1993

Surface Emitting Semiconductor Lasers and Arrays

Gary A. Evans
Southern Methodist University

Jacob M. Hammer

Evans
Hammer

Surface Emitting Semiconductor Lasers and Arrays

ACADEMIC
PRESS

Surface Emitting Semiconductor Lasers and Arrays

edited by
Gary A. Evans
Jacob M. Hammer

QUANTUM ELECTRONICS
Principles and Applications

SURFACE EMITTING SEMICONDUCTOR LASERS AND ARRAYS

Edited by

Gary A. Evans
Southern Methodist University
School of Engineering and Applied Science
Dallas, Texas

Jacob M. Hammer
Photonics Consulting
Seaford, Virginia

ACADEMIC PRESS, INC.
Harcourt Brace & Company, Publishers

Boston San Diego New York
London Sydney Tokyo Toronto

This book is printed on acid-free paper. ♾

ACADEMIC PRESS, INC.
1250 Sixth Avenue, San Diego, CA 92101-4311

United Kingdom edition published by
ACADEMIC PRESS LIMITED
24–28 Oval Road, London NW1 7DX

Library of Congress Cataloging-in-Publication Data
Surface emitting semiconductor lasers and arrays / [edited by] Gary A.
Evans and Jacob M. Hammer.
p. cm. — (Quantum electronics—principles and applications)
Includes bibliographical references and index.
ISBN 0-12-244070-6
1. Semiconductor lasers. I. Evans, Gary A. II. Hammer, J. M.
III. Series.
TA1700.S87 1993
621.36'6—dc20 92-43463
CIP

Printed in the United States of America
93 94 95 96 BB 9 8 7 6 5 4 3 2 1

SURFACE EMITTING SEMICONDUCTOR LASERS AND ARRAYS

QUANTUM ELECTRONICS—PRINCIPLES AND APPLICATIONS

EDITED BY

PAUL F. LIAO

Bell Communications Research, Inc.

Red Bank, New Jersey

PAUL L. KELLEY

Lincoln Laboratory

Massachusetts Institute of Technology

Lexington, Massachusetts

A complete list of titles in this series appears at the end of this volume.

Contents

Preface

Practical demonstrations of diode laser emission from the broad surface area rather than from the cleaved facet of the wafer are relatively recent. This is so despite the fact that the concepts are many years old. The vertical-cavity approach was demonstrated by Melngailis in 1964, and the grating surface-emitting and folded-cavity approach were reported by many authors in the mid to late 1970s. Many, perhaps most, of the concepts discussed in this book were around for many years before they were actively pursued. The advances over the last ten years, mainly in materials, are largely responsible for the capability to implement the ideas presented into working devices. We can look forward to continued progress in materials, processing, and design during the next decade and can expect to see semiconductor laser performance outstripping even our present dreams.

There are now frequent reports on all three principal types of diode laser and diode laser array surface emitters in the literature. Unlike edge-emitting semiconductor lasers, the surface emission approach allows the use of mass production techniques throughout the fabrication process. In addition, the surface-emission approach allows testing of the completed devices at the wafer level, before dicing and packaging. These same capabilities yielded tremendous reductions in cost and enormous increases in the performance and reliability of transistors and other solid state electronic devices. Surface-emitting approaches also allow the integration of single or numerous lasers to form photonic integrated circuits or high power, monolithic, two-dimensional arrays.

Because of the now extensive literature on surface-emitting diode lasers and arrays and the proposed and emerging applications of these exciting and practical new devices in a variety of systems, we feel that this in-depth book

covering the field will be useful to researchers, users, and students interested in the field of lasers, electrooptics, and optical communication. Recent work has been motivated by numerous goals, including low power, integrated sources to replace electrical interconnects with optical interconnects for ultra large-scale integrated circuits; two-dimensional, independently addressable laser arrays for neural networks; steerable output beams for optical computers; high power with large emitting areas for pumping solid-state lasers; and coherent, single frequency, high-power operation with a controlled output beam for space communication and second harmonic generation.

The information in this book is intended to provide the reader with both knowledge about fundamental concepts and the present state of the art of surface-emitting lasers. There are definitive chapters on vertical-cavity, etched-facet-mirror, and grating surface emitters. Additional chapters treat the operation of Bragg grating couplers; edge-emitting diode laser arrays; the theory of phase locking, modes, and beam steering of surface-emitting arrays; external methods of phase locking arrays; coherence and phase control in laser arrays; and thermal considerations in two-dimensional surface-emitting arrays.

We have fortunately been able to enlist some of the leading researchers and developers of surface-emitting diode lasers to contribute to this book. We wish to thank them for many interesting and productive discussions in connection with the preparation of this work. We also wish to thank RCA Laboratories (now the David Sarnoff Research Center), Princeton, New Jersey, for providing both of us with talented collaborators, up-to-date equipment, and a pleasant environment in which most of our work described herein was carried out.

Gary A. Evans
Dallas, Texas

Jacob M. Hammer
Seaford, Virginia

Contributors

Numbers in parentheses indicate the pages on which the authors' contributions begin.

Robert Amantea (351), *David Sarnoff Research Center, CN-5300, Princeton, NJ 08543-5300*

Jerome K. Butler (119), *Southern Methodist University, School of Engineering and Applied Science, Dallas, TX 75275-0335*

Nils W. Carlson (119,351), *David Sarnoff Research Center, CN-5300, Princeton, NJ 08543-5300*

Stephen R. Chinn (9), *Lincoln Laboratory, Massachusetts Institute of Technology, Lexington, MA 02173-9108*

Joseph P. Donnelly (217), *Lincoln Laboratory, Massachusetts Institute of Technology, Lexington, MA 02173-9108*

Gary A. Evans (1, 119), *Southern Methodist University, School of Engineering and Applied Science, Dallas, TX 75275-0335*

William D. Goodhue (217), *Lincoln Laboratory, Massachusetts Institute of Technology, Lexington, MA 02173-9108*

Jacob M. Hammer (1, 119), *Photonics Consulting, 119 Kenneth Drive, Seaford, VA 23696*

Amos A. Hardy (269), *Spectra Diode Laboratories, 80 Rose Orchard Way, San Jose, CA 95134-1356*

Kenichi Iga (71), *Tokyo Institute of Technology, Nagatsuta 4529, Midori-ku, Yokohama 227, Japan*

Fumio Koyama (71), *Tokyo Institute of Technology, Nagatsuta 4529, Midori-ku, Yokohama 227, Japan*

James Leger (379), *Department of Electrical Engineering, 200 Union Street, S.E., University of Minnesota, Minneapolis, MN 55255*

Zong-Long Liau (217), *Lincoln Laboratory, Massachusetts Institute of Technology, Lexington, MA 02173-9108*

Michael Lurie (435), *David Sarnoff Research Center, CN-5300, Princeton, NJ 08543-5300*

Leo J. Missaggia (467), *Lincoln Laboratory, Massachusetts Institute of Technology, Lexington, MA 02173-9108*

William Streifer (269), *Spectra Diode Laboratories, 80 Rose Orchard Way, San Jose, CA 95134-1356*

James N. Walpole (217, 467), *Lincoln Laboratory, Massachusetts Institute of Technology, Lexington, MA 02173-9108*

David F. Welch (269), *Spectra Diode Laboratories, 80 Rose Orchard Way, San Jose, CA 95134-1356*

Richard C. Williamson (217), *Lincoln Laboratory, Massachusetts Institute of Technology, Lexington, MA 02173-9108*

Chapter 1

INTRODUCTION

Gary A. Evans* and **Jacob M. Hammer†**

David Sarnoff Research Center, Princeton, New Jersey

I. BACKGROUND

During the early 1970s, the emphasis in semiconductor laser research was directed at obtaining reliable continuous wave (CW) operation of several milliwatts, a single spatial mode, and reasonable device efficiency, mainly for fiber optics applications. These goals could best be met with semiconductor laser cavities using perfect crystal plane mirrors achieved by simple cleaving techniques, as shown in Fig. 1(a). These partially reflecting cleaved facets, whose reflectivity could be reduced or enhanced with coatings, allowed the laser light to be coupled out of one or both edges of the device.

By the late 1970s and early 1980s, semiconductor laser research was driving towards higher power (tens or hundreds of mWs) with longitudinal mode control and reduced far-field beam divergence. By the mid 1980s, edge-emitting semiconductor lasers had achieved over 100 mW of output in a controlled mode from a single device and electrical to optical efficiencies in the vicinity of 50% were being reported for broad area devices. Edge-emitting arrays, the subject of Chapter 2, had also demonstrated at this time beam divergences as narrow as a few degrees in one dimension. These results were all obtained in AlGaAs lasers emitting in the 0.8 to 0.9 μm region.

* Current address: Southern Methodist University, School of Engineering and Applied Science, Dallas, Texas.

† Current address: Photonics Consulting, Seaford, Virginia.

ISBN 0-12-244070-6

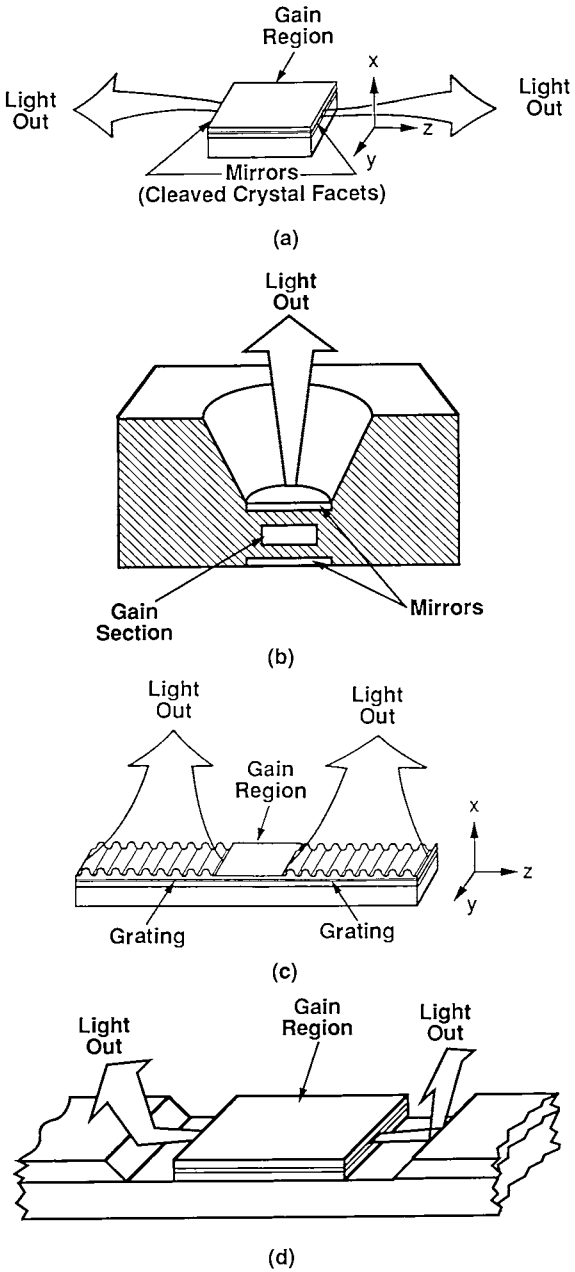

Fig. 1. (a) Conventional semiconductor laser with edge-emission; (b) vertical cavity surface-emitting laser; (c) grating outcoupled surface-emitting laser; and (d) integrated deflector surface-emitting laser.

Development of semiconductor lasers based on InGaAsP, emitting around 1.3 μm and 1.5 μm occurred in parallel. Driven by optical fiber applications, these longer wavelength lasers required dynamic single longitudinal mode operation which is achieved by using a grating to provide distributed feedback (DFB) or distributed Bragg reflection (DBR). Presently, numerous companies are producing both AlGaAs and InGaAsP semiconductor lasers commercially, with the compact audio disc industry alone now requiring a few million AlGaAs lasers per month. Commercial production of InGaAsP devices is estimated at about one-tenth that of the shorter wavelength devices.

II. SURFACE-EMITTING LASERS

In the mid 1980s, the demonstrated performance of diode lasers suggested that they could be used for extensive applications beyond fiber optics, compact optical discs, and optical recording. They could replace flashlamps as solid state laser pumps, provide optical interconnects between integrated circuits or within computers and possibly even replace large gas and solid-state lasers in high power, high coherence applications such as satellite communication and laser machining and welding. These new possibilities caused an increased interest in surface-emitting geometries for semiconductor lasers in an effort to find the best device configuration for a given application or performance level. One expectation was that surface-emitting approaches would allow combining the power of hundreds or thousands of low-power, grain-of-salt sized devices into a monolithic, coherent high power array of semiconductor lasers while maintaining the efficiency and spectral properties of the individual cleaved-facet semiconductor lasers. Results obtained in the last few years and which are described in the chapters of this book are validating the hoped for performance of surface-emitting semiconductor lasers.

In addition to the useful features that make them attractive as replacements for conventional, cleaved-facet semiconductor lasers in some applications, surface-emitting lasers can provide a basis for the use of optics in a number of technologies which cannot easily use cleaved-facet lasers.

A salient feature of the surface-emitters is that they can be grown, fabricated, tested, and used in a monolithic-planar geometry which is similar to the geometry used for electronic integrated circuits. For example, conventional cleaved facet lasers cannot be easily integrated into an optoelectronic-integrated circuit (OEIC) since the act of cleaving separates the laser from

the rest of the chip. This problem can be partially reduced by using etching or micro-cleaving techniques to define the laser facets on the circuit. However, in many integration applications, it is desirable to have the laser connected to an on-chip waveguide, or to have the laser communicate to another chip. Unfortunately, an etched or microcleaved facet is not readily coupled to a monolithic waveguide. In addition, unless the laser is located on the edge of the circuit, the facet emission is difficult to access. Surface-emitting lasers, however, can be located anywhere on an OEIC chip with any orientation, and the light can be easily accessed for external use. Another important feature of all the surface-emitters is that the light is emitted normal (or near-normal) to the surface of the wafer for use in a variety of applications. Of further note, light produced by some types of surface-emitters can, in addition, be simply guided around the wafer and used to optically interconnect coplanar lasers and other optical devices such as switches, modulators and detectors.

Surface-emitting technology also makes the fabrication of monolithic, two-dimensional arrays of semiconductor lasers possible. Phase-locked arrays are obtained by optically interconnecting the lasers on the chip using either on-chip or external means of optical coupling. Such two-dimensional arrays offer the promise of very high powers with narrow beam divergences.

Historically, surface emission dates back almost to the beginning of semiconductor lasers when Melngailis (1965) of MIT's Lincoln Laboratory reported on what has since become known as a vertical cavity structure. The concept (Kogelnick and Shank, 1972) and demonstration (Kogelnick and Shank, 1971) of distributed feedback lasers led to grating-surface-emission in semiconductor lasers largely because of the difficulty of fabricating first-order feedback gratings which required periods of about 0.1 μm at wavelengths around 0.85 μm. Second-, third-, and fourth-order distributed feedback or distributed Bragg reflection gratings were much easier to fabricate but also coupled light out of the surface in lower orders. As a result, initial demonstrations of grating-surface-emission were reported simultaneously by groups from Xerox, (Burnham *et al.*, 1975), the A. F. Ioffe Physico-Technical Institute, (Alferov *et al.*, 1975) and IBM (Zory and Comerford, 1975). A few years later, results were published from Bell Northern, (Springthorpe, 1977) on surface-emitting lasers using 45-degree corner turning mirrors which were etched into the structure. These early demonstrations of surface emission remained relatively dormant until the 1980s, primarily because of fabrication difficulties and more pressing issues related to the performance of conventional semiconductor lasers.

The three basic types of surface-emitting lasers are briefly described in the following sections.

A. Vertical Cavity Surface-emitting Laser

At present there are three basic configurations of surface-emitting lasers. One is the vertical cavity structure, the subject of Chapter 3, in which the feedback mirrors are parallel to the top and bottom surfaces of the semiconductor wafer as shown in Fig. 1(b). The active region can be as thick as several microns, or can be as small as a few tens of angstroms.

The vertical cavity surface-emitting laser (VCSEL) has been extensively and continually developed since 1977 at the Tokyo Institute of Technology. In the last four or five years, many additional researchers from around the world have contributed to the development of vertical cavity lasers. Threshold currents of <1 mA have been reported along with packing densities of about one million lasers/cm^2. Because of their vertical emission, small area, and low threshold, these devices are ideal for optical interconnects with low power consumption. VCSELs have also been considered for generating high power, and two-dimensional arrays have been demonstrated (Orenstein *et al.*, 1991).

B. Grating-outcoupled Surface-emitting Laser

An illustration of a grating-outcoupled surface-emitting (GSE) laser, the subject of Chapter 4, is shown in Fig. 1(c). In these devices, the grating provides in-plane reflection for feedback for laser oscillation and also provides the outcoupling. In coherent arrays of GSE lasers, the grating also allows enough transmission to additional elements to provide optical coupling. The analysis of such gratings is quite complicated, and is discussed in Chapter 6 using coupled mode theory.

In recent years, many research groups have pursued the development of several versions of GSE lasers. Because of a common, uninterrupted waveguide in all sections of a GSE laser wafer, monolithic integration into a coherent 2D array or with other planar optoelectronic devices is straightforward. In addition, a large fraction ($>50\%$) of the two-dimensional surface can be optically emitting. Continuous-wave powers of more than 3 W and peak powers of over 30 W have been reported for GSE arrays. Steering of the surface-emitted beam has been demonstrated by electronic phase adjustment and by wavelength tuning.

C. Integrated Beam Deflector Surface-emitting Lasers

The final type of surface-emitting laser, the topic of Chapter 5, is known as an *integrated beam deflector laser* or *folded cavity laser*, and one version of this device is shown in Fig. 1(d). In a common version of this device,

one or both perpendicular cleaved facets are replaced by an etched perpendicular facet and an etched integrated beam-deflecting mirror. This technology for surface emitters has been developed extensively during the last five years. The use of the mass-transport process, unique to the InGaAsP system, resulted in the first high quality beam-deflecting mirrors and provided device performance equivalent to cleaved edge-emitting lasers (Liau and Walpole, 1985). Although the major thrust in this area has been to fabricate incoherent arrays, a coherent two-dimensional array of etched facet lasers was demonstrated using an external dye laser for the master oscillator (Jansen *et al.*, 1989).

III. HIGH POWER

Coherent, two-dimensional arrays of semiconductor lasers offer the promise of very high power levels with a large area aperture producing a narrow beam divergence with unity aspect ratio. As in one-dimensional edge-emitting arrays, maintaining coherence laterally over a large area is a major challenge in two-dimensional arrays. Coherence, the subject of Chapter 9, is of utmost importance for applications that require power delivered to a point, such as a satellite receiver. For an array with N elements each producing the same output power P, the on-axis power in the far field is $\sim NP$ for an incoherent array, but $\sim N^2P$ for a coherent array. A detailed discussion of the relationship between coherence and "diffraction-limited far fields" from semiconductor lasers is also found in Chapter 9.

Although coherent two-dimensional arrays have been demonstrated to some extent in all three types of surface-emitting arrays, there are many obstacles to maintaining coherent, single frequency operation at very high powers. As the 2D array increases in size, the number of modes increase, and mode discrimination becomes a problem. Because the laser mirrors are no longer formed by near-ideal crystal facets, the quality of the mirrors for all types of surface emitters is critical, requiring careful and sophisticated fabrication techniques to obtain good performance and beam quality. Not only must the compositions and thicknesses of each layer be chosen for high performance, but excellent uniformity and optical flatness need to be maintained over large areas. A network analysis of coherent two-dimensional arrays, along with their limitations and potentials, is the subject of Chapter 7. A coupled mode approach to the same problem is reviewed in Chapter 6.

While an all-monolithic approach to coherent two-dimensional arrays is aesthetically pleasing, external methods of providing or ensuring coherent operation offer a practical alternative and are discussed in Chapter 8.

Another important approach to the realization of high power and high coherence surface-emitting diode lasers has been demonstrated by the use of grating-outcoupled surface-emitting power amplifiers (PA) monolithically integrated with a DBR or DFB master oscillator (MO). This approach, discussed in Chapter 4, has the feature that additional oscillator modes are not introduced with increasing amplifier size. In master oscillator power amplifier (MOPA) devices the output gratings are designed to operate at wavelengths which are not at the Bragg reflection resonance. The emitted beams therefore emerge at an angle to the normal which is chosen to reduce amplifier reflection sufficiently to avoid oscillation of the overall device.

IV. APPLICATIONS

Two-dimensional surface-emitting arrays are expected to find applications in areas where conventional but less efficient high power gas and solid-state lasers are used. Additionally, they are expected to open up new applications which can exploit their unique properties, such as having an outcoupling grating serve as a focusing lens. The power, efficiency and beam properties of individual surface emitters and arrays of surface emitters make them ideally suited for many conventional applications of lasers in data storage, medicine, laser printing, light-activated (remote) switching, solid-state laser pumping, illuminators, rangefinders, proximity fuses, and space and fiber optic communications. The planar nature of surface emitters will allow applications in optical processing, optical computing, neural networks, and in optoelectronic integrated circuit applications where optical interconnects provide a solution to the problem of communicating between integrated circuit (IC) chips. Some applications of surface-emitters, such as optical interconnects, may benefit from a beam-steering capability allowing a full architectural configuration freedom in real time (Hammer and Hendricks, 1989).

V. THE FUTURE

In recent years, the efficiencies and output powers of surface-emitting lasers has increased and the threshold current densities decreased, so that the best reported performance of all three types of surface-emitting lasers is rapidly approaching or has equalled that of conventional edge-emitting lasers. The development of high performance thermal packages, the subject of Chapter 10, for high power surface-emitting lasers is underway at several research

laboratories. Such heat removal capabilities are necessary since, in even the best devices, only about half of the input power is converted to optical power.

In the coming years, we hope we will see coherent 2D surface-emitting laser configurations with circular, submilliradian beam divergences with 50% power conversion efficiency, diffraction-limited beam quality, and with output powers of tens of watts. We also expect to see surface-emitting lasers and arrays with individually addressed elements as part of integrated circuits in computers and neural networks.

REFERENCES

ALFEROV, ZH. I., ANDREYEV, V. M., GUREVICH, S. A., KAZARINOV, R. F., LARIONOV, V. R., MIZEROV, M. N. AND PORTNOY, E. L. (1975). "Semiconductor lasers with the light output through the diffraction grating on the surface of the waveguide layer," *IEEE J. Quantum Electron.*, **QE-11**, 7, 449.

BURNHAM, R. D., SCIFRES, D. R. AND STEIFER, W. (1975). "Single heterostructure distributed-feedback GaAs diode lasers," *IEEE J. Quantum Electron.*, **QE-11**, 7, 439.

HAMMER, J. M. AND HENDRICKS, H. D. (1989). "Optical back plane interconnect technology (OBIT) for computers," (March) paper ThD6, Photonic Switching Conference, Salt Lake City.

JANSEN, M., YANG, J. J., HEFLINGER, L., OU, S. S., SERGANT, M., HUANG, J., WILCOX, J., EATON, L. AND SIMMONS, W. (1989). "Coherent operation of injection-locked monolithic surface-emitting diode laser arrays," *Appl. Phys. Lett.* **54**, 26, 2634.

KOGELNICK, H. AND SHANK, C. V. (1971). "Simulated emission in a periodic structure," *Appl. Phys. Lett.*, **18**, 4, 152.

KOGELNICK, H. AND SHANK, C. V. (1972). "Coupled-wave theory of distributed feedback lasers," *J. Appl. Phys.*, **43**, 2237.

LIAU, Z. L. AND WALPOLE, J. N. (1985). "Surface-emitting GaInAs/InP laser with low threshold current and high efficiency," *Appl. Phys. Lett.*, **46**, 2, 115.

MELNGAILIS, I. (1965). "Longitudinal injection-plasma laser of InSb," *Appl. Phys. Lett.*, **6**, 3, 59.

ORENSTEIN, M., KAPON, E., STOFFEL, N. G., HARBISON, J. P., FLOREZ, L. T. AND WULLERT, J. (1991). "Two-dimensional phase-locked arrays of vertical-cavity semiconductor lasers by mirror reflectivity modulation," *Appl. Phys. Lett.*, **58**, 8, 804.

SPRINGTHORPE, A. J. (1977). "A novel double-heterostructure p-n junction laser," *Appl. Phys. Lett.*, **31**, 8, 524.

ZORY, P. AND COMERFORD, L. D. (1975). "Grating-coupled double-heterostructure AlGaAs diode lasers," *IEEE J. of Quantum Electron.*, **QE-11**, 7, 451.

Chapter 2

REVIEW OF EDGE-EMITTING COHERENT LASER ARRAYS

Stephen R. Chinn*

Electronics Laboratory, General Electric Company, Syracuse, New York

I. INTRODUCTION

Achieving high optical power and brightness have been two of the major goals in the development of semiconductor lasers. A natural means of increasing the power has been to combine many individual lasers into arrays. Before the recent growth in the research of surface-emitting semiconductor laser arrays, described elsewhere in this volume, their edge-emitting precursors provided the basis for a technological foundation and a beginning of theoretical understanding. The primary distinguishing feature of the edge-emitting geometry is the generation and emission of the lasing radiation parallel to the plane of the semiconductor laser's active layer. Some types of surface emitters also generate the stimulated emission in this plane, but emit the radiation in a direction normal to it. The large amount of effort still being devoted to the development of edge-emitting arrays attests to the continued belief in their usefulness for many applications.

This chapter will be devoted to edge-emitting arrays designed for high brightness. In order to achieve this, both high output power and small beam divergence are necessary. The epitaxial layer structure of an edge-emitter determines its optical power density in the plane normal to growth. Many sophisticated forms of epitaxial structures have been developed, including

* Current address: MIT Lincoln Laboratory, Lexington, Massachusetts.

ISBN 0-12-244070-6

those incorporating quantum wells. Constraining laser operation to single-mode, diffraction-limited output in this vertical dimension is relatively easy. Because the epitaxial refractive index variations that cause perpendicular waveguiding are large, the mode behavior is not strongly affected by thermal or carrier effects. Typical dimensions for the mode distribution in the vertical dimension are on the order of a few tenths of microns, which cannot be easily increased without allowing higher-order modes. Even though the vertical beam divergence of typical edge-emitters is large due to the small emitting height, the mode is diffraction-limited and the beam can be readily collimated or focused. A given epitaxial structure will have a lateral power density capability determined by its vertical mode profile and by material damage limits to the semiconductor facet or dielectric coating. In order to keep increasing the total output power, the device must be made wider.

As the emitter width is increased, care must be taken that lateral amplified spontaneous emission does not degrade performance, and that the increasing amount of heat is adequately removed. However, well before these factors play a limiting role, the major problem to be faced in achieving high brightness is to maintain high spatial mode quality over the ever widening emitting aperture. Even if the total output power increases, if the ability to collimate or focus the beam does not improve, the laser may not be useful for many applications.

In the direction along the plane of the active layer, the beam profile can be altered by lateral patterning, growth, or processing variations in this dimension. With larger lateral apertures, the problem of restricting laser operation to a single-mode becomes more difficult. For example, if we wish to construct a single-mode lateral waveguide by means of an effective index variation, the higher mode cut-off condition requires that

$$W\sqrt{n_1^2 - n_2^2} \simeq W\sqrt{2n_1\,\Delta n} \leq \lambda/2, \tag{1}$$

where W is the guide width, n_1 and n_2 are the guide and cladding effective indices of refraction, and λ is the free-space wavelength. For lateral widths beyond a few microns, the limitation on Δn becomes impractically small. Moreover, spatial gain saturation above threshold, as well as thermal and carrier-induced anti-guiding effects and material nonuniformity, make controlled single-mode, diffraction-limited operation from wide-stripe emitters difficult.

A general philosophy for circumventing this problem has been developed, and serves as the basis for this chapter. The method is to force fundamental mode operation in narrow lateral waveguides and combine many of these waveguides in a wider lateral array. In this manner, the mode-control issue

is not eliminated, but transformed into a problem of constraining operation of the multiple emitters in a desired combination of field amplitudes and phases.

In order to achieve this kind of control and obtain high brightness, it is essential that the fields of all the different emitting regions be coherent. A simple example will illustrate this point, and emphasize the difference between arrays that are coherent and those that are not. (In this context, the term "phase-locked" is often used interchangeably with "coherent.") Suppose we have N narrow emitting regions, each of which has a lateral distribution of electric near-field given by $E(x-nD)$, where D is the emitter separation, and n is an integer label for the nth stripe. In the Frauenhofer approximation, the far-field of each element can be found by Fourier transforming the near-field (neglecting an obliquity factor approximately $\cos\theta$). The far-field of each element is denoted by

$$F_n = F(k)\, e^{jknD}, \qquad k = \frac{2\pi}{\lambda}\sin\theta, \tag{2}$$

and θ is the far-field angle. The total far-field intensity is

$$I = \left|\sum F_n\right|^2. \tag{3}$$

If the individual fields have random phases, then

$$I = \sum_n |F_n|^2 = N|F(k)|^2. \tag{4}$$

However, if the individual fields are coherent, or phase-locked, with equal phases,

$$I = |F(k)|^2 \left|\sum_n e^{jknD}\right|^2 = |F(k)|^2 \frac{\sin^2 N\xi}{\sin^2 \xi}, \tag{5}$$

where $\xi = kD/2$. This is the well-known diffraction grating result (Born and Wolf, 1970), and shows that the so-called "in-phase" or "0°" mode has its forward ($\xi = 0$) far-field intensity enhanced by a factor of N over the incoherent result, with a narrower angular full-width, half-maximum

$$\theta_{\text{fwhm}} = \frac{2.78\lambda}{\pi ND}. \tag{6}$$

Equation (5) also indicates that significant diffraction peaks at other than

zero angle may occur if the far-field intensity envelope of the individual emitter is broad, or if the emitters are widely separated. By forcing the individual emitters to be coherent, narrow diffraction angles characteristic of the entire array width can be achieved. However, it is also important to ensure that the proper phase relation exists among the emitters to obtain single-lobe, forward emission.

The most important result to remember is that coherent, in-phase emission can provide brightness comparable to that of a similar-sized broad-area emitter operating in its lowest mode. If the multiple emitters do not maintain coherence, we are merely multiplying the broad intensity distribution of a single narrow element.

In the remainder of this chapter, we will discuss in more detail the means that have been used to obtain diffraction-limited output from edge-emitting coherent arrays. These methods will be grouped according to the similarity of their physical mechanisms into the categories of evanescent, radiative (leaky-mode), diffraction, and intersecting waveguide (Y-branch) coupling. We will concentrate only on edge-emitting arrays that are internally controlled. Other means of mode control, such as use of external optics or resonaters, or injection locking are described elsewhere in this volume, and will be mentioned in this chapter only in elaborating on some fundamental aspects of array operation. Edge-emitting arrays also have great practical importance in applications requiring high power, but not diffraction-limited brightness, such as exciting solid-state lasers. Such incoherent lasers are similar in many respects to their coherent counterparts, but will not be discussed. Earlier useful reviews of phase-locked diode laser arrays are in shorter articles by Streifer *et al.* (1984) and Botez and Ackley (1986).

II. PARALLEL (EVANESCENT) COUPLING

In this section we will describe coherent operation of multi-stripe laser arrays that have colinear, parallel waveguides along the resonator axis, as illustrated in the top view of Fig. 1(a). The interactions among the lasers are caused by the lateral optical fields from the other devices in the array. These fields may be evanescent fields from the bound modes of index-guided lasers, propagating fields from leaky modes, or a quasi-evanescent combination of the two, such as from gain-guided lasers. We shall begin by discussing lasers whose fields interact from an evanescent (or quasi-evanescent) type of overlap. The development of early phased arrays was dominated by gain-guided devices of this type.

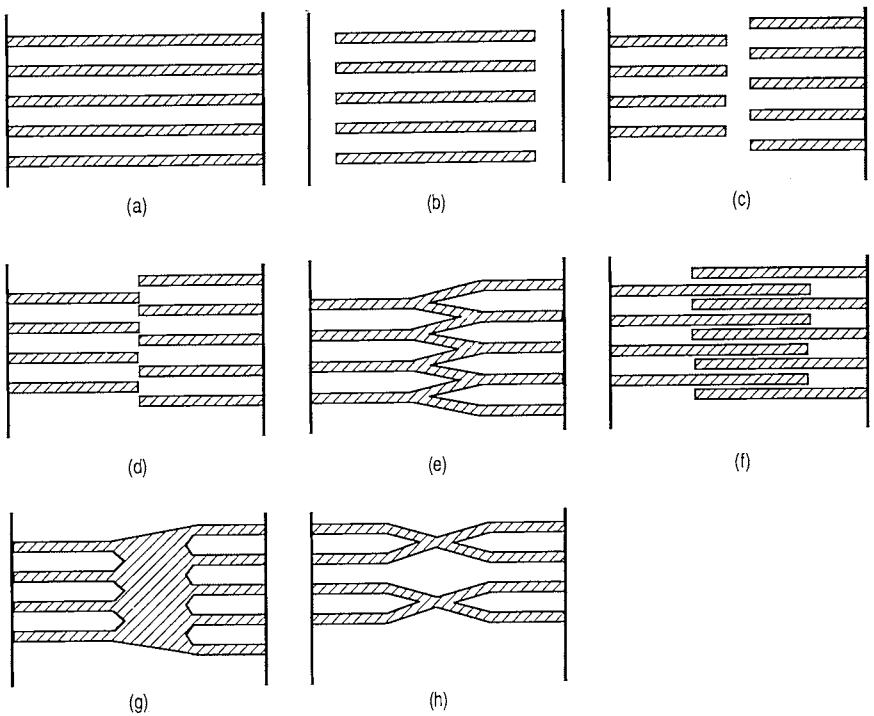

Fig. 1. Schematic (not to scale) top views of some semiconductor laser phased array coupling configurations: (a) Uniform parallel evanescently (or leaky-wave) coupled; (b) Diffraction coupled (Katz *et al.*, 1983c); (c) Talbot-spaced diffraction coupled (Mawst *et al.*, 1989a); (d) Offset-stripe (Welch *et al.*, 1985b); (e) Y-branch (Streifer *et al.*, 1986b); (f) Distributed Y-branch (Chinn, 1988 © IEEE); (g) Wide-waveguide interferometric (Botez *et al.*, 1987); (h) X-junction coupled (Botez *et al.*, 1988d).

A. Experimental Background: Gain-guided Arrays

The first report of internal optical coupling of stripe-geometry diode lasers was by Ripper and Paoli (1970). They showed that two parallel 12 μm-wide gain-guided lasers separated by 12 μm interacted with each other, so as to cause locked oscillation (as measured by their coincident spectra) and some degree of spatial interference. Coherent emission from two coupled sources was demonstrated eight years later by Scifres *et al.* (1978a) with a different configuration. In this example, a single stripe-geometry laser branched

through a curve arc into a second parallel laser, 25 μm apart, having a separate current contact. The far-field radiation pattern from the two parallel separated sources showed multiple deep fringes, characteristic of coherent emission. Since the parallel portions of the two-element array were so widely separated, this example falls into the category of Y-branch coupling described later. We mention it here, however, because it seems to be the precursor of wider parallel arrays by the same workers, some of which have a similar branching scheme.

The first example of what might be called the "modern" phase-locked array was described by Scifres *et al.* (1978b). This was a five-element parallel array of lasers, 3.5 μm wide, on 8 μm centers. The lasers themselves were conventional gain-guided double-heterostructures, with dielectric-masked, Zn-diffused contacts, sharing a common wide metal contact, with schematic cross section shown in Fig. 2(a). The far-field showed a dominant peak $-1{\cdot}4°$ from the facet normal, with a smaller lobe at $+4.3°$. The lobe separation was in excellent agreement with that predicted for diffraction from coherent sources separated by 8 μm (Born and Wolf, 1970),

$$\phi = 57.3°\lambda_0/D, \tag{7}$$

(D = source separation), and the lobe width agreed with the diffraction model for an effective aperture size of 21 μm, half the full aperture of the entire array. The far-field offset was attributed to a $\pi/2$ relative phase shift between elements of unknown origin.

This structure was later enlarged to ten elements (Scifres *et al.*, 1979a, 1979b), with the addition of curved branching elements connecting adjacent stripes, as described previously. An output power of 0.9 W/facet was achieved, with 65% differential quantum efficiency. The far-field had two major lobes at $-2°$ and $+4°$. A series of arrays was made (Scifres *et al.*, 1979b), all with 3 μm stripe widths, but varying separations ranging from 10–27.4 μm. The simplest and cleanest far-field patterns were found for 10 μm separation. From spectral data, multilateral mode operation began to appear at 1.3 times threshold.

A similar 11-element device with 3.5 μm gain guided stripes and the addition of proton implantation between contact stripes to suppress current spreading (but no waveguide branching couplers) was found to emit 200 mW (cw) into one, asymmetric far-field lobe with a divergence of 1.5° (Scifres *et al.*, 1982a). A cross section of this gain-guided structure is shown in Fig. 2(b). The heuristic explanation of the asymmetry simply stated that the associated inter-emitter phase shift minimized the laser threshold, and that

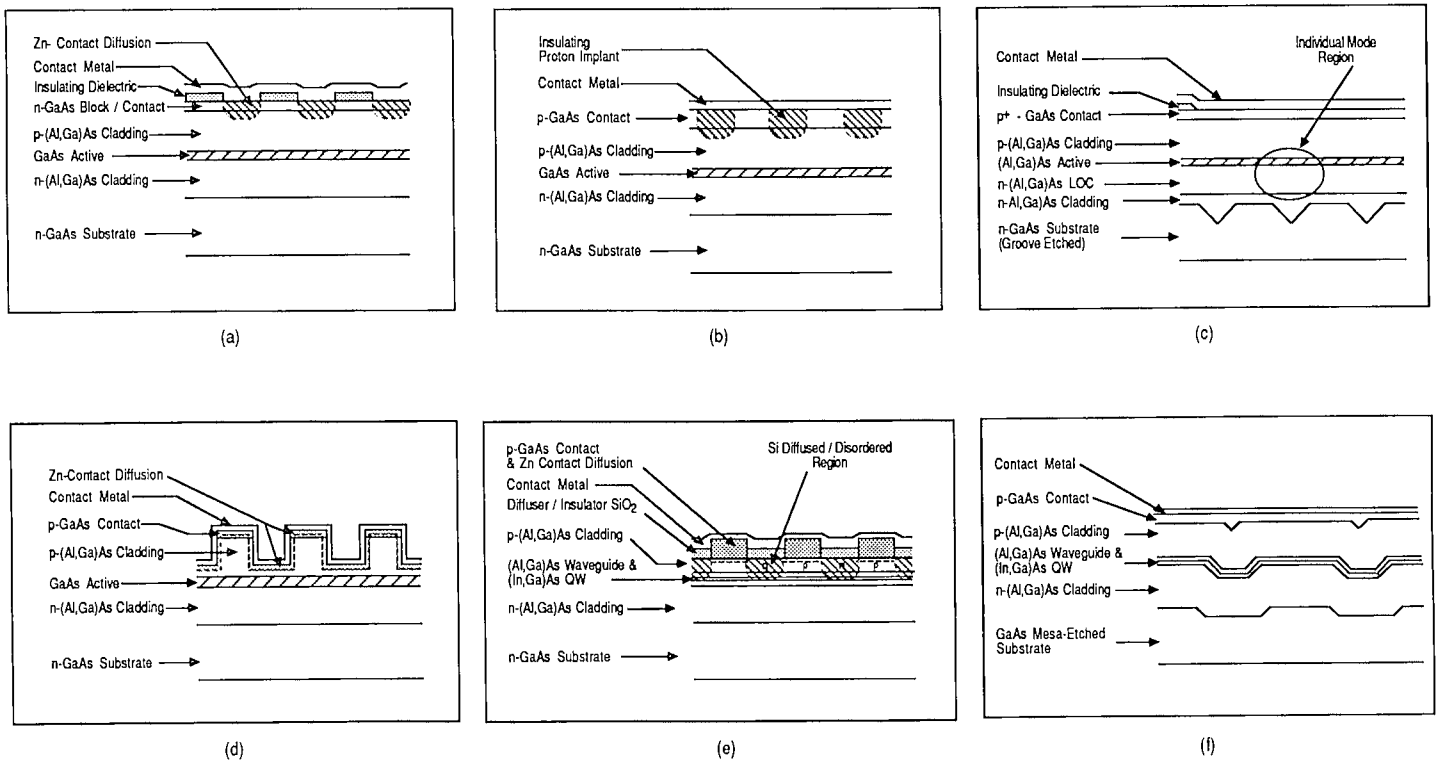

Fig. 2. Schematic (not to scale) cross-section views of some semiconductor laser stripe structures applied to phased arrays: (a) Gain-guided dielectric/blocking defined stripe (Scifres *et al.*, 1978b); (b) Gain-guided proton isolated stripe (Scifres *et al.*, 1982a); (c) Index-guided CSP-LOC (Botez and Connolly, 1983); (d) Index-guided ridge waveguide (Twu *et al.*, 1984); (e) Index-guided disorder-defined stripe (Major *et al.*, 1989); (f) Index-guided non-planar (Baillargeon *et al.*, 1988).

Table I

AlGaAs/GaAs Index-Guided Phased Array Lasers

Structure	Configuration	P/CW	Results	Reference
Strip-buried heterostructure	4–18 element; 5–10 μm width; 15 μm center, LPE	P	1.6 W/facet @ 5 elements; partial spectral locking observed	Tsang *et al.* (1979)
Strip buried heterostructure	2-element; 3–5 μm width; 6–12 μm center; LPE	P, CW	I_{th} = 50–100 mA; partial locking @ 6 μm center	Ohsawa *et al.* (1983)
Lateral grating array	~16 element; 3 μm width, 6 μm center; variable-thickness active layer from substrate grooving; MOCVD	P, CW	I_{th} = 0.325 A(P), 0.35 A(CW); 250 mW/facet (P); multi-lobe, partial locking	Scifres *et al.* (1982d)
CSP-LOC	9 element, 2.8 μm width, 5 μm center, LPE	P, CW	I_{th} = 0.25–0.4 A, 0.15–0.25 DQE, 75 mW(cw) and 400 mW(P) phase locked; generally anti-phase	Botez and Connolly (1983)
Channel guide	10 element, 2 μm width, 4 μm center, MOCVD	CW	I_{th} = 0.2 A, 0.25 DQE/facet, 60 mW(cw) single longitudinal mode; double-lobed far-field	Ackley (1983)
Ridge guide	10 element, 4 μm width, 8 μm center, LPE	P	I_{th} = 0.6–0.75 A, 250 mW, 2–3 times DL	Twu *et al.* (1984)
Ridge guide	5 element, 5 μm width, 8 μm center, LPE, variable contact width	P	I_{th} = 0.25–0.4 A, 110 mW, single-lobe, 2 times DL	Twu *et al.* (1985)
Ridge LOC guide	6–7 element, 3 μm width, 6 μm center, 2-step LPE, $\Delta n \simeq 0.01$	P	I_{th} = 0.16 A, 100 mW, 20% DQE, incomplete locking, multiple array modes, broad lobes	Suemune *et al.* (1984)
Buried ridge	8 element, 4.5 μm width, 9 μm center; 2.5 μm width, 5 μm center; LPE	P	I_{th} = 0.4 A, 1.6° fundamental lobe up to 1.8I_{th}(70 mW)	Mukai *et al.* (1984)
Buried ridge	3–5 element, 5 μm center, LPE/MOCVD, 80%/8% HR/AR	CW	I_{th} = 0.1, 0.15 A; 0.12, 0.15 W (3, 5); fundamental⇒ high-order at high power	Kaneno *et al.* (1985)
Ridge guide	10 element, 6–9 μm center, Schottky barrier confinement, variable-height ridges, LPE	P	I_{th} = 0.22–0.25A, 0.46–0.60 DQE, 300 mW, anti-phase @ 6 μm; Broad lobe (10°) @ 9 μm (uncoupled)	Temkin *et al.* (1985)
CSP (inner stripe)	3 element, 4 μm width, 5 μm center; LPE	CW	I_{th} = 0.1 A, single anti-phase mode up to 50 mW; three supermodes above 50 mW	Matsumoto *et al* (1985)

CSP (inner stripe)	3 element, 2–3 μm wide; 5 μm center; LPE; flat and tapered active layer versions; 90%/7% (HR/AR)	P, CW	$I_{th} \sim 75$ mA, single-lobe to 100 mW (3.6° flat, 5° tapered); 130 mW (CW), 420 mW (P) maximum power	Ohsawa *et al.* (1985)
CSP (inner stripe)	5 element, 5 & 10 μm center, LPE	CW	$I_{th} = 0.1$ A, $T_0 = 110$ C°, 100 mW, junction-down Au–Si solder to Si	Seiwa *et al.* (1987)
CSP (inner stripe)	8 element, 2 μm width, 6 μm center, LPE: 90%/10% (HR/AR)	CW	$I_{th} = 0.25$ A, diffraction-limited anti-phase mode operation to 200 mW	Goldstein *et al.* (1987); Carlson *et al.* (1987)
CSP-LOC	9 element, 5 μm center; LPE.	P, CW	Single-lobe to 80 mW (CW), 200 mW (P).	Carlin *et al.* (1985)
Ridge guide	10-element, 4.5 μm wide, 8 μm center, GRIN-SCH-SQW active layer, MOCVD	P	$I_{th} = 0.1$ A, 0.52 DQE, out-of-phase locked to 1.75 times I_{th} (~50 mW)	Mawst *et al.* (1986)
Buried ridge guide	10/11-element WWI, 4 μm center, GRIN-SCH-DQW active layer, 2-step MOCVD	P	$I_{th} = 325$ mA, 0.35 DQE, 100 mW/facet stable single high-order mode	Mawst *et al.* (1988c)
Buried heterostructure	10 element; 1.5, 2 μm width, 3.5, 4 μm center; MOCVD, two types blocking alloys	P	No phase-locking because of large confinement	Welch *et al.* (1986d)
Impurity-induced disordering	10 element; 2 μm width, 6 μm center; MOCVD; Si-induced disordering of MQW active layer forms low-index cladding	P, CW	$I_{th} = 53$ mA; 0.62 DQE; strong index-guided confinement prevented phase-locking	Thornton *et al.* (1986)
Impurity-induced disordering	10 element; 3 μm widtb, 4 μm center; MOCVD; Si-induced disordering of strained-layer InGaAs SQW-separate confinement active layer forms low-index cladding	P, CW	$I_{th} = 75$ mA; 0.52 DQE; weak index-guided confinement allowed out-of-phase locking over limited current range	Major *et al.* (1989)
Buried optical guide, impurity induced disorder	5-element, MQW active layer, IID MQW optical guide layer, MOCVD or MBE	–	Proposed structure, strong fundamental supermode selection	Zucker *et al.* (1988)
Self-aligned structure, interface layer AlAs (SAS-ILA)	6 element, 5.5 μm wide; 6 μm center; 2-step MOCVD; 4-well MQW active layer.	P, CW	$I_{th} = 125$ mA (P), single out-of-phase mode to 90 mW; slight CW lobe broadening	Sagawa and Kajimura (1989)
Non-planar graded barrier quantum well	Broad-area, ~18 element; 3.6 μm mesa, 3.2 μm groove, 8 μm center; MOCVD	P	$J_{th} = 557$ A/cm^2, double-lobed, 29% DQE	Zmudzinski *et al.* (1989)

the 50% fill-factor of the emitter width leads to a single lobe. With the addition of 15% aluminum to the active layer, the 7700 Å output of this type of device was focused with an astigmatic lens system into a nearly diffraction-limited spot (Scifres *et al.*, 1982b). Beyond powers of 70 mW, the power in the focused spot increased sub-linearly with drive current. This was attributed (Scifres *et al.*, 1983a) to the appearance of a second array mode with different spectral, near-field, and far-field behavior. Paoli *et al.* (1984) resolved multiple modes of a similar array both spectrally and spatially. The two dominant side-lobes of a three-lobe symmetric pattern were identified as grating lobes under the envelope of the gain-guided, single-stripe far-field.

The next advance in this device technology came with the replacement of the double heterostructure (DH) active layer with a multi-quantum-well (MQW) active layer (Scifres *et al.*, 1982c). The same types of asymmetric double-lobed far-field patterns were observed as before but with higher output power capability. Maximum single facet power levels ranged from 240 to 410 mW (cw) for a ten-element array (3 μm stripes on 10 μm centers). When the array size was increased to 40 3.5 μm-wide stripes on 10 μm centers, 1.5 W/facet (cw) was obtained (Scifres *et al.*, 1983b). With the addition of mirror coatings (HR/12%), 2.6W (cw) was emitted from the front facet (Scifres *et al.*, 1983c). In both latter cases, the arrays operated primarily in the out-of-phase mode.

Other means of fabricating gain-guided arrays include use of Schottky barriers (Van der Ziel *et al.*, 1984a) and regrown MOCVD current-confining barrier layers (Welch *et al.*, 1986a). DeFreez *et al.* (1985) have also added a cleaved-coupled-cavity in the longitudinal direction to a 10-stripe proton-implanted array, achieving up to 50 mW in a single longitudinal mode.

B. Experimental Background: Index-guided Arrays

Index-guided arrays are characterized by lateral guiding mechanisms that alter the real part of the index of refraction, instead of the imaginary part (gain/loss). This can be done by means too varied to describe here in detail, including fabrication of rib waveguides, varying layer thicknesses, and post-growth epitaxial material alteration. Schematic cross-sections of some typical index-guiding structures are shown in Figs. 2(c–f). A summary of some results of index-guiding structures applied to phased arrays is given in Tables I (AlGaAs/GaAs) and II (InGaAsP/InP). In general, the evanescent tails of index-guided modes are much smaller than those of gain-guided

Table II

InGaAsP/InP Index-Guided Phased Array Lasers

Structure	Configuration	P/CW	Results	Reference
Ridge guide	2 element, 7 μm wide, 12 μm center; LPE	P	$I_{th} = 0.5$–0.6 A, independent current control of phase locking	Kapon *et al.* (1984g)
Ridge guide	10 element, 3 μm wide, 6 μm center; LPE	P, CW	$I_{th} = 0.3$–0.4 A, 100 mW (CW), 500 mW (P); broad single lobe indicates no phase locking	Dutta *et al.* (1985)
Buried ridge	8 elements, 3 μm wide, 5 μm center; LPE	P	$I_{th} = 0.4$ A, in-phase lobe width 2.7° (1.4 times DL) @ 1.25 I_{th}	Kapon *et al.* (1985, 1986)
Ridge guide	4 element, 3 μm width, non-uniform spacing: 3.5–4.5 μm; LPE	P, CW	$I_{th} = 0.3$–0.35 A, 600 mW/facet (P); phase-locked single-lobe width 6.2°	Dutta *et al.* (1986)
Non-planar	4 μm wide, 8 μm center guides on corrugated GaAs substrate; InGaAs strained quantum well active layer with varying height, 590–1600 μm total array width.	P	$J_{th} = 290$–600 A/cm^2. $\lambda = 1.03$ μm; Double-lobe emission (1.5° width).	Baillargeon *et al.* (1988)

modes. In order to obtain large enough evanescent fields and useful phase-locking interactions among such bound modes, very small differences in the lateral effective indices are required.

C. Coupled-Mode Models

During the early development of semiconductor laser phased arrays, most of the analysis was based on simple diffraction theory from periodic sources with specified phase relationships. It was not until 1984 that models of these arrays were presented as total systems, amenable to a coupled-mode analysis (Butler *et al.*, 1984; Kapon *et al.*, 1984a), yielding the so-called "super-mode" solutions. It is somewhat ironic that most of the experimental impetus for this analysis came from gain-guided arrays, which have proven to be the least accurately described by this methodology. Nonetheless, because this formalism has proven to be an extremely effective and historically important tool for understanding many of the properties of coherent arrays, we shall review its development and results.

Although many of the derivations do not appear the same, in essence they all assume a solution that is a sum of individual wave-guide fields, each of whose coefficients, $A_m(z)$, is allowed to vary slowly with z, the propagation direction (Taylor and Yariv, 1974). When this form is substituted into Maxwell's equations for the entire array structure, and various approximations are made (e.g., neglecting $\partial^2 A_m/\partial z^2$), a set of linear differential equations for the individual guide amplitudes results, in which each amplitude is coupled to all other amplitudes. Each eigenmode coefficient is assumed to have an exponential dependence $A_m(z) = a_m \exp(j\omega t - \gamma z)$, and the eigenvalue $\gamma = \gamma_0 + \delta\gamma$ does not differ appreciably from the unperturbed value, γ_0. Although the general case can always be solved numerically, further analytic simplification results if all guides are assumed identical and equally spaced, and only nearest-neighbor perturbations are considered. It is interesting to note that a similar situation of N identical (but passive) nearest-neighbor-coupled guides was analyzed by Somekh *et al.* in 1973, but they sought only the solution in which one guide was externally excited at $z = 0$. Otsuka (1977) had earlier used coupled-mode equations to examine a special case of evanescently coupled lasers in which only one element had reflective feedback. He later (Otsuka, 1983) presented similar coupled-mode equations for reflection in all elements, but only examined the in-phase and out-of-phase solutions. In a more recent version of the model, the coupled-mode equations become (Wilcox *et al.*, 1987a)

$$\begin{bmatrix} \alpha & \beta & 0 & 0 & 0 & 0 & \cdots & & \cdots \\ \beta & \alpha & \beta & 0 & 0 & 0 & \cdots & 0 & \cdots \\ 0 & \beta & \alpha & \beta & 0 & 0 & & & \\ & & \vdots & & & \ddots & & & \\ & & 0 & & & & \beta & \alpha & \beta \\ & & \vdots & & & & 0 & \beta & \alpha \end{bmatrix} \begin{bmatrix} a_1 \\ a_2 \\ \vdots \\ a_j \\ \vdots \\ a_N \end{bmatrix} = 0 \tag{8}$$

where $\alpha \equiv C_{11} + 2\gamma_0 \delta\gamma B_{11}$, $\beta \equiv C_{12} + 2\gamma_0 \delta\gamma B_{12}$.

The coupling integrals C_{nm} are defined by

$$\begin{aligned} C_{nm} &= k^2 \int \Delta n_m^2(x) E_n(x) E_m(x)\, dx, \\ \Delta n_m^2(x) &= n^2(x) - n_m^2(x - x_m), \end{aligned} \tag{9}$$

and the modal overlaps (with normalized modes) are

$$\begin{aligned} B_{11} &= \int E_1(x) E_1(x)\, dx = 1, \\ B_{12} &= \int E_1(x) E_2(x)\, dx. \end{aligned} \tag{10}$$

This is the same form of equation derived by Butler *et al.* (1984) and Kapon *et al.* (1984a), except it includes the modal overlap factor, B_{12}, neglected by those authors. The eigenvalues of (8) are found when the matrix determinant vanishes. One very simple way of finding the eigenvalues is as follows. Divide all the matrix terms by $-\alpha$, and define $\rho \equiv -\alpha/\beta$, giving a new matrix and determinant with diagonal terms equal to ρ, and off-diagonal terms equal to -1. The determinant of the $N \times N$ matrix, D_N obeys the recursion relation

$$D_N(\rho) = \rho D_{N-1} - D_{N-2}, \tag{11}$$

which is satisfied by the orthogonal Chebyshev polynomial

$$S_N(\rho) = \frac{\sin(N+1)\theta}{\sin\theta} = 0, \qquad \theta = \cos^{-1}\frac{\rho}{2}. \tag{12}$$

The roots of Eq. (12) are given by $\theta_m = m\pi/(N+1)$, so that

$$\rho_m = 2\cos\theta_m = -\frac{C_{11} + 2\gamma_0 \delta\gamma_m}{C_{12} + 2\gamma_0 \delta\gamma_m B_{12}}, \tag{13}$$

$$\begin{aligned} \delta\gamma_m &= -\frac{C_{11} + 2C_{12}\cos\theta_m}{2\gamma_0(1 + 2B_{12}\cos\theta_m)} \\ &= -\frac{(C_{12} - B_{12}C_{11})\cos\theta_m}{\gamma_0(1 + 2B_{12}\cos\theta_m)} - \frac{C_{11}}{2\gamma_0}. \end{aligned} \tag{14}$$

When $B_{12}=0$, the results reduce to the original formulations (Butler *et al.*, 1984; Kapon *et al.*, 1984a), except for the last, constant term in (14) because of a slightly different definition of C_{ij}. From the original definition of γ, the modal gain G is -2 Re γ. G_m has a form similar to (14), but with gain (imaginary index) overlap factors replacing the C_{ij}. It is evident from the form of θ_m and (14) that the difference in mode gain between adjacent modes decreases with the number of stripes. From another point of view, once the near-field distribution has been found, using the sum of the individual near-fields weighted by their amplitude coefficients, the modal gain is the overlap integral of the normalized intensity and local gain/loss distribution. The eigenmodes (waveguide amplitude coefficients) of (8) are

$$a_n^m = \sin n\theta_m, \tag{15}$$

where n labels the nth waveguide, and m labels the mth eigenmode. A picture of the peak-normalized supermode near-field amplitude coefficients is shown at the left in Fig. 3.

In a series of papers, Hardy and Streifer (1985a,b; 1986a,b) have rederived the coupled-mode equations for the general case of nonidentical guides with multineighbor coupling. Although they too find a set of linear coupled equations, the coefficient matrix is considerably more complicated, being neither tridiagonal nor symmetric. Major differences from the simple model can appear, particularly when the guides are closely coupled and nonidentical. This model has recently been applied to the case of twin-stripe, index-guided lasers (Paiss and Hardy, 1989). However, it seems that for the most common situations, the simpler version described above can give an adequate, semiquantitative description of the eigenmodes.

As we saw in the introduction, the far-field of a periodic array of emitters was the product of the individual emitter far-fields and a periodic grating function. When the emitters do not all have the same amplitude, as the previous diffraction model presumed, but have weights given by the supermode amplitudes, the form of the grating function changes. For the mth supermode, the far-field grating function is (Butler *et al.*, 1984)

$$G_m(u) = \left\{ \frac{\sin\left[N(u+\theta_m)/2\right]}{\sin\left[(u+\theta_m)/2\right]} - (-1)^m \frac{\sin\left[N(u-\theta_m)/2\right]}{\sin\left[(u-\theta_m)/2\right]} \right\}^2, \tag{16}$$

where $u = k_0 D \sin\phi$, and ϕ is the angle with respect to the facet normal. Botez (1985) has simplified Eq. (16) to the form

$$G_m(u) = \left\{ \frac{\sin\theta_m \sin\left[(N+1)(u+\theta_m)/2\right]}{\sin^2(u/2) - \sin^2(\theta_m/2)} \right\}^2. \tag{17}$$

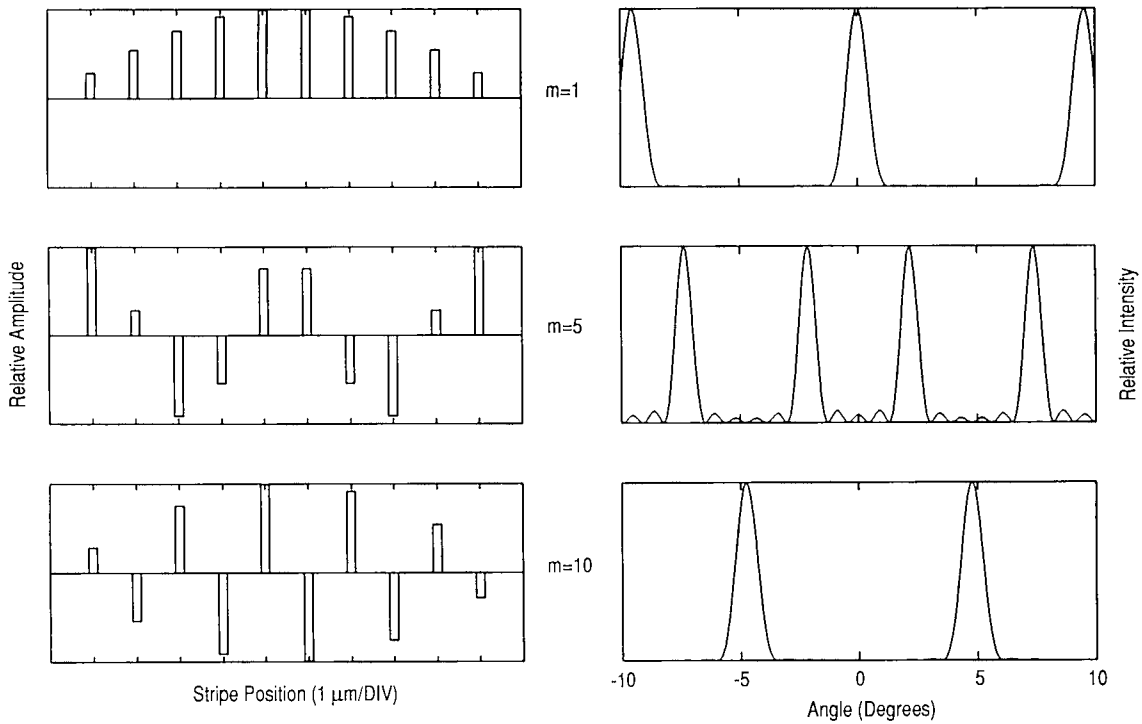

Fig. 3. Near-field amplitude weightings (left) and corresponding far-field grating functions (right) for three super-modes of a 10-element array, calculated from the coupled-mode model (Butler *et al.*, 1984).

This differs from the diffraction model in having slightly larger major lobe widths, and slightly lower side-lobe amplitudes. Considering only the central lobes, the fundamental mode has a major lobe at $\phi = 0°$, and all other modes have a dominant pair of lobes at $\phi \simeq \pm\theta_m / k_0 D$ (rad), the angle increasing with mode order. The peak irradiance of the fundamental supermode is $0.81\,(1+1/N)$ times that for an array of uniform-intensity emitters (Novoseller and Botez 1989). An illustration of some super-mode far-field grating functions is shown at the right in Fig. 3. Similar far-field results were given by Carlson *et al.* (1986). These results were applied by Butler *et al.* (1985) to a channel-substrate-planar (CSP) array of index-guided lasers, with good agreement with experimental data. The role of the gain overlap was found to be critical in determining the closely spaced mode thresholds.

The mode gain of the super-modes depends on the overlap of their near-field functions with the gain/loss distribution in the laser epitaxial layers. As seen from Eq. (15) and Fig. 3, the amplitude coefficients of the $m = 1$ and $m = N$ modes are identical, except for sign. This means that the major differences in the optical intensity overlap with the gain/loss profile will arise from the additive or subtractive differences in the near field functions between the guides. Since the $m = N$ out-of-phase mode has near-field nulls between the waveguides, if there is optical loss in those regions, the modal gain will be higher than for the $m = 0$ mode, which has non-zero intensity between the guides. Streifer *et al.* (1985a,b) have presented a set of design criteria based on uniform step-like distributions of index and gain in the coupled-mode model. In order for the in-phase mode to have the highest gain, they found that the active layer gain had to be larger between the guides than in them, and illustrated a large-optical-cavity (LOC) array designed to provide this. Under conditions that the emitters are in phase, Botez (1988) has found analytic Gaussian approximations for the single-element near-fields to obtain parametric relations for the array parameters required to give 80% of the power in the main lobe.

D. Separate-Contact Arrays

In an effort to understand the coupling mechanism between laser waveguides the use of separate electrical contacts has been a valuable tool. Kapon *et al.* (1983) fabricated an eight-element array of gain-guided lasers, 5 μm wide on 9 μm centers, delineated by proton bombardment. By using two-level metallization, separate contacts were made to each gain-guided stripe. Selecting two nonadjacent lasers and varying the current(s) of the element(s) between them, they demonstrated that the coupling and mutual coherence could be controlled by the intermediate stripe(s) gain. In subsequent work,

Katz *et al.* (1983a,b) operated three and four adjacent elements, and by adjusting the individual laser currents, controlled the array mode, which was monitored by the far-field pattern. Kapon *et al.* (1984b,c) measured the spectrally resolved near-fields of such devices, and showed that for certain ranges of inner stripe currents, the longitudinal mode spectra of the lasers became locked.

The detailed nature of the near-fields measured by Kapon *et al.* (1984c) indicated complicated behavior, not immediately apparent from the supermode amplitude coefficients. For example, secondary mode peaks between the excited contacts appeared, and varied in position with current levels. This can be explained from the non-planar nature of the individual gain-guided laser wavefronts. Gain-guided modes have curved phasé fronts, whose slope varies with the gain/loss profile of the device. When two such adjacent modes combine, the oppositely tilted phase fronts cause a complicated interference pattern to appear, with larger numbers of maxima and minima than stripes (Kapon *et al.*, 1984c,d). The tendency for the individual stripe far-field envelope to have a "rabbit-ear" pattern was also calculated to give a broader modulation envelope to the supermode grating function. They measured different near-field patterns at different frequencies, but for specific current combinations, single longitudinal mode operation could be obtained, with an intensity pattern that depended on the current distribution. The complex coupling coefficient of such gain-guided lasers was calculated by Katz *et al.* (1984a).

Katz *et al.* (1984b) used a simple, steady-state rate-equation analysis for carrier and photon densities above threshold in a multi-element structure. They showed that in order to excite a pure supermode, the individual stripe currents should be selected such that the corresponding photon densities (found from a variational principle that maximizes the total photon density) correspond to the supermode amplitudes. This implies that once a given supermode reaches threshold and begins oscillating, to keep gain saturation from allowing other modes to reach threshold, the currents should be adjusted to compensate for the non-uniform saturation.

E. Nonuniform Single-Contact Arrays

1. Gain-guided

Multiple-contact arrays may be useful for diagnostic purposes, but the most practical devices are likely to have only one electrical contact. Most of the recent effort in monolithic array development has been devoted to finding configurations that can provide greater mode discrimination than the prototypical uniform, evanescently coupled array. One approach to improving

the mode discrimination to favor the lowest-order, in-phase mode has been to reduce the array symmetry. Kapon *et al.* (1984e) have analyzed arrays in which the lateral envelope of the effective index profile has either a linear chirp or an inverted "V" profile, achieved by varying the waveguide widths across the array. The supermode envelopes can be approximated by waveguide solutions corresponding to the effective index envelope. For the linear or "V" chirp, the calculated fundamental mode changed shape and/or location so that its mode gain exceeded that of all the other supermodes. The price that is paid, however, for such discrimination is a narrowing of the fundamental mode near-field distribution, with the resulting disadvantages of greater tendency for spatial gain saturation and lower optical damage threshold. To test these ideas, a six-element, single-contact gain-guided array was fabricated (Lindsey *et al.*, 1984), having stripe widths increasing across the array from 3 to 8 μm (with constant 5 μm separation). At 1.6 × threshold, the predominantly fundamental-mode near- and far-fields were in good agreement with the model, including the off-axis far-field tilt resulting from the near-field phase-front curvature. By decreasing the depth of the proton-implantation between stripes, closer resemblance to a variable-gain broad-area laser was obtained (Lindsey *et al.*, 1985). In subsequent work, Lindsey *et al.* (1987) showed that similar results could be obtained in broad-area lasers having quasi-continuous half-tone grading of the gain across the stripe, thus blurring the distinction between gain-guided arrays and broad-area lasers. This point will be discussed further in a later section. The modes of such tailored-gain arrays or broad stripes are all tilted and single-lobed, with different angles. Welch *et al.* (1985a) have also fabricated chirped-width gain-guided arrays, with the center longitudinal section of stripes offset from the end sections to provide additional mode discrimination. They found single-lobed far-fields, 4° off-normal, with 0.8° (0.7°) beam width at 420 (350) mW in pulsed (cw) operation, and subsequently (Welch *et al.*, 1985b) achieved 575 mW in a single-lobed far-field.

To remove the far-field tilt, an inverted "V" profile to the guide widths was implemented (Kapon *et al.*, 1984f). The center stripe width of the seven element array was 7 μm, decreasing to 4 μm at the edges, with 2 μm separations. The beam full width (half power) increased from 3° at 1.1 × threshold to 4° at 1.5 × threshold. Although not diffraction limited, the far-field was predominantly single-lobed at 0° emission angle.

A longitudinal non-uniformity in the form of internal stripe offset (as well as laterally chirped stripe width) was used by Welch *et al.* (1985b) to equalize the highest and lowest-order supermode gains. They achieved 575 mW in a single-lobed far-field.

2. *Index-guided*

Ackley (1984); Ackley *et al.* (1986) attempted to achieve mode discrimination using differences in stripe separation (as opposed to stripe width) in an index-guided array, but found device operation distributed between in-phase and out-of-phase modes, because of the small difference in mode gains. An interesting special case occurs when the stripe separation is uniform in the interior of the array, but varies at the outer stripes so as to reduce the coupling coefficient by $1/\sqrt{2}$. Analytic solutions to those coupled-mode equations give results somewhat similar to the totally uniform coupling case, but with the important difference that the $m=1$ and $m=N$ modal coefficients have uniform amplitudes at the interior and are reduced by $1/\sqrt{2}$ at the edges (Streifer *et al.*, 1986a). This difference from the previous sinusoidal envelope could cause significant improvement in gain saturation behavior. Unfortunately, the same problem of having similar in-phase and out-of-phase intensity profiles (and therefore, similar modal gains) still occurs.

In another special case, the outer guide propagation coefficients are designed to be $\beta=\beta_0+\kappa$, where β_0 is the interior guide propagation factor. Then, all the fundamental mode amplitude factors are unity (Buus, 1987). However, for mode $m=(N/2)+1$, the absolute values of the amplitude factors are the same as well, leading to small gain discrimination between those modes and similar gain saturation behavior.

In a more general case, Kapon (1987a) calculated the super-modes of index-guided arrays with up to nine elements having variable spacing between them. When the variation of the coupling coefficients caused by the variable spacing is small enough to be handled by perturbation analysis, he found that the mode patterns between supermodes m and $N+1-m$ were almost identical, thereby giving them similar mode gains. When both stripe and separation were varied (Kapon, 1987b), approximately 5% modal gain difference was found between the $m=1$ and closest-gain $m=2,8$ supermodes in a nine-element array. The complexity of introducing both a variable effective index and coupling coefficient precludes an analytic coupled-mode solution, and requires numerical solution of the effective-index Maxwell's equations.

F. Noncoupled Mode Analyses

1. *Linear Models*

For all its usefulness in obtaining good physical insight in array mode behavior with relatively little effort in calculation, the coupled-mode method

has its limitations. When the array is composed of closely spaced or non-uniform guides, or when the complex effective index profile cannot be treated as a perturbation, a more direct and accurate solution of Maxwell's equations may be necessary. As the study of semiconductor laser phased arrays has progressed, these models have become more inclusive and complicated. We shall briefly review their development here.

The simplest subgroup of these models has involved the linear solution of Maxwell's equations below the lasing threshold, using the effective index approximation with a specified index distribution. Prior to the application of the coupled-mode formalism, Chinn and Spiers (1984) had solved such equations using a simple Kronig–Penney type of profile, for pure index or gain-guiding in an infinite (periodic) array. The most significant results of that work were (1) gain is required between the high-index stripes to favor the in-phase mode, and (2) the gain-guided mode discrimination is a sensitive function of the stripe separation, due to the complex nature of the gain-guided near-field, which can also have secondary maxima between the stripes.

A more inclusive model for finite size arrays was developed by Agrawal (1985). Using the effective index approximation to remove the perpendicular spatial dependence, smooth periodic functions were chosen to simulate the effects of a built-in index profile, and diffusion-smoothed carrier profile. The latter property affects the active layer complex index through the optical gain and carrier anti-guiding term. Because of the complicated spatial dependence of the resulting lateral effective index, the waveguide modes were solved using a numerical beam-propagation method. For gain-guided arrays (with no built-in index variation), the carrier anti-guiding effect was found to cause a three-lobed far-field pattern. Agrawal's interpretation relates to the waveguiding competition between the gain under the stripes, and the higher index between the stripes. From another point of view, such a pattern could be regarded as the fundamental mode, with grating envelope greatly altered by the individual stripes' curved phase fronts. Near-field intensity maxima were also predicted to occur between the stripes. For index-guided arrays with uniform gain distributions, modes with predominantly single-lobed far-fields are favored. If the gain is periodic, however, as in a gain-guided array with weak index-guiding, then the out-of-phase double-lobed mode has the lowest threshold.

A very significant point about the number of allowed array supermodes was pointed out by Fujii *et al.* (1985). Treating the case of an index-guided array with uniform pumping, they solved Maxwell's equation using a

transverse propagation matrix technique. In their examples of five and seven stripes, they found additional out-of-phase bound modal solutions with nulls in the high-index regions. These so-called $180°-1$ modes actually correspond to bound modes of the entire broad array, modified by the lateral index and gain functions of the individual stripes. This represents a fundamental, qualitative distinction between a full modal analysis and the coupled-mode approximation, which is constrained to give only N modes for an N-stripe array. Similar results for the number of bound modal solutions exceeding N were found by Marshall and Katz (1986), Buus (1986), Hadley (1986), and Hadley *et al.* (1986a; 1987a,b).

Along with improvements in the electromagnetic field analyses, the self-consistent inclusion of current and carrier spreading has been incorporated in many of the linear array modes. This is an important issue because of the carriers' effect on both the real and imaginary part of the active-layer index of refraction. An early example for a two-stripe array was that of Kumar *et al.* (1985), who used Joyce's (1980; 1982a,b) sheet-current formalism to find the lateral carrier distribution in the active layer. A conformal mapping technique for the lateral current distribution in multiple stripe arrays was developed by Amman and Kappeler (1986). Using numerical methods, Papannareddy *et al.* (1987) found the current-spreading and carrier diffusion in arrays with multiple stripe zinc-diffused contacts. None of these latter three references solved for the corresponding modal solutions.

Twu *et al.* (1986) also included carrier diffusion in their model, but found only five modal solutions for five-element arrays. These results were extended by Kumar (1987), who used a two-dimensional finite-difference solution of Laplace's equation to solve the current-spreading problem (rather than a semi-analytic one-dimensional sheet spreading model). Both these works showed that for typical examples, with small built-in index variation, the lateral gain profile was broad, with a small, periodic modulation. Hadley *et al.* (1987b) included carrier diffusion and pointed out the importance of modeling junction heating as well, which can reverse the effects of carrier-induced anti-guiding on the real part of the refractive index.

Examination of only the near-field patterns of an array may lead to some ambiguity in interpreting results, since both the coupled-mode analysis for arrays with single-stripe phase curvature and the high-order ($>N$) "exact" analysis predict more intensity peaks than the number of elements. Verdiell *et al.* (1989a,b) have studied 10-element gain-guided arrays and concluded from the near- and far-field and spectral data that all of the modes were of the "excess" type, with the number of near-field intensity peaks ranging

from 10 to 17. Their data agreed with a model of the gain-guided array as a broad-area device, perturbed by the periodic gain distribution of the stripe contacts and a quasi-Gaussian lateral temperature profile.

2. *External Mode Selection*

Support for this picture of gain-guided arrays comes from two other types of experiments involving external cavities and injection locking. Although both of these techniques are outside the scope of this review and are treated elsewhere in this volume in more detail, we will briefly discuss their application to the understanding of array behavior. A series of papers by Epler *et al.* (1984; 1985a,b) describes their use of a diffraction-grating external cavity to spectrally force various spatial modes of the array to oscillate. Although their initial interpretation of the data claimed qualitative agreement with the coupled-mode model (Epler *et al.*, 1984), the most recent work (Epler *et al.*, 1985b) presented more detailed evidence in favor of the broad-area interpretation. This was primarily based on the uniformity of the near-field emission under nonlasing conditions (without feedback), the large number of near-field intensity peaks, and an analysis of the wavelength shift versus far-field lobe separation. A uniform broad-area laser would obey the relation

$$\frac{1}{\lambda_x^2}+\frac{n^2}{\lambda_L^2}=\frac{n^2}{\lambda^2}, \tag{18}$$

where $\lambda_x=2\pi/\beta_x$ is the transverse wavelength, λ_L is the free-space wavelength of the longitudinal Fabry–Perot cavity mode having the lowest order (fundamental) lateral mode, n is the modal index of refraction, and λ is the grating-tuned lasing wavelength. This relation gives

$$\Delta\lambda \equiv \lambda_L-\lambda \simeq \frac{\lambda_L^3}{2_n^2\lambda_x^2}. \tag{19}$$

The resulting far-field lobe separation is $\Delta\theta \simeq 1/\lambda_x^2$, which is in excellent agreement with the data and confirms the broad-area interpretation. A more detailed numerical analysis of the lobe angles (Hadley *et al.*, 1986b) also substantiates this interpretation. Andrews *et al.* (1985) performed similar measurements using an external cavity with a mirror to perform mode selection, followed by spectral resolution. However, the mirror tilts made interpretation of the results more difficult.

An alternative to selecting the array mode by external cavity feedback is the use of injection locking. Using a diode-laser master oscillator and a 10-element gain-guided slave array. Goldberg *et al.* (1985) were the first to observe narrow, single-lobe off-axis emission from the injection-locked array. Hohimer *et al.* (1985, 1986) then found similar results by injecting a

low-power dye laser signal, and observed that the narrow, off-axis lobe angle tuned with frequency, and that its angular width at first decreased with emission angle and then remained constant. A numerical simulation of these results was obtained by Hadley *et al.* (1986b), with a simple physical model based on broad-area laser behavior. As an end stripe is injected near its isolated resonant frequency, the array emits into a relatively broad, small-angle lobe. When the master oscillator frequency is increased, the Fabry–Perot resonance condition forces the slave oscillation to become more off-axis, coupling to more elements, and increasing its angle. The single lobe results from the asymmetric injection condition, as compared to the double-lobed patterns obtained with symmetric grating feedback (Epler *et al.*, 1985a,b). When all the elements are coupled, the beam width no longer decreases, but its angle still increases with detuning. This argument, when applied to a given longitudinal resonance, gives (Hadley *et al.*, 1986b)

$$d\theta = -\frac{n^2}{\lambda\theta}\, d\lambda. \tag{20}$$

Note that the incremental change in θ^2 is proportional to the incremental change in λ, as found in the external grating studies by Epler *et al.* (1985).

Hohimer *et al.* (1989a,b) succeeded in monolithically integrating a single-stripe laser diode master oscillator with a 10-stripe gain-guided GRIN-SCH-SQW array. The master oscillator was located to the side of the slave array, and its axis was tilted 1.4°. They obtained up to 125 mW in a single-lobed, near-diffraction-limited beam, with angular steering over a 0.5° range. A significant point is that optical coupling and feedback effects between master and slave presented no problems, even without the use of optical isolation.

All of this evidence reinforces the argument that gain-guided arrays are most easily described in a quasi-analytic manner in terms of their broad-area equivalents, with the addition of an appropriate perturbation from the separate nature of the array contacts. If an accurate numerical model for the array is used, similar results should be obtained, but coupled-mode models are probably inadequate.

3. *Nonlinear (Saturated) Models*

The models previously described have been concerned primarily with analyzing unsaturated modal fields and gains of various array structures. Although they were developed to understand various aspects of measured array behavior, they were capable of finding only the sub-threshold array

properties because the effects of stimulated emission were not included. Even if a linear analysis showed that the fundamental mode of an array were the first to reach threshold, its subsequent saturation of the gain would alter the array's properties, affect all the array modes, and possibly allow higher-order modes to lase. We will now briefly review progress in modeling array behavior above threshold, in the presence of gain saturation.

As mentioned earlier, Katz *et al.* (1984b) performed a steady-state incoherent rate equation analysis to determine a self-consistent supermode condition for local excitation currents and photon densities. Other early analysis was done by Shore (1984) for a two-channel CSP laser, with contact stripes above and between the channel waveguides. The optical power affected the mode behavior through its effects in the diffusion equation for the carrier concentration

$$D\frac{d^2n}{dx^2} = -\frac{J(x)}{ed} + Bn^2 + g(x)P(x), \tag{21}$$

where D is the diffusion coefficient; n, the excess carrier density; J, the injected current density; e, the electron charge; d, the active layer thickness; B, the bimolecular recombination coefficient; g, the gain; and P, the lasing field intensity. The carrier density determines the gain and also alters the real part of the active layer refractive index. Equation (21) is an example of the optical saturating mechanism found in many of the other models. The stimulated recombination term, $g(x)P(x)$, is the key to the non-linear interaction among the optical field, carrier density, and complex index of refraction. Even with a symmetric structure, Shore (1984) found that the carrier concentration and laser mode were asymmetric above threshold, with the latter gradually becoming symmetrically placed between the channels at higher power levels.

Katz and Marshall (1985) examined the general case of an N-element array, using the coupled-mode method with an iterative, self-consistent treatment of the modification of the waveguide parameters by the optical fields. For the baseline example of a three-element array, they found that the power dependence of the ratio of center-to-edge near-field intensities was a very sensitive function of stripe number, anti-guiding factor, and complex coupling angle. A larger, 10-element example was analyzed by Chen and Wang (1985a), also using the coupled-mode method, iterated with the saturating effects of the photon density in each stripe (diffusion and current-spreading were not included). In their example, even though the fundamental, in-phase supermode reached threshold first, at a current only 1% above threshold, three additional modes were also excited.

Also in an iterative fashion, but using an "exact" field analysis (i.e., no coupled-mode approximation), Whiteaway *et al.* (1985) showed that even in chirped, real-index-guided arrays, the combination of carrier-induced index perturbation and spatial hole-burning leads to limitations in obtaining high-power fundamental supermode operation above threshold. However, at least one of their design alternatives (Whiteaway, 1986) gave improved fundamental mode selectivity by narrowing the individual waveguide width, so the array could no longer support a mode corresponding to the out-of-phase supermode. This is another aspect of the broad-stripe nature of array behavior. Conversely, a design that favored the out-of-phase supermode was studied for a 10-element index-guided array, with uniform current injection into the central six elements (Thompson and Whiteaway, 1987). A single-mode operating range up to 625 mW/facet was found.

In an extension of their linear analysis, using finite difference carrier and modal calculations, Twu *et al.* (1987) also found a limited range of single fundamental supermode operation. Comparing different types of five-element arrays, they found the largest range of fundamental mode operation to occur with a broad-contact, index-guided array. This example had a single-mode range 14% above threshold, with 20 mW output power. Worse performance was found for similar stripe-contact index-guided and gain-guided arrays.

A somewhat simpler, but more approximate, numerical method has yielded similar results, and indicates the importance of factors affecting spatial hole-burning (Chinn, 1986). Using the effective index approximation for a ridge-guide structure, the array was subdivided into lateral uniform regions corresponding to the waveguide and interguide cladding. In the interguide regions, a different resistivity material was allowed to fill the valleys between the etched mesas, thus allowing parametric variation of the active layer gain uniformity using a broad-area contact. Joyce's (1980; 1982a,b) method was used to find the current-spreading and carrier diffusion, and the "exact" modal solutions were found using a two-dimensional transfer matrix technique for the multistripe structure. Above threshold, averaged stimulated emission in each region was added to the carrier recombination terms, and the solution iterated for consistency. This analysis indicated that use of p-type substrates and n type layers under the contacts, as suggested by Joyce, could enhance the lateral carrier transport in the active layer, and reduce the effects of spatial hole-burning. The model indicated nearly an order of magnitude improvement in the range of fundamental mode operation above threshold, using high-conductivity n-type layers under the contacts. Results for an optimized, outer-width-apodized

five-stripe array are shown in Fig. 4. Note the narrowing of the fundamental mode at the high power level.

Similar use of stripe width variation to improve array operation was described by Buus (1988). If the desired supermode intensity can be made uniform by such apodization, then its spatial gain saturation should not affect (or increase) the gains of the initially sub-threshold modes. Buus has given perturbation analysis of such spatial hole-burning and some semiquantitative description of its effects. Another self-consistent modal analysis of laser arrays, which uses a transverse resonance technique for finding the modes, has been described by Carroll *et al.* (1987). A somewhat simpler model for current-spreading was used, and no above-threshold results for multistripe arrays were given. Hadley *et al.* (1988) have given a description of their most recent comprehensive numeric model for diode arrays and broad-area devices. It includes the effects of lateral built-in index variation, current-spreading, carrier diffusion, stimulated emission, and thermal gradients. Most of the results presented pertain to broad-area devices.

A rather different philosophy for studying nonlinear effects in arrays has been followed by Chow (1986a,b). He uses the individual stripe fields in a manner similar to that of the coupled-mode formalism, but the nonlinear equations are derived from the coherent, density-matrix rate equations for the slowly varying supermode field amplitude and phase. Imposing the resonator end boundary conditions causes a constraint on the frequencies of the final eigenmodes. Solutions are found from third-order perturbation theory, and only the example of a two-element array is given. An interesting difference between this and previous analyses is evident for the case of two nonidentical guides. In certain regimes, for a given excitation, the array may be either multimode, fundamental mode, or bistable, depending on stripe separation and asymmetry. Hadley (1985) has also solved the two-element asymmetric array using intensity-saturated gain coefficients, Fabry–Perot boundary conditions, and coupled-mode equations for forward and backward propagating fields. Although this approach is different in concept from Chow's the numerical result for an asymmetric gain profile also shows a type of frequency locking for two different array modes below a critical coupling strength.

4. *Passive Phase Compensation*

In many cases described above, the anti-phase mode of an array has a lower threshold and is more stable above threshold. If the array can operate stably

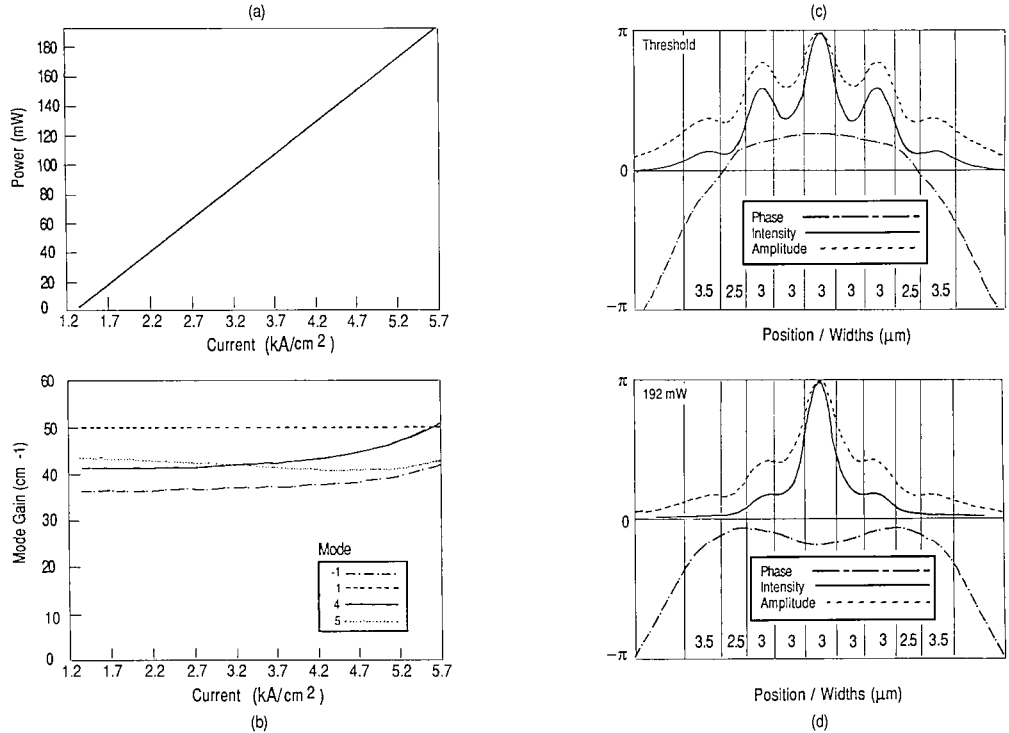

Fig. 4. An example of gain saturation effects in an index-guided array on a p-type substrate: (a) Fundamental mode output power versus current density. (b) Saturated array mode gains versus current density. The fourth-order mode reaches threshold at the maximum current shown. (c) Near-field amplitude, phase, and intensity for the fundamental mode at threshold. (d) Near-field amplitude, phase, and intensity for the fundamental mode at the onset of the next higher-order mode.

in this single high-order mode, then subsequent adjustment of the individual emitter phases (180° shifts on alternating emitters) can convert the double-lobed output into an on-axis, predominantly single-lobed beam. The same idea can apply to any single, high-order mode, with appropriate tailoring of the phase shifts. Ackley *et al.* (1983) proposed such phase adjustment, either by integrated phase shifters within the laser cavity, or by patterned, external thin-films on the laser output facet. The former case is more complicated than they indicate, since the internal nature of the adjacent-stripe phase shift requires an eigenmode analysis of the supermodes. The latter case, using external, alternating $\lambda/2$ coatings is straightforward, though possibly difficult to implement. Heidel *et al.* (1986) demonstrated the concept, although by use of a transferred, magnified near-field image with an external phase plate. A near-field phase plate, mounted adjacent to the diode facet was demonstrated by Thaniyavarn and Dougherty (1987). They used 10 μm silicon nitride strips on 20 μm centers, deposited on a microscope cover slide. Tapering of the dielectric thickness in a direction along the strip axes allowed for variable phase compensation by translation of the phase plate. Most of the double-lobed output of a 10-element, gain-guided array was converted into a single-lobe, with residual sidelobes being explained by multimode laser oscillation, nonideal phase plate separation from the laser, and reflective feedback from the phase plate. Similar results were described by Taneya *et al.* (1987) for a three-element, index-guided array. They obtained 50–70% of the 200 mW output in the central lobe, after phase-shifting the high-order near-field emission. Finally, an integrated version of the phase-plate concept was implemented by Matsumoto *et al.* (1987), who deposited patterned, variable-thickness Al_2O_3 films directly on the laser facet. With a three-element array, they obtained diffraction-limited output in a single lobe up to 1.2 × threshold (5 mW output power). Above that point, higher-order modes of the array lowered the beam quality.

III. LEAKY-MODE COUPLING

Since single-stripe diffraction-limited laser operation benefits from having a waveguide that supports a single bound mode, it is natural that much of the early parallel-stripe array development was based on that concept. As we have discussed earlier, the interaction between such stripes (in the weak coupling limit) can be described in terms of the field overlap from the evanescent tails of the bound modes. However, a different and stronger

optical interaction between stripes can occur if the stripe modes are not bound but leaky (Marcuse, 1974; Engelmann and Kerps, 1980). In a physical description of this type of mode, rays propagating in the waveguide core at a shallow angle are reflected at the cladding interface because of the dielectric discontinuity. However, the cladding has a higher index of refraction than the core, so that the reflection is not total (as for bound modes), and some of the incident core power refracts and radiates into the cladding. The resonant nature of the "mode" is determined from the round-trip phase condition for the reflected core rays. The self-consistent mode constraint requires that $\Delta\phi = 2m\pi$, which for the lowest mode in most practical leaky guides gives an internal, lateral propagation coefficient $h = \pi/d$ (d = core width), and an equivalent lateral wavelength

$$\lambda_0 = \frac{\lambda}{\sqrt{n_0^2 - n_{\text{eff}}^2}}, \tag{22}$$

where n_0 is the local effective index of the anti-guide core, and n_{eff} is the total mode effective index defined by $\beta/k, k = 2\pi/\lambda$, λ = free-space wavelength.

One of the first applications of this concept to multiple stripe lasers was by Ackley and Engelmann (1980). In a twin-stripe configuration, they fabricated buried-heterostructure (BH) AlGaAs lasers with 2 μm widths, separated by 22 μm. The burying layer (lateral waveguide cladding layer) was chosen to have an alloy composition giving it an effective index 0.05 larger than that of the BH stripes. The resulting far-field had two widely separated lobes, modulated by a more densely spaced lobe pattern. The coarse separation was due to the angle of refraction of the leaky mode, determined by the lateral effective index difference. The finer periodicity was caused by coherence between the widely spaced stripes. The initial concept was extended by Ackley and Engelmann (1981) to ten stripes (on 14 μm centers), with improved performance. The overall threshold current density was 900 A/cm^2 with 30% differential quantum efficiency per facet. The laser structure itself was simplified by Ackley (1982), who replaced the BH lasers with channel-guide (CG) devices. These leaky-mode guides were made by etching the p-AlGaAs cladding layers in the 2.5 μm-wide current-injected stripe regions. The index of refraction was lowered in the stripe region because of the larger density of free carriers there. This was verified experimentally by measuring the dependence of far-field leaky-mode diffraction angle on drive current below threshold. Output powers (40 ns pulses) from 1.8 to 2.7 W were obtained with 10-stripe devices.

After a lapse of several years, this leaky-mode array configuration has seen a renewal of interest. Botez and Peterson (1988) and Botez *et al.* (1988a) have demonstrated a closely spaced 10-element array of leaky guides. Major differences from the previous work include the much denser spacing (3 μm leaky guides on 5 μm centers) and a continuous active-layer laser structure. The array was fabricated using a two-step epitaxial process, with the first-stage metal organic chemical vapor deposition (MOCVD) growth forming a two-layer AlGaAs epitaxy, that was etched into channels. The liquid phase epitaxy regrowth provided the remaining waveguide and continuous planar active layer, much as in channel substrate planar (CSP) or SML lasers. In this structure, the unetched mesas formed the high-index cladding regions, and the etched channels formed the low-index regions leaky guides, with an effective index depression of about 0.05. With the dense guide spacing, the amount of leaky, radiative loss relative to coupling decreases. As Botez *et al.* (1988a) show, the total radiative loss coefficient decreases with number of antiguides and shows larger mode discrimination between low order modes than does a similar evanescently coupled array. However, the calculated radiation losses between the 0° and 180° modes are comparable. Depending on details of the structure, stable lasing was obtained in either the 0° mode (up to 166 mW, 3% and 95% facet coating) or 180° mode (up to 110 mW/uncoated facet). An analysis of the modes of this array has been done by Botez and Peterson (1988). They calculate the near-field amplitudes, and show that the large radiative loss from intermediate-order modes comes from their relatively large amplitudes in the outer leaky guides. Moreover, the radiative loss difference between the in-phase and out-of-phase modes is shown to be extremely sensitive to the separation between active layer and etched-mesa top in the high-index regions. An implicit assumption in the model is that the lateral effective index approximation can be used, even though the modes are concentrated in different layers in the channel and mesa regions.

Improvements in this device have incorporated MOCVD growth of the entire structure, and inclusion of diffraction coupling for mode discrimination (Mawst *et al.*, 1988a). In this work the structure resembles the previous one but is grown in an inverted fashion. First, the planar laser epitaxy, which includes a separate-confinement, single-quantum-well active layer, is grown. Mesas are etched in the top cladding layer, and MOCVD regrowth completes the epitaxy. The mesa regions correspond to the previous channel regions, and form the leaky guides. In addition, one end of the array lacks any guides, and forms a broad area diffraction region that couples the leaky modes by reflection from a cleaved facet, 50 μm from the stripe terminations.

This diffraction coupling favors the in-phase mode up to 100 mW/facet output power.

In both of these structures, there is a potential for high-order waveguide modes to interfere with proper operation. In one case, the low-index leaky waveguide can support high-order lateral modes. These tend to be suppressed because of their higher radiation losses, but have been observed (Botez, 1989). In the second case, the perpendicular waveguide in the "high-index" regions can support two perpendicular guided modes (Chinn and Spiers, 1982; Amann, 1986), one with a maximum in the active layer (having a zero-crossing, and a low effective index) and the other with its maximum in the low-aluminum guide layer (having no zero-crossing, and a high effective index). This latter mode is assumed to play a role in the simplest lateral effective index analysis of the anti-guided arrays. In actuality, for greater accuracy the complete set of perpendicular modes should be considered, or else a numerical two-dimensional analysis should be performed. Modeling along these lines has been carried out by Hadley (1989a).

In a manner similar to their use of diffraction coupling to add anti-phase mode discrimination, Mawst *et al.* (1989a) have incorporated a Talbot spatial filter within the laser cavity of a leaky-wave array. By interrupting the guides in the cavity, separating them by half the Talbot distance (here, 65 μm), and offsetting the two portions laterally by half the center-to-center separation, large discrimination between the 0° and 180° modes was achieved. Stable, diffraction-limited output was obtained to over 2× threshold, with output power of 70 mW. Approximately 75% of the power was contained in the central diffraction-limited lobe.

The reason for the structure sensitivity of the modal loss has been described by Botez *et al.* (1988b). For a given anti-guide, the guide width approximately determines the lateral wavelength

$$\lambda_1 = \frac{\lambda}{\sqrt{n_1^2 - n_{\text{eff}}^2}}, \tag{23}$$

where subscript 1 refers to the regions cladding the leaky guides. The leaky guide width approximately constrains λ_0, and thereby determines n_{eff}, giving

$$\lambda_1 = \frac{\lambda}{\sqrt{n_1^2 - n_0^2 + (\lambda/2d)^2}}. \tag{24}$$

The leaky fields from all the anti-guides are in resonance when a half-wavelength across the guide plus an integer number of cladding half-

wavelengths equals the array center separation, Λ, or

$$\Lambda = d + m\frac{\lambda}{\sqrt{n_1^2 - n_0^2 + (\lambda/2d)^2}}. \tag{25}$$

In this resonance condition, the radiation loss is largest, but there is also maximum interaction among all the antiguides. The envelope of in-phase anti-guide intensities is approximately uniform, as opposed to the anti-resonance case where it has a cosinusoidal envelope. Hadley (1989b) has also analyzed the resonant behavior in an infinite array, in the effective index approximation. He finds the ratio of the intensity peaks in the low and high index regions to vary in a resonant manner (similar to that of Eq. 25) with variation in the width of the high-index region.

Further elaboration of this picture by Botez *et al.* (1989a) describes mode discrimination near the lateral resonances in more detail. By very slight detuning from the resonance condition, very large discrimination (on the order of 10 cm^{-1}) between the fundamental and adjacent mode can be achieved. Even more discrimination is achieved when there is inter-guide loss. Diffraction-limited operation of such an array, including an inter-cavity spatial Talbot filter to discriminate against the anti-phase mode, was achieved up to 10 × threshold, with an output power of 450 mW (Mawst *et al.*, 1989b,c). Even without a Talbot filter, interelement loss alone provided diffraction-limited, in-phase operation of a 10-element array up to 2.5 × threshold, and 230 mW total power at 4 × threshold (1.6 × diffraction limit) (Botez *et al.*, 1989b). Proper understanding of the inter-element mode loss in this case comes only from a two-dimensional picture of the modes (Hadley, 1989a).

IV. DIFFRACTION COUPLING

After substantial development of evanescently coupled arrays, it was recognized that suppressing the anti-phase mode was one of the major problems to be faced. Even without considering the problems of spatial gain saturation above threshold, forcing the threshold gain of the in-phase mode to be less than that of the anti-phase mode was not easy to achieve. Another approach was first proposed and demonstrated by Katz *et al.* (1983c), who showed that diffraction coupling between the ends of the array guides could be used to favor different modes. This idea is related to the use of external optic feedback, but the cases discussed in the following paragraphs all involve diffraction and reflection within the epitaxial plane of the array chip.

A schematic drawing of the structure is shown in Fig. 1(b). Light emerging from the end of one of the laser waveguides diffracts, reflects from the cleaved facet, and continues spreading until portions of it are intercepted by the source guide and its neighbors. A major factor that affects mode selection is the phase of the light that is fed back into the surrounding waveguides with respect to the phase re-entering the original guide. If the guide separation and diffraction distance are chosen properly, one can achieve in-phase feedback, and thereby an in-phase lasing mode. If we approximate the field emanating from the reference guide to be a Gaussian, then it can be shown (Katz, 1983c; Wang *et al.*, 1986) that the relative phase difference between neighboring guides is

$$\Delta\phi = \frac{\pi n}{2} \frac{d^2}{\lambda L_d} \frac{1}{1+(\pi w_0^2 n/2\lambda L_d)^2}, \tag{26}$$

where

n = effective refractive index
λ = free-space wavelength
L_d = diffraction distance
d = waveguide center separation
w_0 = Gaussian beam waist parameter.

Simple ray optics yields the same result, without the Gaussian beam correction factor. For example, if we take $\Delta\phi = 2\pi$ (giving in-phase feedback), with $n \simeq 3.6$, $d = 6$ μm, and $\lambda = 0.85$ μm a diffraction distance $L_d = 38$ μm is required.

Katz *et al.* (1983c) fabricated a ten-element array of AlGaAs lasers, 3 μm wide on 9 μm centers, by partially etching through the top *p*-cladding layer. The structure was designed for optical isolation between the waveguides, to ensure that diffraction was the only coupling mechanism. Different diffraction distances could be obtained by cleaving. With different values of L_d (always less than 150 μm), far-fields having either a dominant central lobe or two main sidelobes were obtained, indicative of in-phase or anti-phase operation. These modes were stable over the entire operating range, up to 1.1 W (pulsed) output.

Similar results were reported by Chen *et al.* (1983) for diffraction-coupled arrays fabricated in a similar fashion from an InP/InGaAsP double heterostructure. In this instance, the laser waveguides were separated by only 2 μm, so that direct evanescent coupling was also present. A central lobe about 4°–5° wide was observed for in-phase modes, up to 40% above

threshold. The maximum power measured was 210 mW (pulsed, driver-limited). More recently Yap *et al.* (1989) have used etched, offset-scalloped reflectors to improve the diffraction coupling between InP/InGaAsP laser elements. In addition, similarly fabricated on-axis reflector/lenses at the opposite output end reduced the sidelobe structure, and increased the power into the central lobe.

Diffraction-coupled Schottky-barrier-restricted ridge-waveguide arrays, made from an MOCVD-grown AlGasAs double heterostructure were reported by Yang and Jansen (1986). They found that diffraction regions of 20 μm and 30 μm were needed to couple array elements on 6 and 7.5 μm centers, respectively. For five-element 6 μm-center arrays, they measured a 3.3° lobe width at 1.5 × threshold.

Using the original concept which yields Eq. (26), the idea of a reflectivity matrix between all possible pairs of stripes was formulated by Wang *et al.* (1986). Using the same Gaussian beam approximation, they found the reflection coefficient (diffraction coupling) between stripes n and $n \pm \nu$

$$R_{n,n\pm\nu} = \frac{R(\theta)}{\sqrt{1+iz/z_0}} e^{-ikz} \exp\left(-\frac{ik\rho_n^2}{2(z+iz_0)}\right), \tag{27}$$

where

$$z_0 = \frac{\pi w_0^2 n}{2\lambda L_d},$$

$$k = 2\pi/\lambda,$$

$$\rho_\nu = \nu d,$$

$$R(\theta) = \text{mirror reflectivity at angle } \theta,$$

$$\theta = \tan^{-1}(\rho_n/z).$$

It is usually a good approximation to neglect the θ-dependence of R, and to include only the adjacent stripe diffraction coupling, since the cross-reflectivity amplitude decreases exponentially with stripe separation. In this instance, the reflectivity matrix has a simple, symmetric tridiagonal form that can be easily diagonalized using a method identical to that of the nearest-neighbor evanescently coupled-stripe problem. The eigenmodes are identical to the coupled-stripe supermodes. This means that (in the nearest-neighbor approximation), diffraction coupling will not intermix coupled-stripe supermodes. Even if there is negligible evanescent coupling, these supermodes still provide a diagonal basis for diffraction coupling.

The modal reflectivities are then (Wilcox *et al.*, 1987b)

$$R_\nu = R_0 + 2R_1 \cos\frac{\nu\pi}{N+1}, \qquad \nu = 1, \ldots N$$
$$R_{n,n} \equiv R_0 \tag{28}$$
$$R_{n,n\pm1} \equiv R_1 .$$

(Note that in the corresponding result from Eq. (8) of Wang *et al.* (1986), the sine argument should be divided by 2.)

Incorporating these modal reflectivities, Wilcox *et al.* (1987b) have carried through a complete modal analysis of diffraction-coupled arrays which includes lateral field coupling terms. Even though their parallel-coupling eigenvalues differ slightly from the original simple formulations (Butler *et al.* (1984); Kapon *et al.*, 1984a), the supermode amplitudes are the same. The threshold oscillation condition for the supermodes is expressed from the usual condition for unity round-trip gain:

$$R_n R_0 \exp\left[-2\gamma_{n,\mathrm{thr}}(L_g + L_d)\right] = 1, \tag{29}$$

where L_g = length of coupled-stripe region and γ_n = mode eigenvalue. In Eq. (29) the gain in the diffraction region is approximated by the coupled-region modal gain. The real and imaginary parts of γ_n correspond to supermode gain ($G_n = -2\,\mathrm{Re}\,\gamma_n$) and wave number ($\beta_n = \mathrm{Im}\,\gamma_n$), respectively. Using Eq. (29) gives the threshold gain required for the different supermodes. Wilcox *et al.* (1987b) have examined the dependence of mode discrimination on stripe separation, keeping the diffraction length optimized for in-phase operation. They find ranges of stripe separation that favor the in-phase mode, when "d" exceeds a value that depends on beam waist, guide length, and current-spreading. The theoretical analysis agreed with experimental results on diffraction-coupled arrays using DH or large-optical-cavity (LOC) lasers. Without diffraction coupling, the arrays consistently had double-lobed far-fields, but became single-lobed with diffraction coupling added. The greater increase in beam-width for the LOC arrays was attributed to their greater beam waist and large evanescent mode overlap, which favored high-order mode operation with increasing drive.

In subsequent work, Wilcox *et al.* (1987c) modified such arrays to provide separate contacts and gain levels in the guide and diffraction regions. In that case, Eq. (29) becomes

$$2L_g G_{n,\mathrm{thr}} + 2L_d G_d = \ln\left(1/R_0 R_n\right), \tag{30}$$

where the distinction is made between the modal gains in the stripe region and the uniform gain in the diffraction region. When G_d increases, the

required $G_{n,\mathrm{thr}}$ decreases. Since $G_{n,\mathrm{thr}}$ decreases more for the fundamental mode than others, at high enough G_d, the fundamental mode is favored. This model is in qualitative agreement with results obtained on MOCVD oxide-restricted multiple-quantum-well laser arrays. Near threshold, the far-field was wide and regular, characteristic of uncoupled emission. With increasing gain in the diffraction region, the far-field narrowed, and a dominant 0° lobe emerged. However, a wider base-pattern remained, which was attributed partly to the relatively poor mode discrimination.

Lay *et al.* (1989) have modified the uniform diffraction section by varying the diffraction length for each array element, in a uniform or parabolic fashion, with the center element closest to the facet. This apodization alters the Gaussian beam reflection/diffraction matrix to provide more mode discrimination between fundamental and first-order modes. Selection against the anti-phase modes was provided by internal Y-branch or offset stripe mode filters.

A somewhat different approach to the diffraction-coupling analysis was used by Mehuys *et al.* (1988). Instead of using the Gaussian-beam approximation, they find the diffracted feedback with a reflection matrix that is found from the overlap of the waveguide fields with the set of waveguide modes of the wide diffraction region. Each waveguide field is decomposed into a linear combination of the wide diffraction region modes (which have different propagation coefficients) that travel through the diffraction region, reflect from the laser facet, travel back, and are then re-expressed in terms of a sum of narrow waveguide fields. This reflection matrix is similar in spirit to that found from the Gaussian-beam method. However, in this case the waveguide fields in both the narrow and wide regions are approximated by sinusoids. The supermodes of the array are the eigenmodes of the reflection matrix, which are found numerically. When the supermode threshold gains are calculated as a function of diffracting length, an oscillatory pattern is found, in which the lowest-order mode is favored in some regions, and the highest order in others. This behavior agrees qualitatively with that of the Gaussian-beam approach.

Experimental verification of the model was found with seven-element arrays fabricated with AlGaAs MQW ridge-waveguide lasers, 4.5 μm wide on 9 μm centers. With $L_d = 80$ μm, a fundamental mode far-field was observed up to 100 mW output power. With $L_d = 150$ μm, the highest-order supermode was seen, at similar power. Note that these lengths correspond quite well to phase shifts of 2π and π in the Gaussian beam approximation.

A similar application of a 50 μm-long diffraction region was reported for anti-guiding, leaky-wave arrays (Mawst *et al.*, 1988a). These results have

been previously discussed in Section III, dealing with leaky-wave coupled arrays.

A coupling mechanism related to diffraction has been studied by Salzman and Yariv (1986). They fabricated each resonator element with a negative-curvature etched mirror, to form an array of a dozen adjacent unstable resonators, each of whose fields spreads to other elements. They achieved single lateral mode operation up to 2.5 × threshold, and partial spatial coherence at currents up to 5 × threshold.

A. Talbot Effect Coupling

Another way of viewing diffraction coupling from an infinite array is by means of the Talbot effect (Leger and Snyder, 1984; Leger *et al.*, 1988). This subject is covered more extensively elsewhere in this volume in connection with external feedback. We will merely summarize its major features here to show its relation to the diffraction coupling described above, and to understand its recent application in internal, monolithic array mode discrimination.

If the source field at $z = 0$ is assumed to be periodic in the x coordinate, it can be expanded in a Fourier series. After some manipulation, it can be shown (Leger *et al.*, 1988) that the source field is replicated at distances that are integer multiples of $2d^2/\lambda$, called the Talbot spacing. At half-integer multiples of the Talbot spacing, the field is also replicated, but with a lateral shift of half the source period. This effect has been exploited by Leger *et al.* (1988), Leger and Holz (1988), and Roychoudhuri *et al.* (1988) to control phased array modes with external feedback. It has also been applied by Mawst *et al.* (1989c) in a monolithic configuration within the laser resonator. In this example, a 10-element array of antiguides was separated within the chip 65 μm from a similar 11-element array, which was also laterally offset by half the array period, 4 μm. The longitudinal separation corresponds to half the Talbot distance (λ is the wavelength in the semiconductor). At this distance, the Fourier components having wave vector $q_m = 2\pi m/d$ are (Wilcox *et al.*, 1989)

$$\psi(q_m, z) = \psi(q_m, 0) \exp(ikz - i\pi m^2) \tag{31}$$

$$= \psi(q_m, 0)\ (-1)^m$$

which are also the Fourier components of the original spatial function

$\psi(x-d/2)$, as stated above. Therefore, when the in-phase mode propagates across the diffracting region it is laterally shifted by an amount equal to the array offset, and is well matched to continue propagating in the other portion of the array. If the starting spatial function represents the out-of-phase mode, then it contains only the odd harmonics $q_m=(2m+1)\pi/d$ (note that the spatial period has doubled). The phase shift for the mth harmonic is then

$$\Delta\phi_m=\frac{z}{2k}\left(\frac{(2m+1)\pi}{d}\right)^2. \tag{32}$$

At the first half-Talbot plane ($z=d^2/\lambda$), this phase shift becomes

$$\Delta\phi_m=\frac{(2m+1)^2\pi}{4}=\frac{\pi}{4}+m(m+1)\pi. \tag{33}$$

Since $m(m+1)$ is always an odd integer, all phase shifts are the same, so that apart from a constant phase factor, the out-of-phase field is replicated at the half-Talbot distance. Because the other part of the array has been offset at that position, the out-of-phase nulls are now coincident with the guide centers; from symmetry arguments, the coupling to this mode then vanishes. These arguments apply to an infinite periodic source, but Wilcox *et al.* (1989) have also considered a finite number of array elements using the propagation characteristics of Gaussian beams. Edge effects are present, but the qualitative Talbot results still hold. As well as suppressing the out-of-phase mode, these edge effects may also provide discrimination against low-order modes (Botez, 1989).

The device results of Mawst *et al.* (1989a) were described previously in Section III. To recapitulate, with the half-Talbot-plane diffraction section, they obtained 70 mW of front-facet power, with 72–75% in the diffraction-limited central lobe. When the 10/11-element anti-guide arrays were designed for close-to-resonant coupling to suppress low-order modes and the Talbot filter was incorporated to suppress the anti-phase mode, diffraction-limited operation up to 10×threshold, with 450-mW power was achieved (Mawst *et al.*, 1989b,c; Botez *et al.*, 1989a). Even wider 20/21-element arrays, with internal Talbot filters and optimized coatings, have provided 330 mW front-facet power at 1.8×diffraction limit (Mawst *et al.*, 1989d).

Jansen *et al.* (1989) have made another array configuration that monolithically incorporates a self-imaging Talbot cavity. This device used a 300 μm long section of evanescently coupled ridge-guide lasers with a 165 μm long (1/2 Talbot distance) diffraction region at one end. The outer ends of both

regions were terminated by cleaved facets. Depending on the respective bias currents into both regions, different supermodes were favored. Diffraction-limited single-lobed beams with 100 mW/facet were obtained.

V. Y-BRANCH ARRAYS

In another geometric variation, the use of intersecting waveguides has been applied to phased arrays to select the in-phase mode. Ideally, in such arrays the mode selection properties should be determined primarily by the splitting and combining properties of the waveguide branches. These have also been called "interferometric" arrays, because they rely on coherent interference of the fields to discriminate among modes (Botez and Ackley, 1986). In this case, evanescent coupling between parallel guides is neither necessary nor desirable. The first report of such operation was by Taneya *et al.* (1985), who fabricated a laser with a single waveguide branching into two waveguides (1:2). The internal device structure was a modified V-channeled substrate inner stripe (VSIS), grown by two-step liquid phase epitaxy. They obtained 65 mW in the in-phase mode, with cw threshold currents of approximately 100 mA and slope efficiency 57% (on 96%/2% coated device). No quantitative analysis was given, but the 180° mode suppression was explained by its lower gain in the single-waveguide region. Later results (Taneya *et al.*, 1986) were reported for a 2:3 array, in which 50 mW was obtained in the lowest-order mode ($\nu = 1$). In this case, lasing was observed at higher power in the second-order mode ($\nu = 2$) as well, which has out-of-phase fields in the outer stripes, and zero intensity in the center (of the three-stripe end). Even though the $\nu = 1$ mode had the lowest threshold, $\nu = 2$ oscillation occurred when spatial saturation of the $\nu = 1$ gain allowed the $\nu = 2$ mode to reach threshold.

Streifer *et al.* (1986b, 1987) and Chen and Wang (1986) analyzed the general case of $N-1$ single-mode waveguides branching and recombining into N similar waveguides [Fig. 1(e)]. [An earlier version described by Chen and Wang (1985b) had the wide-end outer guides shortened and absorptively terminated.] The key point of the analysis relates to a scattering matrix description of an individual Y-branch, based on the original formulation by Rediker and Leonberger (1982). In physical terms, a field incident at the one-port side divides equally in power ($1/\sqrt{2}$ in amplitude) into the two branches, assuming that radiation losses due to scattering are negligible. However, two fields incident at the two-port side recombine in the single guide in a manner that depends on their relative phases; if the fields are

out of phase, all the power is radiated since the single guide cannot support a high-order guided mode with a null in its center. If, on the other hand, the fields are in phase, the fields sum coherently into the single-port fundamental mode with no loss of power. For intermediate phase, ϕ, the combined single-port power transmission is $\cos^2(\phi/2)$.

When an array with $N-1:N$ guides is analyzed using the above individual Y-branch transmission properties, the problem can be described by an $N \times N$ tridiagonal matrix, whose solutions can be found analytically by recursion (Streifer *et al.*, 1986b, 1987) or by assuming their form to be a sum of exponentials (Chen and Wang, 1986). The eigenvalues, which describe the total round-trip mode propagation factor, are (normalized to the lowest order mode):

$$\sigma_n = \cos^2\left(\frac{(\nu-1)\,\pi}{(N-1)\,2}\right) \qquad \nu = 1, \ldots, N, \tag{34}$$

with amplitude eigenvectors (at the wide end)

$$U_m^n = \begin{cases} 1/\sqrt{2} & \text{for} \quad m = 1 \\ \cos\left[(m-1)(\nu-1)\pi/(N-1)\right] & \text{for} \quad m = 2, 3, \ldots (N-1) \\ (-1)^{n-1}/\sqrt{2} & \text{for} \quad m = N. \end{cases} \tag{35}$$

These results show that the mode with largest propagation factor (lowest loss) is the in-phase mode with $\nu = 1$, $\sigma_1 = 1$, and the mode with smallest propagation factor (highest loss) is the anti-phase mode with $\nu = N$, $\sigma_N = 0$. This situation is quite different from many of the evanescently coupled supermode models considered previously, where there was little loss discrimination between the 0° and 180° modes. However, there is a problem in mode discrimination between the $\nu = 1$ and low-order modes as N increases. This is shown in Fig. 5, where the gain factor is plotted as a function of mode number for different array sizes. For large N, the separation between the two gain factors approaches $[\pi/2(N-1)]^2$.

Using a totally different approach, Hermansson and Yevick (1989) have attempted to understand the behavior of periodic Y-branch arrays by examining the limit as N approaches infinity. This assumption leads to transverse Floquet-type periodic solutions, which are found from a numeric beam propagation analysis. The analysis also includes evanescent coupling between stripes, making a correspondence with the previous results somewhat unclear. Nevertheless, they find the same type of large discrimination between the 0° and 180° modes, but with differences in some of the intermediate high-order modes. Another technique, the numerical beam propagation

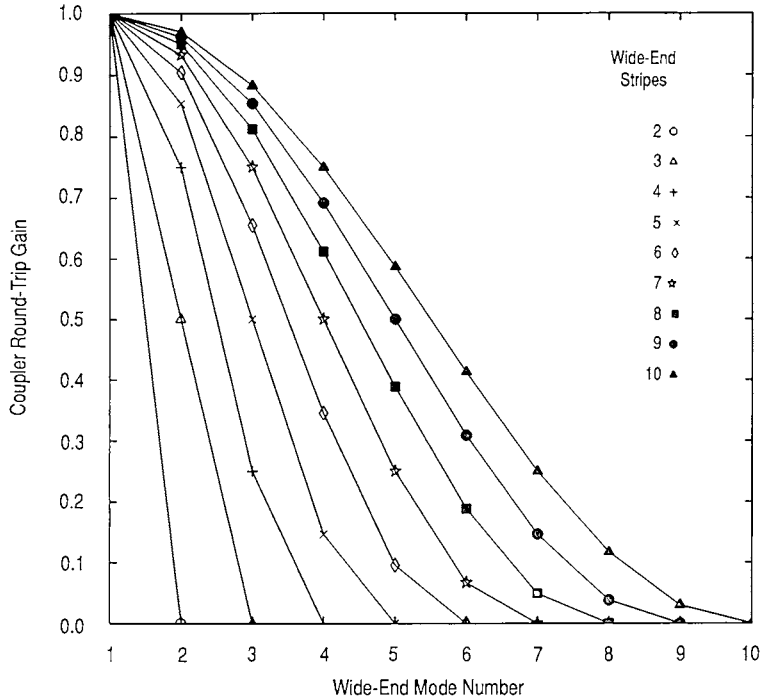

Fig. 5. Relative mode gains for a Y-branch laser as a function of mode number, for different array sizes (Chinn, 1988 © IEEE).

method, has also recently been applied to Y-branch arrays (Reinhoudt and van der Poel, 1989).

In order to minimize the intrinsic radiative scattering loss at the Y-junction, the branching angle must be quite small, typically less than a few degrees, and the corner should be sharp. This can present some practical difficulties in photolithographic patterning of the devices. Chinn (1988) has analyzed an array structure analogous to the Y-branch configuration, but with an evanescent coupling section replacing the branches. The coupling section length is determined by requiring the 0° mode to have $\sigma_1 = 1$. The gain factor for all modes is then

$$\sigma_m = \sin^2 [(\pi/2)(\cos \theta_m / \cos \theta_1)], \tag{36}$$

where $\theta_m = m\pi/(N+1)$.

The gain factor for the distributed-coupler array resembles that of the Y-branch results of Fig. 5, but with less inter-modal discrimination. The

envelope of the $\nu = 1$ amplitude distribution is sinusoidal; it can be made to resemble the more uniform Y-branch eigenmode by increasing the outer guide distributed coupling coefficient by a factor of $\sqrt{2}$. However, in both instances the relative mode discrimination is poorer than that of the Y-guide.

Early experimental results (Welch *et al.*, 1986b, 1986c, 1987a) on 10-element, buried-heterostructure Y-branch arrays showed output power of 200 mW (cw) and 400 mW (pulsed) in the fundamental mode. Similar arrays were made with inverted CSP stripes, but had higher thresholds. Both types were made with two-step MOCVD growth. With conventional 1.5 μm-wide straight waveguides on 4 μm centers the inherently large side-lobe ratio due to the poor aperture fill factor was evident. When the emitting facet stripe ends were flared (Welch, 1987b) to give an 80% fill factor, the side-lobe content decreased markedly, but the maximum in-phase mode power decreased to 150 mW (Welch *et al.*, 1987a,c). A modification of Welch's works (Shinozaki *et al.*, 1989) uses the limit of very short Y's approaching an offset stripe configuration with closely spaced channel-substrate index-guided lasers. Using a 4/5 stripe configuration, 150 mW of fundamental mode power was reported.

There have been recent attempts to improve the modeling of Y-branch arrays to understand their power limits for operating in the fundamental mode. By adding loss terms to the linear analysis, Streifer *et al.* (1988) have examined the effects of having different amounts of loss contributed by the outer waveguide bends versus the Y-junctions. For the more relevant situation where Y-branch losses exceed bend losses, they found that the relative mode discrimination between the $\nu = 1$ and $\nu = 2$ modes decreased significantly. When these modes are nearly degenerate they can be described by admixtures that concentrate the mode intensity at one side of the array or the other. Incoherent oscillation of such spatially separated modes is consistent with many of their laboratory observations.

A more significant effect in limiting $\nu = 1$ mode operation is spatial gain saturation. Since the outer wide-end branches of the array have one-half the intensity of the interior guides, saturated gain above threshold will be higher for the outer guides, and will tend to favor oscillation on the $\nu = 2$ mode. The saturated gain for $\nu = 1$ is clamped near its threshold value, but that for the $\nu = 2$ mode continues to increase. At some point, its gain reaches the threshold value, and it begins to lase, degrading the mode quality of the output beam. In addition, anti-guiding effects at different saturated carrier levels introduce undesirable phase-shifts. This behavior has been numerically analyzed by Streifer *et al.* (1989a,b). They showed that the degradation of the beam, as measured by the Strehl ratio (defined by the

ratio of the far-field intensity at 0° to the 0°-intensity of the diffraction-limited fundamental mode) can occur at powers of tens of mW. However, since this degradation is determined by spatial hole-burning, modifications to the array structure to minimize this effect can be made. Such modifications include shortening the lengths of the wide-end waveguides and increasing the reflectivity at that end. In theory, such improvements should yield approximately 1W of nearly diffraction-limited power (Strehl = 0.85) in a 10-element array.

An extension of the simple Y-branch structure was made by Botez *et al.* (1987) to achieve greater internal fill factor in the array. Using an inverted-rib, index-guided InP/InGaAsP structure, they used closely spaced waveguides and merged the Y-intersection region into a single, slowly tapered wide waveguide. The individual guides gradually broadened until they merged at the edge of the wide-waveguide region. In a qualitative picture, the fundamental super-mode stripe amplitudes (with cosine peak envelope) smooth into a cosine function in the wide waveguide, which then couples well with the fundamental super-mode in the other coupled-guide region. The anti-phase mode, however, evolves into a pattern that has amplitude nulls at the guides of other coupled-guide portion. Although the wide-waveguide region is only 20 μm long (i.e., less than half a Talbot distance), we should note the similarity of this behavior to diffraction-coupling effects discussed previously in Section IV. Nearly diffraction-limited operation up to 70% above threshold, with output power of 60 mW, was achieved. At higher power, spatial gain saturation introduced higher-order modes.

This same array configuration was implemented in an GaAs/AlGaAs CSP-like structure by Botez *et al.* (1988c). The laser structure differed by having an anti-guiding type of inter-channel epitaxy. Without giving a quantitative analysis, Botez *et al.* (1988c) claim that the two significant factors that compete in the mode selection process are transverse antiguiding, which favors high-order operation, and the wide-waveguide interference, which favors low-order modes. In this instance the $L = 8$ mode has the lowest threshold. In addition, such high-order modes tend to be self-stabilizing above threshold, since spatial hole-burning effects cause them to defocus, as opposed to low-order mode self-focusing (Thompson and Whiteaway, 1987). At 3.3× threshold, Botez *et al.* (1988c) achieved 100 mW/facet, with lobes 25% wider than the diffraction limit. At 4.7× threshold (130 mW/facet), the excess broadening increased to 50%.

Further stabilization of the array mode was achieved by coupling first-order modes of the individual waveguides (Mawst *et al.*, 1988b). In this

case, the structure consisted of periodically spaced large-optical-cavity (LOC) $Al_{0.20}Ga_{0.80}As$ ribs over a continuous GaAs active layer. The width of the LOC ribs was such that lateral first-order waveguide modes were allowed. Also, the coupled waveguides had constant width, and were abruptly terminated at the edges of the wide-waveguide interferometer (WWI) section. In one case, with 2 μm guides on 5 μm centers, there is a relatively large amount of field from first-order guide modes between the guides. If these guided fields are out-of-phase, they couple well to the similar first-order, out-of-phase fields across the WWI section. Operation of the first-order waveguide mode stabilizes the out-of-phase mode against spatial hole-burning. At 5 × threshold, 145 mW/facet was obtained, with two dominant lobes 7.5° apart, having widths 1.3 × diffraction limit. When the lasing guides were widened to 3 μm, scattering loss at the WWI boundary was lower for the in-phase array mode (i.e., 10 first-order modes coupled in-phase across the array). However, this mode was more susceptible to spatial hole-burning above threshold.

Another version of interferometric array bears a closer resemblance to the original Y-branch concept, but is X-branched to favor our-of-phase operation (Botez *et al.*, 1988d). Each X-branch consists of a pair of evanescently coupled, single-mode guides that merge into a wide guide, then branch again symmetrically into single-mode guides. The wide guide supports the second-order mode created when the entrant fields are out-of-phase. Since scattering losses will be higher for the first-order wide-guide field (in-phase condition), the X-branch serves as an anti-phase mode discriminator. The natural tendency for anti-phase operation between guides that couple between adjacent X-branch sections causes anti-phase operation of the entire array. The next lower mode has in-phase operation of the center X-branch, and will have higher loss. At 3 × threshold, 230-mW power was obtained, with 1.2° lobe width 10% higher than diffraction limit (approximately 180 mW was in the pure antiphase mode). Near-field data also indicated that the mode was self-stabilizing against spatial hole-burning.

In an effort to avoid the lateral spatial hole burning problem, Whiteaway *et al.* (1989) have made a "tree" array of sequential 1:2 Y-branch sections, starting with one single-mode waveguide, which ultimately branches into four waveguides (from two double-element Y-branches). The starting single element constrains the subsequent phases. By appropriately choosing the high-reflectance facet coating at that end, and the low-reflectance coating at the multielement output end, the internal power can be made approximately the same in all branches. This idea was tested using 3 μm-wide ridge guide InGaAsP/InP lasers. Early results showed output powers of 10 mW

in the in-phase mode, but with considerable sidelobe structure from the large element spacing.

VI. THERMAL, NON-IDEAL, AND TEMPORAL EFFECTS

A. Array Tolerance and Nonuniformity

Most descriptions of array behavior have used the simplest possible models in order to gain understanding without introducing excessive complexity. Real devices, however, do not obey our analytical wishes. Accurate modeling of phased arrays requires an understanding of nonideal effects such as temperature nonuniformity, deviations from design parameters, and structural irregularities.

The earliest analyses of thermal uniformity requirements were by Tavis and Garmire (1984) and Garmire and Tavis (1984). They examined heat sink designs constrained by maximum allowed temperature nonuniformity across a phased array, determined by frequency locking limits (Basov *et al.*, 1965) on nonidentical lasers. Using numerical analysis programs, they determined that optimum heat-sink designs should have a high thermal conductivity pad (e.g., diamond) having the same width as the array, placed on a larger pyramidal or wedge-shaped heat-sink (e.g., copper). This arrangement gives a higher junction temperature for the array but with greater lateral uniformity than a single, broad-area heat-sink. For a typical case, the maximum allowed temperature variation they estimated was 0.4°C between laser diodes.

Another viewpoint for including the effects of thermal non-uniformity is to alter the local indices of refraction due to thermal variation, and then calculate the array modes (Hadley *et al.*, 1987b). The effects of the local variation of the real part of the index from heating (assumed proportional to temperature, and local power dissipation) can significantly alter the modal properties of gain-guided lasers, and should be included in their analysis. Hadley *et al.* (1987b) found that both the near- and far-field intensities were altered with a 10°C quasi-uniform temperature rise in the multistripe region. Also, high-order modal gains varied much less with mode order when the temperature variation was included.

High-power capability of phased-locked arrays has been increased by improving their thermal behavior, through optimization of their length (Aoyagi *et al.*, 1987) and junction-down soldering techniques (Seiwa *et al.*, 1987).

Other types of non-uniformities may also be important in determining array behavior. Garmire (1988) has examined several array parameters that are subject to variation, again from the constraint of frequency locking of non-identical lasers, $\delta\omega/\omega \leq 2\Gamma/nkL$, where Γ is the fraction of optical field coupled in a single pass into an adjacent laser, $k = \omega/c$, L is the laser length, and n is its (modal) refractive index. To obey the weak coupling assumption used in finding this criterion, the locking range will generally be less than a longitudinal mode frequency difference. The locking criterion translates into the approximate requirement that $\delta n/n \leq 10^{-3}\,\Gamma$, where a typical value of Γ is 0.1. This in turn relates to factors that affect n, such as aluminum composition (x), temperature (T), guide thickness, guide width, and carrier density (and related current, I). To summarize Garmire's (1988) results, $\delta x < 1.6 \times 10^{-3}\,\Gamma$, $\delta T < 0.9°\Gamma$, and $\delta I/I < 0.01$. The thickness and width have less stringent direct constraints, but also have indirect constraints (as does the resistivity) through the current uniformity requirement. All of these properties, which are spatial averages over the device length, should be adequately controllable with careful device fabrication.

Nishi and Lang (1985) also examined the uniformity issue, but using a modal analysis with a two-stripe example. For the ideal case, the supermode field is equally divided between the two stripes, but differences in stripe width cause localization of the intensity of the two supermodes in different stripes. This localization affects the gain saturation, and has the result of limiting the range of single supermode (i.e., phase-locked) operation. For example, with a stripe width difference of 0.2 μm out of 3 μm, the second supermode oscillates when the current is only 3% above threshold for the first mode.

Another type of array imperfection that can degrade performance is non-ideal mirror facets (Chen and Wang, 1985c). Microscopic steps or misalignment in the cleaved end can couple supermodes by the imperfect reflection process. Using simulated random cleave positions at each laser stripe corresponding to measured imperfections (average step height from 17 to 90 Å, with standard deviation approximately, 30–40 Å), they showed significant broadening of the far-field patterns and lowering of threshold gain discrimination. Supermode coupling due to facet misalignment was generally less significant, and could be simulated only when the stripe coupling × length product exceeded 1.

B. Temporal Effects

Some temporal behavior has been implicitly described above whenever pulsed operation of arrays has been cited. However, in nearly all those

cases, pulsing was merely a means to reduce heating by lowering the operating duty cycle of the arrays. Little explicit attention was given to differences in pulsed and cw behavior (except for heating effects), and a quasi-cw (albeit lower temperature) mode of operation was assumed during an excitation pulse. We now discuss some explicit time-dependent measurements, which are important for understanding both pulsed behavior and fluctuation phenomena in cw operation.

Short-pulse operation of 10-stripe, gain-guided multi-quantum-well arrays was studied by Van der Ziel *et al.* (1984b), using combined dc and 75 ps current pulses. The far-field had the double-lobed pattern characteristic of gain-guided arrays, interpreted by the authors as resulting from the anti-phase mode (which, as discussed previously, is probably not the exact situation). Gaussian-shaped pulses as short as 62 ps were obtained. Operation was described in terms of a single, high-order spatial mode, and no effects of the array nature of the device, per se, were discussed. Differences from earlier single-stripe BH devices were ascribed to gain parameters associated with the MQW active region of the array.

Dynamic characteristics of the individual array emitters were first measured by Elliott *et al.* (1985) with a streak camera. Current pulses with 50 ns width and 600 ps rise-time were applied to a 10-element, gain-guided array having a MQW active region. Several interesting results were observed: (1) single-pulse output from individual emitters showed quasi-randomly phased spiking output for the entire duration of the 50 ns current pulse; (2) Spikes from adjacent stripes were synchronous, but this synchronism was not present across the entire array, since total output reached a steady state towards the end of the current pulse; (3) The multipulse averaged output from an individual stripe showed regular initial relaxation oscillations, and also tended toward a later steady-state level; and (4) Time evolution of the far-field showed phase-locking within the array to occur within 100 ps of the onset of lasing.

Similar time-resolved studies of the far-field, using a sampling rather than streak camera technique, by Forrest and Abshire (1987) confirmed the finding by Elliott *et al.* (1985) that phase-locking occurs within 100 ps of lasing onset. However, the later study found that the super-mode evolution did not stabilize into a steady-state superposition of modes until one to three ns after the maximum of the current pulse had been reached.

Another system for studying array fluctuations was used by Fuhr (1985) to examine the wavelength distribution of index-guided CSP-LOC arrays having variable spacing between stripes. Using 200-pulse averages, with 10 ns pulses and dc bias, the wavelength spread was less than 2.5 Å in over 70% of the pulses, indicative of single longitudinal mode operation.

The means of understanding such dynamic behavior was discussed by Rozzi and Shore (1985). The interaction of spatial and temporal instabilities can be examined by linearizing the coupled equations for carriers and photons, and applying the Hopf bifurcation method, a stability analysis of the resulting matrix equations of motion. Although the formalism is general, results were cited only for the case of a single-stripe laser. The dynamics of a specific array example were calculated by Wang and Winful (1988). They used a numerical solution of the coupled rate equations for field amplitude, phase, and carrier density in each stripe of a 10-element array. Their simulated results were in excellent agreement with the experimental findings of Elliott *et al.* (1985), showing continuous spiking in an individual emitter output, but regular, damped relaxation oscillations in either the pulse-averaged single-emitter output or the single-pulse output of the entire array. To first-order, locking is established in a time inversely proportional to the inter-stripe coupling coefficient. Their main conclusion was that laser arrays are intrinsically unstable, and provide another example of a system of coupled non-linear oscillators having deterministic chaotic solutions.

Similar results and conclusions have been reported for index-guided Y-branch arrays. Using pulsed excitation, with a synchronized streak camera, DeFreez *et al.* (1987) have shown that the phase-coupled far-field develops within the time resolution limit of the system, 20 ps. Slight time-dependent steering of the central lobe was also observed. When the Y-branch array is operated cw, self-pulsation of the array is observed at GHz frequencies, with slight lagging of the center elements (Yu *et al.*, 1988). Spectral examination of a Y-branch array showed that elements at one end were predominantly single-longitudinal-mode, and others multilongitudinal-mode (DeFreez *et al.*, 1988). Spectral structure on the single-longitudinal-mode was observed, which was associated with the time-dependent amplitude and phase modulation of the array self-sustained pulsations. The array behavior differed from that of gain-guided arrays, in that the individual emitter pulsations had a fixed relation to the lasing onset, and could be coherently averaged over many pulses. This implies that, while dynamic instability is present, its chaotic nature differs from that of gain-guided arrays.

VII. CONCLUSION

As long as the technology for improving single-stripe semiconductor lasers develops, a convenient means of extending their brightness limit will be

through coherent edge-emitting arrays. Although material power density limitations and heat removal geometry will ultimately favor surface-emitters for high-power requirements, linear edge-emitting arrays can be fabricated with methods much like those of single lasers, and should have many moderate power (<1 W) applications. Linear monolithic non-coherent arrays have recently provided 76 W from cm-long bars (Sakamoto *et al.*, 1989), so the hope remains that similar coherent powers might be achievable, with proper mode control.

Apart from thermal and structural non-uniformities, intrinsic size or power limits to coherent single-mode operation are not yet well understood. This area, as well as related dynamic stability questions, is likely to prove fruitful for future modeling efforts.

Arrays will likely improve from further development of individual device technology and from future advances in coupling design. It is likely that as device epitaxy develops (for example, at visible wavelengths, or with better performing strained-layer quantum wells), these improvements will be incorporated in coherent arrays. Another trend that will probably continue is the monolithic, integrated optical incorporation of external, bulk-optic mode control techniques. Examples developed so far include Talbot filtering and injection locking. When the first concept of parallel evanescent coupling was tried, few imagined the more sophisticated techniques (Y-branch interferometric coupling, leaky coupling, Talbot filters, etc.), that have since yielded the highest power devices to date. Hopefully, similar advances will continue to appear.

ACKNOWLEDGMENTS

I would like to acknowledge discussions with and cooperation from D. Botez, G. R. Hadley, J. R. Leger, W. Streifer, and J. Z. Wilcox in preparing this chapter.

REFERENCES

ACKLEY, D. E. AND ENGELMANN, R. W. H. (1980). "Twin-stripe injection laser with leaky-mode coupling," *Appl. Phys. Lett.* **37**, 866.

ACKLEY, D. E. AND ENGELMANN, R. W. H. (1981). "High-power leaky-mode multiple-stripe laser," *Appl. Phys. Lett.* **39**, 27.

ACKLEY, D. E. (1982). "High-power multiple-stripe injection lasers with channel guides," *IEEE J. Quantum Electron.* **QE-18**, 1910.

ACKLEY, D. E. (1983). "Single longitudinal mode operation of high power multiple-stripe injection lasers," *Appl. Phys. Lett.* **42**, 152.

ACKLEY, D. E., BOTEZ, D. AND BOGNER, B. (1983). "Phase-locked injection laser arrays with integrated phase shifters," *RCA Review* **44**, 625.

ACKLEY, D. E. (1984). "Phase-locked injection laser arrays with nonuniform stripe spacing," *Electron. Lett.* **20**, 695.

ACKLEY, D. E., BUTLER, J. K. AND ETTENBERG, M. (1986). "Phase-locked injection laser arrays with variable stripe spacing," *IEEE J. Quantum Electron.* **QE-22**, 2204.

AGRAWAL, G. P. (1985). "Lateral-mode analysis of gain-guided and index-guided semiconductor-laser arrays," *J. Appl. Phys.* **58**, 2922.

AMANN, M.-C. AND KAPPELER, F. (1986). "Analytical solution for the lateral current distribution in multiple stripe laser diodes," *Appl. Phys. Lett.* **48**, 1710.

AMANN, M.-C. (1986). "Rigorous waveguiding analysis of the separated multiclad-layer stripe-geometry laser," *IEEE J. Quantum Electron.* **QE-22**, 1992.

ANDREWS, J. R., PAOLI, T. L., STREIFER, W. AND BURNHAM, R. D. (1985). "Individual spatial modes of a phase-locked injection laser array observed through spectral selection and selected with an external mirror," *J. Appl. Phys.* **58**, 2777.

AOYAGI, T., HINATA, S., SHIGIHARA, K., SEIWA, Y., IKEDA, K. AND SUSAKI, W. (1987). "High-power operation of long-cavity phase-locked laser arrays," *Electron. Lett.* **23**, 1396.

BAILLARGEON, J. N., YORK, P. K., ZMUDZINSKI, C. A., FERNANDEZ, G. E., BEERNINK, K. J. AND COLEMAN, J. J. (1988). "High-power phase-locked InGaAs strained-layer quantum well heterostructure periodic laser array," *Appl. Phys. Lett.* **53**, 457.

BASOV, N. G., BELENOV, E. M. AND LETOKHOV, V. S. (1965). "Diffraction synchronization of lasers," *Sov. Phys.-Tech. Phys.* **10**, 845.

BORN, B. AND WOLF, E. (1970). *Principles of optics*, Sect. 8.5. Pergamon Press, Oxford.

BOTEZ, D. AND CONNOLLY, J. C. (1983). "High-power phase-locked arrays of index-guided diode lasers," *Appl. Phys. Lett.* **43**, 1096.

BOTEZ, D. (1985). "Array-mode far-field patterns for phase-locked diode-laser arrays: coupled-mode theory versus simple diffraction theory," *IEEE J. Quantum Electron.* **QE-21**, 1752. see also, comments by Streifer, W. and Osinski, M., (with Botez reply) *IEEE J. Quantum Electron.* **QE-22**, (1986) 376.

BOTEZ, D. AND ACKLEY, D. E. (1986). "Phase-locked arrays of semiconductor diode lasers," *IEEE Circuits and Dev.* **2**, 8.

BOTEZ, D., PHAM, T. AND TRAN, D. (1987). "0°-phase-shift, single-lobe operation from wide-waveguide interferometric (WWI) phase-locked arrays of InGaAsP/InP ($\lambda = 1.3$ μm) diode lasers," *Electron. Lett.* **23**, 416.

BOTEZ, D. (1988). "Simple design rules for single-lobe operation of (evanescently coupled) index-guided phase-locked arrays of diode lasers," *IEEE J. Quantum Electron.* **QE-24**, 2034.

BOTEZ, D. AND PETERSON, G. (1988). "Modes of phase-locked diode-laser arrays of closely spaced antiguides," *Electron. Lett.* **24**, 1042. See erratum: *ibid.* **24**, 1351.

BOTEZ, D., MAWST, L., HAYASHIDA, P., PETERSON, G. AND ROTH, T. J. (1988a). "High-power, diffraction-limited-beam operation from phase-locked diode-laser arrays of closely spaced "leaky" waveguides (antiguides)," *Appl. Phys. Lett.* **53**, 464.

BOTEZ, D., MAWST, L. J. AND PETERSON, G. (1988b). "Resonant leaky-wave coupling in linear arrays of antiguides," *Electron. Lett.* **24**, 1328.

BOTEZ, D., MAWST, L., HAYASHIDA, P., ROTH, T. J. AND ANDERSON, E. (1988c). "Stable, single-(array)-mode operation from phase-locked, interferometric arrays of index-guided AlGaAs/GaAs diode lasers," *Appl. Phys. Lett.* **52**, 266.

BOTEZ, D., HAYASHIDA, P., MAWST, L. J. AND ROTH, T. J. (1988d). "Diffraction-limited-beam, high-power operation from X-junction coupled phase-locked arrays of AlGaAs/GaAs diode lasers," *Appl. Phys. Lett.* **53**, 1366.

BOTEZ, D. (1989). Private communication.

BOTEZ, D., MAWST, L. J., PETERSON, G. AND ROTH, T. J. (1989a). "Resonant optical transmission and coupling in phase-locked diode laser arrays of antiguides: The resonant optical waveguide array," *Appl. Phys. Lett.* **54**, 2183.

BOTEZ, D., HAYASHIDA, P., MAWST, L. J., ROTH, T. J. AND PETERSON, G. (1989b). "Diffraction-limited in-phase-mode operation from uniform array of antiguides with enhanced interelement loss," *Electron. Lett.* **25**, 1282.

BUTLER, J. K., ACKLEY, D. E. AND BOTEZ, D. (1984). "Coupled-mode analysis of phase-locked injection laser arrays," *Appl. Phys. Lett.* **44**, 293. See also Erratum: *Appl. Phys. Lett.* **44**, 935.

BUTLER, J. K., ACKLEY, D. E. AND ETTENBERG, M. (1985). "Coupled-mode analysis of gain and wavelength oscillation characteristics of diode laser phased arrays," *IEEE J. Quantum Electron.* **QE-21**, 458.

BUUS, J. (1986). "'Excess' modes in gain-guided laser arrays," *Electron. Lett.* **22**, 1296.

BUUS, J. (1987). "Semiconductor laser arrays with enhanced mode stability," *IEEE J. Quantum Electron.* **QE-23**, 757.

BUUS, J. (1988). "Analysis of semiconductor laser arrays with high-intensity uniformity," *IEEE J. Quantum Electron.* **QE-24**, 22.

CARLIN, D. B., GOLDSTEIN, B. AND CHANNIN, D. J. (1985). "High-power diode lasers for optical communications applications," *Proc. IEEE Military Communications Conference*, Boston, MA, Paper 4.4, p. 109.

CARLSON, N. W., BUTLER, J. K. AND MASIN, V. J. (1986). "Coupled mode analysis of wavefront properties of phased array diode lasers," *Electron. Lett.* **22**, 1327.

CARLSON, N. W., MASIN, V. J., LURIE, M., GOLDSTEIN, B. AND EVANS, G. A. (1987). "Measurement of the coherence of a single-mode phase-locked diode laser array," *Appl. Phys. Lett.* **51**, 643.

CARROLL, J. E., WHITE, I. H. AND MACLEAN, D. (1987). "Self-consistent modal field analysis of injection-laser devices," *IEEE Proc.* **134, Pt. A**, 687.

CHEN, T. R., YU, K. L., CHANG, B., HASSON, A., MARGALIT, S. AND YARIV, A. (1983). "Phase-locked InGaAsP laser array with diffraction coupling," *Appl. Phys. Lett.* **43**, 136.

CHEN, K.-L. AND WANG, S. (1985a). "Spatial hole burning problems in evanescently coupled semiconductor laser arrays," *Appl. Phys. Lett.* **47**, 555.

CHEN, K.-L. AND WANG, S. (1985b). "Single-lobe symmetric coupled laser arrays," *Electron. Lett.* **21**, 347.

CHEN, K.-L. AND WANG, S. (1985c). "Effect of mirror imperfections on phase-locked semiconductor laser arrays," *IEEE J. Quantum Electron.* **QE-21**, 264.

CHEN, K.-L. AND WANG, S. (1986). "Analysis of symmetric Y-junction laser arrays with uniform near-field distribution," *Electron. Lett.* **22**, 644.

CHINN, S. R. AND SPIERS, R. J. (1982). "Calculation of separated multiclad-layer stripe geometry laser modes," *IEEE J. Quantum Electron.* **QE-18**, 984.

CHINN, S. R. AND SPIERS, R. J. (1984). "Modal gain in coupled-stripe lasers," *IEEE J. Quantum Electron.* **QE-20**, 358.

CHINN, S. R. (1986). unpublished.

CHINN, S. R. (1988). "Analysis of a laser phased array using a distributed Y-junction analog," *IEEE J. Quantum Electron.* **QE-24**, 687.

CHOW, W. W. (1986a). "Frequency locking in an index-guided semiconductor laser array," *J. Opt. Soc. Am.* B **3**, 833.

CHOW, W. W. (1986b). "Analysis of semiconductor laser arrays," *SPIE* **642** (Modeling and Simulation of Optoelectronic Systems), 61.

DEFREEZ, R. K., PAOLI, T. L., BERNSTEIN, M. AND BURNHAM, R. D. (1985). "CW operation of a cleaved-coupled-cavity array of phase-locked GaAlAs lasers," *Electron. Lett.* **21**, 241.

DEFREEZ, R. K., ELLIOTT, R. A., HARTNETT, K. AND WELCH, D. F. (1987). "Quasi-instantaneous (<20 ps) phase locking in single-lobe Y-coupled laser diode arrays," *Electron. Lett.* **23**, 589.

DEFREEZ, R. K., BOSSERT, D. J., YU, N., HARTNETT, K., ELLIOTT, R. A. AND WINFUL, H. G. (1988). "Spectral and picosecond temporal properties of flared guide Y-coupled phase-locked laser arrays," *Appl. Phys. Lett.* **53**, 2380.

DUTTA, N. K., KOSZI, L. A., SEGNER, B. P., CRAFT, D. C. AND NAPHOLTZ, S. G. (1985). "High-power index-guided multiridge waveguide laser array," *Appl. Phys. Lett.* **46**, 803.

DUTTA, N. K., KOSZI, L. A., SEGNER, B. P. AND NAPHOLTZ, S. G. (1986). "InGaAsP ridge waveguide laser array with nonuniform spacing," *Appl. Phys. Lett.* **48**, 312.

ELLIOTT, R. A., DEFREEZ, R. K., PAOLI, T. L., BURNHAM, R. D. AND STREIFER, W. (1985). "Dynamic characteristics of phase-locked multiple quantum well injection lasers," *IEEE J. Quantum Electron.* **QE-21**, 598.

ENGELMANN, R. W. H. AND KERPS, D. (1980). "Leaky modes in active three-layer slab waveguides," *IEE Proc.* **127**, Pt. I, 330.

EPLER, J. E., HOLONYAK, N., BURNHAM, R. D., PAOLI, T. L. AND W. STREIFER (1984). "Far-field supermode patterns of a multiple-stripe quantum well heterostructure laser operated (~7330 Å, 300K) in an external grating cavity," *Appl. Phys. Lett.* **45**, 406.

EPLER, J. E., HOLONYAK, N., BURNHAM, R. D., PAOLI, T. L. AND W. STREIFER (1985a). "Supermodes of multiple-stripe quantum-well heterostructure laser diodes operated (cw, 300 K) in an external-grating cavity," *J. Appl. Phys.* **57**, 1489.

EPLER, J. E., HOLONYAK, N., BURNHAM, R. D., PAOLI, T. L., THORNTON, R. L. AND BLOUKE, M. M. (1985b). "Transverse modes of gain-guided coupled-stripe lasers: External cavity control of the emitter spacing," *Appl. Phys. Lett.* **47**, 7.

FORREST, K. A. AND ABSHIRE, J. B. (1987). "Time evolution of pulsed far-field patterns of GaAlAs phase-locked laser-diode arrays," *IEEE J. Quantum Electron.* **QE-23**, 1287.

FUHR, P. L. (1985). "Wavelength fluctuations in pulsed variable spacing phase-locked laser diode arrays," *Electron. Lett.* **21**, 697.

FUJII, H., SUEMUNE, I. AND YAMANISHI, M. (1985). "Analysis of transverse modes of phase-locked multi-stripe lasers," *Electron. Lett.* **21**, 713.

GARMIRE, E. M. AND TAVIS, M. T. (1984). "Heatsink requirements for coherent operation of high-power semiconductor laser arrays," *IEEE J. Quantum Electron.* **QE-20**, 1277; and correction: *IEEE J. Quantum Electron.* **QE-21**, 1736 (1985).

GARMIRE, E. M. (1988). "Tolerances for phase locking of semiconductor laser arrays," *Report SD-TR*-88-55, Space Division, Air Force Systems Command, Los Angeles, CA.

GOLDBERG, L., TAYLOR, H. F., WELLER, J. F. AND SCIFRES, D. R. (1985). "Injection locking of coupled-stripe diode laser arrays," *Appl. Phys. Lett.* **46**, 236.

GOLDSTEIN, B., CARLSON, N. W., EVANS, G. A., DINKEL, N. A. AND MASIN, V. J. (1987). "Performance of a channelled-substrate-planar high-power phase-locked array operating in the diffraction limit," *Electron. Lett.* **23**, 1136.

HADLEY, G. R. (1985). "Cavity supermodes for gain-saturated diode laser arrays," *J. Appl. Phys.* **58**, 97.

HADLEY, G. R. (1986). "Numerical simulation of gain-guided diode laser arrays," *SPIE* **642** (Modulation and Simulation of Optoelectronic Systems), 68.

HADLEY, G. R., HOHIMER, J. P. AND OWYOUNG, A. (1986a). "High-order ($\nu > 10$) eigenmodes in ten-stripe gain-guided diode laser arrays," *Appl. Phys. Lett.* **49**, 684.

HADLEY, G. R., OWYOUNG, A. AND HOHIMER, J. P. (1986b). "Modeling of injection-locking phenomena in diode-laser arrays," *Optics Lett.* **11**, 144.

HADLEY, G. R., HOHIMER, J. P. AND OWYOUNG, A. (1987a). "Free-running modes for gain-guided diode laser arrays," *IEEE J. Quantum Electron.* **QE-23**, 765.

HADLEY, G. R., HOHIMER, J. P. AND OWYOUNG, A. (1987b). "Influence of thermal effects on the eigenmodes of gain-guided diode laser arrays," *J. Appl. Phys.* **61**, 1697.

HADLEY, G. R., HOHIMER, J. P. AND OWYOUNG, A. (1988). "Comprehensive modeling of diode arrays and broad-area devices with applications to lateral index tailoring," *IEEE J. Quantum Electron.* **QE-24**, 2138.

HADLEY, G. R. (1989a). "Two-dimensional waveguide modeling of leaky-mode arrays," *Optics Letters* **14**, 859.

HADLEY, G. R. (1989b). "Index-guided arrays with a large index step," *Optics Letters* **14**, 308.

HARDY, A. AND STREIFER, W. (1985a). "Analysis of phased-array diode lasers," *Optics Lett.* **10**, 335.

HARDY, A. AND STREIFER, W. (1985b). "Coupled mode theory of parallel waveguides," *IEEE J. Lightwave Technol.* **LT-3**, 1135.

HARDY, A. AND STREIFER, W. (1986a). "Coupled modes of multiwaveguide systems and phased arrays," *IEEE J. Lightwave Technol.* **LT-4**, 90.

HARDY, A. AND STREIFER, W. (1986b). "Coupled mode solutions of multi-waveguide systems," *IEEE J. Quantum Electron.* **QE-22**, 528.

HEIDEL, J. R., RICE, R. R. AND APPELMAN, H. R. (1986). "Use of a phase corrector plate to generate a single-lobed phased array far field pattern," *IEEE J. Quantum Electron.* **QE-22**, 749.

HERMANSSON, B. AND YEVICK, D. (1989). "Analysis of Y-junction and coupled laser arrays," *Appl. Opt.* **28**, 66.

HOHIMER, J. P., OWYOUNG, A. AND HADLEY, G. R. (1985). "Single-channel injection locking of a diode-laser array with a cw dye laser," *Appl. Phys. Lett.* **47**, 1244.

HOHIMER, J. P., HADLEY, G. R. AND OWYOUNG, A. (1986). "Interelement coupling in gain-guided diode laser arrays," *Appl. Phys. Lett.* **48**, 1504.

HOHIMER, J. P., MYERS, D. R., BRENNAN, T. M. AND HAMMONS, E. (1989a). "Integrated injection locking of high power cw diode laser arrays," Conf. on Lasers and Electro-optics, Baltimore, MD. Pap. THS2.

HOHIMER, J. P., MYERS, D. R., BRENNAN, T. M. AND HAMMONS, B. E. (1989b). "Integrated injection-locked high-power cw diode laser arrays," *Appl. Phys. Lett.* **55**, 531.

JANSEN, M., YANG, J. J., OU, S. S., BOTEZ, D., WILCOX, J. AND MAWST, L. (1989). "Diffraction-limited operation from monolithically integrated diode laser array and self-imaging (Talbot) cavity," *Appl. Phys. Lett.* **55**, 1949.

JOYCE, W. B. (1980). "Current-crowded carrier confinement in double-hetero-structure lasers," *J. Appl. Phys.* **51**, 2394.

JOYCE, W. B. (1982a). "Carrier transport in double-heterostructure active layers," *J. Appl. Phys.* **53**, 7235.

JOYCE, W. B. (1982b). "Role of the conductivity of the confining layers in the DH-laser spatial hole burning effects," *IEEE J. Quantum Electron.* **QE-18**, 2005.

KANENO, N., KADOWAKI, T., OHSAWA, J., AOYAGI, T., HINATA, S., IKEDA, K. AND SUSAKI, W. (1985). "Phased array of AlGaAs multistripe index-guided lasers," *Electron. Lett.* **21**, 780.

KAPON, E., KATZ, J., LINDSEY, C., MARGALIT, S. AND YARIV, A. (1983). "Control of mutual phase locking of monolithically integrated semiconductor lasers," *Appl. Phys. Lett.* **43**, 421.

KAPON, E., KATZ, J. AND YARIV, A. (1984a). "Supermode analysis of phase-locked arrays of semiconductor lasers," *Opt. Lett.* **10**, 125.

KAPON, E., KATZ, J., MARGALIT, S. AND YARIV, A. (1984b). "Longitudinal-mode control in integrated semiconductor laser phased arrays by phase velocity matching," *Appl. Phys. Lett.* **44**, 157.

KAPON, E., LINDSEY, C., KATZ, J., MARGALIT, S. AND YARIV, A. (1984c). "Coupling mechanism of gain-guided integrated semiconductor laser arrays," *Appl. Phys. Lett.* **44**, 389.

KAPON, E., KATZ, J., MARGALIT, S. AND YARIV, A. (1984d). "Controlled fundamental supermode operation of phase-locked arrays of gain-guided diode lasers," *Appl. Phys. Lett.* **45**, 600.

KAPON, E., LINDSEY, C., KATZ, J. AND YARIV, A. (1984e). "Chirped arrays of diode lasers for supermode control," *Appl. Phys. Lett.* **45**, 200.

KAPON, E., LINDSEY, C. P., SMITH, J. S., MARGALIT, S. AND YARIV, A. (1984f). "Inverted-V chirped phased arrays of gain-guided GaAs/GaAlAs diode lasers," *Appl. Phys. Lett.* **45**, 1257.

KAPON, E., RAV-NOY, Z., LU, L. T., YI, M., MARGALIT, S. AND YARIV, A. (1984g). "Phase-locking characteristics of coupled ridge-waveguide InP/InGaAsP diode lasers," *Appl. Phys. Lett.* **45**, 1159.

KAPON, E., LU, L. T., RAV-NOY, Z., YI, M., MARGALIT, S. AND YARIV, A. (1985). "Phased arrays of buried-ridge InP/InGaAsP diode lasers," *Appl. Phys. Lett.* **46**, 136.

KAPON, E., RAV-NOY, Z., MARGALIT, S. AND YARIV, A. (1986). "Phase-locked arrays of buried-ridge InP/InGaAsP diode lasers," *IEEE J. Lightwave Technol.* **LT-4**, 919.

KAPON, E. (1987a). "The supermode structure of phase-locked diode laser arrays with variable channel spacing," *IEEE J. Quantum Electron.* **QE-23**, 89.

KAPON, E. (1987b). "Nonuniform phased arrays of diode lasers for fundamental supermode operation," *Electron. Lett.* **23**, 879.

KATZ, J., KAPON, E., LINDSEY, C., MARGALIT, S., SHRETER, U. AND YARIV, A. (1983a). "Phase-locked semiconductor laser array with separate contacts," *Appl. Phys. Lett.* **43**, 521.

KATZ, J., KAPON, E., LINDSEY, C., MARGALIT, S. AND YARIV, A. (1983b). "Far-field distributions of semiconductor phase-locked arrays with multiple contacts," *Electron. Lett.* **19**, 660.

KATZ, J., MARGALIT, S. AND YARIV, A. (1983c). "Diffraction coupled phase-locked semiconductor laser array," *Appl. Phys. Lett.* **42**, 554.

KATZ, J., KAPON, E., LINDSEY, C., MARGALIT, S. AND YARIV, A. (1984a). "Coupling coefficient of gain-guided lasers," *Appl. Opt.* **23**, 2231.

KATZ, J., KAPON, E., MARGALIT, S. AND YARIV, A. (1984b). "Rate equations analysis of phase-locked semiconductor laser arrays under steady state conditions," *IEEE J. Quantum Electron.* **QE-20**, 875.

KATZ, J. AND MARSHALL, W. K. (1985). "Gain saturation effects in supermodes of phase-locked semiconductor laser arrays," *Electron. Lett.* **21**, 974.

KUMAR, T., ORMONDROYD, R. F. AND ROZZI, T. E. (1985). "Numerical solution of lateral current spreading and diffusion in near-threshold DH twin-stripe lasers," *IEEE J. Quantum Electron.* **QE-21**, 421.

KUMAR, T. (1987). "Steady-state self-consistent analysis of diode-laser arrays," *Appl. Phys. Lett.* **50**, 877.

LAY, T.-S., LEE, S.-C. AND LIN, H.-H. (1989). "Y-Junction and misaligned-stripe diode laser arrays with nonuniform reflective diffraction coupler," *IEEE J. Quantum Electron.* **QE-25**, 689.

LEGER, J. R. AND SNYDER, M. A. (1984). "Real-time depth measurement and display using Fresnel diffraction and white-light processing," *Appl. Opt.* **23**, 1655.

LEGER, J. R., SCOTT, M. L. AND VELDKAMP, W. B. (1988). "Coherent addition of AlGaAs lasers using microlenses and diffractive coupling," *Appl. Phys. Lett.* **52**, 1771.

LEGER, J. R. AND HOLZ, M. (1988). "Binary optical elements for coherent addition of laser diodes," *Conf. Proc., Lasers and Electro-optics Society Ann. Mtg.*, Santa Clara, CA. Pap. FE.2.

LINDSEY, C. P., KAPON, E., KATZ, J., MARGALIT, S. AND YARIV, A. (1984). "Single contact tailored gain phased array of semiconductor lasers," *Appl. Phys. Lett.* **45**, 722.

LINDSEY, C., DERRY, P. AND YARIV, A. (1985). "Fundamental lateral mode oscillation via gain tailoring in broad area semiconductor lasers," *Appl. Phys. Lett.* **47**, 560.

LINDSEY, C. P., MEHUYS, D. AND YARIV, A. (1987). "Linear tailored gain broad area semiconductor lasers," *IEEE J. Quantum Electron.* **QE-23**, 775.

MAJOR, J. S. Jr., HALL, D. C., GUIDO, L. J., HOLONYAK, N. Jr., GAVRILOVIC, P., MEEHAN, K., WILLIAMS, J. E. AND STUTIUS, W. (1989). "High-power disorder-defined coupled stripe $Al_yGa_{1-y}As$-GaAs-$In_xGa_{1-x}As$ quantum well heterostructure lasers," *Appl. Phys. Lett.* **55**, 271.

MARCUSE, D. (1974). *Theory of Dielectric Optical Waveguides*, Sect. 1.5. Academic Press, New York.

MARSHALL, W. K. AND KATZ, J. (1986). "Direct analysis of gain-guided phase-locked semiconductor laser arrays," *IEEE J. Quantum Electron.* **QE-22**, 827.

MATSUMOTO, M., TANEYA, M., MATSUI, S., YANO, S. AND HIJIKATA, T. (1985). "Stable supermode operation in phase-locked laser diode arrays with three index waveguides," *J. Appl. Phys.* **58**, 2783.

MATSUMOTO, M., TANEYA, M., MATSUI, S., YANO, S. AND HIJIKATA, T. (1987). "Single-lobed far-field pattern operation in a phased array with an integrated phase shifter," *Appl. Phys. Lett.* **50**, 1541.

MAWST, L. J., GIVENS, M. E., EMANUEL, M. A., ZMUDZINSKI, C. A. AND COLEMAN, J. J. (1986). "Phase-locked shallow mesa graded barrier quantum well laser arrays," *Appl. Phys. Lett.* **48**, 1337.

MAWST, L. J., BOTEZ, D., ROTH, T. J., PETERSON, G. AND YANG, J. J. (1988a). "Diffraction-coupled, phase-locked arrays of antiguided, quantum-well lasers grown by metalorganic chemical vapor deposition," *Electron. Lett.* **24**, 958.

MAWST, L. J., BOTEZ, D. AND ROTH, T. J. (1988b). "High-power, diffraction-limited-beam operation from diode-laser phase-locked arrays operating in coupled first-order modes," *Appl. Phys. Lett.* **53**, 1236.

MAWST, L. J., BOTEZ, D., ROTH, T. J. AND YANG, J. J. (1988c). "Diffraction-limited beam operation from quantum-well laser phase-locked array grown by metal-organic chemical vapour deposition," *Electron. Lett.* **24**, 570.

MAWST, L. J., BOTEZ, D., ROTH, T. J., SIMMONS, W. W., PETERSON, G., JANSEN, M., WILCOX, J. Z. AND YANG, J. J. (1989a). "Phase-locked array of antiguided lasers with monolithic spatial filter," *Electron. Lett.* **25**, 365.

MAWST, L. J., BOTEZ, D., ROTH, T. J. AND PETERSON, G. (1989b). "High-power, in-phase-mode operation from resonant phase-locked arrays of antiguided diode lasers," IEEE/OSA Conference on Lasers and Electro-Optics, Baltimore, MD. Pap. PD-12.

MAWST, L. J., BOTEZ, D., ROTH, T. J. AND PETERSON, G. (1989c). "High-power, in-phase-mode operation from resonant phase-locked arrays of antiguided diode lasers," *Appl. Phys. Lett.* **55**, 10.

MAWST, L. J., BOTEZ, D., JANSEN, M., ROTH, T. J. AND PETERSON, G. (1989d). "High-power, narrow single-lobe operation from 20-element phase-locked arrays of antiguides," *Appl. Phys. Lett.* **55**, 2060.

MEHUYS, D., MITSUNAGA, K., ENG, L., MARSHALL, W. K. AND YARIV, A. (1988). "Supermode control in diffraction-coupled semiconductor laser arrays," *Appl. Phys. Lett.* **53**, 1165.

MUKAI, S., LINDSEY, C., KATZ, J., KAPON, E., RAV-NOY, Z., MARGALIT, S. AND YARIV, A. (1984). "Fundamental mode oscillation of a buried ridge waveguide laser array," *Appl. Phys. Lett.* **45**, 834.

NISHI, K. AND LANG, R. (1985). "Lateral mode localization in multistripe laser diode," *Jap. J. Appl. Phys.* **24**, L349.

NOVOSELLER, D. E. AND BOTEZ, D. (1989). "Phase-locked laser array far-field normalization," *IEEE J. Quantum Electron.* **QE-25**, 1179.

OHSAWA, J., IKEDA, K., TAKAHASHI, K. AND SUSAKI, W. (1983). "A dual-stripe phase-locked diode laser," *Jap. J. Appl. Phys.* **22**, L230.

OHSAWA, J., HINATA, S., AOYAGI, T., KADOWAKI, T., KANENO, N., IKEDA, K. AND SUSAKI, W. (1985). "Triple-stripe phase-locked diode lasers emitting 100 mW cw with single-lobed far-field patterns," *Electron. Lett.* **21**, 779.

OTSUKA, K. (1977). "A proposal on coupled waveguide lasers," *IEEE J. Quantum Electron.* **QE-13**, 895.

OTSUKA, K. (1983). "Coupled-wave theory regarding phase-locked-array lasers," *Electron. Lett.* **19**, 723.

PAISS, I. AND HARDY, A. (1989). "A coupled-mode analysis of twin-stripe index-guided lasers," *IEEE J. Quantum Electron.* **QE-25**, 1609.

PAOLI, T. L., STREIFER, W. AND BURNHAM, R. D. (1984). "Observation of supermodes in a phase-locked diode laser array," *Appl. Phys. Lett.* **45**, 217.

PAPANNAREDDY, R., FERGUSON, W. AND BUTLER, J. K. (1987). "Current spreading and carrier diffusion in zinc-diffused multiple-stripe-geometry lasers," *Appl. Phys. Lett.* **50**, 1316.

REDIKER, R. H. AND LEONBERGER, F. J. (1982). "Analysis of integrated-optics near 3dB coupler and Mach-zender interferometric modulator using four-port scattering matrix," *IEEE J. Quantum Electron.* **QE-18**, 1813.

REINHOUDT, C. J. AND VAN DER POEL, C. J. (1989). "Array modes of longitudinally varying laser array geometries," *IEEE J. Quantum Electron.* **QE-25**, 1553.

RIPPER, J. E. AND PAOLI, T. L. (1970). "Optical coupling of adjacent stripe-geometry junction lasers," *Appl. Phys. Lett.* **17**, 371.

ROYCHOUDHURI, C., SIEBERT, E., D'AMATO, F., NOLL, R., MACOMBER, S., KINTNER, E. AND ZWEIG, D. (1988). "Review of compact cavities for coherent array lasers," Conf. Proc., Lasers and Electro-optics Society Ann. Mtg., Santa Clara, CA. Pap. FE.4.

ROZZI, T. E. AND SHORE, K. A. (1985). "Spatial and temporal instabilities in multistripe semiconductor lasers," *J. Opt. Soc. Am.* **B2**, 237.

SAGAWA, M. AND KAJIMURA, T. (1989). "Complete single lateral 180° phase mode operation for AlGaAs phased array lasers," *Appl. Phys. Lett.* **55**, 1376.

SAKAMOTO, M., WELCH, D. F., ENDRIZ, J. G., SCIFRES, D. R. AND STREIFER, W. (1989). "76 W cw monolithic laser diode arrays," *Appl. Phys. Lett.* **54**, 2299.

SALZMAN, J. AND YARIV, A. (1986). "Phase-locked arrays of unstable resonator semiconductor lasers," *Appl. Phys. Lett.* **49**, 440.

SCIFRES, D. R., STREIFER, W. AND BURNHAM, R. D. (1978a). "Beam scanning and wavelength modulation with branching waveguide stripe injection lasers," *Appl. Phys. Lett.* **33**, 616.

SCIFRES, D. R., BURNHAM, R. D. AND STREIFER, W. (1978b). "Phase-locked semiconductor laser array," *Appl. Phys. Lett.* **33**, 1015.

SCIFRES, D. R., STREIFER, W. AND BURNHAM, R. D. (1979a). "High-power coupled-multiple-stripe phase-locked injection laser," *Appl. Phys. Lett.* **34**, 259.

SCIFRES, D. R., STREIFER, W. AND BURNHAM, R. D. (1979b). "Experimental and analytic studies of coupled multiple stripe diode lasers," *IEEE J. Quantum Electron.* **QE-15**, 917.

SCIFRES, D. R., BURNHAM, R. D., STREIFER, W. AND BERNSTEIN, M. (1982a). "Lateral beam collimation of a phased array semiconductor laser," *Appl. Phys. Lett.* **41**, 614.

SCIFRES, D. R., SPRAGUE, W., STREIFER, W. AND BURNHAM, R. D. (1982b). "Focusing of a 7700-Å high power phased array semiconductor laser," *Appl. Phys. Lett.* **41**, 1121.

SCIFRES, D. R., BURNHAM, R. D. AND STREIFER, W. (1982c). "High power coupled multiple stripe quantum well injection lasers," *Appl. Phys. Lett.* **41**, 118.

SCIFRES, D. R., BURNHAM, R. D. AND STREIFER, W. (1982d). "Lateral grating array high power cw visible semiconductor laser," *Electron. Lett.* **18**, 549.

SCIFRES, D. R., STREIFER, W., BURNHAM, R. D., PAOLI, T. L. AND LINDSTROM, C. (1983a). "Near-field and far-field patterns of phase-locked semiconductor laser arrays," *Appl. Phys. Lett.* **42**, 495.

SCIFRES, D. R., BURNHAM, R. D., LINDSTROM, C., STREIFER, W. AND PAOLI, T. L. (1983b). "Phase-locked (GaAl)As laser emitting 1.5 W cw per mirror," *Appl. Phys. Lett.* **42**, 645.

SCIFRES, D. R., LINDSTROM, C., BURNHAM, R. D., STREIFER, W. AND PAOLI, T. L. (1983c). "Phase-locked (GaAl)As laser diode emitting 2.6 W cw from a single mirror," *Electron. Lett.* **19**, 169.

SEIWA, Y., AOYAGI, T., HINATA, S., KADOWAKI, T., KANENO, N., IKEDA, K. AND SUSAKI, W. (1987). "High power cw operation over 400 mW on five-stripe phase-locked laser arrays assembled by new junction down mounting," *J. Appl. Phys.* **61**, 440.

SHINOZAKI, K., FURUKAWA, R., FUKUNAGA, T. AND WATANABE, N. (1989). "Supermode control and phase front measurements of phase-locked offset-coupled laser arrays with a large optical waveguide structure," *J. Appl. Phys.* **66**, 1057.

SHORE, K. A. (1984). "Analysis of closely-spaced index-guided semiconductor lasers. I. Multistripe devices," *Optical and Quantum Electron.* **16**, 235.

SOMEKH, S., GARMIRE, E., YARIV, A., GARVIN, H. L. AND HUNSPERGER, R. G. (1973). "Channel optical waveguide directional couplers," *Appl. Phys. Lett.* **22**, 46.

STREIFER, W., BURNHAM, R. D., PAOLI, T. L. AND SCIFRES, D. R. (1984). "Phased array diode lasers," *Laser Focus/Electro-Optics* **20** (June), 100.

STREIFER, W., HARDY, A., BURNHAM, R. D. AND SCIFRES, D. R. (1985a). "Single-lobe phased-array diode lasers," *Electron. Lett.* **21**, 118.

STREIFER, W., HARDY, A., BURNHAM, R. D., THORNTON, R. L. AND SCIFRES, D. R. (1985b). "Criteria for design of single-lobe phased-array diode lasers," *Electron. Lett.* **21**, 505.

STREIFER, W., OSINSKI, M., SCIFRES, D. R., WELCH, D. F. AND CROSS, P. S. (1986a). "Phased-array lasers with a uniform, stable supermode," *Appl. Phys. Lett.* **49**, 1496.

STREIFER, W., CROSS, P. S., WELCH, D. F. AND SCIFRES, D. R. (1986b). "Analysis of a Y-junction semiconductor laser array," *Appl. Phys. Lett.* **49**, 58.

STREIFER, W., WELSH, D. F., CROSS, P. F. AND SCIFRES, D. R. (1987). "Y-junction semiconductor laser arrays: Part I—Theory," *IEEE J. Quantum Electron.* **QE-23**, 744.

STREIFER, W., WELSH, D. F., BERGER. J., CROSS, P. F. AND SCIFRES, D. R. (1988). "Losses in Y-junction semiconductor laser arrays," *Appl. Phys. Lett.* **52**, 1297.

STREIFER, W., WELSH, D. F., BERGER, J. AND SCIFRES, D. R. (1989a). "Above-threshold analysis of ideal Y-junction semiconductor laser arrays," *Appl. Phys. Lett.* **54**, 409.

STREIFER, W., WELSH, D. F., BERGER, J. AND SCIFRES, D. R. (1989b). "Nonlinear analysis of Y-junction laser arrays," *IEEE J. Quantum Electron.* **QE-25**, 1617.

SUEMUNE, I., TERASHIGE, T. AND YAMANISHI, M. (1984). "Phase-locked, index-guided multiple-stripe lasers with large refractive index differences," *Appl. Phys. Lett.* **45**, 1011.

TANEYA, M., MATSUMOTO, M., MATSUI, S., YANO, S. AND HIJIKATA, T. (1985). "0° phase mode operation in phased-array laser diode with symmetrically branching waveguide," *Appl. Phys. Lett.* **47**, 341.

TANEYA, M., MATSUMOTO, M., KAWANISHI, H., MATSUI, S., YANO, S. AND HIJIKATA, T. (1986). "Phased-array with the 'YY' shaped symmetrically branching waveguide (SBW)," *Jap. J. Appl. Phys.* **25**, L432.

TANEYA, M., MATSUMOTO, M., MATSUI, S., YANO, S. AND HIJIKATA, T. (1987). "Stable quasi 0° phase mode operation in a laser array diode nearly aligned with a phase shifter," *Appl. Phys. Lett.* **50**, 783.

TAVIS, M. T. AND GARMIRE, E. M. (1984). "Improved heat-sink design for coherent laser arrays," *Electron. Lett.* **20**, 689.

TAYLOR, H. F. AND YARIV, A. (1974). "Guided wave optics," *Proc. IEEE* **62**, 1044.

TEMKIN, H., LOGAN, R. A., VAN DER ZIEL, J. P., REYNOLDS, C. L. JR. AND THARALDSEN, S. M. (1985). "Index-guided arrays of Schottky barrier confined lasers," *Appl. Phys. Lett.* **46**, 465.

THANIYAVARN, S. AND DOUGHERTY, W. (1987). "Generation of a single-lobe radiation pattern from a phased-array laser using a near-contact variable phase-shift zone plate," *Electron. Lett.* **23**, 5.

THOMPSON, G. H. B. AND WHITEAWAY, J. E. A. (1987). "Analysis of the stability of the highest-order supermode in semiconductor laser arrays," *Electron. Lett.* **23**, 444.

THORNTON, R. L., BURNHAM, R. D., PAOLI, T. L., HOLONYAK, N. JR. AND DEPPE, D. G. (1986). "Highly efficient multiple emitter index guided array lasers fabricated by silicon impurity induced disordering," *Appl. Phys. Lett.* **48**, 7.

TSANG, W. T., LOGAN, R. A. AND SALATHE, R. P. (1979). "A densely packed monolithic linear array of GaAs-$Al_xGa_{1-x}As$ strip buried heterostructure laser," *Appl. Phys. Lett.* **34**, 162.

TWU, Y., DIENES, A., WANG, S. AND WHINNERY, J. R. (1984). "High power coupled ridge waveguide semiconductor laser arrays," *Appl. Phys. Lett.* **45**, 709.

TWU, Y., CHEN, K.-L., DIENES, A., WANG, S. AND WHINNERY, J. R. (1985). "High-performance index-guided phase-locked semiconductor laser arrays," *Electron. Lett.* **21**, 324.

TWU, Y., CHEN, K.-L., WANG, S., WHINNERY, J. R. AND DIENES, A. (1986). "Eigenmode analysis of phase-locked semiconductor laser arrays," *Appl. Phys. Lett.* **48**, 16; and erratum: *ibid*, **48**, 811.

TWU, Y., WANG, S., WHINNERY, J. R. AND DIENES, A. (1987). "Mode characteristics of phase-locked semiconductor laser arrays at and above threshold," *IEEE J. Quantum Electron.* **QE-23**, 788.

VAN DER ZIEL, J. P., MIKULYAK, R. M., TEMKIN, H., LOGAN, R. A. AND DUPUIS, R. D. (1984a). "Optical beam characteristics of Schottky barrier confined arrays of phase-coupled multiquantum well GaAs lasers," *IEEE J. Quantum Electron.* **QE-20**, 1259.

VAN DER ZIEL, J., TEMKIN, H., LOGAN, R. A. AND DUPUIS, R. D. (1984b). "High-power picosecond pulse generation in GaAs multiquantum well phase-locked laser arrays using pulsed current injection," *IEEE J. Quantum Electron.* **QE-20**, 1236.

VERDIELL, J.-M., RAJENBACH, H. AND HUIGNARD, J.-P. (1989a). "Perturbation model for explaining the observed transverse mode patterns in diode laser arrays," Conf. on Lasers and Electro-optics, Baltimore, MD. *Pap. THS*3.

VERDIELL, J.-M., RAJENBACH, H. AND HUIGNARD, J.-P. (1989b). "Array modes of multiple-stripe diode lasers: A broad-area mode coupling approach," *J. Appl. Phys.* **66**, 1466.

WANG, S., WILCOX, J. Z., JANSEN, M. AND YANG, J. J. (1986). "In-phase locking in diffraction-coupled phased-array diode lasers," *Appl. Phys. Lett.* **48**, 1770.

WANG, S. S. AND WINFUL, H. G. (1988). "Dynamics of phase-locked semiconductor laser arrays," *Appl. Phys. Lett.* **52**, 1774.

WELCH, D. F., SCIFRES, D., CROSS, P., KUNG, H., STREIFER, W., BURNHAM, R. D., YAELI, J. AND PAOLI, T. L. (1985a). "High power cw operation of phased array diode lasers with diffraction limited output beam," *Appl. Phys. Lett.* **47**, 1134.

WELCH, D. F., SCIFRES, D., CROSS, P., KUNG, H., STREIFER, W., BURNHAM, R. D. AND YAELI, J. (1985b). "High-power (575 mW) single-lobed emission from a phased-array laser," *Electron. Lett.* **21**, 603.

WELCH, D. F., CROSS, P. S., SCIFRES, D. R., HARNAGEL, G., CARDINAL, M., STREIFER, W. AND BURNHAM, R. D. (1986a). "High-power and high-efficiency phased array lasers grown by a two-step metalorganic chemical vapour deposition," *Electron. Lett.* **22**, 464.

WELCH, D. F., CROSS, P., SCIFRES, D., STREIFER, W. AND BURNHAM, R. D. (1986b). "In-phase emission from index-guided laser array up to 400 mW," *Electron. Lett.* **22**, 293.

WELCH, D. F., CROSS, P. S., SCIFRES, D. R., STREIFER, W. AND BURNHAM, R. D. (1986c). "High-power (cw) in-phase locked 'Y' coupled laser arrays," *Appl. Phys. Lett.* **49**, 1632.

WELCH, D. F., CROSS, P. S., SCIFRES, D. R., STREIFER, W. AND BURNHAM, R. D. (1986d). "Properties of AlGaAs buried heterostructure lasers and laser arrays grown by a two-step metalorganic chemical vapor deposition," *Appl. Phys. Lett.* **48**, 1716.

WELCH, D. F., STREIFER, W., CROSS, P. S. AND SCIFRES, D. R. (1987a). "Y-junction semiconductor laser arrays: Part II—Experiments," *IEEE J. Quantum Electron.* **QE-23**, 752.

WELCH, D. F., CROSS, P. S., SCIFRES, D. R., STREIFER, W. AND BURNHAM, D. (1987b). "High power, AlGaAs buried heterostructure lasers with flared waveguides," *Appl. Phys. Lett.* **50**, 233.

WELCH, D. F., CROSS, P. S., SCIFRES, D. R. AND STREIFER, W. (1987c). "Single-lobe 'Y' coupled laser diode arrays," *Electron. Lett.* **23**, 270.

WHITEAWAY, J. E. A., THOMPSON, G. H. B. AND GOODWIN, A. R. (1985). "Mode stability in real index-guided semiconductor laser arrays," *Electron. Lett.* **21**, 1194.

WHITEAWAY, J. E. A. (1986). "Zero-order supermode discrimination in semiconductor laser arrays," *Electron. Lett.* **22**, 560.

WHITEAWAY, J. E. A., MOULE, D. J. AND CLEMENTS, S. J. (1989). "Tree array lasers," *Electron. Lett.* **25**, 779.

WILCOX, J. Z., YANG, J. J. AND JANSEN, M. (1987a). "Coupled-mode analysis of a periodic array of diode lasers," *Electron. Lett.* **23**, 69.

WILCOX, J. Z., JANSEN, M., YANG, J. J., OU, S. S., SERGANT, M. AND SIMMONS, W. W. (1987b). "Supermode selection in diffraction-coupled semiconductor laser arrays," *Appl. Phys. Lett.* **50**, 1319.

WILCOX, J. Z., JANSEN, M., YANG, J., PETERSON, G., SILVER, A., SIMMONS, W., OU, S. S. AND SERGANT, M. (1987c). "Supermode discrimination in diffraction-coupled laser arrays with separate contacts," *Appl. Phys. Lett.* **51**, 631.

WILCOX, J. Z., SIMMONS, W. W., BOTEZ, D., JANSEN, M., MAWST, L. J., PETERSON, G., WILCOX, T. J. AND YANG, J. J. (1989). "Design considerations for diffraction coupled arrays with monolithically integrated self-imaging cavities," *Appl. Phys. Lett.* **54**, 1848.

YANG, J. J. AND JANSEN, M. (1986). "Single-lobed emission from phase-locked array lasers," *Electron. Lett.* **22**, 2.

YAP, D., WALPOLE, J. N. AND LIAU, Z. L. (1989). "Novel scalloped-mirror diffraction-coupled InGaAsP/InP buried-heterostructure laser arrays," *Appl. Phys. Lett.* **54**, 687.

YU, N., DEFREEZ, R. K., BOSSERT, D. J., ELLIOTT, R. A., WINFUL, H. G. AND WELCH, D. F. (1988). "Self-pulsation in cw operated flared Y-coupled laser arrays," *Electron. Lett.* **24**, 1203.

ZMUDZINSKI, C. A., GIVENS, M. E., BRYAN, R. P. AND COLEMAN, J. J. (1989). "Optical characteristics of high-power nonplanar periodic laser arrays," *IEEE J. Quantum Electron.* **QE-25**, 1539.

ZUCKER, E. P., HASHIMOTO, A., FUKUNAGA, T. AND WATANABE, N. (1988). "Phased-array laser diode with buried optical guides and inverted current injection," *Jap. J. Appl. Phys.* **27**, 2177.

Chapter 3

VERTICAL-CAVITY SURFACE EMITTING LASERS AND ARRAYS

Kenichi Iga and **Fumio Koyama**

Tokyo Institute of Technology, Nagatsuta 4259, Midori-ku, Yokohama 227, Japan

In this chapter, we describe the research progress of vertical cavity surface emitting (SE) injection lasers based on GaAlAs/GaAs, GaInAsP/InP, and GaInAs/GaAs systems. Ultimate laser characteristics, device design, state-of-the-art performances, possible device improvement, and future prospects will also be discussed.

The SE laser is very attractive for future lightwave systems and rather broad applications to opto-electronics by taking advantage of its two-dimensional array configurations.

The authors of this chapter proposed a vertical-cavity SE semiconductor laser in 1977, and efforts to fabricate one were researched. In order to reduce the threshold current, we made several improvements in the laser reflector and introduced a circular buried heterostructure (CBH) for effective current confinement. The micro-cavity structure of 7 μm in length and 6 μm in diameter provided a low threshold operation. A room-temperature cw operation of a vertical cavity SE laser was thus obtained in 1988, and preferable lasing characteristics such as stable single-mode operation and circular narrow beam emission were demonstrated. These results, therefore, triggered the research to challenge the realization of extremely low threshold SE laser devices and densely packed two-dimensional arrays.

ISBN 0-12-244070-6

I. INTRODUCTION

The importance of semiconductor lasers is rapidly increasing along with progress in the opto-electronics field, such as optical fiber communication and optical disk memories. However, in the present structure of cleaved semiconductor lasers, there are still some problems, e.g., the intial probe test of such devices is impossible before separating the device into chips, the monolithic integration of lasers into an optical circuit is limited due to the finite cavity length, etc. The authors suggested a vertical cavity surface emitting (SE) laser in 1977 for the purpose of overcoming such difficulties as mentioned above. Figure 1 shows a model of a Fabry–Perot resonator in vertical cavity SE lasers. The cavity is formed by the two surfaces of an epitaxial layer, and light output is taken vertically from one of the mirror surfaces. This method of laser structure, if utilized, can provide many novel advantages as follows:

1. A huge number of laser devices can be fabricated by fully monolithic processes.
2. A densely crammed two-dimensional laser array can be fabricated.
3. An ultra-low threshold operation can be expected.
4. The initial probe test can be performed before separating devices into discrete chips.
5. Dynamic single mode operation is made possible by a gain difference of neighboring modes with large mode spacing (=100–400 Å).
6. Vertical stacks of multi-thin-film functional optical devices can be integrated intact to an SE laser resonator.
7. A narrow circular beam with negligible astigmatism can be achieved.

A laser structure in which the emission is taken out perpendicular to the electrode was demonstrated by Melngailis (1965), with a bulk InSb at 10 K under an intense magnetic field. After Melngailis, some studies on an optically pumped platelet cavity laser with CdSe or CdS film were made by several groups (Stillman *et al.*, 1966; Basov *et al.*, 1966; Packard *et al.*, 1969; Smiley *et al.*, 1971). The suggestion of a double-heterostructure SE laser was made in 1977. The first lasing operation of a GaInAsP/InP SE laser device, in which the threshold was 900 mA under pulsed condition at 77 K was obtained in 1979 (Soda *et al.*, 1979). Prof. Y. Suematsu of Tokyo Institute of Technology gave the name *surface emitting laser* to this device. Since then, the authors' group has been studying a vertical cavity SE laser device with GaInAsP/InP and GaAlAs/GaAs systems (Soda *et al.*, 1979;

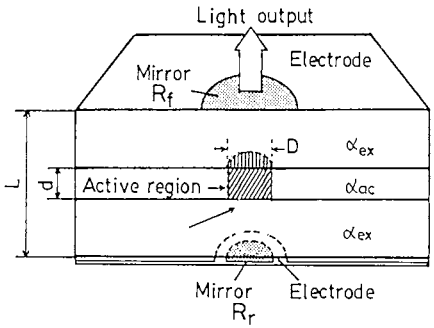

Fig. 1. A schematic diagram of an SE laser. The front side mirror is comparatively large compared with a mode spot size. The diameter of the rear side mirror is almost the same as that of the active region. (From Iga *et al.*, 1988. Copyright © 1988 IEEE.)

Iga *et al.*, 1988). The authors obtained a room-temperature pulsed operation in a GaAlAs/GaAs SE laser in 1983 (Iga *et al.*, 1983). It is advisable for a long-haul system and network to use GaInAsP/InP SE single-mode lasers emitting wavelengths of 1.3 μm or 1.5 μm, if obtainable. On the other hand, GaAlAs SE lasers are attractive for optical disks, optical sensing, and optical parallel processing.

The threshold current density of experimental SE lasers was rather high in comparison with a conventional stripe laser because of short gain region and insufficient reflectivity of the mirrors. For these reasons room-temperature cw operation of SE lasers was prevented until we succeeded in improvement of the structure in 1988. According to preliminary research, we recognized the following points as particularly important to reduce the threshold current of a vertical cavity SE laser;

1. High reflectivity of laser mirrors ($R > 95\%$)
2. Effective current confining structure.

In a preliminary structure (Soda *et al.*, 1979), a gold-zinc alloy mirror was used for a laser reflector and also served as an electrode. Therefore, the reflectivity was poor ($R < 0.8$), which caused a very high threshold current density. To increase the reflectivity of the *p*-side (bonding side) reflector, we introduced a ring electrode in which the reflecting mirror is separated from the electrode (Uchiyama *et al.*, 1984). In addition to this, we used a Au/SiO_2 mirror (Uchiyama and Iga, 1986a), or dielectric multi-layer reflector (Kinoshita *et al.*, 1987a), for improving the *n*-side (output side) reflectivity. For the purpose of effectively confining current in an active

region, various types of current confining structures were also introduced, i.e., a round-low mesa, round-high mesa/polyimid buried, and circular buried heterostructure (Uchiyama *et al.*, 1986b). By using a circular buried-heterostructure (CBH), the threshold was dramatically reduced, and a low threshold was obtained in a GaAlAs/GaAs system (Iga *et al.*, 1987;

Table I

Progress of our SE Laser Research*

Year	GaInAsP/InP SE Laser			GaAlAs/GaAs SE Laser		
1977	Suggestion					
1979	Planar	900 mA	(77 K, P)			
1981	BH	520 mA	(77 K, P)			
	PBH	800 mA	(77 K, P)			
1982	Short cavity	160 mA	(77 K, P)			
1983	Window/cap	50 mA	(77 K, P)	Short cavity	350 mA	(77 K, P)
		180 mA	(140 K, P)		1.2 A	(293 K, P)
1984	Two act.	145 mA	(77 K, P)	Ring electrode	510 mA	(293 K, P)
	Ring electrode	90 mA	(77 K, P)		310 mA	(293 K, P)
		720 mA	(188 K, P)			
	Low-mesa	60 mA	(77 K, P)			
		450 mA	(217 K, P)			
1985		35 mA	(77 K, P)	DMLR	400 mA	(293 K, P)
		700 mA	(252 K, P)			
	DBR	120 mA	(77 K, P)		250 mA	(293 K, P)
	PBH	250 mA	(77 K, P)	MBE	450 mA	(293 K, P)
	HMPB	85 mA	(77 K, P)	DMLR	150 mA	(293 K, P)
		600 mA	(225 K, P)			
	DMLR	65 mA	(77 K, P)			
	Au/SiO_2	18 mA	(77 K, P)			
		400 mA	(263 K, P)			
1986	CBH	24 mA	(77 K, P)	CBH	68 mA	(293 K, P)
	FCBH	20 mA	(77 K, P)		6 mA	(293 K, P)
					4.5 mA	(293 K, P)
				MOCVD	300 mA	(293 K, P)
1987	CBH	15 mA	(77 K, cw)	MOCVD-CBH	50 mA	(293 K, P)
					55 mA	(160 K, cw)
1988	FCBH	12 mA	(77 K, cw)	MOCVD-CBH	30 mA	(293 K, cw)
		6 mA	(77 K, cw)			

HMPB: high-mesa/polyimide-buried. DMLR: dielectric multilayer reflector. PBH: planar buried heterostructure. CBH: circular buried heterostructure. FCBH: flat surface circular buried heterostructure. MOCVD: metalorganic chemical vapor deposition. P: pulse. CW: continuous wave.

* From Iga *et al.*, 1988.

Kinoshita and Iga, 1987b). In 1988, we achieved the first room-temperature cw operation of a GaAlAs/GaAs SE laser (Koyama *et al.*, 1988b). Table I shows the progress of our SE laser research. After we had demonstrated some good characteristics of cw SE lasers, much attention was paid to these lasers, and many research groups such as AT&T, Bellcore and UCSB began to research the vertical-cavity SE laser.

On the other hand, other types of SE lasers, e.g., a distributed Bragg reflector (DBR) or distributed feedback (DFB) method using a higher-order coupling grating (Reinhart and Logan, 1975; Evans *et al.*, 1986; Scifres *et al.*, 1986); an SE laser using a 45° deflector (Springthorpe, 1977; Liau, 1985); and a turn-up or folded cavity structure using a 45° deflecting intra-cavity mirror or a bending waveguide (Wu *et al.*, 1987; Yuasa *et al.*, 1988), are extensively studied. Several fundamental characteristics of these lasers are summarized in Table II from the viewpoints of laser performance, two-dimensional laser array application, and coupling efficiency to other devices. In terms of laser performance itself, it is suggested that an extremely low

Table II

Characteristics of Some Types of SE Lasers*

	Laser Characteristics	2-D Laser Array Capability	Coupling with Other Devices
Vertical cavity	Narrow circular beam Single mode operation	Free arrangement Dense packing	Vertical stacking
Horizontal cavity grating coupling	Narrow beam in one direction	Limited by cavity length	Beam angle sensitive to the change of wavelength
45° Deflector	Single mode operation Compatible with conventional structure Beam quality dependent on mirror flatness	2-D phase-locking Limited by cavity length	Similar to stripe lasers
Turn-up cavity	Limited equivalent reflectivity Simple to manufacture	Limited by cavity length Difficult due to oblique output beam	Similar to stripe lasers Similar to stripe lasers

* From Iga *et al.*, 1988. Copyright © 1988 IEEE.

threshold may be expected in a vertical-cavity SE laser by introducing a microcavity structure with both a cavity length and active region diameter of several microns and a high-reflective mirror. Even if the reflectivity is as high as 95%, high differential quantum efficiency comparable to that of conventional stripe lasers can be achieved by taking advantage of short cavity length.

From the viewpoint of the two-dimensional array application the vertical cavity structure has more flexibility in its arrangement, so a densely packed two-dimensional array can be fabricated. The density of a two-dimensional stripe array is limited by a cavity length of about 300 μm. Moreover, coupling with other devices is easy in the vertical-cavity SE laser, since it emits a circular narrow beam that matches to the mode of a single-mode fiber.

Vertical-cavity SE lasers utilizing semiconductor multilayer reflectors such as a DBR (Chailertvanitkul *et al.*, 1985; Sakaguchi *et al.*, 1988) or DFB structure (Ogura *et al.*, 1984) may enable the integration of thin film functional optical devices onto an SE laser by stacking. This will open up a new scheme of three-dimensional integrated optics (Iga *et al.*, 1982). Such a thin multilayer structure can be obtained by utilizing finer growth techniques, such as metalorganic chemical vapor deposition (MOCVD), molecular beam epitaxy (MBE), or chemical beam epitaxy (CBE) that provide accurate thickness control and good surface morphology. Such growth techniques may accelerate further development of vertical-cavity SE lasers.

In this chapter, we will discuss the progress of vertical-cavity SE injection laser research. First, some anticipated device characteristics of a short-cavity SE laser will be presented. In particular, we shall estimate its threshold current, differential quantum efficiency, condition for cw operation, modulation bandwidth, etc. We will also consider an in-plane superluminescence effect. We shall next present necessary fabrication processes and experimental results on lasing characteristics of CBH SE lasers made of GaInAsP/InP and GaAlAs/GaAs systems. Finally, perspectives toward ultimate performances and future applications, including two-dimensional laser arrays will be discussed.

II. EXPECTED PERFORMANCES OF VERTICAL-CAVITY SURFACE EMITTING LASERS

A. Threshold Current and Quantum Efficiency

The schematic structure of a vertical-cavity SE laser is shown in Fig. 1. We consider a circular buried heterostructure, in which the active region is

buried in a material with smaller bandgap energy, and injected carriers are completely confined in the circular active region with diameter D. The optical loss for the resonant mode must balance the gain to reach the threshold. That is:

$$g_{th} = \alpha_{ac} + \alpha_{ex}\left(\frac{1}{\xi} - 1\right) + \frac{1}{\xi d}\ln\left(\frac{1}{R_f R_r}\right) + \alpha_d \tag{1}$$

where g_{th} is the threshold gain, d is the active layer thickness, L is the cavity length, α_{ac} and α_{ex} are the absorption loss in the active and cladding layers, respectively, R_f and R_r are the reflectivities of the front and rear side reflector, and α_d is the diffraction loss. ξ is the energy confinement factor, which is expressed as the product of the longitudinal confinement factor ξ_l and the transverse factor ξ_t as

$$\xi = \xi_l \cdot \xi_t. \tag{2}$$

ξ_l is expressed as

$$\xi_l = \gamma d / L. \tag{3}$$

When a very thin active layer ($\sim$100 Å) is placed at the maxima of standing wave, γ equals two, and it is unity for a thick active layer. The concept of reducing the threshold by placing the active layer at the maxima which is called *periodic gain structure* is suggested (Geels *et al.*, 1988; Raja *et al.*, 1988). This will be detailed in a later section.

If we assume that $\alpha_{ac} = 10\ \text{cm}^{-1}$, $\alpha_{ex} = 10\ \text{cm}^{-1}$, $\alpha_d = 10\ \text{cm}^{-1}$, $L = 7\ \mu\text{m}$, $d = 3\ \mu\text{m}$, and $g_{th} = 200\ \text{cm}^{-1}$ in Eq. (1), the necessary average reflectivity must be

$$\sqrt{R_f R_r} = 0.95. \tag{4}$$

The threshold gain is expressed in terms of the threshold carrier density N_{th} as

$$g_{th} = A_0 N_{th} - \alpha_{in} \tag{5}$$

where α_{in} is the residual absorption loss, and A_0 is the gain coefficient. Thus, the threshold carrier density N_{th} is expressed as

$$N_{th} = \frac{g_{th} + \alpha_{in}}{A_0}. \tag{6}$$

If we put $g_{th} = 200\ \text{cm}^{-1}$, $\alpha_{in} = 400\ \text{cm}^{-1}$ and $A_0 = 3 \times 10^{-16}\ \text{cm}^2$ for the GaAlAs/GaAs system, $N_{th} = 2 \times 10^{18}\ \text{cm}^{-3}$. The threshold current density

of the SE laser is then expressed as (Soda *et al.*, 1983)

$$J_{\text{th}} = \frac{N_{\text{th}}}{\tau_s} = \frac{edB_{\text{eff}}}{A_0^2}\left(\alpha_{\text{ac}} + \alpha_{\text{in}} - \alpha_{\text{ex}} + \frac{L}{d}\alpha_{\text{ex}} + \frac{1}{2d}\ln\left(\frac{1}{R_{\text{f}}R_{\text{r}}}\right) + \alpha_{\text{d}}\right)^2 \quad (7)$$

where τ_s is a carrier lifetime, e is electron charge, and B_{eff} is the effective recombination constant. Here we have used the following relationship:

$$\tau_s = \frac{1}{B_{\text{eff}}N_{\text{th}}}. \quad (8)$$

If there is no guiding structure in a cladding layer of a device, it results in a divergence of a resonant beam. This causes a diffraction loss, which limits thinning of the diameter to maintain a small diffraction. Assuming that the transverse field distribution has a Gaussian distribution with a spot size of s, the diffraction loss, α_{d} is expressed as follows (Moriki *et al.*, 1987)

$$\alpha_d = \frac{1}{d}\ln\left(\frac{2}{2+3(2l_{\text{c}}/ks^2)^2+(2l_{\text{c}}/ks^2)^4}\right) \quad (9)$$

where l_{c} is the cladding layer thickness, and k is the propagation constant. The reduction of the diameter of the active region results in decreasing the spot size of a resonant beam, causing a large increase in the diffraction loss α_{d}.

Figure 2(a) shows a calculated threshold current density of a GaAlAs/GaAs SE laser against active layer thickness without taking a diffraction loss into account. When $R = 95\%$ and $d = 2$–3 μm, the threshold current density J_{th} is 25 to approximately 30 kA/cm^2. This value is the same as that of high-radiance LEDs and is not a surprisingly high level. The increase of reflectivity can provide further reduction of the threshold current density. A similar result is obtained for a GaInAsP/InP SE laser ($\lambda_{\text{g}} =$ 1.3 μm) as shown in Fig. 2b (Soda *et al.*, 1983). We can find that the threshold current density can be reduced to less than 10 kA/cm^2 by increasing the reflectivity to 99%. This may be achievable by employing a suitably controlled dielectric or semiconductor multilayer reflector. In addition, a quantum well structure can provide a lower threshold by 40% (Uenohara *et al.*, 1988). By reducing the active layer thickness to 100 Å and increasing the reflectivity to 99.9%, a threshold current density of less than 1 kA/cm^2 can be expected. Figure 3 shows a calculated threshold current density and threshold current against the diameter of the active region in a GaAlAs/GaAs SE laser, in which the spot diameter $2s$ is assumed to be equal to the active region diameter D. When the diameter is more than 3 μm, the diffraction loss is

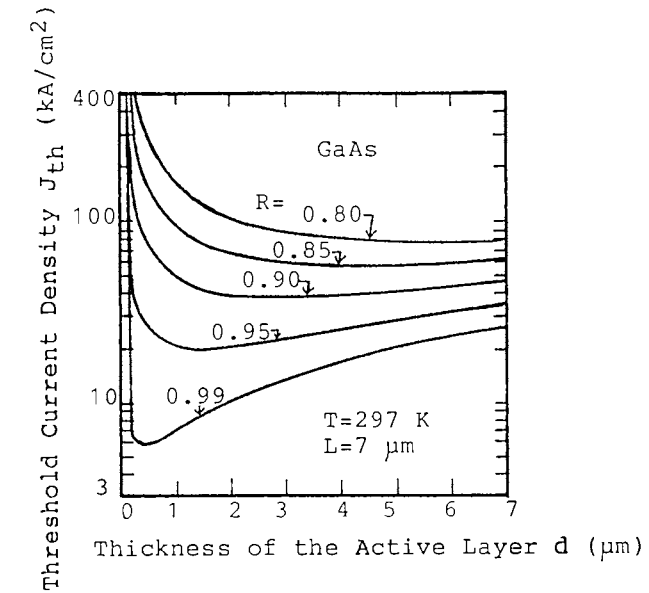

(a)

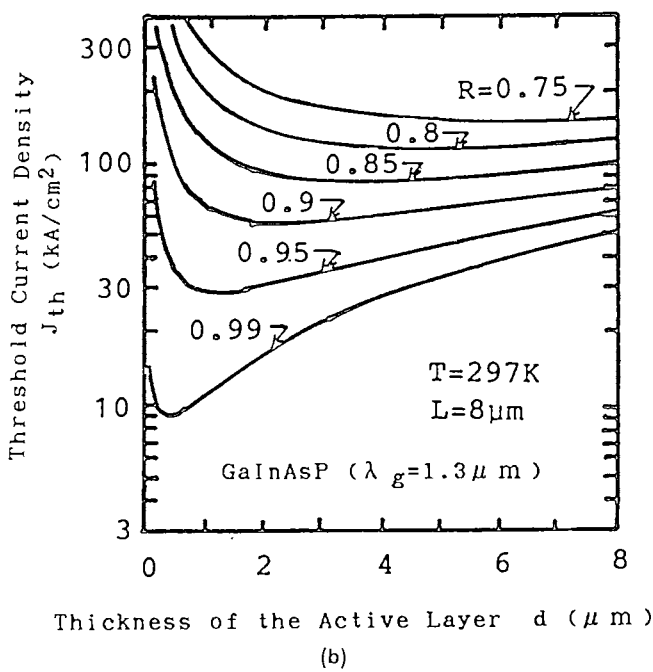

(b)

Fig. 2. Threshold current density against active layer thickness for (a) GaAlAs/GaAs SE laser, (b) GaInAsP/InP SE laser. (Fig. 2a from Kinoshita *et al.*, 1978a; Fig. 2b from Iga *et al.*, 1988. Copyright © 1988 IEEE.)

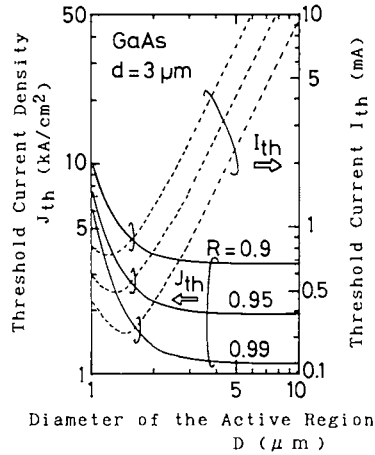

Fig. 3. Threshold current density (solid lines) and threshold current (dashed lines) against active region diameter for a GaAlAs/GaAs SE laser. (From Iga *et al.*, 1988. Copyright © 1988 IEEE.)

negligibly small. Therefore, the threshold current can be decreased in proportion to the square of the diameter in this region. The threshold current is a minimum in the range of the diameter from 1 to 2 μm.

Also, we consider the differential quantum efficiency of the SE laser. If we use a nonabsorbing mirror for the front mirror, the differential quantum efficiency from the front mirror is expressed as (Kinoshita *et al.*, 1987)

$$\eta_d = \eta_i \frac{\ln (1/R_f)}{2\alpha L + \ln (1/R_f R_r)} \tag{10}$$

where η_i is the internal quantum efficiency and α is the internal loss. A calculated result for the GaAlAs/GaAs SE laser is shown in Fig. 4, in which a dielectric multilayer reflector and Au-coated reflector are considered for the front mirror. We have assumed that $R_r = 1.0$, and the internal quantum efficiency $\eta_i = 1$. As for the Au-coated mirror, efficiency deteriorates due to the absorption. In spite of rather high reflectivity of the front mirror (~95%), the differential quantum efficiency stays at 40% because of its short cavity structure.

B. Effect of In-Plane Superluminescence

The emission in the plane of the active layer is enhanced by stimulated emission that may prevent surface emission. When the diameter of the active region is too large, the superradiance of some edge-emitting modes might

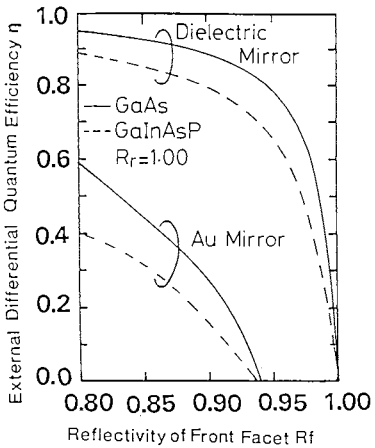

Fig. 4. Differential quantum efficiency versus reflectivity. (From Iga *et al.*, 1988. Copyright © 1988 IEEE.)

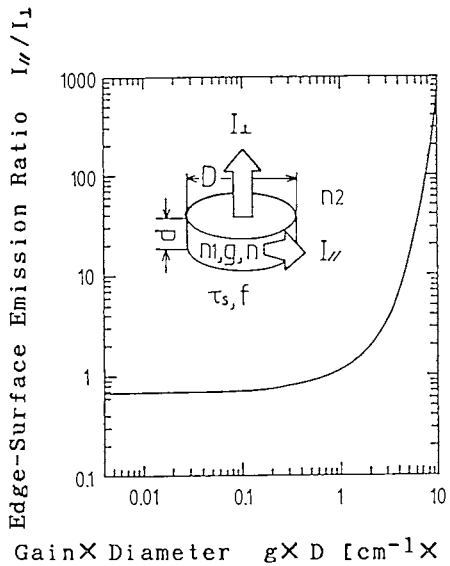

Fig. 5. Ratio of surface and edge emissions taking in-plane superluminescence into account. (From Iga *et al.*, 1988. Copyright © 1988 IEEE.)

dominate. Therefore, such in-plane superluminescence may deteriorate the efficiency of surface emission (Goodfellow *et al.*, 1981). Figure 5 shows the numerical result of the ratio of an edge emission $I_{\parallel}$ to a surface emission $I_{\perp}$ against the gain-diameter product for the active region (Soda *et al.*, 1983), in which we have assumed that the gain is uniform over the whole region.

In order to eliminate the unwanted in-plane superluminescence, the active region diameter should be less than 20 μm, when the gain is equal to 500 cm^{-1}.

C. Longitudinal Mode Behavior

In a short-cavity SE laser, a stable, single longitudinal mode oscillation can be expected due to its large mode spacing. Larger mode spacing between the main lasing mode and neighboring longitudinal modes provides a greater gain difference. The mode spacing $\Delta\lambda$ is expressed as

$$\Delta\lambda = \frac{\lambda^2}{2Ln_{\text{eff}}} \tag{11}$$

where n_{eff} is the effective refractive index. When $L = 7$ μm and $n_{\text{eff}} = 4$, $\Delta\lambda = 135$ Å and 460 Å for a GaAs laser and a GaInAsP laser ($\lambda_g = 1.6$ μm), respectively. The gain difference and resultant mode suppression ratio of neighboring modes, assuming that the gain profile is a parabolic function of wavelength is evaluated as follows:

$$\Delta g = A_0 N - B(\lambda - \lambda_0)^2 \tag{12}$$

Here we have assumed that the main lasing mode coincides with the gain center wavelength λ_0. The side mode suppression ratio is derived from a standard multimode rate equation analysis (Soda *et al.*, 1983) and expressed as

$$P_1/P_0 = \frac{C}{(\Delta g/g_{\text{th}})(I/I_{\text{th}} - 1)} \tag{13}$$

Here, Δg is the gain difference, g_{th} is the threshold gain, I is the injection current, and I_{th} is the threshold current. The parameter C is a spontaneous emission factor (Suematsu and Furuya, 1977) given by

$$C = \xi \frac{\lambda^4}{4\pi^2 n_{\text{eq}}^3 \Delta\lambda_s V} \tag{14}$$

where n_{eq} and $\Delta\lambda_s$ are the refractive index and the spectral width of the spontaneous emission, respectively, ξ is the optical confinement factor that is given by d/L in this case, and V is the volume of the active region. When $L = 7$ μm, $d = 3$ μm, and $D = 10$ μm, C is in the order of 10^{-5} for GaInAsP/InP SE lasers ($\lambda_g = 1.6$ μm).

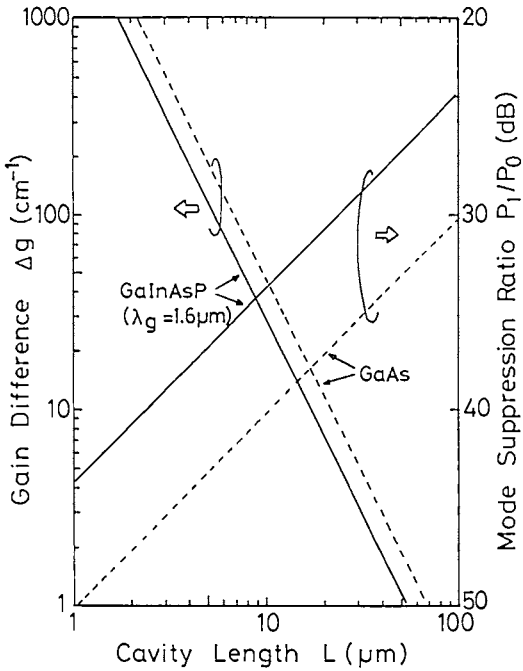

Fig. 6. Gain difference between main mode and neighboring longitudinal mode, and mode suppression ratio against cavity length. (From Iga *et al.*, 1988. Copyright © 1988 IEEE.)

Figure 6 shows a calculated gain difference and side mode suppression ratio as a function of cavity length for GaAlAs/GaAs and GaInAsP/InP ($\lambda_g = 1.6$ μm) SE lasers. With a cavity length < 10 μm, the gain difference is several tens cm^{-1}, which is comparable to that of well-designed DBR- and DFB-type dynamic single-mode lasers (Suematsu *et al.*, 1983). Consequently, the mode suppression ratio of >30 dB can be achievable when $I/I_{th} > 1.5$.

By reducing the size of the cavity volume and spectral width of spontaneous emission in Eq. (14), the spontaneous emission factor may approach unity. A preliminary experiment and theory on the enhancement or suppression of spontaneous emission for a vertical cavity was discussed by Yamamoto *et al.* (1988).

D. Thermal Resistance and cw Condition

When we discuss cw operation of SE lasers, the heat dissipation must be considered. Figure 7 shows a model for calculating the thermal resistance

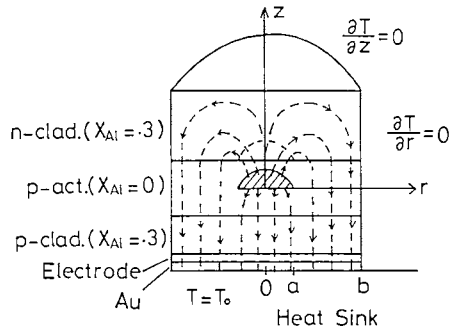

Fig. 7. Calculation model of thermal resistance. (From Iga *et al.*, 1988. Copyright © 1988 IEEE.)

of SE lasers. The thermal resistance against the thickness of *p*-cladding layer as function of device-size is shown in Fig. 8 (Kinoshita *et al.*, 1987c). It is noted that the thermal resistance R_{th} can be decreased by reducing the thickness of the *p*-cladding layer. The increase of chip size causes the decrease in thermal resistance, but this is not critical when chip size is larger than 20 μm square. This fact also implies the limit of separation of arrayed lasers.

We can easily think of five heat sources for a model of a *p*-side down mounted laser, i.e., *n*-cladding, active region, *p*-cladding, cap layer, and *p*-contact. From a rough estimation, the increase of device temperature ΔT

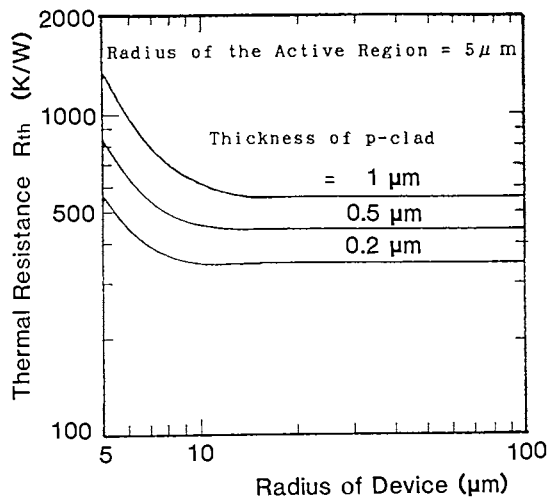

Fig. 8. Thermal resistance of a GaAlAs/GaAs SE laser. (From Iga *et al.*, 1988. Copyright © 1988 IEEE.)

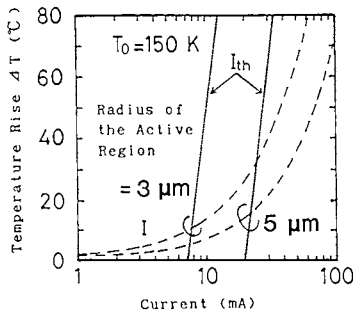

Fig. 9. Temperature rise of active region against injection current. (From Iga *et al.*, 1988. Copyright © 1988 IEEE.)

is expressed as

$$\Delta T = R_{\text{th,ac}} I E_g / e \tag{15}$$

Here, $R_{\text{th,ac}}$ is the thermal resistance of device, and E_g is the band gap energy. On the other hand, the temperature dependence of the threshold is expressed as

$$\Delta T = T_0 \ln (I_{\text{th}} / I_0) \tag{16}$$

If we take the characteristic temperature T_0 of 150 K for GaAs lasers, the temperature increase of the SE laser is shown in Fig. 9, when the radius of the active region is assumed to be 5 μm and 3 μm, respectively. The thermal resistance is estimated as 450 K/W when the radius of the active region is 5 μm. This diagram shows that cw operation can be obtained at the temperature higher than the heatsink temperature by $\Delta T = 25$ K. Moreover, when the radius of the active region can be made to be <3 μm, it is easier to achieve cw operation toward higher heat sink temperature.

E. Modulation Bandwidth

A vertical-cavity SE laser is supposed to be a good light source for optical fiber communications as well as optical interconnection between large-scale-integration circuits (LSIs). For these applications, its modulation bandwidth is one of the important issues. The relaxation oscillation frequency of a semiconductor laser which provides a measure of modulation bandwidth, is denoted by (Ikegami and Suematsu, 1968; Lau *et al.*, 1981) the following expression:

$$f_r = \frac{1}{2\pi} \sqrt{\frac{I/I_{\text{th}} - 1}{\tau_s \tau_p}} = \frac{1}{2\pi} \sqrt{\frac{\xi A_0 P}{\hbar \omega \eta_d V_a}} \tag{17}$$

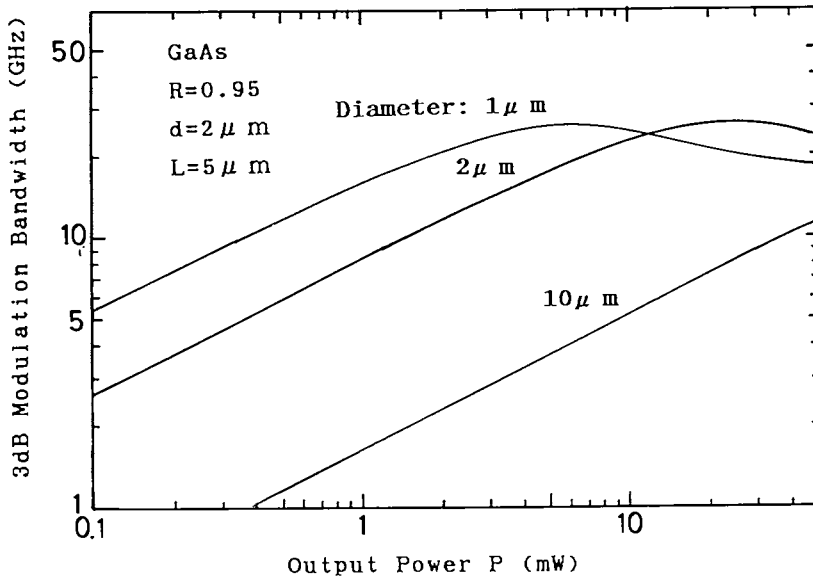

Fig. 10. 3 dB modulation bandwidth of a microcavity laser.

where I_b is the bias current, I_{th} is the threshold current, ξ is the optical confinement factor, A_0 is the gain coefficient, P is the optical output power, ω is the optical angular frequency, η_d is the differential quantum efficiency, and V_a is the volume of the active region. Equation (17) shows that the modulation bandwidth can be increased by decreasing the active volume. We can, then, expect a high-speed modulation in micro-cavity SE lasers. Figure 10 shows the relation between 3 dB modulation bandwidth and optical output power with variation of the active region diameter. In this calculation, we have considered the damping effect due to a nonlinear gain (Olshansky and Su, 1985). A large modulation bandwidth can be obtained even for fairly low output power levels, which is important for the application of densely packed SE lasers in optical interconnection of LSIs. A modulation bandwidth of 8 GHz has already been demonstrated (Jewell *et al.*, 1990).

F. Spectral Linewidth

A narrow linewidth laser diode is a key device for a coherent optical fiber communication system as well as a lightwave sensing system in future electro-optics. The product of spectral linewidth $\Delta\nu$ and output power P

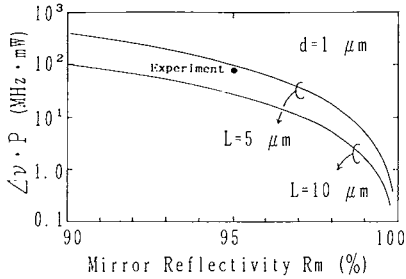

Fig. 11. Calculated spectral linewidth of an SE laser with a high reflective mirror. R_m is the average reflectivity given by $R_m = \sqrt{R_f R_r}$.

is expressed (Henry, 1983) as follows:

$$\Delta\nu P = \frac{\xi^2 v_g h\nu g_{th} n_{sp} \alpha_m (1+\alpha^2)}{8\pi} \tag{18}$$

where ξ is the optical confinement factor, v_g is the group velocity, g_{th} is the threshold gain, n_{sp} is the spontaneous emission rate, and α_m is the mirror loss. We can see that the decrease of ξ, g, and α_m by adding a passive region and by increasing the reflectivity can provide a narrow linewidth. Figure 11 shows a calculated linewidth-power product of an SE laser. A narrow spectral linewidth of <100 kHz can be expected by increasing the mirror reflectivity.

III. FABRICATION AND LASING CHARACTERISTICS OF GaInAsP/InP SE LASERS

A. Structure and Lasing Characteristics

Figure 12 illustrates a structure of a GaInAsP/InP SE laser with a circular buried heterostructure (CBH) (Okuda *et al.*, 1981; Watanabe *et al.*, 1988). These lasers were grown by a two-step liquid phase epitaxy (LPE) growth and successive, fully monolithic fabrication processes. In the first LPE growth, a double heterostructure consisting of five layers was grown, i.e., *n*-type GaInAsP (etch stop layer, Te-doped, 1.5 μm); *n*-type InP (Te-doped, 2.5 μm); *p*-type GaInAsP active layer ($\lambda_g = 1.3$ μm, Zn-doped, 2.5 μm); *p*-type InP (Zn-doped, 1.5 μm); and *p*-type GaInAsP (cap layer, Zn-doped, 0.3 μm) on a (100)-oriented *n*-type InP substrate. A circular SiO_2 mask with 15–17 μm in diameter was formed, and the outer *p*-InP layer was etched off by a Br-CH_3OH solution. In the second LPE growth, the *p*-GaInAsP

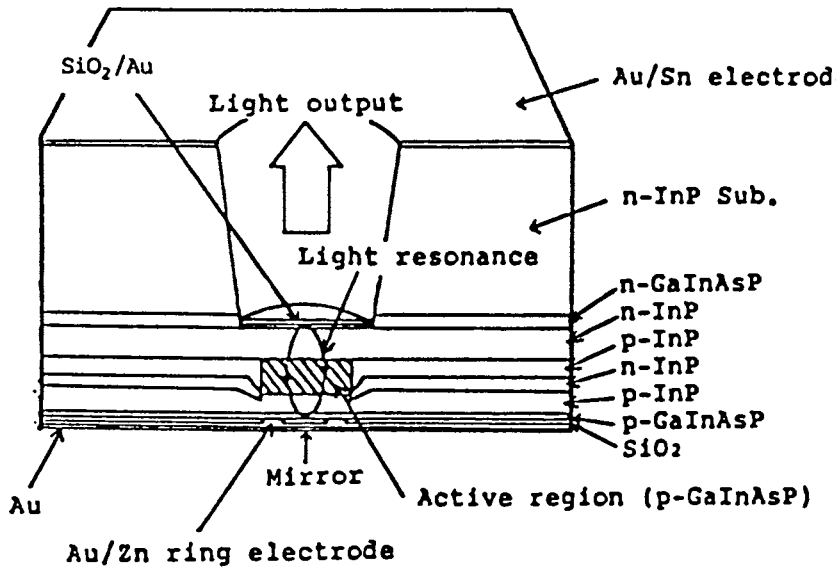

Fig. 12. Schematic view of a CBH GaInAsP/InP SE laser. (From Kawasaki *et al.*, 1988.)

active layer was preferentially melted back by an unsaturated Indium solution (Arai *et al.*, 1980), and the blocking layers consisting of *p*-, *n*-, and *p*-InP layers were regrown on the side bounding area. After the preferential meltback etch, the diameter of the active region was reduced to 18 μm which was estimated from observed spontaneous emission patterns, although the diameter of cap layer was 10 μm. The melted back mesa was considered to have a taper shape. This is why the diameter of the active region was not as small when compared with the diameter of the SiO_2 mask. The *n*-side surface was polished to a thickness of 150 μm, and the *n*-side Au/Sn electrode was formed. The substrate and etch stop layer were then selectively etched to make a cavity whose length was 7 μm. The *p*-side Au/Zn/Au electrode was then formed, but the Au/SiO_2 mirror was prepared only on the surface of the etched well.

Figure 13 shows a light output/current (L–I) characteristic of a typical CBH SE laser device at 77 K under cw condition (Kawasaki *et al.*, 1988). Single longitudinal mode operation was obtained up to $I/I_{th} = 1.4$ without any appreciable sub-transverse modes as shown in Fig. 14. However, the threshold current density was 6.8 kA/cm^2, and this level is still high. This may have been caused by insufficient reflectivity of the mirrors. Also, there is supposed to exist some leakage current through the boundary between the active and blocking region, or through the blocking region. Much lower

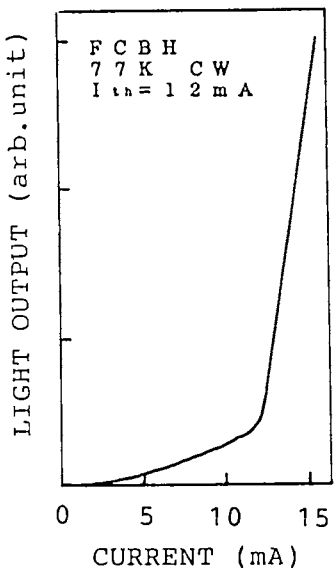

Fig. 13. Light output current characteristic of a GaInAsP/InP SE laser at 77 K under cw condition. (From Kawasaki *et al.*, 1988.)

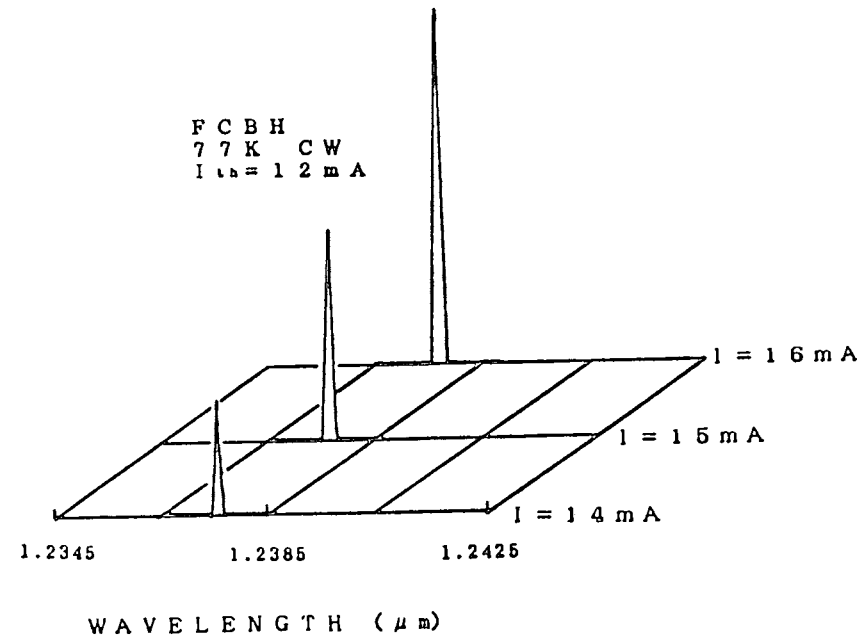

Fig. 14. Lasing spectrum of a GaInAsP/InP SE laser at 77 K under cw condition. (From Kawasaki *et al.*, 1988.)

thresholds could be expected, which leads to room-temperature oscillation after technical improvements such as optimization of the active layer thickness and doping levels of blocking layers, a well-controlled dielectric multilayer mirror with higher reflectivity for the n-side reflector, the reduction of active region diameter, etc.

B. Reflectivity Dependence of Threshold

We tried to introduce a Si/SiO_2 multilayer reflector by taking the advantage of its wide bandwidth providing high reflectivity that comes from a large index difference. To characterize the thresholds of the laser with an Au/SiO_2 mirror and an Si/SiO_2 mirror, we changed the Au/SiO_2 mirror to a Si/SiO_2 multilayer reflector by using the same device. We investigated the variation of I_{th} while changing the reflectivity of the Si/SiO_2 multilayer reflector by increasing the Si/SiO_2 layers (Oshikiri *et al.*, 1989).

A Si/SiO_2 multilayer reflector was designed to have its peak reflectivity at about 1.25 μm, which is the lasing wavelength at 77 K associated with the $Ga_{0.28}In_{0.72}As_{0.61}P_{0.39}$ active medium. We evaporated a Si/SiO_2 multilayer mirror using electron-beam deposition. The experimentally obtained reflectivity of a four-pair Si/SiO_2 mirror is 95% at 1.25 μm.

Figure 15 shows the structure of an SE laser chip that employs a flat surface circular buried heterostructure (FCBH) grown by LPE. The active layer thickness is 2.7 μm, and the cavity length is 7 μm. The active region diameter is about 18 μm as judged from near-field observation. The tested laser device was loaded by an Au/SiO_2 mirror for the light output side. The threshold was 17 mA at 77 K as shown in Fig. 16b. This value is much higher than the expected I_{th} of approximately 2–3 mA, and it is judged to be due to the low reflectivity of the mirror. The threshold current dependence on mirror reflectivity was investigated by the following method. First, we checked the L–I characteristic and the lasing wavelength of the chip with an Au/SiO_2 mirror. Next, we removed the Au/SiO_2 mirror by a chemical wet etch and checked the L–I characteristic without any specific light output mirror (Fig. 16a). After that, we evaporated a two pair Si/SiO_2 reflector by electron-beam evaporator ($R = 90\%$). The L–I characteristic is shown in Fig. 16c. The threshold decreased to 7.5 mA. These observations were performed under 77 K. We successively evaporated another two pairs of Si/SiO_2 layers to raise the reflectivity still further. We found that the I_{th} for a three-pair Si/SiO_2 mirror was 6.2 mA (Fig. 16d), and that for a four-pair Si/SiO_2 mirror the I_{th} decreased to 6.0 mA (Fig. 16e). This value is about 50% of the threshold current obtained by the starting device. In Fig. 16 we

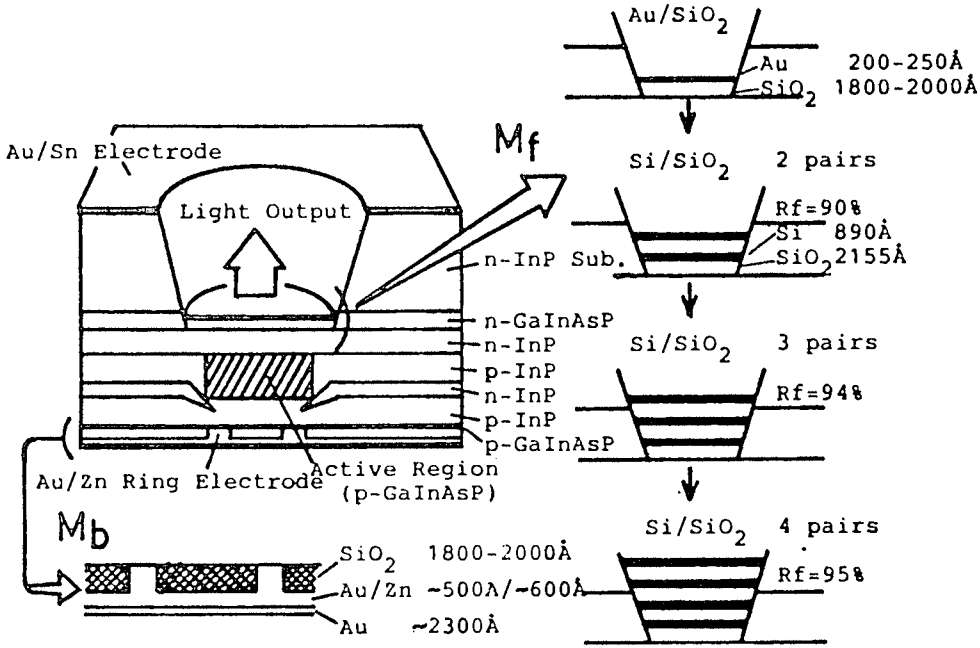

Fig. 15. Structure of a FCBH SE laser and experimental process. (From *IEEE J. Quantum Electron.* **QE-22**, 302–309, Fig. 3a, 1986. Copyright © 1986 IEEE.)

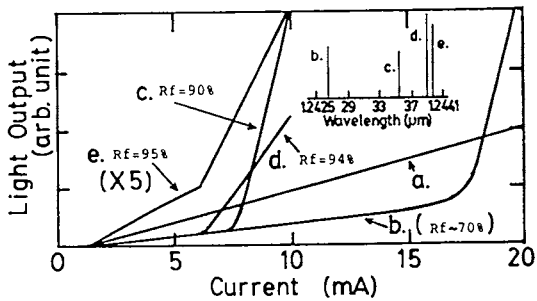

Fig. 16. Light output/current characteristics of an FCBH SE laser with various pair number of multilayer reflector. (From Oshikiri *et al.*, 1989. Copyright © 1989 IEEE.)

can see that there exists a nonradiative floor in the horizontal axis of about 1.5 mA, which may be attributed to the leakage current. If we subtract this from 6.0 mA, the effective threshold is about 4.5 mA.

The change of lasing wavelength with reflectivity is also shown in Fig. 16. The lasing wavelength of the laser with an Si/SiO_2 multilayer reflector is longer than that with an Au/SiO_2 mirror. Lasing wavelength shifted to the longer side also when the reflectivity is improved by increasing the number of Si/SiO_2 layers. The wavelength shifted by a total of about 13 Å. We think that this phenomenon is primarily caused by the increase of the refractive index due to decrease in the cramped carrier density above the threshold.

Figure 17 shows the relationship between I_{th} and the average reflectivity $\sqrt{R_f \times R_r}$. Each point is plotted by using the effective I_{th}, which is defined as the I_{th} minus the leakage current of 1.5 mA. The reflectivity of an Au-Zn-Au film employed in the bonding-side mirror is 82–83% as measured using a test piece. The actual reflectivity of the bonding-side mirror, which

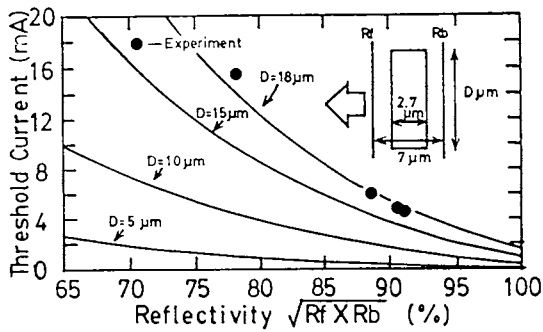

Fig. 17. Reflectivity dependence on threshold current. (From Oshikiri *et al.*, 1989. Copyright © 1989 IEEE.)

has a $\lambda/4$ SiO_2 layer between the epitaxial surface and Au-Zn-Au metal, is estimated to be about 86–89%. We think that this low reflectivity is due to Zn diffusion, and the light output side mirror reflectivity is 90% for two pairs, 94% for three pairs, and 95% for four pairs. From these values, the reflectivity of the forward Au/SiO_2 mirror that was employed first is estimated to be approximately 70%. From this result, we can expect possible fabrication of a sub-mA threshold device at 77 K and room-temperature operation of GaInAsP SE devices by improving the bonding-side mirror. Room-temperature pulsed operation of a 1.55 μm GaInAsP/InP SE laser with a high reflective semiconductor multilayer reflector has already been demonstrated (Kasukawa *et al.*, 1990).

IV. FABRICATION AND LASING CHARACTERISTICS OF GaAlAs/GaAs SE LASERS

A. LPE-Grown SE Laser

A GaAlAs/GaAs laser employs almost the same CBH structure as the GaInAsP/InP laser as shown in Fig. 18. In order to decrease the threshold, the active region was also constricted by the preferential meltback method mentioned above (Kishino *et al.*, 1983). A threshold current of 68 mA was obtained under pulsed operation when the active region was constricted to 14 μm in diameter. Moreover, the threshold was reduced to 6 mA when the diameter was ~6 μm under pulsed operation at 20°C (Iga *et al.*, 1987).

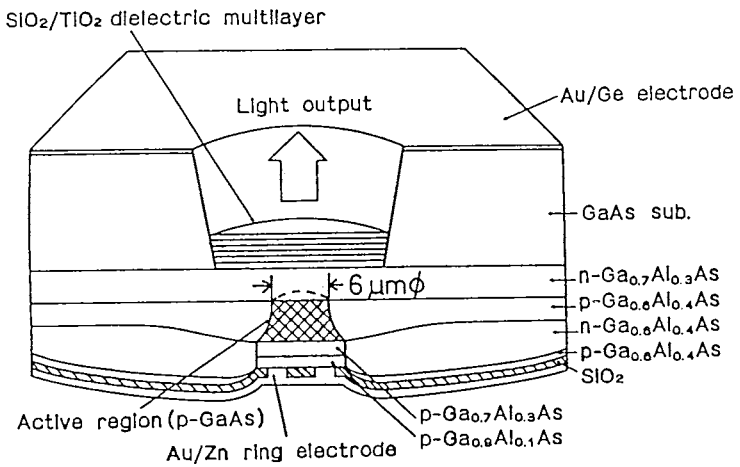

Fig. 18. Schematic view of a CBH GaAlAs/GaAs laser grown by LPE. (From Iga *et al.*, 1987.)

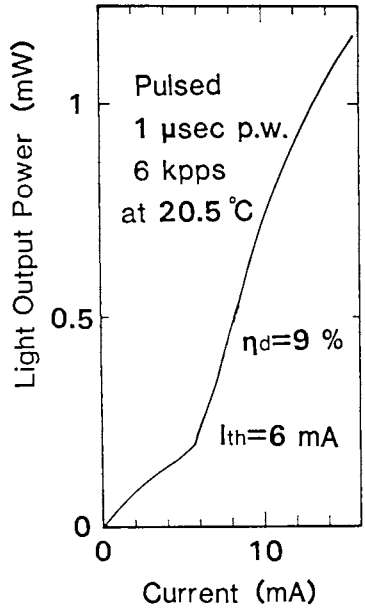

Fig. 19. Light output current characteristic of a GaAlAs/GaAs SE laser under room-temperature pulsed operation. (From Iga *et al.*, 1987.)

Figure 19 shows a light output current characteristic under room-temperature pulsed operation. The threshold current density was 21 kA/cm^2, which agrees with the theoretical value when we postulate the reflectivity of 95%. Figure 20 illustrates a lasing spectrum at $I = 20$ mA and indicates the near-field pattern. This SE laser operated in a single mode, but the linewidth was broadened when the current exceeded 40 mA. The near-field pattern of this SE laser was a circle of 6 μm in diameter. CW operation was obtained with $I_{th} = 4.5$ mA (77 K). This is also a first demonstration of a cw vertical GaAlAs/GaAs SE laser. It is noted that a microcavity of 7 μm length and 6 μm diameter has been realized. From this demonstration of a microcavity SE laser, we found that extremely low threshold current operation with stable single transverse mode can be obtained by decreasing the diameter of the microcavity.

B. MOCVD-Grown SE Laser

We have been fabricating SE lasers mostly by LPE, in which the resulting surface morphology has not been satisfactory in our experiment. In order to improve the surface morphology, which is more important for SE lasers

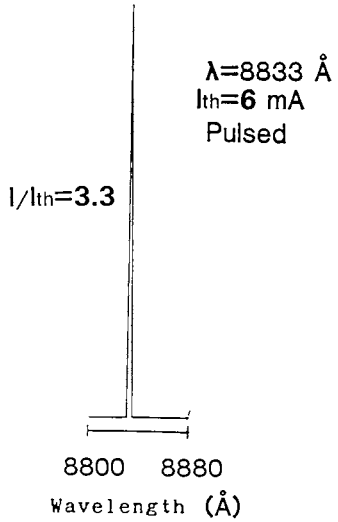

Fig. 20. Lasing spectrum of a GaAlAs/GaAs CBH SE laser. (From Iga *et al.*, 1987.)

than for conventional stripe lasers, we introduced a metalorganic chemical vapor deposition (MOCVD) growth for SE lasers (Koyama *et al.*, 1987). We fabricated GaAlAs/GaAs vertical-cavity SE lasers as shown in Fig. 21 (Koyama *et al.*, 1988a). This device was fabricated by a two-step atmospheric MOCVD. The laser wafer, with an active layer thickness of ~2.5 μm, was grown by an MOCVD and processed by a fully monolithic technology. For presently attainable mirror reflectivities, this thickness is considered to be optimum for a low threshold current density. Current confining layers were grown by a second MOCVD growth. The diameter of a buried circular mesa was 7 μm. In this device structure, the active region was not truncated and the injected current spreads out in the active layer. The effective diameter of the active region was then extended to around 10 μm. A short cavity of about 5.5 μm thick was formed by chemically removing the GaAs substrate. In order to increase the reflectivity of the bonding-side mirror, an $Au/SiO_2/TiO_2/SiO_2$ mirror was prepared. A ring electrode with an outer/inner diameter of 40/5 μm was used for current injection and transverse mode control. After forming the *p*-side electrode, a five-pair SiO_2/TiO_2 dielectric multilayer reflector was evaporated on the output side surface. In addition, the thermal resistance of the device was reduced by bonding the chip on a Cu heatsink for cw operation.

The fabricated devices were initially tested under pulsed conditions (2 kpps, 200 ns duration) at room temperature. Threshold currents of most

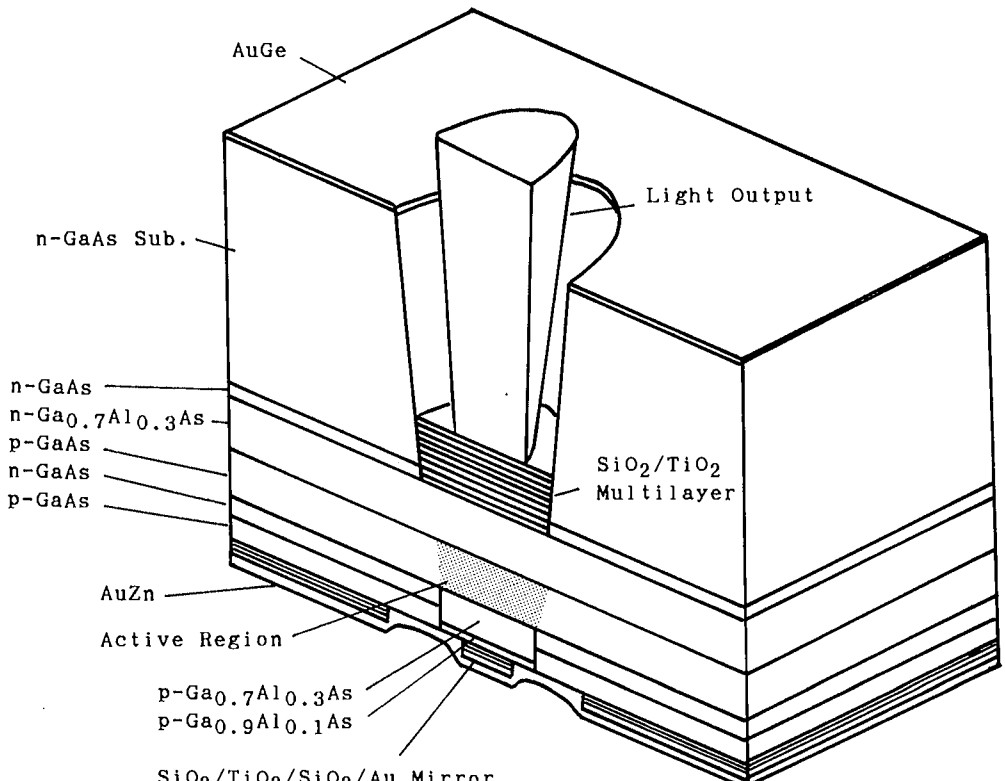

Fig. 21. Schematic view of an MOCVD-grown CBH GaAlAs/GaAs SE laser. (From Koyama *et al.*, 1989.)

of the tested devices ranged from 28 to 40 mA. Maximum output power was 12 mW with a differential quantum efficiency of 10%.

C. cw Lasing Characteristics

Figure 22 shows a typical light output current characteristic and lasing spectrum under cw operation at room temperature (20°C) (Koyama *et al.*, 1988b). The lowest cw threshold current was 30 mA at 20°C. The differential quantum efficiency was 9.3% at 20°C. Stable single mode operation was achieved with neither sub-transverse modes nor other longitudinal modes. The spectral width above the threshold was less than 1 Å which is a resolution of the spectrometer used (Anritsu MS9001A). This indicates a clear cw laser oscillation of this device. The maximum output power of the present device was 2.2 mW at 15°C. The saturation of output power is due to the increase of device temperature. We believe this could be raised by several mW or more by improved heat-sinking.

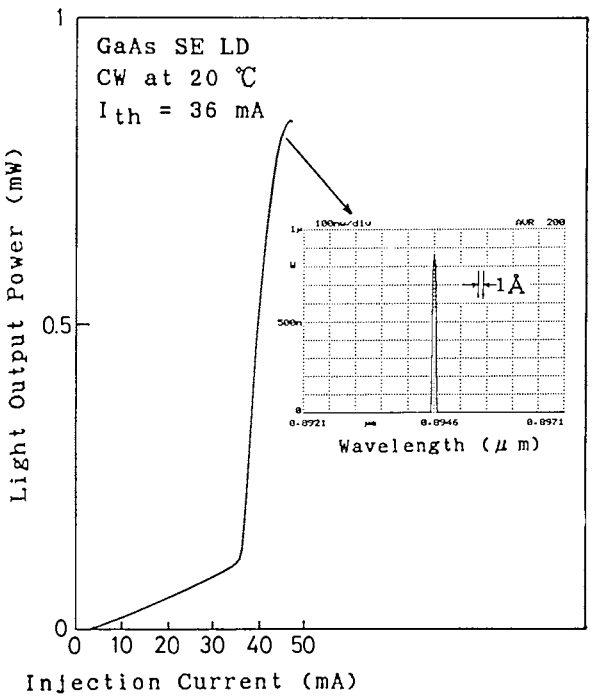

Fig. 22. Light output/current characteristic of an MOCVD-grown GaAlAs/GaAs SE laser under cw condition at room temperature. (From Koyama *et al.*, 1989.)

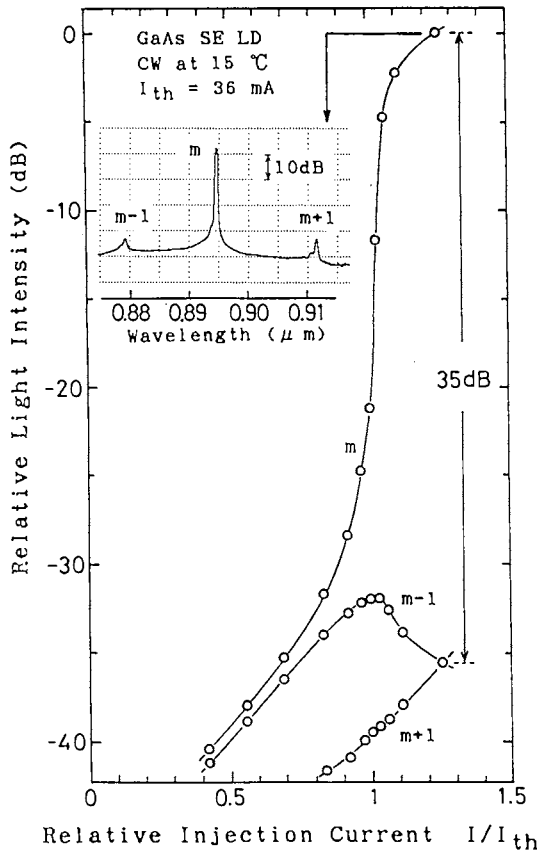

Fig. 23. Side mode suppression ratio. (From Koyama *et al.*, 1989.)

Figure 23 shows the relative intensity of the lasing mode and neighboring longitudinal submodes (Koyama *et al.*, 1989). A side-mode suppression ratio of 35 dB was obtained at $I/I_{th} = 1.25$, which is comparable to that of a well-designed DBR or DFB dynamic single-mode laser. Figure 24 shows the temperature dependence of the threshold and lasing wavelength. The temperature dependence of lasing wavelength was 0.07 nm/K. Single-mode operation was maintained in the temperature range of more than 50 K. This originated from the large mode spacing between neighboring longitudinal modes (~160 Å). The temperature characteristic of the threshold current looks different from that of conventional lasers. The increase in the threshold is caused by gain detuning and heating. Near-field and far-field patterns were also measured as shown in Fig. 25. A circular emission pattern of

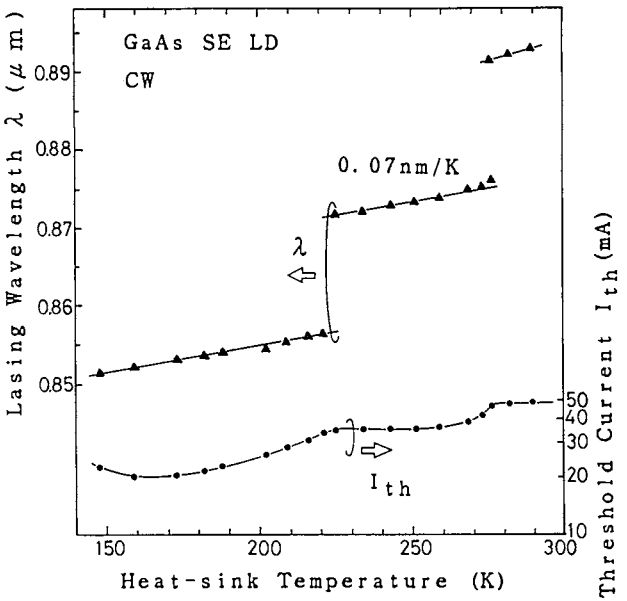

Fig. 24. Temperature dependence of threshold and lasing wavelength. (From Koyama *et al.*, 1989.)

4 μm in diameter was obtained, showing single transverse mode operation. The beam divergence was typically 13° in full width at half maximum. This laser emission property may relieve the problem of coupling the output to a single mode-fiber.

The spectral linewidth was measured by a standard, delayed self-homodyne method (Okoshi *et al.*, 1980) with a 4 km-long single-mode fiber. Two optical isolators, with a total isolation of 60 dB were used to eliminate the effect of external optical feedback. Figure 26 shows the

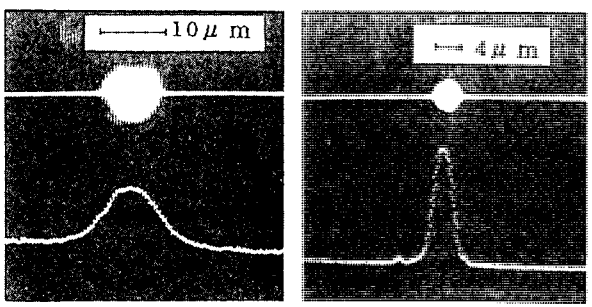

Fig. 25. Near-field patterns of MOCVD grown GaAlAs/GaAs SE laser.

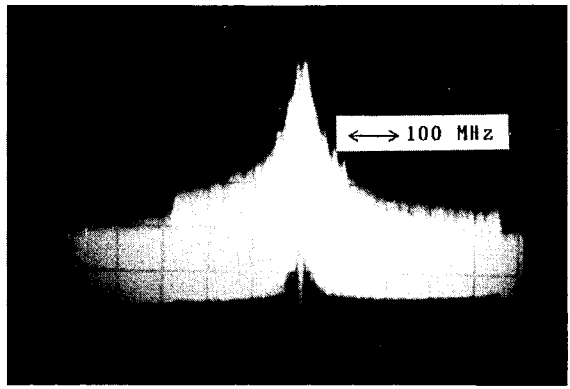

Fig. 26. Self-homodyne beat signal at 1.4 mW output power. (From Sakaguchi *et al.*, 1988.)

self-homodyne beat signal at 1.4 mW output power (Tanobe *et al.*, 1989). A spectral linewidth of 50 MHz was obtained. The linewidth-power product is 89 MHz·mW. Even in such an ultra-short cavity device with a cavity length of <10 μm, a relatively narrow spectral line width was attained. This was due to the high reflectivity of the mirrors. It can be expected that much narrower laser line width can be obtained by increasing the output power and reducing the cavity loss.

D. Polarization Characteristics

For polarization-sensitive applications such as magneto-optic disks and coherent detection, the polarization state of lasers must be well defined. The polarization characteristic of several SE laser samples was measured by detecting the output through a rotating Glan-Thompson prism (Shimizu *et al.*, 1988).

Figure 27 shows a typical polarization profile of intensity versus the polarizer angle with different relative injection levels. No noticeable change in polarization directions was observed with varying injection currents. The output light was linearly polarized along the (011) or $(01\bar{1})$ direction. We considered that the polarization direction was determined by the anisotropy of the crystal surface and an evaporated mirror, the irregularity of the mesa, etc. In order to investigate the polarization selectivity, we introduced a theoretical model to estimate an oscillating mode and a perpendicularly polarized mode. We calculated the relative intensity of modes along two

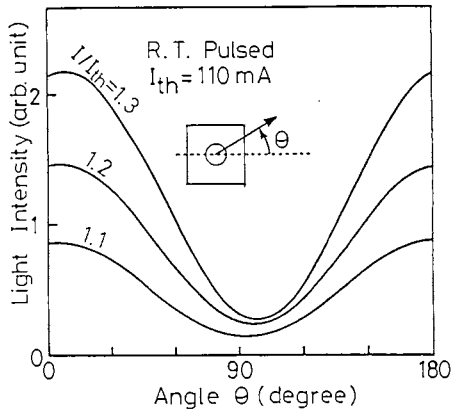

Fig. 27. Polarization characteristic of a GaAlAs/GaAs SE laser. (From Shimizu *et al.*, 1988.)

different directions by using rate equations. These are shown by the solid lines of Fig. 28 against the injection current level below the threshold. The parameter is the cavity loss difference of the two modes. The black and white circles are experimental values of the SE laser and a conventional stripe laser, respectively. The loss difference between polarization states of the SE laser is much smaller than that of a conventional laser. Therefore, a polarization control mechanism is needed for polarization-sensitive applications.

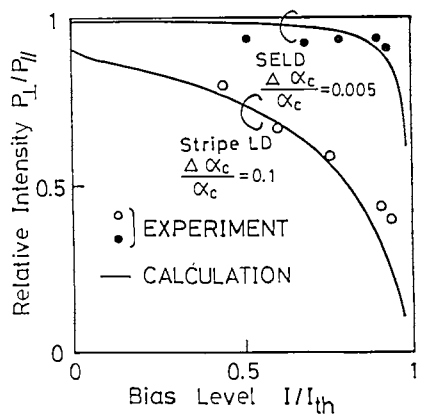

Fig. 28. Relative intensity of the two polarized modes. (From Shimizu *et al.*, 1988.)

E. Perspective of Extremely Low Threshold Devices

Figure 29a shows the relationship between the threshold current and the active region diameter in GaAlAs/GaAs CBH SE lasers. In the model for this calculation, there was no guiding structure considered in the cladding layer, which results in a divergence of a resonant light beam. When the diameter of the active region is large enough to maintain a small diffraction loss, I_{th} is proportional to the square of the diameter of the active region. However, the threshold approaches a minimum when the diameter is reduced since the diffraction loss begins to dominate. The diffraction loss was found to be negligibly small for $D > 3$ μm. The diffraction loss can be eliminated by introducing a cylindrical optical waveguide in the cavity. Figure 29a shows the calculated threshold for this model. A core/cladding index difference of 5% was assumed. An ultra-low threshold of a few μA is expected by decreasing the diameter to less then 1 μm. Experimental data of present devices are plotted in Fig. 29(b). The microampere threshold SE laser device is already within a target of challenge.

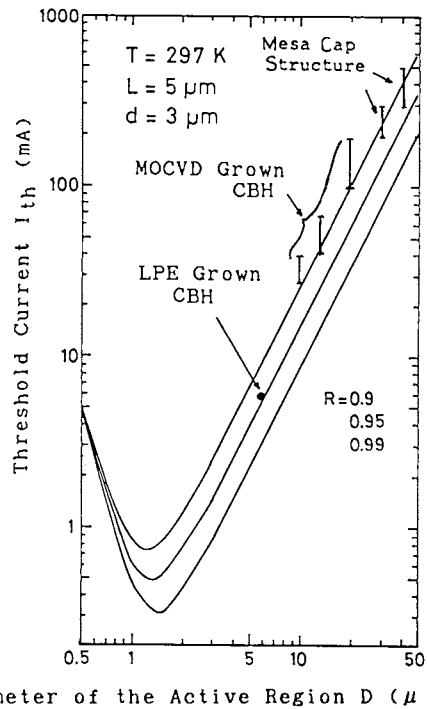

Fig. 29. (a) Threshold current versus active region diameter for a GaAlAs/GaAs SE laser without a guiding structure. (From Oshikiri *et al.*, 1989. Copyright © 1989 IEEE).

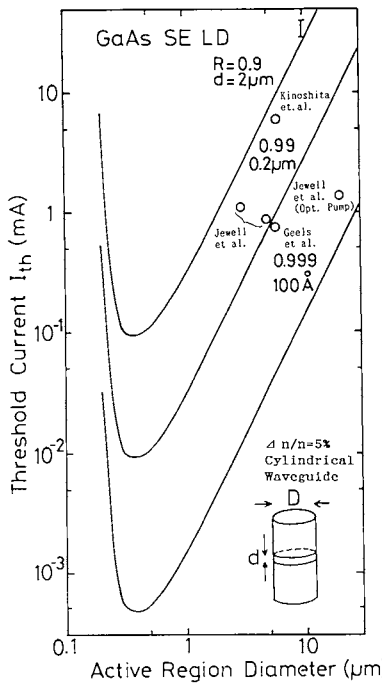

Fig. 29. (b) Threshold current versus active region diameter for a GaAlAs/GaAs SE laser with a cylindrical waveguide.

V. SUPERLATTICE, PERIODIC, AND MULTILAYER STRUCTURE

A. Quantum Well and Periodic Gain Structure

1. Multi-Quantum Well (MQW) Structure

The quantum well laser exhibits some good characteristics such as low threshold current (Lau *et al.*, 1988), high relaxation oscillation frequency (Arakawa and Yariv, 1985), larger characteristic temperatures, etc. Thus, an SE laser with a quantum well for its active region is expected to provide not only a higher gain but also some other better performances. Lasing characteristics of an MQW SE laser by optical pumping was reported by Nomura *et al.* (1985). Laser oscillation of an MQW SE laser by current injection has also been reported (Uenohara *et al.*, 1989).

The schematic model of an MQW SE laser to be fabricated is illustrated in Fig. 30. Its threshold current density has been calculated for a

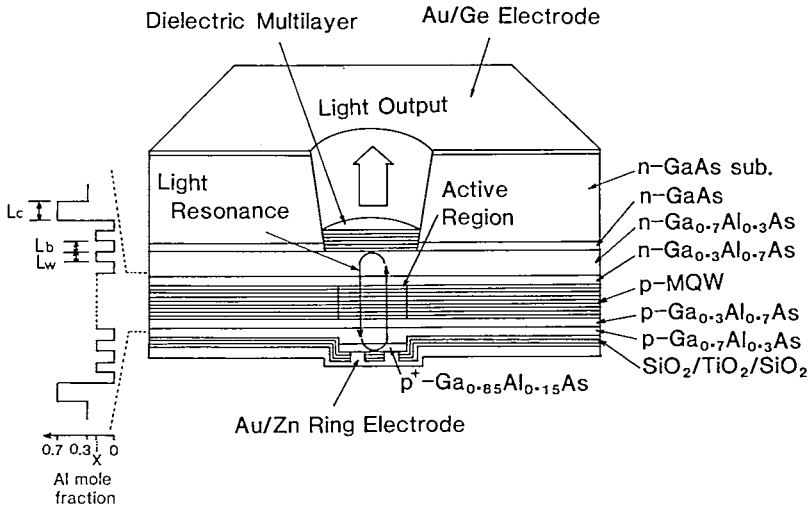

Fig. 30. Structure of an MQW SE laser. (From Uenohara *et al.*, 1989.)

GaAlAs/GaAs system using a density-matrix theory including the relaxation broadening (Asada *et al.*, 1985) to determine how many quantum wells are needed to reach oscillation. The dependence of the resultant threshold current density on the well number is shown in Fig. 31. In this calculation, we have assumed that the cavity length $L = 7\ \mu m$, and the well width $W = 100$ Å. The threshold current density of the MQW structure is found to be about 60% of a bulk active layer. This is due to the increase of the optical gain by quantum size effect. There exists an optimum number of wells versus mirror reflectivity. Note that about 100 wells are required to obtain the minimum threshold current density when the reflectivity is 97%. This is because the cavity length of an SE laser is much shorter than that of an edge-emitting laser. If the reflectivity is increased to 99.9%, a single-quantum well can be used and very low threshold current density can be expected.

An MQW SE laser with a round mesa structure (Fig. 30) was also fabricated. In this device, one hundred wells were used. A pulsed operation by electrical pumping was obtained with a threshold current of 140 mA at 77 K. We believe that this was the first lasing operation of the MQW SE laser by current injection. The threshold current obtained was not as low as expected due to the following problems; (1) nonhomogeneous current injection into each well, and (2) reflectivity of the mirror was insufficient for fulfilling laser operation.

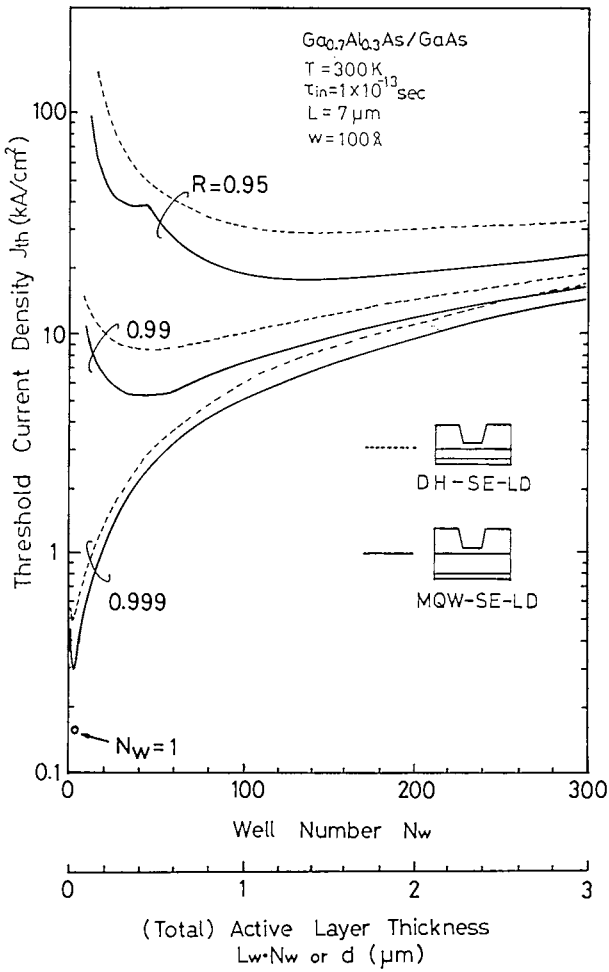

Fig. 31. Calculated threshold current density of an MQW SE laser.

The number of quantum wells required can be reduced by increasing the mirror reflectivity, which may solve the above problem. Jewell *et al.* demonstrated an optically pumped laser operation of a single quantum well SE laser with an extremely high reflective mirror ($R > 99.9\%$) fabricated as shown in Fig. 32(a) (Jewell *et al.*, 1989a). This was a very promising result indicating an ultra-low threshold SE laser device. During the preparation of this manuscript, a 1.2 mA threshold device with current injection was developed as shown in Fig. 32(b) (Jewell *et al.*, 1989b). Subsequently, the threshold further reduced to 0.7 mA (Geels and Coldren, 1990).

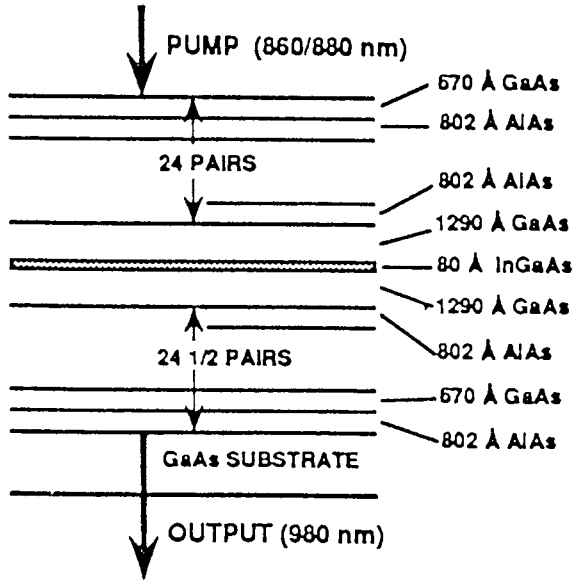

(a)

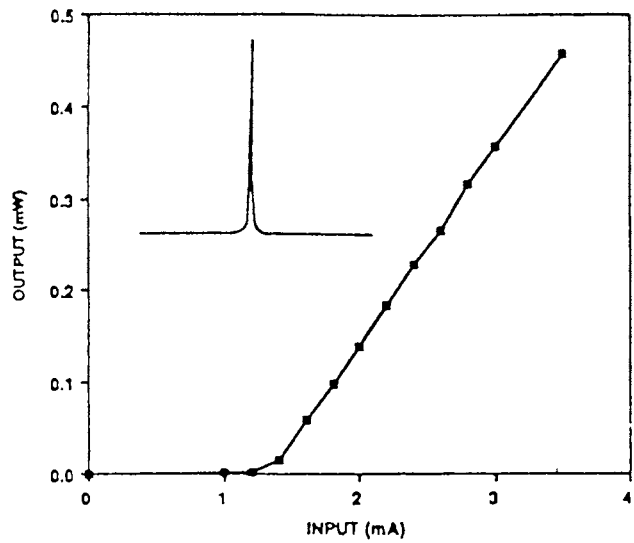

(b)

Fig. 32. GaInAs single quantum well SE laser. (a) Structure, (b) Light output/current characteristic. (Fig. 32a from Jewell *et al. Appl. Phys. Lett.* **55**, 424; Fig. 32b from Jewell *et al.* 1986b with permission.)

2. *Periodic Gain Structure*

The periodic gain concept was proposed by Geels *et al.* (1988) and Raja *et al.* (1988). If the gain region is placed on the maxima of the standing wave of a resonant mode, it is possible to increase the modal gain by a factor of two, and a reduction of threshold current can be expected. Figure 33 shows the conceptional diagram of the SE laser with a periodic gain structure. Optically pumped cw operations of periodic gain SE lasers with a high power conversion efficiency of more than 40%, have been demonstrated (Schaus *et al.*, 1989; Gourley *et al.*, 1989).

B. Semiconductor Multilayer DBR

Fine growth technologies such as MOCVD, MBE, and chemical beam epitaxy (CBE) can provide superlattice structures that enable the fabrication of DFB- and DBR-type SE lasers. For the purpose of demonstrating a DBR SE laser, Bragg reflectors composed of 30-layer GaAlAs and AlAs with quarter wavelength were grown by the aforementioned MOCVD technique. A cross-sectional scanning electron microscope (SEM) photograph of the multilayer Bragg reflector is shown in Fig. 34. The period of the Bragg reflector was 1400 Å. The reflectivity of the multilayer Bragg reflector was measured from the top of the crystal surface. The maximum reflectivity of 97% was obtained at a wavelength of 0.87 μm as shown in Fig. 35, which corresponds to the lasing wavelength of the GaAlAs/GaAs SE laser. Also, it was found that it is possible to inject a carrier into an active region through multilayers approximately 2–3 μm thick by appropriately doping the impurity. Recently, we succeeded in demonstrating the oscillation of a

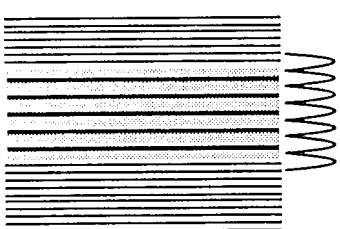

Fig. 33. Schematic structure of a periodic gain SE laser (Geels *et al.*, 1988; Raja *et al.*, 1988).

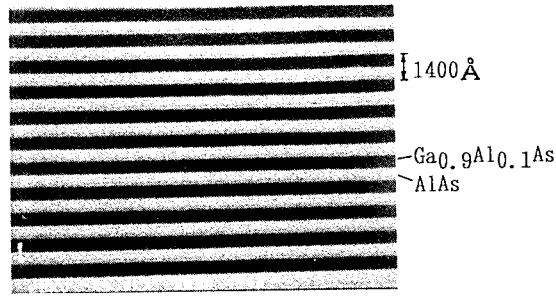

Fig. 34. A cross-sectional SEM photograph of a $Ga_{0.9}Al_{0.1}As/AlAs$ multilayer Bragg reflector.

GaAlAs SE laser that uses a multilayer reflector as one of the mirrors fabricated as shown in Fig. 36 (Sakaguchi *et al.*, 1988). Ibaraki *et al.* (1989) demonstrated a low threshold room-temperature cw operation of a DBR CBH SE laser with $I_{th} = 5.2$ mA as shown in Fig. 37.

By introducing such a periodic configuration, a reduction of the threshold current can be expected (Uchiyama *et al.*, 1986c). To fully activate a multilayered active region such as an MQW and DFB, a transverse or interdigital injection scheme was also proposed (Iga *et al.*, 1985). A DBR or DFB structure without facet mirrors enables the integration of functional optical devices with SE lasers by stacking them. This concept may open a new three-dimensional integrated optics research study.

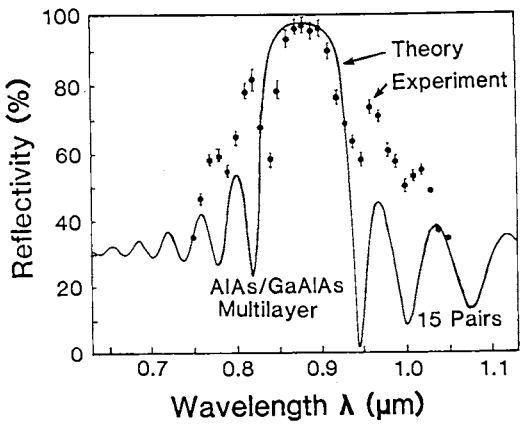

Fig. 35. Measured spectral reflectivity of a 15-pair $Ga_{0.9}Al_{0.1}As/AlAs$ multilayer.

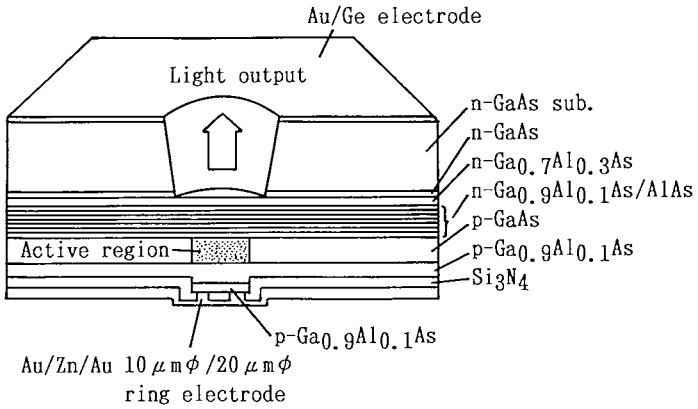

Fig. 36. Structure of GaAlAs/AlAs DBR SE laser. (From Tanabe *et al.*, 1989.)

VI. TWO-DIMENSIONAL SE LASER ARRAY

A conventional injection laser consists of two cleaved end mirrors perpendicular to the active layer, so although one-dimensional laser arrays can be monolithically fabricated, it is necessary to stack wafers to form two-dimensional laser arrays. However, it is also possible to fabricate two-dimensional laser arrays by using the SE laser concept. Specifically, a vertical cavity SE laser can form a high-density two-dimensional array. One application of such a two-dimensional array is for a high power laser, and another is for a stacked planar optics (Iga *et al.*, 1982). The concept of the stacked

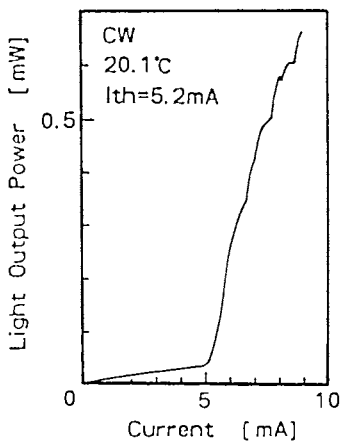

Fig. 37. Light output/current characteristic of CBH DBR SE laser. (From Ibaraki *et al.*, 1989, with permission.)

planar optics is based on a two-dimensional lightwave component array made by stacking two-dimensional planar optical device arrays such as a planar microlens array. This configuration may enable mass production of optical devices with easy alignment. The importance of 2-D arrays are increasing along with the use of optical parallel processing.

The first demonstration of a two-dimensional SE laser array was performed using a GaInAsP system (Uchiyama and Iga, 1985). As another preliminary demonstration, a 5×5 GaAlAs/GaAs SE laser array was fabricated by a two-step MOCVD growth as shown in Fig. 38a (Koyama *et al.*, 1988a). The separation of each device was 20 μm, where the current confining structure was the same as mentioned previously. This device operated under room-temperature pulsed condition with a threshold current

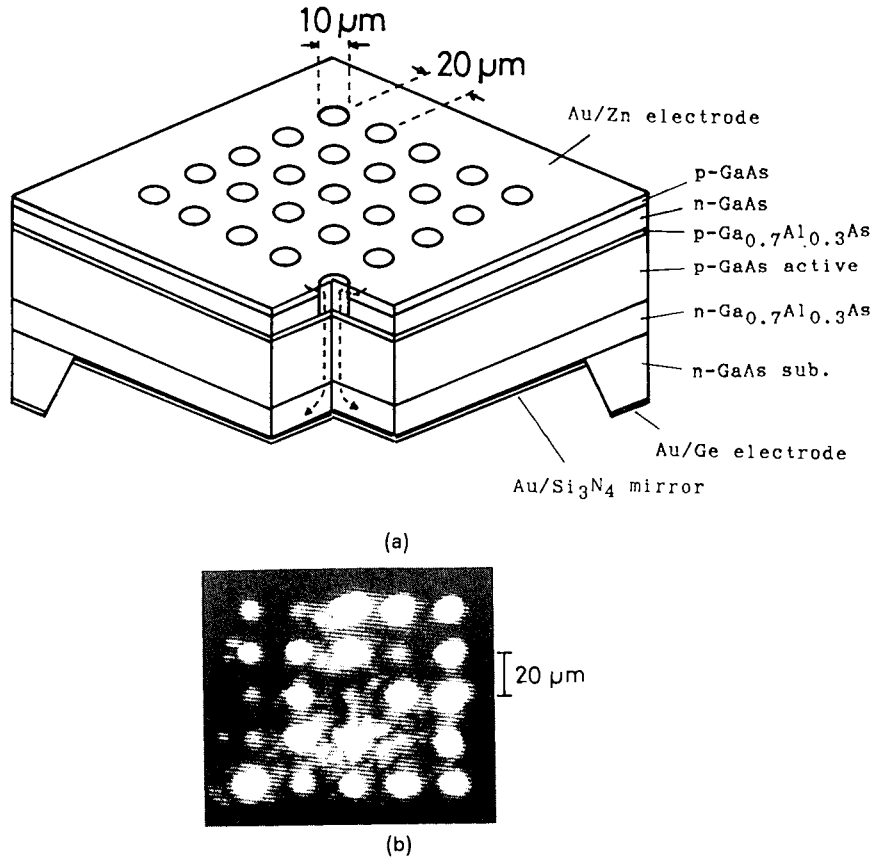

Fig. 38. Two-dimensional SE laser array. (a) Schematic diagram, (b) A near-field pattern of a 5×5 GaAlAs/GaAs SE laser array. (Fig. 38b from Kayama *et al.*, 1988a.)

of 600 mA. Thus, the minimum threshold in 25 SE LDs was estimated to be 24 mA. Figure 38b shows a near-field pattern with a bias current of 2.2 times the threshold. The lasing operation of 19 SE LDs among 25 devices was obtained. Such high density 2-D laser arrays can be formed only by a vertical cavity configuration.

A phase-locked 2-D array is attractive for high-power and narrow circular beam operation. An appropriate design for such a phase-locked 2-D laser array using diffraction-coupling (Leger *et al.*, 1988) may provide stable operation (Ho *et al.*, 1989). A phase-locked array with much closer spacing has been demonstrated (Yoo *et al.*, 1990). The supermode control in a phase-locked SE laser array remains an important problem.

VII. CONCLUSION

A vertical-cavity SE laser possesses many advantages which are not only helpful for mass productivity and the possibility of forming a two-dimensional laser array, but also for providing many excellent laser performances. For example, stable dynamic single-mode operation and an extremely low threshold ($I_{th} < 1$ mA) can be expected by introducing a microcavity structure with a cavity length and active region diameter of less than several microns. In order to reduce the threshold current of SE lasers and to planarize the device surface, a circular buried heterostructure (CBH) was introduced. The laser reflected was also improved by employing a dielectric multilayer mirror. Looking at the progress of SE laser research, it is clear that the present performance characteristics of vertical-cavity SE lasers are not limited by any essential problems, but only by those of a technical nature. Table III summarizes the performance of vertical-cavity SE lasers. The development of basic semiconductor technologies, such as a damage-free micro-fabrication process and the epitaxial growth of ultra-thin layers, may accelerate the research progress of the SE laser.

Detailed lasing characteristics of SE lasers such as transverse mode behavior including polarization state and feedback noise are now under investigation. Further development of the SE laser may open various applications and accelerate the integration of optical devices and optical circuits with the freedom of two-dimensional arrays.

ACKNOWLEDGMENTS

The authors would like to express appreciation to Prof. Y. Suematsu, President of Tokyo Institute of Technology for encouragement of the study.

Table III

Performances of Vertical-Cavity SE Lasers

Character-istic	GaInAsP	GaAlAs	InGaAs
I_{th}	6 mA (77 K) (Tokyo IT) 5 mA (77 K) (AT&T)	5.2 mA (Sanyo) 2.2 mA (AT&T)	0.8 mA (AT&T) 0.7 mA (UCSB)
J_{th}	150 mA (300 K) (Furukawa)	10 kA/cm^2 (TRW) 1.4 kA/cm^2 (AT&T)	1 kA/cm^2 (Bellcore) 600 A/cm^2 (UCSB)
η_d		14% (Tokyo IT) 78% (AT&T)	28% (AT&T)
$\Delta\nu$	<1 Å (Tokyo IT)	50 MHz (Tokyo IT)	85 MHz (UCSB)
$\Delta\nu P$		89 MHz·mW (Tokyo IT)	5 MHz·mW (UCSB)
RIN		<-140 dB/Hz (Tokyo IT)	
P_{out}(cw)		3.2 mW (AT&T)	0.6 mW (AT&T)
P_{out}(pulse)	2 mW (77 K) (Tokyo IT) 3 mW (300 K) (Furukawa)	120 nW (TRW)	18 mW (AT&T)
f_m		300 ps pulse (Tokyo IT)	8 GHz (AT&T)

They also wish to thank Dr. S. Uchiyama (presently with China University), S. Kinoshita (presently with Fujitsu Laboratories), T. Sakaguchi, and other research students for help in performing the study. They also acknowledge support of this study by a Scientific Grant-in-Aid from the Japanese Ministry of Education, Science and Culture.

REFERENCES

ARAKAWA, Y. AND YARIV, A. (1985). "Theory of gain, modulation response and spectral linewidth in AlGaAs quantum well lasers," *IEEE J. Quantum Electron*, **QE-21**, 1666.

ARAI, S., ASADA, M., SUEMATSU, Y., ITAYA, Y., TANBUN-EK, T. AND KISHINO, K. (1980). "New 1.6 μm wavelength GaInAsP/InP buried heterostructure lasers," *Electron. Lett.* **16**, 349.

ASADA, M., KAMEYAMA, A. AND SUEMATSU, Y. (1984). "Gain and intervalence band absorption in quantum well lasers," *IEEE J. Quantum Electron.* **QE-20**, 745.

BASOV, N. G., BOGDANKEVICH, O. V. AND GRASYUK, A. Z. (1966). "Semiconductor lasers with radiating mirrors," *IEEE J. Quantum Electron.* **QE-2**, 9, 594–597.

CHAILERTVANITKUL, A., IGA, K. AND MORIKI, K. (1985). "GaInAsP/InP surface emitting laser ($\lambda = 1.4$ μm) with heteromultilayer Bragg reflector," *Electron Lett.* **21**, 303.

EVANS, G. A., HAMMER, J. M., CARLSON, N. W., ELIA, F. R., JAMES, E. A. AND KIRK, J. B. (1986). "Grating surface emitting laser with dynamic wavelength stabilization and far-field angle of 0.25 degrees," *Conference on Lasers and Electro-Optics*, Postdeadline Paper, ThU3.

GEELS, R., YAN, R. H., SCOTT, J. W., CORZINE, S. W., SIMES, R. J. AND COLDREN, L. A. (1988). "Analysis and design of a novel parallel-driven MQW-DBR surface-emitting diode laser," *The Conf. on Lasers and Electro-Optics*, paper WM-1.

GEELS, R. AND COLDREN, L. A. (1990). 12th IEEE International Semiconductor Laser Conference.

GOURLEY, P. L., BRENNAN, T. M. AND HAMMONS, B. E. (1989). "High-efficiency TEM continuous-wave (Al, Ga)As epitaxial surface-emitting lasers and effect of half-wave periodic gain," *Appl. Phys. Lett.* **54**, 1209.

GOODFELLOW, R. C., CARTER, A. C., REES, G. J. AND DAVIS, R. (1981). "Radiance saturation in small-area GaInAsP/InP and GaAlAs/GaAs LEDs," *IEEE Trans. on Electron Devices* **ED-28**, 365.

HENRY, C. H. (1983). "Theory of the linewidth of semiconductor lasers," *IEEE J. Quantum Electron.* **QE-18**, 259.

HO, E., KOYAMA, F. AND IGA, K. (1989). "Effective reflectivity and threshold of self-imaged surface emitting laser array," *Proc. of MOC/GRIN* **H5**, 228.

IBARAKI, A., ISHIKAWA, S., OHKOUCHI, S. AND IGA, K. (1984). "Pulsed oscillation of GaAlAs/GaAs surface-emitting injection lasers," *Electron. Lett.* **20**, 420.

IBARAKI, A., KAWASHIMA, K., FURUSAWA, K., ISHIKAWA, T., YAMAGUCHI, T. AND NIINA, T. (1989). "Buried heterostructure GaAs/GaAlAs distributed Bragg reflector surface emitting laser with very low threshold (5.2 mA) under room temperature cw conditions," *Jpn. J. Appl. Phys.* **28**, L667.

IGA, K., OIKAWA, M., MISAWA, S., BANNO, J. AND KOKUBUN, K. (1982). "Stacked planar optics; an application of the planar microlens," *Appl. Opt.* **21**, 3456.

IGA, K., SODA, H., TERAKADO, T. AND SHIMIZU, S. (1983). "Lasing characteristics of improved GaInAsP/InP surface emitting injection lasers," *Electron Lett.* **19**, 457.

IGA, K., ISHIKAWA, S., OHKOUCHI, S. AND NISHIMURA, T. (1984). "Room temperature pulsed oscillation of GaAlAs/GaAs surface emitting injection laser," *Appl. Phys. Lett.* **45**, 348.

IGA, K., Japanese Patent (1985).

IGA, K., KINOSHITA, S. AND KOYAMA, F. (1987). "Microcavity GaAlAs/GaAs surface emitting laser with Ith = 6 mA," *Electron. Lett.* **23**, 134.

IGA, K., KOYAMA, F. AND KINOSHITA, S. (1988). "Surface emitting semiconductor lasers," *IEEE J. Quantum Electron.* **QE-24**, 1845.

IKEGAMI, K. AND SUEMATSU, Y. (1968). "Carrier lifetime measurement of junction laser using direct modulation," *IEEE J. Quantum Electron.* **QE-4**, 148.

JEWELL, J. L., LEE, Y. H., TUCKER, R. S., BURRUS, C. A., SCHERER, A., HARBISON, J. P., FLOREZ, L. T. AND SANDROFF, C. J. (1989a). "Surface emitting quantum well lasers," *CLEO'90* (Anaheim), **CFF1**, 500.

JEWELL, J. L., SCHERER, A., MCCALL, S. L., LEE, Y. H., WALKER, S. J., HARBISON, J. P. AND FLOREZ, L. T. (1989b). "Low threshold electrically pumped vertical cavity surface emitting micro-lasers," *Electron. Lett.* **25**, 1123.

JEWELL, J. L., LEE, Y. H., SCHERER, A., MCCALL, S. L., OLSSON, N. A., TUCKER, R. S., BURRUS, C. A., HARBISON, J. P., FLOREZ, L. T., GOSSARD, A. C. AND ENGLISH, J. H. (1990). "Nonlinear FP etalons and microlaser devices," *SPIE*, OE/LASE.

KAWASAKI, H., KOYAMA, F. AND IGA, K. (1988). "Improvement of a flat surface circular buried heterostructure GaInAsP/InP surface emitting laser," *Jpn. J. Appl. Phys.* **27**, 1548.

KASUKAWA, A., IMAJO, Y., KASHIWA, S., FUKUSHIMA, T. AND OKAMOTO, H. (1990). "Room temperature pulsed oscillation of GaInAsP/InP surface emitting laser diode with Bragg reflector grown by MOCVD," DRC, post deadline paper.

KINOSHITA, S., SAKAGUCHI, T., ODAGAWA, T. AND IGA, K. (1987a). "GaAlAs/GaAs surface emitting laser with high reflective TiO_2/SiO_2 multilayer reflector," *Jpn. J. Appl. Phys.* **26**, 410.

KINOSHITA, S. AND IGA, K. (1987b). "Circular Buried Heterostructure (CBH) GaAlAs/GaAs Surface Emitting Lasers," *IEEE J. Quantum Electron.* **QE-23**, 882.

KINOSHITA, S., KOYAMA, F. AND IGA, K. (1987c). "Investigation of the cw operation at room temperature for GaAlAs/GaAs surface emitting laser," Technical Group Meeting, *IECE of Japan*, **OQE86**, 188.

KISHINO, K., KINOSHITA, S., KONNO, S. AND TAKO, T. (1983). "Selective meltbacked substrate inner-stripe AlGaAs/GaAs lasers operated under room temperature cw operation," *Jpn. J. Appl. Phys.* **22**, L473.

KOYAMA, F., UENOHARA, H., SAKAGUCHI, T. AND IGA, K. (1987). "GaAlAs/GaAs MOCVD growth for surface emitting laser," *Jpn. J. Appl. Phys.* **26**, 1077.

KOYAMA, F. AND IGA, K. (1987). "Single longitudinal mode operation of directly modulated GaAlAs/GaAs surface mitting lasers," *Trans. of IEICE of Japan* **E70**, 455.

KOYAMA, F., TOMOMATSU, K. AND IGA, K. (1988a). "GaAs surface emitting lasers with circular buried heterostructure grown by metalorganic chemical vapor deposition and two-dimensional laser array," *Appl. Phys. Lett.* **52**, 528.

KOYAMA, F., KINOSHITA, F. AND IGA, K. (1988b). "Room temperature cw operation of GaAs vertical cavity surface emitting laser," *Trans. of IEICE of Japan* **E71**, 1089.

KOYAMA, K., KINOSHITA, S. AND IGA, K. (1989). "Room temperature continuous wave lasing characteristics of a GaAs vertical cavity surface-emitting laser," *Appl. Phys. Lett.* **55**, 221.

LAU, K. Y. AND YARIV, A. (1985). "Ultra-high speed semiconductor lasers," *IEEE J. Quantum Electron.* **QE-21**, 121.

LAU, K. Y., DERRY, P. L. AND YARIV, A. (1988). "Ultimate limit in low threshold current quantum well GaAlAs semiconductor lasers," *Appl. Phys. Lett.* **52**, 88.

LEGER, J. R., SCOTT, M. L. AND VELDKAMP, W. B. (1988). "Coherent addition of AlGaAs lasers using microlenses and diffractive coupling," *Appl. Phys. Lett.* **52**, 1771.

LIAU, Z. L. AND WALPOLE, J. N. (1985). "Surface-emitting GaInAsP/InP laser with low threshold current and high efficiency," *Appl. Phys. Lett.* **46**, 115.

MORIKI, K., NAKAHARA, H., HATTORI, K. AND IGA, K. (1987). "Single transverse mode condition of surface emitting lasers," *Trans. of IEICE of Japan* **J70-C**, 501.

MOTEGI, Y., SODA, H. AND IGA, K. (1982). "Surface emitting GaInAsP/InP injection laser with short cavity length," *Electron. Lett.* **18**, 461.

MELNGAILIS, I. (1965). "Longitudinal injection-plasma laser of InSb," *Appl. Phys. Lett.* **6**, 59.

NOMURA, Y., SHINOZUKA, K., ASAKAWA, K. AND ISHII, M. (1985). "Lasing characteristics of GaAs/AlGaAs multilayer composing distributed feedback cavity for surface emitting laser," *Extended Abstracts of 17th Conf. on Solid State Devices and Materials*, **71**.

OLSHANSKY, R. AND SU, C. B. (1985). "Effect of nonlinear gain on the bandwidth of semiconductor lasers," *Electron. Lett.* **21**, 721.

OKUDA, H., SODA, H., MORIKI, K., MOTEGI, Y. AND IGA, K. (1981). "GaInAsP/InP surface emitting injection laser with buried heterostructures," *Jpn. J. Appl. Phys.* **20**, 563.

OGURA, M., HATA, T. AND YAO, T. (1984). "Surface emitting laser diode with vertical GaAs/GaAlAs quarter-wavelength multilayers and lateral buried heterostructure," *Jpn. J. Appl. Phys.* **23**, L512.

OKOSHI, T., KIKUCHI, K. AND NAKAMURA, A. (1980). "Novel method for high resolution measurement of laser output spectrum," *Electron. Lett.* **16**, 630.

OSHIKIRI, M., KAWASAKI, H., KOYAMA, F. AND IGA, K. (1989). "Reflectivity dependence of threshold current in GaInAsP/InP surface emitting laser," *Photo. Tech. Lett.* **1**, 11.

RAJA, M. Y. A., BRUECK, S. R. J., OSINSKI, M., SCHAUS, C. F., MCINERNEY, J. G., BRENNAN, T. M. AND HAMMONS, B. E. (1988). "Novel wavelength resonant optoelectronic structure and its application to surface-emitting semiconductor lasers," *Electron. Lett.* **24**, 1140.

REINHART, F. K. AND LOGAN, R. A. (1975). "GaAs-AlGaAs double heterostructure lasers with taper-coupled passive waveguides," *Appl. Phys. Lett.* **26**, 516.

PACKARD, J. R., TAIT, W. C. AND CAMPBELL, D. A. (1969). "Standing waves and single-mode room temperature laser emission from electron beam pumped cadmium sulfide," *IEEE J. Quantum Electron.* **QE-5**, 44.

SAKAGUCHI, T., KOYAMA, F. AND IGA, K. (1988). "Vertical cavity surface emitting laser with an AlGaAs/AlAs Bragg reflector," *Electron. Lett.* **24**, 928.

SCHAUS, C. F., SUN, S., SCHAUS, H. E., RAJA, M. Y. A., MCINERNEY, J. G. AND BRUECK, S. R. J. (1989). "300 K cw operation of MOCVD grown optically

pumped GaAs/AlGaAs resonant periodic gain vertical cavity lasers with 45% efficiency," *Conf. on Lasers and Electro-Optics*, **PD–13**.

SHIMIZU, M., KOYAMA, F. AND IGA, K. (1988). "Polarization characteristics of MOCVD grown GaAs/GaAlAs CBH surface emitting lasers," *Japan. J. Appl. Phys.* **27**, 1774.

SMILEY, V. N., TAYLER, H. F. AND LEWIS, A. L. (1971). "Laser emission in thin dielectric-coated CdSe lasers," *J. Appl. Phys.* **42**, 5859.

SODA, H., IGA, K., KITAHARA, C. AND SUEMATSU, Y. (1979). "GaInAsP/InP surface emitting injection lasers," *Jpn. J. Appl. Phys.* **18**, 2329.

SODA, H., MOTEGI, Y. AND IGA, K. (1983). "GaInAsP/InP surface emitting injection lasers with short cavity length," *IEEE J. Quantum Electron.* **QE-19**, 1035.

SPRINGTHORPE, A. J. (1977). "A Nobel double-heterostructure p–n-junction laser," *Appl. Phys. Lett.* **31**, 524.

STILLMAN, G. E., SIRKIS, M. D., ROSSI, J. A., JOHNSON, M. R. AND HOLONYAK, N. (1966). "Volume excitation of an ultrathin single-mode CdSe laser," *Appl. Phys. Lett.* **9**, 7, 268–269, 1966.

SUEMATSU, Y. AND FURUYA, K. (1977). "Theoretical spontaneous emission factor of injection lasers," *Trans. IECE of Japan*, **E-60**, 467.

SUEMATSU, Y. AND FURUYA, K. (1977). "Theoretical spontaneous emission factor of injection lasers," *Trans. IECE of Japan*, **E-60**, 467.

SUEMATSU, Y., ARAI, S. AND KISHINO, K. (1983). "Dynamic single-mode semiconductor laser with a distributed reflector," *IEEE J. Lightwave Tech.* **LT-1**, 161.

TANOBE, M., KOYAMA, F. AND IGA, K. (1989). "Spectral linewidth of a GaAlAs/GaAs surface emitting laser," *Electron. Lett.* **25**, 1444.

UCHIYAMA, S. AND IGA, K. (1984). "GaInAsP/InP surface emitting injection laser with a ring electrode," *IEEE J. Quantum Electron.* **QE-20**, 1117.

UCHIYAMA, S. AND IGA, K. (1985). "Two-dimensional array of GaInAsP/InP surface emitting laser," *Electron. Lett.* **21**, 162.

UCHIYAMA, S. AND IGA, K. (1986a). "Low threshold GaInAsP/InP surface emitting laser," *Trans. IECE Japan* **E69**, 587.

UCHIYAMA, S., OHMAE, Y., SHIMIZU, S. AND IGA, K. (1986b). "GaInAsP/InP surface emitting lasers with current confining structure," *IEEE/OSA Lightwave Tech.* **LT-4**, 846.

UCHIYAMA, S., IGA, K. AND KOKUBUN, Y. (1986c). "Threshold gain of distributed surface emitting lasers," *12th European Conf. on Optical Commun.* 37.

UENOHARA, H., KOYAMA, F. AND IGA, K. (1989). "Application of the multiquantum well (MQW) to a surface emitting laser," *Jpn. J. Appl. Phys.* **28**, 740.

WATANABE, I., KOYMA, F. AND IGA, K. (1988). "GaInAsP/InP CBH surface emitting laser with a dielectric multilayer reflector," *Jpn. J. Appl. Phys.* **16**, 1598.

WU, M. C., OGURA, M., HSIN, W., WHINNERY, J. R. AND WANG, S. (1987). "Surface emitting laser diode with bent double heterostructure," *Conference on Lasers and Electro-Optics*, **WG4**.

YAMAMOTO, Y., MACHIDA, S., IGETA, K. AND HORIKOSHI, Y. (1988). *XVI Int. Conf. Quantum Electron.*, **WB-2**.

YOO, H. J., SCHERER, A., HARBISON, J. P., FLOREZ, L. T., PEAK, E. G., VAN DER GAAG, B. P., HAYES, J. R., LEHMEN, E., KAPON, E. AND KWON, Y. S. (1990). "Fabrication of a two-dimensional phased array of vertical-cavity surface-emitting lasers," *Appl. Phys. Lett.* **56**, 1198.

YUASA, T., HAMANO, N. AND SUGIMOTO, M., TAKADO, N., UENO, M., IWATA, H., TASHIRO, T., ONABE, K. AND ASAKAWA, K. (1988). "Surface emitting GaAs/AlGaAs multi-quantum well lasers with optical bistability," *Conference on Lasers and Electro-Optics*, **WO6**.

Chapter 4

GRATING-OUTCOUPLED SURFACE EMITTING SEMICONDUCTOR LASERS

Gary A. Evans*, **Nils W. Carlson, Jacob M. Hammer**†

David Sarnoff Research Center, Princeton, New Jersey

and

Jerome K. Butler

Southern Methodist University, Dallas, Texas

I. INTRODUCTION

The ideal semiconductor laser would be 100% efficient while producing high output power (many watts) into a single-lobe far-field with milliradian beam divergence. In addition, this device would have a dynamically stabilized single wavelength capable of multi-GHz modulation rates and low cost. During the past 20 years, the quest to develop such lasers has led to the demonstration of many concepts. The extensive work on edge-emitting arrays, distributed feedback (DFB), coupled-cavity, and distributed Bragg reflector (DBR) lasers is documented in hundreds of publications. Preliminary investigations of many novel semiconductor laser configurations such as multiple-junction (Kosonacky *et al.*, 1968), external Bragg reflector (Hammer *et al.*, 1985), unstable resonator (Bogatov *et al.*, 1980; Craig *et al.*, 1985; Salzman *et al.*, 1985; Tilton *et al.*, 1991), and tailored-gain (Lindsey *et al.*, 1987) lasers were also initiated. Three basic types of surface-emitting, as opposed to edge-emitting, semiconductor lasers have also been considered: the vertical cavity (Chapter 3), the folded-cavity or etched facet (Chapter 5) and the grating-outcoupled surface emitting (GSE) semiconductor laser (Burnham *et al.*, 1975; Alferov *et al.*, 1975; Zory and Comerford, 1975; Reinhart *et al.*, 1975; Ng and Yariv, 1977; Evans *et al.*, 1986; Kojima

* Current address: Southern Methodist University, School of Engineering and Applied Science, Dallas, Texas.

† Current address: Photonics Consulting, Seaford, Virginia.

ISBN 0-12-244070-6

et al., 1987; Hammer *et al.*, 1987; Macomber *et al.*, 1987; Mott and Macomber, 1989; Carlson *et al.*, 1988a; Evans *et al.*, 1988b; Evans *et al.*, 1989; Welch *et al.*, 1989; Waarts *et al.*, 1990; Evans *et al.*, 1991). In this chapter, we review progress towards obtaining high power, narrow bandwidth and dynamic stability in GSE semiconductor lasers. These GSE lasers can consist of single elements, coherent arrays in one or two dimensions, or oscillator-amplifier configurations.

Initial interest (Stoll, 1978a; Evans *et al.*, 1981) for GSE array architectures resulted from a desire to develop coherent, large aperture ($\geq 1\ mm^2$), efficient, lightweight and compact semiconductor lasers for applications such as satellite-to-satellite communication that require several watts of collimated power. Low-power ($\sim 10\ mW$) applications are also presently envisioned and include single-element GSE devices with beam-steering capability for optical interconnects.

The GSE approach to the formation of diode laser arrays includes the following advantages:

- elimination of reflecting cleaved facets, resulting in increased reliability and simpler manufacturing;
- probe testing of devices at the wafer level, resulting in decreased manufacturing costs;
- heat sinking through the broad faces of the wafer, allowing efficient, high-power operation;
- scaling to large areas and high power;
- electronic beam steering by injection current adjustment or wavelength tuning;
- complete passivation of the device with no exposed active regions; and
- realization of high optical fill factors in the emitting aperture.

However, the fabrication of GSE lasers is more complicated compared to the simple edge-emitting lasers. Contemporary designs require multiple independent current controls to provide beam-steering or to provide highly coherent operation. The epitaxial material must have excellent electrical and optical properties, and it must be extremely uniform in composition and layer thickness, and have excellent surface morphology.

II. BASIC CONCEPTS AND OPERATING PRINCIPLES

A. Bragg Gratings

Grating deflections or reflections (deflections through 180°) of guided light in an optical waveguide are caused by constructive interference due to a

resonant phenomena often called Bragg scattering, Bragg deflection, or Bragg reflection because of their similarity to the diffraction of X-rays from crystal lattices (Brillouin, 1953). Bragg scattering through a particular angle requires multiple scattering of a wave by disturbances that are spatially periodic and sufficiently numerous to have a well-defined grating vector in reciprocal lattice space. This process is illustrated in Fig. 1, from which the classical relationship between the spacing Λ of atoms is determined from the X-ray wavelength λ and the angle of incidence θ by the relationship:

$$m\lambda = 2\Lambda \sin \theta \qquad \text{where } m = 1, 2, 3, \ldots \tag{1}$$

For Bragg scattering, only light at certain (resonant) wavelengths λ incident upon a fixed grating period Λ at a fixed angle θ will undergo strong diffraction. As the wavelength departs from resonance the diffracted intensity falls off rapidly although there is generally a weak diffracted intensity (at a fixed angle θ) for wavelengths far from the resonant wavelength.

Bragg scattering similarly occurs if a guided mode is propagating in a dielectric waveguide with a periodic disturbance (Kogelnick and Shank, 1972), such as the surface relief grating shown in Fig. 2(a). For modes propagating in such structures, scattering can result in in-plane reflection or deflection or outcoupling from the waveguide at an angle Θ. The undiffracted light, sometimes referred to as the zeroth order, continues to propagate along the guide. In general, the grating lines are not perpendicular to the direction of propagation in the waveguide. The angle Φ_1 in Fig. 2(b) is a measure of this deviation, which may be either intentional (Stoll, 1978b)

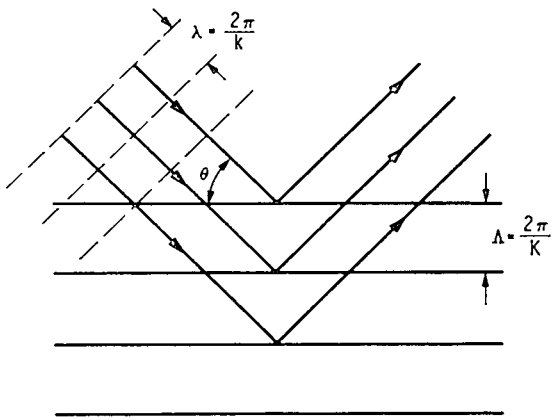

Fig. 1. Bragg scattering of a plane wave from a periodic media. Strong diffraction peaks occur at $m\lambda = 2\Lambda \sin \theta$ due to constructive interference.

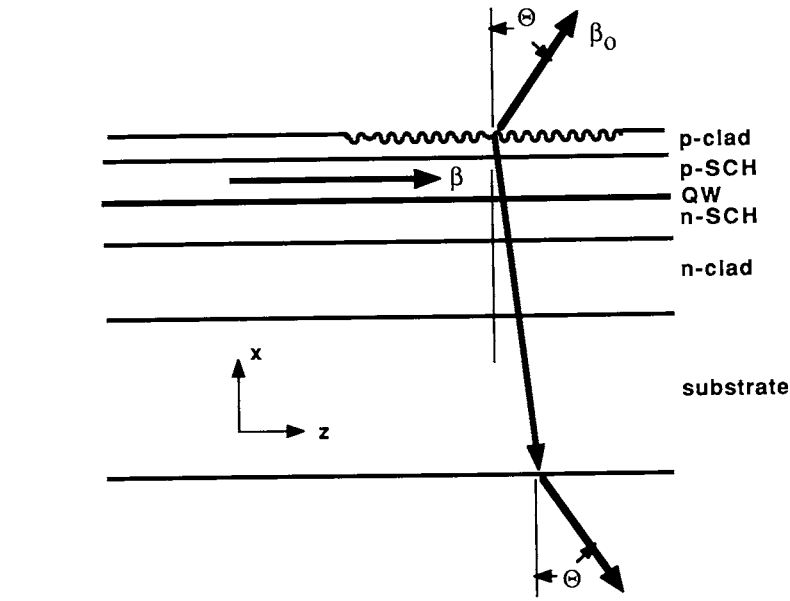

a)

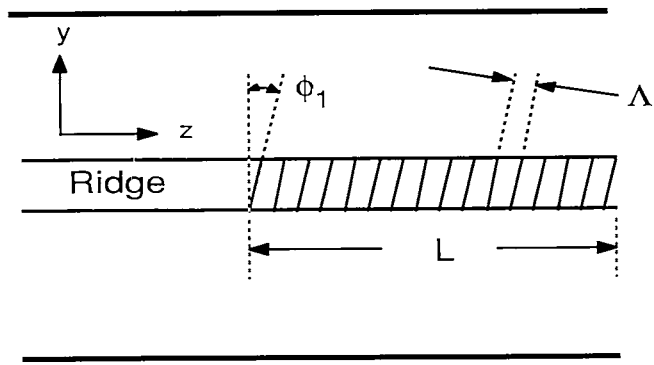

b)

Fig. 2. (a) Sideview of a dielectric waveguide with a periodic surface corrugation; (b) top view showing the grating lines at an angle Φ_1 with respect to the direction of propagation.

or may be the result of inevitable slight misalignments occurring during the device fabrication process.

The directions of the appropriate propagation vectors for the periodic dielectric waveguide structure shown in Fig. 2 are shown in Fig. 3. The waveguide surface and waveguide planes are parallel to the y–z plane. If the grating lines were normal to the propagation direction along the z axis, the grating vector $\mathbf{K}_g$ would also be parallel to z and the guided light (indicated by the wave vector β in Fig. 2) flowing in the $+z$ direction would be reflected into the $-z$ direction by in-plane Bragg scattering. $\mathbf{k}_0$ iss the vector representing the outcoupled light. The deflected light is represented by the vector $\mathbf{k}_e$, which has the same magnitude as the vector $\mathbf{k}_{eff}$.

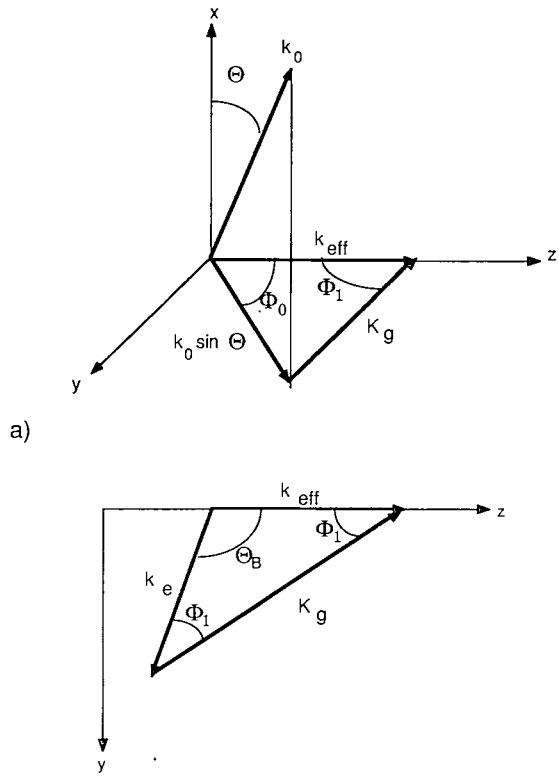

Fig. 3. (a) Propagation vectors and angles for a general waveguide grating outcoupler. y–z is the wafer and waveguide plane; (b) propagation vectors and angles for Bragg scattering (deflection or reflection) in the waveguide plane. k_{eff} is parallel to the z-axis.

By applying the usual conservation laws in reciprocal lattice vector space, it can be shown that

$$n_0^2 \sin^2 \Theta_{m_{out}} = n_{eff}^2 - (2n_{eff} m_{out} \lambda \cos \Phi_1)/\Lambda + m_{out}^2 \lambda^2/\Lambda^2,$$
$$m_{out} = 1, 2, 3, \ldots \tag{2a}$$

where the vector amplitudes are given by

$$k_0 = 2\pi n/\lambda = \beta \tag{2b}$$

$$k_e = k_{eff} = 2\pi n_{eff}/\lambda = \beta \tag{2c}$$

$$K_g = 2\pi m_{out}/\Lambda \tag{2d}$$

and n_0 is the refractive index of the region into which the light is coupled, n_{eff} is the effective index of the guided mode, λ is the free space wavelength of the light and Λ is the grating period.

Similarly,

$$\lambda/\Lambda = -(2n_{eff}/m_B) \sin(\Theta_B/2), \qquad m_B = 1, 2, 3, \ldots \tag{3}$$

The integers m_{out} and m_B correspond to the output coupling order and the in-plane Bragg reflection order, respectively, and Θ_B is the in-plane Bragg diffraction angle (Fig. 2(b)). Equations (2) and (3) are quite general and may be used to find the angles and grating orders that will sustain both in-plane Bragg scattering (reflection or deflection) and output coupling for any waveguide containing a grating. The conditions for both to occur are tabulated for some grating orders in Table I.

If the mode is propagating perpendicular to the gratings, the outcoupling angle for order m_{out}, $\Theta_{m_{out}}$, is given by

$$\sin \Theta_{m_{out}} = \frac{n_{eff} - m_{out}\lambda/\Lambda}{n_0}, \qquad m_{out} = 1, 2, 3, \ldots \tag{4}$$

Equation (4) has solutions only when the absolute value of the right-hand side is less than or equal to one. In a plane parallel geometry such as shown in Fig. 2 if light is coupled to air at an angle Θ above the grating, light will also be coupled to air at the angle Θ after passing through the substrate. The angle in the substrate will be related to that in air by Snell's law. Light can also be coupled into the substrate without being coupled to air. In this case, the light suffers total internal reflection at the substrate air boundary and is a loss mechanism for GSE devices.

For the best outcoupling efficiency, the grating outcoupler should operate in first order ($m_{out} = 1$). The value of λ/Λ required to give first-order outcoupling at angle Θ_1 is found from Eq. (4). Also from Eq. (4) the output

Table I

GSE-BDB Summary. The conditions under which a waveguide mode can simultaneously undergo distributed Bragg deflection (DBD) through an angle Θ_B in the waveguide plane and be coupled out of the waveguide plane (Grating Surface Emission, GSE) through an angle Θ are listed for various grating orders. m_{out} is the grating order for GSE and m_B is the grating order for DBD.

$M = m_{out}/m_B$	$\sin^2\Theta = n_e^2[1-4(M-M^2)\sin^2(\Theta_B/2)]$	Implications
1/1	n_e^2	$n_e \geq 1$, no solutions exist when $\Theta_B = 180°$, $\Theta = 0$;
1/2	$n_e^2 \cos^2 \Theta_B/2$	$\cos \Theta_B/2 \leq 1/n_e$ (e.g. $n_e = 3.4$, $\Theta_B = 145.8°$)
1/3	$n_e^2[1-(8/9)\sin^2(\Theta_B/2)]$	solutions for $n_e < 3$
1/4	$n_e^2[1-(3/4)\sin^2(\Theta_B/2)]$	solutions for $n_e < 2$
2/1	$n_e^2[1+8\sin^2(\Theta_B/2)]$	no solutions for $(M-M^2) < 0$
2/2	same as 1/1	
2/3	same as 1/3	
2/4	same as 1/2	
3/1	$(M-M^2) < 0$	no solutions
3/2	$(M-M^2) < 0$	no solutions
3/3	same as 1/1	
3/4	same as 1/4	
3/5	$n_e^2[1-(4/5)\sin^2(\Theta_B/2)]$	solutions for $n_e < \sqrt{5} = 2.24$
4/1-4/3	$(M-M^2) < 0$	no solutions
4/4	same as 1/1	
4/5	$n_e^2[1-(16/25)\sin^2(\Theta_B/2)]$	solutions for $n_e < \sqrt{5/3}$

angles of higher-order outcoupling with the same grating period and wavelength are given by

$$\sin \Theta_{m_{out}} = \left[(1-m_{out}) \frac{n_{eff}}{n_0} + m_{out} \sin \Theta \right] \tag{5}$$

where $\Delta n = n_{eff} - n_0$.

For negative Θ_1 (backward outcoupling) the absolute value of the right side of Eq. (5),

$$\left| (1-m_{out}) \frac{n_{eff}}{n_0} - m_{out} \sin \Theta \right|,$$

is greater than one for all non-zero values of Θ. Thus, there is no solution for $\Theta_{m_{out}}$ for $m_{out} > 1$, and hence, there will be no outcoupling orders above the first and no losses associated with such outcouplings for gratings chosen to give a negative Θ.

If, however, Θ is positive (forward coupling), then the absolute value of the right side of Eq. (5) becomes

$$\left| m_{out} \sin \Theta + (1 - m_{out}) \frac{n_{eff}}{n_0} \right|,$$

which can either be greater or less than one depending on the order and index values. In particular, solutions can be found for orders coupling into a high index substrate (n_0 = substrate index) but not into air ($n_0 = 1$) for many semiconducting waveguide configurations. For example, if $n_{eff} \approx n_{substrate} \approx 3.3$, $m = 2$, and $\Theta_1 = \{+20°, +10°, +5°\}$ light will be coupled into the substrate at $-18.4°$, $-40.8°$, $-65.9°$ but not into air. In these cases there will be no outcoupling for orders higher than the second. Thus, if the first-order outcoupling grating is chosen to couple to air in a forward direction, light will be lost to the substrate in the second order.

In the special case of first-order outcoupling at 0° (normal to the waveguide plane), the second grating order folds into the second-order in-plane Bragg reflection. The resonant in-plane Bragg reflection wavelength, λ_B, for a period Λ is given by (see Eq. (3))

$$\lambda_B = \frac{2 n_{eff} \Lambda}{m_B}, \qquad m_B = 1, 2, 3, \ldots, \tag{6}$$

where m_B is the Bragg reflection order. In this case, m_B equals 2 and m_{out} equals 1. Alternatively, if the nominal operating wavelength λ_B is specified, the required grating period Λ is chosen (for the Bragg angle $\Theta_B = 180°$) by

$$\Lambda = \lambda_0 / n_{eff} \tag{7}$$

B. Single-Element GSE Lasers

Conventional edge-emitting semiconductor lasers (Figure 4(a)) using cleaved facets to provide both feedback and outcoupling were first fabricated in the early 1960s. The grating surface emitting laser was demonstrated (Burnham *et al.*, 1975; Alferov *et al.*, 1975; Zory and Comerford, 1975; Reinhart *et al.*, 1975) about 15 years later. The simplest GSE laser replaces these cleaved facets with an optical waveguide region with a distributed Bragg reflector (DBR) grating that provides feedback for laser oscillation

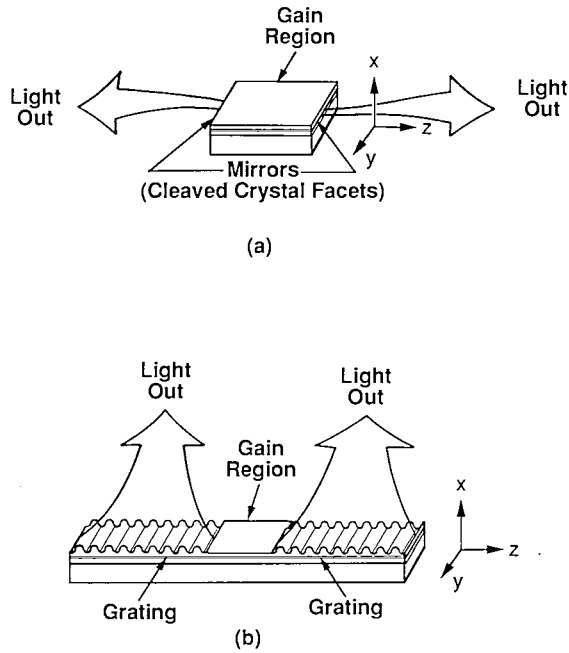

Fig. 4. (a) Conventional edge-emitting semiconductor laser; (b) single element GSE laser.

in second-order and provides outcoupling perpendicular to the laser surface in first-order (Fig. 4(b)). As a result, GSE lasers use horizontal epitaxial layers to provide gain, electrical confinement and optical confinement in the same manner as edge-emitting semiconductor lasers. Some GSE lasers use separate gratings for feedback and outcoupling, in which case the feedback grating can be first-order (Carlson *et al.*, 1990a; Tiberio *et al.*, 1991).

The earliest GSE devices produced far-field patterns with very narrow beam divergences, but suffered from high threshold current density, low power, poor beam quality, and low efficiency. The poor performance was due to the double heterostructure or large optical cavity (LOC) laser structures used and the resulting high absorption of the unpumped active layer in the DBR section. With LOC structures, the active layer was etched away to eliminate absorption, but then the waveguide discontinuity between the gain and DBR sections resulted in substantial scattering loss. The use of tapered transitions was moderately effective in reducing these losses (Evans *et al.*, 1986). The gain section to DBR waveguide discontinuity can be made negligible and the active layer absorption eliminated with the introduction

of an additional growth step after removal of the active layer in the DBR sections. This approach is often used in the InGaAsP material system (Koch *et al.*, 1988; Vangieson *et al.*, 1991).

The use of 'quantum-well' geometries (developed for edge-emitting lasers during the 1980s) for GSE lasers allowed a common waveguide in both the gain and DBR sections as shown in Fig. (5). Because of the step-like density of states, bandgap shrinkage effects (Tarucha *et al.*, 1983), and saturation of the excitonic absorption (Miller *et al.*, 1982), the unpumped quantum-well active region in the DBR section can have low losses ($<5\ \mathrm{cm}^{-1}$). In this simple structure, the cap layer and a large portion of the *p*-clad must be removed in the grating region so that a small portion of the guided mode senses the grating region. The resulting discontinuity between the gain and passive DBR region is very slight, with typical optical mode overlaps (defined in Section 4.3) between 90% and 99%. Use of these quantum well structures has led to single-element as well as to arrays of GSE lasers with power and differential quantum efficiencies equivalent to edge-emitting lasers.

Large far-field beam divergences, which are typically 10° (parallel) and 35° (perpendicular) relative to the plane of the *p–n* junction for edge-emitting lasers are overcome with the use of GSE lasers. Depending on the length of the DBR section and the grating depth, the effective aperture of the GSE laser can be about 100 μm to 1 cm or more, resulting in corresponding beam divergences of 0.5° to 0.005°.

C. One-Dimensional GSE Arrays

Increases in emission power and reductions of beam divergence can be achieved by forming a coherent linear array of GSE lasers (Hammer *et al.*, 1987; Carlson *et al.*, 1988a; Palfrey *et al.*, 1989; Welch *et al.*, 1989; Waarts *et al.*, 1990; Parke *et al.*, 1990a; Liew *et al.*, 1991a). If the strength of the grating in each passive region is such that some of the light is transmitted to adjacent gain sections, then the linear array can operate coherently as one long, multielement, injection-locked array. This can be achieved if the reflectivity of the DBR section is sufficiently low. Both broad-area and narrow-stripe one-dimensional arrays have been demonstrated. Single-frequency operation of 3–5 μm-wide ridge-guided GSEs have been demonstrated at drive currents in the 4–10 times threshold range at wavelengths of 1.3–1.5 μm (Palfrey *et al.*, 1990; Vangieson *et al.*, 1991) and 0.97 μm (Liew *et al.*, 1991a). Differential quantum efficiencies >25%/surface, and cw output powers >1 W have been observed for one-dimensional GSE

arrays (Liew *et al.*, 1991a). Single-element arrays have achieved linewidths of less than 300 kHz (Carlson *et al.*, 1990b).

D. Two-Dimensional GSE Arrays

One approach to expand linear arrays into a two-dimensional array is by expanding each single gain section in the lateral direction as shown in Figs. 5 and 6. As in one-dimensional arrays, the basic building block of two-dimensional arrays is the single-element GSE discussed above. Lateral coupling of the gain sections can be achieved using the methods discussed in Chapter 2 for edge-emitting arrays. Simple evanescent coupling of ridge-guided lasers has been mainly used for lateral coupling (Evans *et al.*, 1988b; Evans *et al.*, 1991), but Y-guide coupling (Streifer *et al.*, 1987; Welch *et al.*, 1987) and 3-dB coupling has also been tried in GSE lasers (Evans *et al.*, 1989). As in one-dimensional arrays, the grating performs several functions that are essential for phase-locked operation of the surface emitting array. The grating period is chosen so that the second diffraction order acts as a Bragg reflector in the waveguide plane, which provides the optical feedback

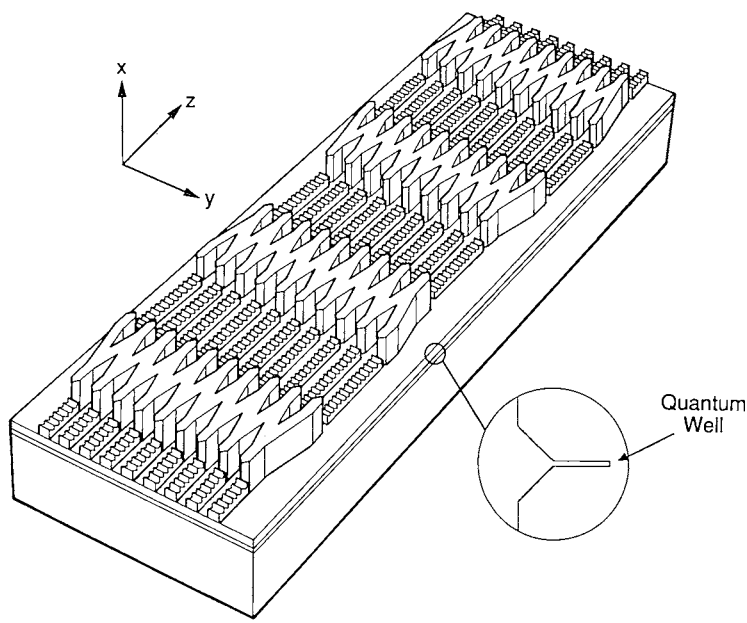

Fig. 5. Sketch of a $10 \times N$ array showing four gain sections with Y-coupling. The quantum-well waveguide is common to both gain and grating regions.

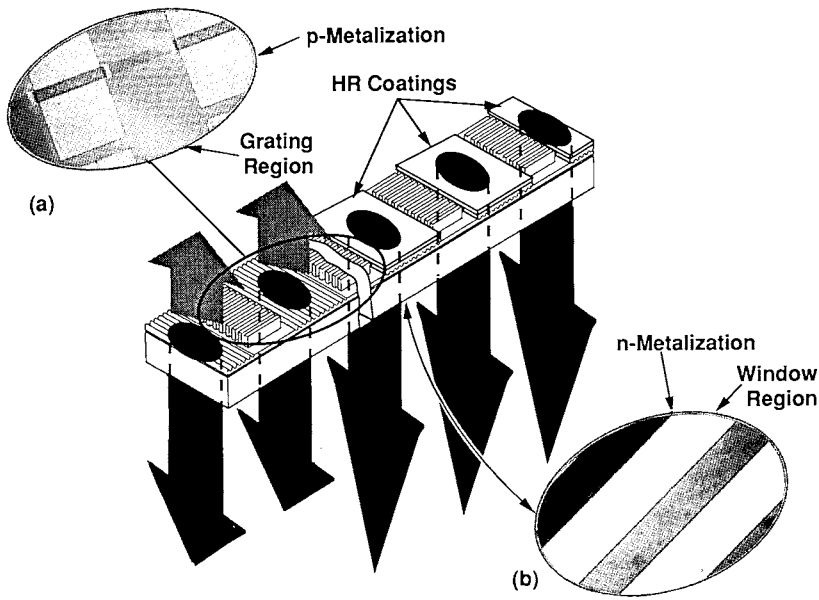

Fig. 6. Sketch of a $10 \times N$ array showing four gain sections with evanescent-coupling of 10 parallel ridge guide lasers in each gain section. The inset photographs shows (a) a completed gain section with contact pad; and (b) the window region for emission from the substrate side.

required for laser oscillation. The first diffraction order of such a grating provides surface emission by coupling guided light normal to and out of the waveguide plane. Finally, the zeroth diffracted order (undiffracted light) is coupled to the adjacent colinear gain section to achieve phase-locking in the longitudinal direction. This optical coupling due to transmitted light has been called mutual-injection-coupling (MIC).

E. Extended-Area GSE Arrays

In the two-dimensional arrays discussed above, the scale of lateral coupling is small (typically 50–100 μm) compared to longitudinal coupling (typically 1 cm or more), and the resulting light emission is therefore from a slit-like aperture. The resulting far-field beam divergence is narrow (~0.01°) along the longitudinal axis and relatively wide (~1°) along the lateral axis. Many systems applications prefer both a circularly symmetric output beam and high output power. These requirements can be satisfied if the device is extended laterally. The number of lateral elements can be increased, and

up to 250 elements have been used in a single gain section for a lateral width of 1 mm (Evans *et al.*, 1990a).

Unfortunately, a large number of lateral elements results in numerous lateral modes, causing problems of mode control especially with material that is not highly uniform. However, for applications such as pumping solid-state lasers, where single-frequency operation is unnecessary, the lower threshold current densities obtained with very wide gain sections (Evans *et al.*, 1990a), due in part to reduced diffraction losses (Dupuy *et al.*, 1992), are helpful in increasing the efficiency.

The use of monolithic corner-turning mirrors to connect parallel columns of one- or two-dimensional arrays on a monolithic chip allows increased lateral extent without increasing the number of lateral modes although the number of longitudinal modes increases. This technique has been demonstrated with one-dimensional (Palfrey *et al.*, 1990; Liew *et al.*, 1991a; Liew *et al.*, 1991b) and two-dimensional (DeFreez *et al.*, 1990; Bossert *et al.*, 1990; Liew *et al.*, 1991a; Liew *et al.*, 1991b) arrays. Figure 7 shows a serpentine of one-dimensional arrays while Fig. 8 shows a simple extended area GSE ring array consisting of multiple elements in each gain section. Figure 9 shows how such a ring configuration can be extended to multiple columns. The corner-turning mirrors operate on the principle of total internal reflection, due to the large index change between the GaAs/AlGaAs or InGaAsP/InP and air interface. Columns of GSE lasers have also been coherently connected by using an extra prism to couple light from a grating section in one column to a grating section in another column (Carlson *et al.*, 1990f), as illustrated in Fig. 10.

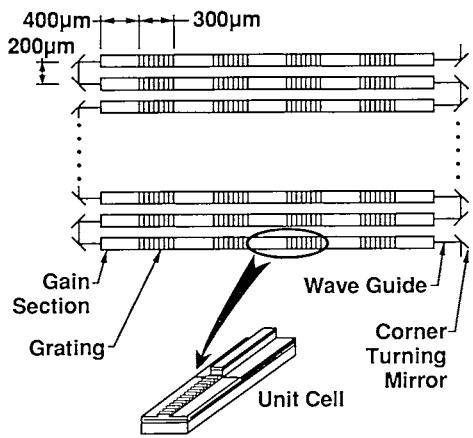

Fig. 7. Sketch of a one-dimensional serpentine GSE array.

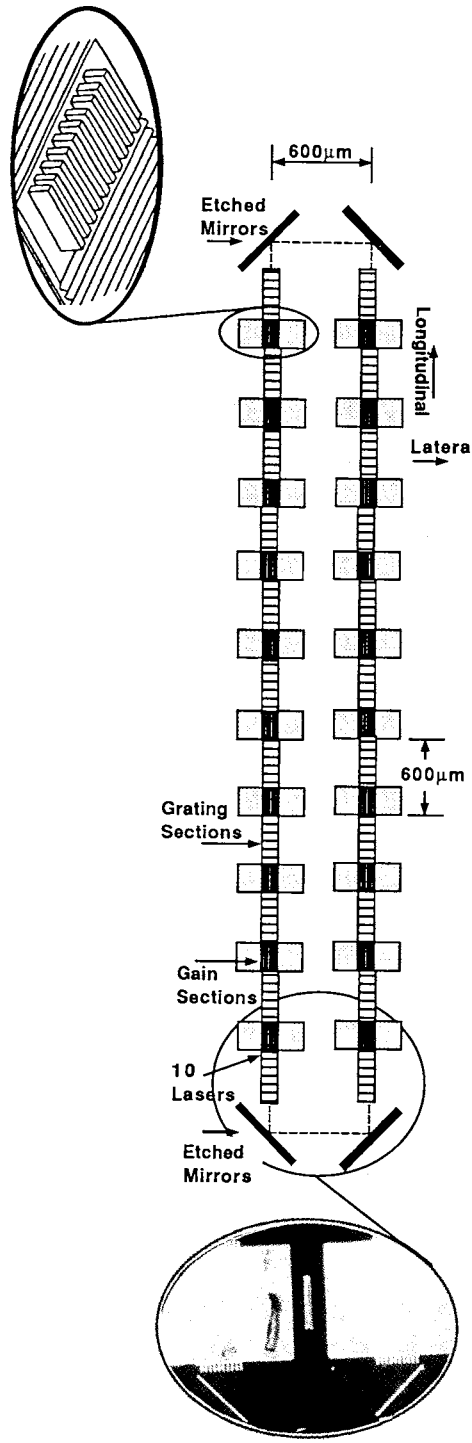

Fig. 8. Sketch of a $10\times10\times2$ GSE ring laser array. Inset shows 10 evanescently coupled ridge-guided lasers in the gain section.

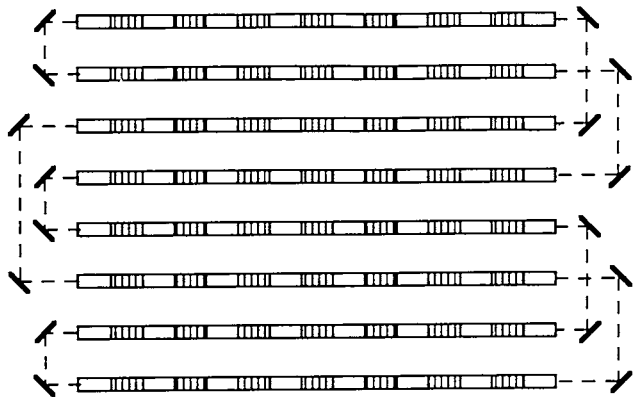

Fig. 9. Sketch of an eight-column GSE array configured in a ring using corner-turning mirrors.

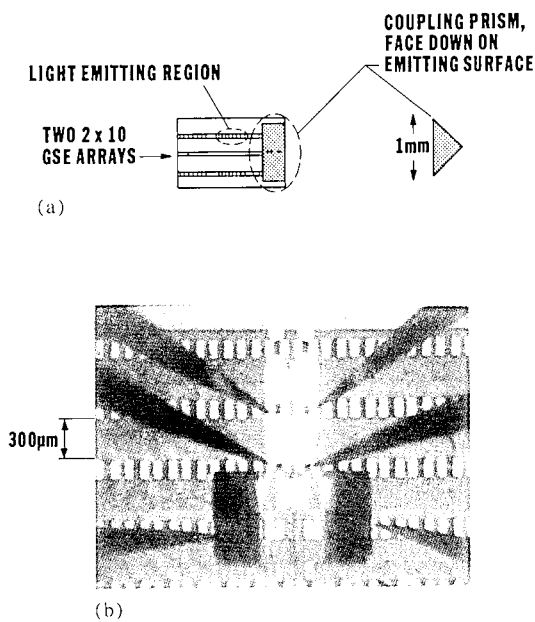

Fig. 10. (a) Sketch of the prism-coupled 10×2 GSE array photographed in (b) during probe testing.

Other approaches to increasing the lateral extent of edge- and surface-emitting lasers and amplifiers, include the use of branching waveguides (illustrated in Fig. 11) (Krebs *et al.*, 1991) to connect parallel columns or a series of multiple branches in a 'tree' configuration (Parke *et al.*, 1991).

F. GSE Amplifier Arrays

Two variations on the basic GSE laser concept are a master oscillator power amplifier (MOPA) configuration with multiple passive grating outcoupling regions (Carlson *et al.*, 1990a; Welch *et al.*, 1990) and a MOPA with a continuous active-grating outcoupler (Carlson *et al.*, 1990g; Mehuys *et al.*,

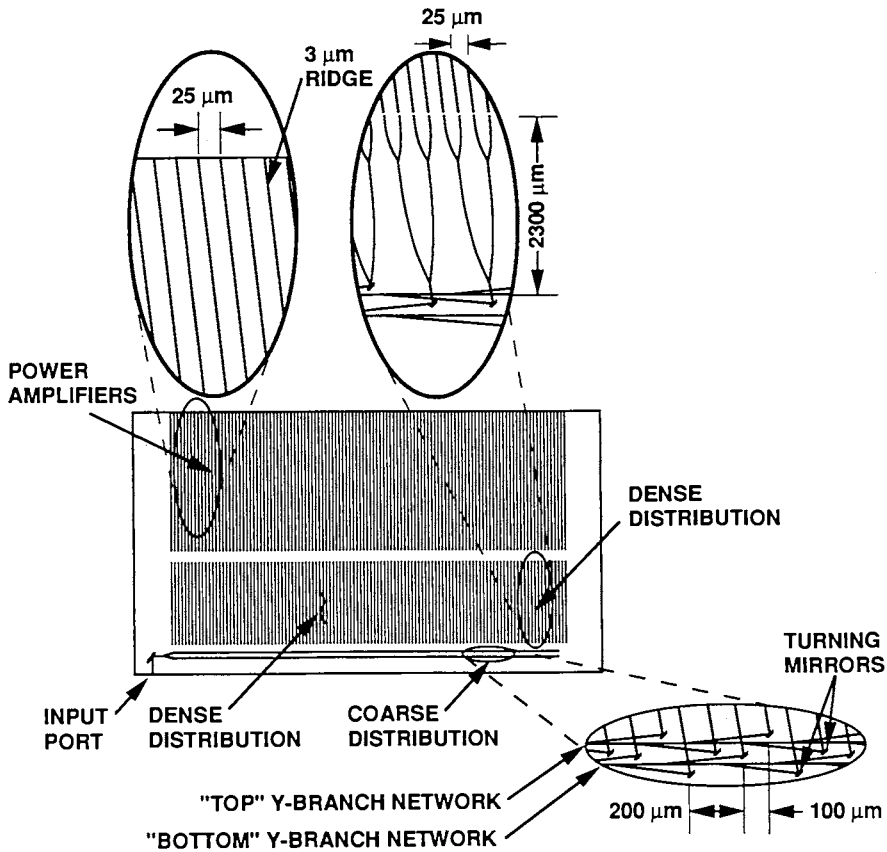

Fig. 11. Sketch of a 400-emitter coherent amplifier chip using branching waveguides (Krebs *et al.*, 1991) (© 1991 IEEE).

1991a). A key feature of these GSE-MOPA devices is that they can be scaled to increase power output by increasing the number or size of the amplifiers, while the oscillator (and number of oscillator modes) is unchanged. As a result, mode discrimination does not become more difficult with increasing size. In addition, excellent noise reduction properties are projected for coherent, high power outputs (Carlson *et al.*, 1990g).

The cascaded GSE-MOPA array shown in Fig. 12 consists of a single-mode GSE-distributed-Bragg reflector laser and a chain of cascaded power amplifiers with passive grating-output coupled waveguide sections after each power amplifier section. The period of the outcoupling gratings is selected so that the Bragg condition for reflection is not satisfied for any wavelength within the gain-bandwidth of the amplifier sections. As a result, the outcoupled light is emitted off-normal, as illustrated by the arrows in Fig. 12.

A GSE amplifier device that offers improved beam quality over the cascaded GSE-MOPA array is obtained by replacing the chain of amplifiers and grating output couplers by a single amplifier with a buried grating output coupler in the active section. A diagram of this type of device is shown in Fig. 13. A DFB (or DBR) laser oscillator that is fabricated along the same waveguide injects coherent light into the amplifying and output coupling region. The injected coherent signal builds up along the amplifier region until the local gain is saturated down to the level of the total (outcoupling and internal) losses. As a result, the local carrier density is 'pinned' along the remaining length of the aperture, which provides a uniform phase relationship and a nearly uniform intensity over the emitting aperture. Ideally, the wavefront of the output coupled light will be planar, and the far-field pattern will have a strong central lobe with minimal side lobes. However material nonuniformities in the device structure and surface variations will give rise to wavefront aberrations. The large aspect ratio and off-normal emission of the output beam can be corrected to near-unity

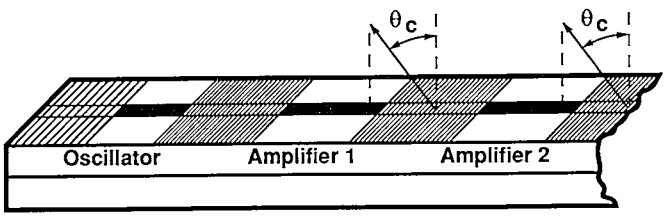

Fig. 12. Sketch of a cascaded GSE-MOPA array. Arrows indicate emission of the grating output coupled light in the "backward" direction.

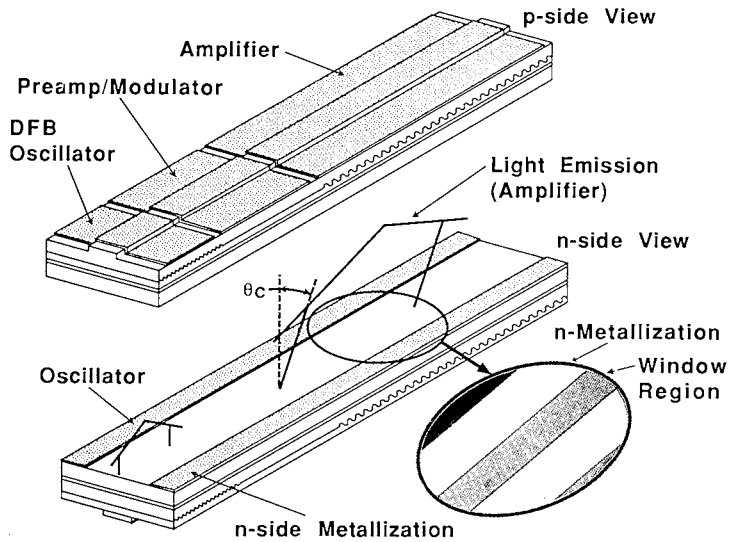

Fig. 13. Sketch of a continuous active grating GSE-MOPA device. Emission of the grating output coupled light is in the "forward" direction. Inset shows the window region for emission from the substrate side.

aspect ratio using the simple external optics shown in Fig. 14 (Carlson *et al.*, 1990g; Liew *et al.*, 1990).

The continuous active-grating MOPA requires only two or three independent electrodes, one for the oscillator, one for the amplifier, and possibly one for a pre-amplifier. A pre-amplifier (without outcoupling) is useful to match the output power of the oscillator to the saturation power of the outcoupling amplifier region, resulting in maximum efficiency and noise suppression.. Additional independent electrodes could be incorporated in the amplifier region by fabricating segmented contacts, allowing some electronic control of the beam pattern. The reduced number of independent electrodes is a significant simplification over present GSE oscillator arrays and chained amplifiers.

III. DESIGN CONSIDERATIONS

A. GSE Oscillator Arrays

1. Structure Considerations

As in most semiconductor lasers, GSE lasers require an active region designed for efficiency and high power. The passive waveguide grating

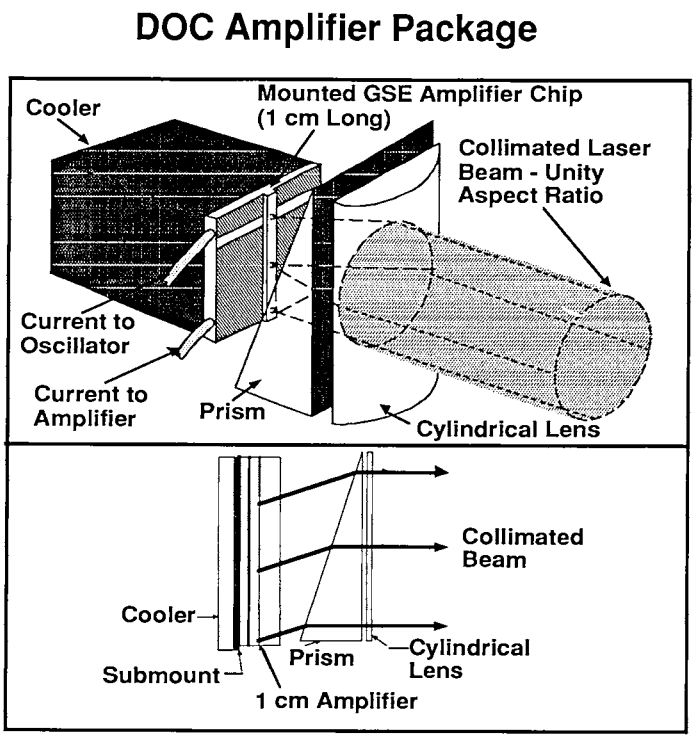

Fig. 14. An external optical arrangement used to correct the aspect ratio and tilt in the output beam of an active grating GSE-MOPA.

region should have low losses and also provide the correct proportions of outcoupled light, transmitted light, and reflected light. In addition, the active region and the grating region must be designed so that the coupling loss between the two regions is low. These objectives have been accomplished by several approaches, but most successfully using single or multiple quantum-well active regions. An additional design consideration is that the subsequent fabrication of the device should be as simple as possible consistent with the performance objectives.

For GSE arrays, the same quantum-well waveguide structure has been continued throughout the unpumped grating region at wavelengths around 1.0 μm and below where the AlGaAs/GaAs and InGaAs/AlGaAs/GaAs material systems are used. Due to the step-like density of states, bandgap shrinkage effects, and saturation of the excitonic absorption, the unpumped quantum-well active region in the DBR section can have low losses ($<5\ cm^{-1}$). This approach has demonstrated very low threshold currents (below 140 A/cm^2) and high cw (>3 W) and pulsed (>30 W) power with

differential efficiencies (both surfaces) of >90% (Evans *et al.*, 1991). Usually, the lasing wavelength (which is determined by the period of the Bragg grating) is chosen so that the emission is slightly (by 50–150 Å) to the long wavelength side of the bandgap edge, in order to reduce absorption losses in the passive region. Although the differential quantum efficiency remains high, the threshold current density can increase to more than 1 kA/cm^2 with the same structure when the grating period is chosen to force the emission wavelength shorter than the bandgap edge (Evans *et al.*, 1991).

In the InGaAsP material system that has emission wavelengths in the 1.3–1.7 μm range, the quantum wells are typically etched away followed by a regrowth to form a waveguide layer in the grating regions (Koch *et al.*, 1988; Palfrey *et al.*, 1989). For this material system, where regrowths are commonplace, and selective etchants are well developed, the placement of the emission wavelength is less critical.

For cw operation, moderately low threshold current densities are required. The mathematical expression for the threshold gain for edge- and surface-emitting semiconductor lasers has the form (Kressel and Butler, 1977; Casey and Panish, 1978; Thompson, 1980; Agrawal and Dutta, 1986) as follows:

$$\Gamma_{\text{active}} \times g = \alpha_{\text{int}} + 1/L \ln (R_{\text{eff}}^2), \tag{8}$$

where Γ_{active} is the active layer confinement factor and represents the fraction of the mode power contained in the active layer; g is the gain of the active layer, α_{int} is the loss in the active region, L is the length of the active region, and R_{eff} is either the facet reflectivity (for edge-emitting lasers) or a measure of the total (outcoupling plus internal) loss of the DBR regions. The threshold gain for GSE lasers is discussed in Chapter 7, where it is shown that the threshold current density decreases as $1/N$, where N is the number of gain sections in the array. The relationship for the differential quantum efficiency (also derived in Chapter 7), indicates the importance of reducing internal losses, maximizing internal efficiency for GSE lasers, and shows that the differential quantum efficiency monotonically increases with N until the maximum value is reached.

For quantum well structures $\Gamma_{\text{qw}} = \Gamma_{\text{active}}$, and is expressed by

$$\Gamma_{\text{qw}} = \int_{\text{qw}} |E_{\text{w}}(x)|^2 \, dx \Big/ \int_{-\infty}^{\infty} |E_{\text{w}}(x)|^2 \, dx. \tag{9}$$

The integration in the numerator is over all the quantum wells in the case

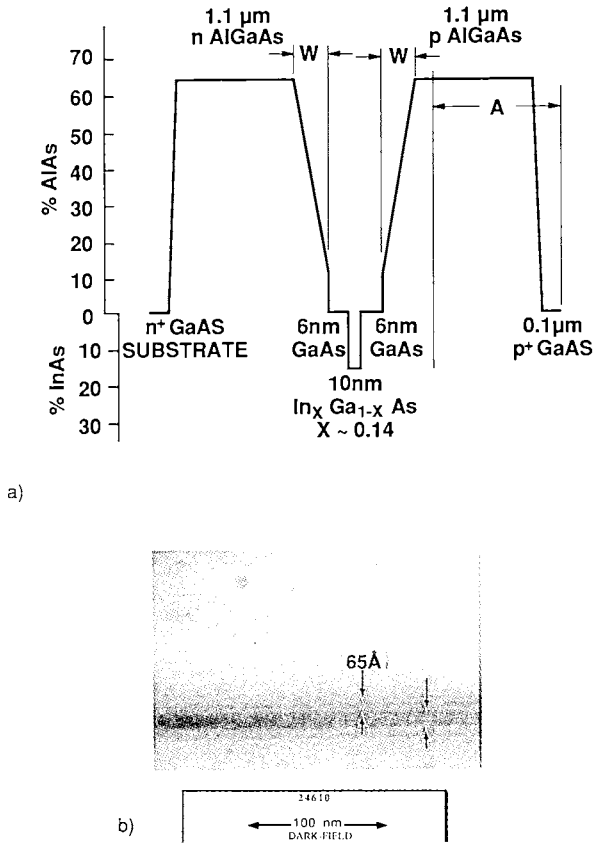

Fig. 15. (a) The thickness and composition profile of a GRIN-SCH laser structure with 66% AlAs in the cladding layers (b) TEM of the quantum-well region.

of multiple quantum wells. Values of Γ_{qw} for single quantum-well graded-index structures corresponding to the laser structure shown in Fig. 15 are shown in Fig. 16 as a function of *p*-cladding compositions for graded region widths varying from 0.1–0.3 μm.

2. *Lateral Guiding*

Chapter 2 discusses many approaches for lateral coupling of edge-emitting arrays, many of which have been applied to GSE arrays. Most all methods for lateral coupling use a lateral index variation. Two of the simplest methods to obtain index-guiding are impurity-induced disordering (Thornton *et al.*,

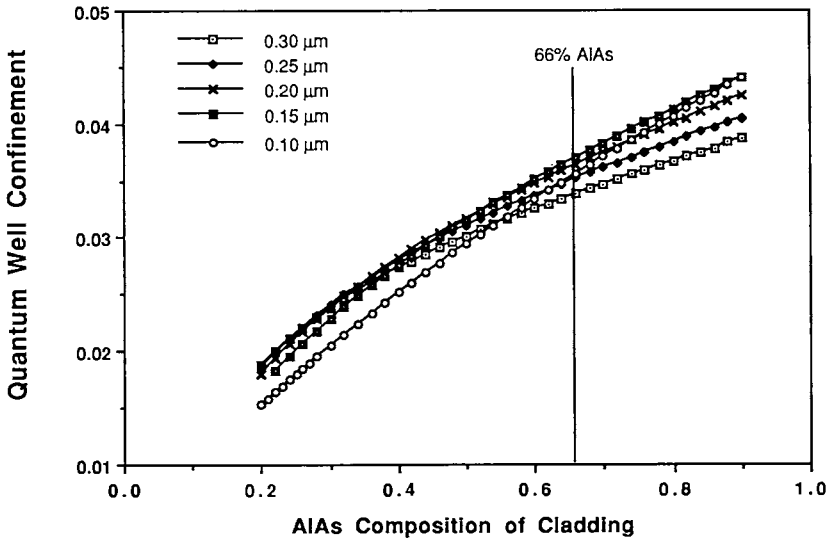

Fig. 16. The quantum-well confinement factor as a function of *p*-cladding composition for graded region thicknesses ranging from 0.1 to 0.3 μm.

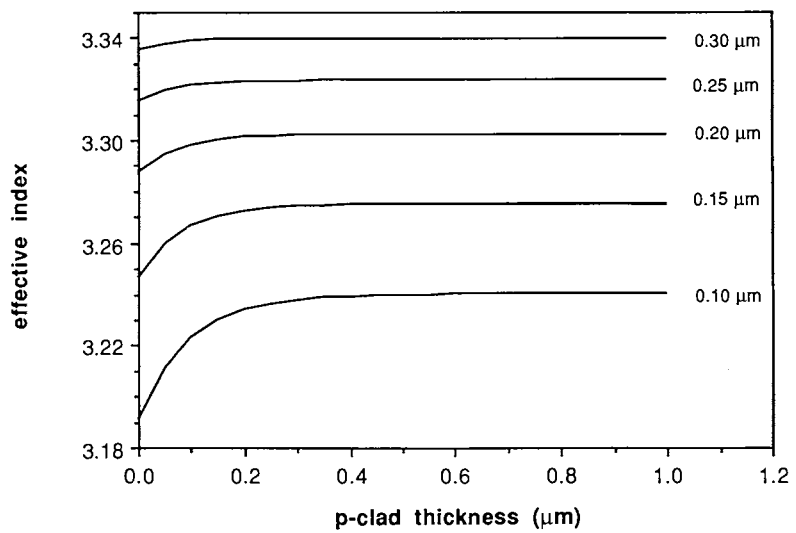

Fig. 17 The effective index of the fundamental waveguide mode for the laser structure shown in Fig. 15 with 60% AlAs in the clad regions for graded region thicknesses ranging from 0.1 to 0.3 μm as a function of remaining *p*-cladding thickness.

1989; Thornton *et al.*, 1990; Zou *et al.*, 1990) and ridges formed by etching. Figure 17 shows the effective index of the fundamental transverse mode in the grating region as the *p*-clad thickness is etched away (after removal of the cap layer) for the graded-index separate confinement heterostructure (GRIN-SCH) single quantum-well geometry shown in Fig. 15. The different curves correspond to graded region widths of 0.1, 0.15, 0.2, 0.25, and 0.3 μm. A lateral index step in the gain region can be achieved by etching away first the cap layer and then most of the *p*-clad material everywhere outside the ridges. The effective index remains almost constant for graded region thicknesses $\gtrsim$0.3 μm. In this case, there would be very little interaction of the optical field with a grating located at the *p*-clad-air interface. For a graded region thickness W of $\lesssim$0.25 μm, substantial changes in the effective index occur as a function of *p*-clad thickness. For the case of a 0.15-μm-thick graded layer, a lateral index step on the order of $3\text{–}8 \times 10^{-3}$ can be obtained by etching the *p*-clad to a thickness of about 1500–800 Å.

The dependence of the quantum-well confinement factor on graded layer thickness for cladding compositions of 66% AlAs and 40% AlAs is shown in Fig. 18.

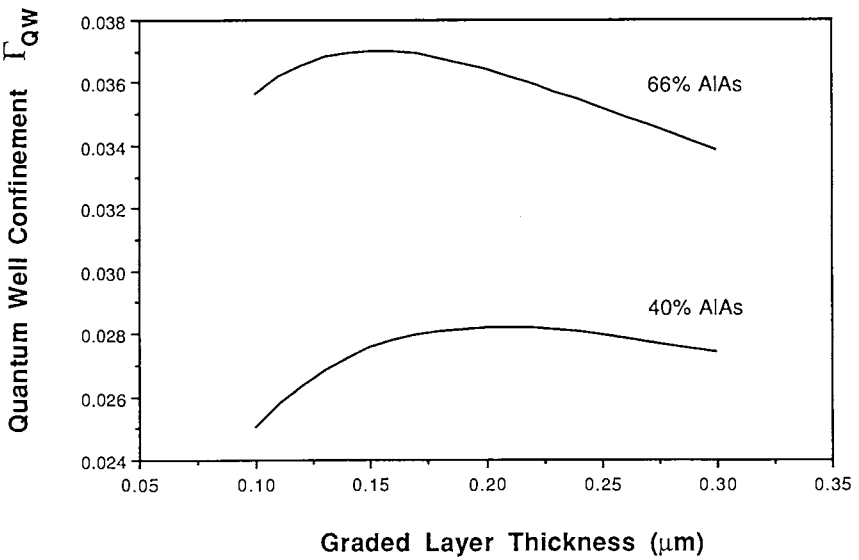

Fig. 18. The quantum-well confinement factor as a function of graded region thicknesses for cladding compositions of 40% and 66% AlAs.

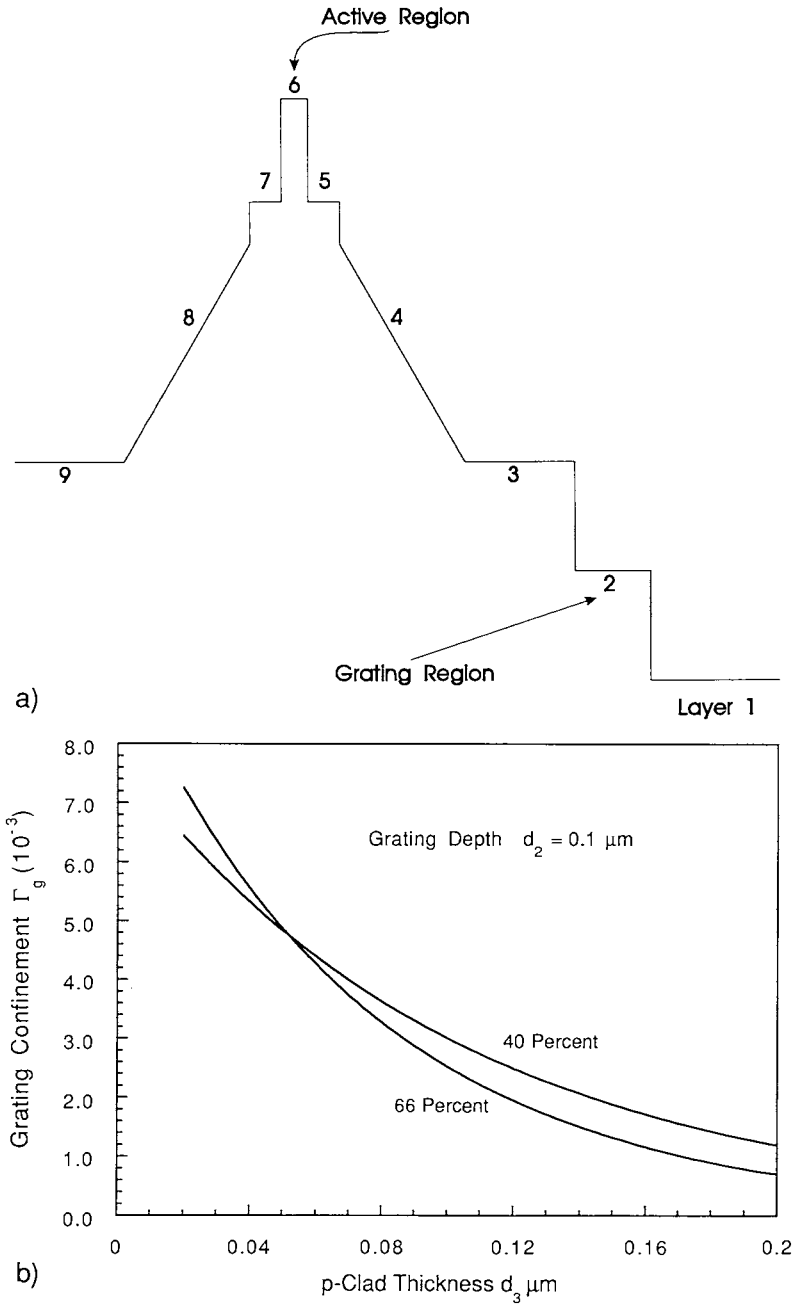

Fig. 19. (a) Index profile of the GRINSCH-SCH structure shown in Fig. 15 with a grating at the *p*-clad/air interface, graded region thickness of 0.15 μm, and 66% or 40% AlAs in the cladding regions; (b) the grating confinement factor for a 1000 Å deep grating as a function of the *p*-clad thickness; (c) the grating confinement factor as a function of grating depth for a *p*-clad thickness of 1000 Å.

3. *Grating Design*

The etching required to produce a lateral index ridge guide exposes a surface in the region between the gain sections that is near the appropriate level for a grating to outcouple radiation. The fraction of the mode power Γ_{gr} interacting with a grating formed at the p-clad/air interface (Fig. 19(a)) is given by

$$\Gamma_{gr} = \int_{gr} |E_w(x)|^2 \, dx \Big/ \int_{-\infty}^{\infty} |E_w(x)|^2 \, dx, \tag{10}$$

where $E_w(x)$ is the transverse field distribution in the waveguide section and the integral in the numerator is performed over the width of the grating region. The variation of Γ_{gr} (which is called the grating confinement factor) is shown in Fig. 19(b) as a function of the distance of the grating above the graded layer, for the laser structure described in Fig. 15 with a p-clad composition of 66% and a graded region thickness of 0.15 μm. In these numerical calculations, the thickness of the grating region is the peak-to-

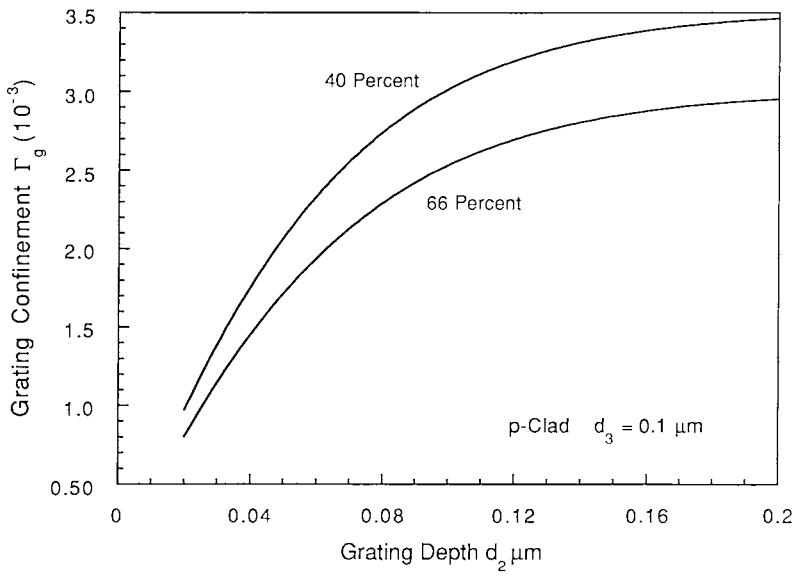

c)

Fig. 19. Continued.

valley distance of the grating. The grating region is assumed to have an uniform dielectric constant equal to the average dielectric constants of the *p*-clad layer and that of the adjacent dielectric layer (Si_3N_4 in this example). This model is consistent with that introduced for an improved perturbational analysis of dielectric waveguides with surface undulations in the propagation region (Handa *et al.*, 1975). From consideration of Figs. 17 and 19, until the grating is located within about 2000 Å of the graded region, very little light can be outcoupled. Even though the *p*-clad layer is mostly removed so that a significant amount of light can be coupled out, the mode in the waveguide section is only slightly distorted from the mode propagating in the gain section. Fig. 19(c) shows the grating confinement factor as a function of grating depth for a fixed grating location of 0.1 μm. This numerical calculation reveals significant changes in the transmission, reflectivity, and outcoupling of the waveguide mode in the grating region as the grating depth is varied from 0.02 μm to about 0.10 μm, but shows very little change with increasing grating depth beyond 0.1 μm.

In the design and fabrication of GSE arrays, one would like to know not only the reflectivity and transmissivity of a grating, but also the amount of power coupled out in the upward and downward directions. Either coupled-wave theory (discussed extensively in Chapter 6) or numerical approaches can be used to calculate these properties for gratings on semiconductor waveguides. In Fig. 20, the reflectivity, transmissivity, and outcoupled powers calculated using a numerical method (Hadjicostas *et al.*, 1990; Butler *et al.*, 1992) are shown for grating lengths of 200, 300, and 400 μm for the graded index structure in Fig. 15, assuming a *p*-clad thickness of 1000 Å in the grating region, a grating depth of 400 Å, and a graded region width of 0.15 μm. The abscissa in Fig. 20 is the normalized wavelength deviation $(\beta - K)/k_0 = \Delta\beta/k_0$ away from the exact Bragg condition ($\beta = K$), where $K = 2\pi/\Lambda$, $\beta = 2\pi/\lambda_g$, $k_0 = 2\pi/\lambda_0$, and λ_g is the wavelength in the waveguide. For the same structure, Fig. 21 shows the amount of power transmitted through a 300 μm-long grating region as a function of grating depth and the *p*-clad thickness remaining between the graded region and the bottom of the grating.

Photoluminescence measurements on the GSE wafer along with measurements of the emission wavelength of edge-emitting lasers fabricated from the same GSE wafer are used to predict the emission wavelength of the GSE device. The layer thicknesses and compositions of the GSE wafer are also measured from which an effective index curve is calculated as a function of remaining *p*-clad thickness (Fig. 17). The grating period can then be calculated once the effective index and emission wavelength is known using either Eq. (1) or (6).

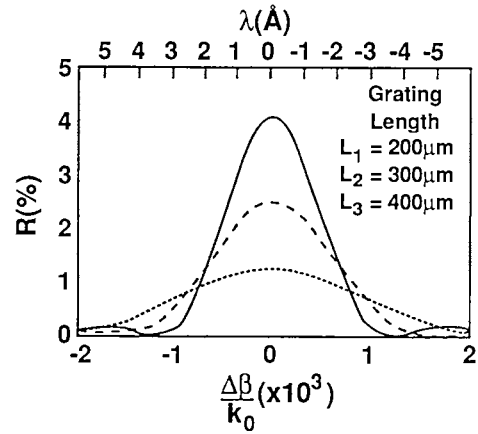

a)

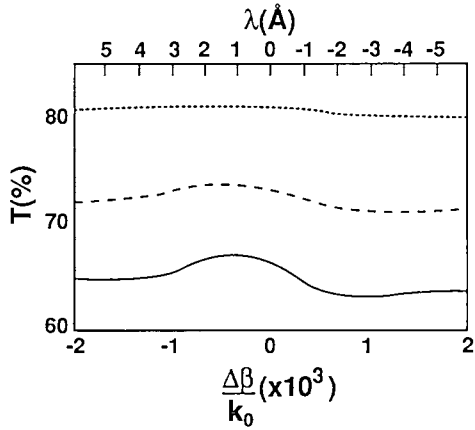

b)

Fig. 20. Calculated (a) reflectivity, (b) transmission, (c) amount of power radiated into air, and (d) amount of power radiated towards the substrate as a function of the normalized wavelength deviation $\Delta\beta/k_0$ away from the exact Bragg condition. The three curves correspond to a grating length of 400 μm (solid line), 300 μm (long dashes) and 200 μm (dotted lines).

4. Gain Section to Grating Section Coupling

An important consideration in the choice of the epi-layer structure is the coupling between the gain and the grating regions since the mode profiles are slightly different in both regions. The resulting mode transmission

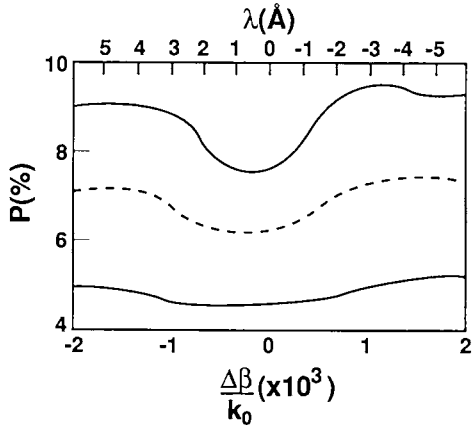

c)

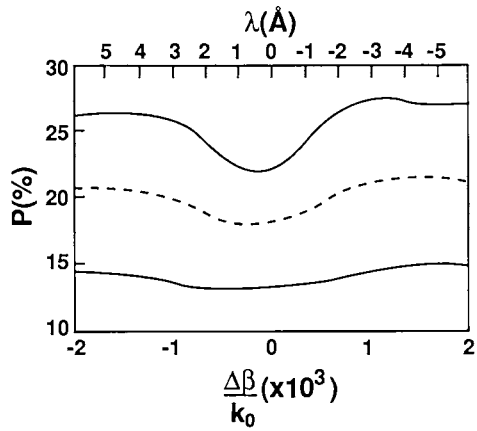

d)

Fig. 20. Continued.

fraction κ_x between the gain and passive waveguide section is given by Evans *et al.* (1986) as follows:

$$\kappa_x = \left| \int_{-\infty}^{\infty} E_g(x) E_w^*(x)\, dx \right|^2 \Big/ \left(\int_{-\infty}^{\infty} E_g(x) E_g^*(x)\, dx \int_{-\infty}^{\infty} E_w(x) E_w^*(x)\, dx \right), \tag{11}$$

where $E_g(x)$ and $E_w(x)$ are the transverse field distributions in the gain and waveguide sections. $E_g^*(x)$ and $E_w^*(x)$ are the complex conjugates of $E_g(x)$ and $E_w(x)$. For the GRINSCH-SQW structure shown in Fig. 15, the mode transmission (κ_x) value ranges from 0.95 to 0.99 for typical p-clad

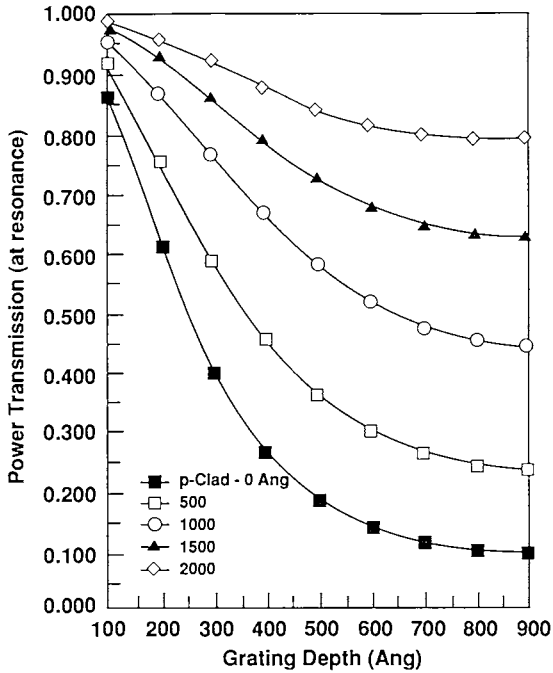

Fig. 21. Power transmitted (on resonance) through a 300 μm long second-order grating region as a function of grating depth for *p*-clad thicknesses remaining between the graded region and the bottom of the grating ranging from 0 to 0.2 μm. The waveguide structure is that shown in Fig. 15 with a graded region thickness of 0.15 μm and 66% AlAs in the cladding region.

thicknesses and graded region thicknesses as shown in Fig. 22. As a result, there is very little scattering loss at the laser-waveguide transition.

5. GSE Oscillator Array Termination

Another design consideration is the method of terminating the GSE laser array. As shown in Chapter 7, an open-ended (terminated in a series of unpumped gain sections or anti-reflective coated cleaved facets) GSE array configuration, such as a linear chain or a serpentine of one- or two-dimensional arrays, requires precise grating parameters to obtain a nearly uniform near-field distribution in the gain regions to prevent spatial hole-burning. On the other hand, by translational symmetry, the near-field pattern of an ideal ring array is identical in each gain section and, therefore, the tolerances on the grating parameters can be reduced if a ring configuration

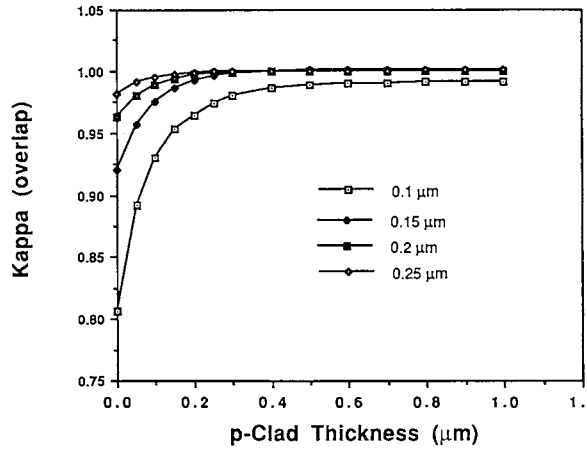

Fig. 22. Mode transmission (κ_x) as a function of remaining *p*-clad thickness after etching for graded region thicknesses ranging from 0.1 to 0.25 μm.

is used. A drawback of the ring configuration is that the corner-turning mirrors may provide a ring feedback path for oscillation independent of the gratings. Especially for small rings, this can lead to mode competition between modes associated predominantly with the mirror feedback and modes associated predominantly with the grating feedback (Evans *et al.*, 1990b). This problem can be avoided or minimized if the ring array is large, and the period of the grating is chosen to provide feedback at the emission wavelength of the mode associated with mirror feedback.

6. *Device Tolerances*

a. Growth and Etching Tolerances. For a GSE array to operate as a coherent unit rather than an incoherent assembly of individual coherent emitters, requires that different elements of the array, when operated individually, have an emission wavelength within the locking bandwidth of the array. One estimate of the locking bandwidth is given by a comparison of the spectral hole-burning width in a quantum-well laser to the reflectivity bandwidth of the grating. As shown in Fig. 23(a), the estimated spectral hole-burning width for a quantum-well laser is on the order of 10 Å (Ahn and Chuang, 1990), while the typical reflectivity bandwidth is about 4 Å (Fig. 20(a)).

Since the bandwidth of the grating reflectivity is narrower than the spectral hole burned in the gain profile, closely spaced ($\leq$1 Å, depending on array dimensions) array modes around the dominant central mode will be suppressed from oscillating due to spectral hole burning. The modes outside

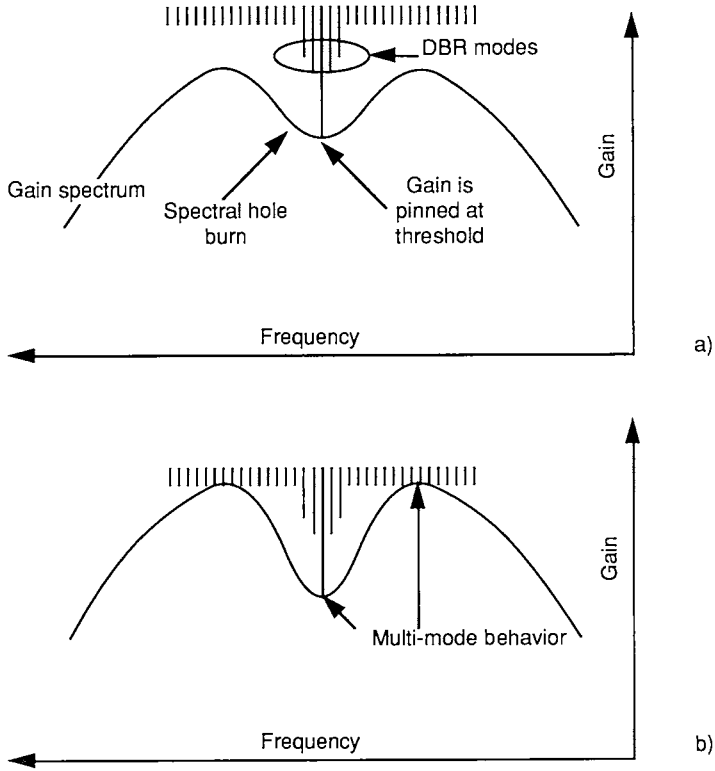

Fig. 23. Spectral hole burning (a) near threshold and (b) at many times threshold.

the grating bandwidth are suppressed by the very low grating reflectivity. Only at very high drive currents is there enough gain away from the hole-burned region of the gain profile for the very-low-reflectivity, off-resonance DBR modes to oscillate, as illustrated in Fig. 23(b). This argument ignores spatial hole burning considerations, but does suggest that, if the uniformity of the array is such that all the individual elements emit within about ±2 Å, the complete array should lock up coherently. A more quantitative analysis of the locking bandwidth awaits more detailed calculations and measurements for hole burning in strained and unstrained quantum-well lasers and a nonlinear theory for GSE arrays.

If the compositions and layer thicknesses of the epitaxial layers of the laser structure vary across the wafer, causing the effective index for the optical model to fluctuate, different elements of the array will tend to emit at different wavelengths. To estimate the resulting wavelength variations, we assume that only compositional and thickness variations produce

emission wavelength changes since the gain spectrum of the quantum well is very broad (Mittelstein *et al.*, 1989). Using a modal analysis, Table II shows such calculated wavelength shifts in a single GSE element assuming a perfect grating period for the laser structure shown in Fig. 15 with a p = clad thickness of 0.1 μm and grating depth of 0.04 μm (see Fig. 19).

Only the graded layers have a significant sensitivity to typical compositional variations: a wavelength shift of ±8 Å results from a variation of 0.5%, while variations of 0.03% result in a shift of $<\pm 1/2$ Å in the emission wavelength.

The layers that are most sensitive to layer thicknesses are both graded layers and the layer between the graded layer and the grating region (grating spacer layer). If the graded region thickness varies by ±50%, the wavelength shift is ±60 Å, a ±10% variation results in ±12 Å, and a ±1% variation produces only a ±1.5 Å variation in the emission wavelength. Similarly, if the grating spacer layer has a 10% thickness variation, a wavelength shift of ±3 Å results, while a 1% variation gives $<\pm 1.5$ Å. Most optimized growth reactors can provide layer uniformities of ±10%, and the very best about ±1%.

The GSE oscillator array results reported in Section V have been grown in a reactor that had compositional variations of about ±0.03% and thickness variations of about ±1% (Wang *et al.*, 1989; Wang and Choi, 1991). The devices also had their p-cap and p-clad layers etched away by ion-beams, and we estimate that the thickness variations due to this process are about ±10%. A noticeable improvement in wavelength uniformity can be obtained if the thickness of the grating spacer is determined by epitaxial growth

Table II

Calculated wavelength shifts in a single GSE element due to changes in the effective index because of compositional and thickness variations assuming a perfect grating period for the laser structure shown in Fig. 15.

Nonuniformity	Variation	Wavelength Shift
Composition (Δ% AlAs)	±0.5%	±7.6 Å
	±0.03%	±0.44 Å
Graded region thickness	±50%	±60 Å
	±10%	±12 Å
	±1%	±1.5 Å
Grating spacer thickness	±50%	±15 Å
	±10%	±3 Å
	±1%	±1.4 Å

rather than dry etching to depths of ~1 μm. Both selective area epitaxy and regrowth have been successful in reducing the variation of the grating spacer layer.

b. Grating Tolerances. The change in emission wavelength $\Delta\lambda$ due to a change in grating period $\Delta\Lambda$ can be estimated from

$$\Delta\lambda = n_{\text{eff}}\Delta\Lambda. \tag{12}$$

Distortions in periodicity for gratings fabricated by holography, even with spherical waves interfering, are reported as one part in 10^7 (Katzir *et al.*, 1977; Suzuki and Tada, 1980). As long as one of the interfering beams in the holographic exposure step of the grating fabrication process is not rapidly diverging, the chirp in the grating period can be maintained to well under 0.1 Å. Electron-beam written gratings may have period variations on the order of 1 Å or more, depending on many factors such as the stabilization of the electronic circuits. Unlike holographically fabricated gratings, e-beam fabricated gratings are exposed one line at a time over a limited region of perhaps 1 mm^2. As a result, e-beam gratings extending 1 cm or more may have several phase errors resulting from the stitching together of the smaller fields.

During the grating fabrication process, there will inevitably be a slight misalignment of the grating with the active region. As a result, the grating lines are not perpendicular to the propagation direction in the plane of the GSE device. If the grating lines are not normal to the propagation direction, there is a wavelength shift and a tilt of the output beam direction away from the normal to the wafer surface. The directions of the appropriate propagation vectors for this problem are shown in Fig. 3. Using Eq. (3) and referring to Fig. 3(b), we find that the resonance wavelength $\lambda_{B'}$ is shifted from the nominal value λ_B (assuming no grating tilt) when the grating is tilted by Φ_1 and is given by

$$\lambda_{B'} = \lambda_B \cos \Phi_1 \tag{13}$$

Equation (13) does not depend on the grating order and thus applies to both GSE and edge-emitting DFB and DBR devices.

Using Eqs. (2) and (13) we find that the output angle to the normal is

$$\Theta = \arcsin (n_c \sin \Phi_1) \tag{14a}$$

or

$$\Theta \approx n_{\text{eff}}\Phi_1 \tag{14b}$$

Thus, tilt angles in the grating result in emission angles departing from the normal direction at angles that are approximately equal to the tilt angle multiplied by the effective refractive index of the waveguide. In addition, the azimuthal angle of the emitted light is rotated through the angle Φ_o which is given by

$$\Phi_o = \arcsin \frac{\lambda_{B'}}{\lambda_B}. \tag{15}$$

When the grating lines are normal to the propagation direction, Φ_o is 90°. In the case that a GSE is lasing with a tilted grating, the outcoupled light propagating in the $+z$ direction will be tilted from the normal at an angle opposite to that undergone by light propagating in the $-z$ direction. Thus, if there is sufficient grating tilt, a double-lobed far-field (in the lateral direction) will be present even though the propagating mode could be a fundamental spatial mode.

From either Fig. 1 or 3(b), $\Delta\Theta_B$, the departure of the deflection angle from 180° is related to the grating tilt angle Φ_1 by

$$\Phi_1 = \Delta\Theta_B/2. \tag{16}$$

For an AlGaAs waveguide with an effective index of ≈3.4, the change in wavelength, Θ, and Φ_o as the grating is tilted through several angles is tabulated in Table III. With moderate care, misalignment of the grating can easily be held to <0.25°. For GSE oscillator arrays with 100 elements and an emitting aperture of ~60 μm × 500 μm, the predicted and measured far-fields have half-widths of ~1° × 0.01° (Evans *et al.*, 1989). Any spread in the beam divergence in such devices due to a grating misalignment of <0.25° would therefore be masked by the 1° lateral beam divergence. As a result of these considerations, expected wavelength shifts of 10 Å or less

Table III

Change in Wavelength, Θ_B, Θ, and Φ_0 for Grating Tilt Angles Φ_1

Φ_1 (°)	$\Delta\Theta_B$ (°)	$(\lambda_0 - \lambda)$ (Å)	Θ (°)	Φ_0 (°)
0	0	0	0	90.0
0.5	1.0	0.3	1.7	89.5
1.0	2.0	1.3	3.4	89.0
1.5	3.0	2.8	5.1	88.5
2.0	4.0	5.1	6.8	88.0

due to growth and fabrication variations over areas of several square centimeters can be expected if the very best epitaxial material is used, and care is taken during the grating fabrication steps.

c. Wafer and Device Flatness. To achieve good beam quality (or a high Strehl ratio) from a GSE device without external optics, the emitting surface should be optically flat. Figure 24(a) shows the measured location of the peak intensities (x's) compared to the ideal location (open circles) for an early GSE array. The resulting geometry of the laser array, calculated from the measured intensity peaks, is shown in Fig. 24(b). The array bar can be flexed during mounting, or it can be warped due to slight lattice mismatches during growth. Figure 25 shows interference fringe measurements on a commercial GaAs substrate before epitaxial growth and on quantum-well structures grown on commercial substrates with 20%, 40%, and 70% AlAs in the cladding layers. Commercial 2 in GaAs substrates commonly have dishing of 5 to 10 μm over the wafer surface. If the cladding layers are limited to about 20% AlAs, there is no additional bowing of the wafer, while the additional bowing with 70% AlAs cladding layers can no longer be measured using interference techniques. Since the surface of the GSE device is an optical element, it should be smooth to between $\lambda/10$ or $\lambda/20$ to provide near-ideal beam quality without corrective optics.

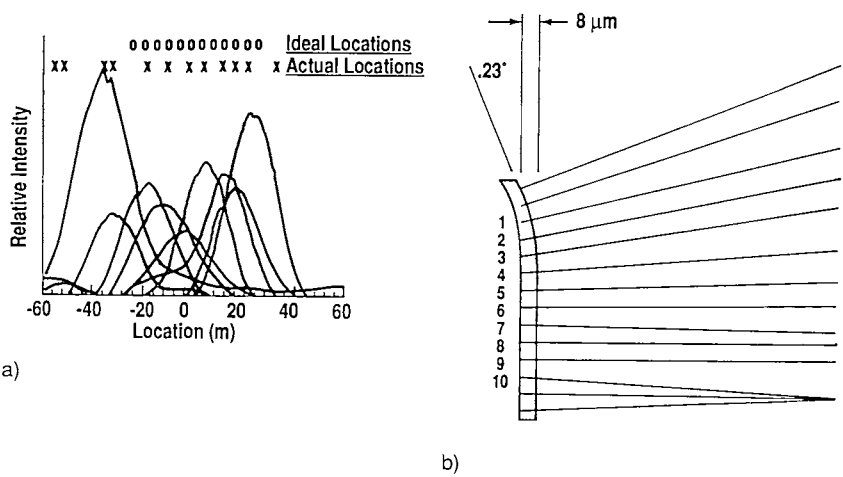

Fig. 24. (a) Ideal (○) and actual (×) locations of the far-field peaks from the individual grating sections of a bowed GSE array. (b) Resulting geometry of the laser array calculated from the measured intensity peaks.

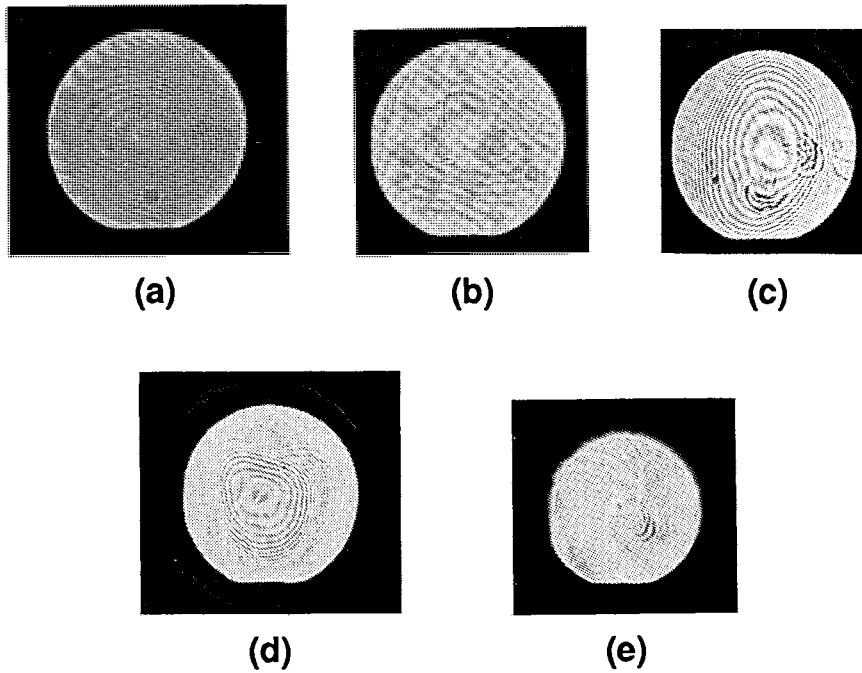

Fig. 25. Interference fringe measurements on (a) a commercial GaAs substrate before epitaxial growth, and on quantum-well structures grown on commercial substrates with (b) 20%, (c) 40%, and (d) 70% AlAs in the cladding layers.

Figure 26 shows a set of theoretical far-fields for a 10×10 GSE array with constant phase and constant field amplitude within each of the 11 grating sections. In Fig. 26(a) there is no phase variation between each of the 11 grating sections, and the corresponding ideal 10×10 GSE far-field is shown in Fig. 26(b). In Fig. 26(c) the random phase variation shown between each of the 11 grating sections produces the distorted far-field shown in Fig. 26(d). Phase variations from DBR section to DBR section can be compensated for by current adjustments to some degree (Evans *et al.*, 1991).

7. *Packaging Considerations*

GSE arrays mounted either junction-up or junction-down have produced watts of cw power. Junction-down mounting facilitates the removal of heat that is generated in the active region, only a micron or two below the surface. This approach requires that the submount have a high thermal conductivity

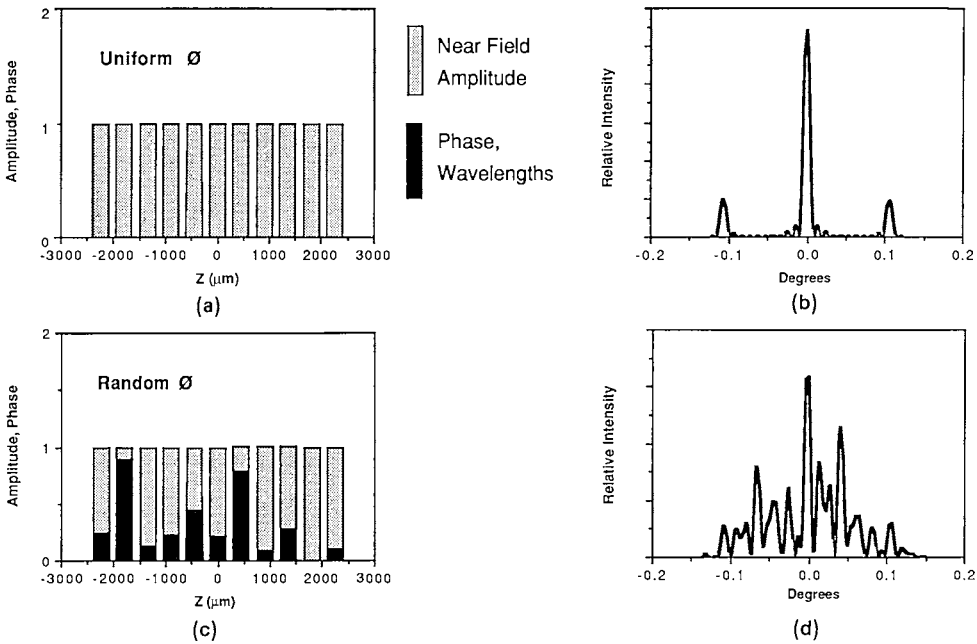

Fig. 26. Calculated far-fields for a 10×10 GSE array. (a) Uniform phase and amplitudes between and in each grating region produces (b) an ideal far-field pattern with low sidelobes; (c) uniform amplitudes and phases in each grating region, but with random phase variations between grating regions produces (d) a far-field pattern with numerous, intense sidelobes.

and be electrically insulating to allow independent current adjustment to each gain section. Such a package, using BeO as the submount is illustrated in Fig. 27 for arrays consisting of one column. Figure 28 shows a similar packaging configuration for a GSE device consisting of eight columns with eight gain sections per column, each containing 10 elements per gain section (640 total elements). The $10 \times 8 \times 8$ GSE chip is shown junction-up in Fig. 28(a), the corresponding BeO submount in Fig. 28(b), and the $10 \times 8 \times 8$ GSE chip mounted junction-down on the submount is shown in Fig. 28(c). The eight stripes on the substrate side of the chip are anti-reflection coated windows for laser emission. An advantage of the junction-down mounting approach is that all the critical electrical connections are between the device and the submount, which contains patterned metal traces matching up with the gain pads of the GSE array. Diamond-like films, which are becoming available at low cost, will offer substantial improvements over BeO for submounts.

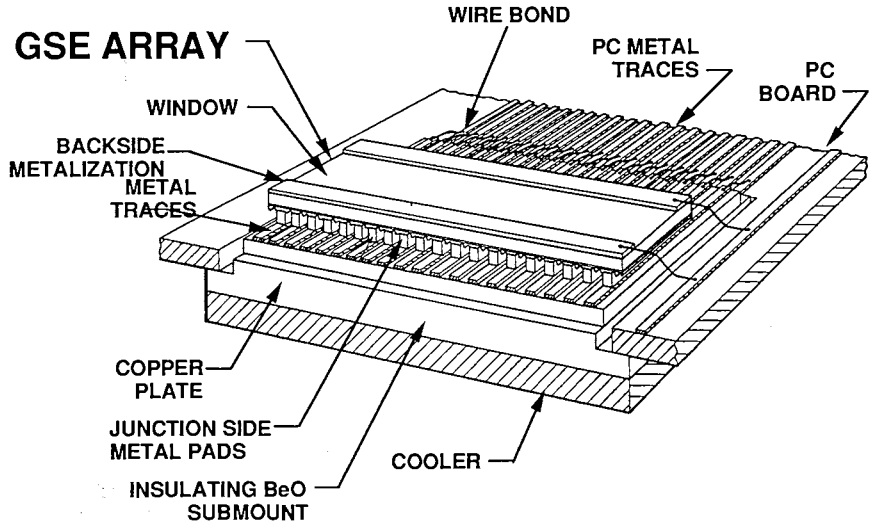

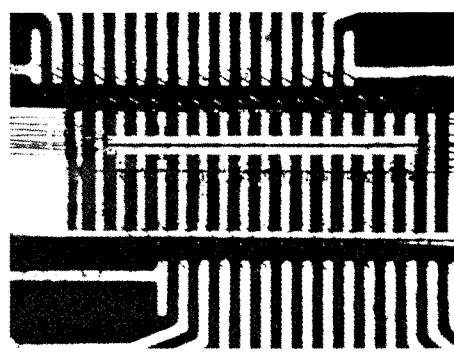

Fig. 27. (a) Sketch of a GSE array mounted junction-down on an insulating BeO submount. The BeO submount has metallized traces corresponding to the GSE gain pads to allow independent electrical control to each gain section; (b) photograph of a GSE array mounted junction-down on a BeO submount.

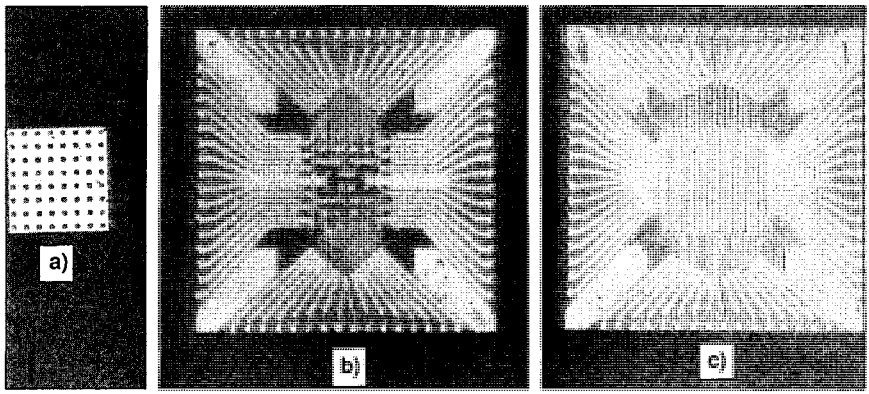

Fig. 28. (a) Micrograph of an eight column GSE ring array with 10 elements per gain section and eight gain sections per column ($10\times8\times8$); (b) micrograph of a BeO submount with independent pads corresponding to the 64 pads shown in (a); (c) micrograph showing the GSE array flip-chip mounted to the BeO submount. The openings in the metallization are windows for emission through the substrate.

Junction-up mounting eliminates the submount and the solder level between the submount and the heatsink (Fig. 27), but the high thermal resistance of the thick (75- to 100-μm) device substrate results in higher junction temperatures than junction-down mounting and leaves the electrical connections exposed.

With either mounting scheme, an anti-reflection coating on the output surface and a high-reflection coating on the opposite surface are desired to obtain the maximum usable power. One or both of these coatings can be a multilayer dielectric stack grown into the epitaxial structure. This configuration, first used in vertical-cavity lasers, has been used to direct most of the outcoupled light towards the emitting surface of a GSE device (Fig. 4 of Chapter 6). The additional series resistance due to the added layers has been either minimized by grading the composition of the interfaces between the layers or eliminated by etching through the layers outside the optical region so that the current path bypasses the multiple layers (Scott and Coldren, 1991).

A simple, alternative approach is to use a single layer of dielectric with an appropriate index and thickness (such as Si_3N_4) as the anti-reflection coating and a similar dielectric layer with an Au coating as the high reflection layer for a GSE device as illustrated on the right-hand side of the sketch in Fig. 6. Such anti-reflection and high-reflection coatings have demonstrated reflections of $<1\%$ and $>80\%$ respectively (Evans *et al.*, 1991). Figure 29 shows an increase in the output power of 63% and a decrease in the threshold

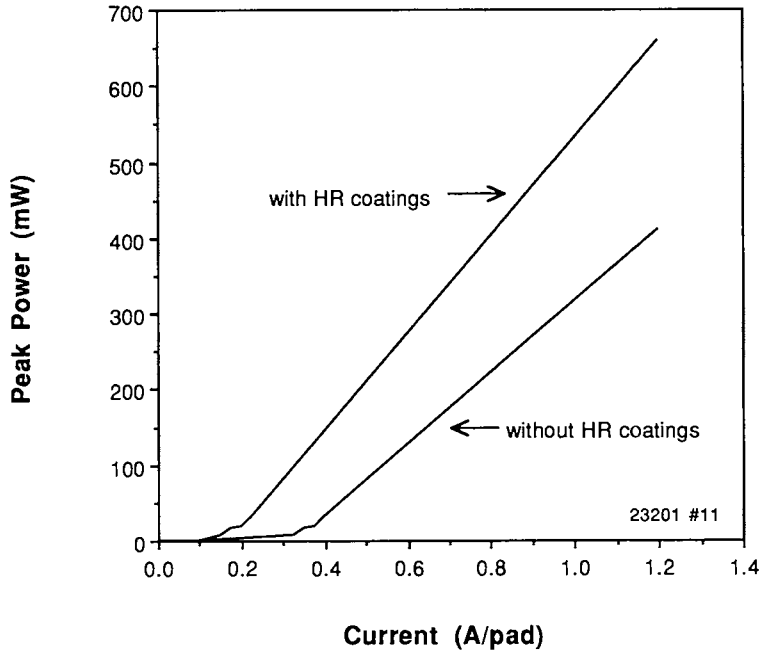

Fig. 29. Power-current curve of a 10×10 GSE array with and without high reflectivity coatings on the grating surface.

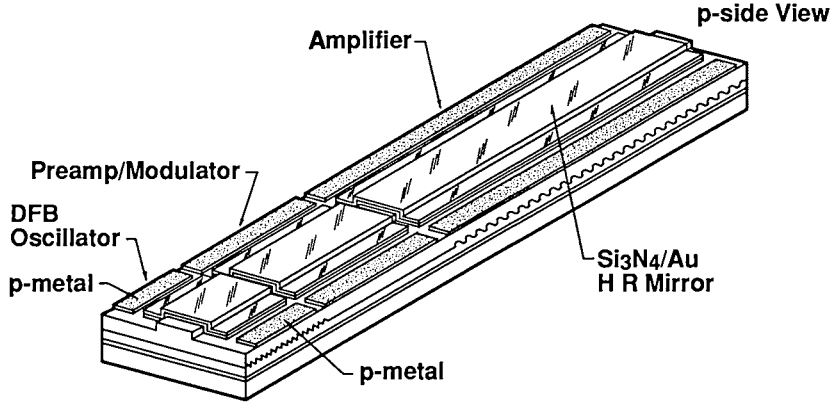

Fig. 30. Sketch of a continuous active grating GSE MOPA with anti-reflection coatings on the substrate side and high-reflection coatings on the junction side.

current of 46% for a 10×10 GSE oscillator array after a high-reflection coating was applied over the grating regions.

Figure 30 shows conceptually how such coatings could be used with a GSE MOPA with active gratings. Another possible approach that could eliminate the need for a high reflectivity coating or grown-in multi-layer reflectors would be to use blazed gratings (Tamir, 1981) in a unidirectional amplifying region to direct the light predominantly towards one surface.

If the GSE arrays are mounted junction-down, the substrate must be transparent (Evans *et al.*, 1991) or must have etched windows (Macomber *et al.*, 1987) in the emitting region. For emission wavelengths above about 0.94 μm, the substrates (GaAs and InP) are transparent. For wavelengths as short as 0.8 μm, AlGaAs substrates have been used (Evans *et al.*, 1989). Another packaging approach is the epitaxial lift-off technique (Yablonovitch *et al.*, 1987), which may be especially useful for GSE arrays operating at visible wavelengths where transparent substrates are not readily available.

B. GSE Amplifier Arrays

1. *Grating Design for MOPAs*

A major issue in the design of an optical amplifier is avoidance of reflections that can cause instabilities in the oscillator or oscillations in the amplifier. Therefore, the period and the strength of the grating output coupler, the transitions between the amplifier and oscillator regions, and the device terminations at the ends of the device are critical.

The period of the output coupling gratings should be selected so that the second-order Bragg condition for feedback is not satisfied over the wavelength region where the amplifier has significant gain. As a result of this requirement, the first-order grating outcoupled light is emitted at an angle with respect to the normal of the surface, rather than normal to the surface as in the case of GSE oscillator arrays.

As discussed in Section II.A, light can also be coupled into the substrate (and/or superstrate) without being coupled to air if the light suffers total internal reflection at the semiconductor-air boundary. Such coupling is undesirable and contributes to the internal losses.

From Eqs. (4) and (5) and the discussion in Section II.A, there is no solution for $\Theta_{m_{out}}$ for $m_{out} > 1$ and, hence, no diffracted orders except the first (and no additional associated losses) if the grating period Λ satisfies

$$\lambda/(n_{eff}+1) < \Lambda < \lambda/n_{eff}. \tag{17}$$

For these conditions, Θ_1 is negative, and the outcoupled light is tilted backwards towards the oscillator as shown in Fig. 12.

However, if the first-order outcoupling grating has a period larger than the wavelength in the material, then

$$\lambda/n_e < \Lambda. \tag{18}$$

The first-order outcoupling to air is in the forward direction (corresponding to positive values of Θ_m as shown in Fig. 13 and light will also be coupled and lost to the substrate in second-order.

Although backward outcoupling results in lower losses, it is not necessarily the best choice for GSE MOPAs. Under very high levels of current injection to the amplifier, significant band filling occurs producing substantial gain at wavelengths as much as 1000 Å shorter than the oscillator design wavelength. As a result, the amplifier region can self-oscillate at a wavelength corresponding to the second-order Bragg in-plane reflection condition of the outcoupling grating.

Self-oscillation due to Bragg resonances is easily avoided by using a forward grating output coupler, since the second-order Bragg condition corresponds to longer oscillation wavelengths and photon energies less than the bandgap of the active layer material.

a. Off-Resonance Bragg Reflections. If a grating period is selected to give an outcoupling angle Θ using Eqs. (2), (3), or (4), for an oscillation wavelength of λ, the corresponding value of the in-plane resonant wavelength λ_B for the same grating may be found using Eq. (6). A plot of Θ for $m_{out} = 1$ and λ_B for $m_B = 2$ as a function of grating period is given in Fig. 31, assuming an emission wavelength λ of 9700 Å and an effective index of 3.3.

As can be seen in Fig. 31, the in-plane resonant wavelength λ_B moves farther from the outcoupling wavelength as the outcoupling angle increases in either the forward ($+\Theta$) or backward ($-\Theta$) direction.

The question of how far from zero degrees to make the outcoupling angle in order to reduce the residual reflection from the Bragg resonance to a value that would avoid oscillation in an amplifier can be estimated by using coupled-mode theory.

The (in-plane) amplitude reflection coefficient, r is given by (Yariv, 1973; Weller-Brophy and Hall, 1985) as follows:

$$r = \frac{-\kappa \sinh \alpha L}{\alpha \cosh \alpha L + i\delta \sinh \alpha L}, \tag{19}$$

where κ is the grating coupling coefficient, L is the grating length, and δ

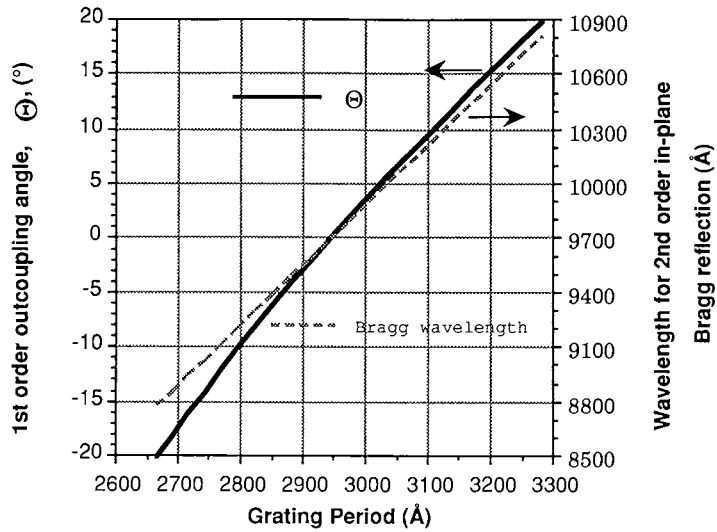

Fig. 31. First-order outcoupling angle (at $\lambda = 9700$ Å) and the wavelength corresponding to the second-order Bragg reflection plotted against grating outcoupler period for a waveguide with effective index of 3.3.

is the detuning parameter (the departure of the source wavelength from the Bragg resonance wavelength) defined as

$$\delta = 2\pi\left(\frac{1}{L} - \frac{n_e}{\lambda_B}\right). \tag{20a}$$

The attenuation (or gain) α is defined by

$$\alpha = \sqrt{\kappa^2 - \delta^2}. \tag{20b}$$

The in-plane power reflectivity, R, is given by $r^* r$. Near resonance, $\kappa^2 > \delta^2$, and then α is real and the power reflectivity becomes

$$R = \frac{\kappa^2 \sinh^2 \alpha L}{\alpha^2 \cosh^2 \alpha L + \delta^2 \sinh^2 \alpha L}. \tag{21}$$

For large departures from resonance, $\kappa^2 < \delta^2$ and α is imaginary. In this case the power reflectivity may be shown to be

$$R = \frac{\kappa^2 \sin^2 (\alpha^* \alpha)^{1/2} L}{\alpha^* \alpha \cos^2 (\alpha^* \alpha)^{1/2} L + \delta^2 \sin^2 (\alpha^* \alpha)^{1/2} L}. \tag{22}$$

The periodic nature and the presence of zeros in Eq. (22) should be noted.

In order to obtain a useful estimate of the actual reflectivity when a grating is chosen as an outcoupler for a GSE MOPA device we make an

estimate of κ. The worst case will occur for a strong grating that will have a broad resonance. As an example, we consider a grating that is 100 μm long and reflects 25% of the light when operated at its second-order Bragg resonant wavelength. In this case, using Eq. (21) with $\delta = 0$ and $L = 10^{-2}$ cm, we calculate that $\kappa = 55\ \text{cm}^{-1}$.

Figure 32(a) shows the in-plane power reflectivity for a grating that couples 9700 Å light out normal to the waveguide plane ($\Theta = 0°$). This is the special case where the first-order outcoupling wavelength and the second-order Bragg reflecting wavelength correspond. Figure 32(b) shows the in-plane reflectivity for a grating period that outcouples 9700 Å light at $\Theta = -20°$. Both plots exhibit the typical characteristics of resonances that consist of a main lobe with smaller side lobes at periodic intervals. For these calculations a nominal waveguide refractive index of 3.3 is assumed. Figure 33 shows the in-plane reflectivity on a log scale for a grating period which outcouples 9700 Å light at $\Theta = -20°$, $+20°$, $-10°$, and $+10°$. Figures 32(b) and 33 show that the in-plane reflectivity of the grating in the vicinity of the emission wavelength (9700 Å) is extremely low.

The peak value of the reflectivity at wavelengths over which the amplifier has sustained gain is of chief interest in determining if the amplifier will oscillate. Far from the grating resonance, $\delta \gg \kappa$ and Eq. (22) reduces to

$$R_{\text{peak}} \approx \kappa^2/\delta^2 = 2\pi n_e(1/\lambda_B - 1/\lambda) \tag{23}$$

Using Eq. 19, the normalized, peak-in-plane reflectivity (R_{peak} at $\lambda = 9700$ Å divided by R at the Bragg resonance wavelength) is plotted against the outcoupling angle in Fig. 34. At $\Theta = 0°$, $R_{\text{peak}} = R$. The normalized value falls to $\approx 5 \times 10^{-4}$ at $\Theta = \pm 5°$, 10^{-4} at $\pm 10°$, and continues to fall off reaching a value $\approx 3 \times 10^{-5}$ at $\pm 20°$. If R at the Bragg wavelength is 0.25, the actual reflectivities will be reduced in proportion.

Although coupled-mode theory is relatively simple and helpful in developing insight while providing analytical expressions, its validity far from resonance is questionable. Numerical methods, while less intuitive, are quite accurate. Figure 35 shows the normalized reflectivity on resonance ($\lambda = 0.955$ μm) and off resonance for the dielectric waveguide profile of Fig. 19(a) as a function of emission wavelength (or outcoupling angle), calculated using a numerical method (Butler *et al.*, 1982). For this calculation, the cladding layers contain 66% AlAs, the graded region thickness is 0.15 μm, the grating period is 2906 Å, the grating depth is 0.1 μm, the *p*-clad thickness (between the graded layer and the bottom of the grating) is 0.1 μm, and the length of the grating is 1 mm. Unlike the simple coupled-mode theory discussed previously, the reflectivity profile calculated using the numerical

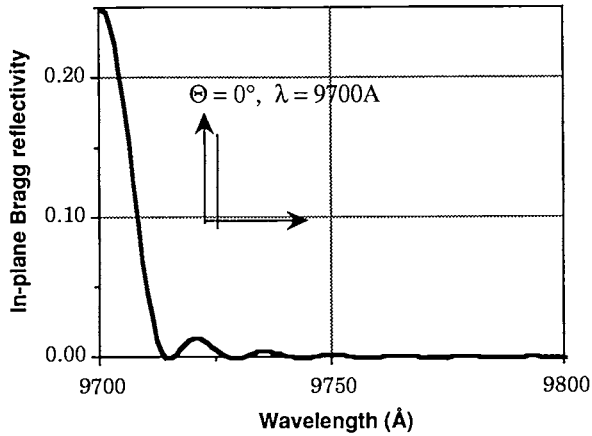

a)

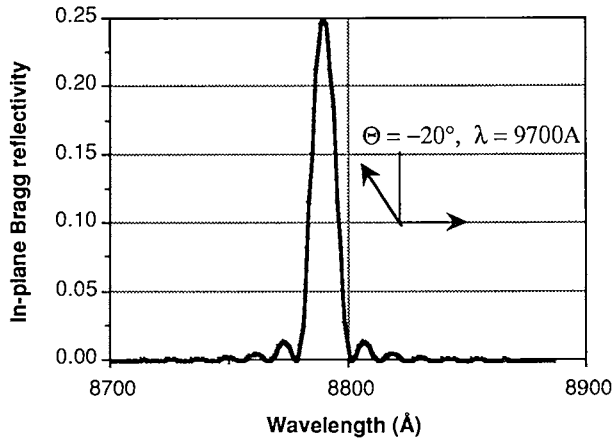

b)

Fig. 32. (a) The in-plane power reflectivity for a grating ($\Lambda = 2939$ Å) which couples light out normal to the waveguide plane ($\Theta = 0°$) in first order. (b) The in-plane reflectivity for a grating ($\Lambda = 2663$ Å) which couples light out at $\Theta = -20°$ in first order. The master oscillator wavelength is 0.97 μm in both cases.

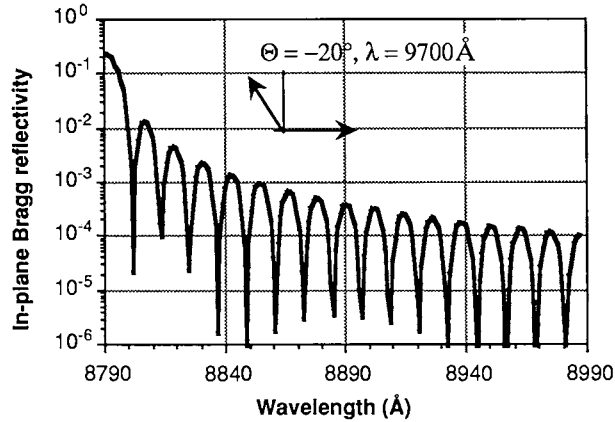

a)

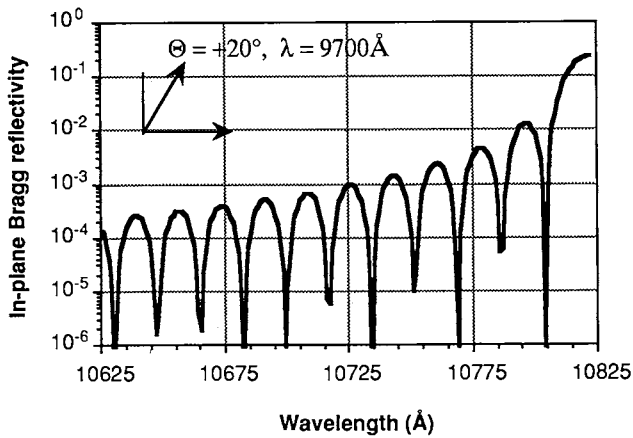

b)

Fig. 33. The in-plane power reflectivity on a log scale for (a) a grating ($\Lambda = 2663$ Å) which couples light out at $\Theta = -20°$ in first order, (b) a grating ($\Lambda = 3279$ Å) which couples light out at $\Theta = +20°$ in first order, (c) a grating ($\Lambda = 2792$ Å) which couples light out at $\Theta = -10°$ in first order, and (d) a grating ($\Lambda = 3102$ Å) which couples light out at $\Theta = +10°$ in first order. The master oscillator wavelength is 0.97 μm in all cases.

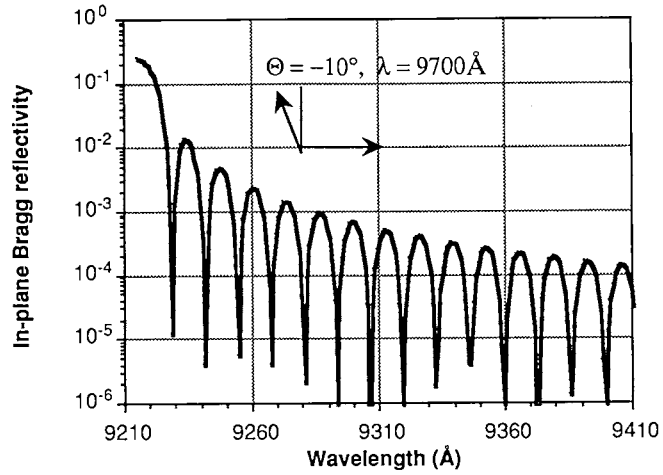

c)

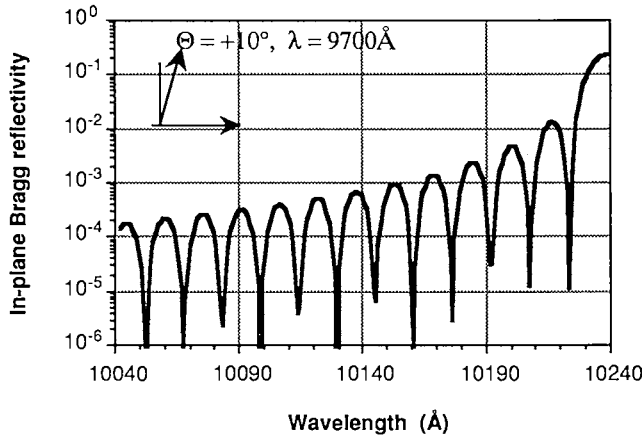

d)

Fig. 33. Continued.

method is not symmetric. However, the agreement between the coupled-mode estimate and the numerical method is within a factor of two for forward outcoupling angles up to 10°, and suggests that the simple coupled-mode theory can be used for initial designs. The reflectivity is sufficiently low to avoid amplifier oscillation for forward outcoupling angles of 5° to 10° or more.

b. Transition and Termination Reflections. Slight changes in mode size and effective index can occur between the waveguide region without a grating

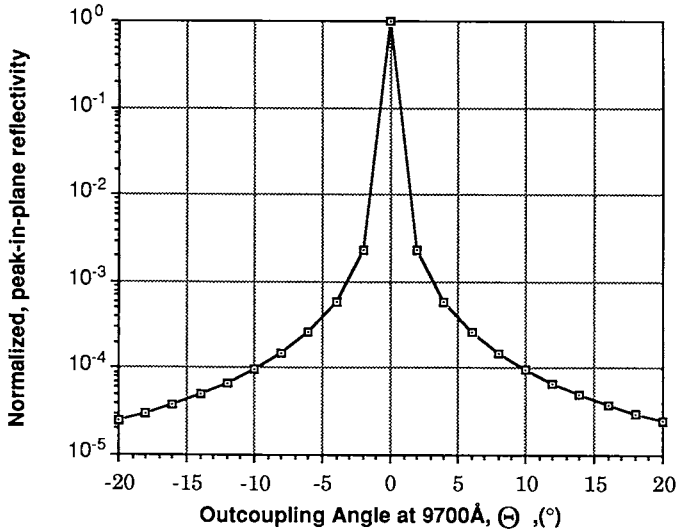

Fig. 34. The normalized, peak-in-plane reflectivity as a function of outcoupling angle as estimated by coupled-mode theory.

and that with a grating. The resulting Fresnel power reflection (R_F) between such regions is given by

$$R_F = \left(\frac{n_e - n_{eg}}{n_e - n_{eg}}\right)^2, \tag{24}$$

where n_e is the effective index in a region without a grating and n_{eg} is the effective index in a region with a grating.

The values of the effective index for the different regions and the mode coupling (using Eq. 11) between the regions are shown in Table IV for both a chained MOPA (Fig. 12) and a buried active grating MOPA (Fig. 13). In one design (Fig. 12), the grating is etched into the *p*-clad region and capped with a dielectric layer. In the second design (Fig. 13), a GaAs grating is buried within a 40% AlAs layer. In both cases, a 50% duty cycle grating is assumed.

The index profile for the buried active grating MOPA in this example is shown in Fig. 36. The *n*-clad region contains 60% AlAs, each graded region is 0.15 μm thick, 60 Å barriers are on either side of the 100 Å quantum well, the spacing between the GaAs grating layer and graded region is 0.1 μm, and the grating layer is 0.1 μm thick. The dashed-line near-field distribution in Fig. 36 is for a section of the device where the grating layer

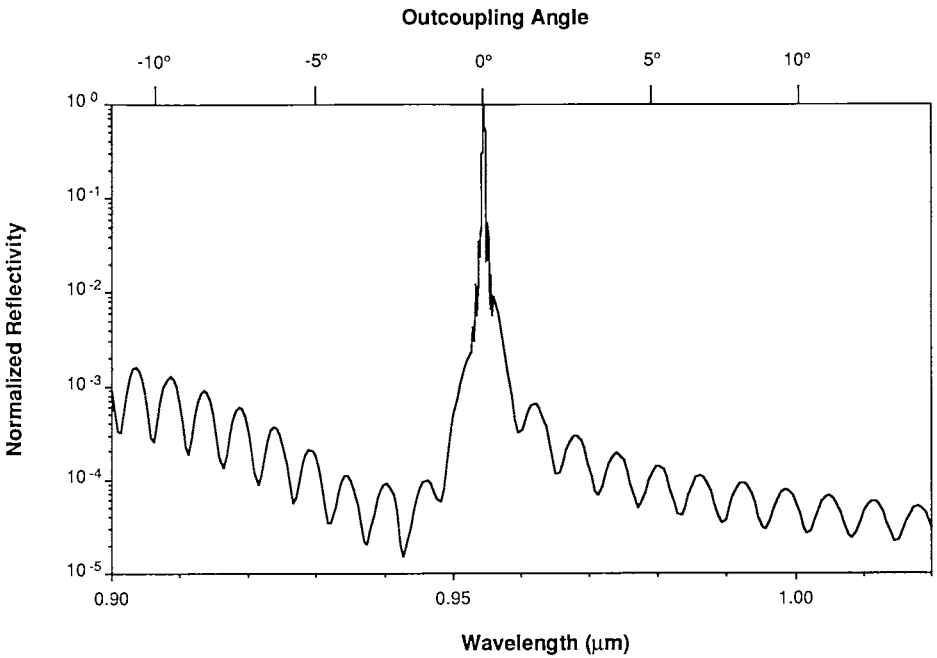

Fig. 35. The normalized, peak-in-plane reflectivity as a function of outcoupling angle calculated numerically for the structure shown in Fig. 15 with 66% AlAs in the cladding layers and a graded region thickness of 0.15 μm.

has been etched completely through with a 50% duty cycle and square wave profile. The solid-line near-field distribution is for a section of the device where the grating layer is completely intact (not etched).

These examples indicate that for such structures, the Fresnel reflection between regions of GSE devices is approximately 10^{-5} or less, and the coupling fractions are >0.97. If necessary, the reflections from such discontinuities in active grating devices can be further reduced by thinning the grating layer in the sections where the grating is not etched, reducing the

Table IV

Mode Coupling and Fresnel Reflection Values for Active and Passive Grating Devices

Device type	n_c	n_{eg}	R_F	κ
Passive grating	3.273	3.266	1.1×10^{-6}	0.975
Active grating	3.335	3.316	8.2×10^{-6}	0.972

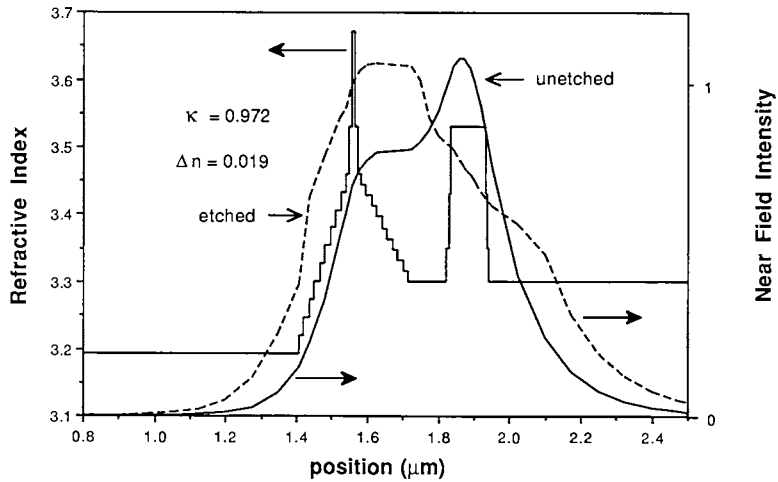

Fig. 36. Index profile for a buried grating MOPA and the near field distributions for a section of the device where the grating layer has been etched completely through with a 50% duty cycle and square wave profile, and a section of the device with the grating layer intact (not etched).

effective index difference and increasing the mode overlap (Eq. 11) between the two regions.

Another source of reflections is from the terminations of the waveguide. If the ends are uncoated cleaved facets, reflections of 30% are expected (Eq. 24). These reflections can be greatly reduced by many techniques including sawing the ends at an angle or applying anti-reflection coatings. Another approach to minimizing reflections is to make the end sections of the waveguide highly lossy by implanting damage or by having an extended, passive grating outcoupling region. Most of these techniques can essentially eliminate end reflections.

2. *Cascaded GSE-MOPA Arrays*

To optimize power and efficiency from a chain of N identical cascaded power amplifiers and output coupler sections, the coupling strength of each grating coupler and the operating level of each amplifier must be selected so that the total losses of each grating section is balanced by the single-pass gain of each amplifier, as explained below (Mehuys *et al.*, 1991b; Carlson *et al.*, 1990a). Also, the transmission of each passive waveguide (with grating output coupler) must be sufficiently large so that the input power to each amplifier in the chain is high enough to saturate the gain to a level where

amplified spontaneous emission noise will be suppressed. A detailed analysis of these topics can be found in Mehuys *et al.* (1991c).

In Fig. 37, the total power output of an amplifier chain is plotted as a function of the number of amplifiers in the chain for different values of the grating transmission. In this calculation, the unsaturated gain of each amplifier was $100\,cm^{-1}$, and the 3 dB saturation power for the gain was 5 mW. For grating transmissions equal to or less than the inverse of the saturated gain, the total power output saturates at powers much less than 1 W as the number of cascaded amplifiers in the chain is increased. This occurs because the input power to each successive amplifier is decreased, so that eventually it drops to the power of the noise, and the coherent power output goes to zero. For grating transmissions greater than the inverse of the saturated gain, the total power output scales linearly with the number of cascaded amplifiers in the chain, and power outputs in excess of 1 W are predicted, as shown in Fig. 37.

For an amplifier chain of a given size, there is a fairly wide range of grating transmissions where appreciable output powers can be obtained. In Fig. 38, this is illustrated for a chain with 20 amplifier sections where the total power output is plotted as a function of the grating transmission. The grating transmission has been displayed on a log scale. In this calculation, the unsaturated gain was $100\,cm^{-1}$ and the saturation power was 5 mW. There is a rapid increase in the power output as the grating transmission is increased above 0.01 and a local maximum in the transmission occurs at

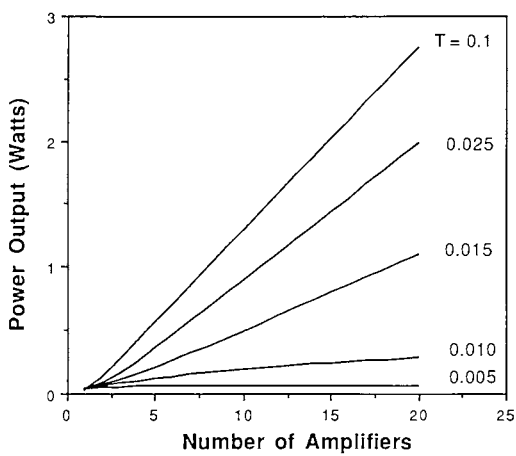

Fig. 37. Calculated power output as a function of the number of cascaded amplifiers.

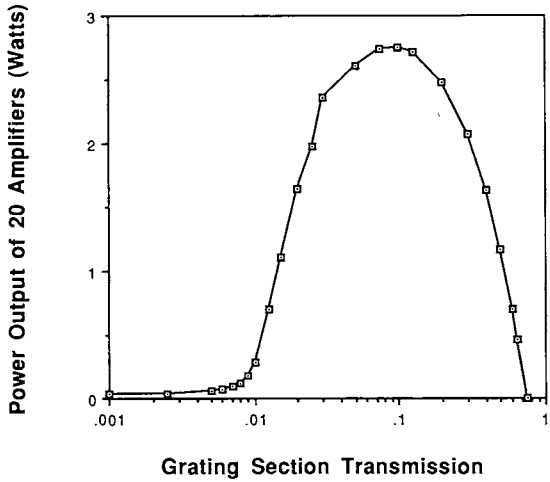

Fig. 38. Calculated power output of 20 cascaded amplifiers as a function of grating output coupler transmission.

0.1. For grating transmission values between about 0.03 and 0.3, the power drops only to about 80% of the maximum at the extremes of the range. Thus, small or even large deviations in the grating transmission from the optimum value will have little effect on the total power output.

3. *Active Grating MOPA*

The characteristics of the amplified light in an active grating GSE amplifier can be modeled using the well-known Rigrod analysis, where the amplification of coherent optical power as a function of position, $P_c(z)$, is governed by (Siegman, 1986; Butler *et al.*, 1989) the following:

$$\frac{dP_c(z)}{dz} = \left[\frac{g_0}{1+[P_c(z)/P_s]} - \alpha - \alpha_o\right] P_c(z) \tag{25}$$

where g_0 is the gain coefficient, P_s is the saturation power of the amplifier active layer, α is the modal loss coefficient, and α_0 is the grating output coupling coefficient. The internal limit power of the amplifier, P_{lim}, obtained from Eq. (25) by setting $dP_c(z)/dz$ equal to zero is given by

$$P_{lim} = P_s\left[\frac{g_0}{\alpha+\alpha_o} - 1\right]. \tag{26}$$

This is the maximum internal power level that occurs when the saturated gain is balanced by the total internal losses. This is often referred to as the loss-limited saturated regime of operation. The total coherent power output due to grating outcoupling, $P_c^{out}(z)$, is given by

$$P_c^{out}(L) = \int_0^L \alpha_0 P_c(z)\, dz, \tag{27}$$

where L is the length of the active grating amplifier. For a sufficiently long amplifier or for $P_c(0) \sim P_{lim}$, the total power output is well-approximated by

$$P_c^{out}(L) = \alpha_0 L P_{lim} = \alpha_0 L P_s \left[\frac{g_0}{\alpha + \alpha_o} - 1 \right]. \tag{28}$$

Even though the active grating amplifier is operated in a completely saturated regime, the emission power scales linearly with amplifier length. With the grating output coupler incorporated into the active section of the amplifier, the amplifier power output is generated by a distributed loss. In contrast, this type of power scaling does not occur in conventional edge-emitting amplifiers, where the maximum power output cannot exceed P_{lim} because the amplifier power output is generated by an end loss.

In order to accurately model the characteristics of active grating amplifiers, a self-consistent calculation (Marcuse, 1983) that accounts for the spatial dependence of the amplified coherent light, gain (carrier density), and amplified spontaneous emission should be used. However, when the input power is equal to P_{lim} maximum noise suppression is obtained and the output power is given by Eq. (28).

The total power output is seen, from Eq. (28), to scale linearly with both the amplifier length, L, the saturation power of the amplifier waveguide mode, P_S, and the unsaturated modal gain coefficient, g_0. There are two competing effects that come into play when the total power output is maximized with respect to the grating output coefficient, α_o. For a fixed operating level (constant current and hence constant g_0), as α_o is increased the fraction of light output coupled from the waveguide will increase, but the modal power in the waveguide (set by P_{lim}) will decrease. This will give rise to a local maximum in the total power output as a function of α_o. Maximizing Eq. (28) with respect to α_o gives,

$$\alpha_o = \sqrt{\alpha g_0} - \alpha. \tag{29}$$

From this result it is seen that the optimum value of α_o is a function only of the modal gain coefficient (and therefore the injected current) and the

internal modal losses, α. Fortunately, the square root reduces the dependence on gain, so high power outputs can be obtained over a wide range of grating output coefficients.

For maximum efficiency (and noise suppression) it is desirable to minimize α. In the loss-limited saturated regime, the differential quantum efficiency (or slope efficiency) η, is given by

$$\eta = \eta_i \alpha_o / (\alpha + \alpha_o) \tag{30}$$

where η_i is the internal quantum efficiency. When α_o is selected for maximum power output at a fixed operating level with an unsaturated modal gain coefficient of g_f, η is given by

$$\eta = \eta_i (1 - \sqrt{\alpha / g_f}). \tag{31}$$

Note that η will increase if α_o is optimized for higher operating level (larger g_f) and the modal losses are decreased. To simultaneously maximize both power output and η, α_o should be much greater than α.

Reports in the literature (Eisenstein *et al.*, 1990) on MQW-SCH InGaAs/InP 1.5 μm amplifiers give the following set of device parameters for buried ridge guide type devices operating at 24 kA/cm^2: $g_0 = 90\ \text{cm}^{-1}$, $P_s = 74$ mW, and $\alpha = 15\ \text{cm}^{-1}$. Using this set of measured device parameters in Eq. (29), it is found that $\alpha_o = 22\ \text{cm}^{-1}$ for maximum power output. Then using Eq. (28), it is seen that the maximum power output per unit length is 2.33 W/cm.

The calculated power current characteristics of a 1 cm long 4 μm wide MOPA are shown in Fig. 39, using the device parameters reported in Eisenstein *et al.* (1990). At 12 A the current density is 24 kA/cm^2, corresponding to the highest reported drive levels. The two curves correspond to different values of the modal loss. As expected, a significant improvement in power output is obtained when the losses are decreased to 5 cm^{-1}, which correspond to some of the lowest losses reported for InGaAs/InP MQW structures.

Similar power outputs are expected for InGaAs/GaAs quantum-well structures operating in the 0.9–1.0 μm wavelength range. In this material system, $P_s \sim 10$ mW, and $\alpha \sim 5\ \text{cm}^{-1}$ or less (Mehuys *et al.*, 1991c). This corresponds to a maximum power output per unit length of about 1.4 W/cm, for $g_0 = 200\ \text{cm}^{-1}$ (for a single quantum-well structure) and optimized $\alpha_o = 27\ \text{cm}^{-1}$, for maximum power output. Higher power output levels would be expected with multiple quantum-well structures. Note that the InGaAs/GaAs material system may produce a more efficient amplifier if the modal losses can be kept small ($\leq 5\ \text{cm}^{-1}$) because the unsaturated

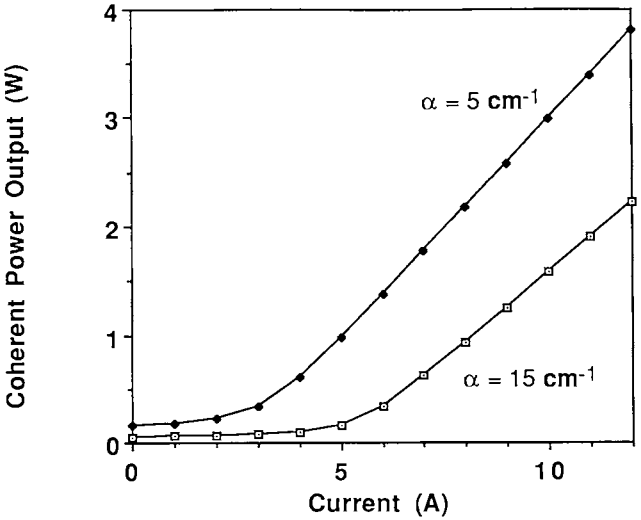

Fig. 39. Calculated power as a function of current for a 1 cm long × 4 μm wide GSE-MOPA.

modal gain coefficient is higher (several hundred cm^{-1}) than that in InGaAsP/InGaAs. In addition, the lower value of P_s in the InGaAs/GaAs material system implies that loss-limited saturated operation is obtained with lower input powers, so there should be less spontaneous emission noise at saturation in InGaAs/GaAs MOPAs than in the InGaAsP/InGaAs devices.

In order to obtain a grating output coefficient of 20 cm^{-1} or more (which is fairly large) without substantially changing the active layer confinement factor or increasing the internal losses, a buried-grating structure (Takemoto *et al.*, 1989; Carlson *et al.*, 1991a; Andrews *et al.*, 1991) is used for the active grating amplifier. Figure 40 shows a plot of the calculated grating output coupling strength versus grating depth for a 1.5 μm MQW-SCH structure (Eisenstein *et al.*, 1990) using a boundary element method (Hadjicostas *et al.*, 1990). Here, the grating layer is InGaAsP (with a bandgap energy corresponding to 1.25 μm) imbedded in InP cladding. Metallized, surface-relief gratings have also been used in active grating devices (Zory and Comerford, 1975; Macomber *et al.*, 1987; Mott and Macomber, 1989).

An important concern in the operation of a long amplifier such as the active-grating GSE is the level of amplified spontaneous emission (ASE) noise. At current densities greater than the transparency level, and with no coherent power input from the oscillator, the spontaneous emission noise power is more than sufficient to saturate the available gain. Spontaneous

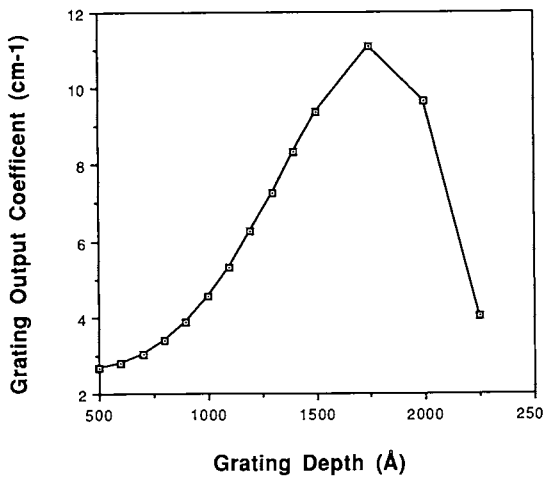

Fig. 40. Calculated grating output coupling coefficient as a function of grating depth for a square grating profile with 50% duty cycle.

emission that is emitted into the same beam divergence as the amplified coherent signal will reduce coherence and degrade the signal-to-noise ratio of a signal in the far field. A dominant contribution to noise in the far-field beam will come from spontaneous emission that is emitted into the waveguide mode. Because of the dispersive nature of the grating and the broad bandwidth (~300 Å) of the spontaneous emission, a small fraction of the isotropically radiated spontaneous emission power is preferentially scattered into the same direction and beam divergence as the coherent beam.

As the coherent input power is increased, the spontaneous emission noise will become suppressed and the amplified coherent signal will build. This is shown in Fig. 41, where the calculated coherent power output and noise power output are plotted as a function of the coherent input power injected by the oscillator. Although the total coherent output begins to saturate at an input power of about 0.1 mW, the minimum noise power output occurs for coherent input powers of 10 mW or more. At this input power level the gain is nearly saturated at the amplifier input by the coherent light, and maximum noise suppression is obtained. When the input power is equal to the limit power and loss-limited saturated operation occurs over the entire extent of the amplifier, the carrier density is pinned over the entire length of the amplifier. Additional carriers that are injected contribute almost exclusively to stimulated recombination, so that the ratio of coherent amplified signal power to noise power will increase with increased injection

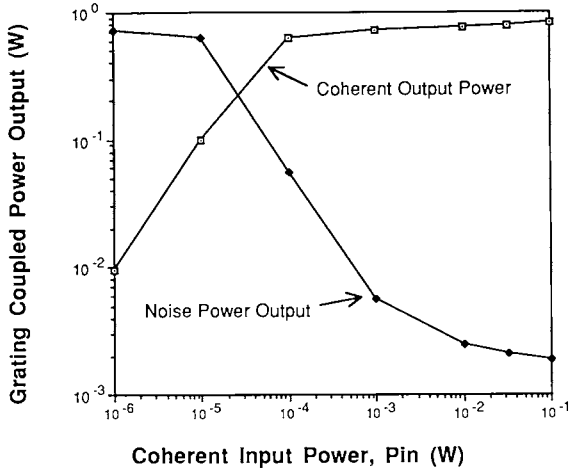

Fig. 41. Calculated coherent output power and noise power output as a function of input power for a 1 cm long active grating GSE-MOPA.

current. This mode of operation is very much like a laser operating above threshold. The origin of the similarity is that the dominant radiative recombination path is stimulated recombination into a single mode for both structures. In a laser, feedback causes amplification of a spontaneously emitted photon in the waveguide mode to a power level where the saturated gain equals the round-trip cavity losses. In the active-grating amplifier, the injected coherent input signal to the amplifier is of sufficiently high power so that the saturated gain per unit length equals the losses per unit length over the entire length of the amplifier, thereby pinning the carrier density.

C. Wavelength Tunable Diode Lasers and GSEs

Many monolithic tunable diode lasers use DFB or DBR gratings. Thus, grating surface emitting lasers may be modified for broadband tuning by use of additional electrodes as outlined in the following paragraphs. In the case of a MOPA-GSE, tuning of the master oscillator will result in angular scanning of the output beam.

A schematic of a general type of tunable distributed-Bragg-reflector (DBR) diode laser is shown in Fig. 42. A DFB laser with a single electrode in the amplifier current region is substantially not tunable. When electrodes and structures are added to allow carrier injection in the grating region I_B, or to allow the insertion of a section to control phase I_P, or to allow both,

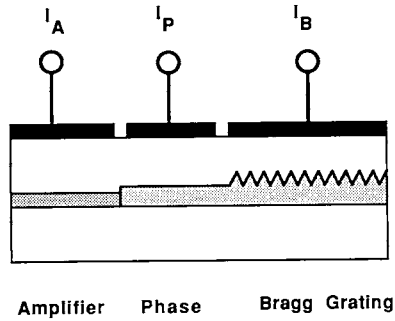

Fig. 42. Sketch of a tunable, three-electrode DBR semiconductor laser.

it becomes possible to tune the operation of the laser and maintain reasonably uniform output and narrow linewidth (Kobayashi and Mito, 1988). Physically a mechanism to allow the maintenance of both the round trip phase and the gain condition for lasing as wavelength is changed is required.

In the case of devices that add only phase control (I_P), the gain can be compensated by changing the current to the amplifier section (I_A) to make up for the loss of reflectivity in the Bragg reflector as the device is tuned off resonance. Such a device demonstrates a relatively small continuous tuning range (~4 Å). As the phase is continuously changed, the wavelength changes monotonically for several Å at which point it reverts back to its initial value and repeats the cycle (Tohmori *et al.*, 1983).

Devices that have a tuned Bragg grating (Broberg and Nilsson, 1988; Kotaki *et al.*, 1988; Koch *et al.*, 1988)—the refractive index in the grating region is changed by injection current so the resonant reflecting wavelength is tuned—can have a very wide but discontinuous tuning range. In these devices the grating resonant wavelength can be tuned over a broad range, but it is not possible to retain the phase condition over the tuning range so the device jumps from one Fabry–Perot mode to another as the tuning continues. A high value of 116 Å was reported (Broberg and Nilsson, 1988).

Three-section devices that include a tuned Bragg grating (I_B) and a phase section (Kotaki and Ishikawa, 1989) are capable of a relatively broad continuous or quasi-continuous tuning range while maintaining a constant output power. In these devices it is necessary to adjust I_A as I_P and I_B are varied if continuous tuning and constant output are required.

Continuous, smooth tuning of 18 Å with a three-section DBR laser has been obtained (Kotaki and Ishikawa, 1989), while 44 Å of continuous and

100 Å of quasi-continuous tuning for three-section DFB lasers has been demonstrated (Kobayashi and Mito, 1988).

D. Beam-steering of GSE Oscillator Arrays

For many applications of high-power, narrow-bandwidth coherent sources (such as space communications, optical recording, optical computing and optical interconnects), electronic beam-steering is desirable. The far-field outputs of edge-emitting phased arrays have been steered both electronically (Katz *et al.*, 1983) and by injection-locking with an external laser (Hohimer *et al.*, 1985; Abbas *et al.*, 1987). Electronic beam-steering has also been observed in grating-coupled Fabry–Perot diode lasers (Kan *et al.*, 1986) and single-element surface-emitting distributed Bragg reflector lasers (Kojima *et al.*, 1987; Evans *et al.*, 1986). Beam-steering from coherent GSE diode laser arrays has been demonstrated in the longitudinal direction (Carlson *et al.*, 1988b) and in the lateral direction (Hammer *et al.*, 1990). In addition, beam-steering has been achieved in GSE laser amplifiers by simply changing the wavelength of the master oscillator or oscillators (Parke *et al.*, 1990b).

A network theory (Amantea *et al.*, 1989; Amantea *et al.*, 1990) has been used to explain the mechanism of electronic beam-steering in GSE oscillator arrays. By adjusting the drive current to each active region, the effective optical length of the active regions is modified. This causes a continuous transformation along the longitudinal axis of the amplitude and phase of the array mode, resulting in a redistribution of the relative phase of the optical field in the different DBR sections (Evans *et al.*, 1989). The far-field pattern of the array is determined by the phase and amplitude of the light coupled out along each DBR section. These output phases and amplitudes in turn depend directly on the phase and amplitude of the standing wave along the DBR section. Because all the outputs are coherent, the relative phases of the standing waves in each DBR section affect the position of the far-field pattern due to interference between the light emitted from different DBR sections. In addition, if the wavelength of the array mode is detuned slightly from the Bragg condition, then the phase will vary across the surface of each grating, resulting in a tilt of the beam coupled out from each DBR section. Varying the current to one or more gain regions changes the index of refraction of those sections of the cavity. This results in both a change in the oscillation condition and a change in the optical path length (phase delay) between the DBR sections. Thus, the relative phases of the field at the grating surface are changed, and the beam is steered in the far

field along the direction that corresponds to the injection coupling. From this conceptual argument it follows that electronic beam-steering can be obtained from injection-coupled surface emitting laser arrays using spatially nonhomogeneous current distributions to drive the array gain elements. Furthermore, this type of beam-steering should be insensitive to the lateral (direction perpendicular to injection-coupled direction) structure of the array.

The far-field patterns of a two-dimensional 10×10 GSE array have been measured in real-time as the current to the ten electrically independent gain sections was varied. These arrays were terminated at each end by a series of unpumped gain sections and DBR sections. Figures 43(a) and 43(b) show the far-field pattern along the longitudinal direction corresponding to two different sets of currents to the ten gain sections. In Fig. 43(a), the gain sections 1 through 10 were simultaneously driven with 100 ns current pulses with the following respective peak values: 765 mA, 370 mA, 310 mA, 300 mA, 380 mA, 840 mA, 730 mA, 445 mA, 245 mA, and 615 mA. These current settings produced a power output of 200 mW. The resulting far-field pattern (Fig. 43) consisted of a dominant single lobe with a full width half-maximum angular divergence of 0.015°. The steered beam in Fig. 43(b) was obtained by increasing the current to the fourth gain section by 50 mA. This current change had a negligible effect on the total output power of the array, and the width of the primary lobe (0.015°) did not measurably change.

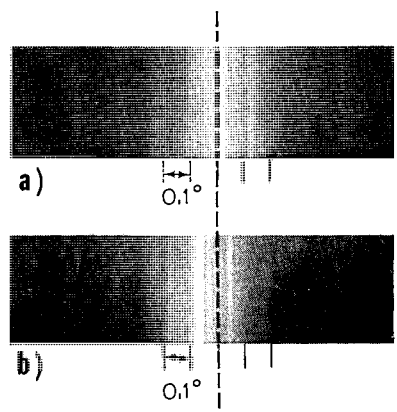

Fig. 43. (a) The far-field pattern of a 10×10 GSE array at one set of currents to the gain sections, and (b) when the current to the fourth gain section was changed by 50 mA. A shift of 0.05° is evident between the far-field patterns shown in (a) and (b). This is equivalent to more than three beam widths.

A shift of 0.05° in the pattern (corresponding to more than three full beam widths at half-maximum) is clearly observed as the current to the fourth gain section was changed. Simple antenna theory predicts that on the order of 10 distinct spots could be resolved in the far-field for this array geometry.

IV. FABRICATION

A. Fabrication Steps

The basic steps involved in making a GSE device is the growth of an appropriate epilayer structure followed by defining the gain regions and the outcoupling regions. Several approaches can be used to obtain lateral index guiding, including etched ridges (Evans *et al.*, 1991) and impurity-induced disordering (Thornton *et al.*, 1989; Thornton *et al.*, 1990; Zou *et al.*, 1990).

B. Fabrication of Passive Grating GSE Devices

The fabrication sequence of a single GSE element or a GSE array is similar. If an etched ridge is used for lateral index guiding, the first step can be metallizing the complete junction side of the wafer. The gain section pattern (single element or multiple element) is then defined in photoresist over the metallized surface. Ion beam-etching is then used to etch away the unprotected metal, the cap layer, and much of the *p*-clad layer. If the layers of each material are known precisely, then a timed etch will result in the desired thickness of the *p*-clad layer. In practice, a small segment of the GSE wafer is often sacrificed when the etching is estimated to be about 75% completed. Measurements on the sacrificed sample provide an indication of the progress and allow a recalculation of the etch time, if necessary. If the gain section consists of a single element, wet chemical etching can be used along with built in etch-stop layers to simplify the process. However, with two-dimensional arrays formed by closely spaced (evanescently coupled or Y-coupled) ridges with a width of 1–3 μm on 2–4 μm centers, the undercutting experienced with wet chemical etching generally precludes their use.

After definition of the gain sections, the grating is fabricated. In most cases, a holographic approach (Heflinger *et al.*, 1981) is used, although gratings formed by electron-beam writing and focused ion-beam micromachining (DeFreez *et al.*, 1989) have been used. The holographic method requires the application of a thin (~1000 Å) layer of photoresist to the wafer surface and subsequent exposure by interfering laser beams to form

a fringe pattern with a period corresponding to the desired grating period of the GSE array. The period of the fringe pattern Λ depends on the wavelength of the exposing light λ_{exp} and the total angle 2θ between the interfering beams and is expressed by the equation

$$\Lambda = \lambda_{exp}/(2 \sin \theta). \tag{32}$$

After development, the resulting photoresist grating is replicated into the *p*-clad layer of the wafer by chemical or dry etching. Dry etching generally results in a more uniform grating, but to minimize damage, the ion-beam acceleration voltages should be low. Figure 44 shows top and profile views of ion-beam (a, b) and chemically assisted ion-beam (c, d) gratings on an exposed surface of AlGaAs using acceleration voltages of 300 V in both cases.

The grating depth is chosen to provide the proper reflection, outcoupling, and transmission and depends on the epi-layer structure, remaining *p*-clad thickness, and grating length, as discussed in Section III. For the structure shown in Fig. 15, typical values for the *p*-clad thickness and grating depth are 0.1 μm and 0.04 μm, respectively for GSE arrays with 300 μm-long grating regions separated by 20 gain sections.

If required, ridges connecting each element in one group of laterally coupled gain sections to corresponding elements in a longitudinally adjacent group of gain sections can be defined in photoresist between the gain sections. An additional 200–500 Å of the *p*-clad layer can then be removed by chemical etching (Evans *et al.*, 1988a) or ion-beam etching outside the ridge regions, producing an index step for the ridges in the grating sections of approximately 3×10^{-3}.

If the GSE device is a MOPA, then the holographic grating fabrication cycle must be repeated a second time since the oscillator gratings and the amplifier gratings require different periods. In this case, before grating fabrication, the wafer surface is covered with a thin (~1500 Å) layer of Si_3N_4 that is then patterned with openings to correspond to the location of the oscillator gratings. After fabrication of the oscillator gratings, the original Si_3N_4 layer is removed and replaced with a new layer. The new layer is then patterned with openings that correspond to the location of the off-resonance, outcoupling gratings, and the grating fabrication sequence is repeated. Of course, if a focused ion- or electron-beam is used to fabricate the gratings, the multiple dielectric depositions and patterning is eliminated.

The grating/etching process is followed by plasma deposition of a 1500 Å-thick layer of Si_3N_4 over the *p*-side of the wafer. Using standard photolithographic techniques, the Si_3N_4 is removed only on the tops of the ridges in

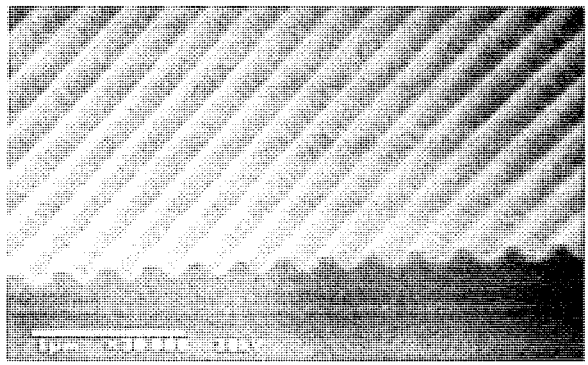

(a)

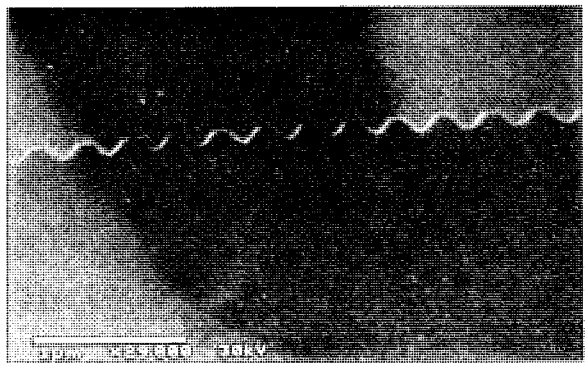

(b)

(c)

Fig. 44. Top and profile views of ion-beam (a, b) and chemically assisted ion-beam etched (c, d) gratings on an exposed surface of AlGaAs.

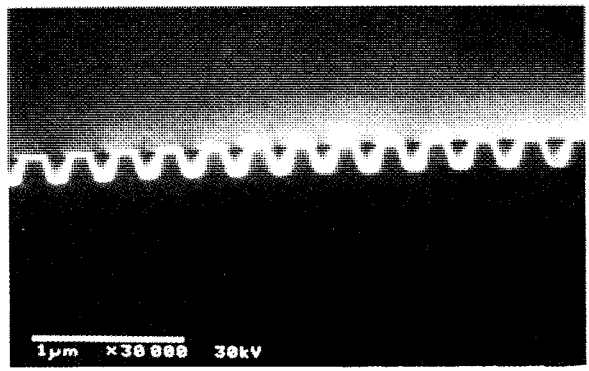

(d)

Fig. 44. Continued.

the gain sections, and the *p*-surface is re-metallized with Ti (500 Å) and Au (1000 Å) by electron-beam evaporation. Gold contact pads for each group of array elements are then plated to a thickness of about 1 μm over the gain sections through openings in a photoresist layer. After photoresist removal, the thin layer of *p*-metal connecting the plated contact pads is removed by ion beam-etching to provide electrical isolation between groups of gain sections. Finally, after thinning and polishing the substrate side of the wafer to about 100 μm, a 1500 Å thick layer of Si_3N_4, which acts as an anti-reflect coating over the *n*-side of the wafer, is applied. Using standard photolithographic steps, the Si_3N_4 is protected in the regions opposite of the gain regions, but removed in continuous 100 μm wide columns on either side, to provide windows in the substrate for light emission as shown in Figs. 6, 13, 27 and 28. Next, Au/Ge/Ni/Au *n*-side contacts are evaporated and sintered. The resulting GSE arrays are capable of emission from both the grating side and the substrate side, assuming that the substrate is transparent to the lasing wavelength. For InGaAsP/InP devices and for strained quantum-well GaInAs devices with the AlGaAs/GaAs material system, the emitting wavelength is such that the substrate is transparent. For GaAs or AlGaAs quantum wells, substrate emission can be obtained by using AlGaAs as the substrate (Evans *et al.*, 1989). A high reflect coating can be obtained on the grating surface by applying a gold coating over the Si_3N_4, as discussed in Section III, directing most of the emission through the substrate.

Figure 45(a) shows a segment of the Y-guide pattern in a gain section after removal of the *p*-cladding (by ion beam-etching) and before fabrication of the submicron grating (period ~2500 Å). An expanded view showing

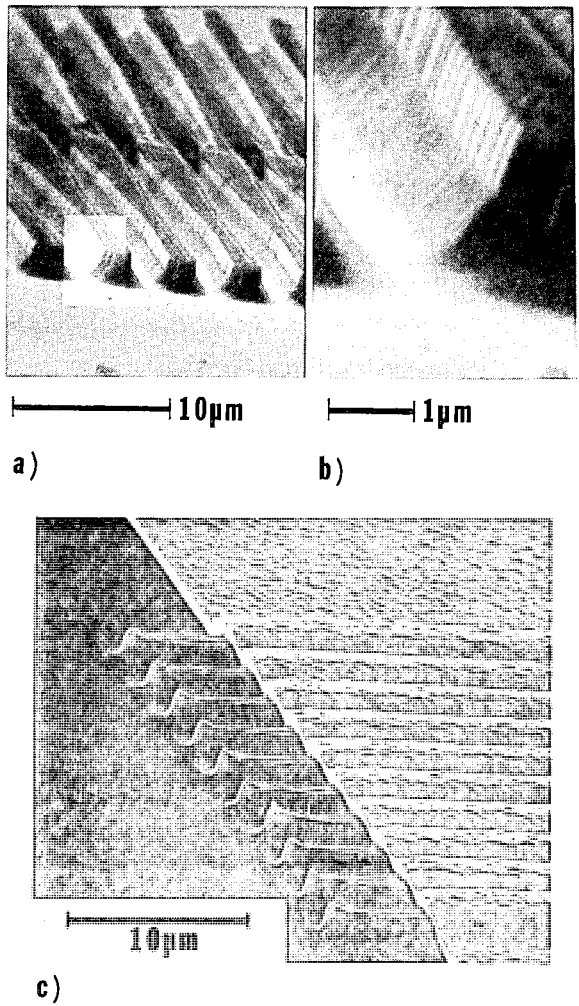

Fig. 45. Scanning electron micrograph view of (a) a Y-coupled gain section prior to the grating fabrication step; (b) an edge of a Y-coupled ridge; (c) an evanescent-coupled ridge gain section after complete processing; and (d) an end view of the ridges in a gain section after complete processing.

the edge of a ridge appears in Fig. 45(b) and corresponds to the bright rectangular region in Fig. 45(a). Portions of a 10-element gain section and grating region of an evanescent-coupled array after complete processing are shown in Fig. 45(c). Figure 45(d) is a close-up showing an end view of two of the ten parallel ridges after complete processing.

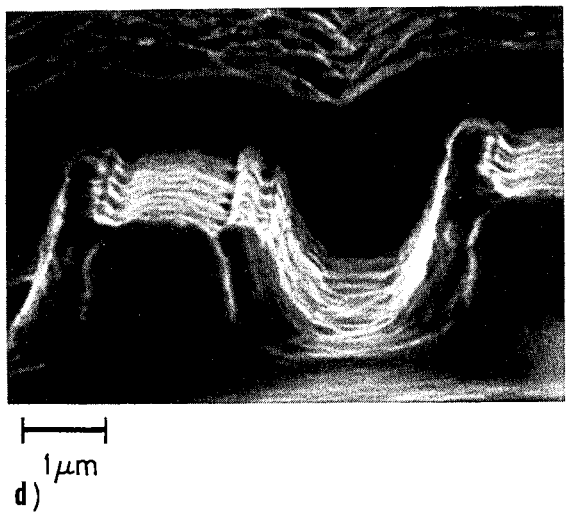

Fig. 45. Continued.

C. Fabrication of Active Grating GSE Devices

The fabrication of GSE devices with active grating outcouplers such as a GSE-DFB (Carlson *et al.*, 1991b) or a GSE-MOPA (Carlson *et al.*, 1991a; Mehuys *et al.*, 1991a) is only slightly different than the process described above. For these devices, the epitaxial growth is stopped at the grating layer. For a MOPA device, two different grating periods can be etched as described above. During regrowth to complete the device structure, care must be taken to prevent deformation of the grating profile by mass transport (Ohata *et al.*, 1986; Bhatt *et al.*, 1990). In the InGaAs/GaAs/AlGaAs material system, a GaAs or InGaAs grating layer (with a bandgap transparent to the emission wavelength) provides the largest index step and, hence, the strongest coupling parameters if all other grating parameters are the same. Such layers require, however, that the grating layer be completely etched through the underlying AlGaAs layer to prevent mass transport (Bour *et al.*, 1991). Alternatively, small amounts of AlAs can be added to the grating layer to prevent mass transport, with a resulting slight reduction in grating strength. For the InGaAsP material system, the grating profile can be maintained if the regrowth is performed in a H_2+PH_3 atmosphere in the presence of a GaAs substrate (Bhatt *et al.*, 1990). Figure 46 shows a TEM cross section through an active grating GSE device. In this case, the

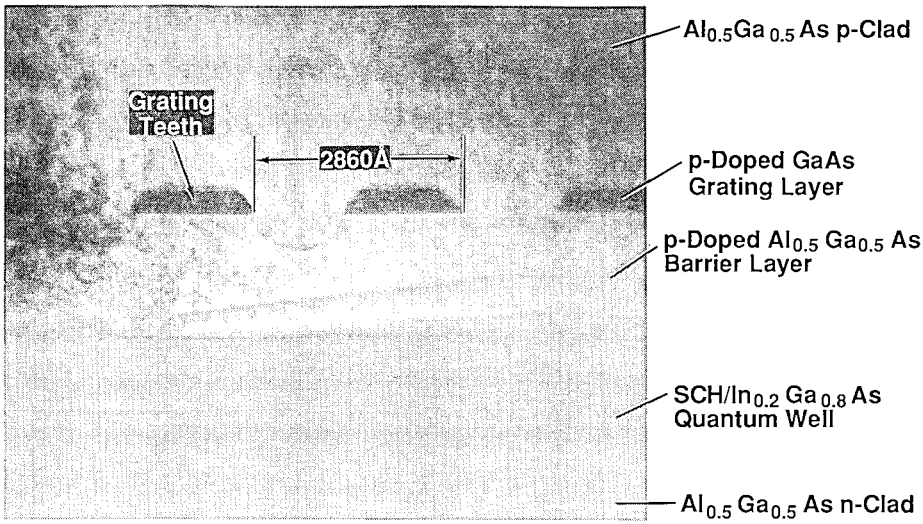

Fig. 46. Transmission electron micrograph cross section through an active grating GSE device.

GaAs grating layer was completely etched through using chlorine-assisted ion beam-etching before regrowth.

V. EXPERIMENTAL RESULTS AND DISCUSSION

A. GSE Oscillator Performance

Figure 47(a) shows a pulsed power current curve of a GSE laser with an output power of 32 W per surface. This GSE array has 10 ridges in each of 30 gain sections. The output power was limited by the power supply to 1.9 A per gain section. With just under 60 A input, the device is putting out 32 W from each surface or more than 1 W of total light output per ampere of drive current. The peak differential quantum efficiency is ~47%/surface. The FWHM of the central spectral line (centered at 9620 Å and shown in the inset of Fig. 47a at 10, 20, and 30 W), increases from 1.1 Å to 3.5 Å. This array had a high differential series resistance of about 9 Ω per gain section, and as a result the cw P-I curve (Fig. 47(b)) was rolling over at about 3.4 W, and the differential quantum efficiency peaked at about 30% per surface at less than 2 W output power per surface.

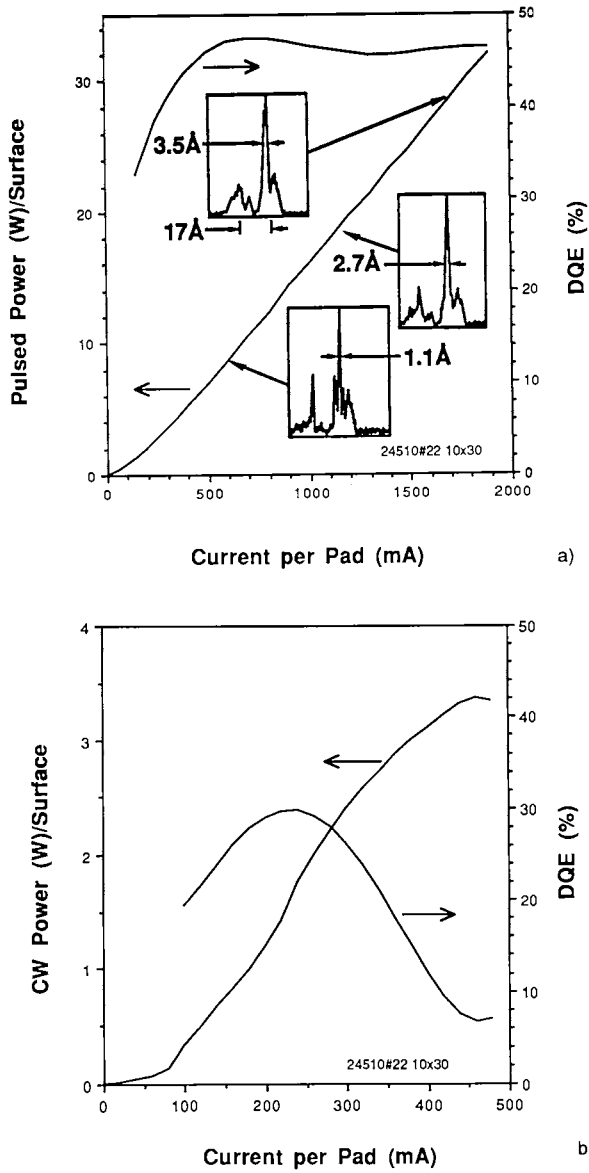

Fig. 47. (a) Power-current curve of a 10×30 GSE array operating with 100 ns pulses, 10 kHz repetition rate, and at a coolant temperature of −2.8°C; (b) cw power-current curve for the same device at −2.8°C. The longitudinal aperture of the array is 1.83 cm.

The power-current curves in Fig. 48 show the effect that the grating period has on the threshold current density. In Fig. 48(a), the grating period resulted in the GSE array emitting at a wavelength of 9600 Å, which is a shift of about 350 Å to the short wavelength side of the emission wavelength (~9950 Å) of conventional cleaved-facet lasers made from the same material. Although such GSEs put out several watts of cw power with, in this case, 21 gain sections, the threshold current density was about 1.3 kA/cm^2. For cw operation, this device had an average differential quantum efficiency of 30% per surface, an average power conversion efficiency

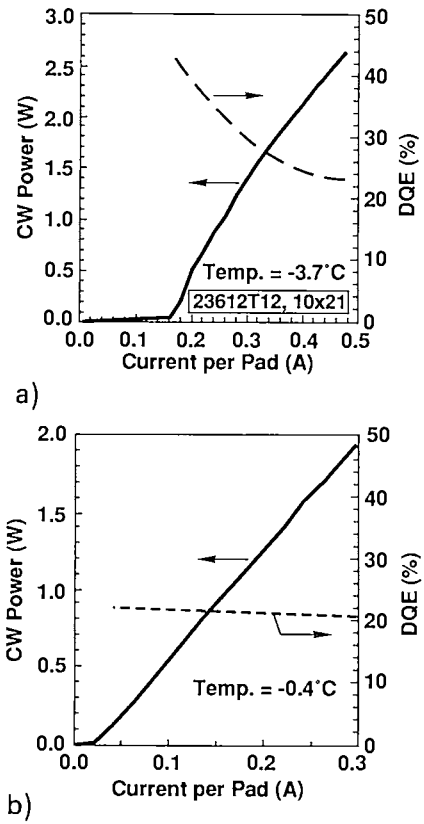

Fig. 48. (a) Power-current curve of a 10×21 GSE array operating cw with a grating period forcing emission on the short wavelength side of the photoluminescence peak. The coolant temperature is −3.7°C. The total aperture of the array is 1.29 cm. (b) Power-current curve of a 10×26 GSE array operating cw with a grating period forcing emission on the long wavelength side of the photoluminescence peak which results in a significantly lower threshold current. The coolant temperature is −0.4°C. The longitudinal aperture of the array is 1.59 cm.

of 7.3% per surface, and a differential series resistance of 2.8 Ω. As shown in Fig. 48(b), by only adjusting the grating period so that the emission wavelength of the GSE array ($\lambda_{GSE} = 9760$ Å) more closely coincided with that of cleaved-facet lasers from the same material ($\lambda_{FP} = 9750$ Å), the threshold current was reduced from 160 mA per gain pad to 24 mA per gain pad, corresponding to about 166 A/cm^2. By choosing the grating period so that emission occurs about 100 to 150 Å to the long wavelength side of the quantum-well photoluminescence peak (where the band to band absorption is significantly reduced), threshold current densities of just under 140 A/cm^2 have been obtained for GSE arrays.

1. *Improvements in Lateral Mode Control*

One of the major remaining challenges in the coupled oscillator GSE approach is to maintain single-mode operation in a narrow linewidth at higher drive currents above threshold (or at higher optical output levels). A limiting factor on being able to operate $10 \times N$ arrays at high drive currents relative to threshold are the complications added by multiple lateral modes. By reducing the number of elements (ridges) in each gain section from ten to one, operation at over eight times threshold in a single longitudinal mode (with a 36-MHz linewidth) has been achieved (Carlson *et al.*, 1990c).

To improve performance of 10-element-wide GSE arrays, mode selective geometries such as Talbot imaging (Dupuy *et al.*, 1992) or ridges in the grating regions (Evans *et al.*, 1991) have been used. In the latter case, an additional ridge-etch is performed in the grating regions after the grating fabrication step. The height of the ridges in the grating regions are about 400 Å and result in a lateral index step of about 5×10^{-3}. The power-current curve of such a GSE array with 20 gain sections pumped with equal currents is shown in Fig. 49. The differential quantum efficiency for this array was 25% per surface. The currents to this array (listed in Table V) could be adjusted to provide a spectrum with a 38 MHz linewidth (Fig. 50) at 2.2 times threshold. The far-field, also corresponding to operation at 2.2 times threshold, is shown in Fig. 51. The device contained 30 gain sections, but only an inner group of 20 gain sections were pumped. The central portion of the near-field, showing emission from 16 gratings, and operating with the drive currents listed in Table V is shown in Fig. 52.

The operation of GSE devices in a single lateral and longitudinal mode resulted in the first semiconductor laser arrays to demonstrate temporal stability (Felisky *et al.*, 1991). Generally, semiconductor laser arrays produce

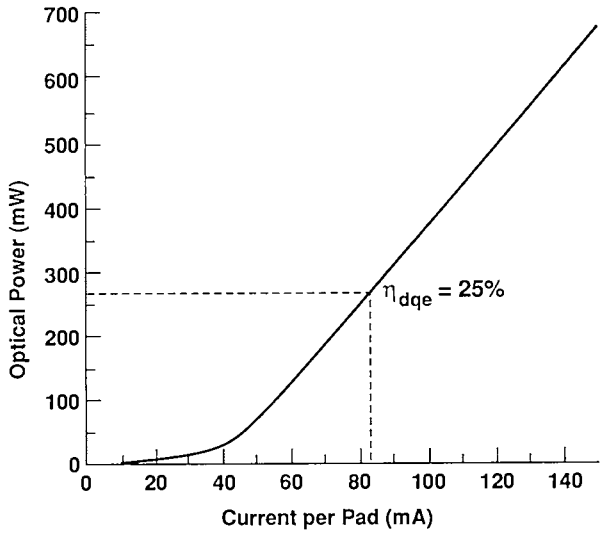

Fig. 49. cw power-current curve of a 10×20 GSE array (24710 #23) at a coolant temperature of 2.0°C. This array had ridges to provide index guiding in the grating regions. The differential quantum efficiency is 25% per surface.

a time-varying output consisting of irregular and even chaotic pulsations, in part due to the beating and mixing of multiple lateral and/or longitudinal modes (Wilson *et al.*, 1991).

2. *Talbot Plane Coupling*

Another approach to lateral coupling makes use of the imaging properties of evenly spaced gain elements. Because the output at the end of the gain

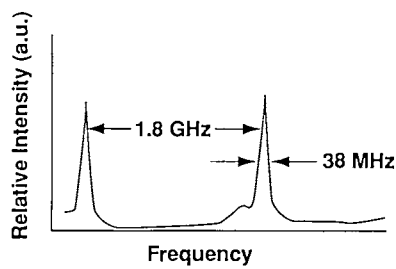

Fig. 50. Measurements of the cw spectrum of a 10×20 GSE array (24710 #23, Fig. 48) operating at 2.2 I_{th} using a scanning Fabry–Perot interferometer, operating at the drive currents listed in Table II.

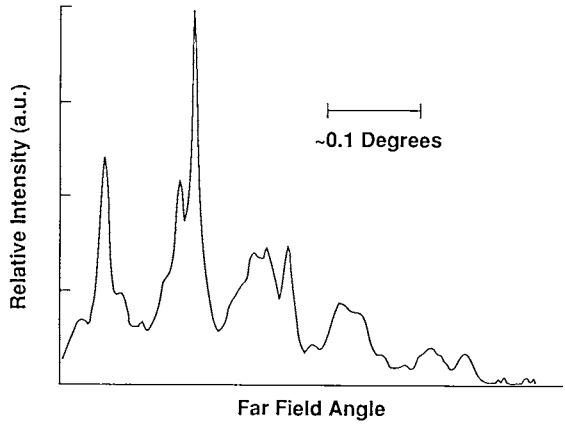

Fig. 51. Far-field of a 10×20 GSE array (24710 #23, Fig. 48) operating at 2.2 I_{th} operating at the drive currents listed in Table II.

sections forms a periodic pattern in the lateral direction, an image of the output occurs at multiple planes located at (Firester *et al.*, 1972; Leger *et al.*, 1988)

$$z = 2pd2/\lambda_m, \qquad p = 1, 2, 3, \ldots, \tag{33}$$

in the Fresnel region where p is an integer, λ_m is the lasing wavelength in the medium, and d is the separation between elements. These planes are sometimes referred to as Talbot planes. For some choices of parameters,

Table V

Gain Section Drive Currents for Device 24710 #23 used to Obtain a 38 MHz Linewidth (Fig. 50)

Gain Section	Current (mA)	Gain Section	Current (mA)
1	101	11	107
2	104	12	91
3	76.5	13	73
4	73.5	14	103
5	76	15	106.5
6	54.5	16	78
7	103.5	17	49
8	92.5	18	74
9	99.5	19	69.5
10	103	20	105

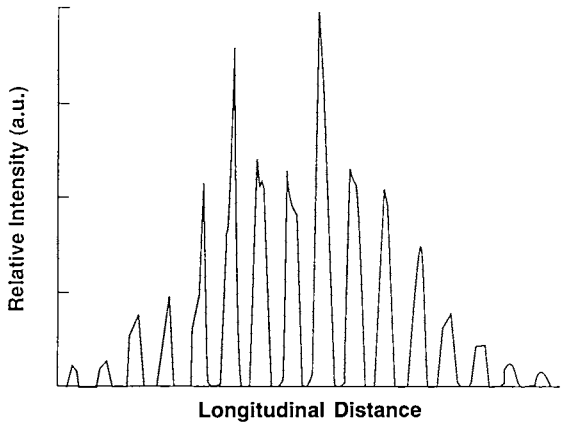

Fig. 52. The central portion of the near-field showing emission from 16 gratings of a 10×20 GSE array (24710 #23, Fig. 48) operating at 2.2 I_{th} operating at the drive currents listed in Table II.

the locations of the Talbot planes can coincide to the gain section spacing (Evans *et al.*, 1989; Wilcox *et al.*, 1989). When this occurs, each point of the re-imaged periodic pattern is a mixture of the peaks of the output from the original periodic pattern. From these considerations, appropriate choice of the grating section length and the lateral element spacing can provide improved lateral coupling between injection-coupled gain sections. The use of filters formed by etching holes at sub-Talbot planes, as shown in Fig. 53, has been demonstrated to increase lateral mode discrimination by blocking all but one of the array supermodes (Dupuy *et al.*, 1992). Since each supermode has different phase distributions, the filters can be shifted to select either the fundamental (in phase) or the highest-order (out-of-phase) mode, as shown in Fig. 54.

3. *Output from Multiple Columns*

As discussed earlier and illustrated in Figs. 8, 9, and 10, multiple columns of GSE arrays can be coherently coupled with monolithic corner-turning mirrors or with external optics. Using prism facets at 45° to couple adjacent GSE columns (Carlson *et al.*, 1990f) as shown in Fig. 10, two-dimensional far-field patterns corresponding to different phases between emitting grating regions were obtained. Figures 55 and 56 indicate the relative phases of the emitting regions and the resulting far-field patterns. Each of the far-field patterns has a well-defined periodic structure in both the lateral and longitudinal directions, indicating a substantial amount of coherence. Spectral

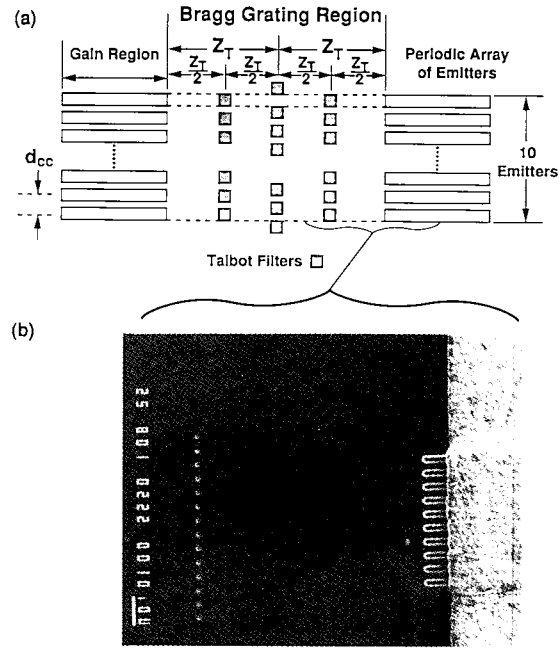

Fig. 53. (a) Sketch of the Talbot filter concept and (b) a scanning electron micrograph of a section from a fabricated device showing the 10 emitters and the first set of Talbot filters. The filters are placed at half multiples of the Talbot distance Z_T (where $Z_T = 2d_{cc}^2 n_{eff}/\lambda_0$).

data were obtained for each of the free-running array columns (Fig. 57(a,b)) and for the coupled array when injection-locked (Fig. 57(c)) in the pattern shown in Fig. 56. In Figs. 57(a) and 57(b), each array column is operating at the same current level as was used to obtain coherent injection of the coupled arrays, but the coupling prism is removed. The wavelength deviation of the modes of the free-running arrays is within 1 Å of that of the injection-locked prism-coupled array. The power output of the locked columns array (91 mW) was slightly greater than the sum of the power outputs (34 mW + 49 mW = 83 mW) from the free-running columns at the same drive currents.

The power-current curve of Fig. 58 shows the power output corresponding to a GSE ring array (Fig. 8) of 200 elements (Liew, *et al.*, 1991b). The characteristic two-dimensional far-field pattern shown in Fig. 59 shows excellent depth of modulation of the visibility in both the lateral and longitudinal directions. Operating near twice threshold, such ring arrays have exhibited an average spatial coherence of 86%, narrow linewidths of

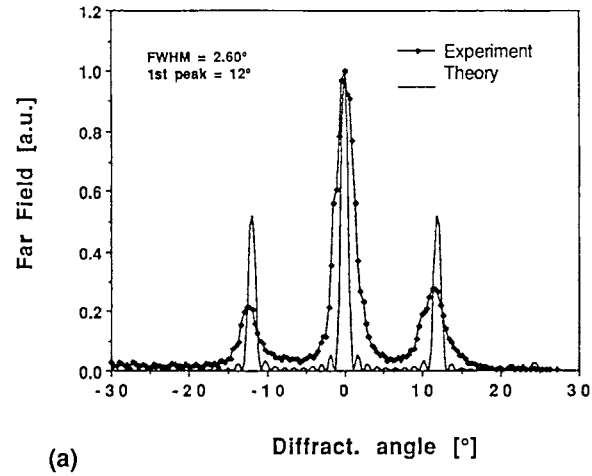

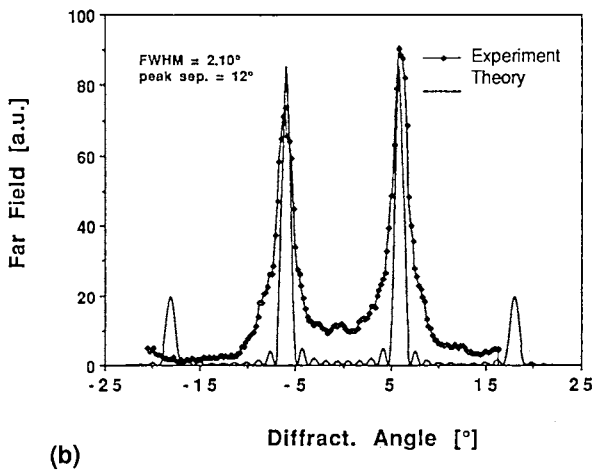

Fig. 54. Lateral far fields for two GSE arrays in which the Talbot filters were positioned to select (a) the fundamental mode and (b) the anti-phase mode. The dotted curves are the experimentally measured far fields, and the solid curve is the far field calculated for a coherent emitter of similar aperture size. The measured far fields are 2.5 times and 2.1 times the diffraction limited FWHM, respectively.

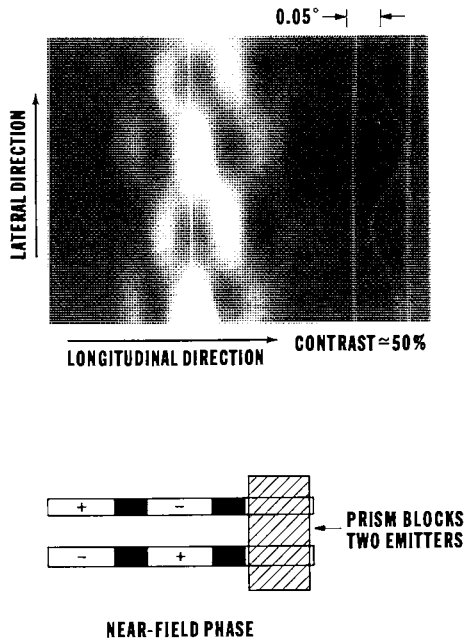

Fig. 55. Two-dimensional picture of the far-field pattern of the injection-locked prism-coupled GSE arrays shown at 91 mW output power. The checkerboard-type-pattern implies out-of-phase emission for adjacent DBR sections along the lateral and longitudinal directions in the array.

28 MHz, and far-field fringe visibilities of 80% (perpendicular to the array columns) and 88% (parallel to the array columns) (Liew *et al.*, 1991b). The mode of the ring array generally remains stable for several hours without adjustment with respect to drive current fluctuations and environmental variations, while that of column or serpentine arrays are stable for only several tens of minutes, suggesting that GSE ring architectures are more robust.

By coupling multiple columns of GSE arrays, any desired beam aspect ratio can be achieved. The fill factor of the GSE emitting aperture can be made equivalent to 100% with a lenticular array to provide a single peak in the far-field with low side-lobes.

4. *Effects of Temperature*

Figure 60 is included to show the dependence of differential quantum efficiency and output power for a GSE oscillator array on heatsink tem-

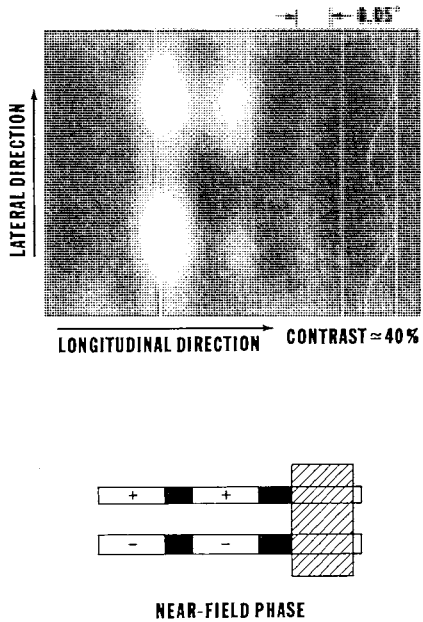

Fig. 56. Two-dimensional picture of the far-field pattern of another pair of injection-locked prism-coupled GSE arrays shown at 80 mW output power. This far-field pattern corresponds to out-of-phase emission for DBR sections adjacent in the lateral direction and in-phase emission for DBR sections that are adjacent to each other in the longitudinal direction.

perature. While there can be a 25% drop in the output power as the coolant temperature increases from 0° to 20°C, the differential quantum efficiency changes by only about 13%.

5. Modulation of GSE Oscillator Arrays

One of the applications envisioned for coherent, high-power grating-surface-emitting (GSE) laser arrays is use as transmitters in free-space coherent communication systems. This application requires that the far-field pattern remain stable during modulation. The electronic beam-scattering that can occur in GSE laser arrays would be undesirable since it would move the transmitter beam off of the detector. Experimental and theoretical studies have demonstrated a set of operating conditions that provide simultaneous spectral and spatial mode stability under GHz modulation rate operation, eliminating beam-steering during modulation (Carlson *et al.*, 1990d). Also,

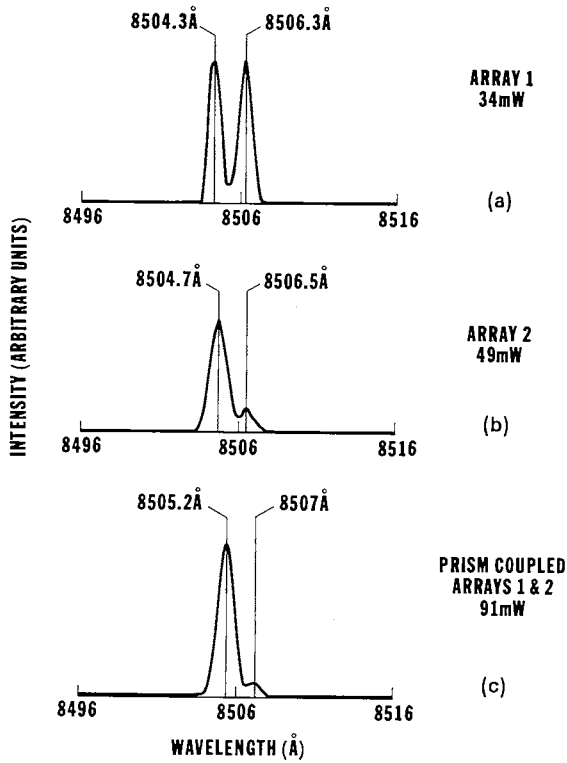

Fig. 57. Spectral outputs and power outputs (a) of column 1, freerunning, (b) of column 2, freerunning, and (c) of both columns injection-locked under the conditions that produced the far-field shown in Fig. 56.

measurements of the modulation bandwidth (Carlson *et al.*, 1990c) and direct modulation characteristics (Carlson *et al.*, 1990e) have also been done.

In experiments that measure beam stability under modulation, single and multi element GSE lasers were operated with a dc bias and were modulated at GHZ frequencies while simultaneous spectral and far-field measurements were made (Carlson *et al.*, 1990d). The GSE laser arrays were similar to those reported to have demonstrated single-mode operation with spectral linewidths as narrow as 290 kHz (Carlson *et al.*, 1990b). Figure 61 shows the simultaneous measurements of far-field and spectral output at the dc bias operating point and at three different power levels of a 1.25 GHz sinewave signal that was used to modulate a three-element GSE laser that was biased to operate in a single longitudinal mode. The spectral measurements were made with a 7.5 GHz free spectral range Fabry–Perot inter-

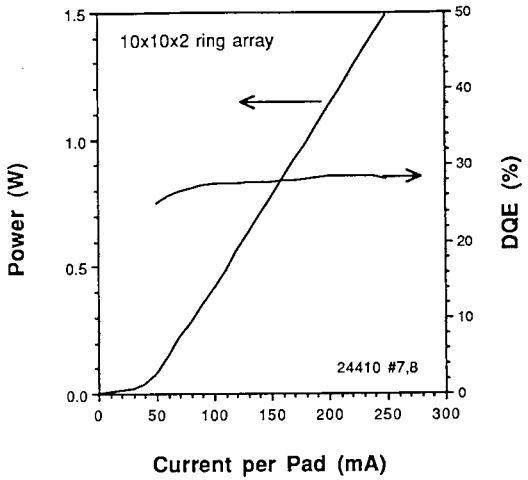

Fig. 58. Power-current characteristics and differential quantum efficiency (η_{dqe}) of a $10 \times 10 \times 2$ GSE ring laser array (Fig. 8).

ferometer, and show that this laser is operating in a single longitudinal mode at the dc bias point corresponding to 12 mW. Direct FM modulation was observed with almost no change in the far-field pattern from that measured in the dc case. The full-width half-maximum of the far-field angular divergence (in Fig. 61) of 0.03° is instrument-limited, so the actual far-field angular divergence is narrower. In the power spectra measurements, there is an increasing asymmetry that appears in the sidebands as the modulation level is increased. This indicates that the phase difference between the FM and AM components of the optical field is changing (Kobayashi *et al.*, 1982). Also, at an rf modulation power of +5 dBm or more the array is no longer operating in a single longitudinal mode as evidenced by the additional structure that appears in the central region of the power spectrum. Even though the array is no longer operating in a single spectral mode, the time-averaged far-field pattern shows only a 5% reduction in the peak intensity of the dominant lobe and essentially no change in the visibility or angular divergence of the lobes. No broadening of the carrier or modulation sidebands is observed in these power spectra measurements. However, at modulation power levels of about +12 dBm or more, broadening of the carrier and sidebands became noticeable, and at +15 dBm the power spectrum was too broad to be resolved by the Fabry-Perot interferometer. In spite of this severe spectral instability, the time-averaged far-field peak intensity was reduced only by about 40% and the fringe visibility dropped to only 58%.

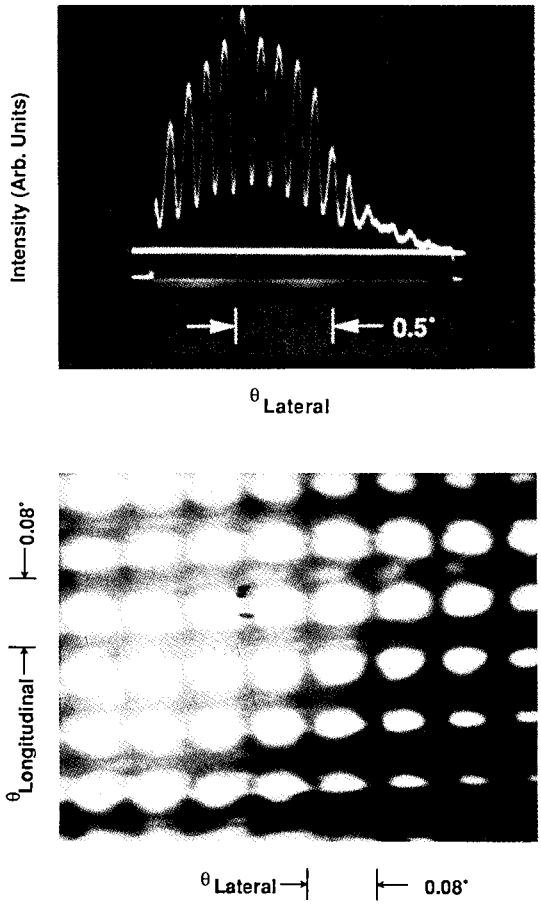

Fig. 59. (a) Image of part of the two-dimensional far-field pattern of a $10 \times 10 \times 2$ GSE array showing two-dimensional structure; (b) video trace of the far-field in the direction perpendicular to the two columns.

The conditions under which it is possible to modulate a GSE array while maintaining spectral and spatial mode stability are expected to be those that result in uniform field distributions in the gain sections, because the mode that produces the most uniform saturation of the gain distribution across the array will have the maximum discrimination against other modes. Additionally, if the current distribution to the gain sections of the array is varied in a symmetric fashion with respect to the center of the array, it is possible to tune the operating frequency without introducing a near-field wavefront tilt that would steer the far-field beam. A calculation is shown in Fig. 62 where the far-field of a three-element array (with uniform power

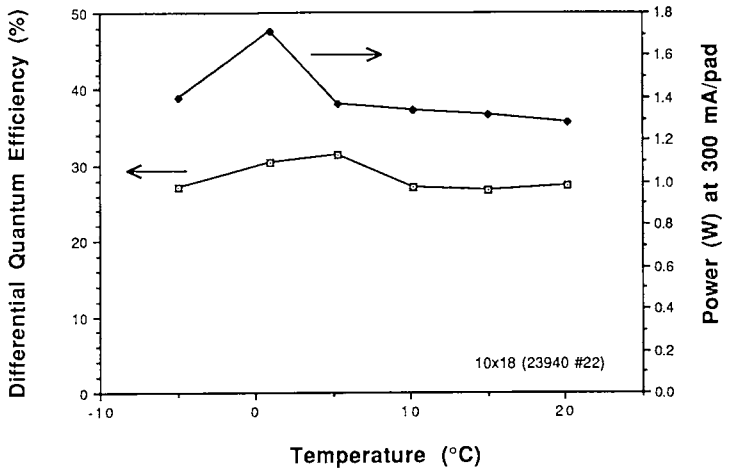

Fig. 60. Differential quantum efficiency and output power at a drive current of 300 mA per gain section as a function of coolant temperature for a 10×16 GSE array.

distribution to the gain sections) operating at 1.5 times threshold is shown. The solid trace is the far-field pattern calculated when the unsaturated gain to each active section is the same, and the dotted trace is the calculated far-field when the unsaturated gain to the center section is increased (in a quasi-static manner) by 12% and the unsaturated gain to the end sections was fixed. The total power output changed by only about 5%. This symmetric change of the unsaturated gain distribution of the array is equivalent to changing the current to the center gain section while the currents to the end gain sections are held fixed. No beam-steering occurs, but there is a change in the relative intensities of the side lobes and the peak intensity of the dominant lobe decreases by about 18%. These quasi-static calculations show that the spatial mode of a GSE array (operating above threshold in a single longitudinal mode) is stable with respect to small symmetric current changes to the gain sections. In order to calculate the amplitude and frequency responses under dynamic conditions, it is necessary to do a small signal analysis (Lang and Yariv, 1985).

B. GSE–MOPA Performance

The power-scaling properties of cascaded GSE-MOPA arrays have been demonstrated under both pulsed (Carlson *et al.*, 1990a; Welch *et al.*, 1990; Mehuys *et al.*, 1991b) and cw operating conditions (Carlson *et al.*, 1991a). Under cw operation, power outputs as high as 300 mW with spectral

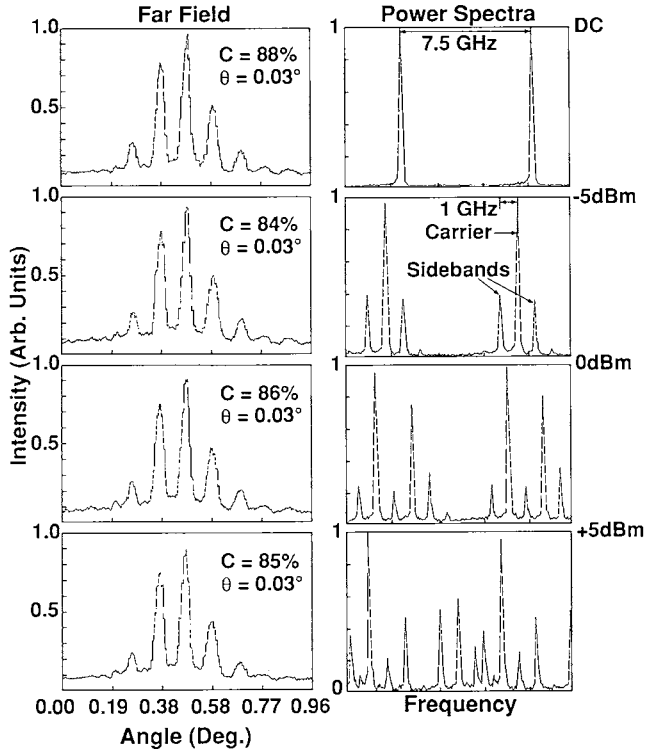

Fig. 61. Simultaneous measurement of the far-field and spectral outputs of a coherent three-element linear GSE laser array as a function of the 1 GHz modulation level applied to the center gain section. The contrast of the far field pattern is given by *C*.

linewidths of 135 MHz have been demonstrated (Carlson *et al.*, 1991a). Figure 63 shows the peak power as a function of total amplifier current to nine amplifiers driven in parallel. A maximum peak power of 1.2 W with 67% slope efficiency was achieved (Mehuys *et al.*, 1991b). This high slope efficiency was possible because a superlattice reflector was incorporated in the substrate increasing the grating output coupling into air.

The spectral control, under pulsed operation, provided by the oscillator is shown in Fig. 64 for the same nine-element amplifier array. With no input from the oscillator, the spectral output of the amplifiers resembles a multi-mode laser (Fig. 64a) because of the Bragg grating before the first amplifier. However, when the oscillator is driven above threshold, the spectral output of the amplifiers (Fig. 64(c)) is seen to correspond to that of the single-mode

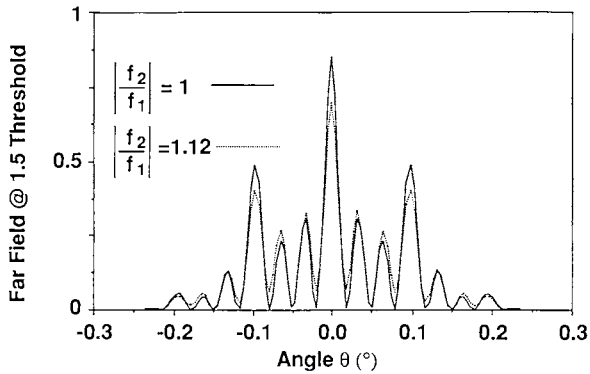

Fig. 62. Nonlinear network model calculation of the far-field output of a uniformly pumped three element GSE array. The solid trace is for a uniformly pumped array. The dotted trace corresponds to the situation when only the unsaturated gain to the center gain sections is increased by 12%.

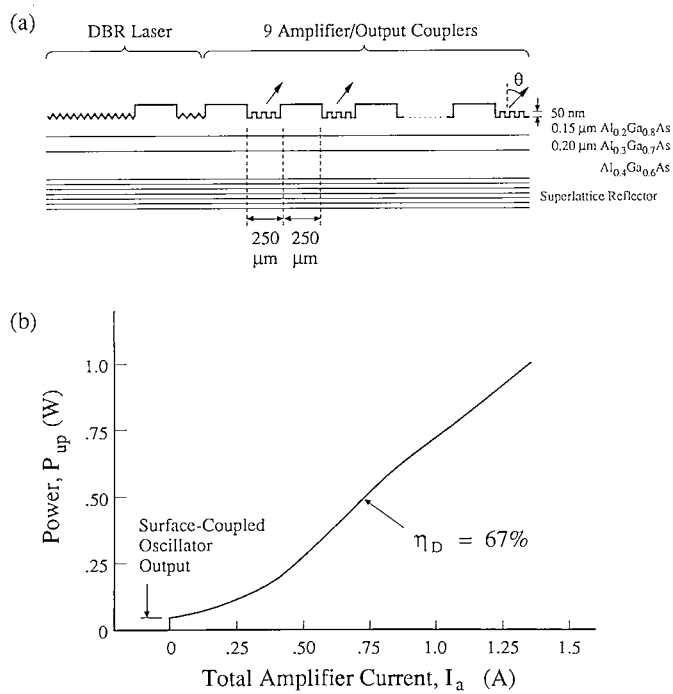

Fig. 63. Peak power as a function of current curve for a nine-element cascaded GSE-MOPA (Mehuys *et al.*, 1991b) (© 1991 IEEE).

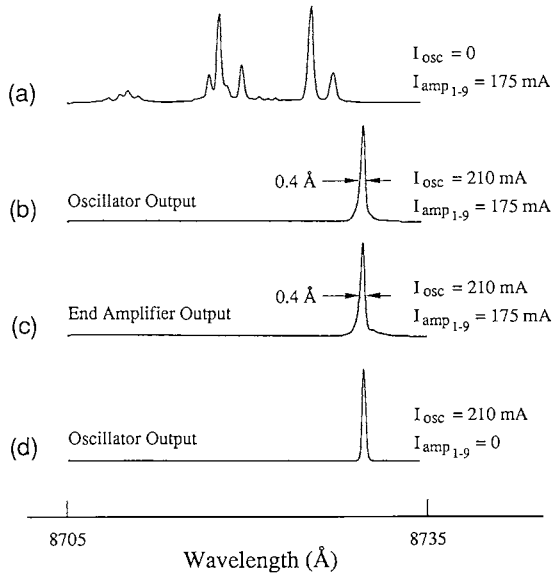

Fig. 64. (a) Spectral output of free-running amplifiers, (b) spectral output of oscillator with amplifiers operating, (c) spectral output of ninth amplifier with oscillator operating, and (d) spectral output of oscillator alone without amplifiers operating (Mehuys *et al.*, 1991b) (© 1991 IEEE).

oscillator (Fig. 64(b)), and single-mode operation of the oscillator is preserved when the amplifiers are operated.

The cascaded GSE-MOPA array is a multiple emitter device and can have random phase variations between separate grating outcoupling elements as do GSE coupled-oscillator arrays. As current to the amplifiers is increased to provide higher power outputs, the gain saturates so that phase tuning, using the amplifier currents, is no longer possible. This contributes to the degradation of the far-field pattern as illustrated in Fig. 65. One solution to phase variations, although it doubles the number of independently controlled electrodes, is to add a small phase tuning section that operates in the vicinity of transparency, providing independent phase control for each amplifier section.

An alternate approach to controlling the phase variation, attractive because of the reduced number of electrodes, is to make one long, continuous active grating as discussed in Section III. The active grating GSE-MOPA has been demonstrated under pulsed operation with peak powers of 370 mW for a 5 mm-long amplifier section (Mehuys *et al.*, 1991a). The corresponding

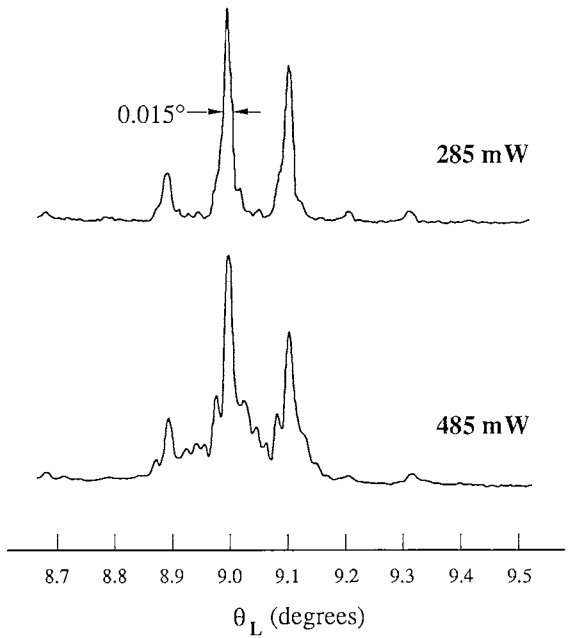

Fig. 65. Far-field pattern of cascaded GSE-MOPA array with eight amplifiers showing degradation at higher output power levels (Mehuys *et al.*, 1991b) (© 1991 IEEE).

near-diffraction-limited far-field is shown in Fig. 66. As discussed in Section IIIB, power outputs of 2–4 W are projected for amplifiers that are ~1 cm long.

VI. CONCLUSION

Figure 67 illustrates the progress made with GSE oscillator arrays over the last five years. The output power (Fig. 67(a)) grew exponentially for both pulsed and cw operation to over 30 W pulsed and 3.5 W cw. This trend of exponential growth in output power is expected to be maintained for applications that do not require highly coherent power. One of the keys to achieving multiwatt cw performance from GSE arrays was the reduction of the threshold current density (Fig. 67(c)) from the 10 kA/cm^2 range to about 100 A/cm^2. The other contribution to high cw power was the improvement in efficiency, shown in Fig. 67(b). The maximum quantum efficiencies of 45–48%/surface of GSE oscillator arrays equaled the maximum values

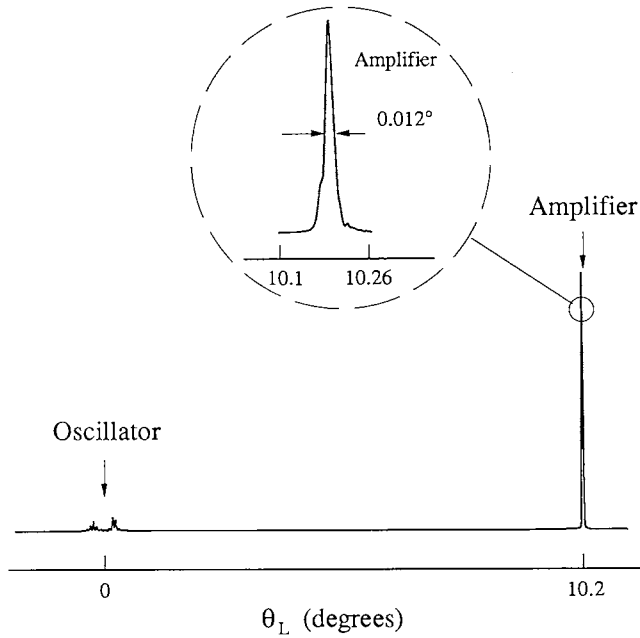

Fig. 66. Far-field pattern of an active grating GSE–MOPA showing single-lobed output of amplifier (Mehuys *et al.*, 1991a, with permission).

per facet that were measured from broad-area edge-emitting lasers from the same material. Figure 67(d) shows an exponential decrease in linewidth with time over the last several years for GSE oscillator arrays. Since the longitudinal and lateral mode spacings of GSE arrays are calculated to be a few GHz, measured linewidths below 100 MHz correspond to highly coherent arrays. The last several points shown are for GSE arrays with 200 coupled elements operating near twice threshold.

Coherent operation of two-dimensional GSE oscillator arrays at much higher power levels may be achieved using several approaches including increased wafer uniformity (producing increased mode discrimination), GSE designs insensitive to fabrication tolerances, improved fabrication techniques to reduce tolerances, and more stable array architectures. Similarly, increased wafer uniformity, improved fabrication techniques, and imaginative designs will result in coherent operation of GSE MOPA devices with several watts of output power.

Advances in packaging and cooling technologies will similarly contribute to the progress in the development of GSE and other semiconductor laser devices. The availability of low-cost synthetic diamond heatsinks along with

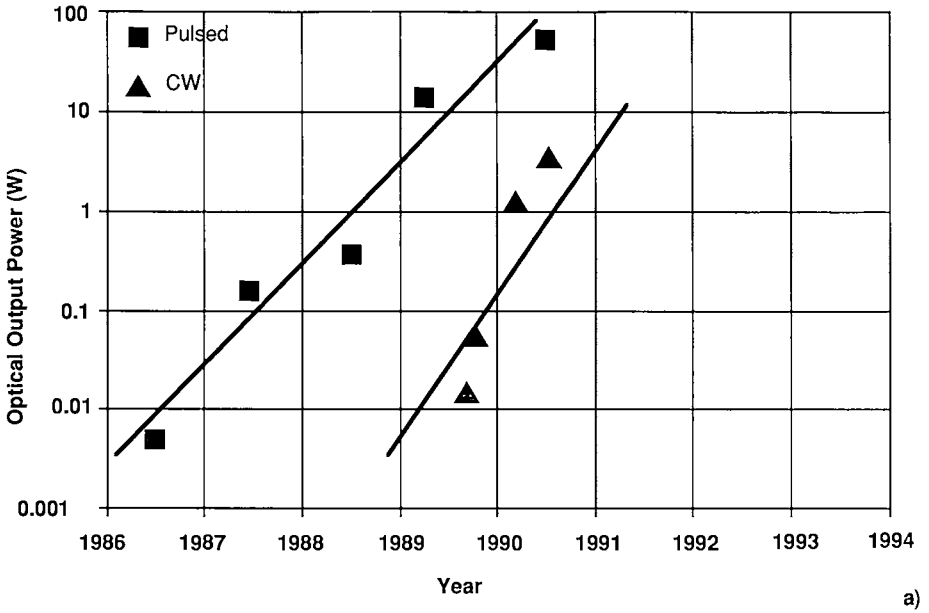

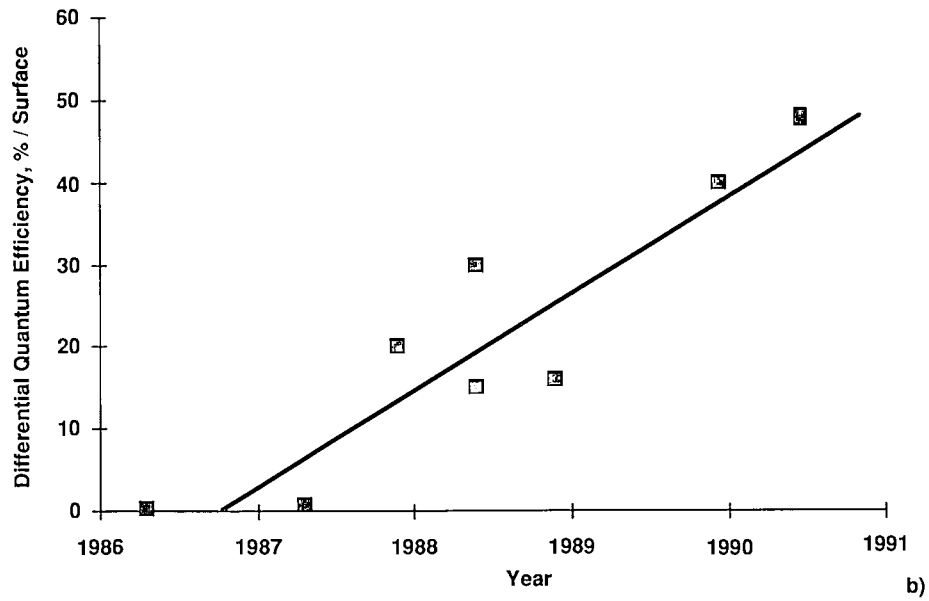

Fig. 67. Progress in GSE laser (a) power, (b) efficiency, (c) threshold, and (d) linewidth with time.

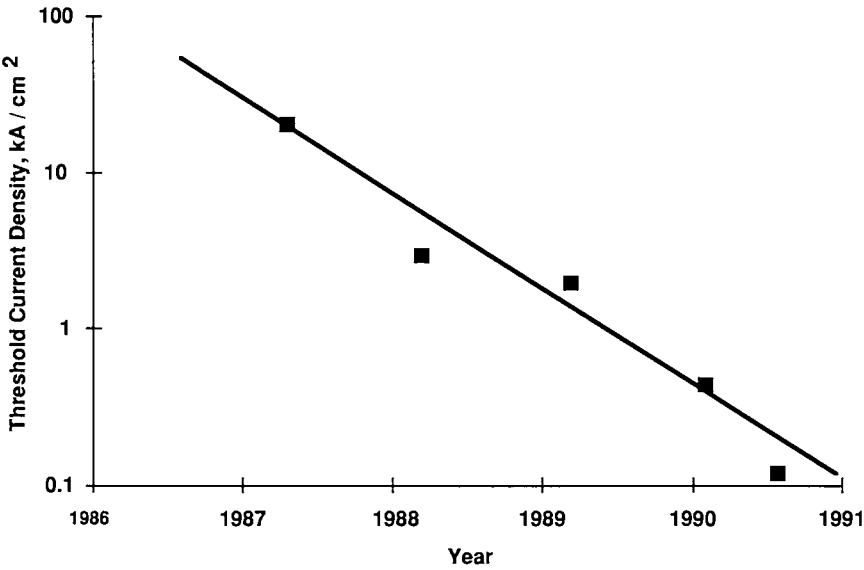

c)

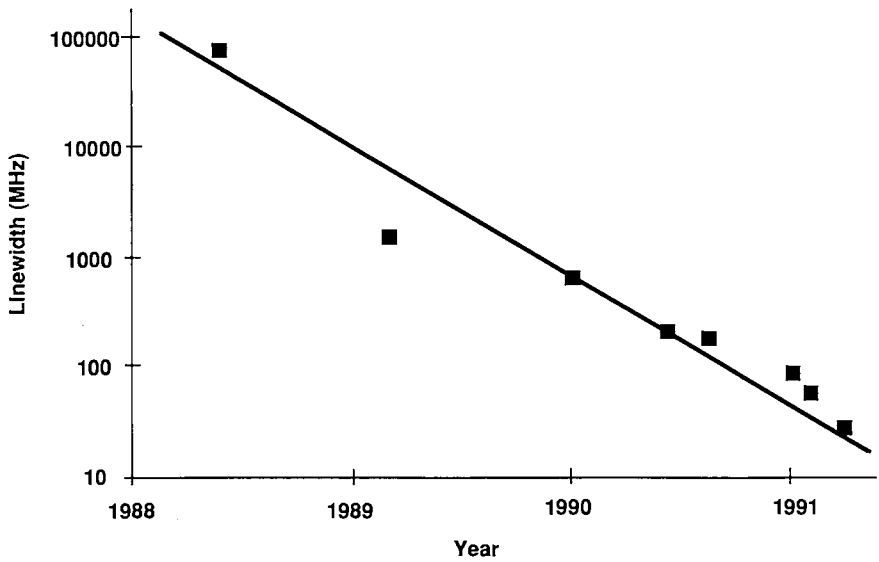

d)

Fig. 67. Continued.

microchannel coolers are two such examples that allow considering the scaling of GSE devices towards emitting and active areas on the order 1 cm^2, with expected cw output powers of many tens if not hundreds of watts.

Improvements in the efficiency of several material systems such as InGaAlP and InGaAsSb/InPSb will result in new families of GSE devices in the visible (0.6–0.8 μm) and the infrared (at wavelengths of 2 μm and beyond).

The final challenge in both the coupled oscillator and the MOPA GSE approaches is to obtain high beam quality at high power. Fill optics (Leger *et al.*, 1988, and the techniques discussed in Chapter 8, section 8.3.4) can compensate for a less than unity fill factor (the ratio of emitting surface to the total aperture) to provide most of the power in a central lobe. But in either configuration, even a narrow linewidth single mode with 100% spatial and temporal coherence can produce a less than acceptable far-field pattern if the GSE surface is not smooth and optically flat. Although phase-conjugate optics could in principle compensate for surface variations, the present research directed at the growth and control of single atomic layers along with the development of improved microfabrication techniques offer the promise of directly providing the desired optical flatness in GSE surfaces.

ACKNOWLEDGMENTS

The authors would like to thank numerous colleagues for their sustained support, contributions, and encouragement relating to GSE laser development over the last five or six years. At the David Sarnoff Research Center, they include Joe Abeles, Bob Amantea, Bob Bartolini, Tom Bibby, David Bour, Don Channin, John Connolly, Nancy Hughes, Chuck Dupuy, Mike Ettenberg, Rob Farkas, Pete Gardner, Norman Goldsmith, Aly Fathy, Dean Gilbert, Maria Harvey, Frank Hawrylo, Ed James, Ernie James, Jay Kirk, Richard Lai, Hao Lee, So Kuen Liew, Mike Lurie, Ray Martinelli, Ray Menna, Yegna Narayan, Steve Palfrey, Wally Reichert, Arye Rosen, Paul Stabile, Dennis Truxal, and Pam York. We also would like to thank Steve Chinn, Mike Finlan, Dick Shealy, and Peter Zory who contributed to the GSE effort at Sarnoff while they were at General Electric. Christine Wang, Hong Choi, and Jim Walpole at MIT Lincoln Laboratories and Chris Schaus and Ms. Sun of the University of New Mexico contributed to our supply of laser material for GSE devices. Rick DeFreez, Dave Bossert, Mark Felisky, H. Ximen, Geoff Wilson, John Hunt and Peter Carleson at the Oregon Graduate Institute assisted with GSE device characterization and

focused-ion-beam micromachining. Warren Ferguson, R. G. N. Ayekavadi, and C. S. Yeh at Southern Methodist University helped to develop a grating theory to aid in the design and prediction of GSE device performance. During this time, the GSE effort at Sarnoff was primarily supported by the Air Force Phillips Laboratory with additional support from Wright Patterson AFB, NASA Langley, and other governmental agencies.

REFERENCES

ABBAS, G. L., YANG, S., CHAN, V. W. S. AND FUJIMOTO, J. G. (1987). "Injection behavior of high-power broad-area diode lasers," *Opt. Lett.*, **12**, 8, 605-607.

AGRAWAL, G. P. AND DUTTA, N. K. (1986). *Long-Wavelength Semiconductor Lasers*, Van Nostrand Reinhold Company, Inc.

AHN, D. AND CHUANG, S. (1990). "Optical gain and gain suppression of quantum-well lasers with valence band mixing," *IEEE J. Quantum Electron.*, **26**, 1, 13-24.

ALFEROV, ZH., I., ANDREYEV, V. M., GUREVICH, S. A., KAZARINOV, R. F., LARIONOV, V. R., MIZEROV, M. N. AND PORTNOY, E. L. (1975). "Semiconductor lasers with the light output through the diffraction grating on the surface of the waveguide layer," *IEEE J. Quantum Electron.* **QE-11**, 7, 449-451.

AMANTEA, R., PALFREY, S. L. AND CARLSON, N. W. (1989). "A network model for two-dimensional coupled laser arrays," *Opt. Lett.*, **30**, 30-32.

AMANTEA, R., CARLSON, N. W., PALFREY, S. L., EVANS, G. A., HAMMER, J. M. AND LURIE, M. (1990). "Network analysis of the modes of two-dimensional grating-surface-emitting diode laser arrays," *IEEE J. Quantum Electron.* **26**, 1023-1038.

ANDREWS, J. T., VANGIESON, E., ENSTROM, R., APPERT, J., KIRK, J. B. AND CARLSON, N. W. (1991). "Buried grating distributed feedback laser at $1 = 1.51$ μm," *Proceedings of third international conference on indium phosphide and related materials*, April 8-11, Cardiff, Wales, U.K., 106-109.

BHATT, R., KOZA, M. A., ZAH, C. E. CANEAU, C., CHANG, C. C., SCHWARZ, S. A., GOZDZ, Z. S., LIN, P. S. D. AND YI-YAN, A. (1990). "A novel technique for the preservation of gratings in InP and InGaAsP and for the simultaneous preservation of InP, InGaAs, and InGaAsP in MOCVD," *Proceedings of the Fifth International Conference on Metalorganic Vapor Phase Epitaxy and Workshop on MOMBE, CBE, GSMBE, and Related Techniques*, 871-877.

BOGATOV, A. P., ELISEEV, P. G., MANKO, M. A., MIKAELYAN, G. T. AND POPOV, Y. M. (1980). "Injection laser with an unstable resonator," *Sov. J. Quantum Electron.* **10**, 5, 620-622.

BOSSERT, D. J., DEFREEZ, R. K., XIMEN, H., ELLIOT, R. A., HUNT, J. M., WILSON, G. A., ORLOFF, J., CARLSON, N. W., EVANS, G. A., LURIE, M.

HAMMER, J. M., PALFREY, S. L. AND AMANTEA, R., (1990). "Grating surface emitting lasers in a ring configuration," *Appl. Phys. Lett.* **56**, 21, 2068-2070.

BOUR, D. P., CARLSON, N. W., EVANS, G. A., LIEW, S. K., KIRK, J. B. AND REICHERT, W. F., (1991). "Surface-emitting, distributed feedback InGaAs/AlGaAs lasers by organometallic vapor phase epitaxy," *J. of Appl. Phys.* **70**, 9, 4687-4693.

BRILLOUIN, L., *Wave Propagation in Periodic Structures*, Dover Publications, New York, 1953.

BROBERG, B. AND NILSSON, S. (1988). "Widely tunable active Bragg reflector integrated lasers in InGaAsP-InP," *Appl. Phys. Lett.* **52**, 1285-1287.

BURNHAM, R. D., SCIFRES, D. R. AND STRIEFER, W. (1975). "Single heterostructure distributed-feedback GaAs diode lasers," *IEEE J. Quantum Electron.* **QE-11**, 7, 439-457.

BUTLER, J. K., EVANS, G. A. AND CARLSON, N. W. (1989). "Nonlinear characterization of modal gain and effective index saturation in channelled-substrate-planar double heterojunction lasers," *IEEE J. Quantum Electron.* **25**, 7, 1646-1652.

BUTLER, J. K., FERGUSON, W. E., EVANS, G. A., STABILE, P. AND ROSEN, A. (1992). "A boundary element technique applied to the analysis of waveguides with periodic surface corrugations," *IEEE J. Quantum Electron.* **28**, 7, 1701-1709.

CARLSON, N. W., EVANS, G. A., HAMMER, J. M., LURIE, M., CARR, L. A., HAWRYLO, F. Z., JAMES, E. A., KAISER, C. J., KIRK, J. B., REICHERT, W. F. AND TRUXAL, D. A. (1988a). "A high power seven element grating surface emitting diode laser array with 0.012° far-field angle," *Appl. Phys. Lett.* **52**, 12, 939-941.

CARLSON, N. W., EVANS, G. A., AMANTEA, R., PALFREY, S. L., HAMMER, J. M., LURIE, M., CARR, L. A., HAWRYLO, F. Z., JAMES, E. A., KAISER, C. J., KIRK, J. B. AND REICHERT, W. F. (1988b). "Demonstration of electronic beam steering in monolithic grating surface emitting diode laser arrays," *Appl. Phys. Lett.* **53**, 23, 2275-2277.

CARLSON, N. W., ABELES, J. H., BOUR, D. P., LIEW, S. K., REICHERT, W. F., LIN, A. S. AND GOZDZ, P. S. D. (1990a). "Demonstration of a monolithic, grating-surface-emitting laser master-oscillator-cascaded power amplifier array," *IEEE Photon. Technol. Lett.* **2**, October, pp. 708-710.

CARLSON, N. W., BOUR, D. P., EVANS, G. A. AND LIEW, S. K. (1990b). "Spectral linewidth narrowing in monolithic grating-surface-emitting laser arrays," *IEEE Photon. Technol. Lett.* **2**, 4, 242-243.

CARLSON, N. W., BOUR, D. P., EVANS, G. A., AMANTEA, R., STABILE, P. J. AND LIEW, S. K. (1990c). "CW operating characteristics and modulation properties of single mode grating-surface-emitting laser arrays," *Conference on Lasers and Electro-Optics*, Technical Digest, p. 430, paper CThJ2.

CARLSON, N. W., BOUR, D. P., EVANS, G. A., AMANTEA, R. AND LIEW, S. K. (1990d). "Stable single mode operation of grating-surface-emitting laser arrays under frequency-modulated operation," *Appl. Phys. Lett.* **57**, 8, 756-758.

CARLSON, N. W., PATTERSON, D. R., STABILE, P. J., LIEW, S. K., BOUR, D. P. AND EVANS, G. A. (1990e). "Demonstration of digital pulse modulation of a grating-surface-emitting diode laser," *Electron. Lett.* **26**, 20, 1695–1696.

CARLSON, N. W., EVANS, G. A., LURIE, M., HAMMER, J. M., KAISER, C. J. AND LIEW, S. K. (1990f). "Coherent operation of injection-locked prism-coupled grating surface emitting arrays," *Appl. Phys. Lett.* **56**, 2, 114–116.

CARLSON, N. W., AMANTEA, R., EVANS, G. A., BOUR, D. P. AND LIEW, S. K. (1990g). "Applications of surface emitting lasers to coherent communications systems," *LEOS '90 Conference Proceedings*, MA, 406–409.

CARLSON, N. W., LIEW, S. K., EVANS, G. A., BOUR, D. P., ABELES, J. H. AND AMANTEA, R. (1991a). "CW operating characteristics of grating-surface-emitting master oscillator power amplifier laser arrays," *Conference on Lasers and Electro-Optics*, Technical Digest, 250–251.

CARLSON, N. W., LIEW, S. K., AMANTEA, R., BOUR, D. P., EVANS, G. A. AND VANGIESON, E. (1991b). "Mode discrimination in undistributed feedback grating surface emitting lasers containing a buried second order grating," *IEEE J. Quantum Electron.* **27**, 6, 1746–1751.

CASEY, H. C. AND PANISH, M. B. (1978). *Heterostructure Lasers, Part A and Part B*, Academic Press, New York.

CRAIG, R. R., CASPERSON, L. W., STAFSUD, O. M., YANG, J. J. J., EVANS, G. A. AND DAVIDHEISER, R. D. (1985). "Etched mirror unstable-resonator semiconductor lasers," *Electron. Lett.* **21**, 2, 62–63.

DEFREEZ, R. K., PURETZ, J., ELLIOT, R. A., CROW, G. A., XIMEN, H., BOSSERT, D. J., WILSON, G. A. AND ORLOFF, J. (1989). "Focused-ion-beam micromachined diode laser mirrors," *SPIE Laser Diode Technology and Applications*, Vol. 1043.

DEFREEZ, R. K., XIMEN, H., BOSSERT, D. J., HUNT, J. M., WILSON, G. A., ELLIOT, R. A., ORLOFF, J., EVANS, G. A., CARLSON, N. W., LURIE, M., HAMMER, J. M., PALFREY, S. L. AND AMANTEA, R. (1990). "Spectral locking in an extended area two-dimensional coherent grating-surface-emitting laser array," *IEEE Photon. Technol. Lett.* **2**, 1, 6–8.

DUPUY, C., G., LURIE, M., HAMMER, J. M., EVANS, G. A. AND DEFREEZ, R. K. (1992). "Lateral mode control of grating surface emitting laser diode arrays by monolithic talbot filtering," *IEEE J. Quantum Electron.* **28**, 5, 1305–1309.

EISENSTEIN, G., TESSLER, N., KOREN, U., WIESENFELD, J. M., RAYBON, G. AND BURRUS, C. A. (1990). "Length dependence of the saturation characteristics in 1.5 μm multiple quantum well optical amplifiers," *IEEE Photon. Technol. Lett.* **2**, 790–791.

EVANS, G. A., GARMIRE, E. M., STOLL, H. H., OSMER, J. A., SOADY, W. E., LEE, A. B. AND ZIEGLER, M. P. (1981). "Progress toward a monolithically integrated coherent diode laser array," Air Force Systems Command, Report SD-TR-81-7.

EVANS, G. A., HAMMER, J. M., CARLSON, N. W., ELIA, G. R., JAMES, E. A. AND KIRK, J. B. (1986). "Surface-emitting second order distributed Bragg reflector laser with dynamic wavelength stabilization and far-field angle of 0.25°," *Appl. Phys. Lett.* **49**(6), 314–315.

EVANS, G. A., CARLSON, N. W., HAMMER, J. M., LURIE, M., BUTLER, J. K., CARR, L. A., HAWRYLO, F. Z., JAMES, E. A., KAISER, C. J., KIRK, J. B., REICHERT, W. F., CHINN, S. R., SHEALY, J. R. AND ZORY, P. S. (1988a). "Efficient, high power (>150 mW) grating surface emitting lasers," *Appl. Phys. Lett.* **52**, 13, 1037-1039.

EVANS, G. A., CARLSON, N. W., HAMMER, J. M., LURIE, M., BUTLER, J. K., PALFREY, S. L., AMANTEA, R., CARR, L. A., HAWRYLO, F. Z., JAMES, E. A., KAISER, C. J., KIRK, J. B., REICHERT, W. F., CHINN, S. R., SHEALY, J. R. AND ZORY, P. S. (1988b)." Coherent, monolithic two dimensional (10 × 10) laser arrays using grating coupling," *Appl. Phys. Lett.* **53**, 22, 2123-2125.

EVANS, G. A., CARLSON, N. W., HAMMER, J. M., LURIE, M., BUTLER, J. K., PALFREY, S. L., AMANTEA, R., CARR, L. A., HAWRYLO, F. Z., JAMES, E. A., KAISER, C. J., KIRK, J. B. AND REICHERT, W. F. (1989). "Two-dimensional coherent laser arrays using grating surface emission," *IEEE J. Quantum Electron.* **25**, 6, 1525-1538.

EVANS, G. A., CARLSON, N. W., BOUR, D. B., HAMMER, J. M., LURIE, M., BUTLER, J. K., LIEW, S. K., KIRK, J. B. AND REICHERT, W. F. (1990a). "Two-dimensional grating surface emitting laser arrays with wide lateral extent," *Electron. Lett.* **26**, 13, 907-908.

EVANS, G. A., CARLSON, N. W., BOUR, D. P., AMANTEA, R., BUTLER, J. K., LURIE, M., HAMMER, J. M., LIEW, S. K., DEFREEZ, R. K., XIMEN, H., BOSSERT, D. J., ELLIOT, R. A. AND HUNT, J. M. (1990b). "An experimental study of the operation of a coherent two-dimensional grating-surface-emitting ring laser array," *Conference on Lasers and Electro-Optics*, Technical Digest, p. 430, paper CThJ3.

EVANS, G. A., BOUR, D. P., CARLSON, N. W., AMANTEA, R., HAMMER, J. M., LEE, H., FARKAS, R., KIRK, J. B., LIEW, S. K., REICHERT, W. F., LAI, R., PELKA, P., WANG, C. A., CHOI, H. K., WALPOLE, J. N., BUTLER, J. K. AND FERGUSON, W. E. (1991). "Characteristics of coherent two-dimensional grating surface emitting diode laser arrays during cw operation," *IEEE J. Quantum Electron.* **27** 6, 1594-1608.

FELISKY, M., DEFREEZ, R. K., WILSON, G. A., EVANS, G. A., CARLSON, N. W., LIEW, S. K., AMANTEA, R., ABELES, J., WANG, C. A., CHOI, H. K., WALPOLE, J. N. AND WINFUL, H. G. (1991). "Dynamics of cw grating-surface-emitting laser arrays," *Technical Digest, CLEO*, Baltimore, MD, Paper CWE6.

FIRESTER, A. H., FOX, E. C., GAYESKI, T., HANNAN, W. J. AND LURIE, M. (1972). "Redundant holograms," *RCA Review*, **33**, 1, 131-153.

HADJICOSTAS, G., BUTLER, J. K., EVANS, G. A., CARLSON, N. W. AND AMANTEA, R. (1990). "A numerical investigation of wave interactions in dielectric waveguides with periodic surface corrugations," *IEEE J. Quantum Electron.* **26**, 5, 893-902.

HAMMER, J. M., NEIL, C. C., CARLSON, N. W., DUFFY, M. T. AND SHAW, J. M. (1985). "Single-wavelength operation of the hybrid-external Bragg-reflector-waveguide laser under dynamic conditions," *Appl. Phys. Lett.* **47**, 3, 183-185.

HAMMER, J. M., CARLSON, N. W., EVANS, G. A., LURIE, M., PALFREY, S. L.,

KAISER, C. J., HARVEY, M. G., JAMES, E. A., KIRK, J. B. AND ELIA, F. R. (1987). "Phase-locked operation of coupled pairs of grating-surface-emitting diode laser," *Appl. Phys. Lett.* **50**, 11, 659-661.

HAMMER, J. M., EVANS, G. A., CARLSON, N. W., BOUR, D. P., LURIE, M., PALFREY, S. L., AMANTEA, R., LIEW, S. K., CARR, L. A., JAMES, E. A., KIRK, J. B. AND REICHERT, W. F. (1990). "Lateral beam-steering in mutual injection coupled Y-branch grating-surface-emitting diode-laser arrays," *Appl. Phys. Lett.* **56**, 3, 224-226.

HANDA, K., PENG, S. P. AND TAMIR, T. (1975). "Improved perturbation analysis of dielectric gratings," *Appl. Phys.* **5**, 325-328.

HEFLINGER, D., KIRK, J., CORDERO, R. AND EVANS, G. (1981). "Submicron grating fabrication on GaAs," *SPIE Proceedings*, **269**, 49-54.

HOHIMER, J. P., OWYOUNG, A. AND HADLEY, G. R. (1985). "Single-channel injection locking of a diode-laser array with a cw dye laser," *Appl. Phys. Lett.* 47, 12, 1244-1246.

KAN, Y., HONDA, Y., SUEMUNE, I. AND YAMANISHI, M. (1986). "Electronic beam deflection in a semiconductor laser diode using grating output coupler," *Electron. Lett.* **22**, 24, 1310-1311.

KATZ, J., KAPON, E., LINDSEY, C., MARGALIT, S. AND YARIV, A., (1983). "Far-field distributions of semiconductor phase-locked arrays with multiple contacts," *Electron. Lett.* **19**, 17, 660-662.

KATZIR, A., LIVANOS, A. C., SHELLAN, J. B. AND YARIV, A. (1977). "Chirped gratings in integrated optics," *IEEE J. Quantum Electron.* **QE-13**, 4, 296-304.

KOBAYASHI, K. AND I. MITO, (1988). "Single frequency and tunable laser diodes," *J. Lightwave Technol.* **6**, 11, 1623-1633.

KOBAYASHI, S., YAMAMOTO, Y., ITO, M. AND KIMURA, T. (1982). "Direct frequency modulation in AlGaAs semiconductor lasers," *IEEE J. Quantum Electron.* **18**, 4, 582.

KOCH, T. L., KOREN, U. AND MILLER, B. I. (1988). "High performance tunable 1.5 μm InGaAs/InGaAsP multiple quantum-well distributed Bragg reflector lasers," *Appl. Phys. Lett.* **53**, 1036-1038.

KOGELNICK, H. AND SHANK, C. V. (1972). "Coupled-wave theory of distributed feedback lasers," *J. Appl. Phys.* **43**, 5, 2237-2335.

KOJIMA, K., NODA, S., MITSUNAGA, K., KYUMA, K. AND HAMANAKA, K. (1987). "Continuous wave operation of a surface-emitting AlGaAs/GaAs multi-quantum-well distributed Bragg reflector laser," *Appl. Phys. Lett.* **50**, 24, 1705-1710.

KOSONACKY, W. F., CORNELY, R. H. AND HEGYI, I. J. (1968). "Multiple GaAs injection laser," *IEEE J. Quantum Electron.* **QE-4**, 4, 176-179.

KOTAKI, Y. AND ISHIKAWA, H. (1989). "Spectral characteristics of a three-section wavelength tunable DBR laser," *IEEE J. Quantum Electron.* **25**, 6, 1340-1345.

KOTAKI, Y., MATSUDA, M., ISHIKAWA, H. AND IMAI, H. (1988). "Tunable DBR laser with wide tuning range," *Electron Lett.* **24**, 8, 503-505.

KREBS, D., HERRICK, R., NO, K., HARTING, W., STRUEMPH, F., DRIEMEYER,

D. AND LEVY, J. (1991). "22 W coherent GaAlAs amplifier array with 400 emitters," *IEEE Photon. Technol. Lett.* **3**, 4, 292–295.

KRESSEL, H. AND BUTLER, J. K. (1977). *Semiconductor Lasers and Heterojunction LEDs*, Academic Press, New York.

LANG, R. J. AND YARIV, A. (1985). "Analysis of the dynamic response of multi-element semiconductor lasers," *IEEE J. Quantum Electron.* **QE-21**, 10, 1683–1688.

LEGER, J. R., SCOTT, M. L. AND VELDKAMP, W. B. (1988). "Coherent addition of AlGaAs lasers using microlenses and diffractive coupling," *Appl. Phys. Lett.* **52**, 21, 1771–1773.

LIEW, S. K., CARLSON, N. W., AMANTEA, R., BOUR, D. P., EVANS, G. A. AND VANGIESON, E. (1990). "Operation of distributed-feedback grating surface emitting laser with a buried grating structure," *LEOS '90 Conference Proceedings*, Boston MA, 410–411.

LIEW, S. K., EVANS, G. A., CARLSON, N. W., AMANTEA, R., BOUR, D. P., BUTLER, J. K., HAMMER, J. M., KIRK, J. B., REICHERT, W. F., STOLZENBERGER, R., WANG, C. A., CHOI, H. K. AND WALPOLE, J. N. (1991a). "Coherent, cw operation of one- and two-dimensional grating surface emitting semiconductor lasers," *CLEO* May 1991.

LIEW, S. K., CARLSON, N. W., EVANS, G. A., AMANTEA, R., BOUR, D. P., HAMMER, J. M., KIRK, J. B., REICHERT, W. F. AND STOLZENBERGER, R. (1991b). "Coherent continuous wave operation of $10 \times 10 \times 2$ grating surface emitting diode laser array in a ring configuration," *J. Appl. Phys.* **70**, 12, 7645–7647.

LINDSEY, C. P., MEHUYS, D. AND YARIV, A. (1987). "Linear tailored gain broad area semiconductor lasers," *IEEE J. Quantum Electron.* **QE-23**, 6, 775–787.

MACOMBER, S. H., MOTT, J. S., NOLL, R. J., GALLATIN, G. M., GRATRIX, E. J., O'DWYER, S. L. AND LAMBERT, S. A. (1987). "Surface-emitting distributed feedback semiconductor laser," *Appl. Phys. Lett.* **51**, 7, 472–474.

MARCUSE, D. (1983). "Computer model of an injection laser amplifier," *IEEE J. Quantum Electron.* **QE-19**, 1, 63–73.

MEHUYS, D., WELCH, D. F., PARKE, R., WAARTS, R. G., HARDY, A. AND SCIFRES, D. (1991a). "High power, diffraction-limited emission from monolithically integrated active grating master oscillator power amplifier," *Electron. Lett.* **27**, 6, 492–494.

MEHUYS, D., PARKE, R., WAARTS, R. G., WELCH, D. F., HARDY, A., STREIFER, W. AND SCIFRES, D. (1991b). "Characteristics of multistage monolithically integrated master oscillator power amplifiers," *IEEE J. Quantum Electron.* **27**, 6, 1574–1581.

MEHUYS, D., WELCH, D. F., WAARTS, R. G., PARKE, R., HARDY, A. AND STREIFER, W. (1991c). "Analysis of monolithic integrated master oscillator power amplifiers," *IEEE J. Quantum Electron.* **27**, 7, 1900–1909.

MILLER, D. A. B., CHEMLA, D. S., EILENBERGER, D. J., SMITH, P. W., GOSSARD, A. C. AND TSANG, W. T. (1982). "Large room temperature optical nonlinearity in GaAs/$Ga_{1-x}Al_xAs$ multiple quantum well structures," *Appl. Phys. Lett.* **41**, 8, 679.

MITTELSTEIN, M., MEHUYS, D. AND YARIV, A. (1989). "Broadband tunability of gain-flattened quantum well semiconductor lasers with an external grating," *Appl. Phys. Lett.* **54**, 12, 1092–1094.

MOTT, J. S. AND MACOMBER, S. H. (1989). "Two-dimensional surface emitting distributed feedback laser arrays," *IEEE Photon. Technol. Lett.* **1**, 8, 202–204.

NG, W. AND YARIV, A. (1977). "Highly collimated broadside emission from room-temperature GaAs distributed Bragg reflector lasers," *Appl. Phys. Lett.* **31**, 9, 613–615.

OHATA, T., HONDA, K., HIRATA, S., TAMAMURA, K., ISHIKAWA, H., MIYAHARA, K., MORI, Y. AND KOJIMA, C. (1986). "AlGaAs/GaAs distributed feedback laser diodes grown by MOCVD," *J. Cryst. Growth* **77**, 637–642.

PALFREY, S., HAMMER, J. M., LONGEWAY, P. A., CARLSON, N. W., EVANS, G. A., ANDREWS, J. T., JAKLIK, J., KIRK, J. B., STOLZENBERGER, R. AND TRIANO, A. R. (1989). "Phase-locked operation of a 3-element InGaAsP/InP grating-surface-emitting diode laser array," *Appl. Phys. Lett.* **54**, 14, 1296.

PALFREY, S., ENSTROM, R., VANGIESON, E., HAMMER, J. M., MARTINELLI, R. U., ANDREWS, J. T., APPERT, J., STOLZENBERGER, R., TRIANO, A., CARLSON, N. W. AND EVANS, G. A. (1990). "Coherent mutually-injection-coupled linear and two-dimensional arrays of InGaAs/InGaAsP/InP multi-quantum-well grating-surface-emitting diode lasers operating at 1.5 μm," *Appl. Phys. Lett.* **57**, 26, 2753–2755.

PARKE, R., WAARTS, R., WELCH, D. F., HARDY, A. AND STREIFER, W. (1990a). "High efficiency, high uniformity, grating coupled surface emitting lasers," *Electron. Lett.* **26**, 2, 125.

PARKE, R., WELCH, D. F., MEHUYS, D., WAARTS, R., CRAIG, R. AND SCIFRES, D. (1990b). "Electronically steerable monolithically integrated master oscillator power amplifier," *Electron. Lett.* **26**, 14, 1076–1077.

PARKE, R., WELCH, D. F. AND MEHUYS, D. (1991). "Coherent operation of 2-D monolithically integrated master oscillator power amplifier," *Electron. Lett.* **27**, 23, 2097–2098.

REINHART, F. K., LOGAN, R. A. AND SHANK, C. V. (1975). "GaAs-$Al_xGa_{1-x}As$ injection lasers with distributed feedback reflectors," *Appl. Phys. Lett.* **27**, 1, 45–48.

SALZMAN, J., VENKATESAN, T., LANG, R., MITTELSTEIN, M. AND YARIV, A. (1985). "Unstable resonator cavity semiconductor lasers," *Appl. Phys. Lett.* **46**, 3, 218–220.

SCOTT, J. W. AND COLDREN, L. A. (1991) "Optimization of vertical-cavity surface emitting lasers: limitations of output power," *LEOS '91 Conference Digest*, November, Paper SDL4.4.

SIEGMAN, A. E. (1986). *Lasers*, Sec. 7.7, University Science Books, Mill Valley, CA, 1986.

STOLL, H. M. (1978a). "High brightness lasers using integrated optics," *SPIE* **139**, 113.

STOLL, H. M. (1978b). "Distributed Bragg Deflector: A multifunction integrated optical device," *Applied Optics*, **17**, 16, 2562–2569.

STREIFER, W., WELCH, D. F., CROSS, P. S. AND SCIFRES, D. (1987). "Y-junction semiconductor laser arrays: Part I—Theory," *IEEE J. Quantum Electron.* **QE-23**, 6, 744–751.

SUZUKI, A. AND TADA, K. (1980). "Fabrication of chirped gratings on GaAs optical waveguides," *Thin Solid Films* **72**, 419–426.

TAKEMOTO, A., OHKURA, Y., KAWAMA, Y., NAKAJIMA, Y., KIMURA, T., YOSHIDA, N., KAKIMOTO, S. AND SUSAKI, W. (1989). "1.3 μm distributed feedback laser diode with a grating accurately controlled by a new fabrication technique," *IEEE J. Lightwave Tech.* **7**, 12, 2072.

TAMIR, T. (1981). "Microwave modeling of optical periodic gratings," *IEEE Trans. MTT*, **MTT-29**, 979–983.

TARUCHA, S., HORIKOSHI, Y. AND OKAMOTO, H. (1983). "Optical absorption characteristics of GaAs-AlGaAs multi-quantum-well heterostructure waveguides," *Jpn. J. Appl. Phys.* **22**, L482.

THOMPSON, G. H. B. (1980). *Physics of Semiconductor Laser Devices*, John Wiley and Sons, New York.

THORNTON, R. L., MOSBY, W. J. AND CHUNG, H. F. (1989). "Demonstration and properties of a planar heterojunction bipolar transistor with lateral current flow," *IEEE Trans. Electron Devices* **36**, 10, 2156–2164.

THORNTON, R. L., MOSBY, W. J., DONALDSON, R. M. AMD PAOLI, T. M. (1990). "Properties of closely spaced independently addressable lasers fabricated by impurity-induced disordering," *Appl. Phys. Lett.* **56**, 1623–1625.

TIBERIO, R. C., PORKOLAB, G. A., ROOKS, M. J., WOLF, E. D., LANG, R. J., LARSSON, A., FOROUHAR, S., CODY, J., WICKS, G. W., ERDOGAN, T., KING, O. AND HALL, D. G. (1991). "Facetless Bragg reflector surface-emitting AlGaAs/GaAs lasers fabricated by electron-beam lithography and chemically assisted ion-beam etching," *J. Vac. Sci. Technol. B* **9**, 6, 2842–2845.

TILTON, M. L., DENTE, G. C., PAXTON, A. H., CSER, J., DEFREEZE, R. K., MOELLER, C. E. AND DEPATIE, D. (1991). "High power, nearly diffraction-limited output from a semiconductor laser with an unstable resonator," *IEEE J. Quantum Electron.* **27**, 2098–2108.

TOHMORI, Y., SUEMATSU, Y., TOSHIMA, H. AND ARAI, S. (1983). "Wavelength tuning of GaInAsP/InP laser with butt-jointed built-in distributed Bragg reflector," *Electron. Lett.* **19**, 17, 656–657.

VANGIESON, E. A., PALFREY, S. L., ENSTROM, R., HAMMER, J. M., MARTINELLI, R. U., CARLSON, N. W., EVANS, G. A., ANDREWS, J. T., APERT, J., STOLZENBERGER, R. AND TRIANO, A. (1991). "Coherent high power arrays of InGaAs/InGaAsP multi-quantum-well grating-surface-emitting diode lasers operating at $\lambda = 1.5$ μm," *Appl. Phys. Lett.* **59**, 22, 2790–2792.

WAARTS, R., WELCH, D. F., PARKE, R., HARDY, A. AND STREIFER, W. (1990). "Coherent linear arrays of grating coupled surface emitting lasers," *Electron. Lett.* **26**, 129.

WANG, C. A., CHOI, H. K. AND CONNORS, M. K. (1989). "Large-area uniform OMVPE growth for GaAs/AlGaAs quantum-well diode lasers with controlled emission wavelength," *J. Electron. Mater.* **18**, 695–701.

WANG, C. A. AND CHOI, H. K. (1991). "Organometallic vapor phase epitaxy of high-performance strained-layer InGaAs/AlGaAs diode lasers," *IEEE J. Quantum Electron.* **27**, 3, 681–686.

WELCH, D. F., STREIFER, W., CROSS, P. S. AND SCIFRES, D. R. (1987). "Y-junction semiconductor laser arrays: Part II—Experiment," *IEEE Quantum Electron.* **QE-23**, 6, 752–756.

WELCH, D. F., PARKE, R., HARDY, A., WAARTS, R., STREIFER, W. AND SCIFRES, D. R. (1989). "High power, 4 W pulsed, grating-coupled surface-emitting laser," *Electron. Lett.* **25**, 1038.

WELCH, D. F., MEHUYS, D., PARKE, R., WAARTS, R., SCIFRES, D. AND STREIFER, W. (1990). "Coherent operation of monolithically integrated master oscillator amplifiers," *Electron. Lett.* **26**, 17, 1327–1329.

WELLER-BROPHY, L. A. AND HALL, D. G. (1985). "Analysis of waveguide gratings: application of Rouard's method," *J. Opt. Soc. Am. A*, **2**, 863–971.

WILCOX, J. Z., SIMMONS, W. W., BOTEZ, D., JANSEN, M., MAWST, L. J., PETERSEN, G., WILCOX, T. J. AND YANG, J. J. (1989). "Design considerations for diffraction coupled arrays with monolithically integrated self-imaging cavities," *Appl. Phys. Lett.* **54**, 19, 1848–1850.

WILSON, G. A., DEFREEZ, R. K. AND WINFUL, H. G. (1991). "Modulation of phased-array semiconductor lasers at K-band frequencies," *IEEE J. Quantum Electron.* **27**, 6, 1696–1704.

YABLONOVITCH, E., GMITTER, T., HARBISON, J. P. AND BHAT, R. (1987). "Extreme selectivity in the lift off of epitaxial GaAs films," *Appl. Phys. Lett.* **51**, 26, 2222–2224.

YARIV, A. (1973). "Coupled-mode theory for guided-wave optics," *IEEE J. Quantum Electron.* **QE-9**, 919–933.

ZORY, P. AND COMERFORD, L. D. (1975). "Grating-coupled double-heterostructure AlGaAs diode lasers," *IEEE J. Quantum Electron.* **QE-11**, 7, 451–457.

ZOU, W. X., LAW, K.-K., GOSSARD, A. C., HU, E. L., COLDREN, L. A. AND MERZ, J. L. (1990). "Low-threshold high-efficiency high-yield impurity-induced layer disordering laser by self-aligned Si–Zn diffusion," *Appl. Phys. Lett.* **57**, 24, 2534–2536.

Chapter 5

HORIZONTAL-CAVITY SURFACE EMITTING LASERS WITH INTEGRATED BEAM DEFLECTORS

R. C. Williamson, J. P. Donnelly, Z. L. Liau, W. D. Goodhue and J. N. Walpole

Lincoln Laboratory, Massachusetts Institute of Technology, Lexington, Massachusetts

I. INTRODUCTION

The performance of horizontal-cavity surface emitting lasers is firmly based upon the characteristics of conventional cleaved-facet edge emitting lasers. Two approaches have been demonstrated to convert this conventional edge emitting structure into a surface emitting laser. Approaches that have been used include gratings and integrated beam deflectors. In the latter approach, an angled (usually 45°) mirror is placed either internal (intracavity deflector) or external (extracavity deflector) to the laser cavity, as shown schematically in Fig. 1. For both types of deflectors, the end facets of the laser cavity are formed by some process other than cleaving. The common advantage of grating and beam deflector designs over vertical-cavity designs is that low series resistance and high power-conversion efficiency, which are difficult to achieve with vertical-cavity lasers, can be obtained by standard techniques. Use of beam deflectors instead of gratings allows for somewhat denser packing of active gain media in two-dimensional arrays. Moreover, cavity reflectivity and output coupling can be independently designed, resulting in arrays with efficiency and output performance approaching that of cleaved-facet lasers.

ISBN 0-12-244070-6

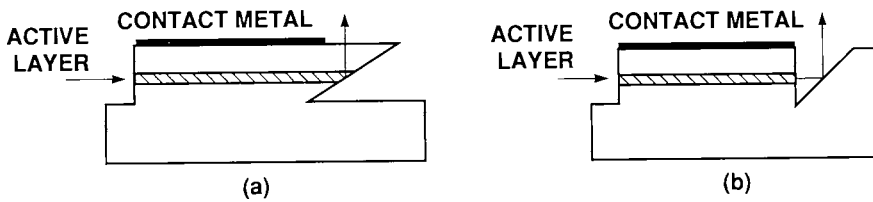

Fig. 1. Basic design of horizontal-cavity surface emitting laser with (a) intracavity and (b) extracavity integrated beam deflector.

An immediate application of two-dimensional arrays of horizontal-cavity surface emitting lasers is the pumping of solid state lasers such as Nd:YAG. Monolithic arrays for this purpose should ultimately have economic advantages over hybrid approaches in which many individual lasers or bars of lasers are mounted together to achieve a two-dimensional array. In addition, horizontal-cavity surface emitting lasers have a favorable geometry for removing heat and can thus sustain higher average powers than stacked edge emitting lasers. Arrays of individually addressable high-efficiency low-power lasers would be useful for optical-interconnection applications. As the performance and uniformity of these arrays are improved, they can be combined with lenslet arrays in external cavities for high-power operation as coherent arrays (see Chapter 8).

Both intracavity and extracavity beam deflector lasers present technological challenges in the fabrication of the facets and deflectors. Devices made in AlGaAs/GaAs, including strained-layer quantum-well structures, require different fabrication processes from devices made in GaInAsP/InP. The fabrication technique must yield sufficiently smooth and accurately controlled shapes that high optical quality can be obtained. For good device performance the rms deviations from the ideal surface typically must be on the order of $\lambda/20$ or smaller, where λ is the optical wavelength.

Intracavity deflector lasers must be designed such that losses that occur as the beam propagates perpendicular to the substrate are minimized. Contact metal must be removed over the emission region, and low doping is preferred in order to minimize absorption, a requirement that conflicts with the high doping normally desired to reduce contact and series resistance. A fundamental problem is the conversion from a guided wave in the active region to a diffracting wave in the top or bottom layer and then reconversion back to a guided wave, because the mismatch of the optical fields introduces additional loss. A design constraint for extracavity deflector lasers involves the efficiency with which the mirror intercepts and deflects a highly divergent semiconductor laser beam, which is typically greater than 30° full width at half-maximum (FWHM).

The feasibility of intracavity deflector lasers was demonstrated in AlGaAs/GaAs by SpringThorpe (1977). His initial device achieved only modest performance with external differential quantum efficiencies (DQE) of 4-6%. This approach languished until 1989, after which several laboratories initiated work on intracavity deflector lasers and laser arrays (Hamao *et al.*, 1989; Takamori *et al.*, 1989; Donnelly *et al.*, 1989, Ou *et al.*, 1991a; Liau and Walpole, 1990; and Stegmüller, 1991).

Meanwhile, the first extracavity deflector lasers were reported by Liau and Walpole (1985) in the GaInAsP/InP system. These devices demonstrated the first use of a parabolic-shaped beam deflector to achieve nearly diffraction-limited collimation of the deflected beam. The first room-temperature two-dimensional arrays of surface emitting lasers were realized in GaInAs/InP (Walpole and Liau, 1986). Subsequently, several other workers fabricated these devices in the AlGaAs/GaAs systems (Windhorn and Goodhue, 1986; Yang *et al.*, 1986a; Puretz *et al.*, 1987; and Shieh *et al.*, 1988) and GaInAsP/InP systems (Saito and Noguchi, 1989; Harriott *et al.*, 1986; and Mutoh *et al.*, 1991). In the AlGaAs/GaAs system, an approach by Donnelly *et al.* (1988a) has been demonstrated in which a linear array bar of edge emitting lasers is mounted onto a Si carrier that has been etched chemically to form extracavity beam deflectors. The result is a hybrid two-dimensional array of surface emitting lasers.

In Section II, the beam deflector lasers and arrays fabricated in AlGaAs/GaAs are reviewed. The topics covered are fabrication technologies used with these materials, work to date on extracavity and intracavity deflector devices, and hybrid arrays. Section III deals with GaInAsP/InP beam deflector lasers and arrays, with a discussion of the mass transport fabrication technology, extracavity deflector devices, and devices with intracavity deflectors and integrated microlenses (Liau *et al.*, 1990; Stegmüller *et al.*, 1991). Also discussed is the technique for monolithic integration of a microlens on the substrate side of a wafer to solve the mode matching problem inherent in folded-cavity designs and to provide collimation of the output beam. Finally, in Section IV, the results for the different types of devices are discussed and compared.

II. AlGaAs/GaAs MATERIAL SYSTEM

A. Fabrication Techniques

The techniques used to fabricate laser facets and deflectors in the AlGaAs/GaAs material system include wet chemical etching

(SpringThorpe, 1977; and Yih and Lee, 1990), ion-beam-assisted etching (IBAE) (Windhorn and Goodhue, 1986), modified IBAE (Tihanyi *et al.*, 1987), reactive ion etching (RIE) (Saito and Noguchi, 1989), ion milling (Yang *et al.*, 1986a; and Shieh *et al.*, 1988), and focused-ion-beam (FIB) milling (Puretz *et al.*, 1987; and Harriott *et al.*, 1986). The last technique has the potential to produce very high optical quality facets and deflectors but has two disadvantages. First, FIB milling requires high energy ions, which can introduce damage and cause reliability problems, and second, the process is very time consuming and may not be practical for production of large-scale arrays. Wet chemical etching is difficult to control since it tends to undercut the mask and to be selective with respect to material composition and crystallographic orientation. The mass transport technique, described later, which is employed for fabrication of facets and deflectors in the GaInAsP/InP material system, is not easily adaptable to the AlGaAs/GaAs system because of the reactivity of the Al constituent. Mass transport has been demonstrated in the GaInAsP/GaAs material system (Groves *et al.*, 1990), however, which has emission wavelengths in the same range as AlGaAs/GaAs lasers, making this an attractive candidate for future work in surface emitting diode lasers in the short-wavelength (less than $\sim$1.0 μm) range.

The IBAE dry etching technique has been used to fabricate several different types of monolithic two-dimensional surface emitting AlGaAs/GaAs diode lasers and arrays. In IBAE, which has been described by Geis *et al.* (1981), the chemical reactant species and the energetic ions can be independently controlled. A schematic illustration of an IBAE system with a load lock, a tiltable sample holder, and a cryopump is shown in Fig. 2. In this system, which routinely reaches a background pressure of 10^{-7} Torr at 15 minutes after sample loading, a chemical reactant species from a local jet and a separately controlled collimated ion beam from an ion source impinge simultaneously upon a sample. Both AlGaAs and GaAs can be etched at room temperature with Cl_2 as the reactant gas and argon as the ion source. Neither is spontaneously etched by Cl_2 at room temperature, so the IBAE is highly directional, with the sidewall slope of a masked etch trench determined essentially by the direction of the argon-ion beam. Therefore, almost any concave slope can be generated with a computer-controlled sample stage that precisely varies the tilt angle between the sample and the ion beam during etching (Goodhue *et al.*, 1990). With appropriate parameters, AlGaAs and GaAs can be etched at essentially the same rate, and no roughness or steps are observed at AlGaAs/GaAs heterointerfaces. Materials such as photoresist, phosphosilicate glass, SiO_2, Ni, and Ti, which have slow etch rates compared to AlGaAs and GaAs, can be used as etch masks.

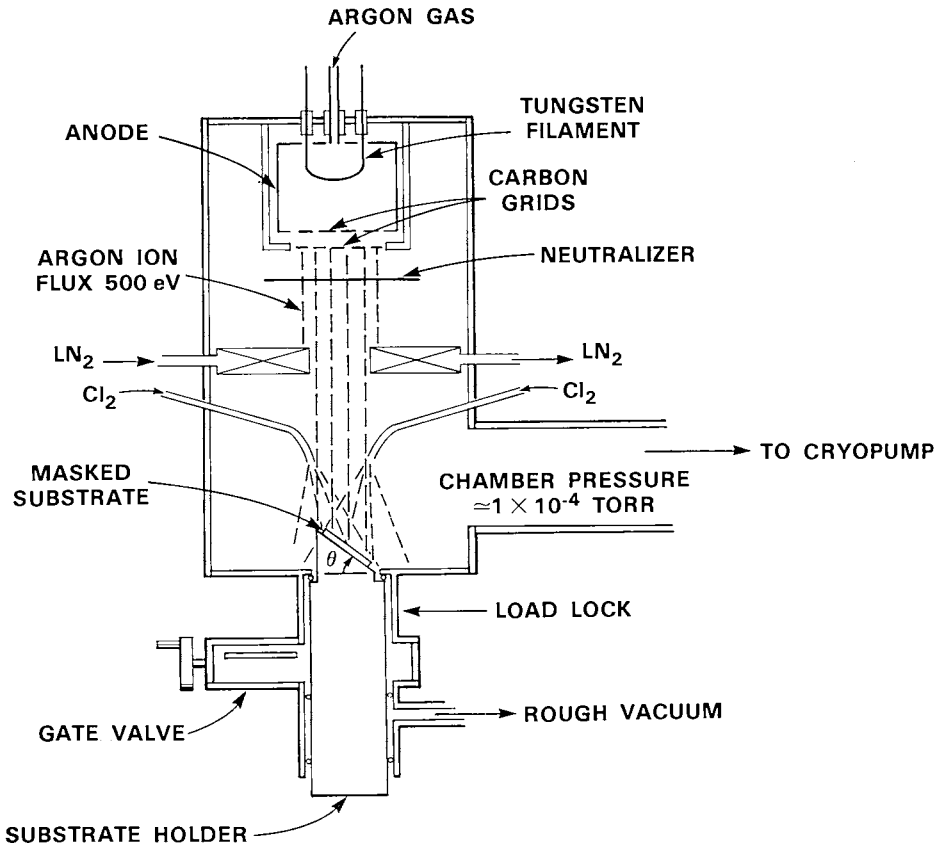

Fig. 2. Schematic illustration of ion-beam-assisted etching apparatus.

As mentioned previously, other dry-etching techniques such as ion milling and RIE for fabricating the facets and deflectors in the AlGaAs/GaAs material system are also being used. However, while ion milling can be highly directional, the facet quality obtained is generally not as good as with IBAE since there is no chemical reaction to carry away etched material in the vapor phase. With RIE, on the other hand, chemical reactions do produce volatile products to remove the etched material and high-quality facets can be obtained, but the directionality is not as good as with IBAE, especially for angled cuts over large areas.

B. Intracavity Deflector Devices

Although surface emitting lasers with intracavity 45° deflecting mirrors were first reported in the AlGaAs/GaAs material system in 1977 (SpringThorpe, 1977), (Fig. 4), only in the last few years has significant progress been made

in increasing the performance of these lasers to acceptable levels. The various generic designs for the lasers include devices that emit light through the top surface of the wafer, through to the back surface of the wafer, and through both top and back surfaces. The three basic cavity configurations from which the various designs have evolved are shown in Fig. 3. The configurations are depicted for a top-surface emitting laser but could be as easily represented for lasers emitting from the back surface or from both surfaces.

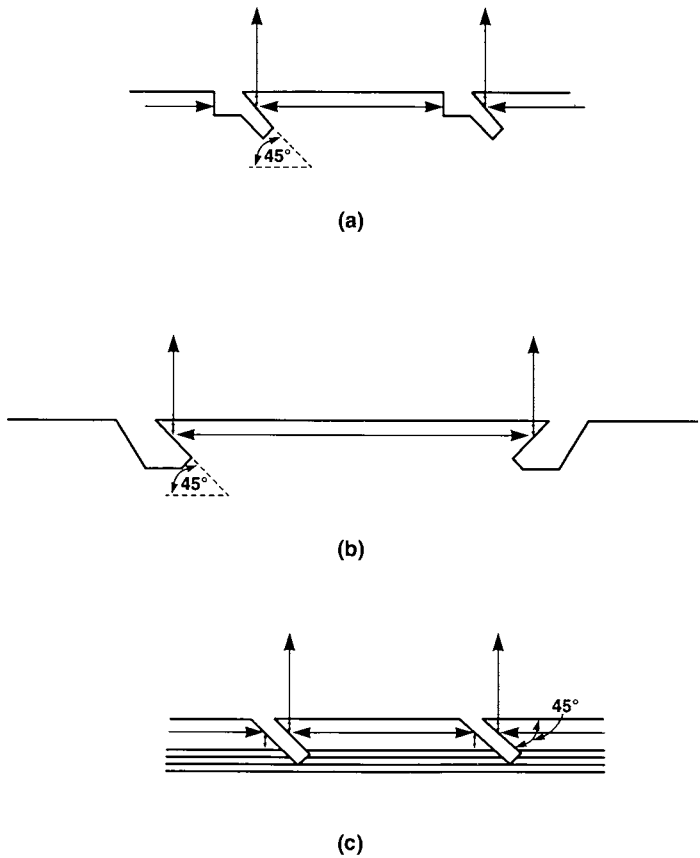

Fig. 3. Schematic diagrams of cavity configurations that have been used in the successful fabrication of lasers with intracavity deflecting mirrors: (a) a folded cavity formed by one vertical etched facet, an etched 45° intracavity mirror, and a top-surface facet; (b) a folded cavity formed by two etched 45° intracavity mirrors and two top-surface facets; (c) a folded cavity formed by a dielectric mirror stack, two etched 45° intracavity mirrors, and a top-surface facet. (Goodhue *et al.*, 1990.)

The first configuration (Fig. 3(a)) employs a folded cavity consisting of a vertical etched facet, a surface etched at 45° forming an intracavity mirror, and a top facet that couples the laser radiation out of the surface of the wafer. SpringThorpe's original laser (1977), shown in Fig. 4, was a back-surface emitting laser of this type in which the 45° folding mirror was formed with wet etching and the vertical facet was formed with cleaving. Ou *et al.* (1991) have demonstrated a similar device with external differential quantum efficiency of 52%, where the vertical facet and 45° mirror are fabricated by RIE and ion-beam milling, respectively. Top-surface emitting lasers in this configuration have been demonstrated by Hamao *et al.* (1989) and Takamori *et al.* (1989, 1990), and monolithic two-dimensional arrays have been reported by Donnelly *et al.* (1989); Goodhue *et al.* (1990). Two-dimensional back-surface emitting arrays have been demonstrated by Jansen *et al.* (1991).

The second configuration (Fig. 3(b)) employs a folded cavity consisting of two surfaces etched at 45° forming two intracavity mirrors and two surface facets that couple the radiation out of the wafer. High-output-power monolithic top-surface emitting two-dimensional arrays in this configuration that emit at 0.815 and 1.03 μm have been reported by Goodhue *et al.* (1991). These devices, which have achieved greater than 50% DQE, are discussed in the following paragraphs.

The third configuration (Fig. 3(c)) employs a folded cavity consisting of an internal dielectric mirror stack, two 45° intracavity mirrors formed in one etch step and one top-surface facet. This design was first demonstrated in a monolithic two-dimensional surface emitting array by Goodhue *et al.* (1990). Recently, Chao *et al.* (1991c) have demonstrated individual ridge waveguide lasers of this type with cw threshold current as low as 10 mA and external DQE of 12%.

Combinations of these configurations are also possible. For example, as illustrated in Fig. 5, a partially reflecting dielectric mirror stack can be used in conjunction with a strained-layer InGaAs quantum well (which yields emission at wavelengths larger than the energy gap of GaAs) to fabricate a back-surface emitting device that does not require the removal of the GaAs substrate under the deflecting mirror (Ou *et al.*, 1991c).

The performance of intracavity deflector devices is critically dependent on the quality and placement of the folding mirrors, dielectric mirror stacks, and etched facets as well as on the heat sinking and bonding. Diffraction losses in the folded-cavity portion of the laser, which must be minimized for efficient operation, depend on both the distance between the 45° mirror and facet and the width of the horizontal-cavity waveguide mode. These

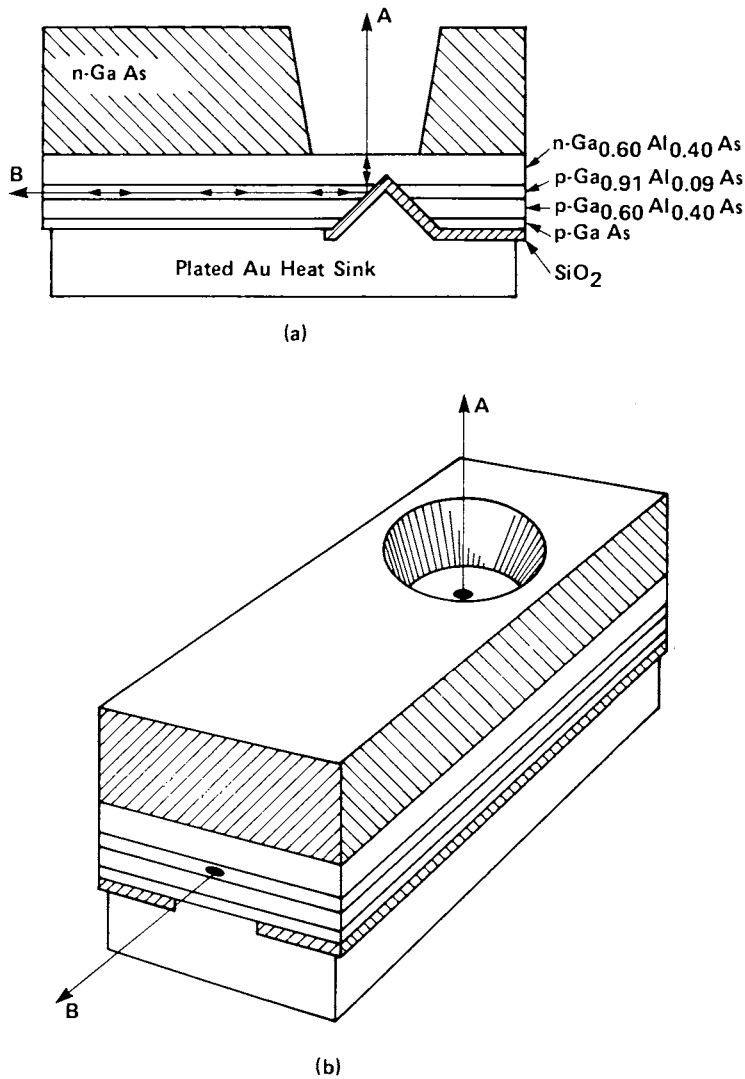

Fig. 4. (a) Cross-sectional and (b) schematic diagrams of the intracavity deflector laser reported by SpringThorpe (1977), showing perpendicular (A) and parallel (B) outputs.

parameters are interactive and cannot be arbitrarily varied, since they also affect the confinement factor and internal loss of the horizontal cavity. For the best results obtained to date, the distance from the active quantum well to the top-surface facet, which sets the distance from the folding mirror to the facet, is about 1.2 to 1.4 μm. The deviation from 45° in the angle of the

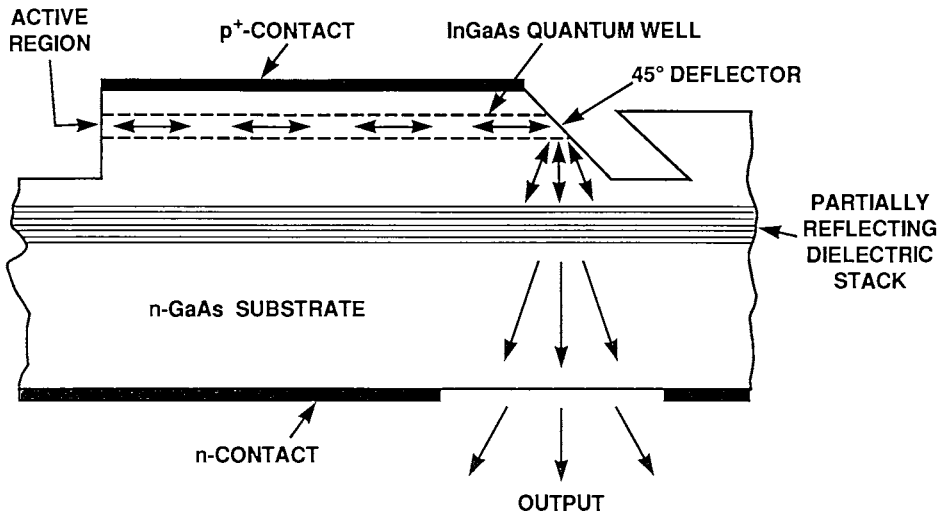

Fig. 5. Schematic illustration of a back-surface emitting diode laser with an internal 45° deflecting mirror and a partially reflecting dielectric mirror stack. The active layer is an InGaAs quantum well. (After Ou *et al.*, 1991c.)

folding mirror must be less than ±2°, and the facet (the top surface) must be parallel to the horizontal cavity to provide good overlap between the reflected wave and the horizontal-cavity waveguide mode. In addition, the smoothness of the facets and mirrors must be maximized. Better-performing devices always have facets and mirrors with variations in surface morphology of less than 40 nm. The optimal characteristics of buried dielectric mirror stacks for folded cavity lasers are currently under investigation.

Monolithic two-dimensional arrays of folded-cavity top-surface emitting strained-layer InGaAs/AlGaAs and AlInGaAs/AlGaAs diode lasers with intracavity deflectors have recently been produced. These lasers, which are configured as shown in Fig. 3(b), are fabricated with a self-aligned process and IBAE. The arrays fabricated in these material systems emitted at 1.03 and 0.815 μm, respectively, and had low threshold current densities and differential quantum efficiencies greater than 50% (Goodhue *et al.*, 1991).

The InGaAs/AlGaAs wafers used for the 1.03-μm arrays contained a single 7 nm-thick $In_{0.25}Ga_{0.75}As$ quantum well symmetrically positioned in a graded-index (GRIN) optical cavity. The GRIN separate-confinement heterostructure (SCH) single-quantum-well (SQW) structure was grown by organometallic vapor phase epitaxy (OMVPE) on an n^+-GaAs substrate and is similar to strained-layer InGaAs/AlGaAs quantum-well structures

previously reported by Choi and Wang (1990). Pulsed broad-area cleaved-facet lasers fabricated from this material with a cavity length of 1000 μm had a threshold current density of 85 A/cm^2 and a differential quantum efficiency of 76%.

The OMVPE-grown AlInGaAs/AlGaAs wafers contained a single 10 nm-thick $Al_{0.18}In_{0.20}Ga_{0.62}As$ quantum well in an SCH structure. AlInGaAs was chosen over AlGaAs as the quantum-well material for 0.815-μm operation because preliminary investigations indicate that strained-layer AlInGaAs/AlGaAs diode lasers have lower threshold current densities and may be less susceptible to defects induced by handling and processing, making them more reliable than their AlGaAs quantum-well counterparts (Wang *et al.*, 1991a,b). Pulsed broad-area cleaved-facet lasers fabricated from this material with a cavity length of 1000 μm had threshold current density of 120 A/cm^2 and differential quantum efficiency of 72%.

The design of the monolithic two-dimensional surface emitting arrays is shown schematically in Fig. 6. Since total internal reflection occurs at the 45° cavity-folding mirror surfaces, high reflectivity coating of these surfaces is not required. Emission occurs through window regions in the top-surface facets at the ends of each laser element. For the AlInGaAs/AlGaAs arrays,

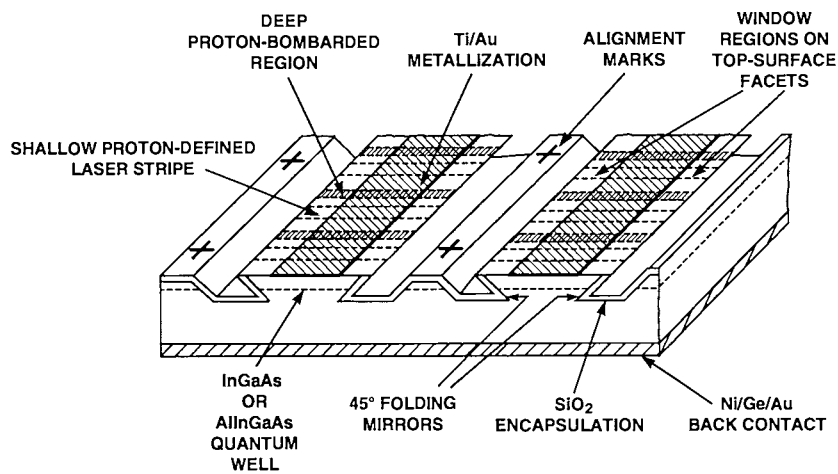

Fig. 6. Schematic illustration of a monolithic two-dimensional surface emitting array of strained-layer InGaAs/AlGaAs or AlInGaAs/AlGaAs diode lasers. Each individual laser utilizes a folded cavity consisting of two etched 45° intracavity mirrors and two top-surface facets.

which operate at a wavelength shorter than the band edge of GaAs, the p^+-GaAs contacting layer is selectively removed from the facet window regions.

The first step in the fabrication process is to deposit a high-quality 75 nm-thick Ni-etch mask on the surface of the wafer with open 5 μm-wide slots for forming the cavity-folding mirrors. The mask is formed by a simple photoresist liftoff technique utilizing a pattern-generator-produced chrome projection mask and a 4:1 projection aligner. Elecron-beam lithography is not used in any of the fabrication or photolithographic mask-making steps. The edges of the Ni mask are very straight, square, and smooth. Photoresist is used to cover one set of slots while the first set of 45° mirrors is formed by IBAE. The photoresist is then removed and reapplied over the etched slots to allow IBAE of the second set of 45° mirrors. The IBAE process used to form such sidewall geometries, has been reported in detail (Goodhue *et al.*, 1990). A scanning electron micrograph (SEM) of an etched 45° mirror is shown in Fig. 7. As seen, the combination of the Ni-etch mask and IBAE results in smooth high-quality 45° mirrors. The distance between the top edges of opposing folding mirrors, which is the effective cavity length, is 1000 μm.

After the 45° mirrors have been etched, the photoresist is removed and reapplied over the etched slots. The residual Ni mask is etched away using a wet-chemical technique. The photoresist is then removed, and the structure is encapsulated in plasma-deposited SiO_2. Encapsulation of the 45° mirrors is required to protect the exposed layers from chemical attack during the rest of the processing. A shallow proton-bombardment schedule (Foyt *et al.*, 1969; Dyment *et al.*, 1973) that penetrates to 0.2 μm above the top

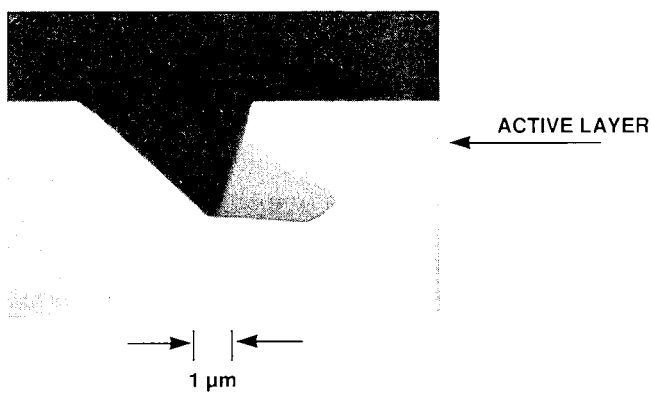

Fig. 7. SEM of an etched 45° mirror formed by IBAE.

AlGaAs confining layer is then used to confine the current in each row to 40 μm-wide laser stripes on 125 μm centers. A second proton-bombardment schedule at higher energies into 12 μm-wide stripes midway between the 40 μm-wide stripes introduces sufficient optical loss to suppress lasing in the transverse direction. The SiO_2 over the contact region on the top surface is opened with RIE, and Ti/Au *p*-type contacts are applied by an electron-beam evaporation and liftoff process. Since the SiO_2 deposition is designed only to protect the 45° mirrors and not to serve as an optimized top-surface facet coating, it is selectively removed from the window regions of these initial arrays. On AlInGaAs quantum-well arrays, the p^+-GaAs contacting layer is also selectively removed from the window regions. The wafer is thinned to approximately 100 μm, Ni/Ge/Au *n*-type contacts are applied to the back surface, and arrays of 16 to 48 laser elements are cleaved from the wafer.

The arrays have been evaluated in pulsed operation with 100 ns pulses and 1 kHz repetition rate. Figure 8 shows the near-field pattern taken at about twice threshold for a AlInGaAs/AlGaAs array consisting of two rows of 24 elements each, all bonded in parallel. The threshold current for this 48-element array is about 4.6 A, which corresponds to a threshold current

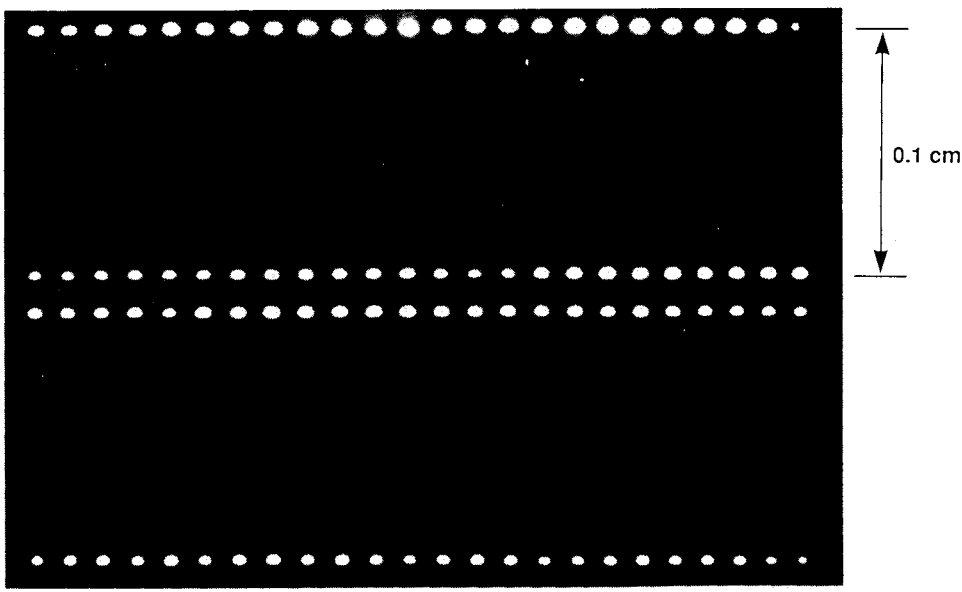

Fig. 8. Near-field pattern of a 48-element strained-layer AlInGaAs/AlGaAs array of folded-cavity lasers. The DQE for this array is 51%.

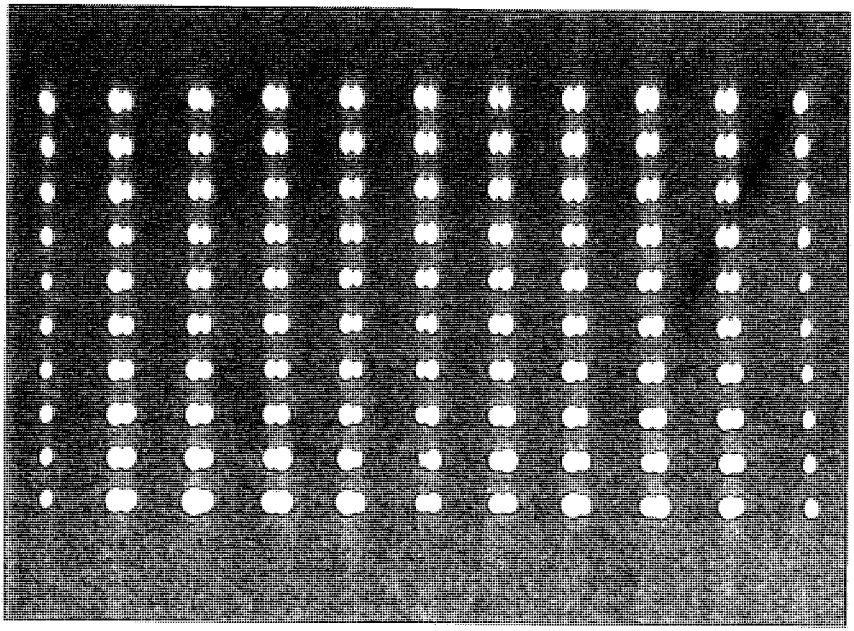

Fig. 12. Near-field pattern of a 100-element monolithic two-dimensional surface emitting array of AlGaAs/GaAs diode lasers with extracavity parabolic deflectors.

stripes is used to introduce sufficient optical loss to suppress transverse lasing. Further details of the fabrication have been reported previously (Donnelly *et al.*, 1989; Goodhue *et al.*, 1990; Donnelly *et al.*, 1987, 1988; Donnelly, 1990).

The L–I characteristic is shown in Fig. 13 for the array whose near-field pattern is represented in Fig. 12. The power is limited to 15 W by the available pulsed current of 62 A. An array consisting of only two rows, a total of 20 elements, fabricated from the same wafer had a pulsed output of 16.5 W at 62 A, which corresponds to a power density of 1.5 kW/cm^2.

The external DQEs of these early arrays is about 20%. Several factors can limit the efficiency, including the quality of the starting material, the quality of the laser facets, the length of the laser cavity, the beam divergence of the laser emission, and the effective f-number of the deflecting mirrors. The latter two factors affect the fraction of the light emitted from the laser facets that is deflected by the mirrors. Several changes can be made to increase the DQE of the arrays. The most obvious are to use a laser material

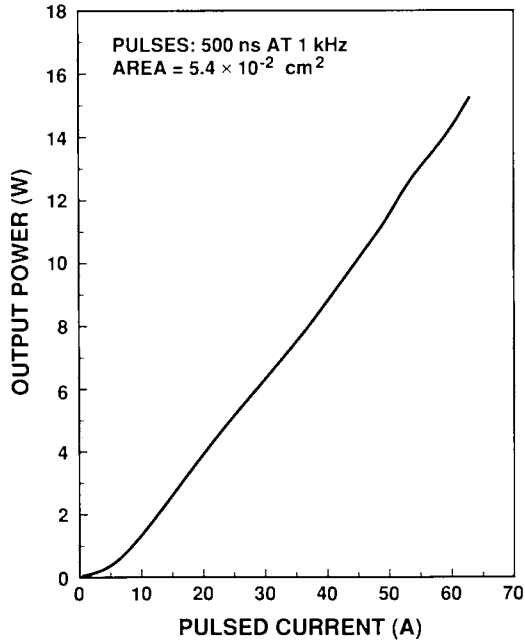

Fig. 13. Power-versus-current characteristic for the 100-element monolithic array whose near-field pattern is shown in Fig. 12.

providing higher cleaved-facet laser performance, including lower threshold current density, higher differential quantum efficiency, and lower beam divergence, and a cavity length more suitable for single quantum-well laser material.

The L–I characteristic of an array recently fabricated in GRIN-SCH-SQW AlGaAs/GaAs material is shown in Fig. 14. The GRIN-SCH SQW material was grown on n^+-GaAs by MOCVD. The quantum well is 10 nm thick and contains approximately 7 mol% AlAs. The GRIN regions on either side of the quantum well are graded from 30 to 60 mol% AlAs over approximately a 200 nm length. Cleaved-facet lasers fabricated in this material have threshold current density of 214 A/cm^2, DQE of 76%, and a beam divergence of $\leq 36°$ (FWHM).

Arrays in this material have been fabricated as described above, except that the laser cavity length was increased to 1000 μm, the lasers were 40 μm wide on 125 μm centers, and 4× projection photolithography was used to define the etch masks for the facets and parabolic cuts. As shown in Fig. 14, small arrays of 17 to 24 elements ($\sim 35 \times 10^{-2}$ cm^{-2}) have threshold

density of 240 A/cm^2 for the active laser area. The differential quantum efficiency is about 51%. Figure 9 shows the output power versus current (L-I) characteristic for a 17-element AlInGaAs/AlGaAs array. The threshold current for this array is about 1.56 A, which corresponds to a threshold current density of 230 A/cm^2. The peak output power is about 15 W at 20 A and the DQE ~ 53%.

Figure 10 shows the L-I characteristic for a 16-element InGaAs/AlGaAs array. The threshold current for this array is about 1.18 A, which corresponds to a threshold current density of 185 A/cm^2. The DQE is about 56%, the highest measured to date on a monolithic array of beam deflector lasers. The output power of 13 W at 20.5 A corresponds to a power density greater than 500 W/cm^2. Other arrays of 16 to 48 elements have demonstrated DQEs of about 50% and threshold current densities ranging from 160 to 200 A/cm^2.

Future work will include schemes to connect high power arrays in serial/parallel configurations, to make the individual elements of the arrays addressable, to integrate microlenses, to assign unique wavelengths to

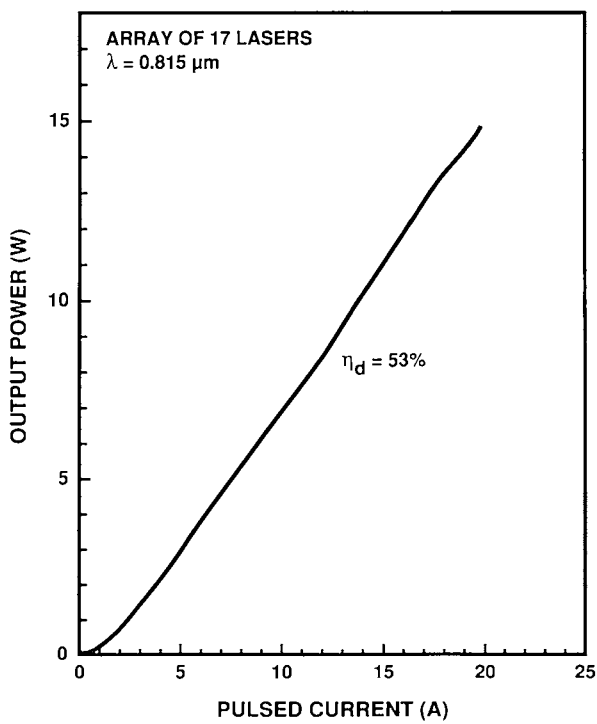

Fig. 9. Power-versus-current characteristic of a 17-element strained-layer AlInGaAs/AlGaAs array of folded-cavity lasers.

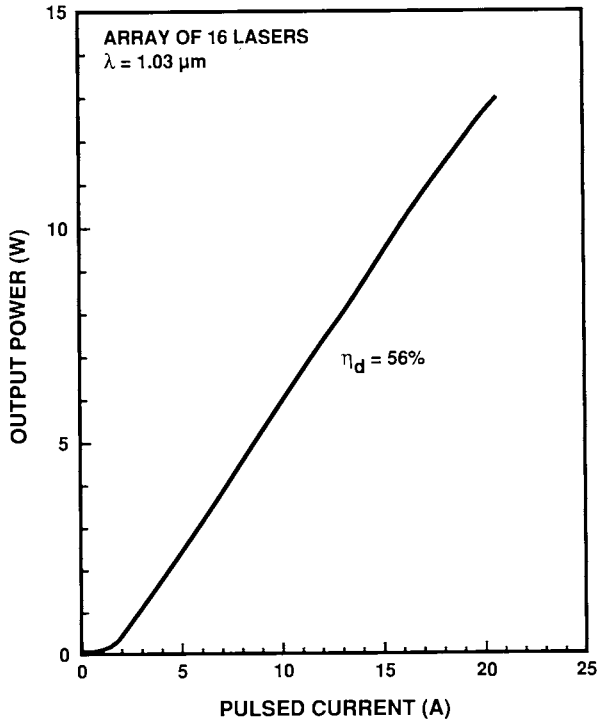

Fig. 10. Power-versus-current characteristic of a 16-element strained-layer InGaAs/AlGaAs array of folded-cavity lasers.

individual elements, and to phase-lock the individual elements of an array. For high output power, the ability to electrically connect the rows in series will be an important consideration. This will entail growing the laser structure on semi-insulating GaAs and developing a reliable, low-series-resistance interconnect scheme. Wu *et al.* (1991) have begun to fabricate simple intracavity deflector arrays with individually addressable elements. Phase-locking can be achieved with either Talbot configurations (Leger *et al.*, 1988) or evanescent coupling schemes, which are described in Chapter 2. Individual wavelength control can be achieved by such techniques as implantation/disordering (Ralston *et al.*, 1989) or segmentation (Fang and Wang, 1984).

C. Extracavity Deflector Devices

Monolithic surface emitting diode lasers with extracavity deflectors have been fabricated in the AlGaAs/GaAs material system using several of the

previously described dry etching techniques. Windhorn and Goodhue (1986) reported the fabrication of a linear array of AlGaAs/GaAs devices in which one of the laser facets was cleaved while the other facet and adjacent deflector were formed by IBAE. Yang *et al.* (1986a,b) reported an array of similar devices in which the noncleaved facet and adjacent deflector were formed by ion milling. Lasers in which the facet and extracavity deflector were formed by a single-step ion milling process were reported by Shieh *et al.* (1988) and Kim *et al.* (1990). An FIB micromachining technique has been used to form the noncleaved facet and 45° deflecting mirror in a device consisting of ten coupled 6 μm-wide laser stripes on 10 μm centers (Puretz *et al.*, 1987). The other facet in this device was a cleaved facet with a highly reflective coating.

The first monolithic two-dimensional AlGaAs/GaAs diode laser array was reported by Donnelly *et al.* (1987). For this array, IBAE was used to dry etch all of the facets and parabolic deflectors. Subsequent versions of this device (Donnelly *et al.*, 1989; Goodhue *et al.*, 1990; Donnelly *et al.*, 1988; and Donnelly, 1990) have produced peak output powers as high as 1.5 kW/cm^2. Jansen *et al.* (1989) reported the injection locking of a monolithic surface emitting diode laser array consisting of six rows of ten coupled ridge waveguide lasers. An external oscillator is injected into the first ridge waveguide, which extends the full length of the device. The other lasers in each row have a vertical etched facet with a highly reflective coating at one end and a vertical etched facet and 45° extracavity deflector at the other end.

Although many of these devices show promise, a major limitation has been that differential quantum efficiency is generally on the order of 20% or less. Ou *et al.* (1991) recently reported the cw operation of a surface emitting laser in which one vertical facet is formed by RIE and the other vertical facet and external outcoupled mirror are formed by ion-beam etching. Although the device had a reasonable threshold current density of 330 A/cm^2, the DQE was only 22%. The discussion that follows on fabrication techniques will describe some recent modifications that have led to substantial increases in DQE (Donnelly *et al.*, 1991, 1992) of surface emitting arrays with external parabolic deflectors. Deflector design and fabrication for light collection efficiency will also be discussed.

A schematic illustration of a monolithic two-dimensional surface emitting array of AlGaAs/GaAs diode lasers with extracavity parabolic deflectors is shown in Fig. 11, and the near-field pattern of a 100-element array is shown in Fig. 12. Each laser is 40 μm in width and has a cavity length of 250 μm. The lasers in each row are on a 180 μm period, and the rows are

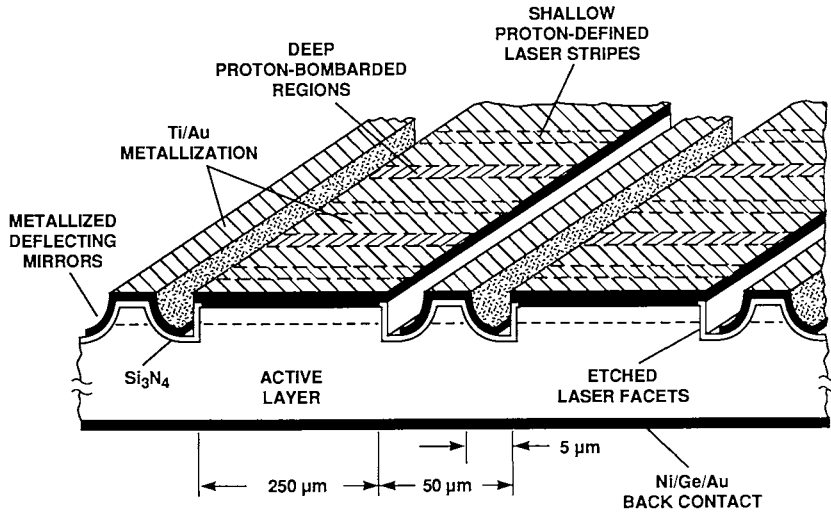

Fig. 11. Schematic illustration of a monolithic two-dimensional surface emitting array of AlGaAs/GaAs diode lasers with extracavity parabolic deflectors.

on a 300 μm pitch. The array is fabricated in SCH-SQW AlGaAs/GaAs material, with an undoped 20 nm-thick GaAs quantum well sandwiched between two 0.32 μm thick $Al_{0.3}Ga_{0.7}As$ confining layers, one *n*-type and one *p*-type. The cladding layers contain 70 mol% AlAs. Cleaved-facet lasers fabricated from this SCH-SQW material have DQEs of about 60%.

The technique used to fabricate the array follows. With photoresist as an etch mask, IBAE is used to etch pairs of straight-sided grooves 2 μm wide and 3–4 μm deep. The outer walls of each pair are the facets of the lasers formed in 250 μm-long rows. Lines approximately 3 μm wide immediately adjacent to the inside edge of one of the grooves in each pair are then opened in a new layer of photoresist, and parabolic deflectors for one side of each row are formed by computer-controlled angled IBAE, which is described below. The deflectors for the other side of each row are then formed in a similar manner.

A layer of Si_3N_4 is plasma-deposited to form a coating approximately 0.22 μm thick on the laser facets. A shallow proton bombardment that penetrates to a depth about 0.2 μm above the top of the upper $Al_{0.3}Ga_{0.7}As$ layer is used to confine the current to 40 μm-wide stripes on 180 μm centers. A second proton bombardment at higher energies midway between the laser

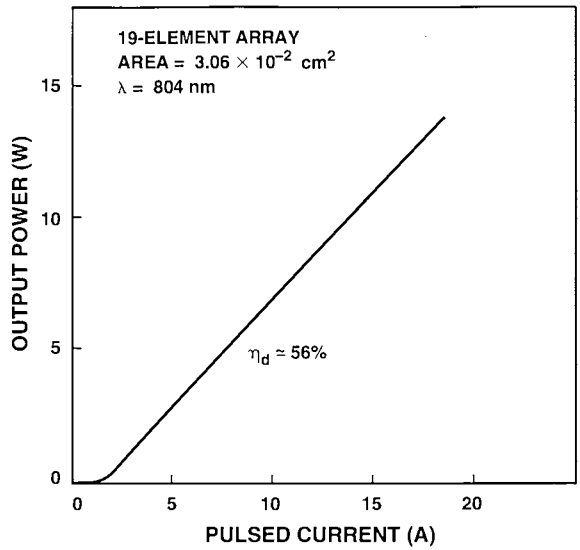

Fig. 14. Power-versus-current characteristic of a recently fabricated 19-element surface emitting array with extracavity parabolic deflectors.

current densities as low as 230 A/cm^2 and DQEs as high as 56%. These threshold current densities compare favorably to those measured on broad-area cleaved-facet lasers made of the same material, indicating high-quality dry etched facets.

Although the DQE is over a factor of two higher than previously obtained in arrays of this type in AlGaAs/GaAs, it is still lower than that observed in cleaved-facet lasers. We believe the primary reason for the lower efficiency is the incomplete collection of light by the deflectors. Larger arrays of 80 to 100 elements (~0.1-0.15 cm^2) have comparable threshold current densities but smaller quantum efficiencies of about 40%. Most of the decrease in overall quantum efficiency is attributable to the difficulty in aligning the parabolic etch masks to the etched facets over a large area. A self-aligned process that sets the edges of the facets and deflectors in one step should increase the uniformity in these arrays.

Use of material with an even smaller divergence angle should further increase the DQE of this type of array. In addition, making the junction slightly deeper (2.5-3 μm instead of 2 μm) and the initial slot cut to form the facet narrower (1-1.5 μm instead of 2 μm) should increase the collection efficiency of the deflectors and make them more tolerant of photolithograhic and etching inaccuracies.

With a planar top surface, an f-number less than one can only be obtained with curved deflectors. Figure 15 shows an integrated parabolic deflector with an f-number less than 0.85. The actual curve etched in the AlGaAs material is now being designed to optimize the f-number, with attention to the following factors: passivation and metal overlap, the depth of the junction, and tolerances in the lithography used to form the etch mask. For the front surface of the deflector to be parabolic, etching a second-order polynomial curve is necessary.

The method for etching the curve in the laser material (Donnelly *et al.*, 1988; Goodhue *et al.*, 1990; Donnelly, 1990) is illustrated in Fig. 16(a). First, the curve is broken down into a number of line segments of length L_n, which is determined by the resolution of the computer-controlled stepping motor. Once an etch rate is established, the time required to etch each segment t_n is calculated from the formula $t_n = L_n/(\sim\cos\phi/n)$, where r is the etch rate and ϕ_n is the incident angle of the argon-ion beam. The resolution of the steps coupled with the slight divergence of the ion beam (~0.5°) creates a smooth surface with the individual etched segments blended together. Figure 16(b) compares a desired calculated curve with an actual etched curve. Note the

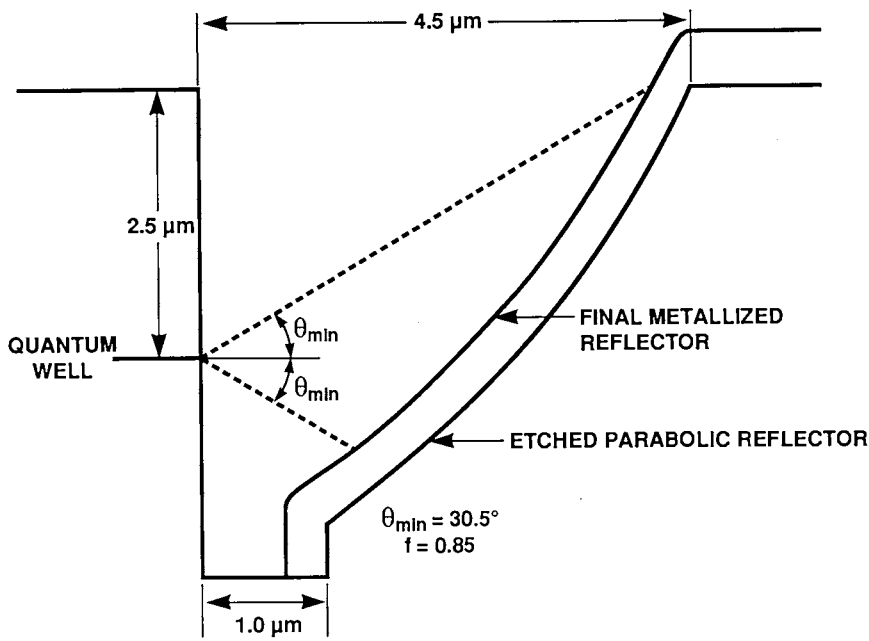

Fig. 15. Schematic illustration of an external deflecting mirror. The effective f-number is less than 0.85 and the minimum θ is 30.5°.

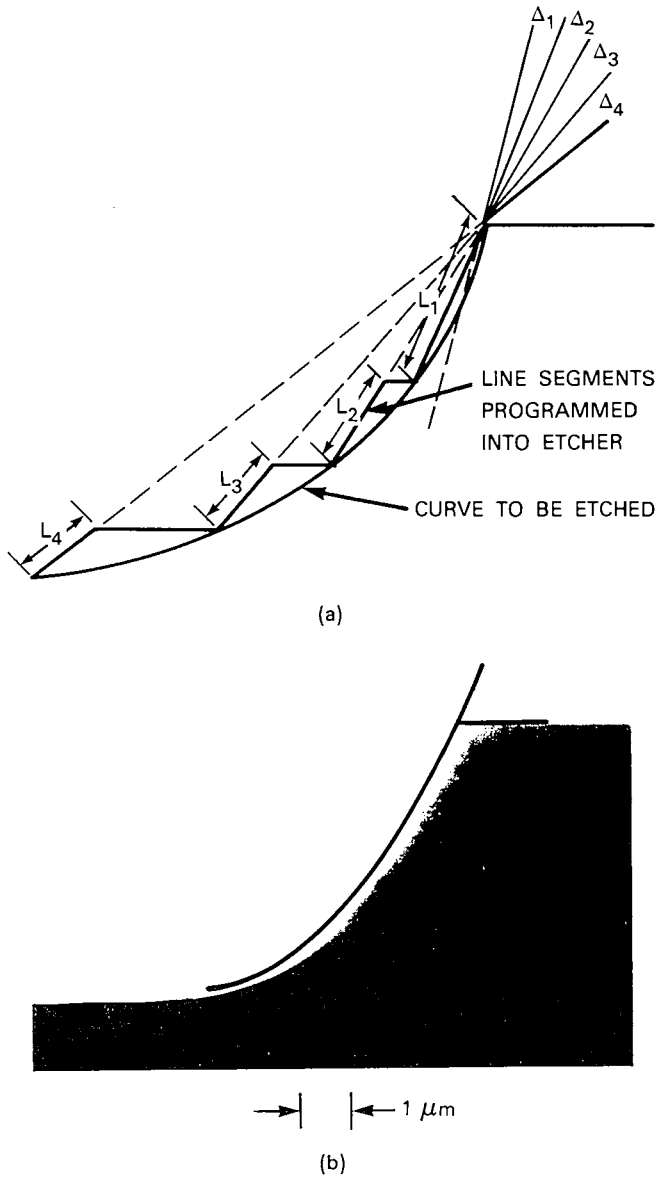

Fig. 16. (a) Dynamic tilting algorithm employed in micromachining the polynomial curve required to produce a parabolic deflector. The quantity Δ_n is the angular displacement generated by a step of the motor, and L_n is the segment length of each step. (b) Optical micrograph of a cleaved cross section of a parabolic deflector. The curved line represents the desired theoretical curve. (Goodhue *et al.*, 1990.)

excellent agreement between the two, with the small amount of deviation most likely due to an error in determining the etch rate. The SEMs in Fig. 17 show the face of a typical etched facet and the surface of an etched deflector recently produced by this method.

Alternative masks to improve smoothness and the use of a self-aligning process are currently under investigation. With these changes it should be possible to fabricate parabolic deflectors with effective f-numbers less than unity and arrays with quantum efficiencies comparable to those of cleaved-facet lasers. Further, by adding a highly reflective coating on one of the facets and taking light out on only one side, series-connected monolithic arrays of this type should be possible.

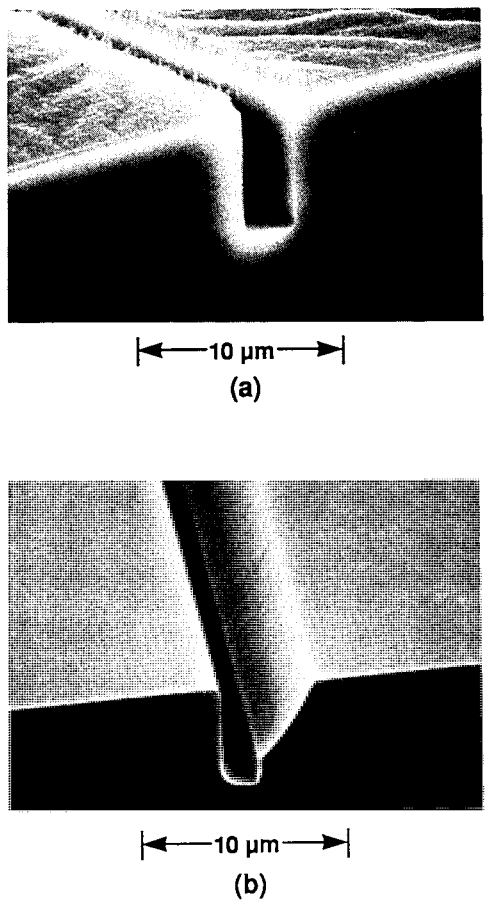

Fig. 17. SEMs of (a) a vertical facet and (b) a vertical facet and parabolic deflector.

D. Hybrid Arrays

Hybrid two-dimensional surface emitting arrays of AlGaAs/GaAs diode lasers that have a geometry similar to horizontal-cavity monolithic arrays have been developed (Donnelly *et al.*, 1989, 1988a, 1990). In addition to having near-term applications, these arrays are excellent devices for experimentally investigating the potential performance of future monolithic arrays.

A hybrid two-dimensional array is illustrated schematically in Fig. 18. The device consists of linear arrays of edge emitting lasers with conventional cleaved facets mounted in grooves with flat bottoms and 45° sidewalls etched in a Si substrate. The Si substrate contains microchannels (Tuckerman and Pease, 1981; Sasaki and Kishimoto, 1986; Phillips, 1987; Phillips *et al.*, 1988; Phillips, 1988; Mundinger *et al.*, 1988; Missaggia *et al.*, 1989; Missaggia and Walpole, 1991) for the flow of cooling fluid. The microchannels provide an efficient means for removing heat resulting from high average dissipated powers. The Cu bar on top of each linear array provides high electrical conductivity along the array and transient heat sinking during pulsed operation.

A photomicrograph of a sawed cross section of a portion of a hybrid array is shown in Fig. 19. The linear array of diode lasers has a cavity length

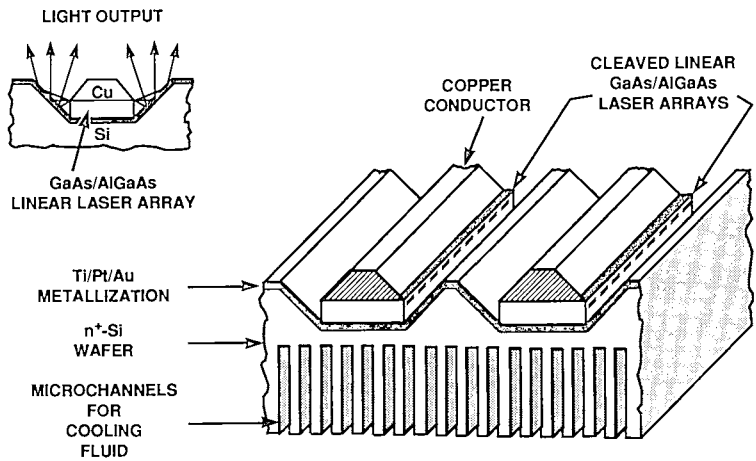

Fig. 18. Schematic illustration of a hybrid two-dimensional surface emitting array of AlGaAs/GaAs diode lasers integrated with a Si heat link.

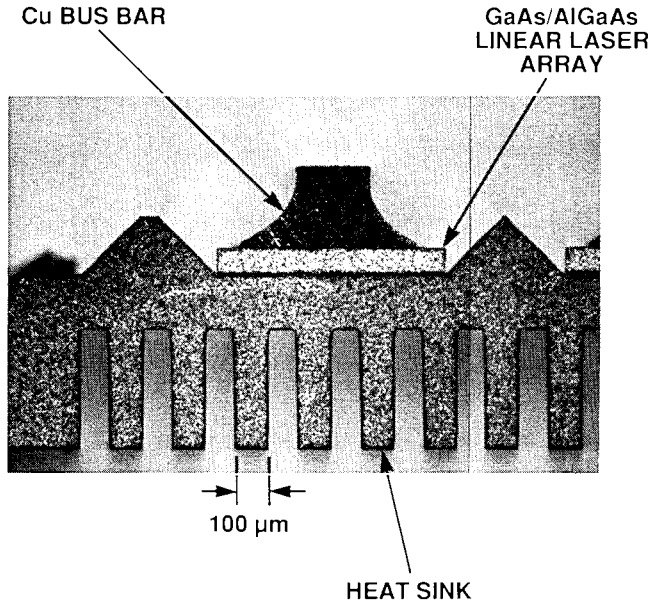

Fig. 19. Photomicrograph of a sawed cross section of an actual hybrid AlGaAs/GaAs diode laser array showing the end of a linear array mounted in an etched groove in a microchannel Si heat sink. The top Cu contact bar is tapered so that it will not block any light that emerges from the surface of the array.

of about 700 μm and is fabricated in GRIN-SCH-SQW n^+-GaAs material grown by OMVPE (Wang *et al.*, 1989; Wang, 1990). The quantum well is 10 nm thick and contains approximately 7 mol% AlGaAs. A proton-bombardment procedure (Foyt *et al.*, 1969; Dyment *et al.*, 1973), similar to that described for monolithic AlGaAs/GaAs arrays, is used to define 40 μm-wide stripes on 125 μm centers. After the wafers are thinned to about 100 μm and ohmic contact is made, 1 cm-long linear arrays are cleaved from the wafers and the facets coated with a layer of Al_2O_3 approximately a half wavelength thick.

The flat-bottom grooves with 45° sidewalls in the heat sink, in which the linear array bars are mounted, are formed in (100) Si with standard photolithography and an orientation-selective etch. A stripe pattern oriented in the (013) direction is first defined in a Si_3N_4 capping layer that serves as an etch mask. The Si is then etched with a KOH–isopropanol–H_2O solution at 80°C. The bottom (100) Si plane etches about 2.5 times faster than the (331) sidewalls. Because the etch ratio is only 2.5, the actual angles between the sidewalls and the top and bottom are closer to 45° than the theoretical

angle of 46.5° between the (331) and (100) planes. A dicing saw is used to cut the microchannels into the bottom of the heat sink. The microchannels are 100 μm wide and spaced every 200 μm. The Si heat sink is metallized with Ti/Pt/Au to form efficient deflecting mirrors, and the linear arrays are soldered onto the bottom of the grooves using a Au/Sn solder. Finally, Cu bars, which are tapered so that they will not block any of the light that emerges from the surface of the array, are In-soldered to the tops of the laser bars.

Figure 20 shows photographs of a completed laser module that contains two 1 cm^2 hybrid arrays, each consisting of eight 1 cm-long linear array bars soldered in eight grooves on a microchannel Si heat sink. In this design, the bars are driven in pairs, whereas in more advanced designs they would be driven in series. Cooling fluid enters the module through the center tube and exits through the two outside tubes. The near-field pattern of the module

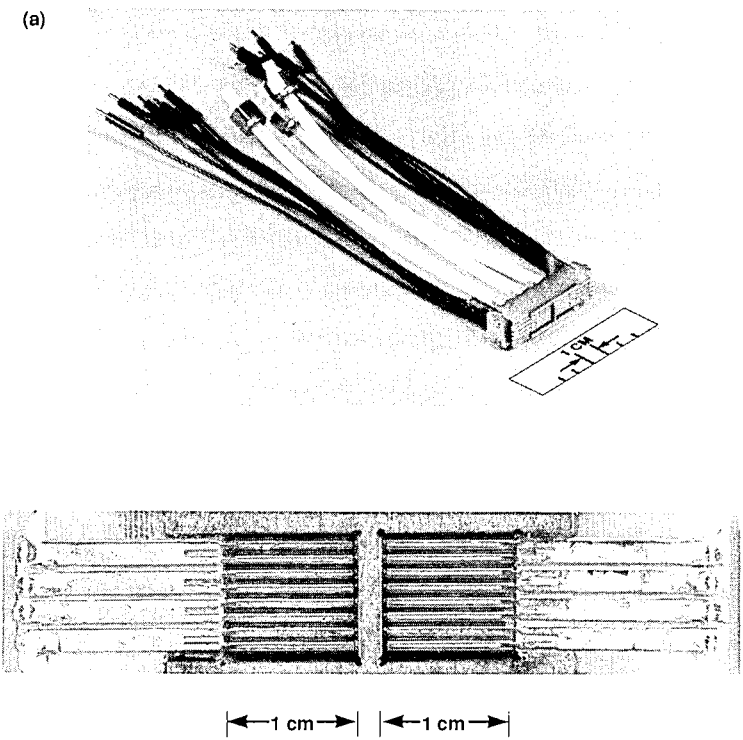

Fig. 20. Photolithographs showing (a) overall and (b) front-face views of a completed laser module containing two 1 cm^2 two-dimensional surface emitting arrays of diode lasers.

is shown in Fig. 21. The uniformity of the bars is very good, as substantiated by power measurements on each pair. The geometry of the hybrid arrays is such that the amount of thermal cross talk between the individual linear array bars is insignificant. Thus, testing the bars individually or in pairs, one pair at a time, provides a good idea of the ultimate performance of the arrays. Separate measurements with the linear array bars driven in pairs and the entire module driven at one time give results within 5% of each other.

The L–I characteristic of a pair of bars driven with 150 μs pulsed currents up to 100 A is shown in Fig. 22. From the data, we estimate that if the entire module was driven with 100 A per pair (50 A/bar), the output energy per pulse would be approximately 120 mJ. Figure 23 shows the integrated output spectra of the pair driven with 40 A (20 A/bar) and 80 A (40 A/bar) 150 μs pulses at 10 Hz. The spectra are typical of most arrays.

By disconnecting one bar of several pairs, the remaining bars have been tested individually at various currents, pulse widths, and repetition rates. Figure 24 shows the L–I characteristics of one 1 cm-long bar of a hybrid array driven with 150 μs pulses at repetition rates up to 500 Hz. Note that at 40 A the decrease in output per pulse at 500 Hz is less than 10% of that at 10 Hz. Output spectra were also obtained for the same bar driven with 150 μs pulses at various currents up to 30 A at 10 Hz, and with 150 μs pulses

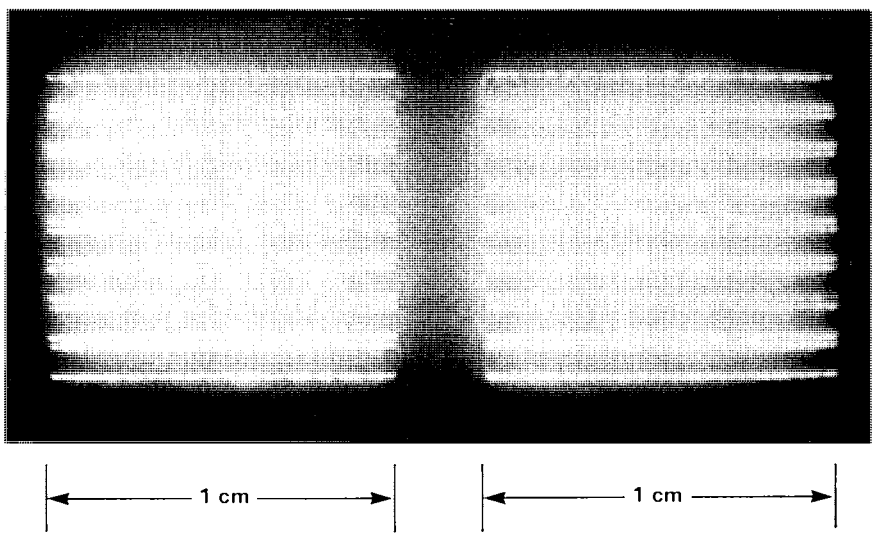

Fig. 21. Near-field pattern of a laser module containing two 1-cm^2 hybrid surface emitting arrays of AlGaAs/GaAs GRIN-SCH-SQW diode lasers.

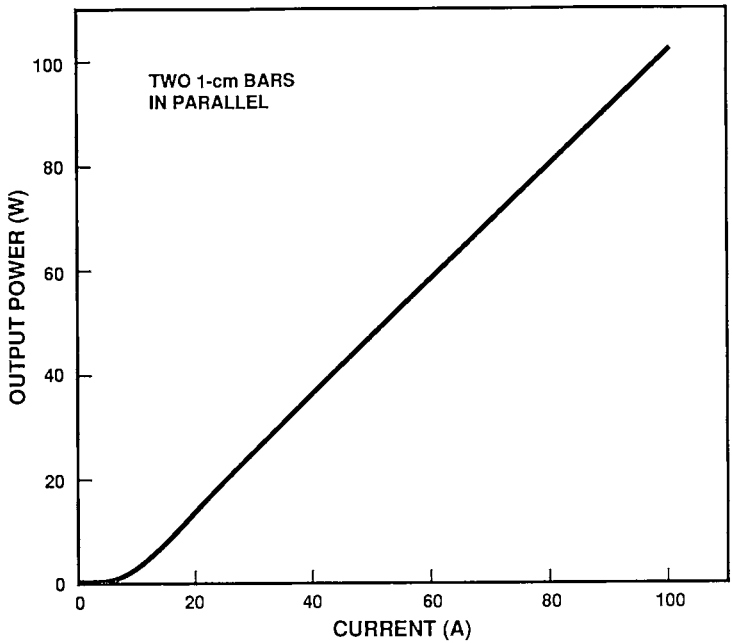

Fig. 22. Power-versus-current characteristics of a pair of parallel 1 cm-long linear array bars of a hybrid array driven with 150 μs pulses at 10 Hz.

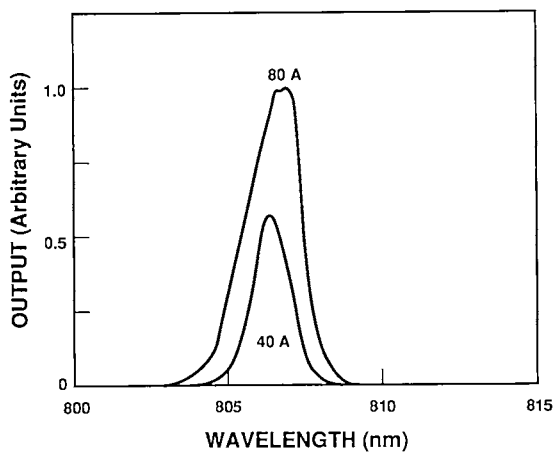

Fig. 23. Output spectra of a pair of parallel 1 cm-long linear array bars of a hybrid array. The bars are driven with 40 A (20 A/bar) and 80 A (40 A/bar) 150 μs pulses at 10 Hz.

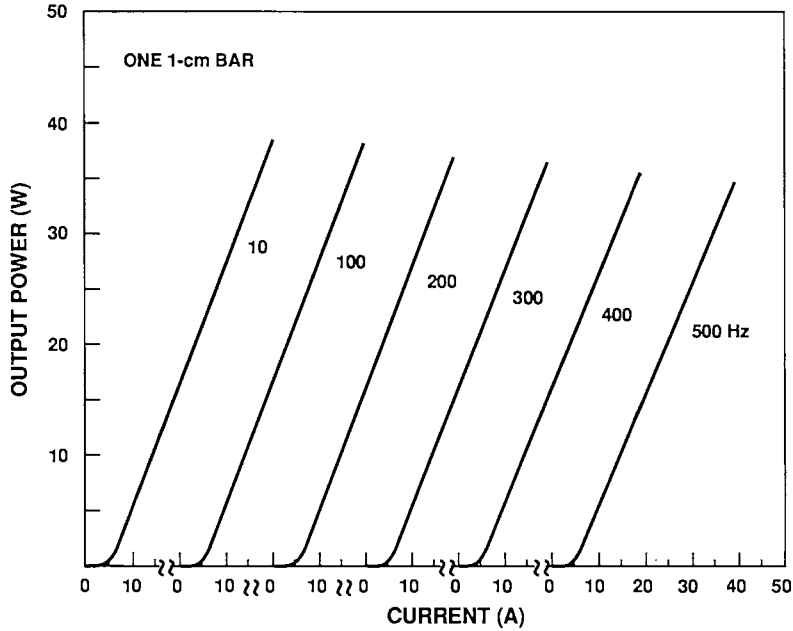

Fig. 24. Power-versus-current characteristics of one 1 cm-long linear array bar of a hybrid array driven with 150 μs pulses at repetition rates from 10 to 500 Hz.

of 30 A at 10 to 500 Hz. At the higher drive currents the output of this bar shows anomalous blue-shifted modes, which are not usually observed. The wavelength change at 30 A compared to that at 7 A indicates a temperature rise of less than 3°C during a 30 A 150 μs pulse. The output spectra of the bar driven with 150 μs pulses at 30 A at repetition rates of 10, 100, 400, and 500 Hz are shown in Fig. 25. The additional temperature rise at the high repetition rates appears to be less than 1°C.

Figure 26 shows the L–I characteristics of a single 1 cm-long bar for pulses ranging from 150 μs to 1 ms at 10 Hz. The figure also shows the cw output for currents up to 25 A. The 18 W cw output indicates that 144 W/cm^2 could be obtained with each bar driven with 25 A. Output spectral data indicate that the temperature rise for 25 A cw operation is about 30°C. The total input power to this 1 cm-long bar at 25 A cw is approximately 40 W. Thus, with an optical output power of 18 W, the power dissipated is about 22 W. With this dissipative power, the cw temperature rise of 30°C gives a total thermal resistance of 0.094°C cm^2/W. This value is in close agreement with heat sink measurements and calculations (Missaggia *et al.*, 1989; Missaggia and Walpole, 1991) with the thermal resistance being approxi-

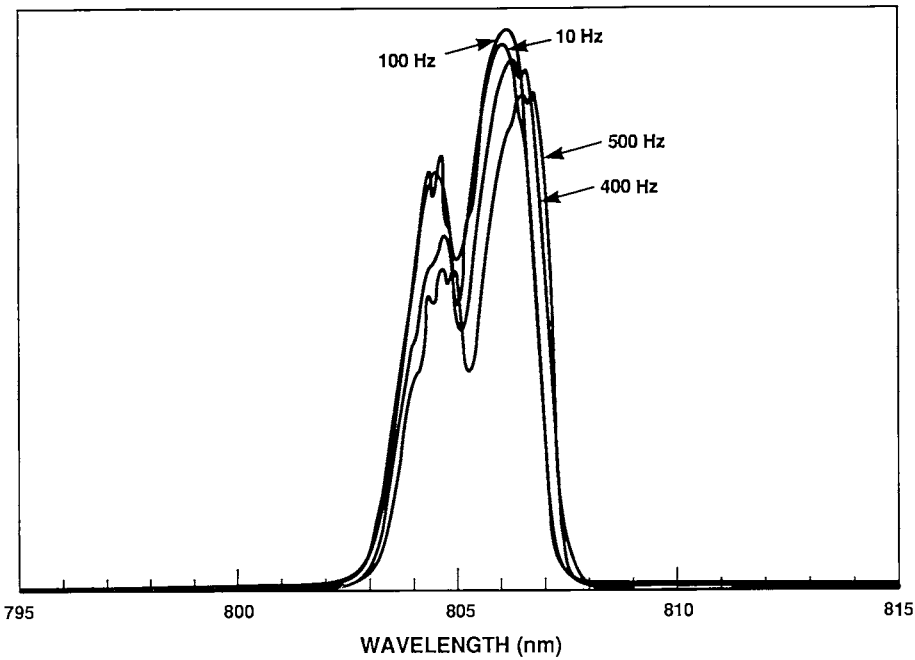

Fig. 25. Output spectra of one 1 cm-long linear array bar of a hybrid array driven with 30 A 150 μs pulses at repetition rates of 10, 100, 400, and 500 Hz.

mately 0.07°C cm^2/W for the Si heat sink and 0.02°C/W for the 100-μm-thick bar.

The cw output power was also measured on six bars (0.75 cm^2) operating in parallel at 25 A per bar for a total current of 150 A. The measured output was 90 W or 120 W/cm^2, which is slightly lower than the 144 W/cm^2 obtained from a single bar.

These results for hybrid arrays demonstrate that both high peak power and high average power can be obtained from arrays mounted junction side up on a microchannel heat sink. Similar results should be possible with monolithic arrays, in which case the fabrication should be somewhat simpler since flat heat sinks can be used. An advantage of monolithic arrays is that materials such as Cu/W, which has a higher electrical and thermal conductivity, could be substituted for Si. In addition, since less space is wasted on mirror formation with monolithic arrays, the thermal fill factor, i.e., the area of active laser material divided by the total heat sink area, should be higher. These variations should offset to some extent the lower performance obtained so far on monolithic arrays compared to cleaved-facet lasers.

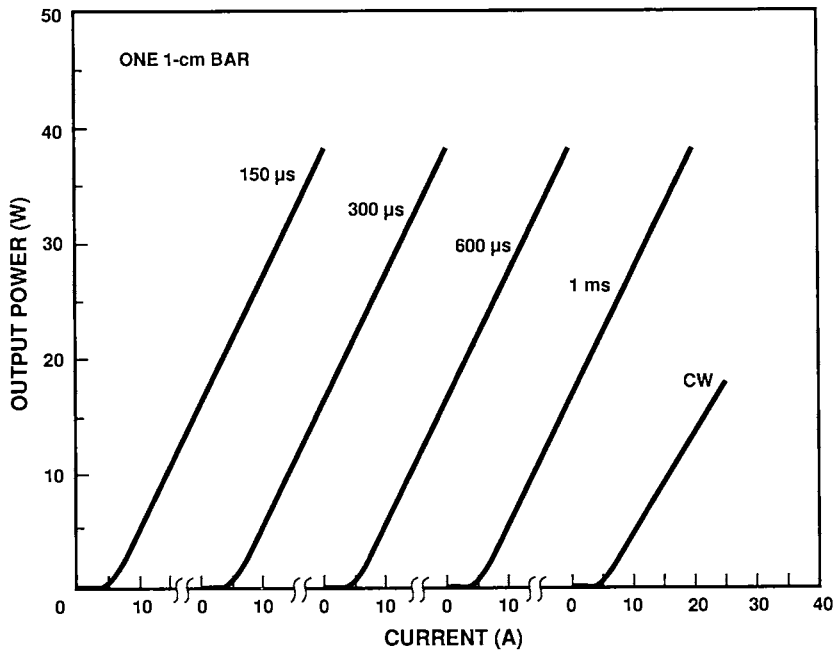

Fig. 26. L–I characteristics of one 1 cm-long linear array bar of a hybrid array driven with 150 μs, 300 μs, 600 μs, and 1 ms pulses at 10 Hz. Also shown is the cw output for currents up to 25 A.

III. GaInAsP/InP MATERIAL SYSTEM

A. Mass Transport

Ion etching techniques similar to those described in Section II for the fabrication of surface emitting lasers in AlGaAs/GaAs have been applied to the GaInAsP/InP material system (Saito and Noguchi, 1989; Mutoh *et al.*, 1991). In GaInAsP/InP, however, because the substrate is transparent and the Al-free cladding layers are more amenable to regrowth, other methods can also be used. In particular, a surface-energy-induced mass transport process can be employed to transform wet-chemical and dry etched structures into smooth high-quality microoptical components (Liau and Walpole, 1985, 1982; Chen *et al.*, 1982; Liau *et al.*, 1984; Walpole *et al.*, 1987; Yap *et al.*, 1988; Liau *et al.*, 1988b, 1989). An example of the use of mass transport to form a 45° mirror (Liau and Walpole, 1985) is shown in Fig. 27. Since this process has played a crucial role in the development of

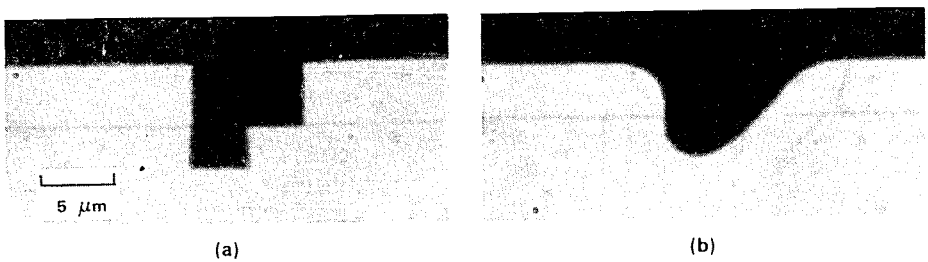

Fig. 27. Optical micrographs showing (a) a stair-shaped structure etched in a GaInAsP/InP double-heterostructure wafer and (b) vertical (left) and 45° (right) smooth mirrors formed after mass transport at approximately 730°C.

surface emitting lasers in the GaInAsP/InP system, it is described in detail here.

Mass transport is caused by surface energy stored in the etched structures and surface atomic mobility at elevated temperatures (Mullins, 1959; Blakeley, 1973; Nagai *et al.*, 1985; Liau and Zeiger, 1990) as illustrated in Fig. 28. As indicated in Fig. 28(a), the thermally dissociated free atoms have an excess concentration proportional to surface energy, which is directly proportional to curvature. Variation of curvature across the surface therefore results in a concentration variation and hence interdiffusion, which

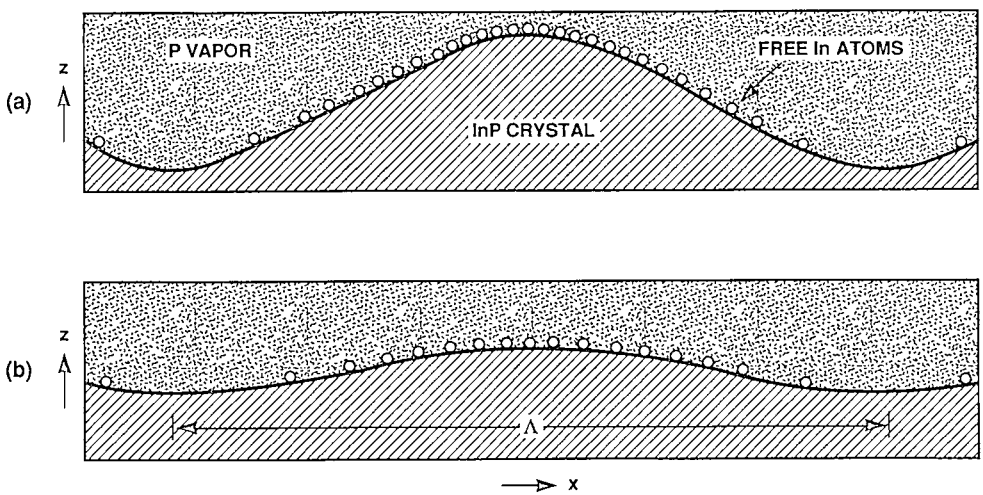

Fig. 28. Model of surface-energy-induced mass transport, showing (a) the effect of surface curvature on thermal dissociation and (b) the resulting diffusion and regrowth.

leads to erosion and growth in the high- and low-energy regions, respectively, resulting in a reduction of the curvature, as shown in Fig. 28(b).

This process can be described quantitatively in the simple case of slowly varying surface profiles, for which curvature is simply the second spatial derivative. By incorporating the second spatial derivative into the (surface) diffusion equation, we arrive at an equation with a fourth spatial derivative of the surface profile (Mullins, 1959; Blakely, 1973; Nagai *et al.*, 1985; and Liau and Zeiger, 1990), as follows:

$$-\frac{\alpha v^2 N_0 D}{kT}\frac{\partial^4 z}{\partial x^4}=\frac{\partial z}{\partial t}, \tag{1}$$

where α is the coefficient of surface tension, v is the molecular volume, N_0 is the equilibrium free-atom concentration in a flat surface, D is the diffusivity, k is the Boltzmann constant, and T is the absolute temperature. A similar equation can be derived for transport through vapor diffusion. The model predicts exponential decay of the amplitude of a sinusoidal surface profile with lifetime proportional to the fourth power of the spatial wavelength. Time evolution of more general profiles can then be obtained by using Fourier expansion. For example, a single mesa step exhibits grading according to a fourth root of time dependence. These predictions can readily be tested experimentally.

A furnace system developed and optimized for mass transport processing (Liau, 1991) is shown in Fig. 29. Because PH_3 flow is used to supply the phosphorus vapor, the system has been specially designed to avoid problems that can be caused by phosphorus condensation in the cooler regions. Experiments using etched stripes with varied periodicities show general agreement with the model (Liau and Zeiger, 1990).

Stages in the fabrication of a microlens by mass transport (Liau *et al.*, 1988b, 1989) are illustrated in Fig. 30. Because of the very strong spatial dependence, the lens profile can be accurately controlled by the etched steps via a simple mass conservation rule, i.e., in each step the volume eroded equals the volume filled. Moreover, the same strong spatial dependence assures an essentially self-controlled process in the microlens formation. The predictions indeed are in good agreement with experiment.

Although the general concepts of the mass transport model are probably correct, some of the detailed mechanisms remain poorly understood. For instance, the physical parameters in Eq. (1) have not been measured directly. Some of these parameters, especially N_0 and D, are probably dependent upon material quality, crystallographic orientation, and surface conditions. Furthermore, some recent studies have shown the need for additional wafer

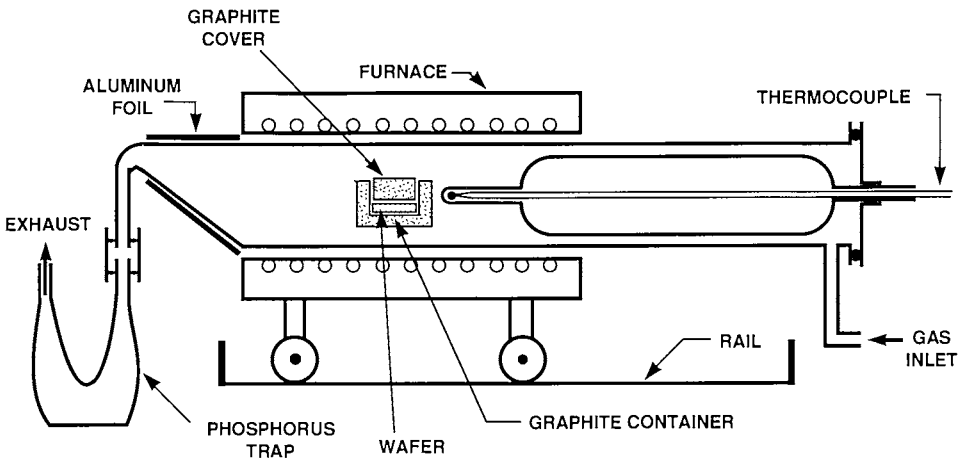

Fig. 29. Schematic illustration of a furnace system for mass transport processing of compound semiconductors. The gas flow, temperature distribution, and furnace movement have been designed for high phosphorus vapor pressure with minimum phosphine consumption and clean phosphorus disposition.

protection against complications due to evaporation loss (Liau, 1991). The possibilities of thermal degradation and defect generation as well as their prevention are still being investigated.

In the fabrication of 45° mirrors, other complications arise. First, the model is not directly applicable, because the surface profile is not slowly varying. More empirical approaches will be needed for accurate control of the mirror angle and profile. Second, a crystallographic orientational effect of the mass transport parameters, as can be seen near the vertical mirror facet in Fig. 31, can play a significant role. Finally, a large area of the exposed GaInAsP contact layer, which is commonly used for lower-resistance ohmic contacts, can become unstable in the phosphorus atmosphere, thereby complicating the InP mass transport. The GaInAsP layer needs to be protected either by deposited oxide or a grown InP layer.

B. Extracavity Deflector Devices

Vertical and parabolic-shaped angled mirror facets have been formed and monolithically integrated with a double-heterostructure laser, as shown in Figs. 27 and 31. The resulting surface emitting laser, whose L–I characteristic is shown in Fig. 32, was the first to operate cw at room temperature (Liau and Walpole, 1985) with performance comparable to cleaved-facet edge

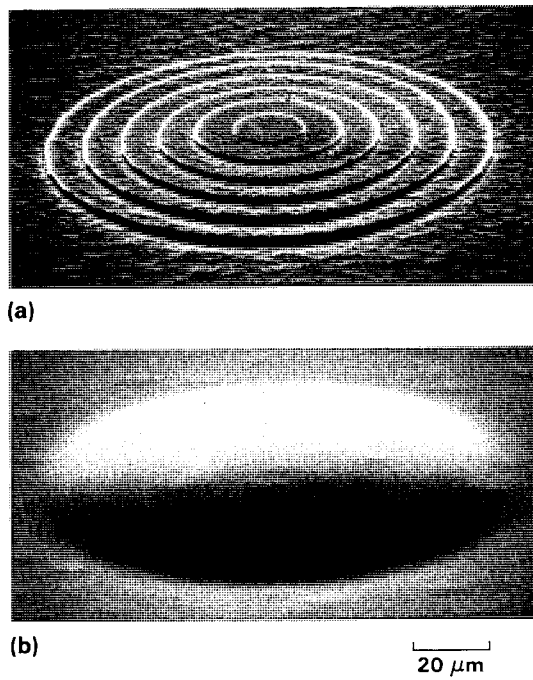

Fig. 30. Optical micrographs of (a) an etched multistep mesa in a GaP substrate and (b) its smoothing to form a microlens.

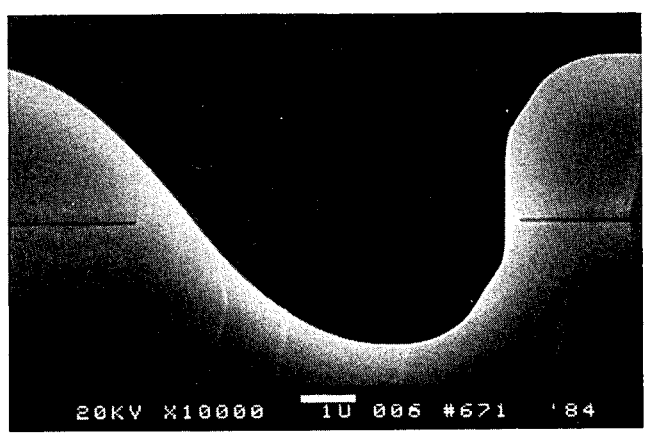

Fig. 31. SEM showing the integrated mirror structure of a surface emitting diode laser.

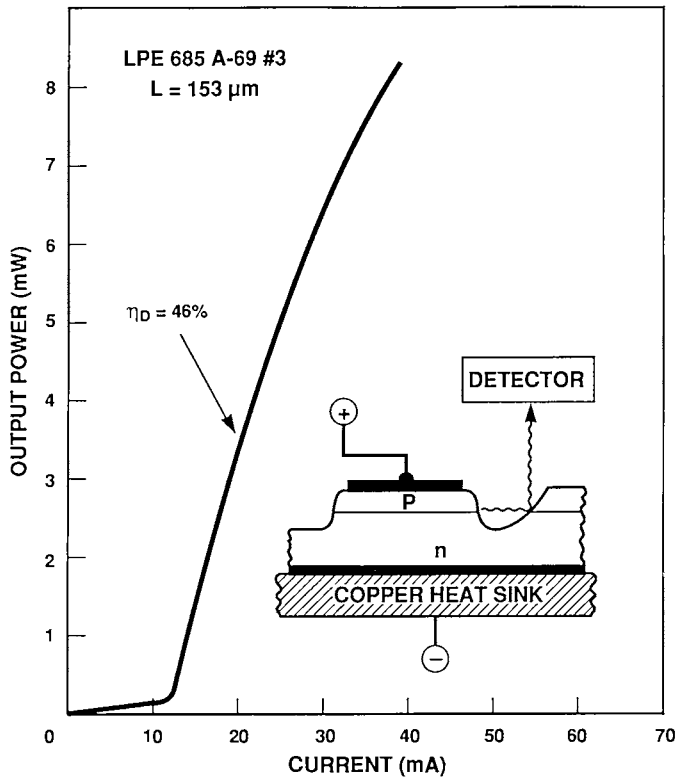

Fig. 32. L–I characteristic for a surface emitting diode laser operated cw at room temperature. This laser, shown in the inset, was the first of its type to demonstrate performance comparable to conventional edge emitting devices.

emitting lasers. This was made possible by the highly smooth mirror facets afforded by the mass transport process (Fig. 31). It is worth noting that these facets are passivated by the mass-transported cladding layer and are potentially advantageous for improved device reliability.

In the fabrication of these lasers, stair-shaped grooves, like the one shown in Fig. 27(a), are first formed in a double-heterostructure wafer by a two-step photolithography and selective chemical etching process. Accurate mask realignment and precision etching are needed to control the step width and height, respectively, for the desired beam deflector profile. Mass transport typically is carried out at 740°C for several hours. The mirror formation can be checked by examining cleaved cross sections. Repeated mass transport runs may be used until the mirror formation is completed. Then, a buried-heterostructure waveguide (Walpole *et al.*, 1987) with a narrow active region width of about 2 μm is formed, again by selective chemical etching

and mass transport, but at a temperature approximately 100°C lower. After the contact alloying, angled evaporation of Ti and Au is carried out to coat the beam deflector and the rear vertical mirror. Thicker Au plating is used to ensure good electrical connection across the nonplanar buried-heterostructure mesa structure, as shown in the finished device in Fig. 33.

The early devices of this type demonstrated room-temperature cw operation with performance quite comparable to that of cleaved-facet edge emitting lasers, as demonstrated in Fig. 32. Later results have shown low threshold current of 6 mA, high differential quantum efficiency of 50%, and cw output powers over 30 mW. The far-field patterns, represented in Fig. 34, evidence narrowing due to the parabolic shape of the beam deflector profile. However, considerable sidelobes are present because of deviation from the exact ideal mirror profile. Also, the numerical aperture of the 45° mirror is often not large enough to fully capture the widely diverging laser light.

These surface emitting lasers can be readily made into monolithic two-dimensional arrays (Walpole and Liau, 1986; Liau and Walpole, 1987). An individually addressable 4×4 array is shown in Fig. 35. With the lower contact resistance afforded by arrays fabricated in *p*-type substrates, the lasers can be tested cw without bonding the array to the heat sink. Figure 36 shows one such test result, with the L–I characteristics demonstrating good uniformity for all but two lasers. The variations can be mapped and

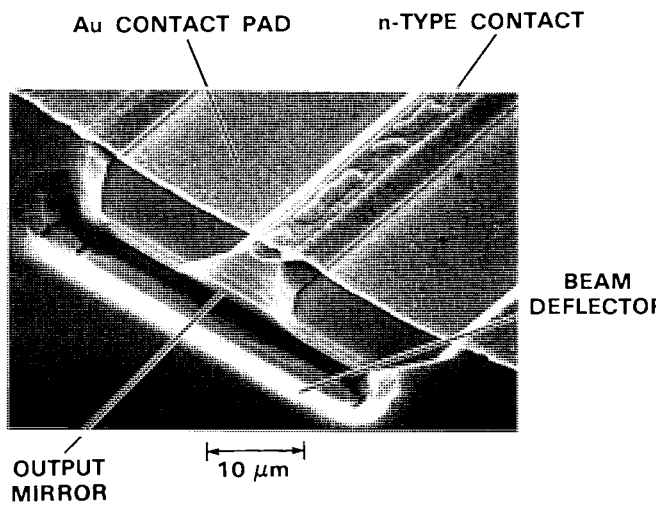

Fig. 33. SEM showing a fabricated surface emitting laser from a perspective near its emission end.

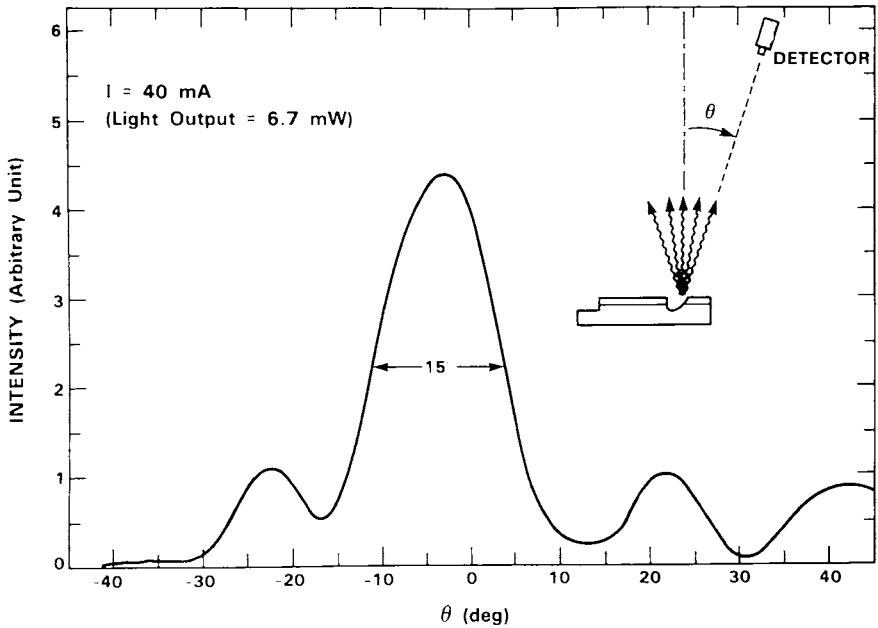

Fig. 34. Far-field pattern of a 1.3-μm GaInAsP/InP surface emitting laser.

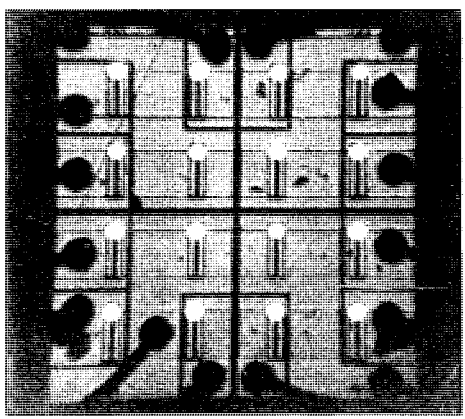

Fig. 35. Infrared micrograph of the first monolithic two-dimensional surface emitting laser array operated cw at room temperature. The center-to-center spacing of the emitting elements is 254 μm in each direction.

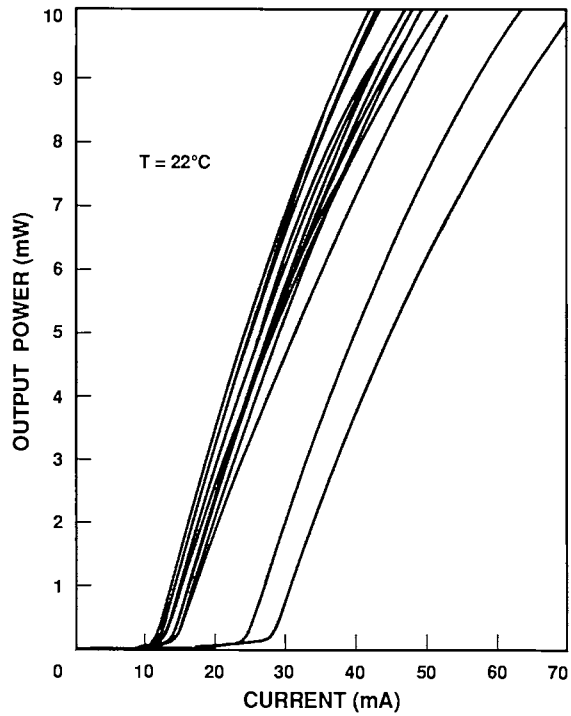

Fig. 36. L–I characteristics for individual lasers of the array in Fig. 35 before bonding to the heat sink. The lasers were operated cw at room temperature.

often correlated with morphological features in the wafer, because liquid-phase epitaxy was used to grow the double heterostructure. Better uniformity could probably be obtained by improved substrate quality and growth technology. Good uniformity in both L–I characteristics and emission wavelengths is very important for many potential applications.

The first large array reported (Liau and Walpole, 1987), 160 devices packed at a density of 4000 lasers/cm^2, is shown in Fig. 37. Similar arrays have demonstrated total cw output of 0.7 W at room temperature and 1.3 W at 11°C. At high packing densities, thermal cross talk can become an important issue. A simple rule for avoiding thermal cross talk is for the separation between the buried-heterostructure lasers to be no smaller than the substrate thickness, since these devices are mounted junction side up. Analytically, the heat flow can be modeled by conformal mapping (Liau *et al.*, 1988a), as shown in Fig. 38. The thermal resistance of heat generated in the active region can then be expressed in a simple analytical formula in terms of the active region width, device spacing, substrate thickness, and

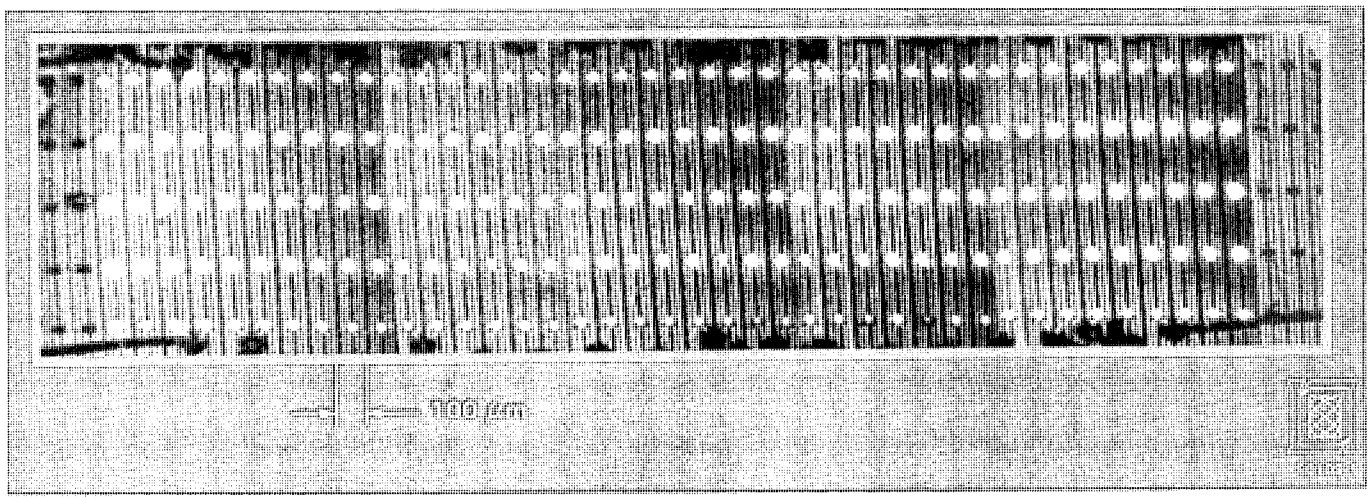

Fig. 37. Composite photograph showing a 160-element laser array packed at 4,000 lasers/cm^2. The individual photographs in the composite were taken of displays on an infrared vidicon system monitor.

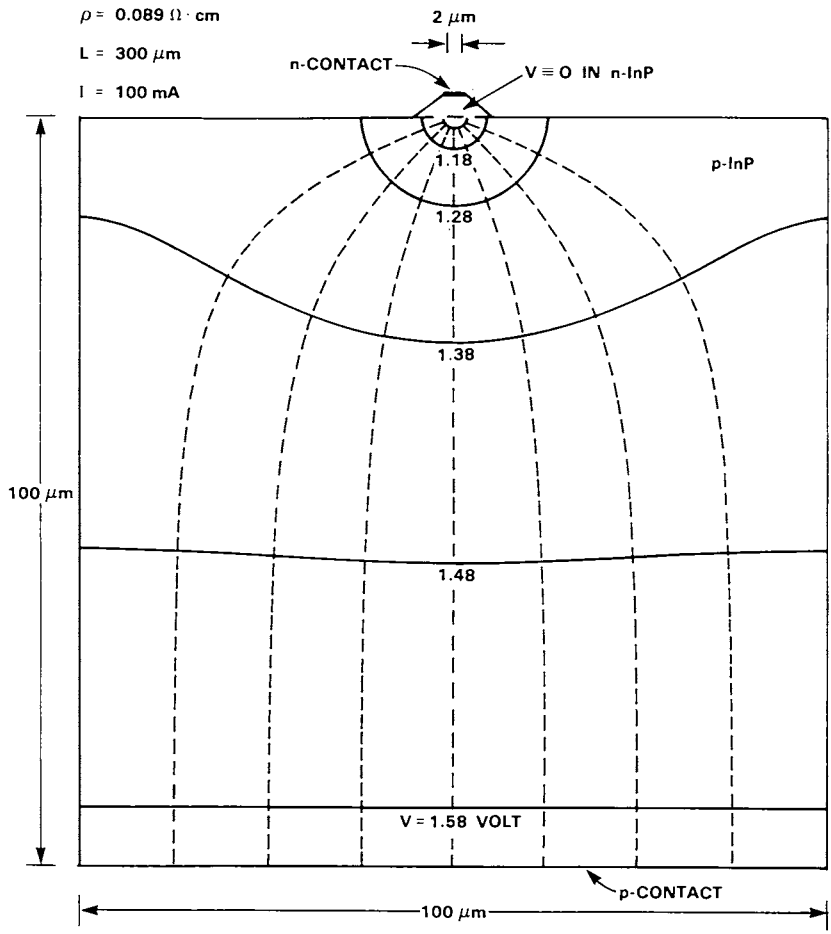

Fig. 38. Conformal mapping calculation of current flow in a substrate. This transverse cross section shows electric current (dashed curves) flowing from the buried-heterostructure active region to the bottom contact at the heat sink. The same calculation can be applied to flows of heat generated both in the active region and in the substrate. (© 1988 IEEE.)

thermal conductivity. It can further be shown that thermal resistance due to ohmic heat in the substrate is exactly half of that generated in the active region (Liau *et al.*, 1988a). This analysis assumes that the Cu heat sink on which the array is bonded is always maintained at a constant temperature. For a very large two-dimensional array, however, the heat flow ino the Cu block becomes one-dimensional and can result in an overall temperature rise for the array, unless measures such as microchannel coolant flow are used to more efficiently remove the heat (see Chapter 10).

In summary, GaInAsP/InP surface emitting lasers with integrated extra-cavity deflectors have demonstrated performance comparable to state-of-the-art cleaved-facet edge emitting lasers. The mass-transported mirror facets are potentially of very high quality and reliability. To make these devices more practical, however, considerably more development in basic materials and fabrication is required. Specifically, uniform high-quality substrates and epitaxial layers, precision lithography and etching techniques, and more understanding of basic material issues and precision control in mass transport are all needed.

C. Surface Emitting Laser Arrays with Integrated Microlenses

The angular width of the emission pattern from a diode laser is typically quite broad (typically several tens of degrees in the direction perpendicular to the active layer) and the emitting area of the lasers in a two-dimensional laser array is typically a small fraction of the total area. These features limit the intensity and brightness that can be obtained with such arrays unless the output of each laser is collimated with its own lens. Arrays of lasers with accurately aligned microlens arrays are important for many applications including end pumping of solid state lasers and coupling of the output from many diode lasers into an optical fiber. Diode laser arrays with lenslets can be used as illuminators by incoherently superimposing, in the far field, the output of each element of the array. With coherent combining of the output of the elements (Chapter 8), a high brightness beam can be obtained for applications such as laser radar or free space optical communications. Other potential applications requiring high intensity lasers are cutting and processing in commercial and medical areas. Therefore, the development of laser arrays creates the need for corresponding microlens arrays. The microlenses must have a large numerical aperture and good efficiency, both of which significantly challenge most microlens technologies. In addition, optical alignment and mechanical fixture of the microlens arrays can be rather difficult to achieve and subject to various instabilities. In these areas, recently

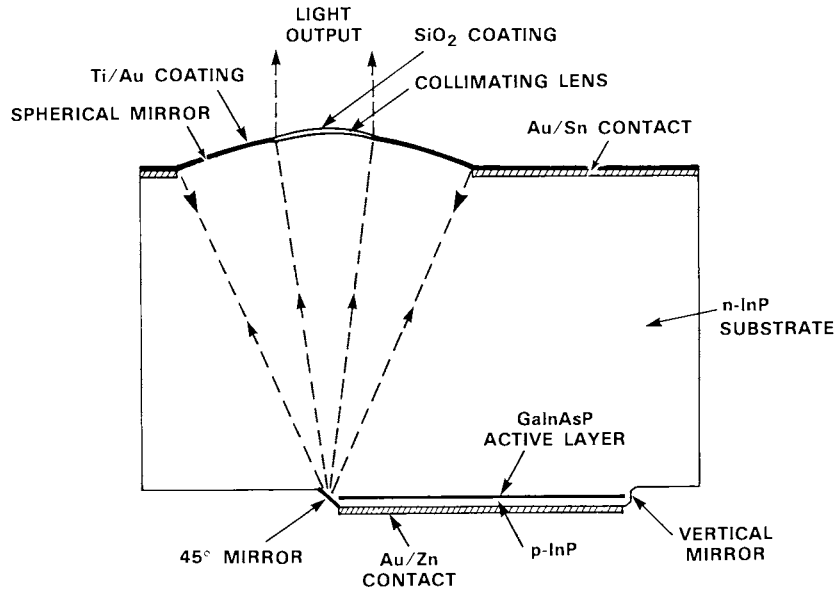

(a)

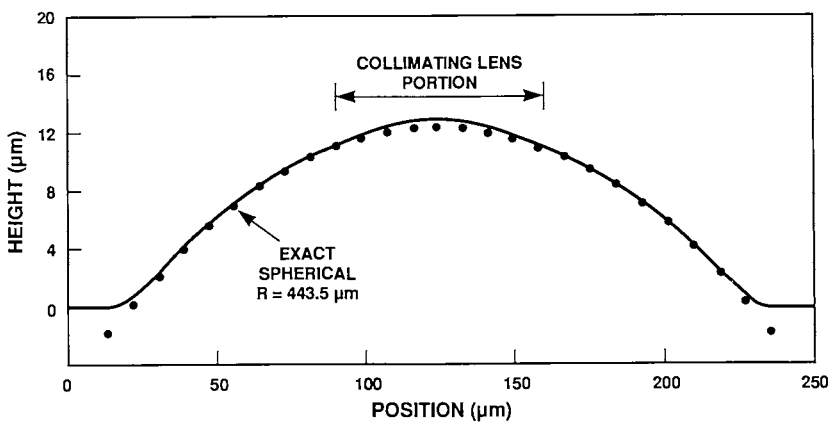

(b)

Fig. 39. (a) Longitudinal cross section of a diode laser with a monolithic integrated microlens, showing the laser cavity formed by the spherical mirror, the waveguide gain region, and the vertical mirror at the far end of the waveguide. The central portion of the microlens collimates the laser output. (b) Actual profile of the bifocal microlens.

developed semiconductor microlenses offer a potential solution because they can be monolithically integrated with lasers.

One possible integration scheme is shown in Fig. 39(a) (Liau *et al.*, 1990). The microlens is first fabricated on one side of the substrate, in this case by mesa etching and mass transport, as described earlier (Fig. 30). The buried-heterostructure gain region is then fabricated on the other side and is coupled to the microlens by a 45° mirror. The outer part of the microlens

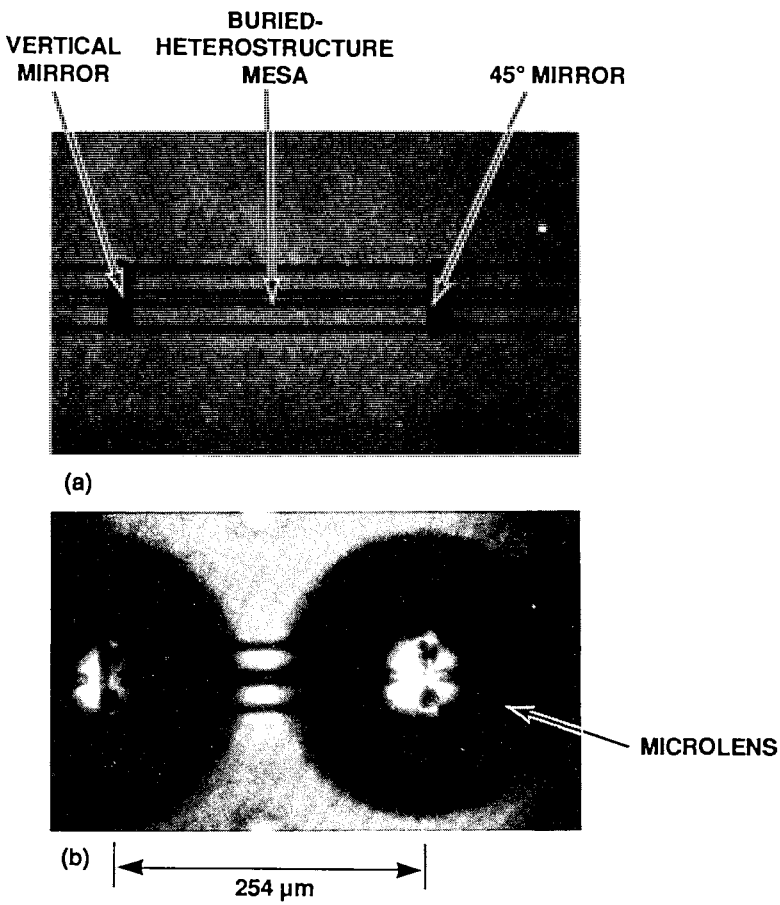

Fig. 40. (a) Visible micrograph of an integrated microlens-laser structure from the laser side. (b) Infrared (transmission) micrograph of the same structure also from the laser side, in which the underlying microlens can be seen. Note that the 45° mirror and buried-heterostructure waveguide are centered on concentrated spots of light produced by this microlens and an adjacent device.

is actually made into a spherical mirror to provide feedback for the laser oscillation, and the inner part is made into a lens to collimate the laser output. An actual profile of a microlens is shown in Fig. 39(b).

Since the buried-heterostructure gain region (Liau and Walpole, 1982) has a width of only approximately 1 μm, the alignment between the microlens and the 45° mirror is rather critical. Accurate alignment can be achieved by shining infrared light through the substrate and using the concentrated spot of light produced by the microlens itself as the reference. If optical feedback can be supplied to the laser cavity by other means, such as distributed feedback or distributed Bragg reflectors, the alignment requirements for the integrated lens is less critical. For example, Stegmüller *et al.* (1991) have recently demonstrated microlens integration utilizing distributed-feedback lasers with 11 mA threshold current and 5 mW output power.

Two micrographs of an integrated microlens-laser structure before metallization are shown in Fig. 40. Fig. 40(a) is an optical micrograph viewed from the laser side, and Fig. 40(b) is an infrared micrograph revealing a microlens on the other side of the substrate as well as the concentrated spots of light produced by this microlens and an adjacent device. Initial results for this device show pulsed threshold currents of 70–100 mA and a collimated output beam divergence of 1.25°. Although these threshold currents are high for buried-heterostructure devices, they represent only the initial results for a device still in its early stage of development. Further perfection of the fabrication technology is expected to improve the device performance. Questions concerning possible material degradation or dopant diffusion during the high-temperature treatment in the fabrication of the microlenses and mirrors also remain to be addressed.

IV. CONCLUSIONS

Differential quantum efficiency is a good measure of the ultimate performance as well as the overall optical quality of surface emitting lasers with integrated beam deflectors. The efficiencies that have been reported to date for these devices are summarized in Table I. For 0.8-μm wavelength lasers, only hybrid arrays have demonstrated total differential efficiency comparable to that obtainable from cleaved-facet edge emitting devices. In the AlGaAs/GaAs material system, substantial improvements have recently been made in the performance of monolithic arrays. Quantum efficiencies as high as 56% have been achieved in arrays of horizontal-cavity surface

Table I

Differential Quantum Efficiency of Surface Emitted Light from Diode Lasers with Integrated Beam Deflectors

Type of Deflector	Reference	Type of Laser	Wavelength (μm)	Surface Differential Quantum Efficiency (%)	Other Facet
Intracavity	SpringThorpe, 1977	Double heterostructure	0.8	6	Cleaved
	Hamao *et al.*, 1989	SQW	0.8	10	Cleaved
	Takamori *et al.*, 1989	Transverse junction stripe	0.8	24	Cleaved
	Ou *et al.*, 1991a	Broad-area GRIN-SCH	0.8	52	High reflectivity, etched
	Goodhue *et al.*, 1991	Strained-layer	0.8, 1.0	56	Etched (double ended arrays)
	Nam *et al.*, 1991	Strained-layer	1.0	28	High reflectivity, etched
Extracavity	Walpole and Liau, 1986	Buried heterostructure	1.3	50	High reflectivity, etched
	Yang *et al.*, 1986b	Large optical cavity	0.8	5	Cleaved
	Donnelly *et al.*, 1987	SQW SCH	0.8	20	Etched with deflector (double ended arrays)
	Puretz *et al.*, 1987	Multiple quantum well	0.8	8	Cleaved
	Shieh *et al.*, 1988	Gain-guided stripe	0.8	6	Cleaved
	Saito and Noguchi, 1989	Buried crescent	1.3	14	Cleaved
	Donnelly *et al.*, 1990	SQW GRIN-SCH hybrid	0.8	80	Cleaved, Si deflector (double ended arrays)
	Mutoh *et al.*, 1991	Buried crescent	1.3	5	Cleaved
	Stegmüller *et al.*, 1991	Buried heterostructure, distributed feedback	1.5	21	Cleaved
	Ou *et al.*, 1991	SQW GRIN-SCH	0.8	22	High reflectivity, etched
	Donnelly *et al.*, 1992	SQW GRIN-SCH	0.8	66	Etched with deflector (double ended arrays)
	Saito *et al.*, 1991	Buried heterostructure	1.5	8	High reflectivity, etched
	Kim and Larsson, 1991	Strained-layer	1.0	15	Etched with deflector (double ended arrays)

emitting laser diodes, both with intracavity deflectors and with extracavity deflectors. (Quantum efficiencies as high as 66% were recently obtained in arrays of lasers with extracavity reflectors (Donnelly *et al.*, 1992).) Threshold currents within 10% of those of cleaved-facet lasers have been obtained in arrays of lasers with extracavity reflectors. Based on these rapid improvements, it is anticipated that arrays with threshold current density and efficiency close to those of cleaved-facet lasers will be achieved in the near future.

In the case of the 1.3-μm wavelength lasers, the best result of 50%, obtained from devices fabricated by mass transport, should be compared with the typical 60–68% total DQE exhibited by double-heterostructure edge emitting lasers. In the GaInAsP/GaAs material system it should be possible to use mass transport to fabricate beam deflector devices that emit in the same wavelength regions as AlGaAs/GaAs devices (Groves *et al.*, 1990). This possibility and further improvement in dry etching technology suggest that still better performance can be expected in the future at any of the wavelengths of interest.

ACKNOWLEDGMENTS

The authors would like to thank the many people who contributed to the work performed at Lincoln Laboratory. In particular, we are indebted to C. A. Wang for providing most of the AlGaAs quantum-well material that was used. We also wish to thank R. J. Bailey, P. S. Day, G. D. Johnson, G. A. Lincoln, M. D. McAleese, S. M. McNeill, L. J. Missaggia, D. Mull, K. Rauschenbach, and J. D. Woodhouse for technical assistance, and K. J. Challberg for technical editing of the manuscript.

This work was sponsored by the Department of the Air Force.

REFERENCES

BLAKELY, J. M. (1973). *Introduction to the Properties of Crystal Surfaces*, Chap. 7, Pergamon, Oxford.

CHAO, C.-P., LAW, K-K. AND MERZ, J. L. (1991). "Low-threshold InGaAs/GaAs strained-layer ridge waveguide surface emitting lasers with two 45° angle etched internal total reflection mirrors," *Appl. Phys. Lett.* **59**, 1532.

CHEN, T. R., CHIU, L. C., YU, K. L., KOREN, U., HASSON, A., MARGALIT, S. AND YARIV, A. (1982). "Low-threshold InGaAsP terrace mass transport laser on semi-insulating substrate," *Appl. Phys. Lett.* **41**, 1115.

CHOI, H. K. AND WANG, C. A. (1990). "InGaAs/AlGaAs strained single quantum well diode lasers with extremely low-threshold current density and high efficiency," *Appl. Phys. Lett.* **57**, 321.

DONNELLY, J. P., GOODHUE, W. D., WINDHORN, T. H., BAILEY, R. J. AND LAMBERT, S. A. (1987). "Monolithic two-dimensional surface-emitting arrays of GaAs/AlGaAs diode lasers," *Appl. Phys. Lett.* **51**, 1138.

DONNELLY, J. P., BAILEY, R. J., WANG, C. A., SIMPSON, G. A. AND RAUSCHENBACH, K. (1988a). "Hybrid approach to two-dimensional surface-emitting diode laser arrays," *Appl. Phys. Lett.* **53**, 938.

DONNELLY, J. P., ANDERSON, K. K., WOODHOUSE, J. D., GOODHUE, W. D., YAP, D., GAIDIS, M. C. AND WANG, C. A. (1988b). "Some applications of ion beams in III–V compound semiconductor device fabrication," *Proc. Mater. Res. Soc. Symp.* **144**, 421.

DONNELLY, J. P., RAUSCHENBACH, K., WANG, C. A., GOODHUE, W. D. AND BAILEY, R. J. (1989). "Two-dimensional surface-emitting arrays of GaAs/AlGaAs diode lasers," *Proc. SPIE* **1043**, 92.

DONNELLY, J. P. (1990). "Two-dimensional surface-emitting arrays of GaAs/AlGaAs diode lasers," *Lincoln Lab. J.* **3**, 361.

DONNELLY, J. P., RAUSCHENBACH, K., WANG, C. A., BAILEY, R. J., WALPOLE, J. N., MISSAGGIA, L. J., WOODHOUSE, J. D., CHOI, H. K., O'DONNELL, F. J. AND DIADIUK, V. (1990). "High-power hybrid two-dimensional surface-emitting AlGaAs diode laser arrays," *Proc. SPIE* **1219**, 255.

DONNELLY, J. P., BAILEY, R. J., LINCOLN, G. A., GOODHUE, W. D., WANG, C. A. AND JOHNSON, G. D. (1991). "Monolithic two-dimensional surface-emitting arrays of AlGaAs horizontal-cavity diode lasers with etched facets and external parabolic deflecting mirrors," *Solid State Research Report*, Lincoln Laboratory, MIT, 1991:4, p. 3.

DONNELLY, J. P., GOODHUE, W. D., BAILEY, R. J., LINCOLN, G. A., WANG, C. A. AND JOHNSON, G. D. (1992). "High quantum efficiency monolithic arrays of surface-emitting AlGaAs diode lasers with dry-etched vertical facets and parabolic deflecting mirrors," *Appl. Phys. Lett.* **61**, 1487.

DYMENT, J. C., NORTH, J. C. AND D'ASARO, L. A. (1973). "Optical and electrical properties of proton-bombarded AlGaAs," *J. Appl. Phys.* **44**, 207.

FANG, Z.-J. AND WANG, S. (1984). "Longitudinal mode behavior and tunability of separately pumped (GaAs) As lasers," *Appl. Phys. Lett.* **44**, 13.

FOYT, A. G., LINDLEY, W. T., WOLFE, C. M. AND DONNELLY, J. P. (1969). "Isolation of junction devices in GaAs using proton bombardment," *Solid-State Electron.* **12**, 209.

GEIS, M. W., LINCOLN, G. A., EFREMOW, N. AND PIANCENTINI, W. J. (1981). "A novel anisotropic dry etching technique," *J. Vac. Sci. Technol.* **19**, 1390.

GOODHUE, W. D., RAUSCHENBACH, K., WANG, C. A., DONNELLY, J. P., BAILEY, R. J. AND JOHNSON, G. D. (1990). "Monolithic two-dimensional GaAs/AlGaAs

laser arrays fabricated by chlorine ion-beam assisted etching," *J. Electron. Mater.* **19**, 463.

GOODHUE, W. D., DONNELLY, J. P., WANG, C. A., LINCOLN, G. A., RAUSCHENBACH, K., BAILEY, R. J. AND JOHNSON, G. D. (1991). "Monolithic two-dimensional surface-emitting strained-layer InGaAs/AlGaAs and AlInGaAs/AlGaAs diode laser arrays with over 50% differential quantum efficiencies," *Appl. Phys. Lett.* **59**, 632.

GROVES, S. H., LIAU, Z. L., PALMATEER, S. C. AND WALPOLE, J. N. (1990). "GaInP mass transport and GaInP/GaAs buried-heterostructure lasers," *Appl. Phys. Lett.* **56**, 312.

HAMAO, N., SUGIMOTO, M., TAKADO, N., TASHIRO, Y., IWATA, H., YUSSA, T. AND ASAKAWA, K. (1989). "Surface-emitting GaAs/AlGaAs lasers with dry-etched 45° total reflecting mirrors," *Appl. Phys. Lett.* **54**, 2389.

HARRIOTT, L. R., SCOTTI, R. E., CUMMINGS, K. D. AND AMBROSE, A. F. (1986). "Micromachining of integrated optical structures," *Appl. Phys. Lett.* **48**, 1704.

JANSEN, M., YANG, J. J., HEFLINGER, L., OU, S. S., SERGANT, M., HUANG, J., WILCOX, J., EATON, L. AND SIMMONS, W. (1989). "Coherent operation of injection-locked monolithic surface-emitting diode laser arrays," *Appl. Phys. Lett.* **54**, 2634.

JANSEN, M., YANG, J. J., OU, S. S., SERGANT, M., MAWST, L., ROZENBERGS, J., WILCOX, J. AND BOTEZ, D. (1991). "Monolithic two-dimensional surface-emitting diode laser arrays mounted in the junction-down configuration," *Appl. Phys. Lett.* **59**, 2663.

KIM, J.-H., LANG, R. J., LARSSON, A., LEE, L. P. AND NARAYANAN, A. A. (1990). "High-power AlGaAs/ GaAs single quantum-well surface-emitting lasers with integrated 45° beam deflectors," *Appl. Phys. Lett.* **57**, 2048.

KIM, J.-H. AND LARSSON, A. (1991). "Pseudomorphic $In_yGa_{1-y}As$/ $GaAs/Al_xGa_{1-x}$ As single quantum-well surface-emitting lasers with integrated 45° beam deflectors," *Appl. Phys. Lett.* **58**, 7.

LEGER, J. R., HOLTZ, M., SWANSON, G. J. AND VELDKAMP, W. B. (1988). "Coherent laser beam addition: an application of binary-optics technology," *Lincoln Lab. J.* **1**, 225.

LIAU, Z. L. AND WALPOLE, J. N. (1982). "A novel technique for GaInAsP/InP buried heterostructure laser fabrication," *Appl. Phys. Lett.* **40**, 568.

LIAU, Z. L., WALPOLE, J. N. AND TSANG, D. Z. (1984). "Low threshold GaInAsP/InP buried-heterostructure lasers with a chemically etched and mass transported mirror," *Appl. Phys. Lett.* **44**, 945.

LIAU, Z. L. AND WALPOLE, J. N. (1985). "Surface-emitting GaInAsP/InP laser with low threshold current and high efficiency," *Appl. Phys. Lett.* **46**, 115.

LIAU, Z. L. AND WALPOLE, J. N. (1987). Large monolithic two-dimensional arrays of GaInAsP/InP surface-emitting diode lasers," *Appl. Phys. Lett.* **50**, 528.

LIAU, Z. L., WALPOLE, J. N., TSANG, D. Z. AND DIADIUK, V. (1988a). "Characterization of mass-transported *p*-substrate GaInAsP/InP buried-heterostructure lasers with analytical solutions for electrical and thermal resistances," *IEEE J. Quantum Electron.* **24**, 36.

LIAU, Z. L., DIADIUK, V., WALPOLE, J. N. AND MULL, D. E. (1988b). "Large-numerical aperture InP lenslets by mass transport," *Appl. Phys. Lett.* **52**, 1859.

LIAU, Z. L., DIADIUK, V., WALPOLE, J. N. AND MULL, D. E. (1989). "Gallium phosphide microlenses by mass transport," **55**, 97.

LIAU, Z. L., WALPOLE, J. N., MISSAGGIA, L. J. AND MULL, D. E. (1990). "GaInAsP/InP buried-heterostructure surface-emitting diode laser with monolithic integrated bifocal microlens," *Appl. Phys. Lett.* **56**, 1219.

LIAU, Z. L. AND ZEIGER, H. J. (1990). "Surface-energy-induced mass-transport phenomenon in annealing of etched compound semiconductor structures: theoretical modeling and experimental confirmation," *J. Appl. Phys.* **67**, 2434.

LIAU, Z. L. (1991). "Prevention of In evaporation and preservation of smooth surface in thermal annealing and mass transport of InP," *Appl. Phys. Lett.* **58**, 1869.

MISSAGGIA, L. J., WALPOLE, J. N., LIAU, Z. L. AND PHILLIPS, R. J. (1989). "Microchannel heat sinks for two-dimensional high-power-density diode laser arrays," *IEEE J. Quantum Electron.* **25**, 1988.

MISSAGGIA, L. J. AND WALPOLE, J. N. (1991). "A microchannel heat sink with alternating directions of flow in adjacent channels," *Proc. SPIE* **1582**, p. 106; also *Solid State Research Report*, Lincoln Laboratory, MIT, 1990: **4**, p. 1.

MULLINS, W. W. (1959). "Flattening of a nearly plane solid surface due to capillarity," *J. Appl. Phys.* **30**, 77.

MUNDINGER, D., BEACH, R., BENETT, S., SOLARZ, R., KRUPLE, W., STAVAN, R. AND TUCKERMAN, D. (1988). "Demonstration of high-performance silicon microchannel heat exchange for laser diode array cooling," *Appl. Phys. Lett.* **53**, 1030.

MUTOH, K., WAKABAYASHI, S., TOYODA, Y. AND NAKAJIMA, M. (1991). "Simultaneous fabrication of vertical and 45° mirrors of InP for surface-emitting lasers using inclined Cl ion beams," *Jpn. J. Appl. Phys.* **30**, 67.

NAGAI, H., NOGUCHI, Y. AND MATSUOKA, T. (1985). "Thermal deformation of surface corrugations on InGaAsP crystals," *J. Cryst. Growth* **71**, 225.

NAM, D. W., WAARTS, R. G., WELCH, D. F. AND SCIFRES, D. R. (1991). "High power monolithic two-dimensional arrays of single mode surface emitting lasers," *IEEE Lasers and Electro-Optics Society 1991 Annual Meeting Conference Digest*, paper SDL 2.5, p. 15.

OU, S. S., YANG, J. J., JANSEN, M., SERGANT, M., MAWST, L. J. AND WILCOX, J. Z. (1991a). "High performance surface-emitting lasers with 45° intracavity micromirrors," *Appl. Phys. Lett.* **58**, 16.

OU, S. S., JANSEN, M., YANG, J. J. AND SERGANT, M. (1991b). "High power cw operation of GaAs/GaAlAs surface-emitting lasers mounted in the junction-up configuration," *Appl. Phys. Lett.* **59**, 1037.

OU, S. S., JANSEN, M., YANG, J. J., MAWST, J. J. AND ROTH, T. J. (1991c). "High-power cw operation of InGaAs/GaAs surface-emitting lasers with 45° intracavity micromirrors," *Appl. Phys. Lett.* **59**, 2085.

PHILLIPS, R. J. (1987). "Forced-convection, liquid-cooled microchannel heat sinks," M.S. Thesis, MIT, Cambridge, MA.

PHILLIPS, R. J., GLICKSMAN, L. R. AND LARSON, R. (1988). "Forced-convection, liquid-cooled, microchannel heat sinks for high-power microelectronics," In *Cooling Technology for Electronic Equipment*, ed. W. Aung, p. 295, Hemisphere, New York.

PHILLIPS, R. J. (1988). "Microchannel Heat Sinks," *Lincoln Lab. J.* **1**, 31; also errata, p. 258.

PURETZ, J., DEFREEZ, R. K., ELLIOTT, R. A., ORLOFF, J. AND PAOLI, R. L. (1987). "300 mW operation of a surface-emitting phase-locked array of diode lasers," *Electron. Lett.* **23**, 130.

RALSTON, J. D., SCHAFF, W. J., BOUR, D. P. AND EASTMAN, L. F. (1989). "Room-temperature exciton eletroabsorption in partially intermixed GaAs/AlGaAs quantum-well waveguides," *Appl. Phys. Lett.* **54**, 534.

SAITO, H. AND NOGUCHI, Y. (1989). "A reflection-type surface-emitting 1.3 μm InGaAsP/InP laser array with microcoated reflector," *Jpn. J. Appl. Phys.* **28**, L 1239.

SAITO, H. AND KONDO, Y. (1991). "4×4 surface-emitting 1.55 μm InGaAsP/InP laser arrays with microcoated reflectors fabricated by reactive ion etching," *Jpn. J. Appl. Phys.*, Part-2-Letters **30**, L599.

SASAKI, S. AND KISHIMOTO, T. (1986). "Optimal structure for microgrooved cooling fin for high-power LSI devices," *Electron. Lett.* **22**, 1332.

SHIEH, C. L., MANTZ, J., ALAVI, K. AND ENGELMANN, R. W. H. (1988). "Low threshold current surface-emitting AlGaAs/GaAs laser with 45° metallized reflector," *Electron. Lett.* **24**, 343.

SPRINGTHORPE, A. J. (1977). "A novel double-heterojunction p-n junction laser," *Appl. Phys. Lett.* **31**, 524.

STEGMÜLLER, B., WESTERMEIER, H., THULKE, W., FRANZ, G. AND SACHER, D. (1991). "Surface-emitting InGaAsP/InP distributed feedback laser diode at 1.53 μm with monolithic integrated microlens," *IEEE Photon. Technol. Lett.* **3**, 776.

TAKAMORI, T., COLDREN, L. A. AND MERZ, J. L. (1989). "Folded-cavity transverse junction stripe surface-emitting laser," *Appl. Phys. Lett.* **55**, 1053.

TAKAMORI, T., COLDREN, L. A. AND MERZ, J. L. (1990). "Lasing characteristics of a continuous-wave operated folded-cavity surface-emitting laser," *Appl. Phys. Lett.* **56**, 2267.

TIHANYI, P., WAGNER, D. K., ROZA, A. J., VOLLMER, H. J., HARDING, C. M., DAVIS, R. J. AND WOLF, E. D. (1987). "High-power AlGaAs/GaAs single quantum-well lasers with chemically assisted ion beam etched mirrors," *Appl. Phys. Lett.* **50**, 1640.

TUCKERMAN, D. B. AND PEASE, R. F. W. (1981). "High performance heat sinks for VLSI," *IEEE Electron Device Lett.* **2**, 126.

WALPOLE, J. N. AND LIAU, Z. L. (1986). "Monolithic two-dimensional arrays of high power GaInAsP/InP surface-emitting diode lasers," *Appl. Phys. Lett.* **48**, 1636.

WALPOLE, J. N., LIAU, Z. L., MISSAGGIA, L. J. AND YAP, D. (1987). "Diode

lasers with cylindrical mirror facets and reduced beam divergence," *Appl. Phys. Lett.* **50**, 1219.

WANG, C. A., CHOI, H. K. AND CONNORS, M. K. (1989). "Highly uniform GaAs/AlGaAs GRIN-SCH-SQW diode lasers grown by organometallic vapor phase epitaxy," *IEEE Photon. Technol. Lett.* **1**, 351.

WANG, C. A. (1990). "A new organometallic vapor phase epitaxy reactor for highly uniform epitaxy," *Lincoln Lab. J.* **3**, 3.

WANG, C. A., WALPOLE, J. N., CHOI, H. K. AND MISSAGGIA, L. J. (1991a). "AlInGaAs-AlGaAs strained single quantum-well diode lasers," *IEEE Photon. Technol. Lett.* **3**, 4.

WANG, C. A., WALPOLE, J. N., MISSAGGIA, L. J., DONNELLY, J. P. AND CHOI, H. K. (1991b). "AlInGaAs/AlGaAs separate-confinement heterostructure strained single quantum-well diode lasers grown by organometallic vapor phase epitaxy," *Appl. Phys. Lett.* **58**, 2208.

WINDHORN, T. H. AND GOODHUE, W. D. (1986). Monolithic GaAs/AlGaAs diode laser/deflector devices for light emission normal to the surface," *Appl. Phys. Lett.* **48**, 1675.

WU, M., CHEN, Y. J., HRYNIEWICZ, J., HO, Y-P. AND MERGERIAN, D. (1991). "A monolithic individually addressable two-dimensional surface-emitting diode laser array," in *IEEE Digest of the IEEE Lasers and Electro-Optics Society Summer Topical Meetings*, p. 51, New York.

YANG, J. J., JANSEN, M. AND SERGANT, M. (1986a). "Surface-emitting GaAlAs/GaAs laser with etched mirrors," *Electron. Lett.* **22**, 438.

YANG, J. J., SERGANT, M., JANSEN, M., OU, S. S., EATON, L. AND SIMMONS, W. W. (1986b). "Surface-emitting GaAlAs/GaAs linear laser arrays with etched mirrors," *Appl. Phys. Lett.* **49**, 1138.

YAP, D., WALPOLE, J. N. AND LIAU, Z. L. (1988). "InGaAsP/InP buried-heterostructure lasers with concurrent fabrication of the stripes and mirrors," *Appl. Phys. Lett.* **53**, 1260.

YIH, S.-J. AND LEE, S.-C. (1990). "AlGaAs/GaAs surface emitting laser diode with curved reflector," *Electron Lett.* **26**, 1506.

Chapter 6

SECOND-ORDER GRATING SURFACE EMITTING THEORY

Amos Hardy*, **David F. Welch**, and **William Streifer**

Spectra Diode Laboratories, San Jose, California

I. INTRODUCTION

Grating coupled surface emitting (GSE) diode lasers are devices with the potential of generating very high levels of coherent radiation from large areas. The lasers employ a sequence of quantum-well gain sections interposed with second-order gratings that provide radiative output coupling, distributed feedback, and power transmission to adjacent sections for coherent locking (Fig. 1). Such GSE structures have been demonstrated to emit substantial output power in short pulses (Hammer *et al.*, 1987; Macomber *et al.*, 1987; Noda *et al.*, 1988; Kojima *et al.*, 1988; Carlson *et al.*, 1988a,b; Evans *et al.*, 1989; Welch *et al.*, 1989a,c), and in the cw mode of operation (Mott and Macomber, 1989). Furthermore, cw thresholds as low as 20 mA for single stripe (Welch *et al.*, unpublished) and 230 mA for pulsed broad areas lasers (Welch *et al.*, 1989b) have also been demonstrated, as well as external differential quantum efficiencies as high as 65% (Parke *et al.*, 1990).

We limit ourselves, here, to the analysis of second-order gratings, used for the coupling of multiple gain sections. Other grating structures, such as nonresonant grating couplers (Buus *et al.*, 1989), vertical-cavity distributed feedback (DFB) and distributed Bragg reflectors (DBR) lasers, have also been reported (Schaus *et al.*, 1989; Dziura and Wang, 1989; Jewell *et al.*, 1989) are not discussed due to the difficulties in 2-D coherent coupling.

*On leave from Tel Aviv University, Israel.

ISBN 0-12-244070-6

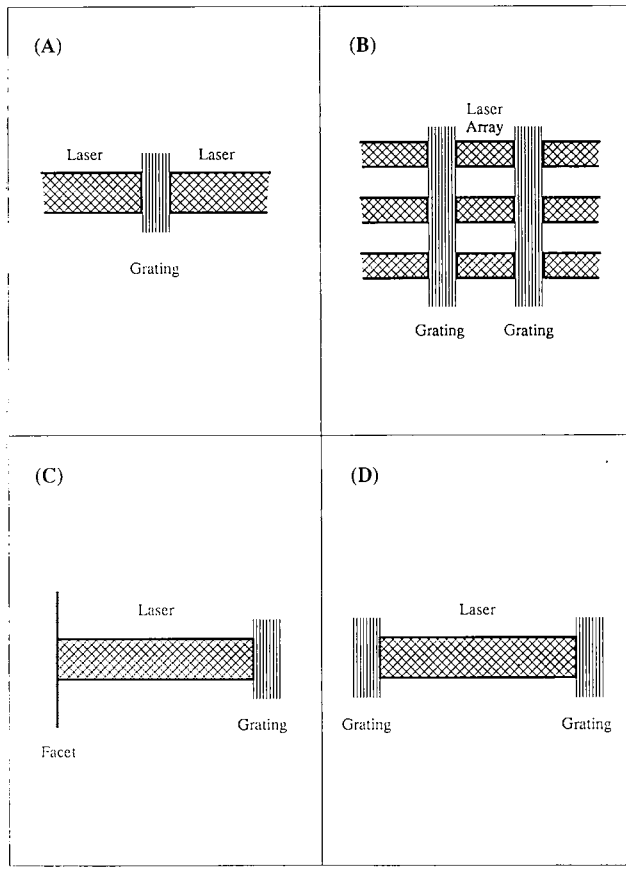

Fig. 1. Various grating-coupled surface-emitting laser geometries.

The behavior of GSE structures is quite complicated and depends on numerous factors. First, there are lateral and longitudinal locking. For the structures shown in Fig. 1, lateral phase locking may be provided either by Y-junction arrays, evanescent coupling, or other means. For simplicity, we consider, in this chapter, only longitudinal effects, the inclusion of lateral effects is straightforward (Amantea *et al.*, 1989). In the longitudinal direction, there exists a sequence of gain and grating sections. The gain sections are pumped and most often the grating sections are composed of the same material. However, the grating regions are generally unpumped so that they display saturable absorption. If desired, the gain sections may be designed and fabricated to be as nearly identical as possible. Similarly, one may strive to obtain virtually identical grating sections. In practice, the sections

may differ in various ways. The material compositions will not be precisely constant over the wafer, the layer dimensions will vary from section to section, and the lengths will not be identical. The pumping currents in the gain sections also may differ.

The gratings will likely have identical periodicity depending on the fabrication technique employed, but as a result of spatial variations in composition and dimensions the propagation constants will differ spatially along the length of the laser in parts of the wafer. Still other factors affecting the behavior are the grating teeth shapes and heights, the lengths of the gratings, their relative phases, and the non-linear effects caused by saturable absorption in the grating sections.

Relative phase relationships of light reflected and transmitted from the gratings, in particular, profoundly affect device operation. Although one may view these as fixed, once the structure has been fabricated, the presence of intensity dependent refractive index (anti-guiding) in the gain sections, has the effect of changing the relative phases as a function of the saturated charge in each gain section. In addition to all these effects, one must also account for temperature variations over the wafer and as a function of time, especially in dynamic situations.

The richness of phenomena influencing device behavior may be viewed as a cause for concern, since the simultaneous control of dimensions, materials, and temperature are difficult. On the other hand, the degrees of freedom are large, which implies that by careful analysis, insight, and clever design, one may achieve a system that is stable to dimensional and other variations from chip-to-chip or with time.

The general case of many emitters is extremely complex. However, to obtain some understanding of structures with many grating regions, we begin with a study of second-order gratings and their properties. We continue with threshold analysis of the simplest laser, which is composed of one gain section located between two grating sections, and then study the two-gain, three-grating GSE, which illustrates many of the effects characteristic of the longer structures.

Corrugated waveguide structures have been analyzed previously either as passive optical elements or as components of lasers (Kogelnik and Shank, 1972; Yariv, 1973; Kogelnik, 1975; Yariv and Nakamura, 1977; Peng and Tamir, 1974; Streifer *et al.*, 1976a; Streifer *et al.*, 1976b; Streifer *et al.*, 1977; Yamamoto *et al*; 1978; Kazarinov and Henry, 1985; Henry *et al*; 1985). In the last application, both DBR and DFB configurations were employed to select and stabilize wavelength. More recently, corrugations have been used in high-power DBR, surface-emitting diode lasers and laser arrays, and

several laboratories are involved in the fabrication of such devices (Noda *et al.*, 1988; Kojima *et al.*, 1988; Carlson *et al.*, 1988a,b; Welch *et al.*, 1989a,b). To date, few analyses have considered the behavior of a grating in the resonant situation, wherein the periodic structure provides reflection, output coupling (radiation), and transmission to another gain section for purposes of mutual injection locking (Hardy *et al.*, 1989).

Consider, for example, the lasers illustrated in Figs. 1(a) and 1(b). In Fig. 1a two gain sections are separated by a grating and in Fig. 1(b) several gain and grating sections alternate. In such geometries, it is essential to determine the light transmitted from one gain section through the grating to the next gain section. The theory is also applicable to the configurations shown in Figs. 1(c) and 1(d), where a grating and cleaved facet form reflectors and where two gratings act as reflectors, respectively. In these cases, transmission is less essential and, as will later be shown, it is even beneficial to reduce it to a minimum in order to increase the external quantum efficiency. The intent of the analysis given in Section II is to increase the understanding and to provide design guidance for such devices as shown in Fig. 1. Furthermore, the results form the basis for the calculation of radiation patterns from GSEs. The analysis of Section II is limited to second-order gratings fabricated on the surface of a passive waveguide, but the theory is equally applicable if the grating is overcoated with a dielectric or (with slight modification) a metal. The formulation is applicable to arbitrary-shaped grating teeth, and a single-mode waveguide whose dimensions, refractive indices, and absorption loss may be varied. Furthermore, we have included the possibility of a reflector located below the waveguide in the substrate to determine its effect on reflection, transmission, and the fractional power radiated in both directions orthogonal to the propagation direction.

In Section III, we analyze the simplest laser that utilizes DBRs, namely a gain section located between two grating sections as shown in Fig. 1(d). Even this relatively simple device displays a variety of phenomena, and clearly it is necessary to understand the many factors influencing the behavior before one can design more complicated devices. Section III analyzes such a laser at threshold and presents the results for several DBR geometries. The analysis is carried out for arbitrary gratings, as are studied in Section II (see also Hardy *et al.*, 1989). That is, the tooth shape and height, the waveguide losses, the presence of a substrate reflector, the section lengths, and indeed the waveguide dimensions and compositions can all be specified. Furthermore, the two grating sections need not be identical. A formulation, which retains this degree of generality, has been developed to

solve for the longitudinal modes of the structure. For each mode the net gain required for threshold and the lasing wavelength are determined, and the differential efficiency and radiation pattern are calculated.

In Section IV, we analyze GSEs that have two gain sections and three gratings in the longitudinal direction. This is the simplest device that includes the effects of light transmitted from one gain section into the other via a grating section. Combined with the light reflected by the grating, back into the gain section, the device becomes sensitive to small changes in its parameters due to phase variations. In Section IV.E.1 we analyze the effects of asymmetric pumping, whereas in Section IV.E.2 the effects of uneven gain sections are explored.

Our objective in Section IV is not to exhaustively quantify the dependence on the large number of parameters that determine device behavior. Rather, we present a formulation that together with earlier sections can be used to evaluate the factors mentioned above. Although only a limited number of situations are considered herein, we hope they are illustrative of some considerations for a successful design. The ultimate objective is to achieve a design that is relatively insensitive to some parameter variations. Such a design is proposed and analyzed in Section IV.E.3. The results are not completely general in that they apply to the two-gain, three-grating case, and they are threshold results, but they are indicative of the directions that can be explored.

The extension of the formulation to a larger number of gain and grating regions is outlined in Section V. An expression for the external quantum efficiency is provided in Section VI.D. The number of parameters that determine behavior is much larger than in the cases discussed in Sections II, III, and IV. Quite a few different designs are possible and are currently under further exploration.

II. SECOND-ORDER GRATINGS

A. Propagating Modes and Partial Waves

Consider the geometry described in Fig. 2, where, for simplicity, only four layers are illustrated. The TE mode satisfies the scalar wave equation

$$\frac{\partial^2 E_y}{\partial x^2}+\frac{\partial^2 E_y}{\partial z^2}+k_0^2 n^2(x, z)E_y(x, z)=0 \tag{1}$$

where k_0 is the free-space wave number and $n^2(x, z)$ is the refractive index

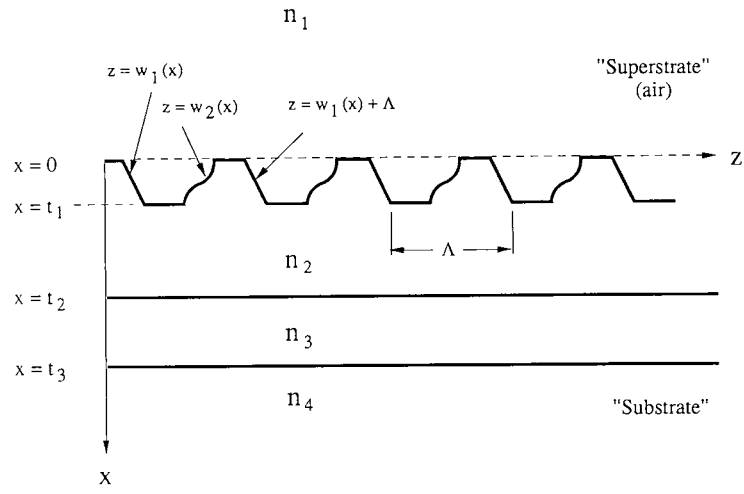

Fig. 2. The waveguide and grating geometry used in the examples.

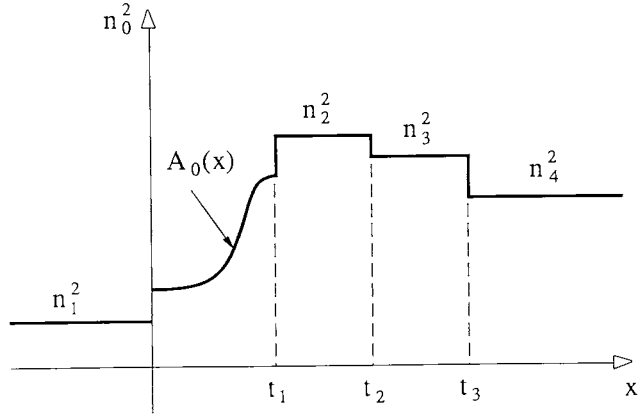

Fig. 3. Refractive index squared of the "unperturbed" waveguide.

distribution squared, which is periodic in z (see Section VI.A). Thus we write

$$n^2(x, z) = [n_0(x) + i\tilde{\alpha}(x)/k_0]^2 + \sum_{\substack{q=-\infty \\ q\neq 0}}^{\infty} A_q(x) \exp(i2\pi qz/\Lambda) \qquad (2)$$

where Λ is the grating period and the first term, in the squared brackets, represents the unperturbed waveguide. The grating periodicity is treated as perturbation and is represented by the $A_q(x)$ Fourier coefficients. The $A_0(x)$ term has been absorbed into the first, squared bracket term (Fig. 3), where

$\tilde{\alpha}(x)$ represents the non-periodic gain ($\tilde{\alpha} < 0$) or loss ($\tilde{\alpha} > 0$) [Section VI.a]. We note that the series expansion in Eq. (2) is only valid for the region $0 \leq z \leq L$ where the grating exists. Thus, within the same region, the field is expanded in partial waves, namely;

$$E_y(x, z) = \sum_{m=-\infty}^{\infty} E_m(x, z) \exp(i\beta_m z) \tag{3}$$

where

$$\beta_m = \beta_0 + 2\pi m/\Lambda \tag{4}$$

and β_0 and $E_m(x, z)$ are to be determined.

In this work we are interested in the resonant case, for which $\beta_{-N} = -\beta_0$ for some integer $m = -N$. To be more specific, surface emitting gratings are typically second order, that is, for $m = -2$, we have

$$\beta_{-1} = 0 \tag{5a}$$

$$\beta_{-2} = -\beta_0 \tag{5b}$$

where the $m = -1$ wave is radiated away in a direction normal to the grating (there are two such waves: one radiates into the air and the other into the substrate), and the $m = -2$ wave is the backward propagating mode. For this resonant situation, both E_0 and E_{-2} are coherent guided waves and both must be considered of comparable importance in the calculation. Using Eq. (4) one finds that the grating period Λ and β_0 are related by the Bragg condition

$$\beta_0 = 2\pi/\Lambda. \tag{6}$$

In the non-resonant situation, Eq. (5) is not satisfied (nor is there any other integer m for which $\beta_m = -\beta_0$). Such gratings are used as input or output couplers for the mode propagating in the waveguide and radiate in a direction that is different than the normal to the grating (see, for example, Streifer *et al.*, 1976b,c). Based on Floquet's theorem, the field E_y is expressed as an infinite series of partial waves in a form similar to Eq. (3) except that $E_m = E_m(x)$ is independent of z. The Floquet theorem is exact for an infinitely long grating but also is a good approximation for E_y in the non-resonant case, when the grating has a finite length. A partial wave at (x, z_0) where $0 < z_0 < L$ and $x < 0$, describes a decaying plane wave (β_0 is complex due to radiation loss) that originates from the grating teeth at some $z < z_0$. Thus some partial waves, in the Floquet expansion, originate at $z < 0$ where the grating does not exist. Similarly, plane waves propagating in the $-z$ direction may originate at $z > L$. Nevertheless, the Floquet expansion

is still a good approximation since, usually, only a small fraction of the total power is carried by any of these partial waves. In the resonant case the situation is different. Since $\mathrm{Im}\,(\beta_m)$ is the same for all m, the partial waves in the Floquet expansion have all the same exponential decaying rate. In particular the counter propagating guided wave E_{-2} does not vanish at $z = L$. Thus, unless light is injected into the grating section at $z = L$, that match E_{-2} both in amplitude and phase, the Floquet expansion fails to describe the actual physical situation. Therefore, one has to lift the restriction on E_m and we assume that it varies with z, i.e., $E_m = E_m(x, z)$. Since $E_m(x, z)$ is yet to be specified, the modified Floquet's expansion of Eq. (3) is always correct. However, it is implicitly assumed that $E_m(x, z)$ vary slowly with z, and the $m = 0$ term is the one which remains in the absence of the grating. In the resonant case, the guided modes ($m = 0, -2$) are expressed in the form

$$E_0(x, z) = R(z)E_0(x) \tag{7a}$$

$$E_{-2}(x, z) = S(z)E_0(x) \tag{7b}$$

where $R(z)$ and $S(z)$ are slowly varying complex functions that are to be determined and $E_0(x)$ satisfies

$$\frac{d^2E_0}{dx^2} + [k_0^2 n_0^2(x) - \beta^2]E_0 = 0. \tag{8}$$

Under the assumption that all the partial waves have a similar z-dependence, i.e.,

$$E_m(x, z) = R(z)E_m^{(0)}(x) + S(z)E_m^{(-2)}(x), \qquad m \neq 0, -2, \tag{9}$$

we find after substantial manipulation (Streifer *et al.*, 1977) that $R(z)$ and $S(z)$ satisfy the modified coupled differential equations

$$dR/dz = (-\alpha + i\delta + i\zeta_1)R + i(\kappa^* + \zeta_2)S \tag{10a}$$

$$-dS/dz = (-\alpha + i\delta + i\zeta_1)S + i(\kappa + \zeta_4)R \tag{10b}$$

where

$$\alpha = \frac{k_0}{\beta_0 Q}\int_{-\infty}^{\infty} n_0(x)\tilde{\alpha}(x)E_0^2(x)\,dx \tag{11}$$

is the mode gain or loss,

$$Q = \int_{-\infty}^{\infty} E_0^2(x)\,dx \tag{12}$$

and κ is the coupling coefficient given by

$$\kappa = \frac{k_0^2}{2\beta_0 Q}\int_0^{t_1} A_{-2}(x)E_0^2(x)\,dx. \tag{13}$$

Note that the integral in Eq. (13) is restricted to the grating's teeth section since $A_q(x) \equiv 0$ outside that region. For a rectangular grating whose teeth occupy half a period, $A_{-2}(x) = 0$, and, therefore, also $\kappa = 0$, but as will be later shown, the reflection is non-zero. In Eq. (10), δ is a measure of the wavelength deviation from the Bragg condition given by (6) namely

$$\delta = \beta - \beta_0. \tag{14}$$

The other constants in (10a) and (10b) are defined below, but first we note that the same constant appears in both equations. Beginning with two different constants, ζ_1 and ζ_3, it can be shown by an involved mathematical argument that they are in fact identical. Furthermore, if the grating teeth are symmetrical, ζ_2 and ζ_4 are related by

$$\zeta_2 = (\kappa^*/\kappa)\zeta_4. \tag{15}$$

In general the constants are defined by the following summations

$$\begin{aligned} \zeta_1 &= \sum_{\substack{q=-\infty \\ q\neq 0,2}}^{\infty} \eta_{q,-q'}^{(0)}, \qquad \zeta_3 = \sum_{\substack{q=-\infty \\ q\neq 0,-2}}^{\infty} \eta_{q,-2-q'}^{(-2)} \\ \zeta_2 &= \sum_{\substack{q=-\infty \\ q\neq 0,2}}^{\infty} \eta_{q,-q'}^{(-2)}, \qquad \zeta_4 = \sum_{\substack{q=-\infty \\ q\neq 0,-2}}^{\infty} \eta_{q,-2-q'}^{(0)} \end{aligned} \tag{16}$$

where

$$\eta_{r,s}^{(j)} = (k_0^2/2\beta_0) \int_0^{t_1} A_r(x) E_0(x) E_s^{(j)}(x)\, dx, \qquad j = 0, -2 \tag{17}$$

and the partial waves $E_s^{(j)}(x)$ are the solutions of

$$\frac{d^2 E_m^{(j)}}{dx^2} + [k_0^2 n_0^2(x) - \beta_m^2] E_m^{(j)} = -k_0^2 A_{m-j}(x) E_0(x), \qquad j = 0, -2, \quad m \neq j. \tag{18}$$

Since $E_{-q}^{(0)}(x)$ is generated by the wave propagating in the $+z$ direction, ξ_1 represents the reaction of all partial waves, both radiating and decaying, back on the $+z$ wave. Similarly, ξ_3 $(=\xi_1)$ represents the reaction of all partial waves excited by the $-z$ wave back on itself. Note that the guided modes $E_0(x, z)$ and $E_{-2}(x, z)$ are not included in these summations; their effect is represented by the coupling coefficient κ [see Eq. (13)]. The quantities ξ_2 and ξ_4 differ from ξ_1. They represent coupling effects via the partial waves and are "corrections" to the coupling coefficient. Thus, for rectangular gratings whose teeth occupy half a period, the coupling coefficient is zero

but the "corrected" one is not. Solutions to Eqs. (8) and (18) are discussed in Section VI.B.

B. Symmetry Relations

1. *Grating Translation*

Suppose the grating is shifted relative to the origin by an arbitrary distance $\Delta z = d$ such that $w_1(x) \to w_1(x) + d$ (w_1 is modified to $w_1 + d$) and $w_2(x) \to w_2(x) + d$ (see Fig. 2). One finds that $A_q(x) \to A_q(x) \exp(-i2\pi qd/\Lambda)$ [see definition of $A_q(x)$ in Section VI.A]. As a result, $\xi_1 \to \xi_1$, $\xi_2 \to \xi_2 e^{-i\phi}$ and $\xi_4 \to \xi_4 e^{i\phi}$ where $\phi = 4\pi d/\Lambda$. The last term in each of the coupled mode equations (10) is multiplied by either $e^{-i\phi}$ or $e^{+i\phi}$ and, therefore, with boundary conditions of $R(0) = R_0$ and $S(L) = 0$, the $R(z)$ wave remains the same whereas $S(z) \to S(z)\, e^{i\phi}$. The partial waves also have a phase change $E_m^{(j)}(x) \to E_m^{(j)}(x) \exp[-i2\pi(m-j)d/\Lambda]$.

2. *Grating Reversal*

Since a grating translation results, as explained above, in constant phase shifts, we may assume with no loss of generality that the x-axis is located on one of the grating teeth (as in Fig. 2). Taking the mirror image through the x-axis we find that $w_1(x)x \to \Lambda - w_2(x)$ and $w_2(x) \to \Lambda - w_1(x)$. Therefore, using the defining equations, one finds that $A_q(x) \to A_q^*(x)$, $\kappa \to \kappa^*$, $\xi_1 \to \xi_3$, and $\xi_3 \to \xi_1$. Since $\xi_1 = \xi_3$ in the first place, neither is affected by the grating reversal operation. On the other hand, ξ_2 and ξ_4 are interchanged namely $\xi_2 \to \xi_4$ and $\xi_4 \to \xi_2$. The coupled mode equations (10) are the same except that $\kappa + \xi_4$ and $\kappa^* + \xi_2$ are interchanged. Thus, for boundary conditions of $R(0) = R_0$ and $S(L) = 0$, we find that $R(z)$ is unchanged whereas $S(z) \to S(z)(\kappa^* + \xi_2)/(\kappa + \xi_4)$. The partial waves have a somewhat more complicated symmetry, namely $E_m^{(0)}(x) \to E_{-m-2}^{(-2)}(x)$, $E_m^{(-2)}(x) \to E_{-m-2}^{(0)}(x)$.

Combining translation and grating reversal one finds for symmetric teeth, that Eq. (15) is satisfied, and if the x-axis is located at the center of the symmetric tooth then $\kappa = \kappa^*$ (real) and $\xi_2 = \xi_4$.

C. Solutions to the Coupled Mode Equations

Consider a guided mode propagating in the uncorrugated waveguide and entering the corrugated region at $z = 0$ (see Fig. 4). Its complex amplitude at that point is denoted $R(0)$. The corrugated section is assumed to extend for a length L and to be characterized by the constants κ, ζ_1, ζ_2, and ζ_4.

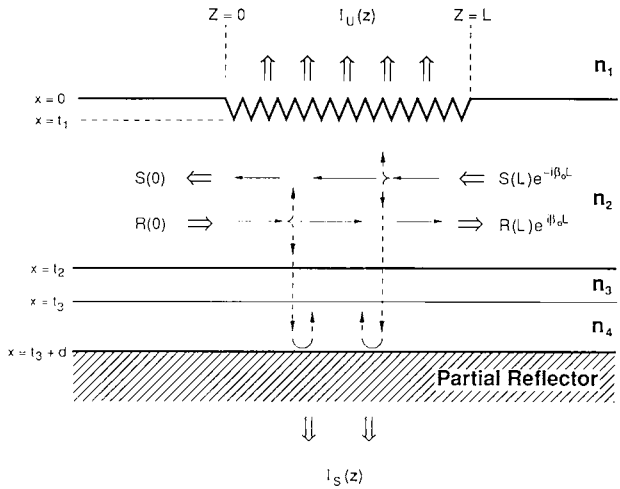

Fig. 4. Illustrating the waveguide-grating structure and the reflected, transmitted, and radiated waves.

Furthermore, the propagation constant in the corrugated waveguide is β, which may differ from the Bragg condition of $\beta_0 = 2\pi/\Lambda$ by $\delta = \beta - \beta_0$. Similarly, let us assume that a counter propagating guided mode impinges on the corrugated region at $z = L$ with complex amplitude of $S(L) \exp(-i\beta_0 L)$. The guided wave in the corrugated region, in accordance with Eqs. (3) and (7), is expressed in terms of the two counter propagating modes as

$$E(x, z) = E_0(x)R(z) \exp(i\beta_0 z) + E_0(x)S(z) \exp(-i\beta_0 z), \tag{19}$$

where $R(z)$ and $S(z)$ satisfy the coupled mode equations (10) with the boundary conditions specified above. The solutions to Eq. (10) are given by

$$R(z) = \frac{\gamma \cosh[\gamma(L-z)] - (-\alpha + i\delta + i\xi_1) \sinh[\gamma(L-z)]}{\gamma \cosh(\gamma L) - (-\alpha + i\delta + i\xi_1) \sinh(\gamma L)} R(0)$$

$$+ \frac{i(\kappa^* + \xi_2) \sinh(\gamma z)}{\gamma \cosh(\gamma L) - (-\alpha + i\delta + i\xi_1) \sinh(\gamma L)} S(L) \tag{20a}$$

$$S(z) = \frac{i(\kappa + \xi_4) \sinh[\gamma(L-z)]}{\gamma \cosh(\gamma L) - (-\alpha + i\delta + i\xi_1) \sinh(\gamma L)} R(0)$$

$$+ \frac{\gamma \cosh(\gamma z) - (-\alpha + i\delta + i\xi_1) \sinh(\gamma z)}{\gamma \cosh(\gamma L) - (-\alpha + i\delta + i\xi_1) \sinh(\gamma L)} S(L) \tag{20b}$$

where

$$\gamma = [(-\alpha + i\delta + i\zeta_1)^2 + (\kappa^* + \zeta_2)(\kappa + \zeta_4)]^{1/2}. \tag{21}$$

In particular, for $R(L)$ and $S(0)$ we can use a scattering matrix notation, namely

$$\begin{bmatrix} E^{(+)}(L) \\ E^{(-)}(0) \end{bmatrix} = \begin{bmatrix} \tau^{(+)} & \rho^{(-)} \\ \rho^{(+)} & \tau^{(-)} \end{bmatrix} \begin{bmatrix} E^{(+)}(0) \\ E^{(-)}(L) \end{bmatrix} \tag{22}$$

where

$$E^{(+)}(0) = R(0) \tag{23a}$$

$$E^{(-)}(L) = S(L) \exp(-i\beta_0 L) \tag{23b}$$

are the guided mode field amplitudes incident on the grating and

$$E^{(-)}(0) = S(0) \tag{23c}$$

$$E^{(+)}(L) = R(L) \exp(i\beta_0 L) \tag{23d}$$

are the field amplitudes propagating away from the corrugated region. The $+$ or $-$ superscript denote propagation in the positive $+z$ or negative $-z$ direction. The field transmissivity is independent of the direction of propagation, i.e., $\tau^{(+)} = \tau^{(-)} = \tau$ for any tooth shape where

$$\tau = \frac{\gamma \exp(i\beta_0 L)}{\gamma \cosh(\gamma L) - (-\alpha + i\delta + i\xi_1) \sinh(\gamma L)}. \tag{24}$$

The field reflectivities are given by $\rho^{(\pm)}$ where

$$\rho^{(+)} = \frac{i(\kappa + \xi_4) \sinh(\gamma L)}{\gamma \cosh(\gamma L) - (-\alpha + i\delta + i\xi_1) \sinh(\gamma L)} \tag{25a}$$

and

$$\rho^{(-)} = \frac{i(\kappa^* + \xi_2) \sinh(\gamma L) \exp(i2\beta_0 L)}{\gamma \cosh(\gamma L) - (-\alpha + i\delta + i\xi_1) \sinh(\gamma L)}. \tag{25b}$$

The power reflection for the R wave at $z = 0$ is given by $|\rho^{(+)}|^2$ when $S(L) = 0$, and similarly $|\rho^{(-)}|^2$ is the power reflection coefficient for the S wave at $z = L$ when $R(0) = 0$. The power transmissions are given by $|\tau|^2$.

The near-field intensity of the guided modes is given by $|E(x, z)|^2$ of Eq. (19). However, due to rapid complex exponentials in Eq. (19), one obtains a high-frequency, nearly periodic wave. Averaging that standing wave we find that the guided wave intensity pattern is proportional to

$$I_g(z) = |R(z)|^2 + |S(z)|^2 \tag{26}$$

and, in general, it is nonzero throughout the laser, including the grating regions as well as the gain sections between any two gratings.

We note that cross terms do not appear in Eq. (26) since they average to zero over each spatial period for the guided waves. These results are not directly applicable to the evaluation of the near field that causes radiation in the grating regions. Since power conveyed by both $R(z)$ and $S(z)$ are each converted into a near normal wave with the same propagation constant in the same direction by the grating, their contributions to the radiated field add. Thus, the locally radiated power up into the superstrate (usually air) of index n_a (n_1 in Fig. 2) is expressed as

$$I_u(z) = \frac{k_0 n_a}{2\omega\mu_0} \left| C_{-1,1}^{(0)} R(z) + C_{-1,1}^{(-2)} S(z) \right|^2 \tag{27}$$

and the locally radiated power into the substrate of index n_s (n_4 in Fig. 2)

$$I_S(z) = \frac{k_0 n_s}{2\omega\mu_0} (1 - |R_m|^2) \left| C_{-1,M}^{(0)} R(z) + C_{-1,M}^{(-2)} S(z) \right|^2 \tag{28}$$

where the coefficients $C_{-1,m}^{(j)}$ are defined in Section VI.B. The values of these coefficients depend on the presence of a substrate reflector, which is specified by the complex field reflectivity R_m. The parameter μ_0 is the vacuum permeability and ω is the angular frequency of the light. Note that for symmetric teeth the constants multiplying $R(z)$ and $S(z)$ are identical, and the locally radiated power, either up or into the substrate, is proportional to

$$I_r(z) = |R(z) + S(z)|^2. \tag{29}$$

Equations (27) through (29) are nonzero only in the grating regions where the guided waves are converted into radiation.

The useful power output from the grating, due to radiation up into the air (superstrate), is obtained by integrating Eq. (27) over the grating length namely

$$P_u = \int_0^L I_u(z)\, dz \tag{30a}$$

and similarly the power radiated into the substrate is

$$P_s = \int_0^L I_s(z)\, dz. \tag{30b}$$

The power incident on the grating at either end is given by

$$P_{in}(0) = \frac{\beta_0 Q}{2\omega\mu_0} |R(0)|^2 \tag{31a}$$

$$P_{in}(L) = \frac{\beta_0 Q}{2\omega\mu_0} |S(L)|^2 \tag{31b}$$

where Q is defined by Eq. (12).

In the special case that power is incident on the grating region at one end only [say $S(L)=0$], we may find it useful for later application to define normalized power radiated into the air or into the substrate, namely

$$U = P_u/P_{in}(0) = \frac{k_0 n_a}{\beta_0 |R(0)|^2} \int_0^L |C_{-1,1}^{(0)} R(z) + C_{-1,1}^{(-2)} S(z)|^2 \, dz \tag{32a}$$

$$S = P_s/P_{in}(0) = \frac{k_0 n_s}{\beta_0 |R(0)|^2} (1 - |R_m|^2) \int_0^L |C_{-1,M}^{(0)} R(z) + C_{-1,M}^{(-2)} S(z)|^2 \, dz. \tag{32b}$$

Finally, the far-field pattern of the wave radiated up into the air is given by (Goodman, 1968)

$$H(\vartheta) = \cos(\vartheta) \int_0^L E_y^{(-1)}(x=0, z) \exp[-ik_0 z\vartheta] \, dz, \tag{33}$$

where $E_y^{(-1)}(x=0, z)$ is the complex radiating field just above the grating

$$E_y^{(-1)}(x=0, z) = C_{-1,1}^{(0)} R(z) + C_{-1,1}^{(-2)} S(z). \tag{34}$$

We note that for the second-order gratings discussed here, the peak of $|H(\vartheta)|^2$ is close to, but not exactly at $\vartheta = 0$. In particular for $\delta \neq 0$, the peak of $|H(\vartheta)|^2$ is close to $\vartheta = \delta/k_0 n_a$ (Streifer *et al.* 1976b).

D. TM Modes

Most corrugated devices are designed to operate with TE modes. However, gratings for TM mode couplings were also considered in the past. In order to couple TM modes preferentially, the grating period should satisfy Eq. (6) with β_0 at or close to the propagation constant of the lowest-order TM mode. In such a case, Eq. (5) will still be valid with radiation emerging nearly perpendicularly to the grating surface. The analysis of such a device is more complicated though. The reason for this is that the electric field component is no longer continuous across the tooth boundary. The coupled mode formalism (Kogelink, 1975) expands the electric and magnetic field components in a complete set of modes of the unperturbed waveguide. Usually, for TE modes, one ignores all terms but those that are related by the Bragg condition [Eq. (6) for second-order gratings], since their field amplitudes are significantly larger than the others. In the case of the second-order gratings, some of the radiation terms may also be included (Yamamoto *et al.*, 1978). However, for TM modes, due to the field discontinuities the expansion coefficients have a jump across the tooth boundary and their derivatives are very large (strictly speaking, they are proportional

to Dirac's delta-functions). It is not clear then which terms in the expansion can be ignored and which cannot. Ignoring some important terms may violate the boundary conditions of the perturbed waveguide.

An example that underscores this problem is the calculation of the coupling coefficient κ. Instead of Eq. (13) for TE modes, Streifer *et al.*, (1976a) derive two different integral expressions for TM mode-coupling coefficients. These two expressions may differ quite significantly when the index difference across the tooth boundary is large [Hardy, A., unpublished] as is the case in many surface emitting devices where the corrugations are at the air-semiconductor interface. Nevertheless, in the limit of very shallow gratings, exact analytical expressions for the coupling coefficient are available. Various approaches are used for gratings with different tooth shapes (Verly *et al.*, 1980; Stegeman *et al.*, 1981; Hardy, 1984). It turns out that in all cases the coupling coefficient for the TM modes is obtained through multiplying the expression for the TE coupling coefficient by the same reduction factor. Since these analytic expressions may not be useful for deeper gratings, we shall restrict ourselves to the more common TE mode coupling devices.

E. Examples

The basic waveguide geometry used in most of the examples in this section has a $t_3 - t_1 = 200$ nm-thick waveguide of index $n_2 = n_3 = 3.6$, which is bounded below by $n_4 = 3.4$ index material (referred to as the substrate), and above by air (sometimes referred to as the superstrate) with unity index. The grating teeth are assumed here to be rectangular in shape, but results were also presented for triangular teeth (Hardy *et al.*, 1989). In the analysis, rectangular gratings that extend 20 nm or 100 nm above the waveguide were considered. These tooth heights, t_1, encompass the range of gratings used in experimental devices. Furthermore, various grating lengths, L, were studied. Unless otherwise specified, the modal field absorption loss is set equal to 10 cm^{-1}, and the deviation from the Bragg condition is zero. The wavelength is 0.8 μm, and the grating period for the geometry equals one wavelength of the laser light in the waveguide. The grating period, Λ, is, therefore, approximately 232 nm, but the precise value of Λ depends on the tooth height and shape. Moreover, if the refractive indices or waveguide thickness are changed, the grating period at which resonance occurs must be modified so that the Bragg condition is satisfied.

For our first study we consider the effect of a multistack reflector (Thornton *et al.*, 1984) located some distance below the waveguide in the

substrate. Such a substrate reflector is characterized by a complex field reflectivity, whose impact on the grating radiation, reflection, and transmission is to be determined. The presence of the reflector should reduce the power lost to the substrate and redistribute that power into the air or into the guided modes. Since the fields propagating toward and back from the reflector both traverse some distance, the effect of the reflector will vary depending on its precise location. Rather than model the distance dependence directly, we assign a phase to the complex reflectivity that accounts for various reflector positions. Because the light travels back and forth from the grating to the substrate reflector, and since the substrate index is 3.4, a change in the location of the reflector of only 120 nm corresponds to full 2π phase shift in the reflection coefficient. The substrate reflector is assumed to be located sufficiently below the waveguide (>1 μm) so that the evanescent tails of the guided and non-radiating partial waves have decayed before being influenced by its presence.

The grating to be analyzed is assumed to extend 100 nm into the air and its tooth width, Δ_1, is taken to be $\Lambda/2$. In Fig. 5 the amplitude of the substrate field reflectivity has been set equal to 0.95 (for a power reflection of $0.9 = 0.95^2$) and the phase has been varied through 2π. The power radiated into the substrate is quite small. At its peak, which occurs just below π, slightly over 8% of the power is lost and for most reflector locations, that value is much smaller. However, we also observe that the power radiated into the air is not always enhanced by the presence of the reflector. Indeed at $0.85\ \pi$, the radiated power into the air approaches zero. This may be a desirable situation if an edge emitter with maximum grating reflectivity and minimum surface emission is desired. The conclusion to be drawn from this data is that a substrate reflector can be helpful either for a surface or edge emitter, but only if it can be precisely located to produce the appropriate behavior.

The same calculation was repeated for $t_1 = 20$ nm and $L = 300$ μm (Hardy *et al.*, 1989) in order to determine the dependence of the reflection, radiation, etc. on the tooth height when phase (R_m) is varied. Although the shapes of the curves are not very similar to those of Fig. 5, they do have some features in common. Namely, the general dependence of the radiation into the air and the reflectivity on the phase.

In a second example illustrated in Fig. 6, the grating height is again set equal to $t_1 = 100$ nm, the tooth width is $\Delta_1 = 0.5\ \Lambda$, and the grating length $L = 50$ μm. The phase of the substrate reflector is fixed at π and the amplitude reflection coefficient is varied. The dependences of reflection, radiation, etc., are uncomplicated. As expected with increasing reflectivity,

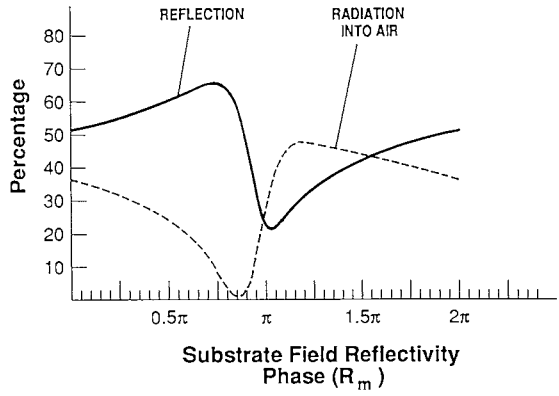

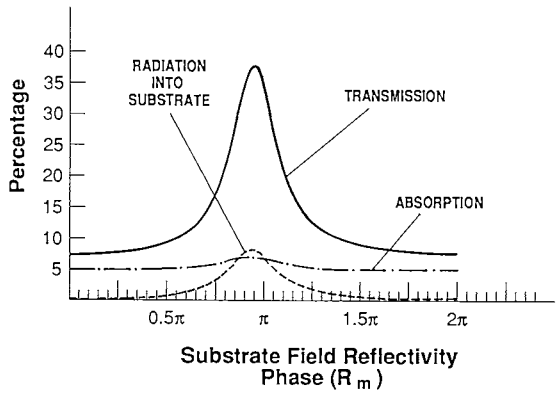

Fig. 5. Reflection, transmission, radiation, and absorption versus the phase of the substrate field reflectivity [magnitude $(R_m) = 0.95$] for a rectangular grating with $t_1 = 100$ nm, $\Delta_1 = 0.5\Lambda$, and $L = 50$ μm.

the substrate reflector minimizes the radiated power into that medium. The important and somewhat unexpected result is that the radiated power into the air is not strongly dependent of the substrate reflection magnitude. The calculation was repeated with phase $(R_m) = \pi/2$. The dependencies of the radiation, reflection, etc., on the magnitude of R_m, differ slightly from those obtained with phase $(R_m) = \pi$. The same geometry was evaluated also with $t_1 = 20$ nm, rectangular teeth of width $\Delta_1 = 0.5\Lambda$, and $L = 300$ μm, and phase $(R_m) = 0.5\pi$. All the dependences illustrated in Fig. 6 were qualitatively unchanged, although with this shallow grating the radiation into the air

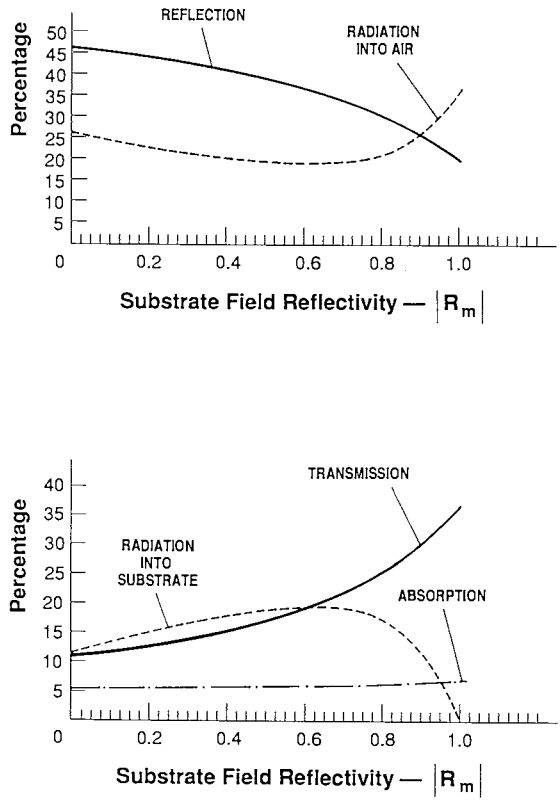

Fig. 6. Reflection, transmission, radiation, and absorption versus the amplitude of the substrate field reflectivity [phase $(R_m) = \pi$] for a rectangular grating with $t_1 = 100$ nm, $\Delta_1 = 0.5\Lambda$, and $L = 50$ μm.

was enhanced. These calculations lead to the general conclusion that the phase of the substrate reflectivity affects the performance of the device profoundly, whereas the magnitude of R_m is much less critical in determining device behavior. Because the substrate reflector position is difficult to control precisely with presently available technology, and because the phase of R_m is so critical, we set $R_m = 0$ in the remainder of this section.

Another interesting fact is also revealed by the previous calculations. When conventional coupled-mode theory, which ignores radiation, is applied to calculate grating reflection for the rectangular grating with teeth equal to one-half period, i.e., $\Delta_1 = 0.5\Lambda$, it predicts that the coupling coefficient for reflection, κ, is identically zero. In the above examples where $\Delta_1 = 0.5\Lambda$, the coupling coefficient κ remains zero, however, ζ_2 and ζ_4 are

not zero and the power reflectivity is quite substantial. The large reflection results from the interaction of the radiating fields with the grating to couple power back into the guided modes. This effect is enhanced by the reflected field from the substrate reflector for phase $(R_m) = 0.8\pi$ as shown in Fig. 5 for $t_1 = 100$ nm.

The effect of the tooth width Δ_1 on the grating performance is illustrated in Fig. 7. At the leftmost end, the teeth vanish and only the 200 nm-thick waveguide remains. The reflectivity and radiation are zero. Near the other extreme, the grating teeth almost equal the period, and the grating, in effect, consists of very narrow 100 nm-deep groves in a 300 nm-thick waveguide. The grating length is $L = 50$ μm. Note that at the extremes where $\Delta_1 = 0$ and $\Delta_1 = \Lambda$, the grating vanishes and the waveguide thicknesses become 200 and 300 nm, respectively. These different thicknesses cause the modes near $\Delta_1 = 0$ and $\Delta_1 = \Lambda$ to differ quite significantly and therefore their interactions with the grating are asymmetrical. Another contributing factor to the asymmetry is the quite strong interaction of the guided and radiated fields with the high teeth for all values of Δ_1. Note also that at $\Delta_1/\Lambda = 0.5$ the power reflectivity approaches 46% despite the fact that the coupling coefficient, κ, is identically zero and no substrate reflector is included. As mentioned previously, this results entirely from the reaction of the radiation and the other partial wave fields on the guided modes as represented by ζ_2 and ζ_4 in Eqs. (10a) and (10b). Furthermore, the reflectivity dips to slightly above 15% for $\Delta_1/\Lambda = 0.4$, but even this value may be adequate to achieve a low threshold in a DBR laser.

The effect of varying the tooth height for a grating with $\Delta_1/\Lambda = 0.5$, $L = 50$ μm, and no substrate reflector present is illustrated in Fig. 8. We observe that for small tooth heights the substrate power exceeds that radiated into the air, but for greater tooth heights the situation is reversed. Qualitatively similar results are obtained for $\Delta_1/\Lambda = 0.25$ and 0.75. We note that the curves for radiation into the air and radiation into the substrate, intersect near $\lambda/4$ and $\lambda/2$. This indicates that some transverse resonance effects take place within the tooth. These data demonstrate that rectangular second-order gratings with $\Delta_1/\Lambda = 0.5$ can be employed to provide feedback in DBR lasers. Specifically, a power reflectivity of 30%, attained in Fig. 8 at $t_1 > 52$ nm is equivalent to that of an edge emitter with a cleaved facet. For longer gratings, however, a given power reflectivity is obtained with still smaller tooth heights.

The next calculation examines the importance of loss in the corrugated waveguide region. Here the rectangular grating teeth extend 50 nm above the waveguide; $\Delta_1 = 0.5\,\Lambda$ and $L = 500$ μm. No substrate reflector exists. As

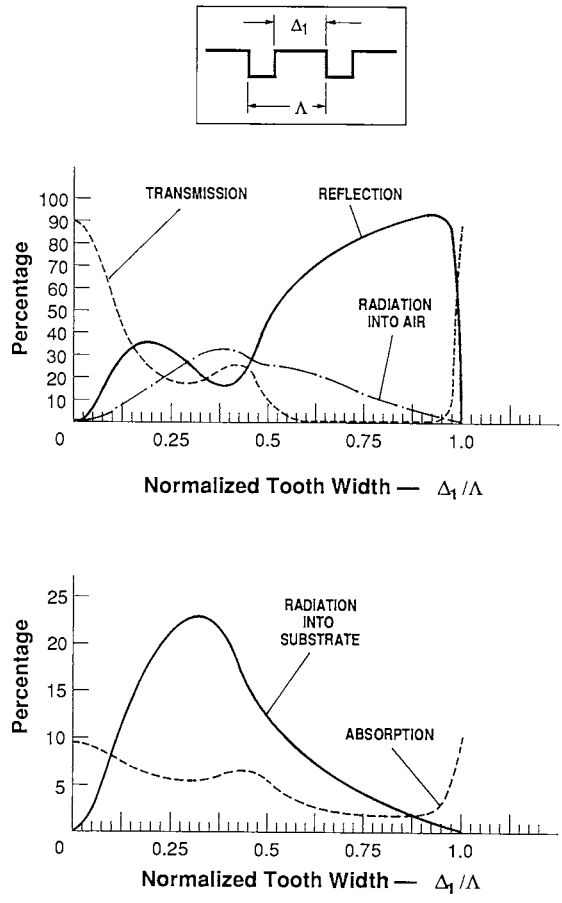

Fig. 7. Reflection, transmission, radiation, and absorption versus the tooth width, Δ_1, for a rectangular grating with $t_1 = 100$ nm, and $L = 50$ μm, with no substrate reflector.

the modal field absorption coefficient is increased, we observe in Fig. 9 that the reflection decreases, but the radiated power is relatively insensitive to the variations. For all values of α the transmitted power is negligible as one would expect for a 500 μm-long grating. Results for a symmetrical triangular grating are quite similar.

The next example is in some ways the most important, since it addresses deviations from the Bragg condition. When a laser of the types illustrated in Figs. 1(a)-(d) is pumped to threshold, the condition that must be satisfied is that the round-trip gain equal unity in magnitude and be a multiple of

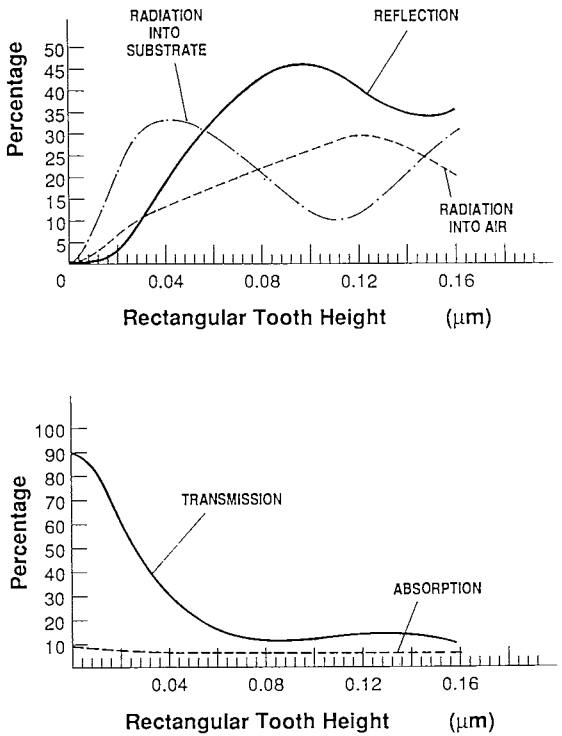

Fig. 8. Reflection, transmission, radiation, and absorption versus the tooth height for a rectangular grating with $\Delta_1 = 0.5\Lambda$, and $L = 50$ μm, with no substrate reflector.

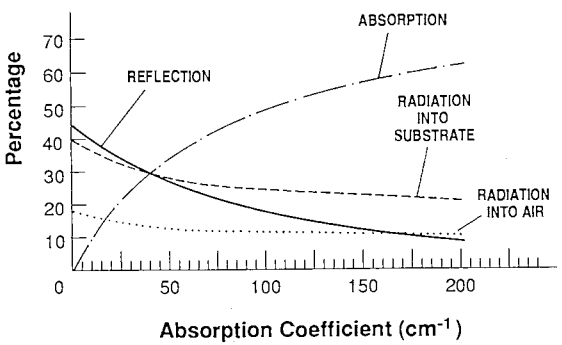

Fig. 9. Reflection, transmission, radiation, and absorption versus the modal field absorption coefficient, α, for a rectangular grating with $t_1 = 50$ nm, $\Delta_1 = 0.5\Lambda$, and $L = 500$ μm.

2π in phase. Since the optical length of the gain region is not well controlled and, in fact, changes as the active region refractive index is modified by the injected charges, it is not possible to precisely predetermine the wavelengths at which the round-trip condition will be satisfied. In addition, when a series of gain regions separated by gratings are arranged as in Fig. 1(b) to implement injection-locking, all the gain regions will oscillate in a mutually coherent fashion and the optical frequency in all the grating regions will be identical. The gratings or waveguides may, however, differ slightly and even small variations in dimension or material composition will cause some detuning from the Bragg condition.

Figure 10 is a plot for a 100 nm-high, symmetrical rectangular ($\Delta_1 = 0.5\Lambda$) grating of 100 μm length. No substrate reflector is present and the absorption

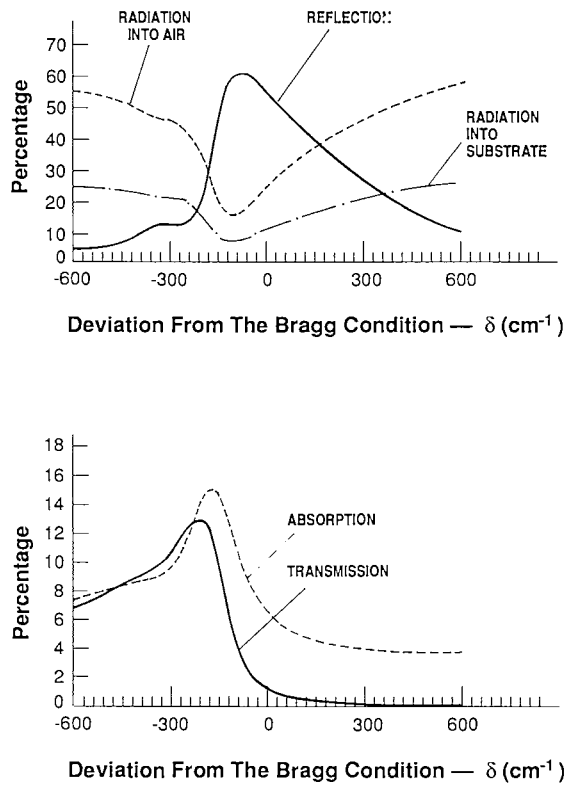

Fig. 10. Reflection, transmission, radiation, and absorption versus the deviation from the Bragg condition, δ, for a rectangular grating with $t_1 = 100$ nm, $\Delta_1 = 0.5\Lambda$, and $L = 100$ μm.

coefficient is 10 cm^{-1}. The horizontal axis is marked in units of cm^{-1} and for 0.8 μm light, the guided mode propagation constant is 27.07 μm^{-1}. Thus, a deviation of $\delta = 300\ cm^{-1}$ corresponds to a wavelength shift of -0.89 nm from the Bragg condition. The peak reflectivity shown in Fig. 10 is 62% and the full-width at half-maximum is approximately 430 cm^{-1}. Actually, semiconductor lasers will function quite well even with much smaller reflectivities and the width between 10% points in Fig. 10 is on the order of 1000 cm^{-1} or 2.95 nm. The radiated power increases away from the reflectivity peak, which itself does not occur precisely at the Bragg condition. The peak shift from the Bragg condition is in fact caused by the complicated interaction of the two counter-propagating modes with the radiation fields. We observe too that the transmitted power is much larger for negative deviations, which as noted previously correspond to longer wavelengths. For wavelengths below the Bragg condition, the radiation is strong and the transmitted power is quite small.

A similar study was carried out for $t_1 = 20$ nm, $\Delta_1 = 0.5\Lambda$, and $L = 300$ μm. The curves have approximately the same dependence on δ as Fig. 10 with two differences. First, they are more nearly symmetric about $\delta = 0$, as expected for shallow gratings (Kogelnik, 1975), and second, the substrate radiation exceeds the power radiated into the air for $t_1 = 20$ nm, which is just the reverse of the situation for $t_1 = 100$ nm.

Finally, the near-field and far-field patterns of the radiating mode are shown in Fig. 11. The grating parameters are the same as in Fig. 10, and $\delta = 0$. Such a radiation pattern is expected for a surface emitter with a single grating as in Fig. 1(c), although due to the resonance condition (see Section IV), the laser may operate at a wavelength that slightly deviates from the Bragg condition. Note that the far-field peak slightly deviates from $\vartheta = 0°$ (despite having $\delta = 0$) due to a slow near-field phase variation along the grating.

F. Conclusions

In this section, results of an analysis of second-order gratings used as DBRs in surface emitting lasers, have been presented. The analysis yields parametric dependences that should prove useful in the understanding and design of GSEs. The data are also essential for calculating radiation patterns produced by such lasers. It has been shown that the use of substrate reflectors, of the type previously demonstrated, can have beneficial effects on the grating reflectivity and, to a lesser extent, on the radiated power. However, since the overall behavior of the device is very sensitive to the

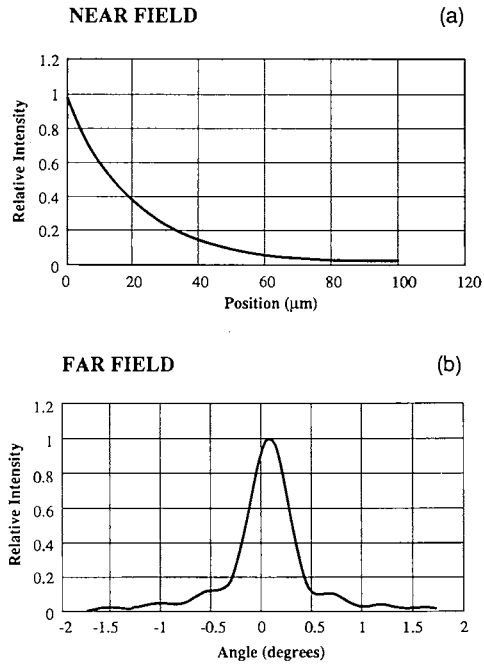

Fig. 11. The radiating mode near-field and far-field intensity patterns for a rectangular grating with $t_1 = 100$ nm, $\Delta_1 = 0.5\Lambda$, and $L = 100$ μm.

reflector position, the substrate reflector must be precisely located relative to the waveguide and grating.

The analysis also shows that the interaction of the radiating modes with the grating serves to modify the effective grating reflectivity. This effect can be so pronounced as to dominate the predictions of conventional coupled-mode theory, which neglects radiation effects. Other data relate to variations in tooth shape and height. Insofar as sensitivity is concerned, the grating height is also a very important parameter.

The effects of losses and detuning from the Bragg condition have also been studied. In a representative case we find that significant reflectivity (within 10% of the peak reflectivity) can occur over substantial wavelength bands on the order of 2 to 3 nm, that the reflection and the other power fractions as functions of the deviation from the Bragg condition are not symmetric, and that the peak reflectivity does not occur precisely at the Bragg condition. These effects are caused by the complicated interactions of the guided modes, the radiation fields, and the evanescent partial waves.

III. TWO GRATINGS–ONE GAIN SECTION

A. Geometry and Definitions

The simplest GSE laser geometry, with a DBR configuration, is shown schematically in Fig. 12. It consists of a gain or active section of length L, located between two waveguide sections with second order gratings of length L_{g1} and L_{g2}. The grating period Λ is identical for both corrugations (thus, β_0 is identical) and is assumed to closely approximate the optical wavelength in each guide. However, the situation in which the two waveguides differ slightly is encompassed by the analysis.

Near the resonant wavelengths the second order gratings act as DBRs and as output couplers (see Section II). When excited by a guided wave, the induced polarization in the grating teeth generates a reflected guided wave, and radiating waves into both the substrate and superstrate. In general, some incident power is also lost in the waveguide, and some may be transmitted after passing along the length of the grating. The various fractions of the incident power are denoted by R = reflected, T = transmitted, U = radiated into the air (superstrate), and S = radiated into the substrate. The parameters U and S are defined in Eq. (32) whereas $T = |\tau|^2$ and $R = |\rho^{(\pm)}|^2$ are obtained by Eqs. (24) and (25a, b) respectively.

The fractional power lost in the grating to optical absorption and scattering is then given by

$$A = 1 - R - T - U - S \tag{35}$$

When appropriate, subscripts 1 and 2 will be used to designate the radiation,

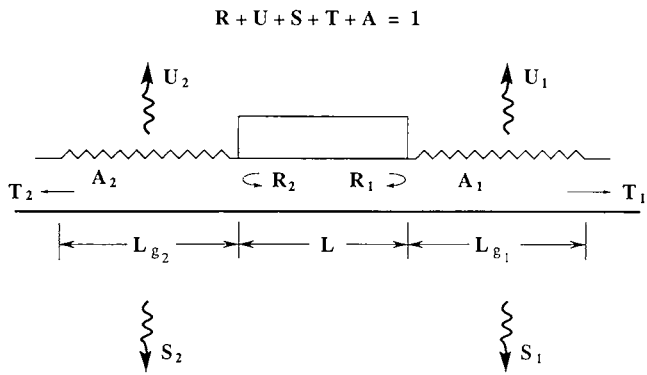

Fig. 12. Schematic of the geometry of a laser composed of two gratings and one gain section, and the fractional powers reflected, radiated, transmitted, and absorbed.

transmission, etc., in the two grating sections. In particular, we note that $R_1 = |\rho_1^{(+)}|^2$ and $R_2 = |\rho_2^{(-)}|^2$.

B. Threshold Condition

Upon increasing the gain in the central section the laser will attain threshold. Since the grating reflectivities for the optical fields are complex, the threshold condition is given by (Yariv and Nakamura, 1977) as

$$R_1 R_2 \exp(2gL) = 1 \tag{36a}$$

and

$$\phi_1 + \phi_2 + 2\beta_a L = 2\pi q, \tag{36b}$$

where g is the net modal power gain in the active section of length L, and $\phi_1(\lambda)$, $\phi_2(\lambda)$ are the phases of the complex modal field reflectivities ρ_1 and ρ_2 of the gratings. Furthermore, $\beta_a(\lambda)$ is the modal propagation constant in the gain section and q is an integer approximately given by $\beta_a L/\pi$. Note that β_a is not necessarily identical to β_0 or to $\beta_0 + \delta$. To solve for the longitudinal modes of the system, i.e., the active section plus the two DBR sections, we evaluate (according to the analysis of Section II) R_1, R_2, ϕ_1, and ϕ_2 as functions of the deviation from the Bragg condition in the grating sections

$$\delta_j(\lambda) = \beta_j(\lambda) - \beta_0, \qquad \text{where } j = 1, 2 \tag{37}$$

where $\beta_0 = 2\pi/\Lambda$ and $\beta_j(\lambda)$ is the propagation constant in grating section j. We note that β_0 is the same for the two gratings if the period Λ is the same. However, $\beta_1(\lambda) \neq \beta_2(\lambda)$ (for the same λ) if the two waveguides differ in material composition or thickness. With a knowledge of the variations in these quantities as functions of λ, the threshold gain $g(\lambda)$ is determined to satisfy Eq. (36a). Then the imposition of the resonance condition Eq. (36b) with $\beta_a(\lambda)$ yields the various longitudinal mode wavelengths. Each of these is associated with a value of q. The variation in the active section real refractive index with gain, which modifies $\beta_a(\lambda)$, can also be included in the formulation if so desired.

C. The Radiation Differential Efficiency

For each longitudinal mode resonance, the field distributions in the grating sections can be found by the equations of Section II. In that process it is first necessary to determine the relative amplitudes of the fields incident on

each grating-gain section boundary. Just as for a laser with two dissimilar, discrete reflectors, the ratio of power flow impinging on the two grating sections is given by (Thompson, 1980)

$$P_1/P_2 = (R_2/R_1)^{1/2}. \tag{38}$$

Knowledge of the superstrate grating parameters U_1 and U_2 together with Eq. (38) suffice to compute the differential efficiency for radiation from the gratings into the air. We obtain

$$\eta_D = \eta_i \eta_0 \frac{(U_2\sqrt{R_1} + U_1\sqrt{R_2})}{(1-R_2)\sqrt{R_1} + (1-R_1)\sqrt{R_2}} \tag{39}$$

where η_i is the internal differential efficiency, and

$$\eta_0 = \frac{\ln(1/R_1R_2)}{2\alpha_l L + \ln(1/R_1R_2)} \tag{40}$$

represents the fractional net power entering the grating sections. This term is similar to the power coupled through the end mirrors in edge emitters (Yariv, 1989). In Eq. (40), α_l is the optical power loss per unit length of the mode in the active section and the actual modal threshold gain exceeds g by α_l. Eq. (39) is derived in Section VI.C. The derivation neglects the effects of losses at the boundary between the grating and the gain sections of the laser. For identical, symmetrical gratings, $R_1 = R_2$, $U_1 = U_2$, and

$$\eta_D = \eta_i \eta_0 U/(1-R) \tag{41}$$

where $U/(1-R) < 1$, which follows from Eq. (35) since A, T, S are all positive quantities.

It is important to recognize that the factor $U/(1-R)$ or the more complicated expression in Eq. (39) reduces the maximum differential efficiency of a GSE in comparison with a conventional edge emitter. To maximize the differential efficiency so that $\eta_D = \eta_i \eta_0$, the grating should be designed and fabricated for low substrate radiation ($S \ll 1$), low transmission ($T \ll 1$), and low loss ($A \ll 1$). Then U may approach $(1-R)$ and the surface emitter differential efficiency will increase toward that of an edge emitter with the same reflectivities. Finally, if so desired, the useful radiation could be extracted via the substrate. Equations (38) through (41) are still valid except that $U_j (j = 1, 2)$ must be replaced everywhere by $S_j (j = 1, 2)$.

D. Far-Field Radiation Patterns

To evaluate the far-field pattern for a particular longitudinal mode, it is necessary to determine the relative phases and magnitudes of the modes in each grating section. The complex modal amplitudes entering the grating sections 1 and 2 are denoted $R_j (j = 1, 2)$, and each incident mode generates

a counter-propagating mode with amplitude $S_j (j = 1, 2)$ (see Section II). If z is set equal to zero at the junction of the gain and grating section j (at the left end of grating 1 and the right end of grating 2 in Fig. 12), with z increasing into the grating section, R_j and S_j satisfy the coupled differential equations (10a, b), with boundary conditions $S_j(L_{gi}) = 0$ for each grating separately. The solutions for R_j, S_j, and the field reflectivities are given in Section II. Note that α in Eq. (10) represents the modal field absorption, whereas in diode laser theory α_l [see Eq. (40)] is the modal power loss. Thus, modal power loss in the grating sections is characterized by 2α in this chapter. When the grating heights or tooth shapes are not identical in waveguide sections 1 and 2, or when the waveguide's losses, dimensions, or compositions differ, the constants κ, ζ_1, ζ_2, ζ_4, α, and δ will not be the same for the two gratings.

The far-field radiation pattern of a single emitter extending from $z = 0$ to $z = L_g$ is given by Eq. (33) in Section II, where ϑ is measured relative to the normal to the emitter. Note that Eq. (33) is an expression for the optical field and not the intensity (power). Thus, the radiation field of grating 1 is $H_1(\vartheta)$. To evaluate the field radiated by grating 2, we observe first that laterally shifting the grating by d, so that it extends from $z = d$ to $z = d + L_g$, modifies the far-field pattern $H_1(\vartheta)$ by a multiplicative factor $\exp[-ik_0 d\vartheta]$. We then define the ratio of the incident, complex modal amplitudes to be

$$R_2/R_1 = \eta \exp(i\phi), \tag{42}$$

where ϕ is the relative phase and

$$\eta = \frac{R_1^{1/4}}{R_2^{1/4}} = \left(\frac{P_2}{P_1}\right)^{1/2} \tag{43}$$

[see also Eq. (38)]. The combined intensity pattern of two gratings excited as described above is given by

$$F(\vartheta) = |H_1(\vartheta) + \eta \exp(i\phi) \exp[+ik_0 L\vartheta] H_2(-\vartheta)|^2, \tag{44}$$

where L is the length of the active section or equivalently the grating separation and the angle in H_2 is reversed to compensate for having let z increase into both grating sections. The subscript for grating 2 has been changed to signify that its geometry may not be the same as that of grating 1.

E. Examples

The refractive index variation of the waveguide/grating geometry to be studied in the following examples is shown in Fig. 3, with $n_1 = 1$ (air),

$n_2 = 3.49$, $n_3 = 3.42$ and $n_4 = 3.36$. It represents the continuation of a single-quantum-well, separate-confinement-heterostructure laser into an unpumped waveguide region. In this model, the 10 nm-thick active layer is neglected in the grating section and the discontinuity experienced by the guided mode between the gain and grating section is disregarded. The grating is etched into the 3.49 material of thickness $t_2 = 200$ nm to a depth $t_1 = 50$ nm. The 3.42 material has thickness of $t_3 - t_2 = 200$ nm, and the free space wavelength is equal to 0.8 μm.

The propagation constant β_j, $j = 1, 2$, in the waveguide just described can then be determined as a function of λ for each grating geometry. The grating period, Λ, is then specified by setting $\beta_j(\lambda) = \beta_0$, for $\lambda = 0.8$ μm, in these examples if the two gratings and waveguides are identical. If the waveguides or gratings differ, β_0 and Λ are fixed by choosing $\beta_1(\lambda) = \beta_0$, for $\lambda = 0.8$ μm. In the following examples the grating sections in all the devices are identical and $L = L_{g1} = L_{g2} = 300$ μm [see Fig. 12], and unless otherwise noted, the modal *field* absorption in the grating region is $\alpha = 10\ \text{cm}^{-1}$. The power loss in the gain section is $\alpha_l = 5\ \text{cm}^{-1}$ and we set $\eta_i = 0.95$ [see Eqs. (39) and (40)].

For our first example the grating tooth has a sawtooth shape as shown in the insert of Fig. 13, where the tooth orientation is such that the mode travels from left to right in grating region 1 and oppositely in grating region 2. Figure 13 is a plot of net threshold modal power gain in the active section as a function of deviation from the Bragg condition computed by solving Eq. (36a). On that scale $\delta = 10\ \text{cm}^{-1}$ corresponds approximately to $\Delta\lambda = -0.03$ nm. The vertical lines in Fig. 13 are the longitudinal mode resonances at the solutions of Eq. (36b), and it is evident that the mode nearest the Bragg condition has the lowest threshold. For that mode at $\delta = 7.5\ \text{cm}^{-1}$, the net threshold modal power gain is $g = 26\ \text{cm}^{-1}$. Since the sawtooth grating is not symmetrical, the various power fractions R_j, U_j, S_j, A_j, and T_j, differ for $j = 1$ and 2. Their values are listed in Table I.

For this device, the reflection from grating 1 is about three times stronger than that for grating 2, and the fractional power radiated from grating 2 into the air exceeds that from grating 1 by almost a factor of five. The actual power radiated from each grating also depends on the relative incident powers. If the power incident on grating 1 is normalized to 1.0, then the power incident on grating 2 is 1.67. The relative powers radiated into the air are the product of this ratio and U_j. Therefore, that value for grating 2, normalized to 1.0 for grating 1, is 8.3, or for this device grating 2 radiates 8.3 times the power of grating 1 into the air. Similarly, the ratio of grating 2 to grating 1 substrate radiated power is 42.3, and overall less than 25%

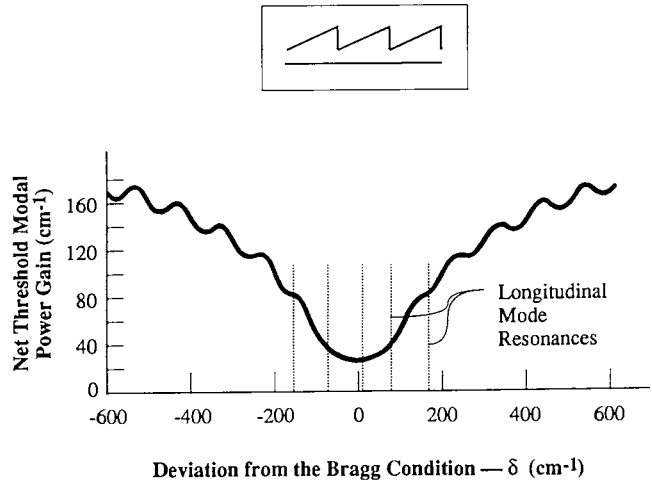

Fig. 13. Net threshold modal power gain versus deviation from the Bragg condition for a grating surface emitter with sawtooth shaped teeth. For this example $\alpha = 10\ \text{cm}^{-1}$ $t_1 = 50$ nm, $L = L_{g1} = L_{g2} = 300\ \mu$m, and $\delta = 10\ \text{cm}^{-2}$ corresponds to $\Delta\lambda \approx -0.03$ nm. The longitudinal mode resonances are shown.

Table I

Fractional power flows and relative powers for a grating surface emitter with sawtooth-shaped teeth. For this example $\alpha = 10\ \text{cm}^{-1}$ $t_1 = 50$ nm, $L = L_{g1} = L_{g2} = 300\ \mu$m, and $\delta = 10\ \text{cm}^{-1}$ corresponds to $\Delta\lambda \approx 0.03$ nm.

	Grating 1	Grating 2
R	0.759	0.273
U	0.025	0.124
S	0.018	0.456
T	0.008	0.008
A	0.190	0.139
P_{inc}(grating)*	1.0	1.67
P_{rad}(air)*	1.0	8.3
P_{rad}(substrate)*	1.0	42.3

* Normalized.

of the radiated power is emitted into the air. The effect of the low radiation efficiency calculated above is to lower the differential efficiency. If we set $\eta_i = 0.95$, and take $\alpha_l = 5\ \text{cm}^{-1}$, then $\eta_0 = 0.84$, $\eta_g = 0.159$, and $\eta_D = 0.127$.

The radiation pattern of the lowest threshold mode of this laser is plotted in Fig. 14. Because of the differences in the individual radiation patterns and the powers from the two gratings, the far field is not symmetric. Indeed from the relative power values one might expect a still more exaggerated distortion, but we recall that the pattern results from the interference of the fields, which are proportional to the square root of the power. The peak is off-center at 0.015°, and the lobe width is 0.053° full-width at half-maximum (FWHM).

As a second example, we consider a laser with the same dimensions as studied above and rectangular gratings with half-a-period tooth width. In order to determine the effect of losses in the grating region, the device is evaluated for modal field absorptions of $\alpha = 10$, 100, and 200 cm^{-1}. Threshold gain versus δ for the two extreme cases are plotted in Fig. 15, where

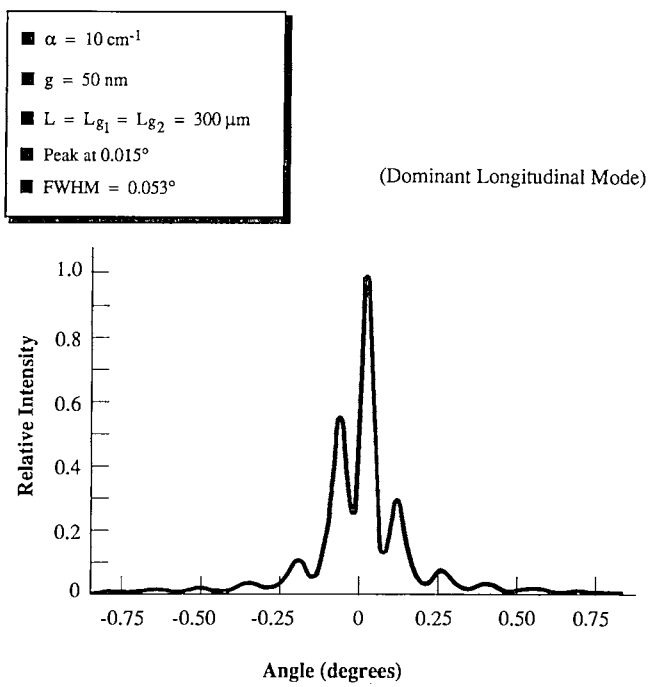

Fig. 14. Far-field radiation pattern for the dominant mode in the geometry of Fig. 13. The central lobe peak is at 0.015° and the lobe full-width half-maximum (FWHM) = 0.053°.

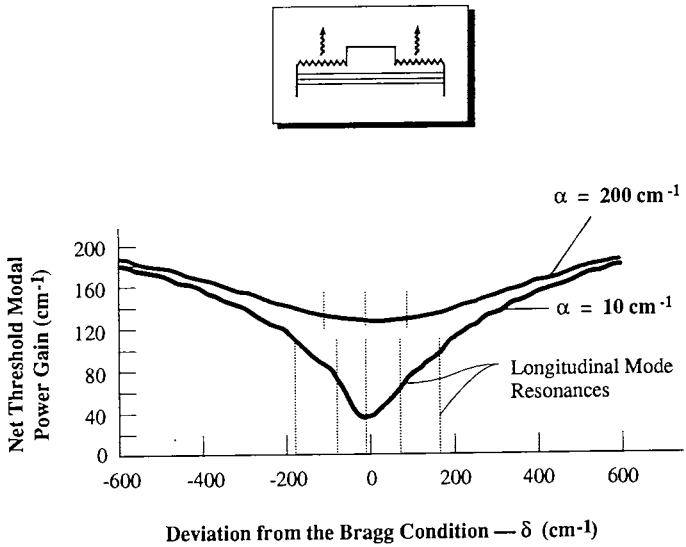

Fig. 15. Comparison of the net threshold modal power gain versus deviation from the Bragg condition for a grating surface emitter with rectangular shaped teeth and $\alpha = 10\ \text{cm}^{-1}$ and $\alpha = 200\ \text{cm}^{-1}$. For this example $t_1 = 50$ nm, $L = L_{g1} = L_{g2} = 300\ \mu$m, $\Delta_1 = \Lambda/2$ and $\delta = 10\ \text{cm}^{-1}$ corresponds to $\Delta\lambda \approx 0.03$ nm. The longitudinal mode resonances are shown.

the longitudinal mode resonances are shown. As expected, the relative longitudinal mode discrimination is much greater for the low-loss case.

Data for the dominant longitudinal mode, including deviation from the Bragg condition, the threshold power gain, the fractional power distributions in the gratings, and the efficiencies with $\eta_i = 0.95$, are tabulated in Table II. Since the gratings are symmetric, both are excited and radiate equally. The laser with the lowest loss in the grating section again has the highest differential efficiency of $\approx 15\%$, and we also note that if the output were taken through the substrate that value would be more than doubled.

The effect of grating absorption on the radiation pattern is illustrated in Fig. 16. With increasing absorption, the central lobe broadens, more power is contained in the side lobes, and the side lobe separation increases. All these phenomena follow from the decreased penetration of the mode into the grating section with increasing absorption. Specifically, for $\alpha = 100\ \text{cm}^{-1}$ the intensity decreases approximately three times more rapidly than for $\alpha = 10\ \text{cm}^{-1}$. Furthermore, if one attempts to relate the calculated patterns to those produced by two discrete (point) radiators spaced by D, the lobe

Table II

Comparison of the longitudinal mode resonances, the threshold gains, the fractional power flows, and the differential efficiencies for a grating surface emitter with rectangular-shaped teeth and $\alpha = 10\ \text{cm}^{-1}$, $\alpha = 100\ \text{cm}^{-1}$, and $\alpha = 200\ \text{cm}^{1}$.

Parameters	$\alpha = 10\ \text{cm}^{-1}$	$\alpha = 100\ \text{cm}^{-1}$	$\alpha = 200\ \text{cm}^{-1}$
$\delta(\text{cm}^{-1})$	−10.27	−9.83	−10.57
$\Delta\lambda(\text{nm})$	0.031	0.030	0.032
$g(\text{cm}^{-1})$	34	94	126
R	0.349	0.060	0.023
U	0.120	0.082	0.060
S	0.274	0.187	0.140
T	0.028	0.000	0.000
A	0.229	0.670	0.880
η_0	0.875	0.949	0.962
η_g	0.184	0.087	0.061
$\eta_D = \eta_i\eta_0\eta_g$	0.153	0.078	0.056

separation obtained from λ/D for $\alpha = 10\ \text{cm}^{-1}$, yields $D = 591\ \mu\text{m}$ for 0.8 μm light. This value agrees well with the penetration of the mode into the grating sections as do the results for $\alpha = 100\ \text{cm}^{-1}$, $D = 422\ \mu\text{m}$ and for $\alpha = 200\ \text{cm}^{-1}$, $D = 385\ \mu\text{m}$.

To understand the effects of variations in the grating tooth height, the previous calculation has been repeated with $\alpha = 10\ \text{cm}^{-1}$ for $t_1 = 20$ and $t_1 = 80$ nm (Hardy *et al.*, 1990a). Noteworthy is the large decrease in threshold that occurs when t_1 is increased from 20 to 50 nm. The drop in threshold with a further increase in tooth height to $t_1 = 80$ nm is much smaller, but the differential efficiency improves substantially to 29% for the highest teeth. With $t_1 = 80$ nm, approximately the same power is radiated into the substrate and the air (see Section II.E).

Radiation patterns for $t_1 = 20$ and 80 nm (see Hardy *et al.*, 1990a) both exhibit two symmetrical lobes, which is characteristic of an out-of-phase mode. Thus, for these two grating heights, the waves in gratings 1 and 2 associated with the lowest threshold longitudinal mode have opposite phases, whereas for $t_1 = 50$ nm the two grating fields are in-phase for the dominant mode, resulting in one central lobe at $\vartheta = 0°$ [see Fig. 16(a)]. We observe that the second mode for $t_1 = 50$ nm is double lobed (Fig. 17). Not

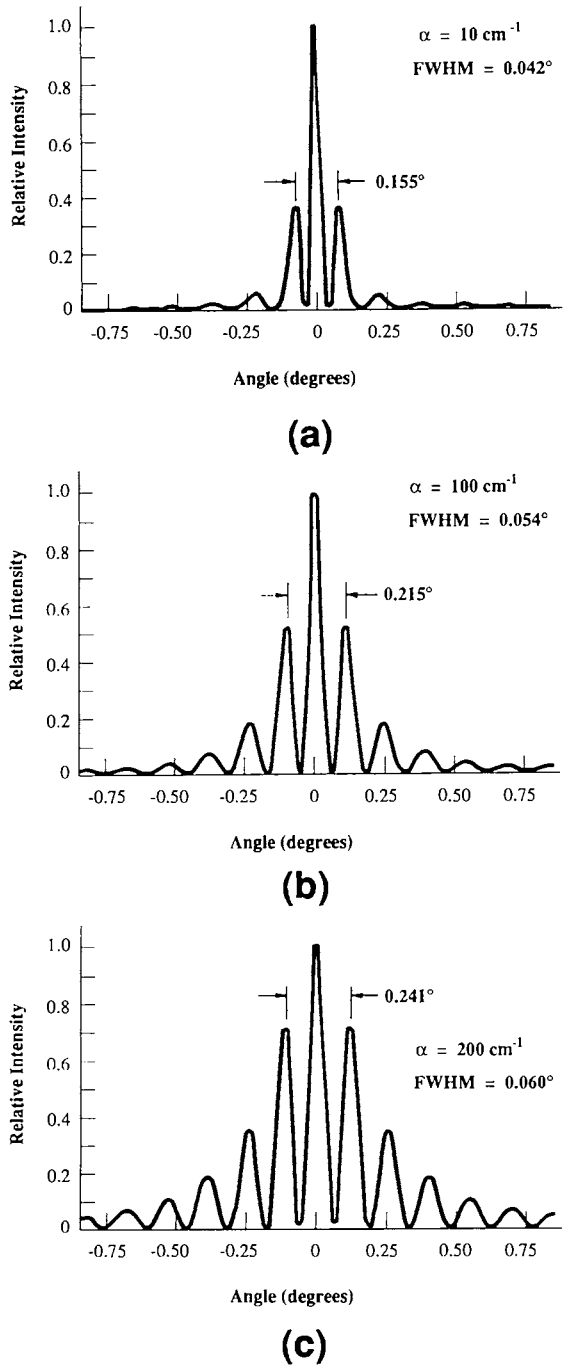

Fig. 16. Far-field radiation patterns for the dominant mode in the geometry of Fig. 15 with (a) $\alpha = 10\ \mathrm{cm}^{-1}$, (b) $\alpha = 100\ \mathrm{cm}^{-1}$, and (c) $\alpha = 200\ \mathrm{cm}^{-1}$.

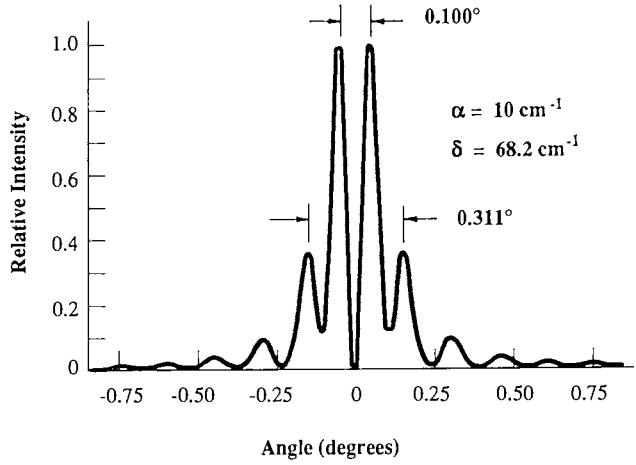

Fig. 17. Far-field radiation patterns for the second longitudinal mode in the geometry of Fig. 15 with $\alpha = 10\ \text{cm}^{-1}$ and $t_1 = 50$ nm.

surprisingly the longitudinal modes alternate in phase as a function of δ or equivalently λ.

The effect of a multistack reflector (Thornton *et al.*, 1984) located some distance below the waveguide in the substrate is assessed in the following example. A similar superstrate reflector was suggested previously (Yamamoto *et al.*, 1978). Such a reflector located below the active region above the substrate reduces the power radiated into the substrate (Hardy *et al.*, 1989), and redistributes that power among the other quantities R, U, T, and A. As previously noted, the substrate reflector may be characterized by a complex field reflectivity whose phase is determined by its precise position below the waveguide. In this example, the grating teeth are rectangular (occupying half a period) $t_1 = 50$ nm, and the modal field absorption in the grating region is $\alpha = 10\ \text{cm}^{-1}$. The magnitude of R_m, which is the field reflectivity of the substrate reflector, is assumed equal to 0.95 and both phase $(R_m) = \pi$ and 0.5π are considered.

Figure 18(a) is a plot of net threshold power gain g versus δ for phase $R_m = \pi$, and we note that two longitudinal modes have very nearly the same thresholds. Values of g, δ, the grating parameters, and the differential efficiency are listed in Table III. The lowest threshold longitudinal mode in this device is displaced $\Delta\lambda = 0.192$ nm from the Bragg condition, and its far-field (not shown) is double lobed. The second lowest threshold mode lases virtually at resonance, $\delta = 0.24\ \text{cm}^{-1}$ or $\Delta\lambda = -7 \times 10^{-4}$ nm, and radiates predominantly in a single lobe. For the particular value of phase R_m in this

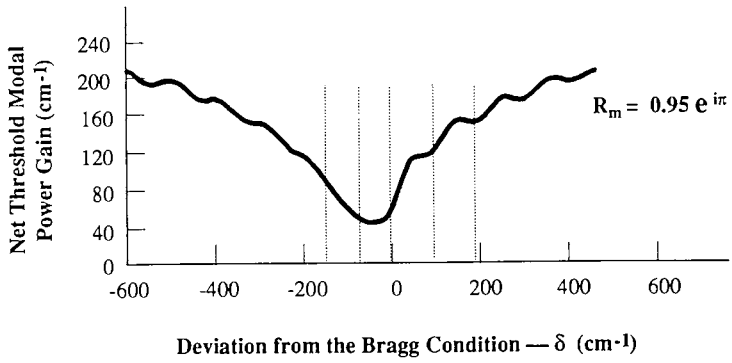

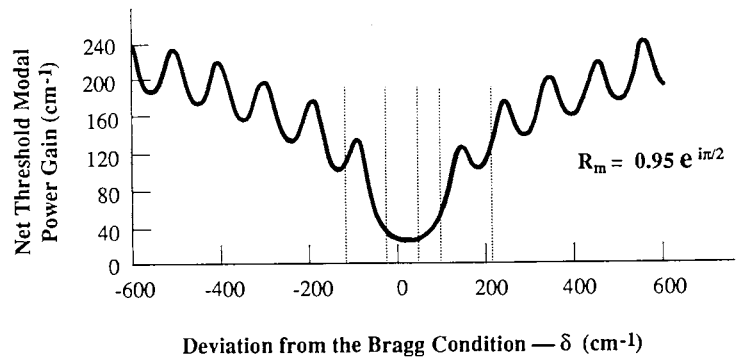

Fig. 18. Net threshold modal power gain versus deviation from the Bragg condition for a grating surface emitter with rectangular shaped teeth and a substrate reflector. In this example, $\alpha = 10\ \text{cm}^{-1}$, $t_1 = 50$ nm, $L = L_{g1} = L_{g2} = 300\ \mu$m, $\Delta_1 = \Lambda/2$ and $\delta = 10\ \text{cm}^{-1}$ corresponds to $\Delta\lambda \approx 0.03$ nm. The longitudinal mode resonances are shown. (a) $R_m = 0.95e^{i\pi}$, and (b) $R_m = 0.95e^{i\pi/2}$.

example, the differential efficiency is substantially increased to 42% for the lowest threshold mode; however, that is not the case for other values of phase R_m as will be shown. Net threshold power gain versus δ for magnitude $R_m = 0.95$ and phase $R_m = 0.5\pi$ is plotted in Fig. 18(b) and data are tabulated in Table IV. Once again the two lowest threshold modes are approximately degenerate in threshold; the dominant longitudinal mode is farther from the Bragg condition; it radiates in two lobes (not shown). The second

Table III

Comparison of the lowest and second threshold longitudinal mode resonances, the threshold gains, the fractional power flows, and the differential efficiencies for a grating surface emitter with rectangular shaped teeth and a substrate reflector. For this example $R_m = 0.95e^{i\pi}$, $\alpha = 10\ \text{cm}^{-1}$ $t_1 = 50$ nm, $L = L_{g1} = L_{g2} = 300\ \mu\text{m}$, and $\delta = 10\ \text{cm}^{-1}$ corresponds to $\Delta\lambda \approx -0.03$ nm.

Parameters	Lowest Threshold	2nd Lowest Threshold
$\delta(\text{cm}^{-1})$	−63.6	0.24
$\Delta\lambda$(nm)	0.192	−0.0007
$g(\text{cm}^{-1})$	44.5	58.7
R	0.263	0.172
U	0.364	0.291
S	0.068	0.055
T	0.066	0.148
A	0.239	0.335
η_0	0.899	0.922
η_g	0.494	0.352
η_D	0.422	0.308

threshold mode radiates in a single lobe. The most remarkable data are the lower thresholds and the low differential efficiencies for this case. Thus changing the phase of R_m from π to 0.5π, which corresponds to shifting the substrate reflector by $\approx 0.03\ \mu$m, has the effect of increasing the grating reflectivity by a factor of ≈ 2.5 and reducing the differential efficiency by a factor of 5. We thus conclude that the phase of the substrate reflectivity affects the behavior of the device profoundly, and the position of the substrate reflector must be precisely controlled if it is to be utilized.

The final device to be studied in this section is one in which the grating periods are identical as previously so that β_0 is the same in both grating sections. However, as the result of either minute compositional or dimensional differences, the propagation constants in the two grating sections are not identical. In grating 1 we assume the waveguide dimensions and indices are such that $\beta_1 = \beta_0 = 2\pi/\Lambda$ at $\lambda = 0.8\ \mu$m, and $\delta_1(\lambda) =$

Table IV

Comparison of the lowest and second threshold longitudinal mode resonances, the threshold gains, the fractional power flows, and the differential efficiencies for a grating surface emitter with rectangular-shaped teeth and a substrate reflector. For this example $R_m = 0.95\, e^{i\pi/2}$, $\alpha = 10\ \text{cm}^{-1}$, $t_1 = 50$ nm, $L = L_{g1} = L_{g2} = 300\ \mu\text{m}$, and $\delta = 10\ \text{cm}^{-1}$ corresponds to $\Delta\lambda \approx -0.03$ nm.

Parameters	2nd Lowest Threshold	Lowest Threshold
$\delta(\text{cm}^{-1})$	−20.0	45.0
$\Delta\lambda$(nm)	0.060	−0.14
$g(\text{cm}^{-1})$	27.2	26.2
R	0.442	0.454
U	0.025	0.055
S	0.039	0.087
T	0.159	0.115
A	0.336	0.289
η_0	0.845	0.840
η_g	0.044	0.100
η_D	0.035	0.080

$\beta_1(\lambda) - \beta_0$. For grating 2, however, the waveguide is slightly modified to increase its effective index. Thus $\beta_2 = \beta_0$ at some wavelength longer than 0.8 μm, and with the definition $\delta_0(\lambda) = \beta_2(\lambda) - \beta_1(\lambda)$ (δ_0 is a weak function of the lasing wavelength) we have $\delta_0(\lambda) = 141\ \text{cm}^{-1}$, which corresponds to an 0.425 nm shift in the vicinity of 0.8 μm. Under the conditions outlined above, the reflectivity of grating 1 peaks at $\delta_1(\lambda) = -18\ \text{cm}^{-1}$, in immediate proximity to the Bragg condition. The maximum reflectivity of grating 2 occurs at $\delta_1(\lambda) = -159\ \text{cm}^{-1}$. Now by using the calculated reflectivities for the gratings as described above, we compute the curve of net modal power gain at threshold and the longitudinal mode resonances, which are plotted in Fig. 19.

Several features of these results are worthy of discussion. First we note that two longitudinal modes, each corresponding to one grating resonance, have comparable thresholds, but not surprisingly these thresholds are higher than for the devices previously studied. The dominant mode with $g = 58.9\ \text{cm}^{-1}$ lases at $\delta_1 = -23.4\ \text{cm}^{-1}$ or $\lambda = 0.80007\ \mu\text{m}$, whereas the second

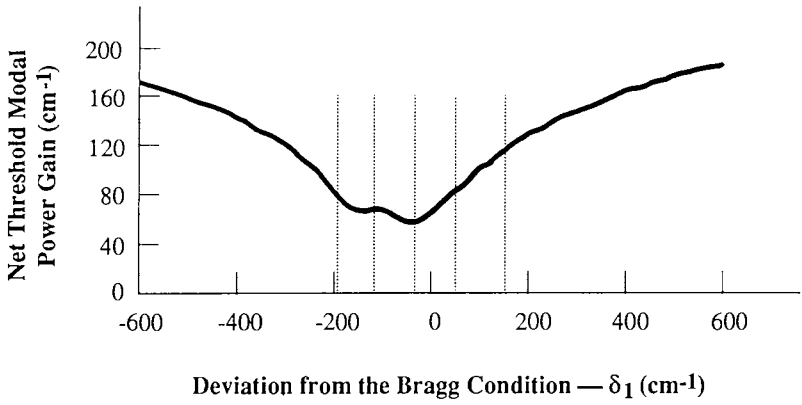

Fig. 19. Net threshold modal power gain versus deviation from the Bragg condition of grating 1, for a grating surface emitter with rectangular-shaped teeth. The peak reflectivity of grating 1 occurs very near $\lambda = 0.8$ μm whereas that of grating 2 is at $\lambda = 0.8005$ μm. In this example, $\alpha = 10\ \text{cm}^{-1}$, $t_1 = 50$ nm, $L = L_{g1} = L_{g2} = 300$ μm, $\Delta_1 = \Lambda/2$ and $\delta_1 = 10\ \text{cm}^{-1}$ corresponds to $\Delta\lambda \approx -0.03$ nm. The longitudinal mode resonances are shown.

has a threshold gain of $g = 67.3\ \text{cm}^{-1}$ and a resonance at $\delta_1 = -108\ \text{cm}^{-1}$ or $\lambda = 0.80033$ μm. Were the length of the active region increased slightly so as to shift the longitudinal mode resonances slightly to more negative values of δ_1, the modes would shift toward the peak reflectivity of grating 2 and would become more nearly threshold degenerate. However, because of the asymmetry in the threshold curve of Fig. 19, which results from the asymmetry of the individual reflectivity curves, it appears as if the dominant mode will lie nearer to $\delta_1 = 0$ than $\delta_1 = -140\ \text{cm}^{-1}$ regardless of changes in the active section length.

The longitudinal modes discussed in the preceding paragraph have approximately equal differential efficiencies of 21% and both radiate in asymmetric patterns. The far-field pattern for the dominant mode is shown in Fig. 20(a), and the radiation pattern emitted by the second longitudinal mode at $\lambda = 0.80033$ μm is plotted in Fig. 20(b). Note the reduced radiation contrast as compared to Figs. 16(a) and 17. One may observe a similar contrast reduction when the two gratings do not emit coherently.

These results illustrate the sensitivity of the radiation pattern to differences in the two waveguide regions. For a difference in resonant Bragg wavelength of half the above value, i.e., $\delta_0(\lambda) = 70.7\ \text{cm}^{-1}$, the longitudinal mode, which is resonant near $\lambda = 0.8$ μm is again dominant and radiates in a pattern similar to that shown in Fig. 20, but the subsidiary lobe is now much reduced

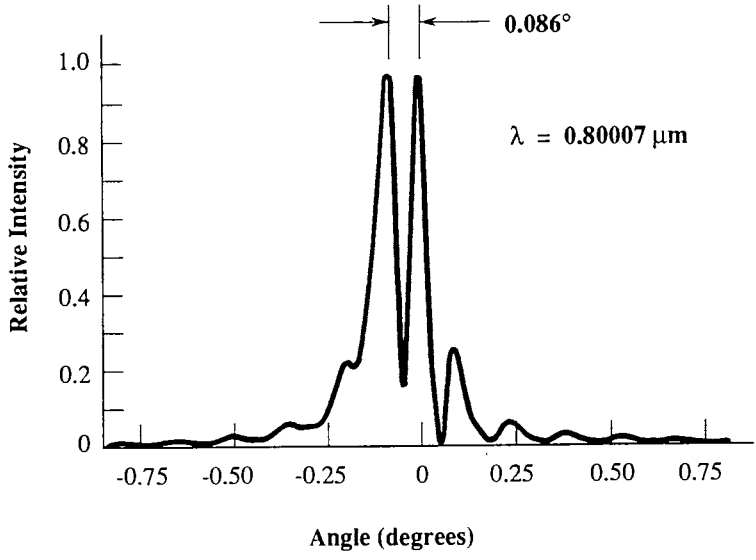

(a)

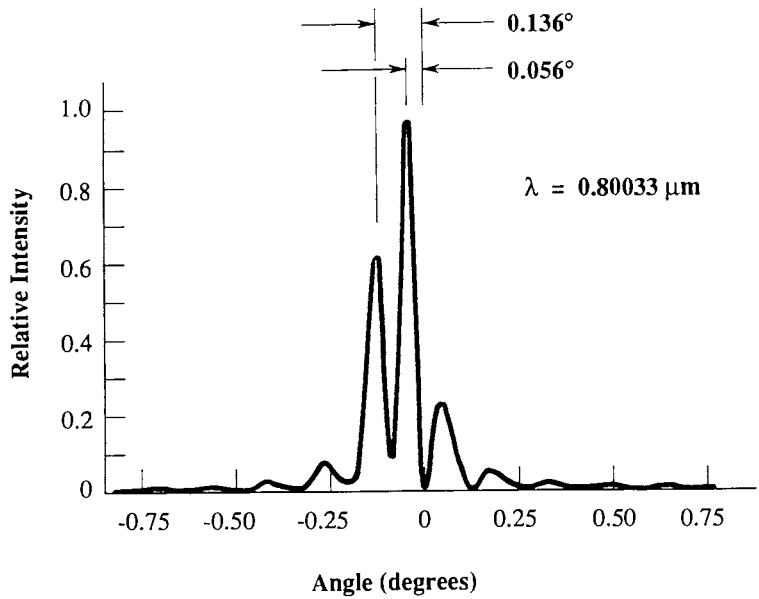

(b)

Fig. 20. Far-field radiation patterns for (a) the lowest threshold longitudinal mode, and (b) the second threshold longitudinal mode in the geometry of Fig. 19.

in amplitude and power. The longitudinal mode discrimination is also improved, and we conclude that a waveguide-grating mismatch of 0.25 nm between two grating sections is acceptable.

F. Conclusions

In this section results of a GSE analysis for lasers with a gain section interposed between two second-order gratings have been presented. The analytical results include an expression for differential efficiency in terms of the grating parameters and expressions for the radiation pattern. Computations, based on the formulation, solve for the longitudinal modes of the device. For each longitudinal mode, the threshold gain, differential efficiency and the far-field radiation pattern are evaluated.

The data show that the spacings of the longitudinal mode resonances are determined primarily by the length of the gain region between the gratings, and the lowest threshold mode usually lases at some wavelength close but not identical to that predicted by the Bragg condition. Longitudinal mode selectivity is enhanced for higher grating teeth and lower losses in the grating sections. As expected, asymmetrical grating tooth shapes generate asymmetric radiation patterns, but even gratings with symmetric teeth usually emit in a direction, at least slightly displaced from the normal to the grating. The far-field patterns alternate between predominantly single- and double-lobe output, and in roughly half the cases, the latter pattern will be favored.

In general, differential efficiency is reduced from that of a coated, cleaved-facet laser because of several effects. Some power is transmitted through the grating section, some is lost to absorption in the grating sections, and if the output is taken from the radiation into the air, the power radiated into the substrate is lost as well. The last source of loss can be eliminated by the use of a substrate reflector, and the inclusion of such a reflector is generally beneficial. However, it is also possible to locate the reflector such that it acts to cancel the radiation and the laser then has a still lower differential efficiency.

The effect of differing Bragg wavelengths in the two grating sections has also been examined. Such differences can be caused by small variations in waveguide dimensions or compositions, even if the grating periods are identical. For a laser whose Bragg wavelengths differ by 0.5 nm, we find that two longitudinal modes are almost threshold degenerate, and the mode patterns are significantly distorted and displaced from the normal. With the difference reduced to 0.25 nm, the situation is much improved, and the device behaves in an acceptable manner.

IV. THREE GRATINGS–TWO GAIN SECTIONS

A. Discussion of the Geometry

We consider a GSE geometry in which there are two gain sections, flanked by two grating sections and separated by a central grating section as shown in Fig. 21. The gratings all have identical periods and the gain sections may or may not have equal lengths L_1 and L_3. But even if $L_1 = L_3$, the fact that they can be differentially pumped, in effect, encompasses to some degree cases where they may differ in gain or length. Consider two situations as discussed in the following paragraphs.

In the first case, the three gratings are assumed to be fixed in position relative to each other. Now suppose that the center grating is increased or decreased in length by a relatively small amount, on the order of a fraction of a period to several periods. The increase or decrease can be characterized by a change in the phase of the light transmitted and reflected by the grating. If the change in effective grating length is compensated by an identical phase increase or decrease of either or both gain sections, the relative phases of the reflections and transmission from the center grating are to a good approximation unchanged, and our calculations indicate that device performance is also virtually unaffected. We note that the modified gain section(s) with the same pumping current will have a slightly different optical length under these conditions as a result of anti-guiding, but that change is insignificant. This situation is illustrated schematically in Fig. 22. Here we show three gratings fixed on a wafer relative to one another. We visualize

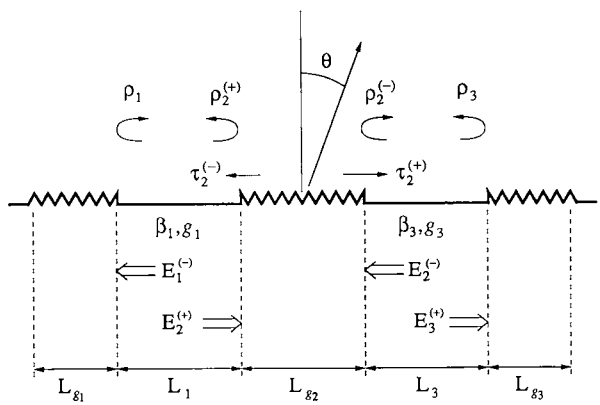

Fig. 21. A two-gain, three-grating surface emitter illustrating the parameters, reflections, and transmission.

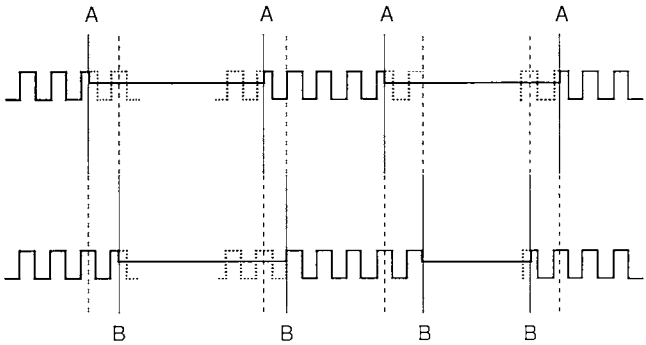

Fig. 22. Illustration of two gratings that behave equivalently.

that the planes labelled "A" are the boundaries of the gratings on one GSE, and those denoted "B" are the boundaries on another GSE. According to our argument given previously both devices behave very similarly.

For the second case, the position of the central grating is not fixed as in the previous case. Instead we envision it being shifted along the laser length such that the new teeth positions do not coincide with the former positions. Now the device behavior may be radically modified. Such effects are also observed with a fixed grating if the two pump currents are separately adjusted to achieve threshold. Assume one current is set at a relatively low level, and the second is increased to attain threshold. At and above the threshold condition, the charge densities in the two sections saturate at different levels and the effective optical lengths differ. Thus, in effect, the central grating has been shifted. In Section IV.E we study that situation in more detail.

B. The Threshold Condition

The geometry to be modeled is shown in Fig. 21. The two gain regions are L_1 and L_3 in length and the complex field reflectivities $\rho_1, \rho_2^{(\pm)}, \rho_3$, and transmissivities $\tau_2^{(\pm)}$, are all functions of wavelength (or equivalently β) and in all cases $\tau_2^{(+)} = \tau_2^{(-)}$, as discussed in Section II. Note that $\rho_1 = \rho_1^{(-)}$ and $\rho_3 = \rho_3^{(+)}$. In terms of these quantities, the threshold condition is given by (Hardy *et al.*, 1990b)

$$\begin{aligned}\rho_1\rho_3\tau_2^{(+)}\tau_2^{(-)} \exp\left[i2(\beta_1 L_1 + \beta_3 L_3)\right] \exp\left[(G_1 + G_3)(1 - ib)\right] \\ = \{1 - \rho_1\rho_2^{(+)} \exp\left(i2\beta_1 L_1\right) \exp\left[G_1(1 - ib)\right]\} \\ \times \{1 - \rho_3\rho_2^{(-)} \exp\left(i2\beta_3 L_3\right) \exp\left[G_3(1 - ib)\right]\}\end{aligned} \tag{45}$$

where $G_1 = g_1 L_1$, $G_3 = g_3 L_3$ are the net power gain-length products of the two gain sections, b is the anti-guiding factor, and β_1, β_3 are the propagation constants for the condition of zero gain or, equivalently, transparency. Note that this condition is attained at some non-zero injected charge density where the gain just compensates for the internal losses. Below that charge density the gain is negative.

In Eq. (45), G_1, G_3, and the lasing wavelengths of the longitudinal modes are the unknowns. They are determined by requiring that the magnitudes of both sides of Eq. (45) be equal and identical in phase at threshold. This problem is underspecified since there are many pairs of G_1, G_3. For example, one may set the two equal and find $G = G_1 = G_3$ and λ. More generally, one may specify a ratio between G_1 and G_3, or a fixed difference $G_3 - G_1$. The equation then contains only one unknown gain and resonant λ.

To solve Eq. (45), the propagation constant (or the wavelength) is varied in the vicinity of the Bragg condition. For each wavelength the complex reflectivities and transmissivities of the gratings are computed, and the resulting quadratic equation is solved for the remaining gain variable G_1 or G_3. Only real values of G are physically acceptable and each corresponds to a longitudinal mode solution. The various resonant wavelengths are determined by this technique, and one longitudinal mode has the lowest threshold. The solution with the lowest gain is dominant, and all other longitudinal modes can be ordered according to increasing threshold. In this manner one can determine the stability of a mode relative to its nearest competitors.

C. The Radiation Quantum Efficiency

As for the two-grating case (Section III), the field reflectivities, transmissivities and relative field amplitudes incident on each grating section (Fig. 21) must be found for the longitudinal mode resonances. With these parameters known, we can calculate the total power loss in gain section j ($j = 1, 3$)

$$P_l^{(1)} = \left(\frac{\beta_1 Q_1}{2\omega\mu_0}\right)\{|\rho_1 E_1^{(-)}|^2 + |\rho_2^{(+)} E_2^{(+)} + \tau_2 E_2^{(-)}|^2\}\left(\frac{\alpha_1}{g_1}\right)\{\exp(G_1) - 1\} \tag{46a}$$

$$P_l^{(3)} = \left(\frac{\beta_3 Q_3}{2\omega\mu_0}\right)\{|\rho_3 E_3^{(+)}|^2 + |\rho_2^{(-)} E_2^{(-)} + \tau_2 E_2^{(+)}|^2\}\left(\frac{\alpha_3}{g_3}\right)\{\exp(G_3) - 1\} \tag{46b}$$

where $G_j = g_j L_j$ ($j = 1, 3$) and $\tau_2^{(+)} = \tau_2^{(-)} = \tau_2$ was assumed. The normalizing factor Q_j is defined in (12) and for identical waveguides as considered here

(except for length) $Q_1 = Q_3 = Q$ and $\beta_1 = \beta_3 = \beta$ where $\beta = \beta_0 + \delta$. The power lost in each grating section via all channels (see Fig. 12) is

$$P_g^{(1)} = |E_1^{(-)}|^2 (1 - |\rho_1|^2) \left(\frac{\beta Q}{2\omega\mu_0} \right) \tag{47a}$$

$$P_g^{(3)} = |E_3^{(+)}|^2 (1 - |\rho_3|^2) \left(\frac{\beta Q}{2\omega\mu_0} \right) \tag{47b}$$

for gratings 1 and 3, and

$$P_g^{(2)} = (|E_2^{(+)}|^2 + |E_2^{(-)}|^2 - |\rho_2^{(+)} E_2^{(+)} + \tau_2 E_2^{(-)}|^2 - |\rho_2^{(-)} E_2^{(-)} + \tau_2 E_2^{(+)}|^2) \left(\frac{\beta Q}{2\omega\mu_0} \right). \tag{47c}$$

The useful power output $P_u^{(j)}$ ($j = 1, 2, 3$) from any of the three gratings, due to radiation up into the air (refractive index n_1) is given by Eq. (30a). In particular, using Eq. (32a) for the two end gratings ($j = 1, 3$) we have

$$P_u^{(1)} = |E_1^{(-)}|^2 U_1 \left(\frac{\beta Q}{2\omega\mu_0} \right) \tag{48a}$$

$$P_u^{(3)} = |E_3^{(+)}|^2 U_3 \left(\frac{\beta Q}{2\omega\mu_0} \right) \tag{48b}$$

but for the center grating the integration of Eq. (30a) yields a more complicated expression. With the above definitions, we find that the external differential quantum efficiency is given by

$$\eta_D = \eta_i \left[\frac{P_u^{(1)} + P_u^{(2)} + P_u^{(3)}}{P_l^{(1)} + P_l^{(3)} + P_g^{(1)} + P_g^{(2)} + P_g^{(3)}} \right] \tag{49}$$

or, in analogy to the dual grating case (Section III)

$$\eta_D = \eta_i \eta_0 \eta_g \tag{50}$$

where η_i is the internal quantum efficiency, and

$$\eta_0 = \left[\frac{P_g^{(1)} + P_g^{(2)} + P_g^{(3)}}{P_l^{(1)} + P_l^{(3)} + P_g^{(1)} + P_g^{(2)} + P_g^{(3)}} \right] \tag{51a}$$

$$\eta_g = \left[\frac{P_u^{(1)} + P_u^{(2)} + P_u^{(3)}}{P_g^{(1)} + P_g^{(2)} + P_g^{(3)}} \right]. \tag{51b}$$

It is straightforward to show that for a laser composed of two gratings (e.g., $P_l^{(3)} = P_g^{(3)} = 0$), Eq. (50) reduces to Eq. (39). More detailed calculations of the quantum efficiency are given in Section VI.D.

D. The Radiation Far-Field Pattern

As in the case of two gratings (Section III), one determines, first, the relative phases of the modes in each grating section. The far-field pattern, radiated by gratings 1 and 3 are similar to those derived for the two gratings in Section III. However, for the center grating, one finds it more convenient to separate the contribution of the forward propagating mode, $E_2^{(+)}$, from that of the backward propagating mode, $E_2^{(-)}$ (Fig. 21). Assuming that for each of the incident waves (i.e., $E_1^{(-)}$, $E_3^{(+)}$, $E_2^{(+)}$, and $E_2^{(-)}$) separately, z is set equal to zero at the junction of the gain and grating section, with z increasing into the grating section, one finds that the far-field intensity pattern satisfies

$$\begin{aligned} F(\vartheta) = |&E_1^{(-)} H_1(-\vartheta) \exp[i k_0 (L_1 + L_{g2}/2)\vartheta] \\ &+ E_2^{(+)} H_2^{(+)}(\vartheta) \exp[i k_0 (L_{g2}/2)\vartheta] \\ &+ E_2^{(-)} H_2^{(-)}(-\vartheta) \exp[-i k_0 (L_{g2}/2)\vartheta] \\ &+ E_3^{(+)} H_3(\vartheta) \exp[-i k_0 (L_3 + L_{g2}/2)\vartheta]|^2 \end{aligned} \tag{52}$$

where the superscript $(\pm)$ in H_2 is to include non-symmetric gratings for which Eq. (33) may differ depending on the propagation direction [for symmetric gratings $H_2^{(+)}(\vartheta) = H_2^{(-)}(-\vartheta)$]. The angle in $H_2^{(-)}$ and H_1 is reversed to compensate for having let z increase in the opposite direction. The various exponential multiplicative factors in Eq. (52) are due to the lateral grating shifts as in Section III for two gratings.

E. Examples

1. *Asymmetric Pumping*

As an example, we consider a symmetric situation in which both gain sections are exactly 300 μm in length and the anti-guiding factor, b which is variously assumed to lie between 1.5 and 6 (Osinski and Buus, 1987), is set equal to 2. The three grating sections are also all identical, their teeth are rectangular and occupy half the grating period. The gratings are located

as shown in Fig. 21. The waveguide dimensions and refractive indices are (see Fig. 3) $n_1 = 1, n_2 = 3.49, n_3 = 3.42, n_4 = 3.36, t_1 = 50$ nm, $t_2 = 200$ nm and $t_3 = 400$ nm. The propagation constant in the grating regions for $\lambda = 0.8$ μm is $\beta_0 = 26.525$ μm^{-1}, so that the second-order grating period is $\Lambda = 2\pi/\beta_0 = 0.23688$ μm. For simplicity we assume that β_1 and β_3 equal β_0.

Each grating, without loss of generality, is assumed to consist of an integer number of teeth. In light of our earlier discussion, the precise number of teeth and/or fractional teeth do not profoundly influence device behavior subject to maintaining the relative phases of the light transmitted and reflected by the gratings. Thus, without loss of generality, the number of teeth is arbitrarily set exactly to 844 for a length of 199.925 μm. This choice covers a variety of similar cases. To be specific, for example, if the central grating length is extended to the left by half a grating period, i.e., $\Lambda/2$, then a reduction in the optical length of the adjacent gain section ΔL will compensate if $\beta \Delta L = \beta_0 \Lambda/2$, where β is the propagation constant in the gain section, and ΔL is the reduction in length of the gain section. The change in a gain section length ΔL has a minor secondary effect on the refractive index because of the anti-guiding, but that has been neglected, and as noted previously $\beta = \beta_0$.

Figure 23 illustrates the locus of g_1 versus g_3 (where $G_i = g_i L_i$) for the dominant and second lowest threshold longitudinal modes of the symmetric GSE described above. As expected the results are symmetric in g_1, g_3, although the axes have different scales in Fig. 23. The threshold for the lowest threshold mode with identical pumping is $g_1 = g_3 = 30.2$ cm^{-1}, and

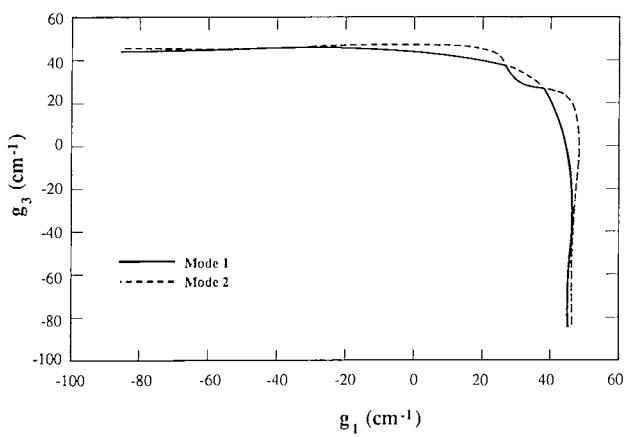

Fig. 23. Threshold plot for the lowest two modes with g_3 versus g_1.

for this case the second-mode threshold is given by $g_1 = g_3 = 33.2\ \text{cm}^{-1}$. We note that between $(g_1, g_3) = (37.6, 27.1)\ \text{cm}^{-1}$ and $(g_1, g_3) = (27.1, 37.6)\ \text{cm}^{-1}$, one mode is dominant. At those limiting values the two modes become degenerate and their thresholds are reversed outside this range. The situation is represented more clearly in Fig. 24, which displays an expanded plot of Fig. 23.

Over most of the range the dominant and second-mode threshold differ by roughly 10%, whereas the third mode threshold gain is approximately double the first and second. The maximum difference between modes 1 and 2 occurs at about $(g_1, g_3) = (20, 40)\ \text{cm}^{-1}$ for the dominant mode. Near degeneracy also occurs for $(g_1, g_3) = (-40, 46)\ \text{cm}^{-1}$, but when one of the gain sections is not pumped to above transparency, the situation may be less interesting in the applications. For near-symmetric pumping when $g_1 \approx g_3$, the dominant mode is near the Bragg condition with a deviation of $\delta \approx 13\ \text{cm}^{-1}$ or ≈ -0.04 nm. The second-mode deviation is $\approx -54\ \text{cm}^{-1}$ or $+0.16$ nm. The dependences of deviation on g_1 are shown to be rather weak in Fig. 25.

The guided wave intensity $I_g(z)$ and the radiating near-field $I_r(z)$ [see Eqs. (26) and (29)] for the symmetric case with $g_1 = g_3 = 30.2\ \text{cm}^{-1}$ are plotted in Fig. 26. Since both the geometry and excitation are symmetrical, the fields must be either symmetric or anti-symmetric. Clearly the near-field guided wave power is symmetric, as shown by the curve of Fig. 26. The radiating field $I_r(z)$, however, passes through zero at the center of the structure indicating that the phase changes at that point. We also observe that the radiating intensity is much reduced in the center grating region, as compared with the outer grating sections. The lower radiating near field in

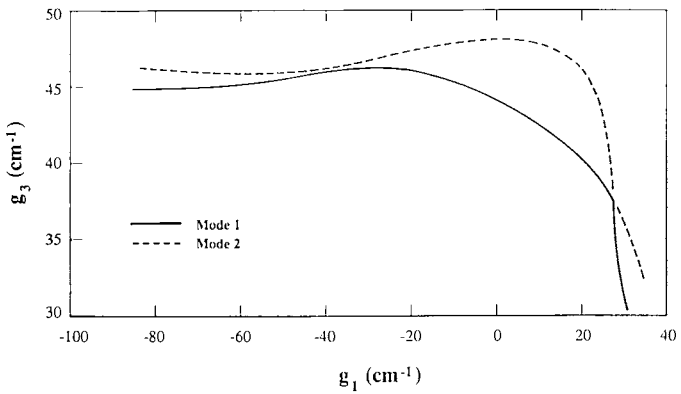

Fig. 24. Expanded view of Figure 23.

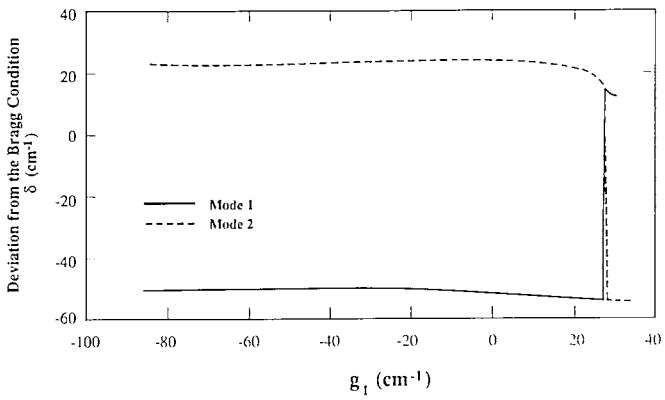

Fig. 25. Deviations from the Bragg condition versus g_1 for the two lowest threshold modes.

the center grating section indicates that the overall radiation losses are smaller, resulting in a lower threshold. This is as expected since the lowest threshold mode has a combination of lower losses and higher gain than the second, third, etc.

In this geometry, the second-order mode is also antisymmetric and the third-order, higher threshold mode, whose deviation from the Bragg condition is $-52.5\ \text{cm}^{-1}$, is symmetric. The high third-mode threshold directly results from its large radiation power, which acts as a loss mechanism. The near-fields for this mode are shown in Fig. 27, where it is evident that the high optical intensity in the central grating causes the large radiation.

The far-field (radiation) pattern of the dominant asymmetric mode of a symmetrically pumped laser is shown in Fig. 28. A null is evident at the center as is expected from the asymmetry, and many lobes exist because of the interference between the two outer gratings. Figures 29 and 30 present the same results for asymmetric pumping, i.e., $(g_1, g_3) = (-8.5, 45.1)\ \text{cm}^{-1}$. Here, as expected, we observe very little optical energy in the lightly pumped gain section and the corresponding outer grating. Once again, the far-field has a null at zero indicating that the radiation from the two radiating gratings are out-of-phase.

As a second example we consider the effect of small differences in gain. Assume $(g_1, g_3) = (27.4, 36.2)\ \text{cm}^{-1}$, which could result from material variations. Note too that since these numbers refer to net gain in excess of transparency and internal losses, the pumping currents need not differ greatly. The near- and far-field patterns for this pumping situation are shown in Figs. 31 and 32. The latter is especially interesting since we observe that

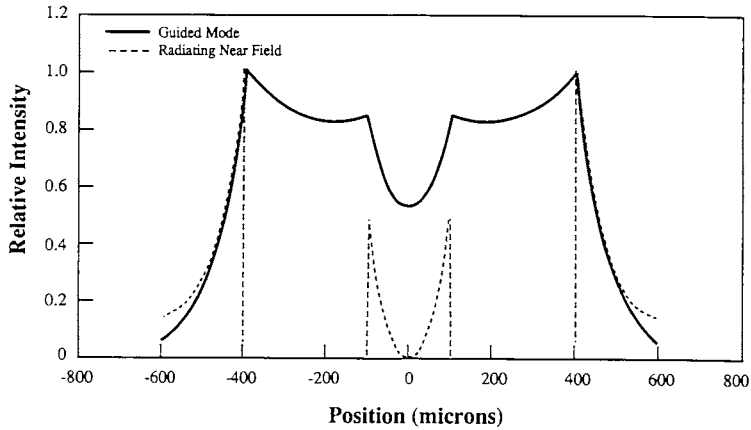

Fig. 26. The near-field intensity pattern for the dominant longitudinal mode with threshold gains of $g_1 = g_3 = 30.2\ \text{cm}^{-1}$. This mode oscillates at $\partial \sim 12.3\ \text{cm}^{-1}$ ($\Delta\lambda = -0.37$ Å) away from the Bragg condition. Due to the symmetry of the structure, the near field is either symmetric or antisymmetric (the intensity pattern is symmetric). The solid line represents the local intensity of the propagating guided mode. It does not vanish anywhere along the structure. The radiating near-field intensity pattern is represented by the broken line, and is non-zero only in the grating regions. Note the radiation null at the center of the second grating, which minimizes loss and reduces the model threshold gain.

the contrast in the far-field pattern is reduced. In this case, the radiation from each of the gratings is fully coherent, but the pattern does not exhibit full contrast.

Before concluding the discussion in this subsection, it is interesting to ask if all the points for the lowest threshold mode in Figs. 23 and 24 are accessible. First, we recall that one cannot adjust the gains, but only the currents. Thus, to speak of setting a value of gain implies that the laser is below or just at threshold. With this in mind, consider for example, setting g_3 equal to $45\ \text{cm}^{-1}$ and increasing g_1 from its unpumped negative value. Then threshold would be attained at $g_1 \approx -80\ \text{cm}^{-1}$. According to the calculations, if g_1 were further increased, the laser would cease lasing. This is a

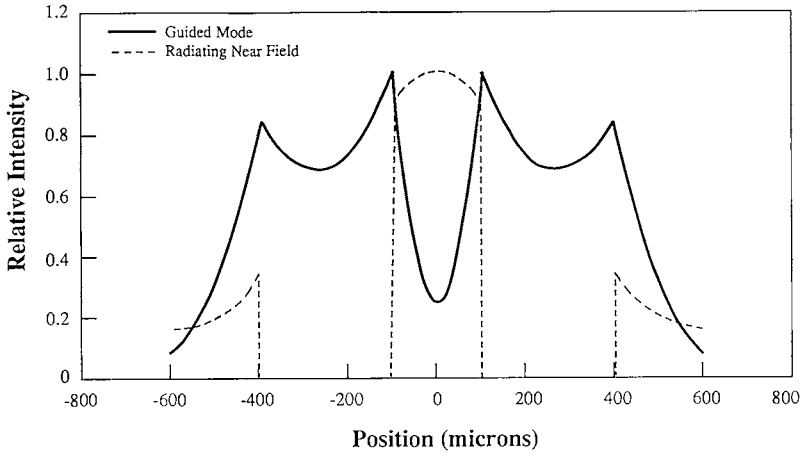

Fig. 27. Near fields for the third-order mode showing the high radiation intensity in the central grating.

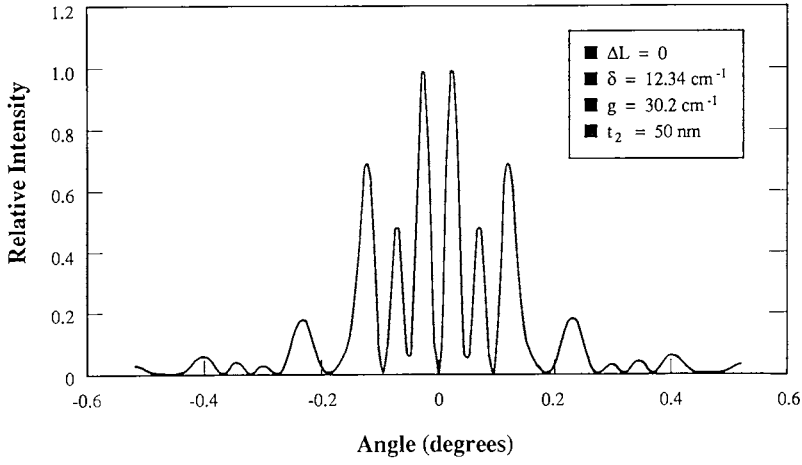

Fig. 28. Far-field of the dominant longitudinal mode with $g_1 = g_3 = 30.2\ \text{cm}^{-1}$.

direct result of the anti-guiding, which modifies the phase relationships as a function of gain to require a still higher gain, g_3, to satisfy the resonance condition and is analogous to a laser with a wavelength selective external

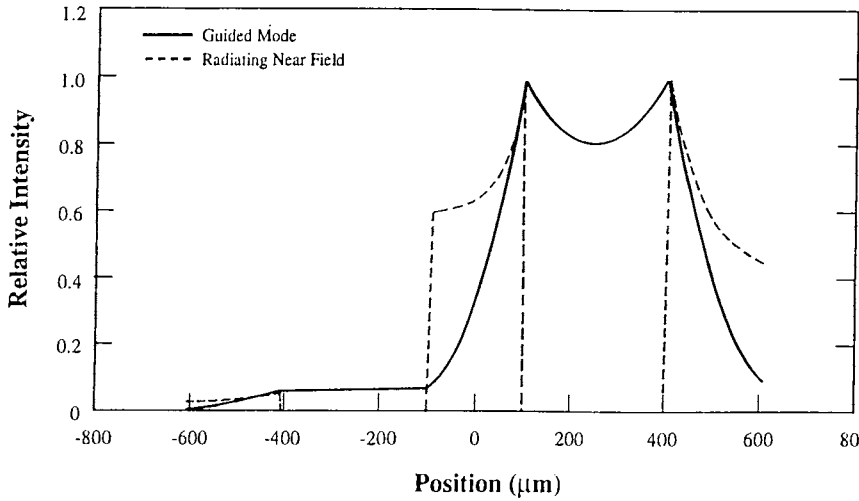

Fig. 29. Near-field intensity pattern for the dominant longitudinal mode. The structure is symmetric about the center of the middle grating. However, it is pumped nonsymmetrically. The gain in the first gain section is $g_1 = -8.5\ \text{cm}^{-1}$, whereas the gain in the other gain section is $g_3 = 45.1\ \text{cm}^{-1}$. The mode oscillates near $\partial = -5.2\ \text{cm}^{-1}$ ($\Delta\lambda \sim 1.5$ Å) away from the Bragg condition. Note that most of the power of the propagating guided mode (solid line) is concentrated in the more strongly pumped gain section. Thus, significant radiation (broken lines) is emitted only from two gratings, whereas the leftmost outer grating radiates very little energy. In this case the structure behaves like a DBR laser.

element. Depending on adjustment, the feedback from the element can cause the laser to quench at particular placements.

To verify the analytic results, a two-gain, three grating section surface emitter has been tested using a specially designed apparatus (Waarts, 1990) by differentially pumping the gain sections. The near-fields were observed under several conditions. When one gain section was pumped just slightly above threshold with 400 mA, with the other unpumped, the output was

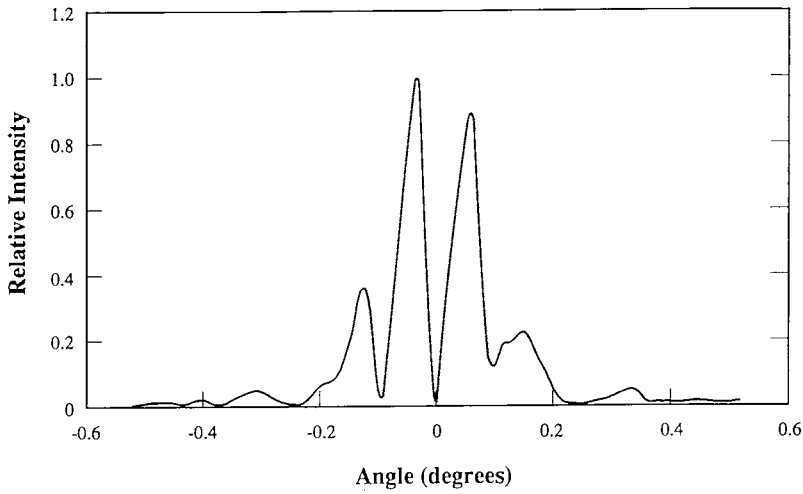

Fig. 30. Far field of the dominant longitudinal mode with $g_1 = -8.5\ \text{cm}^{-1}$, and $g_3 = 45.1\ \text{cm}^{-1}$.

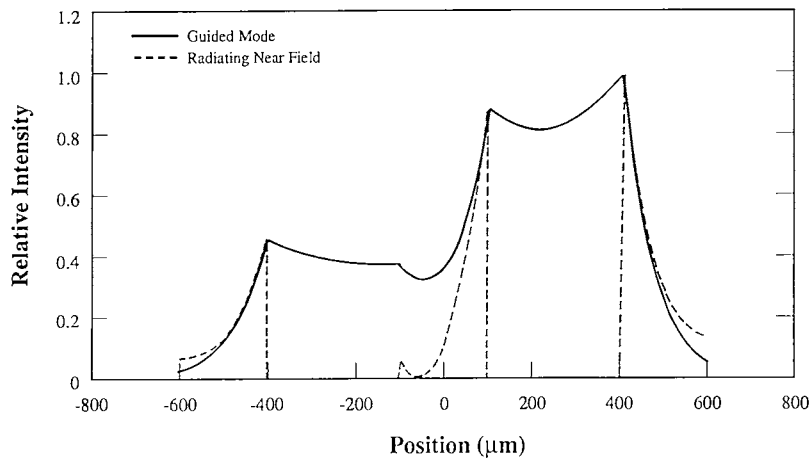

Fig. 31. Near fields of the dominant longitudinal mode with $g_1 = 27.4\ \text{cm}^{-1}$, and $g_3 = 36.2\ \text{cm}^{-1}$.

measured. Then the current to the second gain section was increased to 100, 200, and 300 mA. The results are shown in Fig. 33. We observe that the output power is substantially decreased at 100 mA, it increases again at 200 mA, but does not yet attain its initial value. For 300 mA, not only is the initial level recovered, but output light is also evident at the third grating

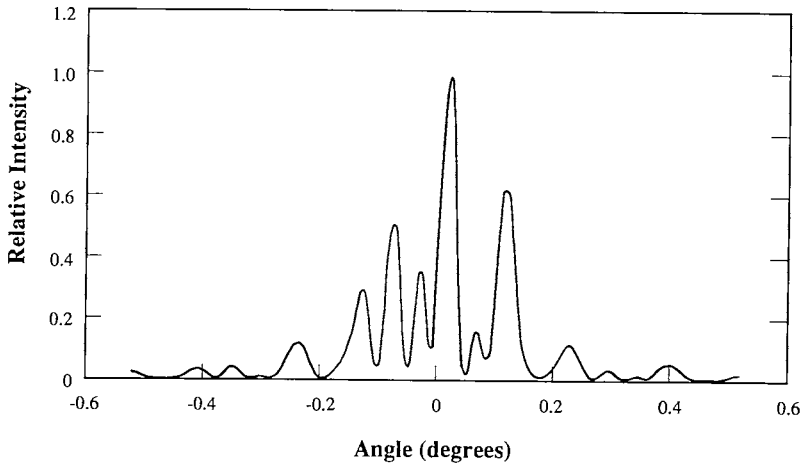

Fig. 32. Far field of the dominant longitudinal mode with $g_1 = 27.4\ \text{cm}^{-1}$, and $g_3 = 36.2\ \text{cm}^{-1}$.

section. At 400 mA the pattern, which is not shown, is very close to being symmetric as predicted by the theory.

The behavior discussed in the preceding paragraph corresponds qualitatively well with the theory. When the device lases at $(g_1, g_3) = (-80, 45)\ \text{cm}^{-1}$, increases in g_1 initially raise the threshold value of g_3, which manifests itself as a decrease in output power ($I_1 = 100$ mA). Then beyond the peak at $g_1 \approx -30\ \text{cm}^{-1}$, the power begins to increase ($I_1 = 200$ mA), until at $g_1 \approx -10\ \text{cm}^{-1}$ ($I_1 = 300$ mA) the power again attains its value with $I_1 = 0$. These results are qualitatively consistent with the data of Figs. 23 and 24.

2. *Modal Sensitivity to Length-Induced Phase Variations*

To illustrate the sensitivity of GSE lasers to asymmetric, length-induced phase variations, we describe in this subsection the evolution of the lowest threshold longitudinal modes of a two-gain section, three-grating laser under an asymmetric change in one of the gain section lengths. In particular, the optical length of one gain section is shortened with respect to the other by up to one grating period. Along with the changes in threshold gain and resonant frequency, the near- and far-fields are found to be dramatically changed. For example, radiation from one of the three gratings can be completely suppressed for even the lowest threshold mode. When the asymmetry so introduced is small, symmetry can be restored by differential current pumping as has been verified experimentally (Waarts, R., un-

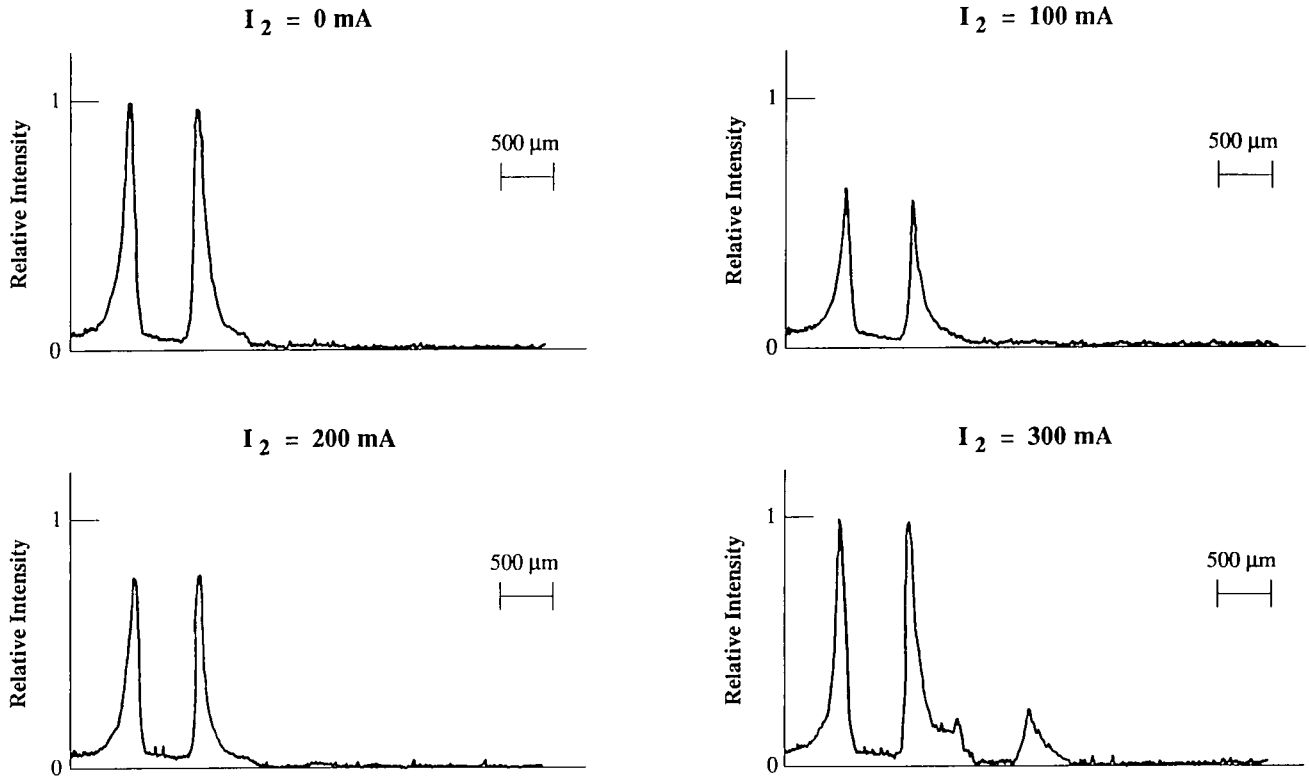

Fig. 33. Measured near field patterns with $I_1 = 400$ mA and various currents I_2. The vertical scale for all the patterns are identical.

published), but in general this is not necessarily the case. However, by studying the causes of this sensitivity, we are able to demonstrate an improved design that trades off increased threshold gain for reduced sensitivity to length-induced phase variations (Hardy *et al.*, 1990c). In all cases, though, the analysis implies that for stable, single-mode operation to occur, it may be necessary to control the optical length of gain and grating sections to better than a wavelength.

As in the previous subsection, we consider the case of $n_1 = 1$, $n_2 = 3.49$, $n_3 = 3.42$, $n_4 = 3.36$, $t_1 = 50$ nm, $t_2 = 200$ nm, and $t_3 = 400$ nm (see Fig. 3). The number of grating periods in 844 ($L_{g1} = L_{g2} = L_{g3} \simeq 199.925$ μm) and, in our first example, a symmetrical configuration is considered where $L_1 = L_3 = 300$ μm (see Fig. 21). In a further section we will allow for L_3 to be slightly longer than L_1, by a fraction of a wavelength, but, in all cases, $g_1 = g_3 = g$ will be assumed.

The two sets of curves in Fig. 34 plot the magnitude and phase of $G = gL$ corresponding to the two solution branches of Eq. (45), as a function of deviation δ from the Bragg condition ($\delta = \beta - \beta_0$). Since the threshold gain is a real quantity, longitudinal mode resonances are defined by the condition phase $(G) = 2\pi m$, m an integer (for convenience, the phase has been normalized so as to vary between +0.5 and −0.5 in Fig. 34). At each

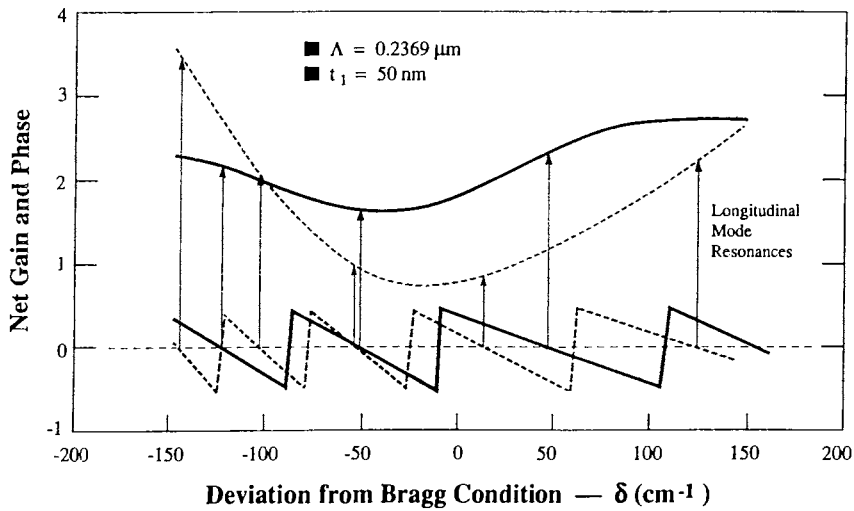

Fig. 34. Longitudinal mode structure for the symmetrical case, $L_3 = L_1$. The upper solid (dashed) curve gives the threshold gain $G_1 = G_3 = gL$ while the lower solid (dashed) curve gives the corresponding phase for the symmetrical (anti-symmetrical) branch as a function of deviation from the Bragg condition. Resonances correspond to zeros of the phase.

resonance condition so defined, the value of the magnitude of G represents its corresponding threshold gain. This first example establishes a baseline for the longitudinal mode resonant frequencies and their respective threshold gains.

The two lowest threshold modes oscillate at $\delta = 12.3\ \text{cm}^{-1}$ ($\Delta\lambda = -0.037$ nm) with $g_{\text{th}} = 30.2\ \text{cm}^{-1}$, and at $\delta = -54.89\ \text{cm}^{-1}$ with $g_{\text{th}} = 33.2\ \text{cm}^{-1}$. Both are antisymmetric with a zero in the near field radiation pattern at the center of grating 2. The near-field and far-field patterns of the lowest threshold longitudinal mode are depicted in Figs. 26 and 28, respectively. The third mode, which oscillates at $\delta = -52.5\ \text{cm}^{-1}$, has a symmetric near-field pattern (Fig. 27) without a null in the center of the device, resulting in much more radiation loss and higher threshold ($g_{\text{th}} = 54.7\ \text{cm}^{-1}$).

to small length variations, and in particular asymmetric variations. Certainly, when both gain section lengths L_1 and L_3 are modified simultaneously so that $\Delta L_1 = \Delta L_3$, the structure remains symmetric with an antisymmetric or symmetric mode distribution and the gain curves virtually remain the same as in Fig. 34. The only noticeable change is in the location of the resonances, which shift as $\Delta L_1 = \Delta L_3$ is changed. This, however, is not the case when L_1 is held fixed and only L_3 is varied. In Fig. 35, we describe the effect of a small variation ΔL_3 in the length L_3 on the modal gains g (Fig. 35a) and on the mode resonance locations (Fig. 35b). The first-order mode is defined to be the one having lowest threshold and is indicated by solid lines in Figs. 35a and 35b. The next higher-order mode is given by the dotted line and the third mode by the broken line. We note that several gain degeneracies appear between $\Delta L_3 = 0$ and $\Delta L_3 = \Lambda$ and that the mode resonances frequently hop from one wavelength to another. In the following paragraphs the variation in near- and far-field patterns that accompany the gain and frequency variations of Fig. 35 are described.

Since for $\Delta L_3 \neq 0$ the structure is no longer symmetric about the center of the middle grating, neither are the modal fields. To illustrate the variety of asymmetric distributions encountered, in Figs. 36, 37, and 38 we describe the near-field and far-field patterns at three different values of ΔL_3. First, in moving from $\Delta L_3 = 0$ [point (a) in Fig. 35] to $\Delta L_3 = 0.01\ \mu\text{m} \cong 0.042\ \Lambda$ [point (b) in Fig. 35], note that the resonance location and threshold gain are only slightly altered ($\delta = 11\ \text{cm}^{-1}$, $g_{\text{th}} = 32.3\ \text{cm}^{-1}$). However, the near-field and far-field intensity patterns become quite asymmetric (Fig. 36) with nearly 30% more light in the left-hand gain section. The field asymmetry is due to the interference effects between fields reflected from and transmitted through the middle grating. At this point, the asymmetry is small enough

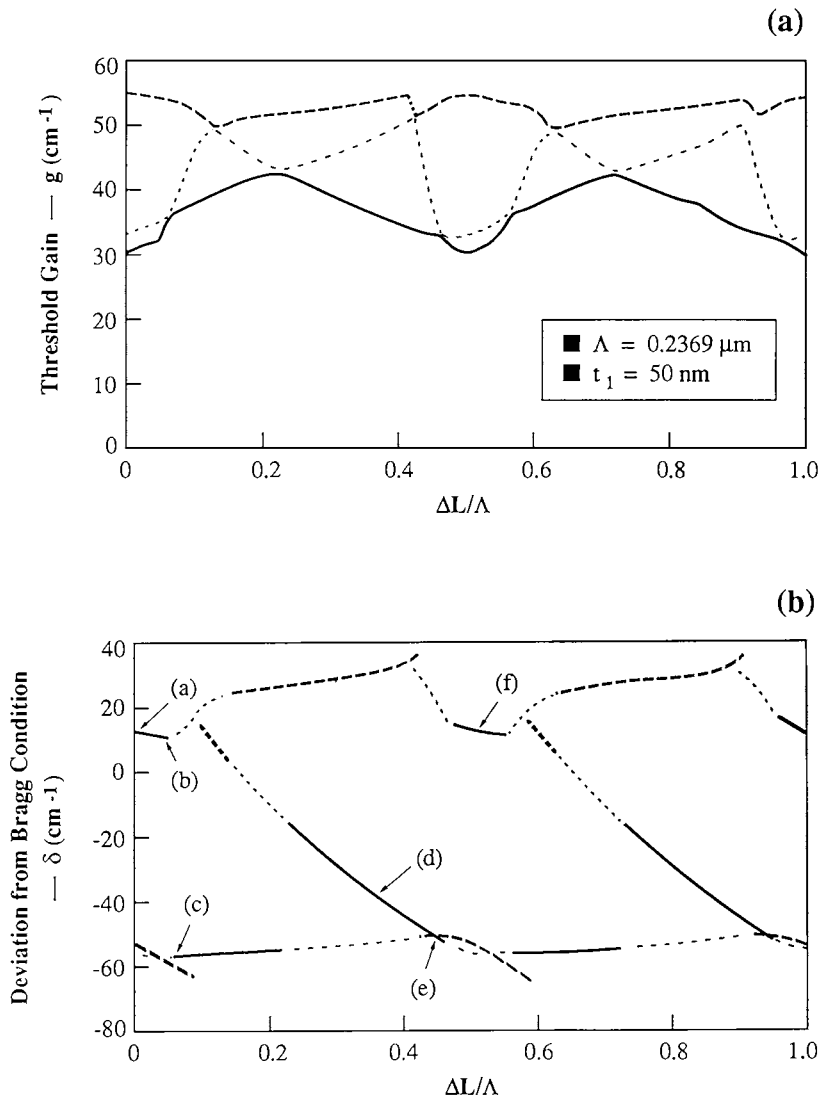

Fig. 35. (a) Threshold gain, and (b) oscillation frequency, of the three lowest threshold-gain modes as a function of $\Delta L/\Lambda = (L_3 - L_1)/\Lambda$.

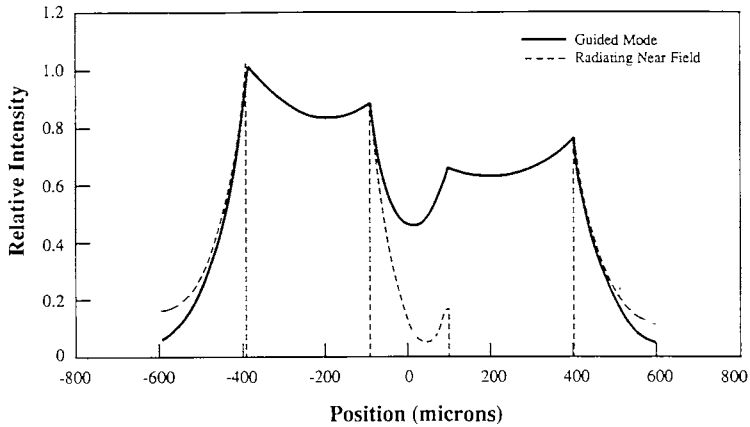

(a)

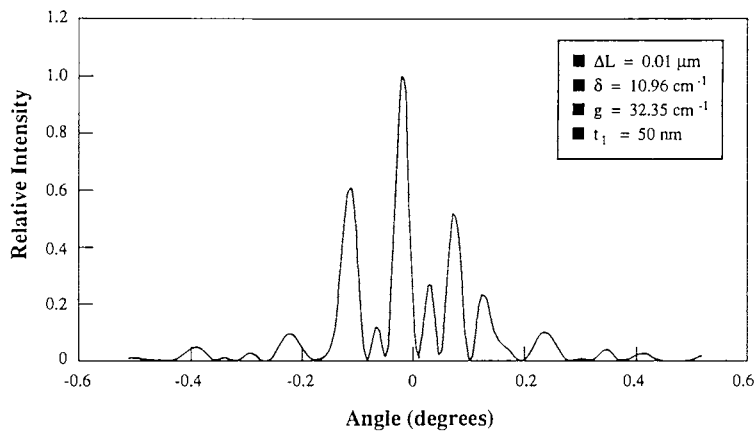

(b)

Fig. 36. Lowest threshold mode at $\Delta L_3 = 0.01$ μm ($\approx 0.042\,\Lambda$) [point (b) in Fig. 35]. (a) Guided mode (solid) and radiating (dashed) near field, (b) far field.

to be compensated by pumping one of the two gain sections slightly harder than the other, thereby altering the relative phases via the anti-guidance factor and virtually restoring near-field symmetry ($g_{\text{th}}^{(1)} = 29.3\ \text{cm}^{-1}$, $g_{\text{th}}^{(3)} = 32.2\ \text{cm}^{-1}$, $\delta = 9.5\ \text{cm}^{-1}$). We note that these threshold gains are *net* gains, i.e., gain above the transparency level and, therefore, the actual current differences in the two sections may be quite small.

The mechanism for restoring symmetry by differential current pumping is as follows: The right-hand gain region, which was lengthened by 0.01 μm relative to the left-hand one, is pumped a little harder to provide more gain. This tends to equalize the near-field intensities of Fig. 36a. At the same time, the increased injected carrier density reduces the effective index of refraction $n_{\text{eff},3}$ via the anti-guidance factor. The optical length $n_{\text{eff},3}L_3$ is also reduced, and eventually equals that of gain section 1. At this point, far-field symmetry is restored, albeit at a different current level than that required to restore near-field symmetry. However, as we show in the next paragraph, one can no longer restore field symmetry when ΔL_3 is larger, at least not by modifying the currents alone.

By further increasing ΔL_3 slightly, the two lowest-order modes go through a degeneracy point and separate again. At $\Delta L_3 = 0.015$ μm [point (c) in Fig. 35] the wavelength hops to $\delta = -56.43\ \text{cm}^{-1}$. In addition, the location of the far field lobes is shifted (not shown). The resulting near-field pattern is similar to that of Fig. 36, but the intensity pattern asymmetry is more pronounced. This asymmetry continues to worsen as the length variation $\Delta L_3/\Lambda$ approaches the mode hop at $\Delta L_3/\Lambda = 0.22$. Just to the left of the jump point, at $\Delta L_3/\Lambda = 0.21$, virtually only the left two gratings radiate. To the right of the jump, however, it is the right two gratings that strongly radiate. In Fig. 37 we describe the near-field and far-field patterns at $\Delta L_3 = 0.317\,\Lambda$ [point (d) in Fig. 35]. The near-field asymmetry is now extreme, as virtually only grating 2 and grating 3 radiate. The far-field pattern, characteristic of two-grating radiation is now broader, with fewer and wider lobes. This mode oscillates at $\delta = -31.1\ \text{cm}^{-1}$ and has a threshold of $g_{\text{th}} = 38.3\ \text{cm}^{-1}$. The second-order mode (not shown) has a threshold of $g_{\text{th}} = 46.0\ \text{cm}^{-1}$ and oscillates at $\delta = -52.8\ \text{cm}^{-1}$. Its near field-pattern is also asymmetric but, as opposed to that of point (d), occupies exactly the left-hand gain section (where the field intensity is low in Fig. 37). The small mode discrimination between such spatially segregated modes is an invitation to spatial hole-burning, and leads one to expect that the two lowest-order modes may oscillate simultaneously above threshold. The near-field pattern of the combined two modes will now be nearly symmetric, taking better advantage of the available gain than either one alone. However, the spectrally resolved near-field will reveal that the radiation from the two end gratings differ in wavelength. Since the far-field lobes of the second mode are located between those of the first mode, the combined far-field pattern is broader, with lower lobe visibility. In the case of $\Delta L_3 = 0.317\Lambda$, mode symmetry could not be restored by differential current pumping. When pumping any of the two gain sections harder to bring the relative phases

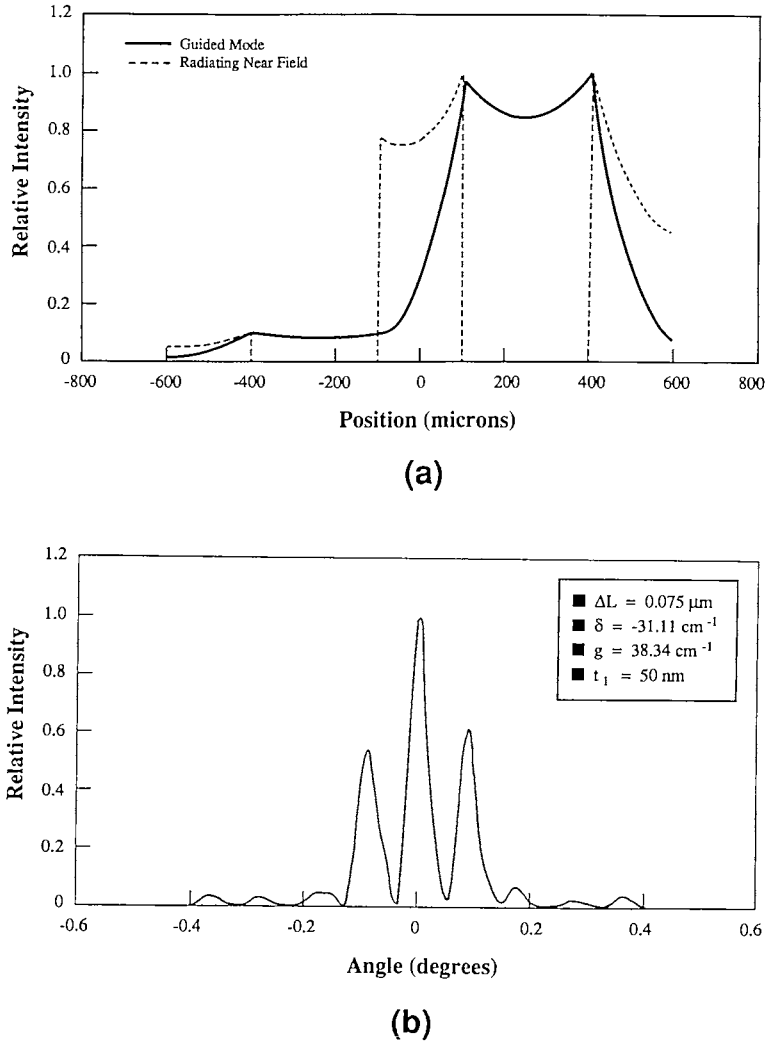

Fig. 37. Lowest threshold mode at $\Delta L_3 = 0.317\ \Lambda$ [point (d) in Fig. 35]. (a) Guided mode (solid) and radiating (dashed) near field, (b) far field.

back to symmetry, the gain imbalance becomes too high to sustain a symmetric pattern. Pumping gain section 3 harder to reduce its optical length only increases the near-field asymmetry. Thus, the intensity pattern remains asymmetric.

In moving to the right of point (d) in Fig. 35, towards point (e) at $\Delta L_3/\Lambda = 0.464$, the near- and far-fields again change rapidly as grating 1

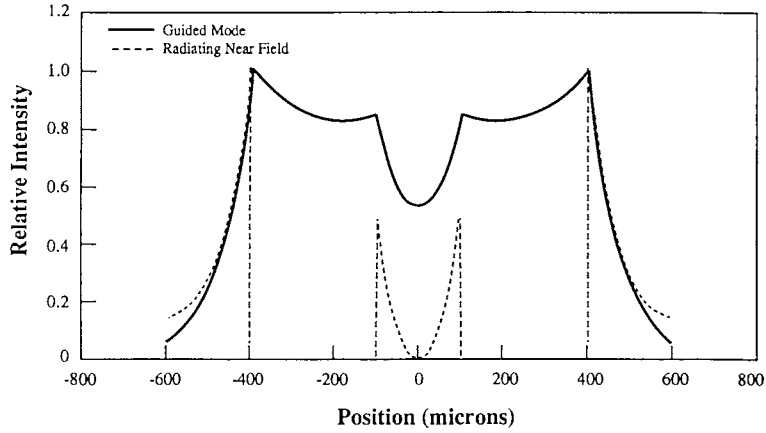

(a)

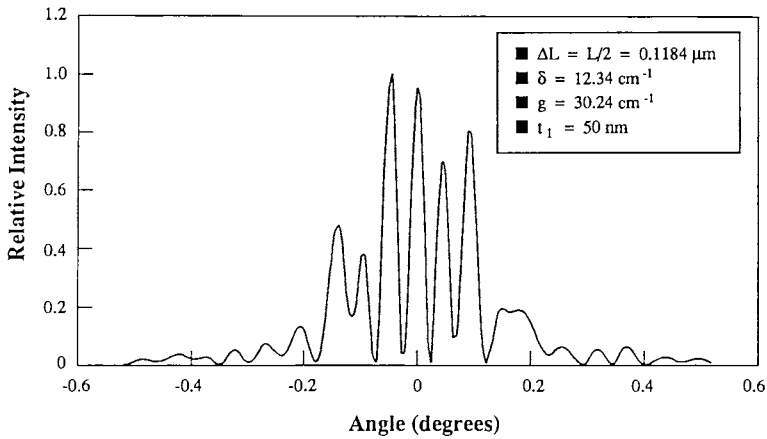

(b)

Fig. 38. Lowest threshold mode at $\Delta L_3 = 0.5\,\Lambda$ [point (f) in Fig. 35]. (a) Guided mode (solid) and radiating (dashed) near field, (b) far field.

starts to participate once again. Here the near-field pattern is close to that at point (b) (Fig. 36), and the far-field again has several narrow lobes although they do not coincide with those of Fig. 36. In Fig. 38 we depict the near- and far-field patterns at $\Delta L_3 = 0.5\Lambda$ [point (f) of Fig. 35]. The threshold gain, resonance location, and near-field patterns are almost iden-

tical to those for $\Delta L_3 = 0$ (see Fig. 26). This is expected since, by shifting the third grating to the right by half a period, from the symmetry point, the field propagates back and forth a total extra distance of $\Delta L_3 = \Lambda = \lambda$. The far-field pattern, however, is not exactly the same as in Fig. 28. Due to the grating shift of $\Delta L_3 = 0.5\Lambda$, there is an additional phase shift of π between the two end gratings. Therefore, we should have a maximum at $\vartheta = 0°$ as opposed to the zero at $\vartheta = 0°$ in Fig. 28. Furthermore, there are small phase differences between the two end mirrors. These phase differences add up to give a slight asymmetry in the far-field pattern at point (f). These small phase differences cancel each other when $\Delta L_3 = \Lambda$ so that at that point the near-field and far-field patterns of Figs. 26 and 28 are fully restored.

In stepping through points (a) to (f) of Fig. 35, we have found the lowest-order mode to be extremely sensitive to length variations on the order of one-tenth of a grating period. We can conclude, therefore, that the near- and far-field instabilities are related to having several modes with nearly degenerate threshold gains. That is, the source of modal sensitivity to length or current perturbations is the relatively poor mode discrimination. This sensitivity results, in part, from the several mode hops that occur within a gain length shift ΔL_3 of Λ.

3. *An Improved Design*

In this subsection we investigate the sources of the sensitivity to length-induced phase variations and demonstrate that the effects of these sources can be minimized in an improved design. The improved design has far less sensitivity to small perturbations. Close examination of Fig. 34 reveals several sources for the poor mode discrimination. First, the gain curves are broad and quite flat, which reduces discrimination among resonances located on the same gain branch. Second, the two gain branches themselves may be too close to discriminate effectively between resonances located on different gain branches. Third, the longitudinal mode spacing, as a function of δ, should be increased as much as possible, thereby pushing most longitudinal modes to higher gain regions. We shall address improvements to the baseline design by considering these sources in sequence.

First, observe that the width of the gain curve is closely related to the width of the reflectivity curve, as a function of δ, for each grating. The width of the reflectivity curve, in turn, is largely affected by the losses in the grating region (Hardy *et al.*, 1989). The higher the loss, the broader the reflectivity curve. Thus, one would like to minimize material and other losses in the grating region in order to steepen the increase of threshold

gain away from the Bragg wavelength. However, this parameter is only partially under our control. In our examples we assume $\alpha = 10\ \text{cm}^{-1}$ (power loss $= 2\alpha = 20\ \text{cm}^{-1}$). With improved fabrication control, one would expect to reduce it by factor of 2–4.

Once the loss parameter is fixed, in order to narrow the reflectivity curve, one must reduce the coupling coefficient κ (Yariv and Nakamura, 1977). In our particular case, with 50% teeth, the coupling coefficient κ is zero. However, the forward- and backward-propagating waves in a second-order grating are coupled not only directly through the grating, but indirectly through the radiative and other partial waves. This indirect coupling is characterized by additional coupling constants ζ_i [see Eq. (10)], so that the effective coupling coefficient $\kappa + \zeta_i$ is not zero. These coupling parameters are reduced by decreasing the tooth height. However, by making the gratings shallower, the peak of the reflectivity curve also decreases. Thus, one should make longer and shallower gratings, in order to have narrower reflectivity curves without compromising much of the peak reflectivity. This was indeed verified by several numerical studies. Although one should strive for longer and shallower gratings, there is a limit to this process, due to problems associated with wafer uniformity and material loss. A reasonable and practical number would be $L_g = 1$ mm with tooth height about 20 to 30 nm.

Regarding the second issue, i.e., the separation between the two gain branches, we note that the lower branch generally corresponds to antisymmetric modes with a null in the radiation near-field at the center of the middle grating. The upper branch with the higher losses corresponds to symmetric modes with a maximum in the radiation near-field in the center of the middle grating. This is physically reasonable since radiation represents a power loss for these devices, resulting in higher thresholds. When the middle grating is lengthened so that transmission is negligible, the field incident on either of its ends decays and is quite small at the center. Thus their superposition at the center of the grating, whether it is destructive or constructive should give about the same near-field intensity. Thus, for a long middle grating one would expect little discrimination between the symmetric and antisymmetric modes, and indeed this was verified numerically. To increase the gain discrimination between branches, one would, therefore, shorten the middle grating as much as possible. On the other hand there is a lower limit to this procedure before the device resembles only two gratings. Thus, when the middle grating is too short, it perturbs the guided wave so little that the amount of power radiated away (whether symmetric or antisymmetric) diminishes. Thus, for too short a middle grating, the discrimination between the symmetric and antisymmetric modes

drops again. It appears that there is an optimum length for the middle grating. With $L_g = 1$ mm for the side grating, $L_g = 0.5$ mm for the middle grating is close to optimum in discrimination between the two branches.

Consider the third issue, that of increasing the resonance spacings. For Fabry-Perot resonators, it is well known that decreasing the length increases the mode spacing. In our case we have two gain sections separated by one middle grating of finite length. It behaves more as a C^3-laser rather than a Fabry-Perot resonator. Nevertheless, we expect that for long middle gratings with only moderate transmissions (i.e., coupling between the gain sections is not too high) the mode spacing increases as the length of the gain section decreases. We also note that in Fig. 34 the solutions are $G = gL$ for the various modes. Decreasing L while G remains about the same, increases g and with it also $\Delta g = g_i - g_j$ for any two modes. The penalty, of course, is that the threshold gain itself is higher and the differential quantum efficiency may drop. Thus an optimum seems to be about $L =$ 150-200 μm.

By combining the three considerations we select 3800 teeth for the two side gratings ($L_g = 898.334$ μm) and 1900 teeth for the middle grating ($L_g =$ 449.167 μm). The tooth height is $t_1 = 20$ nm, and the gain section length is $L_1 = L_3 = 149.96$ μm. Figure 39 shows the gain curve for this structure. Note

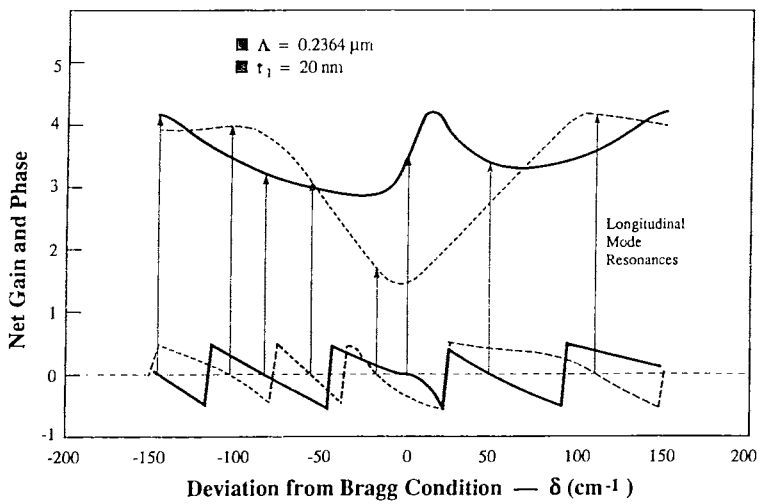

Fig. 39. Longitudinal mode structure (as in Figure 34) for the improved design, with $L_1 = L_3 = 149.95$ μm, $L_{g1} = L_{g3} = 898.334$ μm (3800 teeth), $L_{g2} = 449.167$ μm (1900 teeth).

the excellent mode discrimination: the lowest threshold mode at $\delta = -16.9\ \text{cm}^{-1}$ has $g_{\text{th}} = 106.9\ \text{cm}^{-1}$ while the next higher-order mode near $\delta = -57\ \text{cm}^{-1}$ has $g_{\text{th}} = 194\ \text{cm}^{-1}$. By slightly modifying the gain section length ($L_1 = L_3 = 150.05\ \mu\text{m}$), the lowest threshold mode can be brought to the minimum of the gain curve, thus further reducing its threshold. In any case with $L_1 \equiv L_3 \simeq 150\ \mu\text{m}$ the lowest order mode fluctuates not far away from the minimum of the gain curve. In Fig. 40 we show the near- and

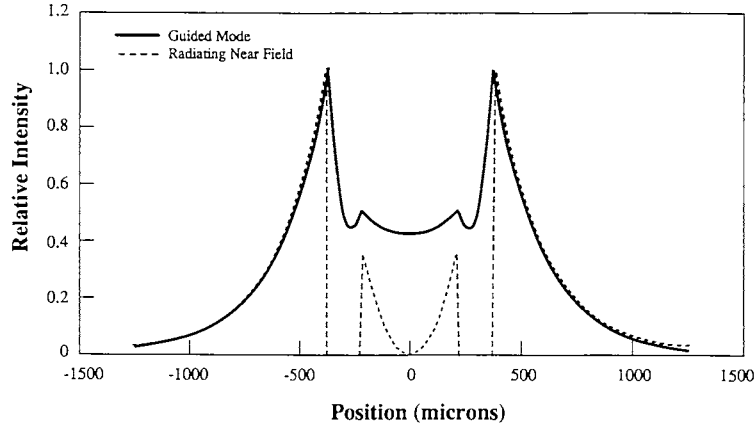

(a)

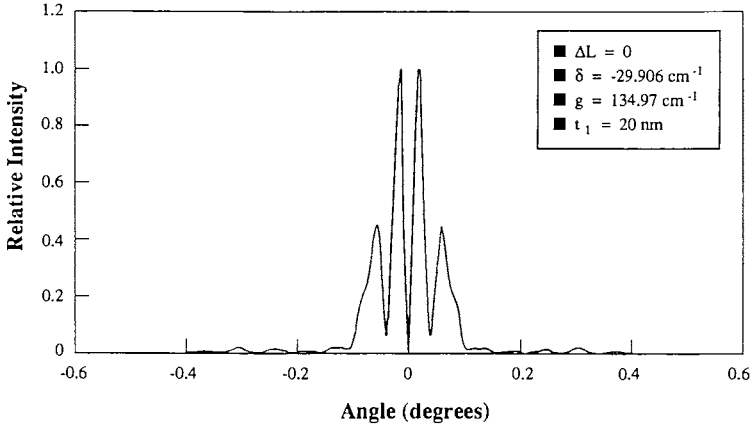

(b)

Fig. 40. Lowest-threshold mode for the symmetrical improved design, with $L_1 = L_3 = 150\ \mu\text{m}$. (a) Guided-mode (solid) and radiating (dashed) near field, and (b) far field.

far-field patterns of the lowest-order mode at $\delta = -29.9\ \text{cm}^{-1}$ for $L_1 = L_3 = 150\ \mu\text{m}$. Note, in particular, the much improved far-field pattern [Fig. 40(b)] mainly due to the longer penetration into the side gratings as compared to Fig. 28. In fact we chose the worst possible length near $L = 150\ \mu\text{m}$. For $L_1 = L_3 = 149.96\ \mu\text{m}$ (which was used in Fig. 39) the side lobes are about half the size of those in Fig. 40.

In general, not only the far-field pattern is improved with the better design, but also its sensitivity to small length fluctuations. In Fig. 41 we describe the sensitivity of the gain and resonance locations for the three lowest-order modes of the improved design, to small length variations ΔL_3 of one of the gain sections. The other gain section length is held constant at $L_1 = 150\ \mu\text{m}$. Since the figure is periodic we show here only one period of $\Delta L_3 = 0.5\Lambda$. Compared to Fig. 35 we note the remarkable improvement both in mode discrimination and resonance stability. There is only one degeneracy where the resonance hops from $\delta = -31.19\ \text{cm}^{-1}$ [at point (c) in Fig. 41(b)] to $\delta = -2.69\ \text{cm}^{-1}$ [at point (d) in Fig. 41(b)]. Between points (a) and (c), the modal oscillation frequency is nearly constant. Along this curve the near- and far-field both change, but significantly less than for the deeper gratings. In fact, there is always enough power in either gain section so that all three gratings radiate. To demonstrate this we show in Fig. 42 the near- and the far-field patterns at $\Delta L_3 = 0.059\ \mu\text{m} = 0.250\Lambda$ [point (c) in Fig. 41(b)]. In Fig. 43 we show the near- and far-field patterns at $\Delta L_3 = 0.060\ \mu\text{m} = 0.254\Lambda$ [point (d) in Fig. 41(b)]. We note the much improved near- and far-field patterns. In particular, the far-field patterns, although distorted [compared to Fig. 40 for point (a)], still exhibit narrow lobes with much smaller side lobes.

F. Conclusions

A GSE with two gain sections and three grating sections has been analyzed. The results show that for a symmetric geometry the two lowest threshold longitudinal modes are asymmetric. However, because a structure with three or more coupled gratings must establish a resonant mode in which the reflections from all three gratings are commensurate, the device is very sensitive to the relative phases of the reflections. Thus small changes in grating position or variations in material parameters or pumping current affect the far field patterns. On the other hand if two differing structures with approximately the same dimensions have quite similar phase relationships their performances will be almost identical.

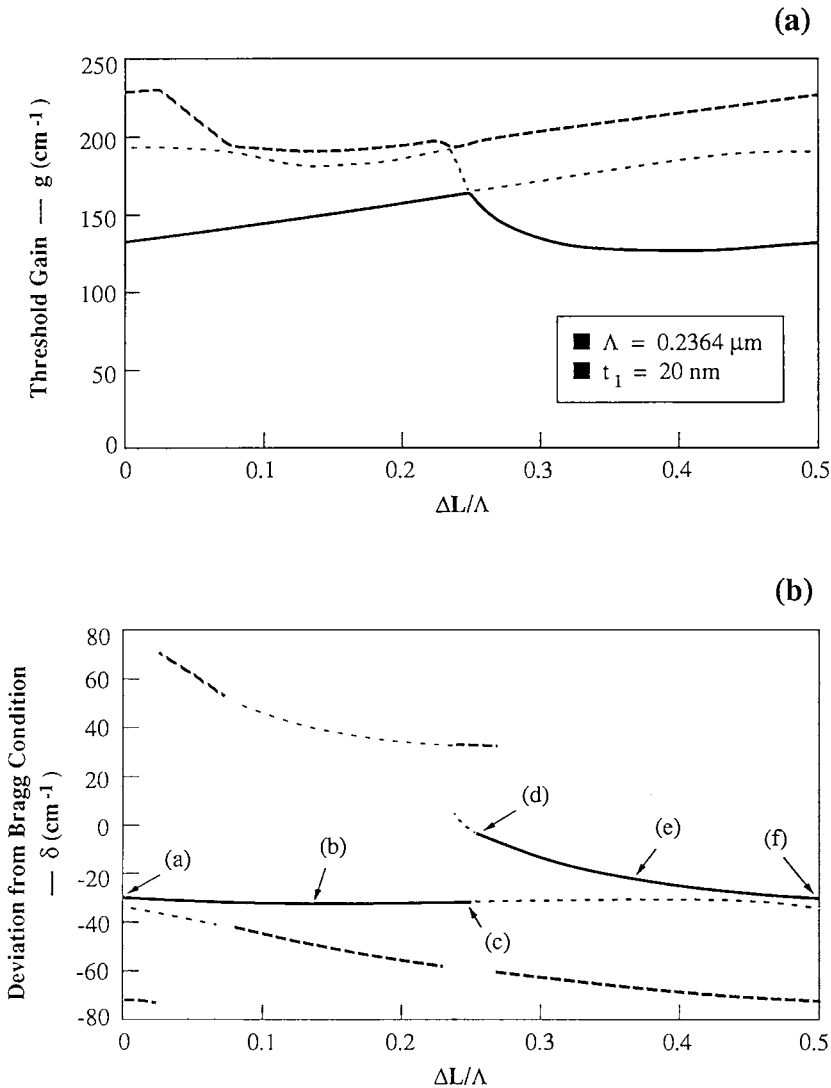

Fig. 41. (a) Threshold gain, and (b) oscillation frequency of the three lowest-threshold gain modes of the improved design as a function of $\Delta L/\Lambda = (L_3 - L_1)/\Lambda$.

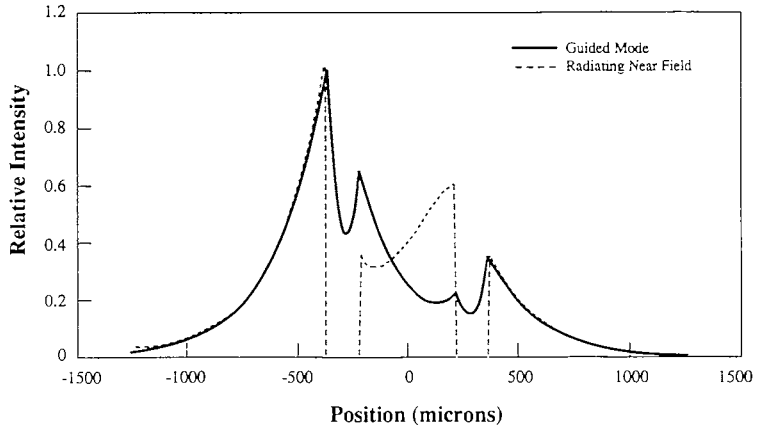

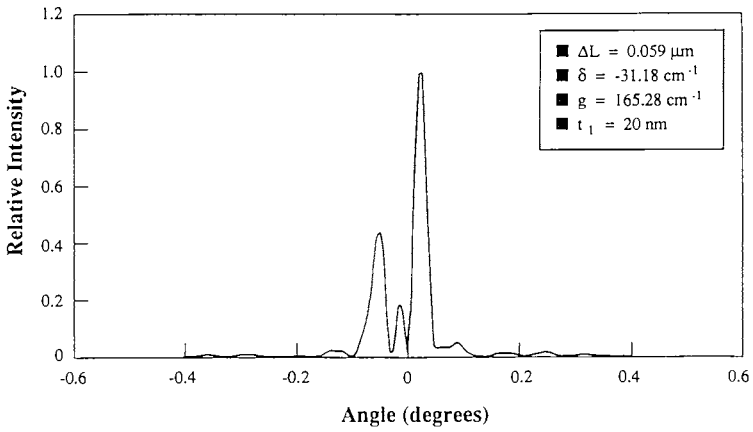

Fig. 42. Lowest-threshold mode of the improved design at $\Delta L_3 = 0.250\Lambda$ [point (c) in Fig. 41(b)]. (a) Guided-mode (solid) and radiating (dashed) near field, and (b) far field.

First, we examined the effect of asymmetric pumping of an otherwise symmetric structure. Threshold gains as functions of the two gain-section currents were calculated and the variations in near- and far-fields were presented. Predications of the analytic theory compared well with results from an experimental device in the regime of near threshold operation.

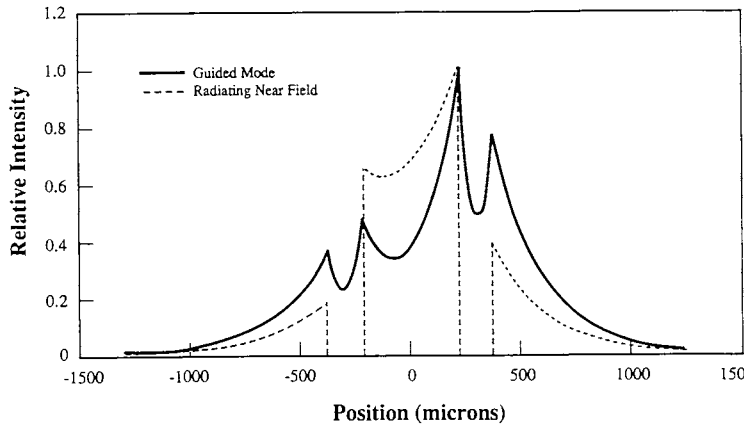

(a)

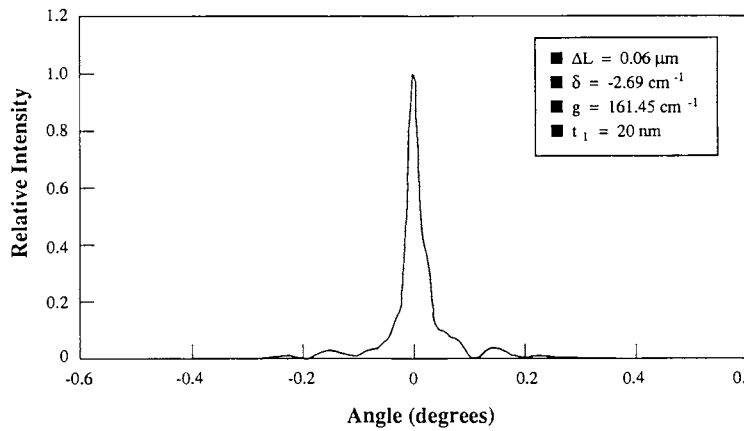

(b)

Fig. 43. Lowest-threshold mode of the improved design at $\Delta L_3 = 0.254\Lambda$ [point (d) in Fig. 41(b)]. (a) Guided-mode (solid) and radiating (dashed) near field, and (b) far field.

Second, we have demonstrated that GSE laser arrays have a longitudinal mode structure that is extremely sensitive to length-induced phase variations. For a laser composed of two gain and three grating sections, an asymmetric variation in the length of one gain section of only one-tenth of a grating period is enough to cause a longitudinal mode hop. For this configuration,

adjacent longitudinal modes have different symmetry with respect to near- and far-fields (i.e., either symmetric or antisymmetric). Thus, mode hops are characterized not only by a jump in wavelength but by a discontinuity of radiation pattern. In practice, such small variations in optical length can be caused by fluctuations in current density, temperature, or material characteristics across the wafer. Conversely, small asymmetries can be compensated by differential current pumping; larger asymmetries, however, cannot.

The cause of this sensitivity is the poor mode discrimination inherent in baseline designs. We set out, therefore, to design a GSE laser with improved mode discrimination. Increased gain discrimination between modes of like symmetry was achieved by incorporating longer, shallower grating sections and shorter gain sections into the design, in order to further separate the resonances in frequency and to narrow the grating reflectivity spectrum. Furthermore, discrimination between symmetric and antisymmetric modes was increased by optimizing the length of the center grating. The resulting design demonstrated improved sensitivity to length-induced phase variations, but at a cost of increased threshold gain for the lowest-order modes. Initial experiments with such gratings showed promising results (Waarts *et al.*, 1990).

In general, however, the sensitivity to phase variations of all GSE structures is at a level high enough to cause at least one mode hop when the asymmetry in optical path lengths of adjacent gain sections exceeds one half of a grating period. In practice, this implies that for a fixed operating condition (temperature profile and material inhomogeneity), the currents to individual emitters of the array may need to be optimized in order to achieve single-mode, coherent operation.

V. EXTENSION TO AN ARBITRARY NUMBER OF GRATINGS

In order to extend the analysis to more than three gratings, it is convenient to adopt a scattering matrix approach. Consider, for example, the schematic array representation shown in Fig. 44. Odd-numbered sections represent grating regions, whereas even numbered sections represent gain regions. It is straightforward to show that

$$\begin{bmatrix} E_t^{(+)} \\ E_i^{(-)} \end{bmatrix} = M \begin{bmatrix} E_i^{(+)} \\ E_t^{(-)} \end{bmatrix} \tag{53}$$

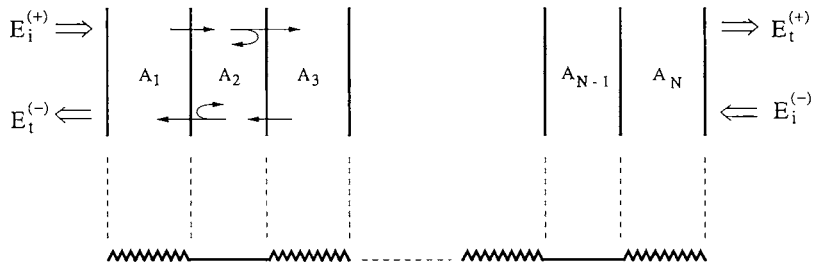

Fig. 44. Schematic representation of a linear array with N grating and gain sections.

where the 2×2 matrix M is the product, in reversed order, of the matrices A_j for each of the sections,

$$M = A_N A_{N-1} \ldots A_1. \tag{54}$$

The even-numbered matrices A_i, representing gain sections, are diagonal. The odd-numbered matrices for the grating sections, are derived by using Eqs. (22) through (25). The threshold condition for lasing is detained by requiring $E_i^{(+)} = E_i^{(-)} = 0$. This requirement yields

$$M_{22} = 0 \tag{55}$$

where M_{22} is the lower right diagonal element of the matrix M. As in the case of three gratings (see Section III), the problem is under specified since there may be many combinations of gains (or currents), for which the solution of (55) yields different results for the lowest threshold mode. Note that even if the relationship between the various gain sections is specified (e.g., by requiring that all gains are the same) one still has many solutions to Eq. (55), namely the various resonances, but only one (or two in case of degeneracies) corresponds to the lowest threshold mode.

A similar approach has been used by Amantea *et al.*, (1989). They extended the analysis to include two-dimensional arrays that are evanescently coupled in the lateral direction and injection-coupled in the longitudinal direction. They specialized, however, in analyzing identical gratings and identical gain sections. Furthermore, only approximate matrix elements were used and their exact wavelength dependence, or the effect of various grating parameters, was ignored.

An alternative approach to the problem is the shooting method (Shakir *et al.*, 1989). The analysis has been extended to include gain saturation

effects in the gain sections and coupled-mode equations were used in the grating sections. However, the parameters in the coupled-mode equations were only approximately estimated. One also should be careful, when using this approach, not to miss some of the lowest-order modes. Combining the two methods, i.e., solving Eq. (55) at threshold and then using the shooting method above threshold may be the most efficient approach. An interesting result of the shooting method analysis for a linear array of five gratings (Shakir and Salvi, 1988), is that an in-phase array mode can be made the dominant one by driving the coupled gain sections nonuniformly. This is expected since, for a larger number of grating sections, the difference between the near-field intensity pattern of the symmetric and antisymmetric modes diminishes. As a result, the radiation loss from the center grating is nearly the same for the symmetric and antisymmetric modes. Note, in particular, that for an even number of grating sections, the center of symmetry is in a gain section and, thus, radiation losses for symmetric and antisymmetric modes are the same.

VI. APPENDICES

A. Fourier Expansion Coefficients

Consider the structure illustrated in Fig. 2. The refractive index squared is expressed analytically as

$$n^2(x, z) = \begin{cases} n_1^2, & x < 0 \\ \displaystyle\sum_{p=-\infty}^{\infty} [n_1^2\{u[z - w_1(x) - p\Lambda] - u[z - w_2(x) - p\Lambda]\} \\ \qquad + n_2^2\{u[z - w_2(x) - p\Lambda] \\ \qquad - u[z - w_1(x) - (p+1)\Lambda]\}], & 0 < x < t_1 \\ n_2^2, & t_1 < x < t_2 \\ n_3^2, & t_2 < x < t_3 \\ n_4^2, & t_3 < x \end{cases} \tag{A-1}$$

where the functions $w_1(x)$ and $w_2(x)$ express the tooth shape as shown in Fig. 2 and u is the unit step function. Then since $n^2(x, z)$ is periodic in z, we expand it in a Fourier series as in Eq. (2). The Fourier coefficients are zero outside the grating region and are functions of the tooth shape within

that region viz.,

$$A_q(x) = \frac{1}{\Lambda}\int_{-\Lambda/2}^{\Lambda/2} n^2(x, z)\exp(-i2\pi qz/\Lambda)\,dz$$

$$= \frac{(n_2^2 - n_1^2)}{i2\pi q}\{\exp[-i2\pi q w_2(x)/\Lambda] - \exp[-i2\pi q w_1(x)/\Lambda]\}, \quad 0 < x < t_1 \tag{A-2}$$

with $q \neq 0$.

Note that, if n_j^2 are real, $A_q(x) = A_{-q}^*(x)$. Usually $\mathrm{Im}\{n_j^2\} \ll \mathrm{Re}\{n_j^2\}$ so that we may assume that n_j^2 are all real and the loss or gain is represented entirely by $\tilde{\alpha}(x)$ in Eq. (2). Furthermore, we also drop $\alpha^{\sim 2}$ since $|\tilde{\alpha}| \ll k_0 n_0$. The unperturbed waveguide is represented by $n_0^2(x)$

$$n_0^2(x) = \begin{cases} n_1^2, & x < 0 \\ n_2^2 + (n_1^2 - n_2^2)[w_2(x) - w_1(x)]/\Lambda, & 0 < x < t_1 \\ n_2^2, & t_1 < x < t_2 \\ n_3^2, & t_2 < x < t_3 \\ n_4^2, & t_3 < x \end{cases} \tag{A-3}$$

Note that the $A_0(x)$ term has been absorbed into $n_0^2(x)$, so that the waveguide geometry, with periodicity ignored (i.e., the "unperturbed" waveguide), is a five region structure. (See Fig. 3.)

B. Partial Wave Coefficients

To increase the generality of the analysis, one may approximate the grating teeth by a series of N sublayers of constant width. Within each sublayer the squared refractive index is set constant and equal to its average value in that layer. The total number of layers with constant refractive index, including air (superstate) and the substrate, is M. The solutions for the radiating and evanescently decaying partial waves are given by

$$E_m^{(j)}(x) = \begin{cases} C_{m,1}^{(j)}\exp(-ik_{m,1}x), & x < x_1 = 0 \\ C_{m,p}^{(j)}\cos[k_{m,p}(x - x_{p-1})] + D_{m,p}^{(j)}\sin[k_{m,p}(x - x_{p-1})] + T_{m,p}^{(j)}(x - x_{p-1}), & x_{p-1} < x < x_p,\ p = 2, 3, \ldots, M-1 \\ C_{m,M}^{(j)}\{\exp[ik_{m,M}(x - x_{M-1})] + R_m\exp[-ik_{m,M}(x - x_{M-1})]\}, & x_{M-1} < x < x_{M-1} + d \end{cases} \tag{B-1}$$

where $j=0, -2$ and the $x_p (p=1, \ldots, M-1)$ are the layers boundaries. The parameters $k_{m,p}$ are defined

$$k_{mp}^2 = \mathrm{k}_0^2 n_p^2 - \beta_m^2. \tag{B-2}$$

In (B-1) $x=0$ is the upper boundary, and the reflector is located at $x = x_{M-1} + d$. The reflector is modeled by the symbol R_m for the radiating $(m=-1)$ wave, which is set equal zero for the other partial waves and the guided waves. The layers numbered $p=2, 3, \ldots, N+1$ represent the grating, and the domain $x<0$ is the air (superstrate). The layers numbered $p = N+2, \ldots, M-1$ represent all other waveguide regions and $p=1$ and $p=M$ represent the superstrate and substrate, respectively.

In the grating layers of Eq. (B-1) the terms $T_{mp}^{(j)}$ are driving terms originating from the guided wave interaction with the grating. They are given by

$$T_{mp}^{(j)}(x-x_{p-1}) = a_{mp}^{(j)} \cos\left[k_{0,p}(x-x_{p-1})\right] + b_{mp}^{(j)} \sin\left[k_{0,p}(x-x_{p-1})\right], \quad 2 \le p \le N+1 \tag{B-3}$$

where

$$a_{mp}^{(j)} = -[\mathrm{k}_0^2/(k_{mp}^2 - \mathrm{k}_{0_p}^2)] A_{m-j,p} C_{0,p}, \quad j=0, -2 \tag{B-4a}$$

$$b_{mp}^{(j)} = -[\mathrm{k}_0^2/(k_{mp}^2 - \mathrm{k}_{0,p}^2)] A_{m-j,p} D_{0,p}, \quad j=0, -2 \tag{B-4b}$$

and $A_{m-j,p}$ are the squared refractive index Fourier expansion coefficients in layer p of the grating region. For $p = N+2, \ldots, M-1$, $T_{m,p}^{(j)} = 0$. The constants C_{mp} and D_{mp} in Eq. (B-1) are determined by imposing the boundary conditions for field and field derivative continuity. Note that Eq. (B-1) also holds for $m=0$ (the guided mode), but in this case $T_{0_p}^{(j)} \equiv 0$ and one of the coefficients (say $C_{0,1}$) is arbitrary. The boundary conditions of field and field derivative continuity, determine all other constants $C_{0,p}$, $D_{0,p}$ and also provide the characteristic equation for the propagation constant β.

C. Calculating Equation (39)

In each grating, power is dissipated via several channels, namely $P_j \mathrm{U}_j$, $P_j \mathrm{S}_j$, $P_j \mathrm{T}_j$, $P_j \mathrm{A}_j$, where P_j $(j=1, 2)$ is the power incident on grating j. The fraction of useful power radiated up into the air, from the two gratings, versus the total amount of power dissipated in the gratings is

$$\eta_{\mathrm{g}} = \frac{P_1 \mathrm{U}_1 + P_2 \mathrm{U}_2}{P_1(\mathrm{U}_1 + \mathrm{S}_1 + \mathrm{T}_1 + \mathrm{A}_1) + P_2(\mathrm{U}_2 + \mathrm{S}_1 + \mathrm{T}_2 + \mathrm{A}_2)}. \tag{C-1}$$

The power radiated up is given by

$$P_u = (I - I_t)(h\nu/e)\eta_i\eta_0\eta_g \tag{C-2}$$

where η_i is the internal quantum efficiency, η_0 is defined by (40), I is the injected current, I_t is the injected current at threshold ($I > I_t$), h is Planck's constant, ν is the light frequency, and e is the electron's charge. The external differential quantum efficiency η_D is defined as (Yariv, 1989),

$$\eta_D = \frac{d(P_u/h\nu)}{d(I/e)} = \eta_i\eta_0\eta_g. \tag{C-3}$$

Using Eqs. (35) and (38), to substitute for A_j and $P_j (j = 1, 2)$, we obtain Eq. (39).

D. The External Differential Quantum Efficiency for *N*-Grating, $N-1$ Gain Sections

Consider the geometry described in Fig. 45. The power generated in gain section j due to the injected electric current I_j is given by

$$P_e^{(j)} = (1/e)(I_j - I_{tj})h\nu\eta_i, \qquad j = 1, \ldots, N-1 \tag{D-1}$$

where I_{tj} is the current required to reach threshold, h is Planck's constant, e is the electron charge, ν is the optical frequency and it is assumed that

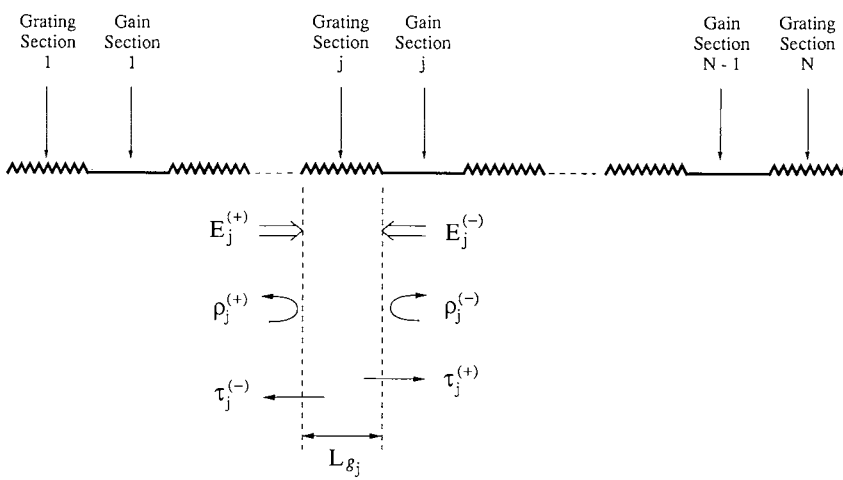

Fig. 45. An N grating, $N-1$ gain section surface emitter, illustrating the parameters, reflections and transmissions.

all gain sections have the same internal quantum efficiency η_i. The power loss in gain section j due to the power loss $\alpha_l^{(j)}$, per unit length, is given by

$$P_e^{(j)} = \int_0^{L_j} \alpha_l^{(j)} P_j^{(+)}(0) \exp(g_j z)\, dz = \left(\frac{\alpha_l^{(j)}}{g_j}\right)[\exp(g_j L_j) - 1] P_j^{(+)}(0) \quad \text{(D-2)}$$

where $P_j^{(+)}(0)$ is the optical power injected into the gain section j at $z = 0$ and propagate in the $+z$ direction. A similar expression is obtained when power $P_j^{(-)}(L_j)$ is injected at $z = L_j$ and propagate in the $-z$ direction. Combining the two and substituting for the injected powers, we find

$$P_e^{(j)} = (|\rho_j^{(-)} E_j^{(-)} + \tau_j^{(+)} E_j^{(+)}|^2 + |\rho_{j+1}^{(+)} E_{j+1}^{(+)} + \tau_{j+1}^{(-)} E_{j+1}^{(-)}|^2) \times (\alpha_l^{(j)}/g_j)(\exp[g_j L_j] - 1)\left(\frac{\beta Q}{2\omega\mu_0}\right), \qquad j = 1, \ldots, N-1, \quad \text{(D-3)}$$

where for gain section $j = 1$, $E_1^{(+)} = 0$ is assumed and for gain section $j = N - 1$ we take $E_N^{(-)} = 0$. In order to calculate the power lost on the grating sections, we note that for the two end gratings, power which is *not* reflected is lost. Thus,

$$P_g^{(1)} = |E_1^{(-)}|^2 (1 - |\rho_1^{(-)}|^2)\left(\frac{\beta Q}{2\omega\mu_0}\right) \quad \text{(D-4a)}$$

$$P_g^{(N)} = |E_N^{(+)}|^2 (1 - |p_N^{(+)}|^2)\left(\frac{\beta Q}{2\omega\mu_0}\right) \quad \text{(D-4b)}$$

The power lost on all the other grating sections j, $j = 2, \ldots, N-1$, is given by

$$P_g^{(j)} = \{(|E_j^{(+)}|^2 + |E_j^{(-)}|^2) - (|\rho_j^{(+)} E_j^{(+)} + \tau_j^{(-)} E_j^{(-)}|^2 + |\rho_j^{(-)} E_j^{(-)} + \tau_j^{(+)} E_j^{(+)}|^2)\}\left(\frac{\beta Q}{2\omega\mu_0}\right) \quad \text{(D-5)}$$

Here, unlike for the end gratings, power transmitted through the grating is *not* lost, but is injected into the next gain section. The useful power output $P_u^{(j)}$, $j = 1, \ldots, N$, from each of the gratings, due to radiation up into the air, is given by Eq. (30a). Thus, the total useful power output is

$$P_u = \sum_{j=1}^{N} P_u^{(j)} = \left(\sum_{j=1}^{N-1} P_e^{(j)}\right)\left(\frac{\sum_{j=1}^{N} P_u^{(j)}}{\sum_{j=1}^{N-1} P_l^{(j)} + \sum_{j=1}^{N} P_g^{(j)}}\right) \quad \text{(D-6)}$$

Defining

$$\eta_D = \frac{d(P_u/h\nu)}{d(I/e)} \tag{D-7}$$

where $I = \sum_{j=1}^{N-1} I_j$, we find that

$$\eta_D = \eta_i \eta_0 \eta_g \tag{D-8}$$

where

$$\eta_0 = \frac{\sum_{j=1}^{N} P_g^{(j)}}{\sum_{j=1}^{N-1} P_l^{(j)} + \sum_{j=1}^{N} P_g^{(j)}} \tag{D-9a}$$

and

$$\eta_g = \frac{\sum_{j=1}^{N} P_u^{(j)}}{\sum_{j=1}^{N} P_g^{(j)}}. \tag{D-9b}$$

REFERENCES

AMANTEA, R., PALFREY, S. L. AND CARLSON, N. R. (1989). "Network model for two-dimensional coupled laser arrays," *Opt. Lett.* **14**, 30.

BUUS, J., WILLIAMS, P. J., GOODRIDGE, I., ROBBINS, D. J., URQUHART, J., WEBB, A. P., REID, T., NICKLIN, R., CHARLES, P., REID, D. C. J. AND CARTER, A. C. (1989). "Surface-emitting two-dimensional coherent semiconductor laser array," *Appl. Phys. Lett.* **55**, 331.

CARLSON, N. W., EVANS, G. A., HAMMER, J. M., LURIE, M., CARR, L. A., HAWRYLO, F. Z., JAMES, E. A., KAISER, C. J., KIRK, J. B., REICHERT, W. F., TRUXAL, D. A., SHEALY, J. R., CHINN, S. R. AND ZORY, P. S. (1988a). "High-power, seven-element grating surface emitting diode laser array with 0.012° far-field angle," *Appl. Phys. Lett.* **52**, 939.

CARLSON, N. W., EVANS, G. A., HAMMER, J. M., LURIE, M., BUTLER, J. K., PALFREY, S. L., ETTENBERG, M., CARR, L. A., HAWRYLO, F. Z., JAMES, E. A., KAISER, C. J., KIRK, J. B., REICHERT, W. F., SHEALY, J. R., SPRAGUE, J. W., CHINN, S. R. AND ZORY, P. S. (1988b). "Dynamically stable 0° phase mode operation of a grating-surface-emitting diode laser array," *Opt. Lett.* **13**, 312.

DZIURA, T. G., AND WANG, S. C. (1989). "Emission properties of surface-emitting distributed-feedback and distributed-Bragg reflector semiconductor lasers," *Opt. Lett.* **14**, 491.

EVANS, G. A., CARLSON, N. W., HAMMER, J. M., LURIE, M., BUTLER, J. K., PALFREY, S. L., AMANTEA, R., CARR, L. A., HAWRYLO, F. Z., JAMES, E. A., KAISER, C. J., KIRK, J. B. AND REICHERT, W. F. (1989). "Two-dimensional coherent laser arrays using grating surface emissions," *IEEE J. Quantum Electron.* **QE-25**, 1525.

GOODMAN, J. W. (1968). *Introduction to Fourier optics*, McGraw-Hill, New York, Ch. 4.

HAMMER, J. M., CARLSON, N. W., EVANS, G. A., LURIE, M., PALFREY, S. L., KAISER, C. J., HARVEY, M. G. JAMES, E. A., KIRK, J. B. AND ELIA, F. R. (1987). "Phase-locked operation of coupled pairs of grating-surface emitting diode lasers," *Appl. Phys. Lett.* **50**, 659.

HARDY, A. (1984). "Exact derivation of the coupling coefficient in corrugated waveguides with rectangular tooth shape," *IEEE J. Quantum Electron.* **QE-20**, 1132. Erratum, (1984). *IEEE J. Quantum Electron.* **QE-22**, 376.

HARDY, A., WELCH, D. F. AND STREIFER, W. (1989). "Analysis of second-order gratings," *IEEE J. Quantum Electron.* **QE-25**, 2096.

HARDY, A., WELCH, D. F. AND STREIFER, W. (1990a). "Analysis of a dual grating-type surface emitting laser," *IEEE J. Quantum Electron.* **QE-26**, 50.

HARDY, A., WAARTS, R. G., WELCH, D. F. AND STREIFER, W. (1990b). "Analysis of three grating coupled surface emitters," *IEEE J. Quantum Electron.* **QE-26**, 843.

HARDY, A., MEHUYS, D., WAARTS, R. G., WELCH, D. F. AND STREIFER, W. (1990c). "Sensitivity of grating-coupled surface emitters to length-induced phase variations," *IEEE J. Quantum Electron.* **QE-26**, 1467.

HENRY, C. H., KAZARINOV, R. F., LOGAN, R. A., AND YEN, R. (1985). "Observation of destructive interference in the radiation loss of second-order distributed feedback lasers," *IEEE J. Quantum Electron.* **QE-21**, 151.

JEWELL, J. L., SCHERER, A., MCCALL, S. L., LEE, Y. H., WALKER, S., HARBISON, J. P. AND FLOREZ, L. T. (1989). "Low-threshold electrically pumped vertical-cavity surface-emitting microlasers," *Electr. Lett.* **25**, 1123.

KAZARINOV, R. F. AND HENRY, C. H. (1985). "Second-order distributed feedback lasers with mode selection provided by first-order radiation losses," *IEEE J. Quantum Electron.* **QE-21**, 144.

KOGELNIK, H. AND SHANK, C. V. (1972). "Coupled-wave theory of distributed feedback lasers," *J. Appl. Phys.* **43**, 2327.

KOGELNIK, H. (1975). "Theory of dielectric waveguides," in *Integrated Optics*, Tamir T., Editor, Chapter 2. Springer-Verlag, New York.

KOJIMA, K., KAMEYA, M., NODA, S. AND KYUMA, K. (1988). "High efficiency surface-emitting distributed bragg reflector laser array," *Electr. Lett.* **24**, 283.

MACOMBER, S. H., MOTT, J. S., NOLL, R. J., GALLATIN, G. M., GRATIX, E. J., O'DWYER, S. L. AND LAMBERT, S. A. (1987). "Surface-emitting distributed feedback semiconductor laser," *Appl. Phys. Lett.* **51**, 472.

MOTT, J. S., AND MACOMBER, S. H. (1989). "Two-dimensional surface-emitting distributed feedback laser arrays," *IEEE Photonics Tech. Lett.* **1**, 202.

NODA, S., KOJIMA, K. AND KYUMA, K. (1988). "Surface-emitting multiple quantum well distributed feedback laser with a broad-area grating coupler," *Electr. Lett.* **24**, 277.

OSINSKI, M. AND BUUS, J. (1987). "Linewidth broadening factor in semiconductor lasers-an overview," *IEEE J. Quantum Electron.* **QE-23**, 9.

PARKE, R., WAARTS, R., WELCH, D. F., HARDY, A., AND STREIFER, W. (1990). "High efficiency, high uniformity, grating coupled surface emitting lasers," *Elect. Lett.*, **26**, 125.

PENG, S. T. AND TAMIR, T. (1974). "Directional blazing of waves guided by asymmetrical dielectric gratings," *Opt. Comm.* **11**, 405.

SCHAUS, C. F., SCHAUS, H. E., SUN, S., RAJA, M. Y. A. AND BRUECK, S. R. J. (1989). "MOCVD growth of GaAs/AlGaAs wavelength resonant periodic gain vertical cavity surface-emitting laser," *Electr. Lett.* **25**, 538.

SHAKIR, S. A. AND SALVI, T. C. (1988). Internal Report, R&D Associates.

SHAKIR, S. A., SALVI, T. C. AND DENTE, G. C. (1989). "Analysis of grating-coupled surface-emitting lasers," *Opt. Lett.* **14**, 937.

STEGEMAN, G. I., SARID, D., BURKE, J. J. AND HALL, D. G. (1981). "Scattering of guided waves by surface periodic gratings for arbitrary angles of incidence: perturbation field theory and implications to normal-mode analysis," *J. Opt. Soc. Amer.* **71**, 1497.

STREIFER, W., SCIFRES, D. R. AND BURNHAM, R. D. (1976a). "TM-Mode coupling coefficients in guided-wave distributed feedback lasers," *IEEE J. Quantum Electron.* **QE-12**, 74.

STREIFER, W., SCIFRES, D. R. AND BURNHAM, R. D. (1976b). "Analysis of grating-coupled radiation in GaAs:GaAlAs lasers and waveguides," *IEEE J. Quantum Electron.* **QE-12**, 422.

STREIFER, W., BURNHAM, R. D. AND SCIFRES, D. R. (1976c). "Analysis of grating-coupled radiation in GaAs:GaAlAs lasers and waveguides—II: Blazing Effects," *IEEE J. Quantum Electron.* **QE-12**, 494.

STREIFER, W., SCIFRES, D. R. AND BURNHAM, R. D. (1977). "Coupled wave analysis of DFB and DBR lasers," *IEEE J. Quantum Electron.* **QE-13**, 134.

THOMPSON, G. H. B. (1980). *Physics of Semiconductor Laser Devices*, Wiley, New York, p. 98.

THORNTON, R. L., BURNHAM, R. D. AND STREIFER, W. (1984). "High reflectivity GaAs-AlGaAs mirrors fabricated by metalorganic chemical vapor deposition," *Appl. Phys. Lett.* **45**, 1028.

VERLY, P., TREMBLAY, R. AND LIT, J. W. Y. (1980). "Application of the effective-index method to the study of distributed feedback in corrugated waveguides: TM polarization," *J. Opt. Soc. Amer.* **70**, 1218.

WAARTS, R. (1990). "Optical characterization of grating surface emitting semiconductor lasers," *Appl. Opt.* **29**, 2718.

WAARTS, R., WELCH, D. F., PARKE, R., HARDY, A. AND STREIFER, W. (1990). "Coherent linear arrays of grating coupled surface emitting lasers," *Electr. Lett.*, **26**, 129.

WELCH, D. F., PARKE, R., HARDY, A., STREIFER, W. AND SCIFRES, D. R. (1989a). "High-power grating-coupled surface emitters," *Electr. Lett.* **25**, 819.

WELCH, D. F., PARKE, R., HARDY, A., STREIFER, W. AND SCIFRES, D. R. (1989b). "Low threshold grating-coupled surface-emitting lasers," *Appl. Phys. Lett.* **55**, 813.

WELCH, D. F., PARKE, R., HARDY, A., WAARTS, R., STREIFER, W. AND SCIFRES, D. R. (1989c). "High power, 4W pulsed, grating-coupled surface-emitting laser," *Electr. Lett.* **25**, 1038.

WELCH, D. F., WAARTS, R. G., PARKE, R., HARDY, A. AND STREIFER, W. (unpublished).

YAMAMOTO, Y., KAMIYA, T. AND YANAI, H. (1978). "Improved coupled mode analysis of corrugated waveguides and lasers," *IEEE J. Quantum Electron.* **QE-14**, 245.

YARIV, A. (1973). "Coupled-mode theory for guided-wave optics," *IEEE J. Quantum Electron.* **QE-9**, 919.

YARIV, A. AND NAKAMURA, M. (1977). "Periodic structures for integrated optics," *IEEE J. Quantum Electron.* **QE-13**, 233.

YARIV, A. (1989). *Quantum Electronics*, 3rd Ed. Wiley, New York.

Chapter 7

NETWORK ANALYSIS OF TWO-DIMENSIONAL LASER ARRAYS

R. Amantea and **N. W. Carlson**

David Sarnoff Research Center, Princeton, New Jersey

I. INTRODUCTION

The development of semiconductor diode laser arrays has experienced rapid growth over the last decade. Many types of one-dimensional laser array structures have been fabricated and demonstrated and models of these arrays have also been developed (see Chapter 2). A group of parallel gain elements sufficiently close to each other comprises laterally-coupled edge-emitting laser array structures. Butler *et al.* (1984) have shown that coupled-mode theory can be used to model arrays of lasers with weak lateral coupling. Such arrays are often referred to as evanescently coupled because the strength of the coupling adjacent lasers in the array is characterized by the overlap of their evanescent electric fields in the common cladding region. In order to model array structures with arbitrary lateral coupling, numerical models such as those of Agrawal (1985) and Hadley *et al.* (1988) have been developed. The model of Hadley used a self-consistent approach to include the effects of two-dimensional current flow, carrier diffusion, and heating of the array structure. Incorporation of charge and thermal effects provides accurate modeling of the array characteristics well above threshold.

Besides the lateral-coupled laser array, there is also the injection-coupled laser array, where gain elements are coupled end-to-end in a serial arrangement. In this type of longitudinally coupled multielement laser array,

ISBN 0-12-244070-6

adjacent elements are injection-coupled to each other. Injection coupling in semiconductor lasers is attractive because it can be implemented at the wafer level so that monolithic structures can be fabricated. The threshold characteristics and linewidth of linear arrays of injection coupled lasers was first modeled by Fleck (1963). More recently, generalized approach for modeling the dynamic response and noise characteristics of multielement arrays has been developed by Lang and Yariv (1985).

All of the aforementioned laser array models were developed for one-dimensional array structures. With the recent development of two-dimensional laser arrays such as the grating-surface-emitter, a need has arisen to extend array modeling capabilities to two dimensions. The modal analysis of such two-dimensional laser array structures is more complicated than that of conventional one-dimensional arrays. The existing one-dimensional models apply to lateral coupling distributed along the length of the array or injection (longitudinal) coupling where the coupling occurs at the boundary between serially connected gain elements. These two types of coupling are referred to as distributed and boundary coupling respectively. In two-dimensional arrays such as the grating-surface-emitter, both boundary coupling and distributed coupling can occur together. Therefore, a general two-dimensional array model must provide a framework that will allow for a uniform treatment of the various types of coupling that can occur.

By transforming the two-dimensional laser array into a network representation (Amantea *et al.*, 1989; Amantea *et al.*, 1990) such a unified treatment becomes possible. All the essential elements of the arrays, i.e., the gain sections, DBR sections and their interfaces, are treated in terms of network components. Coupling (even distributed coupling) between array elements is transformed into the mathematical equivalent of boundary coupling, so it occurs at the interfaces between the network components. In this way, the array behavior can be studied at a level of abstraction above the device physics. Although this hides some of the details of the behavior of the array elements, it facilitates the modeling, understanding and designing of arrays. Furthermore, new models for the elements can be incorporated into the network. For example, above-threshold operation can be modeled in a straightforward manner by incorporating non-linear models for the laser gain elements.

This chapter will deal with the development and application of the network approach to analyze the modes of two-dimensional GSE arrays that are evanescently-coupled through the gain elements in the lateral direction, and mutually injection-coupled through DBR sections in the longitudinal direction. A diagram of this array architecture is shown in

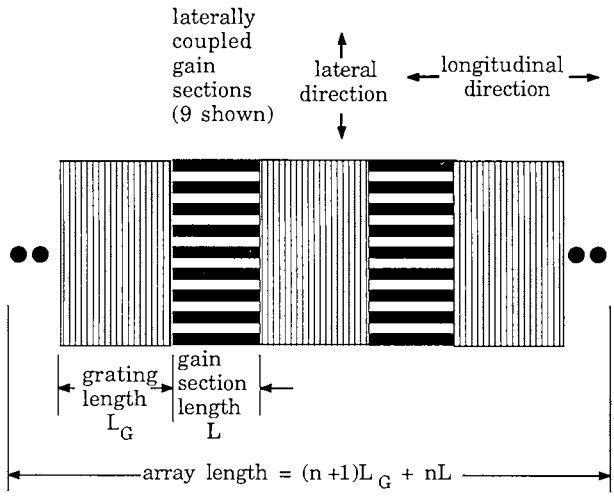

Fig. 1. A representation of the structure.

Fig. 1. The analysis of various other coupling schemes, such as Y-coupling, would be straightforward. The formalism presented here, however, is limited to cases in which the longitudinal coupling is nearest neighbor and in which any lateral coupling that occurs in the DBR sections is similar in form to the lateral coupling that occurs in the gain elements (e.g., evanescent coupling occurs in both the gain and DBR sections).

The network model consists of state variables and network scattering elements. The state variables correspond to the electric field at various points in the array, namely, at the inputs to the gain sections. The scattering elements correspond to the array gain sections and DBR sections. The array is then described by relating all the state variables through a coupling matrix that is obtained from the scattering matrices of the array components. The nontrivial solution of the resulting state equation yields the threshold gain and frequency of each array mode. In order to solve the oscillation condition in a numerically efficient way, the problem of finding the zeros of the determinant of the coupling matrix is transformed to an eigenvalue problem. For the limitations on the coupling discussed above, the lateral and longitudinal coupling are separable, and the oscillation condition for the entire array can be written as an equivalent Fabry-Perot lasing condition with a multibranch frequency-dependent effective modal reflectivity. As a result, the analysis of the coupling in each dimension can be done separately. The total number of branches is equal to the number of gain sections in the

array. Each branch corresponds to the frequency dependent effective reflectivity for a distinct mode of the array. The exact operating frequency depends on the propagation delay in the gain sections. Since the effects of the two coupling schemes are separable in the oscillation condition, the extensive results in the literature on the laterally-coupled case (the longitudinal case here is new because of the DBR sections) are therefore directly applicable to the two-dimensional case.

From the oscillation condition, the complete mode spectrum and threshold gain discrimination between modes is obtained, as well as the internal field intensity and phase. The near-field and the resulting far-field radiation pattern can be obtained from this internal field. This analysis, has shown that a critical parameter in obtaining a uniform power distribution to the gain elements of the array is the ratio of the grating transmissivity to reflectivity.

In Section II, we describe the network model for two-dimensional GSE arrays and its solution. Details of the matrix algebra are provided in the appendices. In Section III, we consider two specific examples, one of a 3 times 3 array, and another of a one-dimensional array of 10 injection-coupled DBR lasers. Finally, in Section IV, we compare experimental measurements of the threshold and near-field to the calculations and find excellent qualitative agreement.

II. THEORY

A. Introduction

In the process of developing a network model for two-dimensional laser arrays, the overall mathematical problem facing us is to formulate a methodology for analyzing large arrays of coupled laser cavities, where large can mean hundreds or thousands of cavities. A similar problem occurs in integrated-circuit technology where large numbers of transistors are interconnected. The circuit problem is handled by the definition of state variables, describing the interconnection of the elements with matrices, and the application of algebraic techniques to form a network theory. It is the goal of this work to introduce a similar methodology for laser arrays.

Fortunately a network formulation exists for waveguide circuits (i.e., scattering matrices) thus all we need to do is to reformulate the array problem into this format. This is done by treating the individual gain elements as a pair of unilateral linear amplifiers interconnected by the longitudinal couplers each of which is represented by a scattering matrix.

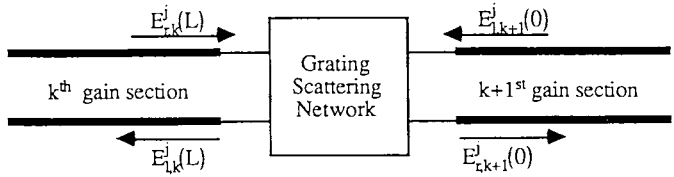

Fig. 2. Schematic network.

This, in effect, neglects the nonlinear interaction between the right and left travelling waves in the gain section.

If lateral coupling in the array occurs primarily in the gain sections and not in the DBR sections or if the lateral coupling in both the gain section and the DBR section are similar, then the lateral and longitudinal coupling become separable and may be treated independently. In this case, each of the lateral coupled gain sections behaves as $2m$ coupled unilateral linear amplifiers, where m is the number of lateral gain elements.

The longitudinal coupling is incorporated into the array theory via a scattering matrix formulation. The two-port network representation is shown in Fig. 2 where the gain sections are shown as a pair of thick parallel horizontal lines to depict the linear transmission-line nature of the gain section and the grating is a symmetric, reciprocal 2-port network which is characterized by a lossy scattering matrix $\begin{bmatrix} r & t \\ t & r \end{bmatrix}$, where r is the reflectivity and t is the transmittivity of the DBR, both functions of wavenumber, β. The dissipative and radiative losses are represented by a, where $|r|^2+|t|^2+|a|^2=1$.

An alternative schematic representation is the signal flow graph shown in Fig. 3. This figure depicts the relationships between the wave amplitudes now written in terms of the state variables, **x**. Each amplifier represents m laterally coupled gain elements and the boxes represent the coupling of gain sections. This picture is useful in establishing the longitudinal coupling equations.

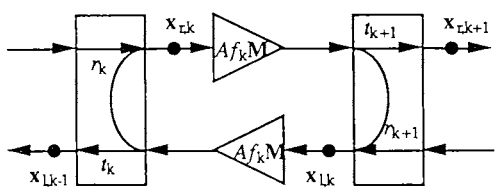

Fig. 3. Signal flow graph representation.

B. One-Dimensional Longitudinal Coupling

Let us first consider a one-dimensional longitudinally-coupled array and ignore the lateral coupling. Each DBR couples two adjacent gain sections, for example the kth and $(k+1)$st gain sections are coupled by the $(k+1)$st DBR, thus

$$E_{l,k}(L) = r_{k+1}E_{r,k}(L) + t_{k+1}E_{l,k+1}(0) \tag{1}$$

and the $(k-1)$st and kth are coupled by the kth DBR

$$E_{r,k}(0) = r_k E_{l,k}(0) + t_k E_{r,k-1}(L) \tag{2}$$

where 0 corresponds to the left end, L corresponds to the right end of a gain section, r_k and t_k are the wave reflectivity and transmittivity of the kth DBR respectively, and E is the amplitude of the electric field.

To cast these relationships into algebraic form, the state variable vector, $\mathbf{x}_r = [x_{r,1}, x_{r,2}, \ldots, x_{r,n}]^T$ is defined to be the n-dimensional vector of all the right travelling wave amplitudes at the left of all the gain elements, e.g., $x_{r,k} = E_{r,k}(0)$ where n is the number of gain sections in the array. Similarly, $\mathbf{x}_l$ is defined as the vector of the left travelling wave amplitudes at the right of the gain sections, e.g., $x_{l,k} = E_{l,k}(L)$. These are the input waves to either side of the gain sections in contrast to $E_{r,k}(L)$ and $E_{l,k}(0)$ which are the output waves.

With these definitions Eqs. (1) and (2) become

$$\begin{aligned} \mathbf{x}_{r,k} &= r_k \boldsymbol{A} f_k \mathbf{x}_{l,k} + t_k \boldsymbol{A} f_{k-1} \mathbf{x}_{r,k-1} \\ \mathbf{x}_{l,k} &= r_{k+1} \boldsymbol{A} f_k \mathbf{x}_{r,k} + t_{k+1} \boldsymbol{A} f_{k+1} \mathbf{x}_{l,k+1}. \end{aligned} \tag{3}$$

The boundary conditions at the ends of the array can be absorbed into the reflectivity of the first and last DBRs so that $x_{r,0} = 0$ and $x_{l,n+1} = 0$, without loss of generality. Specifically, let Γ_1 be the complex reflection coefficient terminating the left end of the left-most DBR in the array. With reference to Fig. 4, the DBR scattering equations relate the outgoing waves, b_1 and b_2 to the incoming waves to a_1 and a_2, e.g., $b_2 = ra_2 + ta_1$ and $b_1 = ta_2 + ra_1$. Solving for b_2/a_2 results in the equivalent terminated DBR reflectivity $r_{1T} = r_1 + \Gamma_1 t_1^2/(1 - r_1\Gamma_1)$.

Equation (3) is a set of n homogeneous linear equations in the variables $x_{r,k}$. In matrix notation $\mathbf{Tx} = 0$. Thus to have a nontrivial solution the

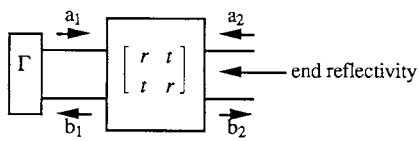

Fig. 4. Array termination equivalent reflectivity.

determinant of the coefficient matrix, **T**, must be zero. This is the oscillation condition. Since this matrix is generally large, the determinant cannot be found analytically so that an iterative method is required to find the complex value of A that makes the determinant zero. Because this method will be numerically very inefficient, this approach is not very desirable. If a similarity transformation can be found that will transform **T** into an eigenvalue form, e.g., $(\mathbf{K}-\mu\mathbf{I})\mathbf{x}=0$, where **K** is independent of A and μ depends upon A then a significant simplification results.

Equation (3) is shown in matrix form in Eq. (4).

$$\begin{bmatrix} -1 & 0 & \cdots & & 0 & Ar_1f_1 & 0 & \cdots & & 0 \\ At_2f_1 & & & & \vdots & 0 & & & & \vdots \\ 0 & & \ddots & \ddots & & & & & \ddots & \\ \vdots & \ddots & & & 0 & \vdots & & \ddots & \ddots & 0 \\ 0 & \cdots & 0 & At_nf_{n-1} & -1 & 0 & & & 0 & Ar_nf_n \\ & & & & & -1 & At_2f_1 & 0 & \cdots & 0 \\ Ar_2f_1 & 0 & \cdots & 0 & & 0 & & & \ddots & \vdots \\ 0 & & & \vdots & & \vdots & & \ddots & & 0 \\ \vdots & \ddots & & 0 & & & \ddots & & & At_nf_{n-1} \\ 0 & \cdots & 0 & Ar_{n+1}f_n & & 0 & \cdots & & 0 & -1 \end{bmatrix} \begin{bmatrix} \mathbf{x}_r \\ \mathbf{x}_l \end{bmatrix} = 0. \tag{4}$$

Equation (4) can be written as

$$\begin{bmatrix} \mathbf{S}_r & \mathbf{C}_l \\ \mathbf{C}_r & \mathbf{S}_l \end{bmatrix} \begin{bmatrix} \mathbf{x}_r \\ \mathbf{x}_l \end{bmatrix} = 0 \tag{5}$$

where $\mathbf{S}_r$ couples right-travelling waves to right-travelling waves across gain sections via the DBR transmissivity similarly $\mathbf{S}_l$ couples left-travelling waves to left-travelling waves. The **C** matrices couple right to left travelling waves via the DBR reflectivity. These matrices can be expressed in more compact form as $\mathbf{S}_l = -\mathbf{I} + A\mathbf{s}^T\boldsymbol{\tau}\mathbf{f}$, $\mathbf{S}_r = -\mathbf{I} + A\mathbf{s}\boldsymbol{\tau}_+\mathbf{f}$, $\mathbf{C}_r = A\boldsymbol{\rho}_+\mathbf{f}$, and $\mathbf{C}_l = A\boldsymbol{\rho}\mathbf{f}$. The matrix **s** is the subdiagonal shift matrix,

$$\mathbf{s} = \begin{bmatrix} 0 & & \cdots & & 0 \\ 1 & & & & \\ 0 & & \ddots & & \vdots \\ \vdots & \ddots & & & \\ 0 & \cdots & 0 & 1 & 0 \end{bmatrix}$$

The matrices ρ, ρ_+, τ, τ_+, and **f** are diagonal matrices with diagonal elements $[r_1, r_2, \ldots, r_n]$, $[r_2, r_3, \ldots, r_{n+1}]$, $[t_1, t_2, \ldots, t_n]$, $[t_2, t_3, \ldots, t_{n+1}]$, $[f_1, f_2, \ldots, f_n]$, respectively.

Equation (5) can simplified by eliminating $\mathbf{x}_l$, e.g., $\mathbf{x}_l = \mathbf{S}_l^{-1}\mathbf{C}_r\mathbf{x}_r$, factoring $\mathbf{C}_r$ from the right, and multiplying by the inverse of $\mathbf{C}_l$ from the left to obtain $[\mathbf{S}_l^{-1} - \mathbf{C}_l^{-1}\mathbf{S}_r\mathbf{C}_r^{-1}]\mathbf{C}_r\mathbf{x}_r = 0$ which reduces the size of the problem by two.

The inverse of $\mathbf{S}_l$ can be obtained from the matrix series expansion of $(\mathbf{I}-\mathbf{X})^{-1}$. If $\mathbf{X}^n = \mathbf{O}$, where $\mathbf{O}$ is the zero matrix, then by direct substitution it can be shown that $(\mathbf{I}-\mathbf{X})^{-1} = \mathbf{I}+\mathbf{X}+\mathbf{X}^2+\ldots+\mathbf{X}^{n-1}$.

Since $\mathbf{S}_l = -\mathbf{I} + A\mathbf{s}^T\tau\mathbf{f}$, let $\mathbf{X} = A\mathbf{s}^T\tau\mathbf{f}$ then $\mathbf{X}^k = (A\mathbf{s}^T\tau\mathbf{f})^k$. It can be easily demonstrated that the nth power of the shift matrix is zero (each shift operation moves a vector's coefficients down one position so that after n shifts the vector is zero). Furthermore, since $\tau\mathbf{f}$ is diagonal then $(\mathbf{s}^T)^n = \mathbf{O}$ implies $(\mathbf{s}^T\tau\mathbf{f})^n = \mathbf{O}$ which then implies $\mathbf{X}^n = \mathbf{O}$ so that the expansion of $(\mathbf{I}-\mathbf{X})^{-1}$ is valid. For example, let $s_k = t_k f_k$ then

$$s^2 = \begin{bmatrix} 0 & s_2 & 0 & \cdots & 0 \\ \vdots & & \ddots & & \vdots \\ & & & & 0 \\ & & & & s_n \\ 0 & & \cdots & & 0 \end{bmatrix} \begin{bmatrix} 0 & s_2 & 0 & \cdots & 0 \\ \vdots & & \ddots & & \vdots \\ & & & & 0 \\ & & & & s_n \\ 0 & & \cdots & & 0 \end{bmatrix}$$

$$= \begin{bmatrix} 0 & 0 & s_2 s_3 & 0 & \cdots & 0 \\ \vdots & & & \ddots & & \vdots \\ & & & & & 0 \\ & & & & & s_{n-1}s_n \\ & & & & & 0 \\ 0 & & & \cdots & & 0 \end{bmatrix}$$

$$s^{n-1} = \begin{bmatrix} 0 & s_2 & 0 & \cdots & 0 \\ \vdots & & \ddots & & \vdots \\ & & & & 0 \\ & & & & s_n \\ 0 & & \cdots & & 0 \end{bmatrix}^{n-1}$$

$$= \begin{bmatrix} 0 & \cdots & 0 & & \Pi_{k=2}^{n} s_k \\ \vdots & & & \ddots & 0 \\ & & & & \vdots \\ 0 & & \cdots & & \end{bmatrix}.$$

Thus

$$\mathbf{S}_l^{-1} = -\mathbf{I}_n - \begin{bmatrix} 0 & h_{1,2} & \cdots & h_{1,n} \\ \vdots & & \ddots & \vdots \\ & & & h_{n-1,n} \\ 0 & & \cdots & 0 \end{bmatrix} = -\begin{bmatrix} 1 & h_{1,2} & \cdots & h_{1,n} \\ 0 & & \ddots & \vdots \\ \vdots & \ddots & & h_{n-1,n} \\ 0 & \cdots & 0 & 1 \end{bmatrix} \tag{7}$$

where the $h_{i,j}$ are given by

$$h_{i,j} = A^{j-i} \prod_{k=i+1}^{j} \tau_k f_k = \frac{A^j \prod_{k=1}^{j} \tau_k f_k}{A^i \prod_{k=1}^{i} \tau_k f_k} = \frac{\eta(j)}{\eta(i)}. \tag{8}$$

Thus

$$[\mathbf{S}_l^{-1} - \mathbf{C}_l^{-1}\mathbf{S}_r\mathbf{C}_r^{-1}] = \begin{bmatrix} 1 & h_{1,2} & \cdots & h_{1,n} \\ 0 & \ddots & \ddots & \vdots \\ \vdots & \ddots & \ddots & h_{n-1,n} \\ 0 & \cdots & 0 & 1 \end{bmatrix}$$

$$\overbrace{-A^{-2}((\rho\rho_+)^{-1}\mathbf{f}^{-2})}^{\text{diagonal terms}} + \overbrace{A^{-1}\rho^{-1}\mathbf{f}^{-1}s\tau_+\rho_+^{-1}}^{\text{subdiagonal terms}}. \tag{9}$$

Let $\mathbf{Y}$ be the matrix on the right-hand side of Eq. 9. If $\mathbf{Y}$ is operated on with a diagonal similarity transformation, i.e., $\mathbf{P}^{-1}\mathbf{Y}\mathbf{P}$, with elements p_i then the diagonal portion of the matrix $\mathbf{I}_n - A^{-2}(\rho\rho_+)^{-1}\mathbf{f}^{-2}$ is unchanged, the $i-j$th entry of the upper triangle (e.g., $h_{i,j}$) is multiplied by $p_i^{-1}\, p_j$, and the subdiagonal portion, $A^{-1}\rho^{-1}\mathbf{f}^{-1}\mathbf{s}\tau_+(\rho_+)^{-1}$, is multiplied by $p_{i+1}^{-1}\, p_i$. The goal is to select p_i to eliminate the powers of A from the off-diagonal terms, e.g., $p_i^{-1} p_j\, h_{i,j} = 1$ for $i \leqq j$. Since $h_{i,j}$ is separable, e.g., $h_{i,j} = \eta(j)/\eta(i)\; p_i$ can easily be found to satisfy this requirement, e.g., $p_i^{-1} = \eta(i)$.

Thus let $p_i^{-1} = A^i \Pi_{k=1}^{j}\, t_k f_k$ then

$$p_{i+1}^{-1} p_i = \mathrm{A}t_{i+1} f_{i+1} \quad \text{and} \quad p_i^{-1} p_j = \mathrm{A}^{i-j} \prod_{k=1}^{i} \mathrm{t}_k \mathrm{f}_k \Big/ \prod_{k=1}^{j} \mathrm{t}_k \mathrm{f}_k.$$

Define $q_k = t_k / r_k$, then $\tau(\rho)^{-1} = \mathbf{q}$ and $\tau_+(\rho_+)^{-1} = \boldsymbol{q}_+$, where $\mathbf{q}$ is the diagonal matrix with elements $[q_1, q_2, \ldots, q_n]$ and $\mathbf{q}_+$ is the diagonal matrix with elements $[q_2, q_3, \ldots, q_{n+1}]$ so that the subdiagonal terms are $\mathbf{P}^{-1}\{A^{-1}(\rho\mathbf{f})^{-1}\mathbf{s}\mathbf{q}_+\}\mathbf{P}$. Noting that $(\rho\mathbf{f})^{-1} = \mathbf{q}(\tau\mathbf{f})^{-1}$ and $\mathbf{s}\mathbf{q}_+ = \mathbf{q}\mathbf{s}$, the subdiagonal terms become $\mathbf{P}^{-1}\{A^{-1}\mathbf{q}^2(\tau\mathbf{f})^{-1}\mathbf{s}\}\mathbf{P}$. Utilizing the diagonal nature of $\mathbf{q}$, $\mathbf{P}^{-1}\mathbf{q}^2 = \mathbf{P}^{-1}\mathbf{q}^2\mathbf{P}\mathbf{P}^{-1} = \mathbf{q}^2\mathbf{P}^{-1}$, we can factor this to $\mathbf{q}^2\mathbf{P}^{-1}\{A^{-1}(\tau\mathbf{f})^{-1}\mathbf{s}\}\mathbf{P}$. Finally note $\mathbf{P}^{-1}\{A^{-1}(\tau\mathbf{f})^{-1}\mathbf{s}\}\mathbf{P} = \mathbf{s}$ so that

$$\mathbf{P}^{-1}[\mathbf{S}_l^{-1} - \mathbf{C}_l^{-1}\mathbf{S}_r\mathbf{C}_r^{-1}]\mathbf{P} = \begin{bmatrix} 1 & \cdots & 1 \\ 0 & \ddots & \vdots \\ \vdots & \ddots & \\ 0 & \cdots 0 & 1 \end{bmatrix} \overbrace{-A^{-2}((\rho\rho_+)^{-1}\mathbf{f}^{-2})}^{\text{diagonal terms}} + \overbrace{\mathbf{q}^2\mathbf{s}}^{\text{subdiagonal terms}}. \tag{10}$$

Let

$$\mathbf{L}=\begin{bmatrix}1 & \cdots & 1\\ 0 & \ddots & \vdots\\ \vdots & \ddots & \vdots\\ 0 & \cdots & 1\end{bmatrix}+\mathbf{q}^2\mathbf{s}=\begin{bmatrix}1 & \cdots & & 1\\ q_2^2 & & & \\ 0 & \ddots & & \vdots\\ \vdots & \ddots & & \vdots\\ 0 & \cdots & 0 & q_n^2 \quad 1\end{bmatrix}. \tag{11}$$

Then the lasing condition becomes

$$[\mathbf{S}_1^{-1}\mathbf{C}_r-\mathbf{C}_1^{-1}\mathbf{S}_r]\mathbf{x}_r=\mathbf{P}\{\mathbf{L}-A^{-2}\mathbf{f}^{-2}(\rho\rho_+)^{-1}\}\mathbf{P}^{-1}(\rho_+\mathbf{f})\mathbf{x}_r=0. \tag{12}$$

Factoring $\mathbf{f}^{-2}(\rho_+\rho)^{-1}$ from the left results in

$$\mathbf{P}\{\mathbf{f}^{-2}(\rho\rho_+)^{-1}\}\overbrace{\{\rho\rho_+\mathbf{f}^2\mathbf{L}-A^{-2}\mathbf{I}_n\}}^{\text{eigenvalue equation}}\mathbf{P}^{-1}\mathbf{C}_r\mathbf{x}_r=0. \tag{13}$$

Since $\mathbf{P}\{\mathbf{f}^{-2}(\rho\rho_+)^{-1}\}$ is not singular, A^{-2} are the eigenvalues and $\mathbf{P}^{-1}\mathbf{C}_r\mathbf{x}_r$ are the eigenvectors of the longitudinal coupling matrix $\mathbf{K}=\rho\rho_+\mathbf{f}^2\mathbf{L}$. The eigenvalue equation contained in (13) can be reformulated as,

$$\frac{1}{A_\eta^2}=\mu_{L\eta} \tag{13a}$$

where μ_{L_η} is the ηth eigenvalue of the longitudinal coupling matrix **K**. Equation (13a) is a generalized Fabry–Perot oscillation condition, where $\mu_{L\eta}$ can be thought of as the effective modal reflectivity.

C. A One-Section Example

Let us consider a simple array with one gain section so that

$$\mathbf{K}=[r_1r_2f_1^2] \tag{14}$$

this results in the oscillation condition

$$\left(r_1r_2f_1^2\frac{1}{A^2}\right)=0. \tag{15}$$

The quantity f_kA is complex gain of the kth gain section. $G_{pk}=|f_kA|^2$ is the power gain and $\arg(f_k\mathrm{A})=\arg(e^{j\beta L})=j\beta L$ is the phase delay of the kth gain section. Thus

$$(r_1r_2G_{\mathrm{P1}}\,e^{2j\beta_1L_1}-1)=0. \tag{16}$$

Recall that the end gratings must be terminated so that the reflectivity is replaced by its equivalent terminated reflectivity. Thus the general oscillation condition for a DBR terminated laser is

$$\left[\left(r_1+\frac{\Gamma_1 t_1^2}{1-r_1\Gamma_1}\right)\left(r_2+\frac{\Gamma_2 t_2^2}{1-r_2\Gamma_2}\right)\left(G_{\mathrm{P1}}\, e^{2j\beta_1 L_1}-1\right)\right]=0. \tag{17}$$

When the frequency is far away from the Bragg condition then $r\to 0$ and $t\to 1$ so that

$$(\Gamma_1\Gamma_2 G_{\mathrm{P1}}\, e^{2j\beta_1 L_1}-1)=0, \tag{18}$$

which is the standard Fabry-Perot result.

D. A Two-Section Example

Let us consider a simple array with two gain sections so that

$$\mathbf{K}=\begin{bmatrix} r_1 r_2 f_1^2 & r_1 r_2 f_1^2 \\ r_2 r_3 f_2^2 q_2^2 & r_2 r_3 f_2^2 \end{bmatrix}. \tag{19}$$

Then the oscillation condition is

$$\left(r_1 r_2 f_1^2-\frac{1}{A^2}\right)\left(r_2 r_3 f_2^2-\frac{1}{A^2}\right)-r_1 r_2 f_1^2 r_2 r_3 f_2^2 q_2^2=0. \tag{20}$$

We can put this into more conventional form by multiplying through by A^4 and substituting t/r for q, thus

$$(r_1 r_2(f_1^2A^2)-1)[r_2 r_3(f_2^2A^2)-1]-(f_1^2A^2)(f_2^2A^2)r_1 r_3 t_2^2=0. \tag{21}$$

Substituting for A results in

$$(r_1 r_2 G_{\mathrm{P1}}\, e^{2j\beta_1 L_1}-1)(r_2 r_3 G_{\mathrm{P2}}\, e^{2j\beta_2 L_2}-1)-r_1 r_3 t_2^2 G_{\mathrm{P1}} G_{\mathrm{P2}}\, e^{2j(\beta_2 L_2+\beta_1 L_1)}=0, \tag{22}$$

which is, except for notation and ignoring antiguiding, the same oscillation condition as that found in Hardy and Streifer (1985).

E. A Ten-Section Example

With reference to Fig. 1, the nominal array specifications for the device to be considered are given in Table I.

Figure 5(a) shows a plot of the phase of the square of the effective reflection coefficient for a one-dimensional grating-coupled array as a function of $\delta=\Delta\beta/\beta_{\mathrm{B}}$ for a 10-section array with DBR parameters $\kappa=10\ \mathrm{cm}^{-1}$,

Table I

Nominal specifications for 2-D GSE arrays that are evanescently-coupled through the gain elements in the lateral direction and are mutually injection-coupled through DBR sections in the longitudinal directions

Parameter	Value
Λ_G	2401.5 Å
N_G	1250
L	150 μm
n	10
m	1
s	4 μm
W_R	4 μm

$\alpha = 8\ \text{cm}^{-1}$, and $\xi = 2\ \text{cm}^{-1}$ $\delta = 0$. Note that the vertical scale has been normalized to π. As expected, the phase of the effective reflection coefficient is split into 10 branches, labeled 1 through 10 each of which decreases nearly linearly as δ increases. The phase of each branch has been adjusted by adding integral multiples of 2π so that it crosses $\delta = 0$ in the range $0 \leq \text{phase} \leq 2\pi$.

The gain-section phase delay is shown as the series of positive-slope straight lines overlaying the effective reflection phase curves in Fig. 5(a). The intersections of the effective reflection phase curves and the linear phase delay curve of the gain section define the wavenumbers of the modes of the array. Figure 5(b) is a plot of the threshold gain, $g_{\text{th}} = \ln(|\Re|)/L + \alpha$, for each of these modes.

F. One-Dimensional Lateral Coupling

In this section we outline the conversion of a coupled-wave model into a network model. We use evanescently-coupled ridge-guided gain elements with nearest-neighbor coupling to formulate the theory. Other types of lateral coupling could be used without any change in the formulation, for example, Streifer *et al.* (1987) establishes the coupling matrices for Y-junction lateral coupling.

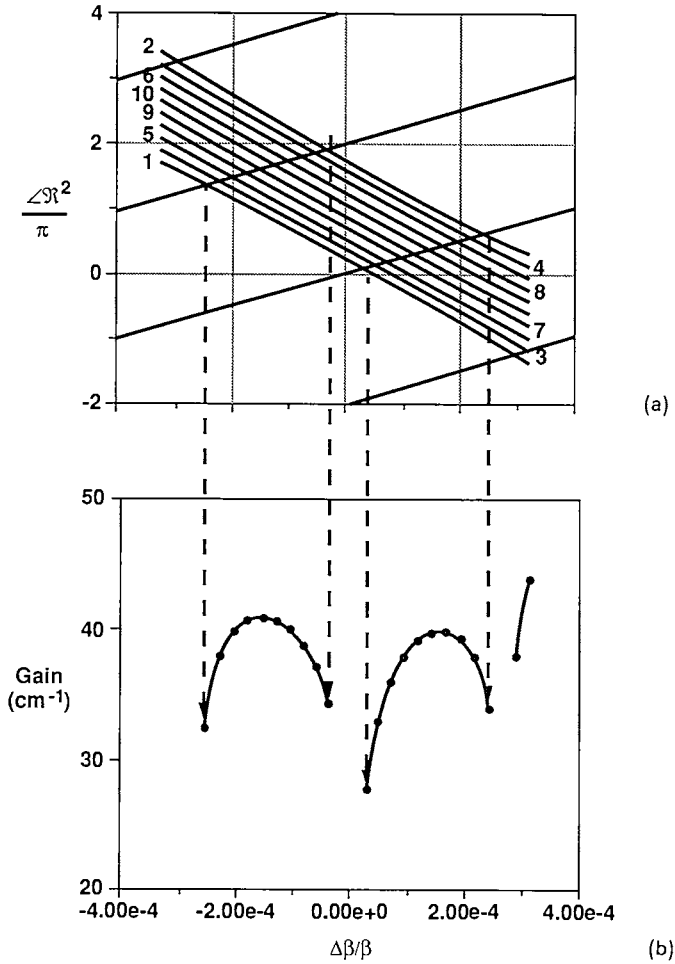

Fig. 5. A 10×1 example.

If we assume that an isolated ridge-guided gain element supports a single mode then a travelling wave in the positive z direction will be given by

$$E(x, y, z, t) = E_r(z)e(x, y) \exp(-jwt + \gamma_0 z) \tag{23}$$

where $E_r(z)$ is a slowly varying complex wave amplitude and $e(x, y)$ is the normalized lateral and transverse wave shape. To characterize the ensemble of right travelling waves in the lateral-coupled gain region of a single gain section of the array we use the amplitude vector $E_r^j(z) = [E_r^1(z), E_r^2(z), \ldots, E_r^m(z)]^T$ where the superscript represents the right travelling

wave amplitude in the jth lateral element. If we assume that opposite travelling waves do not couple in the gain medium, then the behavior of the group of waves can be modeled by m coupled-wave equations in the form

$$\frac{\partial \mathbf{E}_r(z)}{\partial z} - \gamma_0 \mathbf{E}_r(z) = \hat{\mathbf{M}} \mathbf{E}_r(z) \tag{24}$$

where γ_0 is the unperturbed propagation constant and $\hat{\mathbf{M}}$ is the distributed lateral coupling matrix, e.g., for four lateral evanescently coupled lasers with the nearest-neighbor interaction with strength κ,

$$\hat{\mathbf{M}} = \begin{bmatrix} 0 & \kappa & 0 & 0 \\ \kappa & 0 & \kappa & 0 \\ 0 & \kappa & 0 & \kappa \\ 0 & 0 & \kappa & 0 \end{bmatrix}.$$

We have two sets of these m equations; one set of m for both the right and left travelling waves. Our goal is to replace the set of $2m$ differential equations in the gain section by an algebraic relationship between the wave amplitudes at the boundaries.

We begin with the solution of coupled-wave equations (24) which relate the array mode propagation constants γ_j to the isolated mode propagation constant γ_0, by a mode-splitting factor, e.g., $\gamma_j - \gamma_0 = \mu_{M_j}$. We define the vector $\mathbf{v}(z) = [e^{\mu_{M_1} z}, e^{\mu_{M_2} z}, \ldots, e^{\mu_{M_m} z}]^T$ to represent the slowly varying part of the mode amplitude due to lateral coupling. The solution to Eq. (24) will be in the form given by $\mathbf{E}_r(z) = \exp(\gamma_0 z)\mathbf{C}\mathbf{v}(z)$, where $\mathbf{C}$ is a matrix of coefficients. Substituting this proposed solution into the coupled-mode equations results in

$$\mathbf{C}\mu_M \mathbf{v}(z) = \hat{\mathbf{M}}\mathbf{C}\mathbf{v}(z) \tag{25}$$

where μ_M is the diagonal matrix composed of the μ_{M_j}. This result shows that $\mathbf{C}$ is the similarity transformation that diagonalizes the distributed lateral coupling matrix, $\hat{\mathbf{M}}$, $\mathbf{v}(z)$ are the eigenvectors, and μ_{M_j} are the eigenvalues.

To relate the wave amplitudes at either end of the gain section we note that $E_r(L) = \exp(\gamma_0 L)\mathbf{C}\mathbf{v}(L)$ and $E_r(0) = \mathbf{C}\mathbf{v}(0)$ and

$$\mathbf{v}(L) = \begin{bmatrix} e^{\mu_{M_1} L} & 0 & \cdots & 0 \\ 0 & & & \vdots \\ \vdots & & \ddots & 0 \\ 0 & & \cdots 0 & e^{\mu_{M_m} L} \end{bmatrix} \boldsymbol{v}(0). \tag{26}$$

So that

$$\mathbf{E}_r(L) = \exp(\gamma_0 L)\mathbf{C}\begin{bmatrix} e^{\mu_M{}^1 L} & 0 & \cdots & 0 \\ 0 & \ddots & \ddots & \vdots \\ \vdots & \ddots & \ddots & 0 \\ 0 & \cdots & 0 & e^{\mu_M{}^m L} \end{bmatrix}\mathbf{C}^{-1}\mathbf{E}_r(0), \tag{27}$$

which in matrix notation is

$$\mathbf{E}_r(L) = \exp(\gamma_0 L)\mathbf{M}\mathbf{E}_r(0) = A\mathbf{M}\mathbf{E}_r(0) \tag{28}$$

where $A = \exp(\gamma_0 L)$. We define the lumped lateral coupling matrix for the gain region by $\mathbf{M} = C\exp(\mu_M L)C^{-1} = \exp(\hat{\mathbf{M}}L)$. We see that $A\mathbf{M}$ is the travelling wave amplitude matrix transfer function across a nominal gain section. Finally note that nothing in this treatment restricts the approach to nearest-neighbor interaction.

G. Two-Dimensional Coupling

To combine the longitudinal and lateral network approaches into a two-dimensional model we start by redefining the state vectors $\mathbf{x}_r$ and $\mathbf{x}_l$, e.g.,

$$\mathbf{x}_r = [x_{r,1}^1, x_{r,2}^1, \ldots, x_{r,n}^1, x_{r,1}^2, x_{r,2}^2, \ldots, x_{r,n}^2, \ldots, x_{r,1}^m, x_{r,2}^m, \ldots, x_{r,n}^m]^T$$

then the kth segment of $\mathbf{x}_r$, $\mathbf{x}_{r,k} = [x_{r,k}^1, x_{r,k}^2, \ldots, x_{r,k}^m]^T$, corresponds to the lateral components in the kth gain section. Thus Eq. (3) becomes

$$\begin{aligned} \mathbf{x}_{r,k} &= r_k A f_k \mathbf{M}\mathbf{x}_{l,k} + t_k A f_{k-1}\mathbf{M}\mathbf{x}_{r,k-1} \\ \mathbf{x}_{l,k} &= r_{k+1} A f_k \mathbf{M}\mathbf{x}_{r,k} + t_{k+1} A f_{k+1}\mathbf{M}\mathbf{x}_{l,k+1}. \end{aligned} \tag{29}$$

As before in Eq. (5), Eq. (29) is equivalent to the set of matrix homogeneous equations

$$\begin{bmatrix} \mathbf{S}_r & \mathbf{C}_l \\ \mathbf{C}_r & \mathbf{S}_l \end{bmatrix}\begin{bmatrix} \mathbf{x}_r \\ \mathbf{x}_l \end{bmatrix} = 0. \tag{30}$$

However, in this case the submatrices are n times m on a side. We utilize the Kronecker (Pearson, 1983) matrix product to simplify notation. The Kronecker matrix product is a distributive, associative operator that has the following properties:

1. If $\mathbf{A} = [a_{ij}]_n$ and $\mathbf{B} = [b_{kl}]_m$ where n denotes an $n \times n$ matrix then $(\mathbf{A} \otimes \mathbf{B}) = [\mathbf{F}_{ij}]_n$ where $\mathbf{F}_{ij} = a_{ij}\mathbf{B}$. Thus each element of the matrix $\mathbf{A}$ is replaced by the matrix $a_{ij}\mathbf{B}$.
2. If $\mathbf{A} \sim \mathbf{C}$ and $\mathbf{B} \sim \mathbf{D}$ where $\sim$ denotes same size matrices then $(\mathbf{A} \otimes \mathbf{B}) \times (\mathbf{C} \otimes \mathbf{D}) = (\mathbf{AC} \otimes \mathbf{BD})$.

3. $(\mathbf{A}\otimes\mathbf{B})^n = (\mathbf{A}^n\otimes\mathbf{B}^n)$.
4. If $\mathbf{A}$ and $\mathbf{B}$ are nonsingular then $(\mathbf{A}\otimes\mathbf{B})^{-1} = (\mathbf{A}^{-1}\otimes\mathbf{B}^{-1})$.
5. If μ_j $(j = 1, 2, \ldots, n)$ are the eigenvalues of $\mathbf{A}$ and λ_k $(k = 1, 2, \ldots, m)$ are the eigenvalues of $\mathbf{B}$ then $\mu_j\lambda_k (j = 1, 2, \ldots, n;\ k = 1, 2, \ldots, m)$ are the eigenvalues of $\mathbf{A}\otimes\mathbf{B}$).
6. $\mathrm{Det}\,(\mathbf{A}\otimes\mathbf{B}) = [\mathrm{Det}\,(\mathbf{A})]^m[\mathrm{Det}\,(\mathbf{B})]^n$.

Thus $\mathbf{S}_l = -\mathbf{I}_n\otimes\mathbf{I}_m + A\mathbf{s}^T\tau\mathbf{f}\otimes\mathbf{M}$, $\mathbf{S}_r = -\mathbf{I}_n\otimes\mathbf{I}_m + A\mathbf{s}\tau + \mathbf{f}\otimes\mathbf{M}$, $\mathbf{C}_r = A\rho + \mathbf{f}\otimes\mathbf{M}$, and $\mathbf{C}_l = A\rho\mathbf{f}\otimes\mathbf{M}$, where $\mathbf{I}_n$ denotes the n times n identity matrix. As before the inverse of $\mathbf{S}_l$ can be obtained from the matrix expansion of $(\mathbf{I}-\mathbf{X})^{-1}$. Since $\mathbf{S}_l = -\mathbf{I}_n\otimes\mathbf{I}_m + A\mathbf{s}^T\tau\mathbf{f}\otimes\mathbf{M}$, let $\mathbf{X} = A\mathbf{s}^T\tau\mathbf{f}\otimes\mathbf{M}$. Using property (3) we get $\mathbf{X}^k = (\mathbf{A}\mathbf{s}^T\tau\mathbf{f})^k\otimes\mathbf{M}^k$. We have already shown that $(\mathbf{s}^T\tau\mathbf{f})^n = \mathbf{O}$ thus $\mathbf{X}^n = 0$ so that the method of inversion remains valid. Performing the expansion results in

$$\mathbf{S}_l^{-1} = -\mathbf{I}_n\otimes\mathbf{I}_m - \begin{bmatrix} 0 & h_{1,2} & \cdots & h_{1,n} \\ \vdots & & \ddots & \vdots \\ & & & h_{n-1,n} \\ 0 & & \cdots & 0 \end{bmatrix} = -\begin{bmatrix} \mathbf{I}_m & h_{1,2} & \cdots & h_{1,n} \\ 0 & & \ddots & \vdots \\ \vdots & \ddots & & h_{n-1,n} \\ 0 & \cdots & 0 & \mathbf{I}_m \end{bmatrix} \tag{31}$$

where the $m\times m$ submatrices $h_{i,j}$ are given by

$$h_{i,j} = (A\mathbf{M})^{j-i}\prod_{k=i+1}^{j}\tau_k f_k. \tag{32}$$

Equation (9) now generalizes to

$$[\mathbf{S}_l^{-1} - \mathbf{C}_l^{-1}\mathbf{S}_r\mathbf{C}_r^{-1}] = \begin{bmatrix} \mathbf{I}_m & h_{1,2} & \cdots & h_{1,n} \\ 0 & & \ddots & \vdots \\ \vdots & \ddots & & h_{n-1,n} \\ 0 & \cdots & 0 & \mathbf{I}_m \end{bmatrix} - \overbrace{((\rho\rho_+)^{-1}\mathbf{f}^{-2}\otimes(A\mathbf{M})^{-2})}^{\text{diagonal terms}} + \overbrace{\rho^{-1}\mathbf{f}^{-1}\mathbf{s}\tau_+\rho_+^{-1}\otimes(A\mathbf{M})^{-1}}^{\text{subdiagonal terms}}. \tag{33}$$

As before this can be transformed into eigenvalue form by a similarity transformation, however, in this case the transformation is an $n\times m$ by $n\times m$ matrix composed of $m\times m$ submatrices along a diagonal, e.g.,

$$\mathbf{P} = \begin{bmatrix} \mathbf{p}_1 & \mathbf{O} & \cdots & \mathbf{O} \\ \mathbf{O} & & \ddots & \vdots \\ \vdots & \ddots & & \mathbf{O} \\ \mathbf{O} & \cdots & \mathbf{O} & \mathbf{p}_n \end{bmatrix} \tag{34}$$

where **O** are $m \times m$ matrices with all zero entries, and the $m \times m$ diagonal matrices are given by

$$\mathbf{p}_i^{-1} = (A\mathbf{M})^i \prod_{k=1}^{j} t_k f_k. \tag{35}$$

Performing this transformation results in

$$\mathbf{P}^{-1}[\mathbf{S}_l^{-1} - \mathbf{C}_l^{-1}\mathbf{S}_r\mathbf{C}_r^{-1}]\mathbf{P} = \begin{bmatrix} 1 & \cdots & & 1 \\ 0 & \ddots & & \vdots \\ \vdots & \ddots & & \vdots \\ 0 & \cdots & 0 & 1 \end{bmatrix}$$

$$\otimes \mathbf{I}_m - A^{-2}((\rho\rho_+)^{-1}\mathbf{f}^{-2}) \otimes \mathbf{M}^{-2} + \mathbf{q}^2\mathbf{s} \otimes \mathbf{I}_m. \tag{36}$$

Finally

$$\mathbf{P}(\mathbf{f}^{-2}(\rho\rho_+)^{-1}\}\overbrace{\{\rho\rho_+\mathbf{f}^2\mathbf{L} \otimes \mathbf{M}^2 - A^{-2}\mathbf{I}_n \otimes \mathbf{I}_m\}}^{\text{eigenvalue equation}}\mathbf{P}^{-1}\mathbf{C}_r\mathbf{x}_r = 0. \tag{37}$$

The eigenvalue equation part of (37) can be rewritten as,

$$\frac{1}{A_{\nu,\eta}^2} = \exp(2\mu_{M\nu}L)\,\mu_{L\eta} \tag{37a}$$

where $\mu_{L\eta}$ is the ηth eigenvalue of the longitudinal coupling matrix **L**, $\mu_{M\nu}$ is the νth eigenvalue of the lateral coupling matrix **M**, and L is the length of a gain section. This is an equivalent Fabry-Perot oscillation condition where $\exp(2\mu_{M\nu}L)\mu_{L\eta}$ can be thought of as the effective modal reflectivity.

H. A 3×3 Example

To illustrate some of the features discussed we consider a 3×3 matched uniform array. The lateral coupling matrix is given by

$$\hat{\mathbf{M}} = \begin{bmatrix} 0 & \kappa & 0 \\ \kappa & 0 & \kappa \\ 0 & \kappa & 0 \end{bmatrix}$$

where κ is the lateral coupling coefficient. The eigenvalues of $\hat{\mathbf{M}}$ are given by

$$\mu_{M_\nu} = 2\kappa \cos\left(\frac{\nu\pi}{4}\right).$$

The longitudinal coupling matrix is given by

$$\mathbf{K} = r^2 \begin{bmatrix} 1 & 1 & 1 \\ q^2 & 1 & 1 \\ 0 & q^2 & 1 \end{bmatrix}$$

with eigenvalues given by

$$\mu_{L\eta} = r^2\{1 + 2\sqrt{2/3}\, q \cos[\cos^{-1}(3\sqrt{3}\, q/4\sqrt{2})/3 + 2\eta\pi/3]\}.$$

Thus the lasing condition is

$$\frac{1}{A_{\nu\eta}^2} = r^2\{1 + 2\sqrt{2/3}\, q \cos[\cos^{-1}(3\sqrt{3}\, q/4\sqrt{2})/3 + 2\eta\pi]\} \exp\left(2\kappa L \cos\left(\frac{\nu\pi}{4}\right)\right)$$

where j and k take on the values of 1 through 3. This leads to the phase

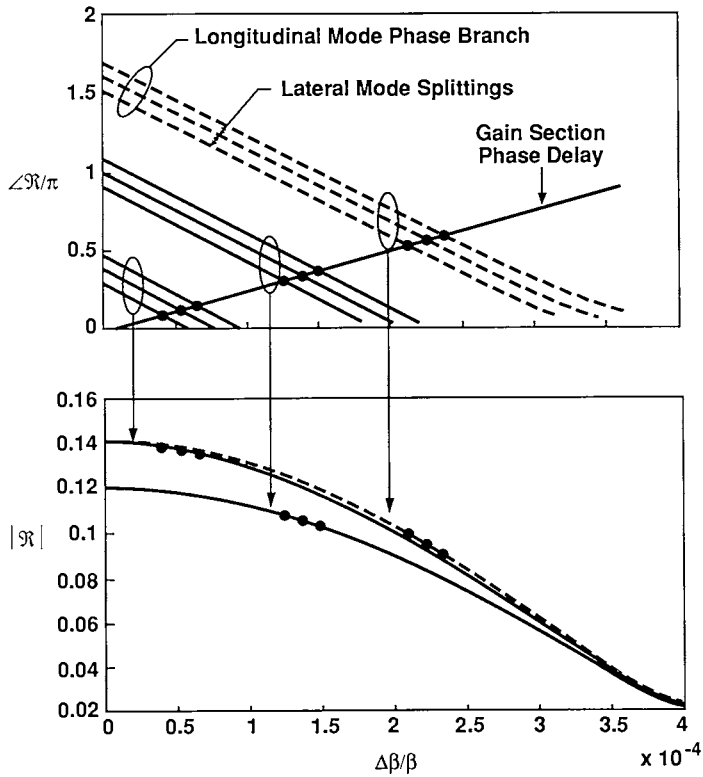

Fig. 6. A 3×3 example.

condition

$$4\pi N_L \delta_{\nu\eta\xi} + 2\xi\pi = \arg\,(r^2\{1 + 2\sqrt{2/3}\; q \cos\,[\cos^{-1}\,(3\sqrt{3}\; q/4\sqrt{2})/3 + 2\eta\pi/3]\} + 2\,\mathrm{Im}\,[\kappa]L\cos\,(\nu\pi/4)$$

where r and q are both functions of $\delta_{\nu\eta\xi}$. Note that the imaginary part of the lateral coupling coefficient leads to a three-fold splitting of each of the branches of the longitudinal phase.

The phase and amplitude conditions for this 3×3 case are shown in Fig. 6. As expected there are nine branches to the phase of the effective reflectivity, however, in this figure we have shown only one of the branches associated with the mode number ξ. The bullets at the intersections of the two sets of curves are the relative wave numbers of one set of allowable modes corresponding to a single value of ξ. The modes with the larger effective reflectivity require less threshold gain and are the ones most likely to oscillate. Note that the real part of κ has been assumed zero so that there is no splitting of the amplitude of the effective reflectivity.

III. EXPERIMENT

A. Approximate Analytic Expressions and Comparison with Experiment

In the previous sections, the formal development of the network theory was presented, and example calculations of the modal gain spectra were given for specific array structures. It is also possible to calculate the scaling properties of a specific array structure. Characteristics such as threshold gain, differential quantum efficiency, and intra-cavity power distributions can be modeled as a function of the array size (i.e. number of gain and DBR sections) using the network theory. Such model calculations of the array scaling properties are of practical value because they can be used to identify the critical parameters associated with optimizing the array design.

The threshold properties of a 2-D array can be obtained from the maximum effective modal reflectivity (defined in Eqs. (13a) and (37a)) that occurs for the allowable modes, e.g.,

$$|\Re^2_{\max}| = \max_{\delta_{\nu\eta\xi}} |\Re^2_{\nu\eta}(\delta_{\nu\eta\xi})| \tag{38}$$

since the threshold gain per unit length is

$$g_{\mathrm{th}} = \alpha_L \frac{1}{L} \ln\,(|\Re^2_{\max}|) \tag{39}$$

where α_L is optical absorption loss coefficient for the gain sections. Results of calculations show that in an uniform array (i.e. identical gain sections and identical DBR sections) the natural log of the maximum effective modal reflectivity varies nearly inversely with the number of sections. Therefore, $|\Re^2_{\max}|$ must have a nearly exponential dependence on $1/n$. The exact form of this dependence can be obtained from $|\Re^2_{\max}|$ for $n=1$ and $|\Re^2_{\max}|$ for $n=\infty$, since these cases can easily be derived by physical arguments. When $n=1$, $|\Re^2_{\max}|$ is exactly that of a single grating, thus

$$a^2+|r|^2+|t|^2=1 \Rightarrow |\Re| = \sqrt{\frac{1-a^2}{1+q_0^2}} \tag{40}$$

where $q_0=|t/r|$ at $\Delta\beta/\beta=0$. As n goes to infinity, the contribution of the end losses becomes negligible. Then, in the case of a uniform array, the threshold gain must equal the sum of the losses in the DBR section and the gain section. Therefore, the effective power reflectivity as seen by a single gain section is $|\Re^2_{\max}| = r^2+t^2 = 1-a^2$. Placing the limiting results for $n=1$ and $n=\infty$ into an exponential relationship between $|\Re^2_{\max}|$ and $1/n$ results in

$$|\Re_{\max}| = \sqrt{1-a^2}\exp\left(\ln\left(\sqrt{1+q_0^2}\right)/n\right). \tag{41}$$

The lowest threshold mode occurs very near the Bragg condition. Therefore, the frequency dependence of $|\Re^2_{\max}|$ can be ignored and the value of $|\Re^2_{\max}|$ at $\Delta\beta/\beta_B=0$ can be used. So it is not necessary to calculate the details of the frequency dependence of $|\Re^2_{\max}|$ in order to model the threshold characteristics of an array. This is an important result because it makes it possible to do analytic calculations of the scaling properties of the threshold characteristics of GSE arrays. Using this approximation, and substituting Eq. (22) into Eq. (20) gives the following result for the threshold gain

$$g_{\text{th}}(n) = \overbrace{\alpha_L}^{\text{active section loss}} \overbrace{-\frac{1}{L}\ln\sqrt{1-a^2}}^{\text{DBR loss}} + \overbrace{\frac{1}{nL}\ln\left(\sqrt{1+q_0^2}\right)}^{\text{end loss}}. \tag{42}$$

This equation predicts an inverse relationship between the modal threshold gain and the number of laser sections. Each term in this equation corresponds to a distinct loss mechanism. The first term, as explained above, is the optical loss per unit length in each gain section. The second term is the total optical loss per unit length (including out-coupled light) in each DBR section. The third term represents the end losses, when the array has been terminated by DBR sections and unpumped gain sections. For sufficiently large n, this last (end loss) term is negligible, and the threshold gain simply equals the sum of losses due to optical absorption in a gain section and the total losses (absorption and output coupling) in a DBR section.

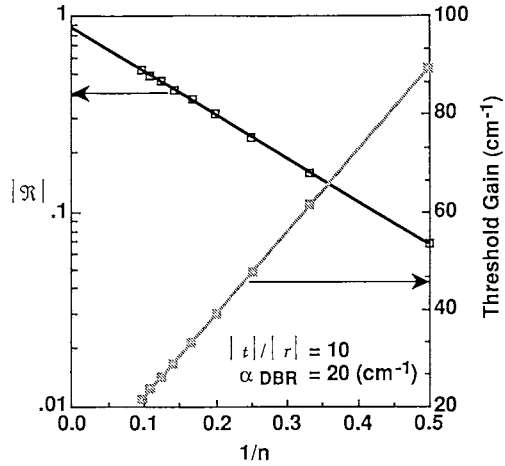

Fig. 7. Reflectivity and threshold gain versus reciprocal of number of array elements.

Figure 7 shows the calculated maximum effective modal reflectivity (shown on a semi-log plot) and threshold gain as a function of $1/n$ from both the network theory (points) and the approximate theory (lines). Because of the good agreement between the numerical result of the network theory and the analytic result of the approximate theory, the analytic result, which is computationally less demanding, can be used to study the effects of the various parameters on the threshold properties of the array gain. Both the threshold current density and the differential quantum efficiency can be calculated directly from the threshold gain.

To obtain the threshold current density from the threshold gain, the current-gain relationship for the active layer structure must first be known. The arrays that we have fabricated and studied experimentally typically have gain sections consisting of a graded index separate confinement heterostructure with a single quantum well (GRIN-SCH-SQW) active layer. For this type of structure, Chinn *et al.* (1988) have shown that the threshold current density, J_{th}, is well approximated by $\ln(J_{th}/J_0) = (G_{th}/G_0)$, where J_0 and G_0 are empirical constants that depend on the dimensions and composition of the GRIN-SCH-SQW (Chinn *et al.*, 1988). Experimental measurements of J_{th} for injection-coupled GSE arrays as a function of n, the number of gain sections, have shown that the logarithm of J_{th} exhibits a linear dependence on $1/n$ (Carlson *et al.*, 1988). In this respect, the network theory exhibits good qualitative agreement with experiment. Figure 8 shows one example of experimental data on the threshold current density

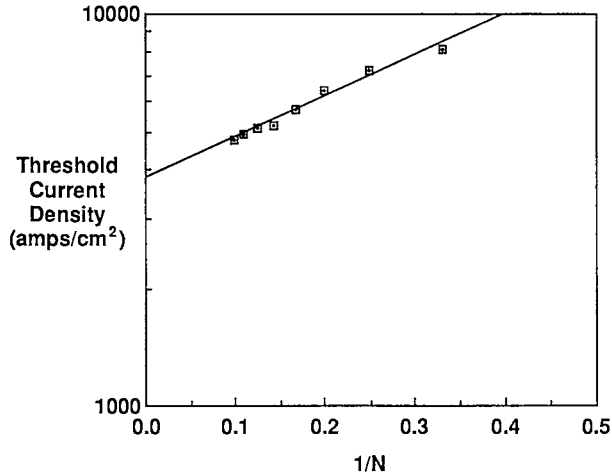

Fig. 8. Measured threshold current density versus reciprocal of number of array elements.

versus $1/n$. This particular array had gain sections that consisted of ten evanescently-coupled ridge-guided lasers. The exponential dependence of threshold current density on $1/n$ has also been measured for GSE arrays with Y-guide coupling in the gain sections, as well as linear GSE arrays (Carlson *et al.*, 1988). These experimental results show that the linear dependence of $\ln J_{\text{th}}$ on $1/n$ is a general property of injection-coupled GSE laser arrays, and the predictions of the network theory are also consistent with this observation. Although the qualitative behavior is well understood, a quantitative verification of the threshold current density dependence on n is still lacking because some of the device parameters (e.g. DBR section reflectivity and transmissivity and absorption losses in DBR sections and gain sections) are not known with sufficient accuracy.

At threshold, the external quantum efficiency, η_{ext}, for any laser is defined as the ratio of the useable output power to the total simulated power in the laser. For a GSE array, the approximate analytic expressions can be used to derive the following analytic expression for the external quantum efficiency,

$$\eta_{\text{ext}} = \frac{1}{g_{\text{th}}(n)} \left[\frac{1}{L} \ln \sqrt{1-a^2} + \left(\frac{1}{nL} \ln \sqrt{q_0^2+1} \right) \frac{\ln \sqrt{1-a^2}}{\alpha_L L - \ln \sqrt{1-a^2}} \right] \left\{ \frac{\alpha_{\text{DBR}}^{\text{rad}}}{\alpha_{\text{DBR}}} \right\} \eta_0 \tag{43}$$

where $\alpha_{\text{DBR}}^{\text{rad}}/\alpha_{\text{DBR}}$ is the ratio of useable output coupled light to total losses

in the DBR and η_0 is the internal quantum efficiency. The physical justification for the above equation is as follows. gth is the total stimulated power at threshold per unit length. The first term of the factor in square brackets is the total power lost in the DBR sections. This is multiplied by $\alpha_{\mathrm{DBR}}^{\mathrm{rad}}/\alpha_{\mathrm{DBR}}$ to obtain the fraction of usable surface emitted power. Since it has been assumed that the array has been terminated by uniform regions of unpumped gain sections and DBR sections, some of the power lost out the ends of the array will be out-coupled by DBR sections beyond the pumped sections of the array. The second term of the factor in square brackets represents this contribution to the power, and it too must be multiplied by $\alpha_{\mathrm{DBR}}^{\mathrm{rad}}/\alpha_{\mathrm{DBR}}$. A different type of array termination would give a slightly different external quantum efficiency, since there would be a different fraction of the end loss power coupled out as useful power. As the number of gain sections is increased, the power contribution from the end losses becomes negligible, and the differential quantum efficiency is independent of the array termination. Therefore, in the limit of large n, this result is valid for all types of array termination.

Figure 9 shows a plot of the threshold gain and external differential quantum efficiency as a function of the number of injection-coupled gain sections in the array. These curves were calculated using the analytic forms derived from the approximate theory. The values of the parameters were inferred from experimental data. They are best estimates of the parameters for the arrays that have been reported in Carlson *et al.* (1988); Evans (1989). The ratio of useable output coupled light to total losses in the DBR,

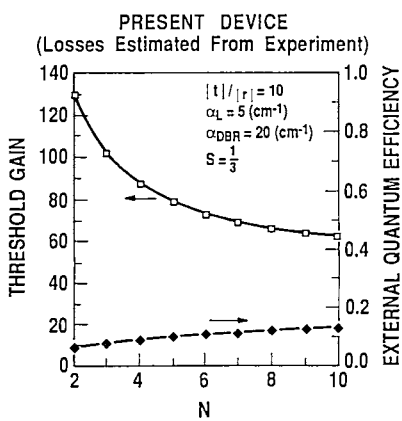

Fig. 9. Calculated threshold gain and external quantum efficiency versus number of array elements for devices reported in Carlson *et al.* (1988).

$\alpha_{DBR}^{rad}/\alpha_{DBR}$, is chosen as 1/3 because the early experimental results reported were for arrays mounted p-side up (see Chapter 4). A comparable level of light will usually be out-coupled on the n-side and radiated into the substrate. In Figure 9, the differential quantum efficiency slowly increases as n increases. For $n = 10$, it is 12% which agrees well with the measured values of 12–15% for 10×10 GSE arrays reported in Carlson *et al.* (1988), and Evans (1989). The threshold gain drops by about a factor of two as n is increased from 2 to 10.

Figure 10 also shows a plot of the threshold gain and external differential quantum efficiency as a function of the number of injection-coupled gain sections in the array. However, the parameters used here correspond to those of a theoretically optimized array. The best GRIN-SCH-SQW lasers have losses typically of about 5 cm^{-1}. The amount of useable surface emitted light ($\alpha_{DBR}^{rad}/\alpha_{DBR}$) can be increased by growing arrays on substrates that are transparent to the operating wavelength of the array, so that when mounted p-side down (for better heat sinking) the light will be transmitted out the n-side of the wafer (Evans *et al.*, 1989). In this configuration, the n-side of the array would be anti-reflect coated and the p-side would be high reflect coated so that the maximum amount of grating-coupled light will be emitted out the n-side of the wafer. This should increase $\alpha_{DBR}^{rad}/\alpha_{DBR}$ to about 0.8. The optimized 10-element array in Fig. 10 has a differential quantum efficiency greater than 75%, which is comparable to what has been reported for the best edge-emitting lasers (Welch *et al.*, 1987). Also, for an array with $n = 10$, the threshold gain of the optimized array is reduced by

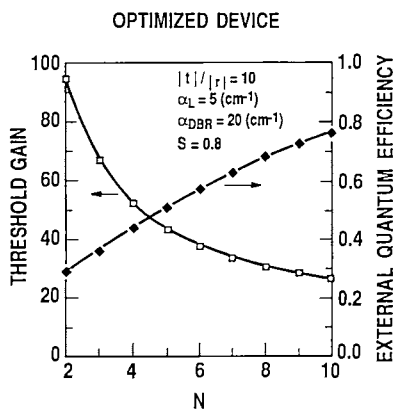

Fig. 10. Calculated threshold gain and external quantum efficiency versus number of array elements for optimized structure.

about a factor of two relative to that calculated for the present arrays in Fig. 9. This will decrease the threshold current density resulting in a higher total conversion efficiency for the array.

As discussed in the previous section, the linear network theory can also be used to calculate the field distribution inside the array. This can be very useful for optimizing the array for single mode operation. In an optimized GSE array design, the power flowing into each gain section in the array should be as uniform as possible over the extent of the array. This is important for obtaining maximum utilization of the available gain in the array. Besides optimizing the conversion efficiency, a uniform power distribution can improve mode discrimination at power levels where nonlinear gain saturation effects occur (Streifer *et al.*, 1986). Also, as the size of the array increases, a uniform power distribution will help to prevent the array from decoupling into smaller sub-arrays that oscillate incoherently with respect to each other. A figure of merit which can be used for characterizing the uniformity of the power flow to the gain sections is the root-mean-square power deviation, $\overline{\Delta P^2}$, which is given by

$$\overline{\Delta P^2} = \sum_{m=1}^{n} [P_m - \bar{P}]^2$$

where P_m, the total power flowing into the mth gain section, is given by

$$P_m = |E_{l,m}(L)|^2 + |E_{r,m}(0)|^2$$

here $E_{l,m}(L)$ and $E_{r,m}(0)$ are the left and right travelling input waves to each end of the mth gain section. As described earlier, the travelling waves are the eigenvector of state-variable vector components. The average power to each gain section is given by

$$\bar{P} = \frac{1}{n} \sum_{m=1}^{n} P_m.$$

Optimization of an array can then be accomplished varying the design parameters to obtain a minimum in the rms power deviation, $\overline{\Delta P^2}$. Note that $\overline{\Delta P^2} \geq 0$, but because of end losses $\overline{\Delta P^2}$ will not actually go to zero. Also, the characteristics of the second order grating have a great influence on $\overline{\Delta P^2}$. This occurs because the output coupling of the second order grating represents a coherent loss, because it depends on the relative phase of the oppositely propagating waves in the DBR waveguides. In general, the lowest loss mode will be the one where the radiative losses in the DBR waveguide sections are minimized. In a uniform array, this occurs when the radiated fields associated with each travelling wave destructively interfere. For non-uniform arrays, it is not generally true that the lowest loss mode radiates

the least amount of light, and in some cases nearly uniform near fields can be obtained.

In order to calculate the resulting near-field distributions of the grating-coupled light output, a detailed model for the second order DBR sections is required. This model will have to calculate the electric field distribution in the gain and DBR sections, as well as the field distribution of the light out-coupled by the grating. The inputs to the DBR model will be the near-field inputs to the DBR sections that are provided by the network theory calculations. There are many such models of second order gratings in the literature, however, at this time there is no consensus as to which is most accurate. To date, only the coupled-mode approach (Streifer and Scifres, 1976) has been used to model second order DBR sections in GSE arrays (Shakir *et al.*, 1989). This approach does not explicitly calculate the field distribution of the radiated light. However, the near field can be taken to be proportional to the sum of the forward and reverse travelling waves. Since the network model can be used with any grating model, more detailed models under development (see Chapter 4 on gratings) that explicitly calculate the radiation field due to the grating coupling could be incorporated into the network model.

In conclusion, this network theory calculates the threshold properties of an arbitrary two-dimensional laser array structure from a set of parameters associated with the individual elements that comprise the array. From these results critical elemental parameters for optimizing the array performance have been identified. The network theory predictions of the threshold characteristics of injection-coupled GSE arrays show good qualitative agreement with the experimental results. A quantitative comparison between the network theory and experiment awaits the development and application of improved models for the DBR section and more accurate measurements of the parameters associated with the gain sections and the DBR sections.

REFERENCES

AGRAWAL, G. P. (1985). "Lateral-mode analysis of gain-guided and index-guided semiconductor-laser arrays," *J. Appl. Phys.* **58**, 2922.

AMANTEA, R., PALFREY, S. L. AND CARLSON, N. W. (1989). "Network model for two-dimensional coupled laser arrays," *Opt. Lett.* **14**, pp. 30–32.

AMANTEA, R., CARLSON, N. W., PALFREY, S. L., EVANS, G. A., HAMMER, J. M. AND LURIE, M. (1990). "Network analysis of the modes of two-dimensional grating-surface-emitting diode laser arrays," *IEEE J. Quantum Electron.*, **26**, 6.

BUTLER, J. K., ACKLEY, D. E. AND BOTEZ D. (1984). "Coupled-mode analysis of phase-locked injection laser arrays," *Appl. Phys. Lett.* **44**, 293.

CARLSON, N. W., EVANS, G. A., AMANTEA, R., PALFREY, S. L., HAMMER, J. M., LURIE, M., CARR, L. A., HAWRYLO, F. Z., JAMES, E. A., KAISER, C. J., KIRK, J. B. AND REICHERT, W. F. (1988). "Performance characteristics of coherent two-dimensional grating surface emitting diode laser arrays," *1988 LEOS Annual Meeting Conference Proceedings*, Nov. 2-8, 444-446.

CHINN, S. R., ZORY, P. S. AND REISINGER, A. R. (1988). "A model for GRINSCH-SQW diode lasers," *IEEE J. Quantum Electron.* **24**, 2191-2214.

EVANS, G. A., BOUR, D. P., CARLSON N. W., HAMMER, J. M., LURIE, M., BUTLER, J. K., PALFREY, S. L., AMANTEA, R., CARR, L. A., HAWRYLO, F. Z., JAMES, E. A., KIRK, J. B., LIEW, S. K. AND REICHERT, W. F. (1989). "Coherent, monolithic two-dimensional strained InGaAs/AlGaAs quantum well laser arrays using grating surface emission," *Appl. Phys. Lett.* **55**, 26.

FLECK, J. A. Jr. (1963). *J. Appl. Phys.* **34**, 2997.

HADLEY, G. R., HOHIMER, J. P. AND OWYOUNG, A. (1988). "Comprehensive modeling of diode arrays and broad-area devices with applications to lateral index tailoring," *IEEE J. Quantum Electron.* **QE-24**, 2138.

HARDY, A. AND STREIFER, W. (1985). "Analysis of phased-array diode lasers," *Opt. Lett.* **10**, 335.

LANG, R. J. AND YARIV, A. (1985). "Analysis of the dynamic response of multielement semiconductor lasers," *IEEE J. Quantum Electron.* **QE-21**, 10, 1683-1688.

PEARSON, C. E. (1983). *Handbook of Applied Mathematics*, p. 919, Van Nostrand Reinhold, New York.

SHAKIR, S. A., SALVI, T. C. AND DENTE, G. C. (1989). "Analysis of grating-coupled surface-emitting lasers," *Opt. Lett.*, **14**, 937-939.

STREIFER, W. AND SCIFRES, D. R. (1976). "Analysis of grating-coupled radiation in GaAs:GaAlAs lasers and waveguides," *IEEE J. Quantum Electron.* **QE-12**, 422-428.

STREIFER, W., OSINSKI, M., SCIFRES, D. R., WELCH, D. F. AND CROSS, P. S. (1986). "Phased-array lasers with a uniform, stable supermode," *Appl. Phys. Lett.* **49**, 22, 1496-1498.

STREIFER, W., WELCH, D. F., CROSS, P. S. AND SCIFRES, D. R. (1987). "Y-junction semiconductor laser arrays: Part 1—Theory," *IEEE J. Quantum Electron.* **QE-23**, 744.

WELCH, D. F., CARDINAL, M., STREIFER, W., SCIFRES, D. R. AND CROSS, P. S. (1987). "High-brightness, high-efficiency, single-quantum-well laser diode array," *Electron. Lett.* **23**, 1240-1241.

Chapter 8

EXTERNAL METHODS OF PHASE LOCKING AND COHERENT BEAM ADDITION OF DIODE LASERS

James R. Leger

Department of Electrical Engineering, University of Minnesota, Minneapolis, Minnesota

A diode laser array is capable of producing very high optical powers from a relatively small emitting region. Applications requiring simple illumination such as solid-state laser pumping take direct advantage of the high power and efficiency of these sources. In addition to power, however, a large class of applications require a high-quality wavefront profile as well. Several on-chip techniques for establishing wavefront coherence and phase control are reviewed in Chapter 2.

In this chapter, we explore wavefront control methods applied externally to the laser array chip. The laser cavity is no longer restricted to a planar topology, providing a degree of flexibility and control over a two-dimensional array that does not exist in a monolithic structure. Micro-optics can be introduced to shape and modify each laser beam; other optical devices such as spatial filters and gratings can affect the entire ensemble of beams, assisting in establishing mutual coherence and wavefront control.

This chapter is divided into three parts. The first section reviews the basic concepts of laser beam combining. Incoherent multiplexing schemes are briefly described, and their limitations noted. The radiance theorem is then introduced in the context of coherent beam addition, and the two basic methods of increasing radiance are shown.

The second section describes the far-field behavior of a two-dimensional diode laser array in detail. The Strehl ratio is introduced as a measure of

ISBN 0-12-244070-6

source radiance, and equations relating array magnitude and phase nonuniformities to the Strehl ratio are developed. Finally, we describe the effects of partial coherence and laser position on the far-field.

In the third section, several external methods are explored for establishing coherence, controlling lateral modes, and combining the individual laser beams. Fourier-plane spatial filtering and diffractive coupling both utilize a common cavity to establish coupling between lasers and provide coherence. The differences between these two techniques are explored. External master oscillators offer an alternative method of phase-locking lasers. Both laser injection-locking and master-oscillator-power-amplifier (MOPA) systems are described. Finally, we review a few of the methods available for combining the individual coherent laser beams into a single beam with high Strehl ratio.

I. REQUIREMENTS FOR LASER BEAM ADDITION

A. Coherent versus Incoherent Laser Combining

Laser arrays consist of a collection of individual lasers, each with its own characteristic properties and light distribution. Laser beam *addition* converts this complicated superposition of wavefronts into a common beam that appears to have come from a single laser. The properties of the resultant wavefront (e.g., wavelength and polarization) must be identical to those of a single laser. A conceptual block diagram of the beam addition process is shown in Fig. 1.

Laser beam *multiplexing* is also concerned with coupling light from several laser sources into a single beam. In this case, however, the different properties of each beam are retained, and the resultant wavefront is more complex than any single laser. For example, a polarizing beamsplitter can be used to multiplex two laser beams of orthogonal polarization into a common beam (Fuhr, 1987). But, unless the lasers are locked together in phase, the

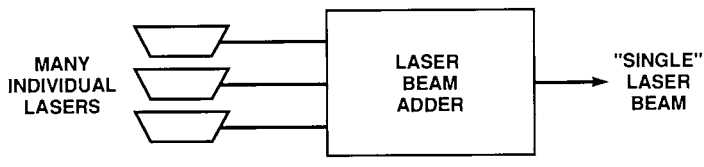

Fig. 1. Conceptual block diagram of the beam addition process.

resultant beam will be randomly polarized, increasing the complexity of the wavefront. A second method of beam multiplexing uses diffraction gratings (Minott and Abshire, 1987) to superimpose laser beams of different wavelength. Each beam is incident on the grating at a different angle corresponding to its wavelength, and the combined beams exit the grating along a common direction. In theory, this method is capable of coupling a large number of lasers into a single beam, but the bandwidth of the result is much wider than any single laser. Dichroic mirrors have also been employed for wavelength multiplexing (Blau *et al.*, 1987; Smith, 1987).

This chapter is concerned exclusively with laser beam addition, where the complexity of the output beam does not increase. We start by considering two simple optical systems for beam addition and compare the performance of each with mutually coherent and incoherent laser sources. The simplest optical component for combining two beams is a beam splitter (Fig. 2). We imagine two *mutually incoherent* sources, each producing a wave with intensity I_0, incident on a 50% reflective beam splitter. The mutual incoherence allows us to calculate the intensity of each beam separately, and sum the two resultant intensities. Clearly, each source beam is split into a transmitted beam and reflected beam of equal intensity $I_0/2$. With both lasers present, the intensities of the beams exiting the beam splitter are simply double the value from a single laser. Hence, the exiting beams each have an intensity I_0, and no increase in beam power is obtained.

Consider now the identical experiment with two sources that are *mutually coherent.* The complex amplitudes from the two sources must now be summed. Referring to Fig. 2 the amplitudes of the two exiting beams $\hat{b}_1$

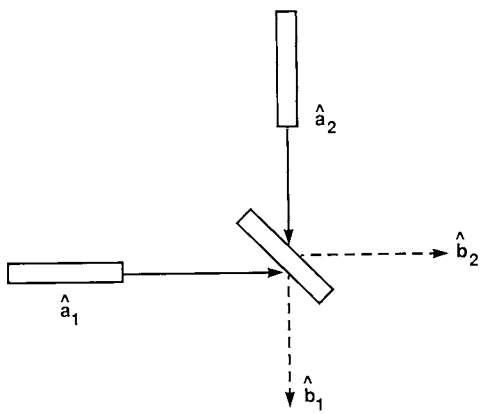

Fig. 2. Combining two laser beams with a beam splitter.

and $\hat{b}_2$ are related to the input beam amplitudes $\hat{a}_1$ and $\hat{a}_2$ by (Haus, 1984)

$$\hat{b}_1 = -\frac{\hat{a}_1}{\sqrt{2}} + j\frac{\hat{a}_2}{\sqrt{2}}, \qquad \hat{b}_2 = j\frac{\hat{a}_1}{\sqrt{2}} - \frac{\hat{a}_2}{\sqrt{2}}, \tag{1}$$

where $j = \sqrt{-1}$. If the two beams differ in phase by $\pi/2$ radians, $\hat{a}_1 = \sqrt{I_0}$ and $\hat{a}_2 = j\sqrt{I_0}$. From Eq. (1), the beams leaving the splitter are given by

$$\begin{aligned} \hat{b}_1 &= -\frac{2\sqrt{I_0}}{\sqrt{2}}, & I_1 &= 2I_0 \\ \hat{b}_2 &= 0, & I_2 &= 0. \end{aligned} \tag{2}$$

The light is completely coupled into I_1, doubling its intensity. Other relative phases result in different amounts of light in the two beams. Clearly, coherence appears to be necessary for beam addition using beam splitters.

We now examine a second common optical system for combining beams called aperture sharing. We compare the on-axis far-field power from a single source with a collection of sources that share the same aperture (Fig. 3). The on-axis far-field power can be estimated by the following simple argument. (A more precise treatment of the far-field behavior is contained in Section II.A.) The main diffraction lobe from a single source with a square aperture of width D has a full angular extent given by

$$\theta \approx \frac{2\lambda}{D}, \tag{3}$$

where λ is the wavelength of light. The area of this lobe at a distance z is

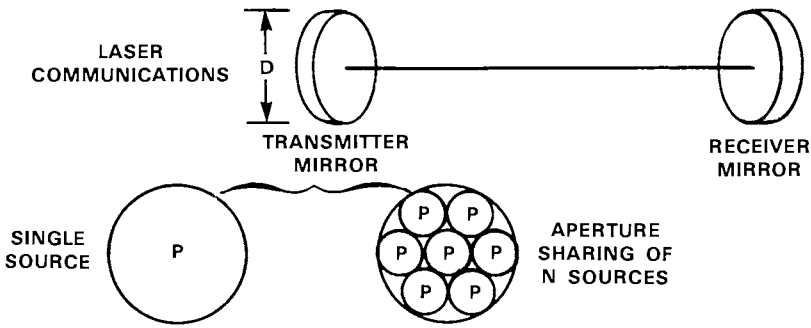

Fig. 3. Comparison of the power deposited in a distant receiver mirror using a single laser and multiple laser sources to illuminate the transmitter mirror of a free-space laser communications link.

then simply given by

$$\text{area} = (\theta z)^2 = \left(\frac{2\lambda z}{D}\right)^2. \tag{4}$$

If we assume that the entire power P from the lasing aperture is uniformly distributed over this area, the average intensity in the central lobe region is given by

$$I_{\text{ave}} \approx \frac{PD^2}{4\lambda^2 z^2}. \tag{5}$$

Since the intensity distribution is actually peaked in the center, it can be shown that the intensity $I_1(0, 0)$ at the center of the far-field lobe from a single aperture is actually given by:

$$I_1(0, 0) = \frac{PD^2}{\lambda^2 z^2}. \tag{6}$$

We now compute the on-axis power of a 2×2 array of *mutually incoherent* lasers, each with power P, sharing the same $D \times D$ aperture. The size of a single laser aperture is now $(D/2) \times (D/2)$, and its on-axis intensity from Eq. (6) is

$$I_{\text{single}} = \frac{P(D/2)^2}{\lambda^2 z^2} = \frac{PD^2}{4\lambda^2 z^2}. \tag{7}$$

Since the lasers are mutually incoherent, the on-axis intensity from all four is simply the sum of the four individual intensities

$$I_{4,\text{incoh}} = 4I_{\text{single}} = \frac{PD^2}{\lambda^2 z^2} = I_1. \tag{8}$$

We conclude the on-axis far-field intensity does not increase by aperture sharing from mutually incoherent sources.

Finally, we consider the same aperture sharing arrangement with *mutually coherent* lasers. Again, Eq. (7) gives the on-axis intensity for a single aperture. However, if the mutually coherent apertures all have the same phase, the on-axis *amplitudes* add and the resultant intensity is given by

$$I_{4,\text{coh}} = \left|\frac{2\sqrt{P}D}{\lambda z}\right|^2 = \frac{4PD^2}{\lambda^2 z^2} = 4I_1. \tag{9}$$

We conclude that coherent aperture sharing sums the power of the individual laser sources in the center of the far-field.

It is apparent from these two examples that mutual coherence is required for laser beam addition. For a clearer understanding of this point, we introduce the concept of radiance in the next section.

B. Radiance and the Radiance Theorem

The total optical power of a laser array is often given as the measure of array performance. Although this is appropriate for some applications, the power specification alone contains no information about the wavefront quality of the beam. Specifically, when we need to focus the light to a small spot or propagate the light a long distance from the array, additional measures of array performance are required.

The power per unit solid angle (called the radiant intensity[1] by the radiometric community) depends a great deal on the original wavefront quality of the source. Light from a highly aberrated source will be diffracted over a much larger angle than light from a nonaberrated source, and hence will have a lower radiant intensity. However, this quantity is dependent on the specific optical system used to collimate the array as well as the array itself. For example, the diffraction-limited collimated beam of radius R in Fig. 4 has a radiant intensity $\mathscr{I}$ of

$$\mathscr{I} \cong \frac{P}{\pi(0.61\lambda/R)^2}, \tag{10}$$

where P is the total power of the beam, and we assume uniform illumination with $R \gg \lambda$. Clearly, the radiant intensity is dependent on the size of the aperture R created by the collimating lens.

A more useful measure of laser performance is given by the power per unit area per unit solid angle. This quantity is called *radiance* (or sometimes brightness), and is independent of the optical system that follows the array. Returning to Fig. 4, the diffraction-limited radiance is given by

$$\mathscr{L} \cong \frac{P}{(\pi R^2)\pi(0.61\lambda/R)^2} \propto \frac{P}{\lambda^2}. \tag{11}$$

The radiance is seen to be solely a function of the laser array, and is proportional to the total power divided by the square of the wavelength for a diffraction-limited source.

[1] The radiometric term for incident power per unit area is *irradiance*. However, in this chapter we will refer to this quantity as the *intensity* and reserve the term *radiant intensity* for power per unit solid angle.

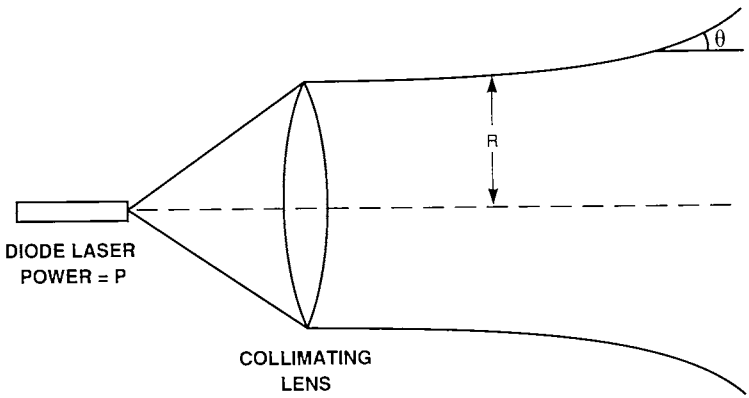

Fig. 4. Calculation of the radiant intensity and radiance of a collimated diffraction-limited laser beam. The radiance is independent of the collimating optics.

Laser beam addition can now be defined as the process of summing radiances from individual laser sources. There are two important theorems that govern our ability to perform beam addition. The first, called the radiance theorem (Boyd, 1983), states that the radiance of a light distribution produced by any imaging system is always less than or equal to the original source radiance. The second related theorem states that the radiance of a collection of mutually incoherent sources cannot be increased by a passive linear optical system to a level greater than the radiance of the single brightest source. These two theorems show that mutual coherence across all laser elements is a necessary (but not sufficient) condition for laser beam addition.

In addition to mutual coherence, the laser beams must be combined (perhaps by some external optical system) to create an output beam that is uniform in magnitude and phase. (These will be described at the end of Section III.) The definition of radiance suggests a useful way to categorize methods of combining coherent sources. The method of superposition, shown schematically in Fig. 5(a), requires the light from all N laser sources to illuminate a common spot. The optical system changes the propagation angles of the beams, resulting in a single output direction. The power per unit area is increased by N, and the divergence is the same as a single laser. Consequently, the radiance is increased by N. The second method, called aperture filling, requires the laser sources to all have a common output direction [Fig. 5(b)]. The optical system simply expands the beams until they form a continuous wavefront. The power per unit area of the resultant beam is the same as a single expanded laser beam, but the divergence is

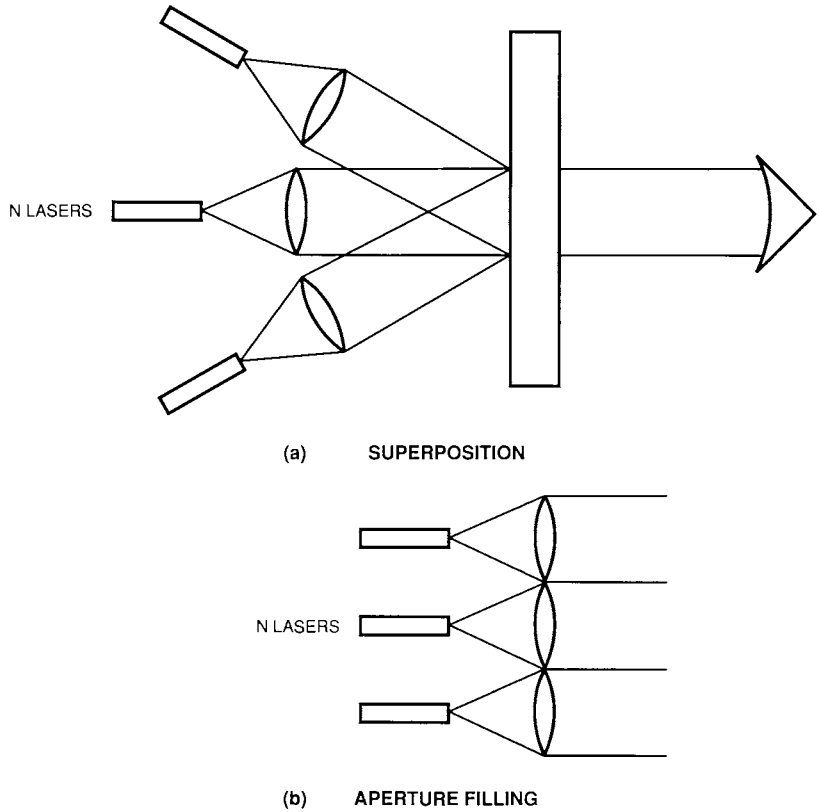

Fig. 5. Two methods of laser beam combining. (a) Superposition increases the power per unit area. (b) Aperture filling increases the power per unit solid angle.

reduced by a factor of N. The net result is an increase in radiance by N as before. Note that even though these two methods result in beams of different size and divergence, they are entirely equivalent from a radiance standpoint, and a beam-expanding telescope can be used to convert one distribution into the other.

II. FAR-FIELD PROPERTIES

Many coherent laser array applications require light to propagate over large distances, and the intensity distribution in this distant plane is of principal importance. In other applications, the beam is focused by a lens to a small

point, and the light distribution at this focal point is of most interest. The far-field diffraction pattern is a key measure of performance in both these cases. In this section, the far-field behavior of a light field is calculated. The Strehl ratio is introduced as a measure of overall performance, and the effects of laser nonuniformities in magnitude, phase, position, and mutual coherence are computed.

A. The Strehl Ratio

We start with a general near-field complex amplitude distribution $\hat{a}(x, y)$ from a surface-emitting diode laser array contained within the region $\mathcal{R}$. We assume for the moment that the distribution is spatially coherent. The intensity distribution at a distance $z \gg d^2/\lambda$ (where d is the maximum spatial extent of $\mathcal{R}$) is given by

$$I(x', y', z) = \frac{1}{(\lambda z)^2}\left|\iint_{\mathcal{R}} \hat{a}(x, y) \exp\left[-j\frac{2\pi}{\lambda z}(xx' + yy')\right] dx\, dy\right|^2. \quad (12)$$

Using this equation, a uniformly illuminated circular aperture of amplitude A and radius R produces the familiar Airy disk far-field intensity pattern illustrated in Fig. 6

$$I(x', y', z) = |A|^2\left(\frac{\pi R^2}{\lambda z}\right)^2\left|\frac{J_1(2\pi R\sqrt{x'^2 + y'^2}/\lambda z)}{\pi R\sqrt{x'^2 + y'^2}/\lambda z}\right|^2, \quad (13)$$

where J_1 is the first-order Bessel function of the first kind.

Often, the most important feature of the far-field pattern is the intensity at the center ($x' = 0$, $y' = 0$). For example, the critical parameter for optical satellite communication is the amount of power deposited in a receiver mirror located at the very center of the diffraction pattern. This intensity is given by evaluating Eq. (12) at the origin

$$I(0, 0, z) = \frac{1}{(\lambda z)^2}\left|\iint_{\mathcal{R}} \hat{a}(x, y)\, dx\, dy\right|^2. \quad (14)$$

The uniformly illuminated circular aperture described above has an on-axis intensity of

$$I(r' = 0, z) = \frac{1}{(\lambda z)^2}\left|\int_0^{2\pi}\int_0^R A\, r\, dr\, d\theta\right|^2 = |A|^2\left(\frac{\pi R^2}{\lambda z}\right)^2, \quad (15)$$

where $r = \sqrt{x^2 + y^2}$. Note that the on-axis intensity decreases as z^{-2} according to the inverse square law; it also increases as R^4. This fourth power dependence on aperture size is characteristic of a spatially coherent aperture,

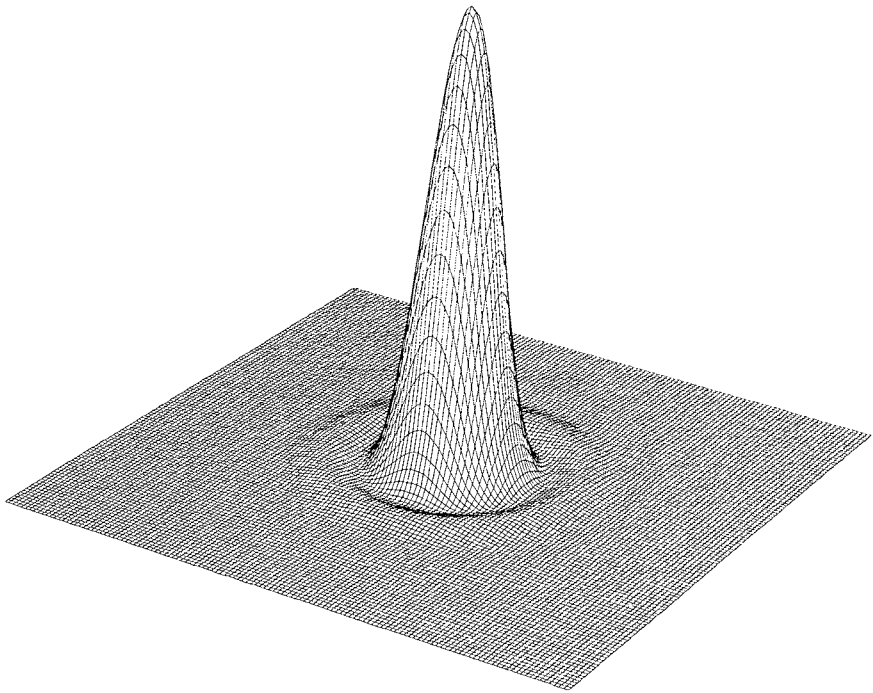

Fig. 6. Far-field intensity pattern from a circular aperture.

and results from two factors. First, the total power radiating from a uniformly illuminated aperture is proportional to the aperture area, or πR^2. Second, the beam divergence from the aperture is given by $\sin \theta = 0.61\lambda/R$, resulting in a solid angle proportional to R^{-2}. The increased total power combined with the decreased angular spread results in an on-axis far-field intensity proportional to the fourth power of the aperture size.

It is sometimes convenient to express laser array performance independent of aperture size and propagation distance. We can define the Strehl ratio as the ratio between the on-axis far-field intensity of a test array and a uniformly illuminated constant phase aperture with the same total power and overall dimensions.[2] Consider again a circular laser array of radius R with a complex amplitude distribution $\hat{a}(r, \theta) = a(r, \theta) \exp[j\phi(r, \theta)]$, where $a(r, \theta)$ and $\phi(r, \theta)$ are the magnitude and phase of $\hat{a}(r, \theta)$. The total power

[2] The Strehl ratio is usually defined for uniformly illuminated test apertures only (Born and Wolf, 1970). We use a more general definition in this chapter to include the effect of non-uniform test aperture illumination.

in this test array is given by

$$P_t = \int_0^{2\pi} \int_0^R |a(r, \theta)|^2 r \, dr \, d\theta. \tag{16}$$

Consequently, a uniformly illuminated aperture with the same power P_t must have a constant amplitude of

$$\bar{a} = \sqrt{\frac{1}{\pi R^2} \int_0^{2\pi} \int_0^R |a(r, \theta)|^2 r \, dr \, d\theta}. \tag{17}$$

The on-axis far-field intensities of the test laser array I_t and uniformly illuminated aperture I_{dl} are given by

$$I_t(r' = 0, z) = \frac{1}{(\lambda z)^2} \left| \int_0^{2\pi} \int_0^R a(r, \theta) \exp[j\phi(r, \theta)] r \, dr \, d\theta \right|^2, \tag{18}$$

and

$$I_{dl}(r' = 0, z) = \frac{1}{(\lambda z)^2} \left| \int_0^{2\pi} \int_0^R \left\{ \sqrt{\frac{1}{\pi R^2} \int_0^{2\pi} \int_0^R |a(r, \theta)|^2 r \, dr \, d\theta} \right\} \rho \, d\rho \, d\varphi \right|^2. \tag{19}$$

The Strehl ratio S is given by the ratio of Eqs. 18 and 19:

$$S = \frac{I_t(r' = 0, z)}{I_{dl}(r' = 0, z)} = \frac{\left| \int_0^{2\pi} \int_0^R a(r, \theta) \exp[j\phi(r, \theta)] r \, dr \, d\theta \right|^2}{\pi R^2 \int_0^{2\pi} \int_0^R |a(r, \theta)|^2 r \, dr \, d\theta}. \tag{20}$$

It is easy to show the conditions that maximize the Strehl ratio. The Cauchy-Schwarz inequality can be expressed in integral form as

$$\left| \int_0^{2\pi} \int_0^R \hat{a}(r, \theta) \hat{b}(r, \theta) r \, dr \, d\theta \right|^2 \leq \int_0^{2\pi} \int_0^R |\hat{a}(r, \theta)|^2 r \, dr \, d\theta \int_0^{2\pi} \int_0^R |\hat{b}(r, \theta)|^2 r \, dr \, d\theta, \tag{21}$$

where the equality holds only when $\hat{a}(r, \theta) = K\hat{b}(r, \theta)$, and K is a complex constant. If $\hat{b}(r, \theta) = 1$, then a modified inequality results:

$$\left| \int_0^{2\pi} \int_0^R \hat{a}(r, \theta) r \, dr \, d\theta \right|^2 \leq \int_0^{2\pi} \int_0^R |\hat{a}(r, \theta)|^2 r \, dr \, d\theta (\pi R^2), \tag{22}$$

where the equality holds only when $\hat{a}(r, \theta)$ equals a complex constant. Comparing the inequality of Eq. 22 to the Strehl ratio of Eq. 20, it is clear that the Strehl ratio $S \leq 1$, and that unity Strehl is achieved only when the magnitude $a(r, \theta)$ and phase $\phi(r, \theta)$ are constant.

By defining the average of the distribution as

$$\overline{\hat{a}(r,\theta)} = \frac{1}{\pi R^2} \int_0^{2\pi} \int_0^R \hat{a}(r,\theta) r \, dr \, d\theta \tag{23}$$

and the average square of the distribution as

$$\overline{|\hat{a}(r,\theta)|^2} = \frac{1}{\pi R^2} \int_0^{2\pi} \int_0^R |\hat{a}(r,\theta)|^2 r \, dr \, d\theta, \tag{24}$$

the Strehl ratio can be expressed as

$$S = \left|\overline{\hat{a}(r,\theta)}\right|^2 / \overline{|\hat{a}(r,\theta)|^2}. \tag{25}$$

The ideal diode laser array should produce a near-field distribution that is constant in magnitude and phase, and is spatially coherent. The remaining parts of this section consider the effects of magnitude and phase nonuniformities, coherence, and laser source distribution on the Strehl ratio.

B. Effects of Nonuniform Magnitude

Magnitude variations across a diode laser array can result from a variety of causes. Each diode laser produces a Gaussian-like intensity profile, rather than the desired uniform profile. In addition, the output facets of the array usually are separated by non-radiating regions, enhancing the nonuniformity. Finally, the intensities may vary from laser to laser due to nonuniformities in lasing thresholds and efficiencies, or as a result of operating in a particular array mode (see Chapter 2).

The Strehl ratio can easily be calculated for a nonuniform light field using Eqs. (23)–(25). As an example, consider the surface-emitting laser shown in Fig. 7 consisting of a two-dimensional array of mutually coherent apertures on a square grid. The size of each aperture is $c \times c$, and the spacing between apertures is b in each dimension. The complex amplitude is assumed to have a constant magnitude A and uniform phase across each

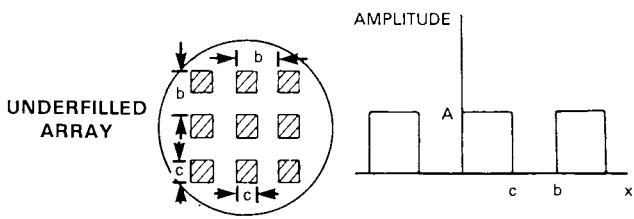

Fig. 7. An underfilled array with a two-dimensional fill factor of c^2/b^2.

aperture. The magnitude between apertures is zero. The mean value of the magnitude is $\overline{a(x, y)} = A(c^2/b^2)$, and the mean square is $\overline{|a(x, y)|^2} = A^2(c^2/b^2)$. The Strehl ratio is given as the square of the mean divided by the mean square

$$S = \left|\overline{\hat{a}(r, \theta)}\right|^2 / \overline{|\hat{a}(r, \theta)|^2} = \frac{c^2}{b^2}. \tag{26}$$

The ratio of the emitting aperture area to the device area c^2/b^2 is referred to as the fill factor of the array; the Strehl ratio in this case is simply equal to the array fill factor. Many array geometries have inherently low fill factors that reduce the Strehl ratio significantly. External optics are required to increase the fill factor and thus the Strehl ratio.

As a second example of the effect of magnitude nonuniformity, consider a one-dimensional array with a magnitude profile of a half sine wave. This approximates the distribution of the fundamental array mode from an evanescently coupled array. The squared mean of this distribution is $4/\pi^2$, and the mean square is $1/2$, resulting in a Strehl ratio $S = 0.81$.

We now restrict the analysis to a periodic array of apertures most commonly found in surface-emitting laser arrays, and calculate the entire far-field diffraction pattern. Assume a two-dimensional laser array distribution where the lasing apertures are spaced by b in each direction. Each lasing aperture is described by the complex amplitude distribution $h(x, y)$. Variations in magnitude and phase from aperture to aperture are expressed by $g(x, y)$. The near field is given by

$$\hat{a}(x, y) = \left[\sum_{m=-\infty}^{\infty} \sum_{n=-\infty}^{\infty} \delta(x - mb, y - nb) \cdot g(x, y)\right] * h(x, y), \tag{27}$$

where $\delta(x, y)$ is a two-dimensional Dirac delta function and $*$ indicates a two-dimensional convolution. The function $g(x, y)$ is chosen to be zero outside the array, and therefore limits the number of lasing apertures.

From Eq. (12), the far-field intensity is given by the squared magnitude of the Fourier transform of $\hat{a}(x, y)$

$$I(x', y', z) = \frac{1}{\lambda^2 z^2 b^4} \left| \left\{ \sum_{m=-\infty}^{\infty} \sum_{n=-\infty}^{\infty} \delta\left(\frac{x'}{\lambda z} - \frac{m}{b}, \frac{y'}{\lambda z} - \frac{n}{b}\right) * G\left(\frac{x'}{\lambda z}, \frac{y'}{\lambda z}\right) \right\} \times H\left(\frac{x'}{\lambda z}, \frac{y'}{\lambda z}\right) \right|^2, \tag{28}$$

where $G(x', y')$ and $H(x', y')$ are the Fourier transforms of $g(x, y)$ and $h(x, y)$ respectively. If there are many lasing apertures in the array, the extent of $g(x, y)$ is much larger than the aperture spacing b, and the

convolution of $G(x'/\lambda z, y'/\lambda z)$ with the array of shifted delta functions leads to discrete copies of $G(x'/\lambda z, y'/\lambda z)$ with very little overlap. In this case, an approximate expression for the intensity results:

$$I(x', y', z) \approx \frac{1}{\lambda^2 z^2 b^4} \sum_{m=-\infty}^{\infty} \sum_{n=-\infty}^{\infty} \left| G\left(\frac{x'}{\lambda z} - \frac{m}{b}, \frac{y'}{\lambda z} - \frac{n}{b}\right)\right|^2 \cdot \left| H\left(\frac{x'}{\lambda z}, \frac{y'}{\lambda z}\right)\right|^2. \tag{29}$$

As an example, consider an $N \times N$ square array of Gaussian laser beams with beam waists $\omega_0/\sqrt{\pi}$. The amplitude of each laser can be written as

$$h(x, y) = A \exp\left[-\pi \frac{(x^2+y^2)}{\omega_0^2}\right]. \tag{30}$$

We assume for simplicity that there is no variation in magnitude or phase from laser to laser. Hence,

$$g(x, y) = \text{rect}\left(\frac{x}{Nb}\right) \text{rect}\left(\frac{y}{Nb}\right), \tag{31}$$

$$\text{where rect}\,(x) = \begin{cases} 1, & |x| \leq \frac{1}{2} \\ 0, & \text{otherwise.} \end{cases}$$

Using the Fourier transform relationships

$$\mathcal{F}\left\{\text{rect}\left(\frac{x}{Nb}\right)\right\} \triangleq Nb \frac{\sin(\pi Nbu)}{\pi Nbu} \triangleq Nb\ \text{sinc}\,(Nbu) \tag{32}$$

and

$$\mathcal{F}\left\{\exp\left[-\pi \frac{(x^2+y^2)}{\omega_0^2}\right]\right\} = \omega_0^2 \exp\left[-\pi\omega_0^2(u^2+v^2)\right], \tag{33}$$

Eq. (29) becomes

$$I(x', y', z) \approx \frac{A^2 N^4 \omega_0^4}{\lambda^2 z^2}\left\{\sum_{m=-\infty}^{\infty} \sum_{n=-\infty}^{\infty} \text{sinc}^2\left[Nb\left(\frac{x'}{\lambda z} - \frac{m}{b}\right)\right] \times \text{sinc}^2\left[Nb\left(\frac{y'}{\lambda z} - \frac{n}{b}\right)\right]\right\} \exp\left[-\pi \frac{2\omega_0^2(x'^2+y'^2)}{\lambda^2 z^2}\right]. \tag{34}$$

Equation (34) is plotted in Fig. 8. The light distribution consists of a two-dimensional array of sinc functions called grating lobes located at $x'/\lambda z = m/b$ and $y'/\lambda z = n/b$, $m, n =$ integers. The off-axis lobes reduce the power of the main lobe and contribute to a smaller Strehl ratio.

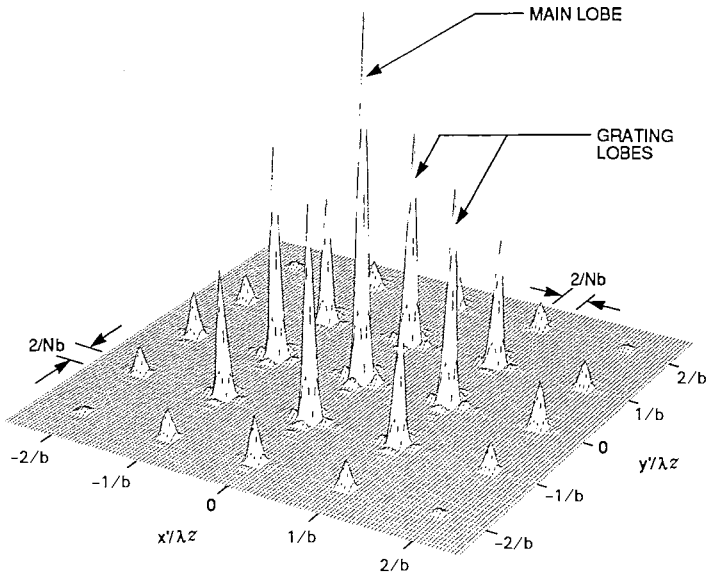

Fig. 8. Far-field intensity pattern from an 8×8 coherent array of Gaussian apertures. The equivalent fill factor ω_0^2/b^2 is 8%.

Each sinc function (corresponding to a specific grating lobe) contains a central peak and several sidelobes. The width of this central peak x'_{width} is determined solely by the width of the array:

$$\frac{x'_{\text{width}}}{\lambda z} = \frac{2}{Nb} = \frac{2}{\text{width of array}}. \tag{35}$$

A similar situation exists when the magnitude varies from laser to laser. $g(x, y)$ is no longer a simple rect function and the functional form of $G(x', y')$ changes. As a consequence, the central peak width of each grating lobe increases or decreases somewhat.

The intensity of each grating lobe falls off according to the Gaussian function in Eq. (34) and is down to $1/e^2$ when $\sqrt{x'^2+y'^2}/\lambda z = 1/(\sqrt{\pi}\omega_0)$. The total number of major grating lobes L contained in this central part of the Gaussian is given by

$$L = b^2/\omega_0^2. \tag{36}$$

By defining an equivalent fill factor for Gaussian beams as ω_0^2/b^2, we have the simple result that L is equal to the reciprocal of the fill factor.

C. Effects of Nonuniform Phase

We now consider a laser array with a uniform magnitude distribution but a phase that varies from laser aperture to laser aperture. Perfect spatial coherence is still assumed. The near-field complex amplitude distribution of an $M \times N$ periodic array of laser apertures can be expressed by a modification of Eq. (27):

$$\hat{a}(x, y) = \left[\sum_{m=1}^{M} \sum_{n=1}^{N} \delta(x - mb, y - nb) \exp(j\phi_{mn}) \right] * A \operatorname{rect}\left(\frac{x}{b}\right) \operatorname{rect}\left(\frac{y}{b}\right), \quad (37)$$

where ϕ_{mn} is the phase associated with the (m, n)th laser aperture, and A is the constant magnitude. The far-field intensity becomes

$$I(x', y', z) = \frac{A^2 b^4}{\lambda^2 z^2} \left| \sum_{m=1}^{M} \sum_{n=1}^{N} \exp\left[-j2\pi \frac{(mbx' + nby')}{\lambda z} \right] \exp(j\phi_{mn}) \right.$$
$$\left. \times \operatorname{sinc}\left(\frac{bx'}{\lambda z}\right) \operatorname{sinc}\left(\frac{by'}{\lambda z}\right) \right|^2. \quad (38)$$

Evaluating Eq. (38) at the origin ($x' = 0$, $y' = 0$) and expanding the square of the sum gives

$$I(0, 0, z) = \frac{A^2 b^4}{\lambda^2 z^2} \sum_{m=1}^{M} \sum_{m'=1}^{M} \sum_{n=1}^{N} \sum_{n'=1}^{N} \exp(j\phi_{mn}) \exp(-j\phi_{m'n'}), \quad (39)$$

where we recall $\operatorname{sinc}(x' = 0) = 1$. The Strehl ratio compares the intensity in Eq. (39) to the intensity of an aperture with no phase errors

$$I_{\mathrm{dl}} = \frac{A^2 b^4}{\lambda^2 z^2} M^2 N^2, \quad (40)$$

resulting in

$$S = \frac{1}{M^2 N^2} \sum_{m=1}^{M} \sum_{m'=1}^{M} \sum_{n=1}^{N} \sum_{n'=1}^{N} \exp(j\phi_{mn}) \exp(-j\phi_{m'n'}). \quad (41)$$

When the phase distribution of an array is known explicitly, Eq. (41) can be used to calculate the Strehl ratio. Often, however, the exact phase relationships are unknown, and a statistical analysis must be employed. If the phase ϕ_{mn} can be expressed as a random variable with a known distribution function, we can calculate the expected value of the Strehl ratio $\mathscr{E}\{S\}$:

$$\mathscr{E}\{S\} = \frac{1}{M^2 N^2} \sum_{m=1}^{M} \sum_{m'=1}^{M} \sum_{n=1}^{N} \sum_{n'=1}^{N} \mathscr{E}\{\exp(j\phi_{mn}) \exp(-j\phi_{m'n'})\}, \quad (42)$$

where $\mathscr{E}\{\ldots\}$ indicates the expected value. If in addition, we assume the phases ϕ_{mn} and $\phi_{m'n'}$ are uncorrelated, the expected value of the Strehl ratio becomes

$$\mathscr{E}\{S\} = \frac{1}{M^2N^2} \sum_{m=1}^{M} \sum_{m'=1}^{M} \sum_{n=1}^{N} \sum_{n'=1}^{N} \mathscr{E}\{\exp(j\phi_{mn})\}\mathscr{E}\{\exp(-j\phi_{m'n'})\}. \quad (43)$$

We will calculate $\mathscr{E}\{S\}$ for two different distribution functions. The first assumes that ϕ_{mn} is distributed as a Gaussian random variable with a mean value of zero and a variance of σ_ϕ^2. We then have

$$\begin{aligned}\mathscr{E}\{\exp(j\phi_{mn})\} &= \frac{1}{\sigma_\phi\sqrt{2\pi}} \int_{-\infty}^{\infty} \exp\left[-\frac{u^2}{2\sigma_\phi^2}\right] \exp(ju)\, du \\ &= \frac{1}{\sigma_\phi\sqrt{2\pi}} \int_{-\infty}^{\infty} \exp\left[-\frac{(u-j\sigma_\phi^2)^2}{2\sigma_\phi^2}\right] \exp\left[-\frac{\sigma_\phi^2}{2}\right] du \\ &= \exp\left[-\frac{\sigma_\phi^2}{2}\right]. \end{aligned} \quad (44)$$

Since we also have

$$\mathscr{E}\{\exp(-j\phi_{mn})\} = \exp\left[-\frac{\sigma_\phi^2}{2}\right], \quad (45)$$

the expected value of the Strehl ratio becomes

$$\mathscr{E}\{S\} = \frac{1}{M^2N^2} \sum_{m=1}^{M} \sum_{m'=1}^{M} \sum_{n=1}^{N} \sum_{n'=1}^{N} \exp(-\sigma_\phi^2) = \exp(-\sigma_\phi^2). \quad (46)$$

Equation (46) gives the general result for a Gaussian-distributed random phase with variance σ_ϕ^2. For small σ_ϕ^2, the exponential can be expanded in a power series and approximated by the first two terms:

$$\mathscr{E}\{S\} \approx 1 - \sigma_\phi^2 = 1 - \mathscr{E}\{\phi^2\}. \quad (47)$$

For this case, we have the simple result that the Strehl ratio is decreased from unity by an amount equal to the variance of the phase.

We also calculate $\mathscr{E}\{S\}$ for phases that are uncorrelated and uniformly distributed between $-\alpha$ and α. The distribution function is given by

$$p(\phi) = \begin{cases} 1/(2\alpha), & -\alpha < \phi < \alpha \\ 0, & \text{otherwise.} \end{cases} \quad (48)$$

We then have

$$\mathscr{E}\{\exp(j\phi_{mn})\} = \frac{1}{2\alpha} \int_{-\alpha}^{\alpha} \exp(ju)\, du = \frac{\sin(\alpha)}{\alpha} \quad (49)$$

We note that $\mathscr{E}\{\exp(-j\phi_{mn})\} = \mathscr{E}\{\exp(j\phi_{mn})\}$. Hence, for a uniform uncorrelated distribution, Eq. (43) reduces to

$$\mathscr{E}\{S\} = \mathscr{E}\{\exp(j\phi_{mn})\} \cdot \mathscr{E}\{\exp(-j\phi_{mn})\}$$
$$= \left[\frac{\sin(\alpha)}{\alpha}\right]^2 \triangleq \operatorname{sinc}^2\left(\frac{\alpha}{\pi}\right). \tag{50}$$

As an example, the Rayleigh limit for good beam quality requires the phase variations to stay within $\pm\pi/4$ of the mean. If the phase errors are uniformly distributed over this interval, the expected value of the Strehl ratio is

$$\mathscr{E}\{S\} = \left|\frac{\sin(\pi/4)}{\pi/4}\right|^2 = 0.81. \tag{51}$$

A small phase expansion of Eq. (50) results in an expression similar to Eq. (47)

$$\mathscr{E}\{S\} \approx \left|\frac{\alpha - (\alpha^3/6)}{\alpha}\right|^2 \approx 1 - \frac{\alpha^2}{3} = 1 - \mathscr{E}\{\phi^2\}. \tag{52}$$

Section III describes several external cavity techniques for correcting and controlling the phase of a diode laser array.

D. Effects of Partial Coherence

The coherence of a wavefront can be categorized into two types. The first type, temporal coherence, is a measure of wavefront correlation at two different times. A perfectly monochromatic source is completely temporally coherent, whereas a source with finite spectral bandwidth is temporally coherent only over a finite length of time (given by the reciprocal of the bandwidth). The second type, spatial coherence, measures the correlation between any two spatially separated points in the wave field at the same instant of time.

Returning to the simple beam splitter for combining two lasers, we imagine two lasers with total spatial coherence but only partial temporal coherence. The two lasers must produce identical (but nonmonochromatic) wavefronts. If the wavefronts incident on the beam splitter are displaced in time by less than the coherence time, they will add coherently. Since the propagation delays of the different lasers can in general be adjusted to be quite small, this implies that broad-band multilongitudinal mode lasers can be used as readily as single-mode lasers. The spatial coherence must be high, however, for effective beam addition. We examine the effect of partial spatial coherence on the Strehl ratio in this section.

As in the previous section, we start with an $M \times N$ array of laser apertures with uniform intensity across each aperture. However, we must now indicate the temporal behavior of each source. The complex time-varying amplitude of the (m, n)th source is given by $\hat{E}_{m,n}(t)$, and Eq. (37) becomes

$$\hat{a}(x, y, t) = \left[\sum_{m=1}^{M} \sum_{n=1}^{N} \delta(x - mb, y - nb) \hat{E}_{m,n}(t) \right] * \operatorname{rect}\left(\frac{x}{b}\right) \operatorname{rect}\left(\frac{y}{b}\right). \quad (53)$$

We will assume in this analysis that the time-average intensities of all the apertures are equal:

$$\langle |\hat{E}_{m,n}(t)|^2 \rangle = \langle |\hat{E}_{m',n'}(t)|^2 \rangle, \quad (54)$$

where the angular brackets denote the time average

$$\langle \cdots \rangle \triangleq \lim_{T \to \infty} \frac{1}{T} \int_0^T (\cdots)\, dt. \quad (55)$$

Following the steps of the previous section, we evaluate the squared magnitude of the Fourier transform of Eq. (53) at the origin. A time average of this expression results in an expression similar to Eq. (39)

$$\langle I(0, 0, z) \rangle = \frac{b^4}{\lambda^2 z^2} \sum_{m=1}^{M} \sum_{m'=1}^{M} \sum_{n=1}^{N} \sum_{n'=1}^{N} \langle \hat{E}_{m,n}(t) \hat{E}^*_{m',n'}(t) \rangle. \quad (56)$$

For an array with perfect spatial coherence and uniform phase, Eq. (56) becomes

$$\langle I'(0, 0, z) \rangle = \frac{b^4}{\lambda^2 z^2} M^2 N^2 \langle |\hat{E}_{m,n}(t)|^2 \rangle. \quad (57)$$

The Strehl ratio is given as the ratio between Eqs. (56) and (57):

$$\langle S \rangle = \frac{\sum_{m=1}^{M} \sum_{m'=1}^{M} \sum_{n=1}^{N} \sum_{n'=1}^{N} \langle \hat{E}_{m,n}(t) \hat{E}^*_{m',n'}(t) \rangle}{M^2 N^2 \langle |\hat{E}_{m,n}(t)|^2 \rangle}$$

$$= \frac{1}{M^2 N^2} \sum_{m=1}^{M} \sum_{m'=1}^{M} \sum_{n=1}^{N} \sum_{n'=1}^{N} \hat{\gamma}_{m,n,m',n'}, \quad (58)$$

where the normalized complex spatial coherence function $\hat{\gamma}_{m,n,m',n'}$ is defined as

$$\hat{\gamma}_{m,n,m',n'} = \frac{\langle \hat{E}_{m,n}(t) \hat{E}^*_{m',n'}(t) \rangle}{\langle |\hat{E}_{m,n}(t)|^2 \rangle}, \quad (59)$$

and the normalization ensures that $|\hat{\gamma}_{m,n,m',n'}| \leq 1$. For perfect spatial coherence and uniform phase across all the apertures, $\hat{\gamma}_{m,n,m',n'} = 1$ for all (m, n) and (m', n'), and the Strehl ratio of Eq. (58) is unity.

Equation (58) expresses the average Strehl ratio in terms of a general four-dimensional spatial coherence function. Frequently, however, the spatial coherence is only a function of the relative distance $(m - m', n - n')$ between the lasers. In this case, the space-invariant form of the coherence function $\hat{\gamma}_{p,q}$ can be used, where $p = m - m'$ and $q = n - n'$. Equation (58) can then be cast into a more revealing form:

$$\begin{aligned}
\langle S \rangle &= \frac{1}{M^2 N^2} \sum_{m=1}^{M} \sum_{m'=1}^{M} \left[\sum_{n=1}^{N} \sum_{n'=1}^{N} \hat{\gamma}_{m-m',n-n'} \right] \\
&= \frac{1}{M^2 N^2} \sum_{m=1}^{M} \sum_{m'=1}^{M} \left\{ N \hat{\gamma}_{m-m',0} + \sum_{q=1}^{N-1} (N-q)(\hat{\gamma}_{m-m',q} + \hat{\gamma}_{m-m',-q}) \right\} \\
&= \frac{1}{MN} \hat{\gamma}_{0,0} + \frac{2}{M^2 N} \sum_{p=1}^{M-1} (M-p) \operatorname{Re}\{\hat{\gamma}_{p,0}\} + \frac{2}{MN^2} \sum_{q=1}^{N-1} (N-q) \operatorname{Re}\{\hat{\gamma}_{0,q}\} \\
&\quad + \frac{2}{M^2 N^2} \sum_{p=1}^{M-1} \sum_{q=1}^{N-1} (M-p)(N-q) \operatorname{Re}\{\hat{\gamma}_{p,q} + \hat{\gamma}_{p,-q}\}, \qquad (60)
\end{aligned}$$

where $\operatorname{Re}\{\hat{\gamma}_{p,q}\}$ denotes the real part of the complex spatial coherence function $\hat{\gamma}_{p,q}$. The first term in Eq. (60) is a result of self-interference from each of the MN apertures. The second and third terms result from interference between lasers separated in x and y respectively, and the fourth term results from interference in the two cross-diagonal directions.

For a completely spatially incoherent array, $\hat{\gamma}_{p,q} = 0$ everywhere except when $p = 0$ and $q = 0$, where $\hat{\gamma}_{0,0} = 1$. All terms except for the first term are zero, and the Strehl ratio of an incoherent array is simply equal to $1/(MN)$. This is reasonable, since we know the radiance of an incoherent array can be no greater than the radiance of the greatest single laser. But a single laser only occupies $1/(MN)$ of the array area, and by Eq. (26) must have a Strehl ratio equal to this fill factor.

An array with perfect coherence in the x direction and no coherence in the y direction retains the first two terms in Eq. (60). Since $\hat{\gamma}_{p,0} = 1$ for perfect x coherence, the second summation results in $(M-1)/MN$, and the total Strehl ratio is given by $\langle S \rangle = (1/N)$.

In practice, many laser arrays have a spatial coherence that decreases with increasing separation. As a final example, we analyze a one-dimensional array of M lasers with an exponentially decreasing real spatial coherence

function

$$\hat{\gamma}_p = \xi^p, \qquad \xi \leq 1. \tag{61}$$

Substituting this spatial coherence function into a one-dimensional form of Eq. (60) yields

$$\langle S \rangle = \frac{1}{M} + \frac{2}{M^2} \sum_{p=1}^{M-1} (M-p)\xi^p. \tag{62}$$

By recognizing the finite summation in Eq. (62) as an arithmetic-geometric series (Spiegel, 1968), the Strehl ratio can be written as

$$\langle S \rangle = \frac{2(1-\xi^M)}{M(1-\xi)} - \frac{2\xi[1 - M\xi^{M-1} + (M-1)\xi^M]}{M^2(1-\xi)^2} - \frac{1}{M}. \tag{63}$$

If M is sufficiently large such that $\xi^M \ll \xi$, Eq. (63) simplifies to

$$\langle S \rangle = \frac{M - 2\xi - M\xi^2}{M^2(1-\xi)^2}. \tag{64}$$

A plot of Eq. (63) is shown in Fig. 9 as a function of ξ for $M = 20$. There are two important features to be noted. First, the Strehl ratio approaches

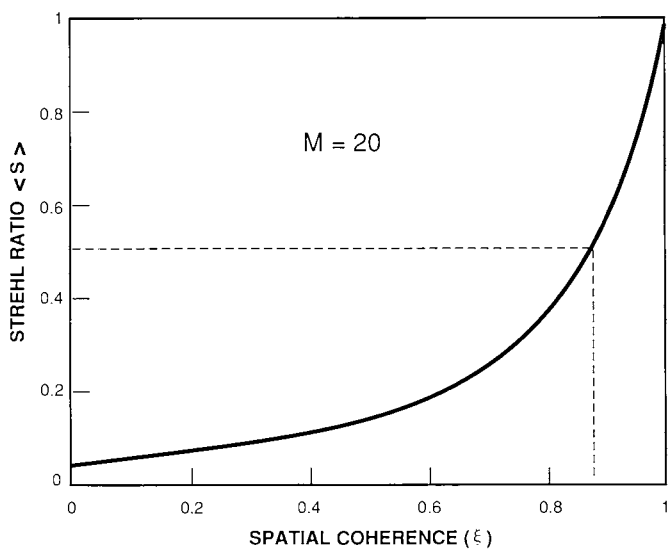

Fig. 9. Strehl ratio of 20-element linear array as a function of spatial coherence between lasing elements. Dashed line corresponds to coherence required for a Strehl ratio of 0.5.

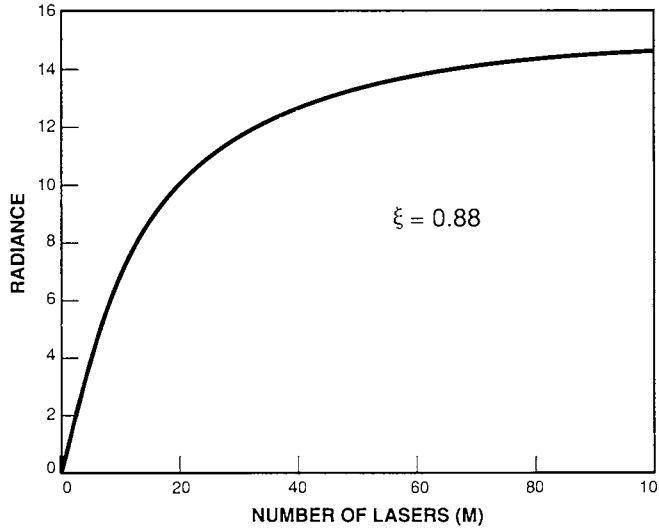

Fig. 10. Radiance from a linear laser array as a function of number of lasers. Nearest-neighbor coherence is 0.88.

$1/M = 0.05$ as the coherence approaches zero. Second, a nearest-neighbor coherence of $\xi = 0.88$ is required for a Strehl ratio of 0.5. This high value of ξ is necessary because the coherence was assumed to degrade exponentially with laser separation. With a nearest-neighbor coherence of $\xi = 0.88$, lasers separated by half the array length have a coherence of 0.28, and lasers on opposite ends of the array have a coherence of only 0.086. The Strehl ratio can be interpreted as the fraction of the array that is effectively coherent.

Figure 10 illustrates the radiance from an array with $\xi = 0.88$ as a function of laser number. Note that operating an array with more than 20 lasers does not significantly increase the array radiance. Section III explores some external methods of establishing and enhancing spatial coherence in diode laser arrays.

E. Effects of Laser Source Distribution

We saw from Eqs. (27)-(34) that a periodic array of apertures gives rise to a main lobe and several additional off-axis grating lobes. Although periodic laser arrays are most common, aperiodic and random placement arrays are important to understand for several reasons. First, a formerly periodic array

can become aperiodic by random device failure. Second, some periodic array fabrication techniques can lead to small aperture location errors. We need to determine the effect of partial device failure and placement error on the Strehl ratio and the far-field pattern. Finally, we would like to determine whether any benefits can be derived from designing arrays with nonperiodic spacing.

It can be seen from Eq. (25) that both the numerator and denominator of the Strehl ratio are average quantities, where the average extends over the entire laser array. Hence, the relative locations of the individual lasing apertures have no effect on the Strehl ratio, and we conclude that random arrays and periodic arrays of the same overall size have identical on-axis performance.

Although aperiodic aperture placement does not affect the size of the main lobe, it can have a dramatic effect on the distribution of power in the other grating lobes. This can be understood qualitatively by modeling the laser array as a diffraction grating. A periodic diffraction grating gives rise

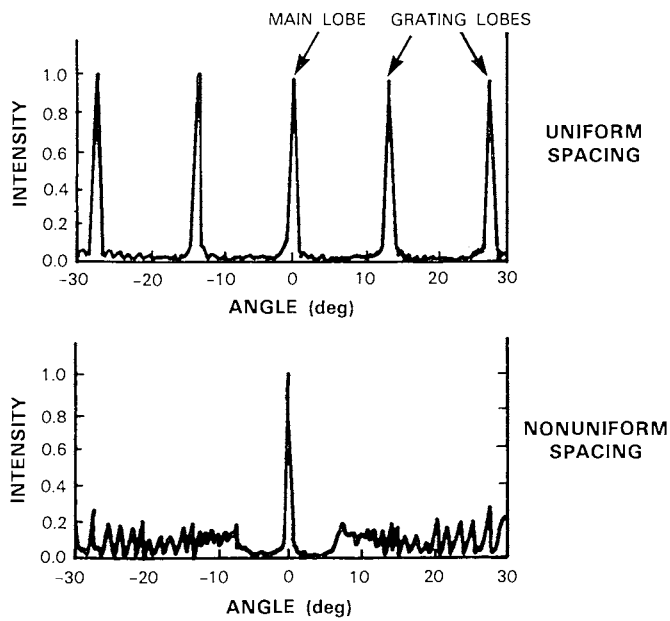

Fig. 11. Effect of laser aperture placement on the far-field pattern. (a) corresponds to the far-field pattern from a linear array of equally spaced point sources. (b) corresponds to the far-field pattern from an array with linearly increasing spacing (Abeles and Deri, 1988).

to discrete diffraction orders (grating lobes). A simple quasi-nonperiodic array can be constructed by superimposing several periodic arrays, each with a different array spacing. Since each subarray contributes diffraction orders at a different set of angles, the off-axis power is distributed over the far field. Note, however, that the on-axis order of each subarray is not a function of the array period, and consequently the on-axis power from the superposition is identical to the on-axis power from a periodic array.

The actual structure of the off-axis far field depends greatly on the locations of specific apertures. In radar and radio telescope arrays, the presence of large grating lobes is often detrimental, and it is advantageous to spread the off-axis power out as uniformly as possible. Special aperiodic and random array designs have been studied to optimize the off-axis behavior (Lo, 1963, 1968). Diode laser arrays with spacing based on a geometric series (Suhre, 1986) and a linearly increasing spacing (Abeles and Deri, 1988) have also been suggested. The results of a computer model are shown in Fig. 11 for a one-dimensional array with linearly increasing spacing. Point sources are used in the model, giving rise to equal intensity grating lobes for the periodic case. In contrast, the array with linearly increasing spacing spreads the power of the off-axis grating lobes over virtually the entire far field. The amount of power in the main lobe and hence the Strehl ratio are unchanged, however.

III. COHERENCE, LATERAL MODE CONTROL, AND BEAM COMBINING

We showed in Section I that mutual coherence is required to sum the radiances of individual lasers in an array. In addition, the optimum Strehl ratio is obtained only when the amplitude and phase across the laser array are uniform. In this section, we explore various external methods of establishing coherence among a two-dimensional array of lasers, controlling the phase profile of the resulting coherent wavefront, and combining the laser outputs into a single beam.

We start by analyzing the effect of a spatial filter on an incoherent and coherent laser array in an external cavity. Spatial filtering systems are then described that establish mutual coherence across incoherent arrays and control the lateral modes of partially coherent arrays.

Next, we describe diffractive coupling in an external cavity for establishing coherence combined with Fresnel-plane spatial filtering for lateral mode control. This technique leads to simple and compact external optical systems.

The third part reviews techniques that employ an external master oscillator. Injection-locking by a master oscillator laser is shown to augment the coherence of a partially coupled array, promote the desired lateral mode, and narrow the spectrum of the array. The master-oscillator-power-amplifier configuration is also explored.

Finally, we review a few of the methods available for combining individual coherent sources into a single quasi-uniform beam with desirable far-field properties.

A. Fourier-Plane Spatial Filtering

Experiments coupling semiconductor lasers to external optical cavities were performed as early as 1964 (Crowe and Craig, 1964a, b; Crowe and Ahearn, 1966, 1968) and later extended by Rutz (Philipp-Rutz and Edmonds, 1969). Since then, the effects of an external cavity on diode laser spectral characteristics and far-field patterns have been studied by many researchers (Fleming & Mooradian, 1981; Hardy *et al.*, 1986; Seo *et al.*, 1989). An external cavity is useful by itself to improve certain diode laser characteristics such as spectral linewidth. However, the principal advantage from our point of view is the ability to insert additional optical elements into the cavity to promote mutual coherence and improve the Strehl ratio of the resulting wavefront. We begin this section by analyzing a simple external cavity Fourier-plane spatial-filtering system.

1. Spatial Filter Analysis

Figure 12(a) shows a highly simplified diode laser array in an external cavity (only one dimension is shown for simplicity). We assume that the front facets of all the diode lasers are perfectly antireflection-coated, and are enlarged (e.g., by microlenses) so that their width b is equal to their separation. The entire laser array consists of an $N \times N$ array of these square apertures. The array is placed in the front focal plane of a lens, with a spatial filter in the back focal plane. The spatial filter consists of an adjustable square aperture to block a portion of the light from the lens. A second lens and output mirror are provided to form a feedback beam. In the absence of the spatial filter, the two lenses form an afocal imaging system with an image of the laser array formed at the output mirror (inverted). The returning light from the mirror is reimaged by the two lenses and inverted again to make an erect image at the laser array. Thus, light from a single aperture in Fig. 12(a) is returned only to that aperture, and the array lases as N^2 independent laser cavities.

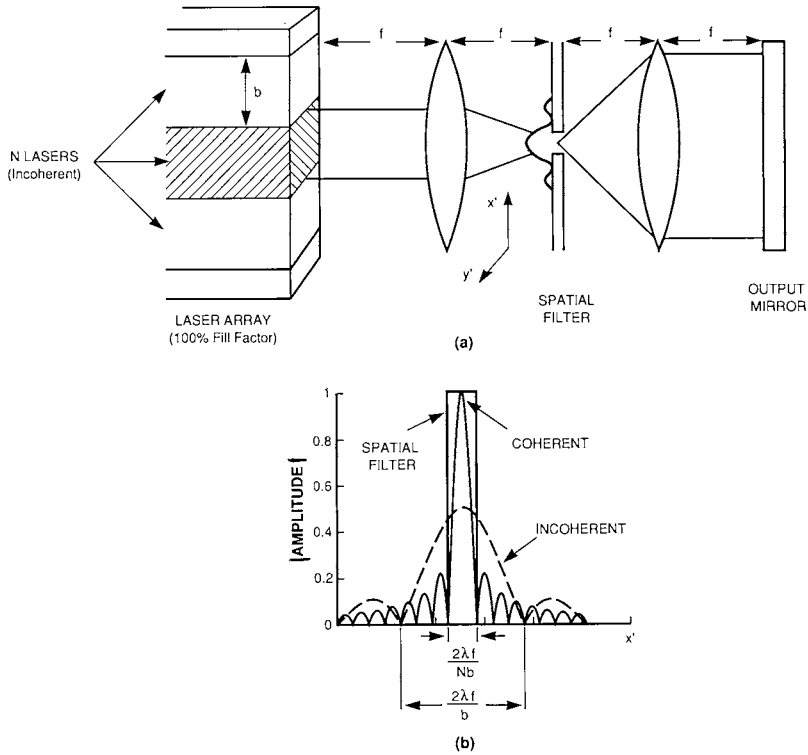

Fig. 12. Establishing mutual coherence by spatial filtering. (a) shows a simplified optical configuration assuming a linear laser array with 100% fill factor. (b) shows the light magnitude at the spatial filter plane for an incoherent (dashed) and coherent (solid) laser array. The spatial filter is adjusted to pass the central lobe of the coherent array.

We now consider the effect of the spatial filter on both a coherent and incoherent laser array. If the array is mutually coherent and uniform in magnitude and phase, its complex amplitude distribution $g(x, y)$ can be expressed as

$$g(x, y) = A \operatorname{rect}\left(\frac{x}{Nb}\right) \operatorname{rect}\left(\frac{y}{Nb}\right), \tag{65}$$

$$\text{where rect}\,(x) = \begin{cases} 1, & |x| \leq \frac{1}{2} \\ 0, & \text{otherwise,} \end{cases}$$

and A is the magnitude of the complex amplitude distribution.

The complex amplitude distribution at the spatial filter is given by the Fourier transform of Eq. (65)

$$G(x', y') = \frac{AN^2b^2}{j\lambda f} \operatorname{sinc}\left(\frac{Nbx'}{\lambda f}\right) \operatorname{sinc}\left(\frac{Nby'}{\lambda f}\right), \tag{66}$$

where $\operatorname{sinc}(x) = \sin(\pi x)/\pi x$, f is the focal length of the lens, λ is the wavelength of light, and $j = \sqrt{-1}$. The absolute value of this distribution, plotted as the solid curve in Fig. 12(b) consists of a single main lobe and several sidelobes.

Consider the effect of a spatial filter (shown in Fig. 12(b)) that only passes the central lobe of the sinc function in Eq. (66). Since this lobe contains 82% of the power, the filter allows most of the light to continue to the end mirror. We assume for simplicity that the second lens and end mirror form a perfect folded afocal imaging system; the light field directly behind the spatial filter passes through the second lens, is reflected by the end mirror, and is reimaged (inverted) by the second lens onto the back side of the filter. Since we assume perfect imaging, this feedback light passes through the filter from right to left with no further attenuation. The original sinc function of Eq. (66) has been clipped by the filter, however, and the first lens can only produce an aberrated image of the $N \times N$ apertures at the laser array. This aberration causes a small amount of the light from a single aperture to be imaged outside the aperture, resulting in a total round-trip coherent mode attenuation of approximately 0.75.

We now calculate the loss from the spatial filter when there is no coherence between apertures. In this case, the light pattern at the filter plane is given by the superposition of intensities from each laser aperture. A single aperture has a complex amplitude $g(x, y)$ given by

$$g(x, y) = A \operatorname{rect}\left(\frac{x}{b}\right) \operatorname{rect}\left(\frac{y}{b}\right), \tag{67}$$

resulting in a complex amplitude distribution at the filter plane of

$$G(x', y') = \frac{Ab^2}{j\lambda f} \operatorname{sinc}\left(\frac{bx'}{\lambda f}\right) \operatorname{sinc}\left(\frac{by'}{\lambda f}\right). \tag{68}$$

The absolute value of this distribution is shown as a dashed curve in Fig. 12(b). With the spatial filter adjusted as before, all light is blocked outside the region $|x'| \leq \lambda f/Nb, |y'| \leq \lambda f/Nb$. The light amplitude directly behind

the spatial filter is then given by

$$G_f(x', y') = \frac{Ab^2}{j\lambda f} \operatorname{sinc}\left(\frac{bx'}{\lambda f}\right) \operatorname{rect}\left(\frac{Nbx'}{2\lambda f}\right) \operatorname{sinc}\left(\frac{by'}{\lambda f}\right) \operatorname{rect}\left(\frac{Nby'}{2\lambda f}\right). \quad (69)$$

If $N \gg 1$, then $\operatorname{sinc}(bx'/\lambda f) \approx 1$ for $|x'| \leq \lambda f / Nb$. Hence, Eq. (69) simplifies to

$$G_f(x', y') \approx \frac{Ab^2}{j\lambda f} \operatorname{rect}\left(\frac{Nbx'}{2\lambda f}\right) \operatorname{rect}\left(\frac{Nby'}{2\lambda f}\right). \quad (70)$$

Again we assume perfect reimaging by the second lens and the end mirror, so the return beam has the complex amplitude of Eq. (70) at the spatial filter plane and is completely passed by the filter on route to the laser array. The final image of a single laser aperture at the laser array is given by the Fourier transform of Eq. (70),

$$g_i(x, y) = \frac{A}{(N/2)^2} \operatorname{sinc}\left(\frac{2x}{Nb}\right) \operatorname{sinc}\left(\frac{2y}{Nb}\right). \quad (71)$$

We would like to calculate the power contained in the single $b \times b$ laser aperture. Again, if $N \gg 1$, $\operatorname{sinc}(2x/Nb) \approx 1$ for $|x| \leq b/2$, and the power P in the laser aperture is given by

$$P = \int_{-b/2}^{b/2} \int_{-b/2}^{b/2} |g_i(x, y)|^2 \, dx \, dy \approx \frac{A^2 b^2}{(N/2)^4}. \quad (72)$$

The power in the original aperture is simply given by $P_0 = A^2 b^2$, resulting in an attenuation by the spatial filter of

$$\frac{P}{P_0} \approx \frac{1}{(N/2)^4}, \qquad N \gg 1. \quad (73)$$

Two things are apparent from this derivation. First, the loss suffered by a mutually incoherent laser array is much greater than that from a coherent array even for a small number of lasers. Consequently, the threshold of the incoherent state will be much greater, and the system will prefer to lase as a mutually coherent ensemble.

Second, the spatial filter provides coupling between lasers by diffraction. The round-trip light distribution from a single laser aperture is given by Eq. (71) regardless of the coherence between this aperture and its neighbors. This sinc function profile has a central lobe of size $Nb \times Nb$ covering the entire laser array. Consequently, feedback light from each aperture is spread

among all the apertures of the array, thereby establishing the coupling necessary for coherent operation. Note that mutual coherence across the array does not alter this coupling, but rather provides the proper interference at the filter plane to allow the light to pass through the filter.

2. *Applications*

Spatial filters of the type described previously have been used by researchers to establish coherence across broad-area lasers (Philipp-Rutz, 1972), incoherent laser arrays (Philipp-Rutz, 1975), and discrete lasers (Rediker *et al.*, 1985; Anderson and Rediker, 1987). Many variations on this structure have also been implemented. The coherence of broad-area lasers has been enhanced using a retroreflecting mirror as a spatial filter to feed back a specific off-axis plane-wave component (Goldberg and Weller, 1989). Single-mode fibers have also been employed as spatial filters (Eisenstein *et al.*, 1987). Alternatively, nondegenerate external cavities have been designed that use the aperture of the broad-area laser itself as a spatial filter (Sharfin *et al.*, 1989).

Complementary filters consisting of blocking wires rather than slits have been used to establish coherence across a linear array of lasers while inducing operation in specific lateral modes (Leger, 1989). Figure 13 shows

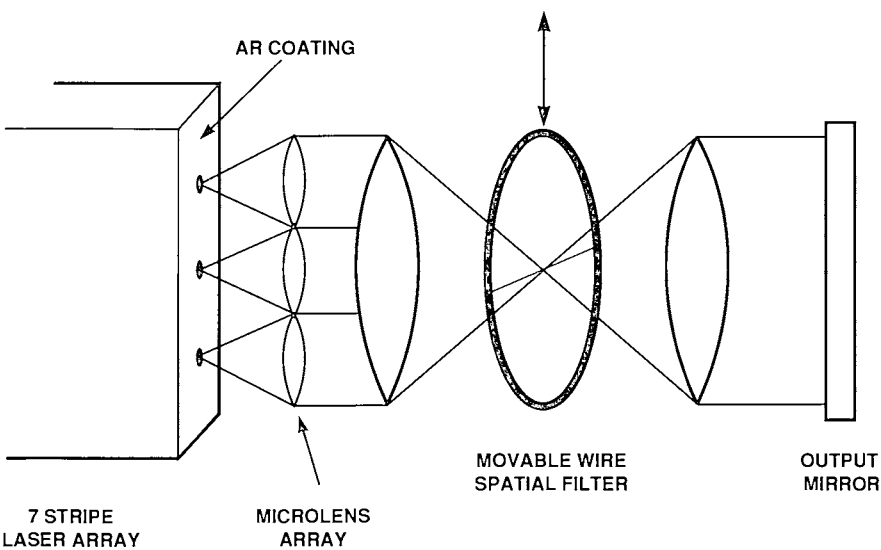

Fig. 13. Spatial filtering experimental set-up. A microlens array increases the effective fill factor, and a movable wire is used as a complementary spatial filter (Leger, 1989).

the elements of the external cavity. The laser array consisted of seven gain-guided multiple-quantum-well diode lasers on 50 μm centers (Spectra Diode Labs. custom order). The front facet of the array was given an antireflection coating, while the back facet was coated for high reflectivity. An array of anamorphic microlenses expanded and collimated the lasers (see Section III.D), while an afocal imaging system produced an image of the microlens array at the flat output mirror. A spatial filter consisting of a thin wire was placed in the back focal plane of the first lens.

As an initial test, the array was operated with no wire present. The far-field pattern shown in Fig. 14(a) has a width characteristic of a single emitter, consistent with incoherent array operation. By placing the wire in the filter plane slightly to the right or left of the optical center, the laser radiated as a mutually coherent ensemble corresponding to the fundamental lateral mode (Fig. 14(b)). Placing the wire in the optical center prohibited this mode from lasing. Instead, the laser array ran in the highest-order lateral mode, characterized by a 180° phase shift between adjacent lasing elements (Fig. 14(c)).

Spatial filtering has also been used to augment the coherence of partially coherent arrays and control their lateral modes. Gain-guided lasers fabricated on 10 μm centers couple light through evanescent fields to establish coherence across the array. The array can still lase in a variety of lateral modes characterized by the phase profile across the array. In many of these structures, the highest-order lateral mode is preferred, and the array produces a far-field diffraction pattern with two off-axis peaks. At high powers,

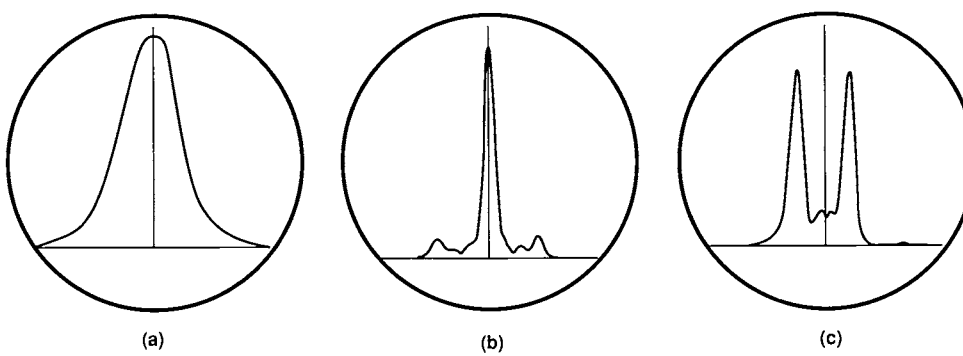

Fig. 14. Far-field patterns from spatial filtering in an external cavity. (a) Spatial filter wire removed. (b) Wire positioned in null of on-axis far-field pattern. (c) Wire adjusted to block center of on-axis pattern, permitting operation of highest-order lateral mode (Leger, 1989).

the coherence degrades and the width of these peaks increases as additional lateral modes are excited.

In one of the first demonstrations of lateral mode control by spatial filtering, a ten-stripe multiple-quantum-well laser was given an antireflection coating and placed in the front focal plane of a lens (Yaeli *et al.*, 1985). The spatial filtering system of Fig. 12 was simplified by placing the output mirror directly after the spatial filter and eliminating the second lens. The feedback light in this system consisted of an inverted image at the array. Proper placement of the spatial filter preferentially excited the lowest-order mode and produced a single-lobed, on-axis output beam. A similar spatial filter was designed to increase the coherence of a Y-junction laser array (Berger *et al.*, 1988).

A more compact system utilizing a graded-index (GRIN) lens together with a linear diode array and spatial filter is shown in Fig. 15 (Chang-Hasnain *et al.*, 1986, 1987, 1989). A high reflectivity mirror is placed at the end of the 0.25 pitch GRIN lens. The width and location of this mirror is chosen to reflect only one of the two lobes from the highest-order lateral mode; the output is taken from the other lobe. This configuration permits

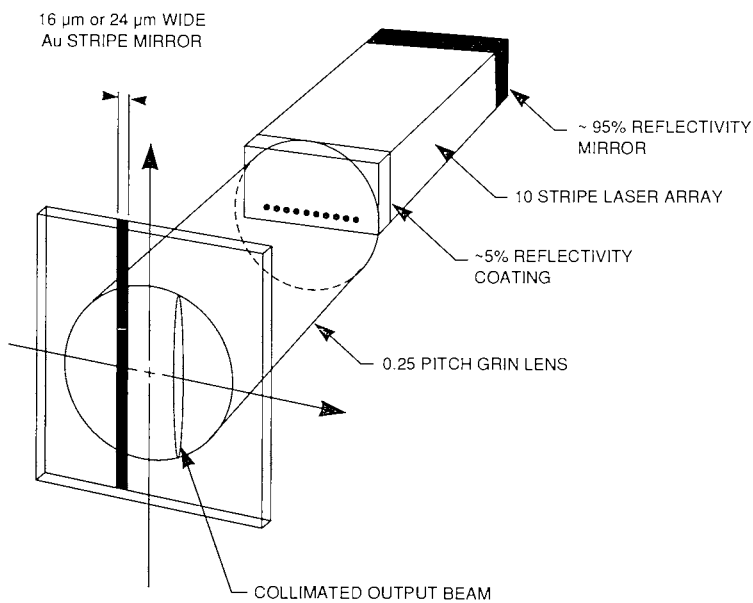

Fig. 15. Spatial filtering with a graded index lens. The output mirror is patterned to reflect only a selected portion of the far-field pattern at the end of the lens (Chang-Hasnain *et al.*, 1987).

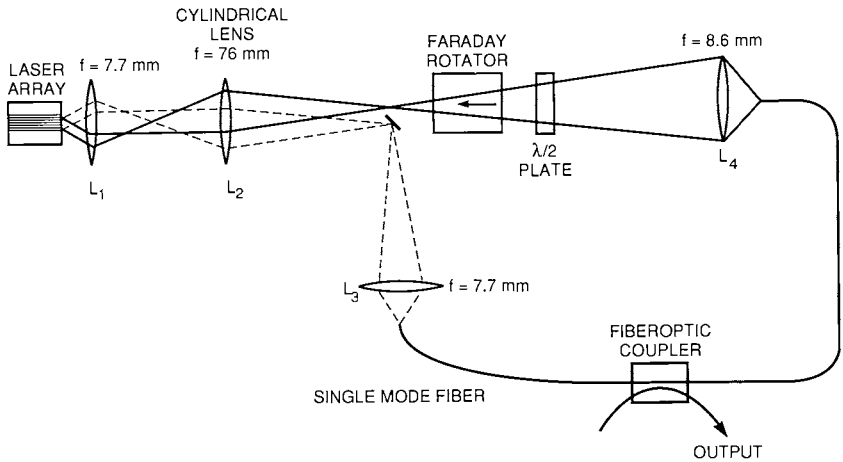

Fig. 16. Spatial filtering using a fiber in an external ring resonator (Goldberg and Weller, 1987a).

operation in a lateral mode that matches the current/gain profile of the original array; the resulting differential efficiency was as high as 70%. 700 mW of pulsed power and 208 mW of cw power were observed in an essentially diffraction-limited peak.

A 40-stripe evanescently coupled laser array is configured as a ring resonator in Fig. 16 (Goldberg and Weller, 1987a). As in the previous example, the array is allowed to operate in a high-order lateral mode to optimize the array efficiency. In this case, however, the light from one lobe of the array diffraction pattern is focused into a single-mode polarization-holding fiber. The fiber acts as a spatial filter by rejecting any light outside of a diffraction-limited spot. The fiber output is then fed back into the array along the other emission lobe. A Faraday polarization rotator ensures that this ring cavity oscillates in one direction only, and the output power is removed through a fiberoptic coupler. With a laser array power of 500 mW, a single longitudinal-mode power of 90 mW was measured from the output fiber.

B. Diffractive Coupling and Fresnel-Plane Spatial Filtering

In the previous section, spatial filtering in the Fourier plane provided coupling between lasers. In this section, we explore coupling by diffraction of unguided light. Monolithic diffractively-coupled structures have been studied by several groups for linear laser arrays (Katz *et al.*, 1983; Chen *et al.*, 1983; Yang and Jansen, 1986; Wang *et al.*, 1986; Wilcox *et al.*, 1987a, b;

Mehuys *et al.*, 1988; Mawst *et al.*, 1989). These devices consist of laser waveguide arrays with a common unguided section. The planar waveguide in this common region allows light to diffract in one dimension before reflection by the end mirror. The feedback light from a single aperture is thus spread over several neighboring lasers in the linear array.

Diffractive coupling can also be applied to an external optical cavity (Basov *et al.*, 1965a,b). Since the diffraction is no longer confined to a planar substrate, mutual coherence can be established across both one- and two-dimensional laser arrays. This technique has been applied to CO_2 laser arrays (Glova *et al.*, 1985; Antyukhov *et al.*, 1986) as well as semiconductor laser arrays (Darznek *et al.*, 1975; Leger *et al.*, 1988a; Leger and Holz, 1988; Roychoudhouri *et al.*, 1988; Leger, 1989; D'Amato *et al.*, 1989; Leger and Griswold, 1990).

1. *Talbot Self-Imaging*

The effect of diffractive coupling can be understood easily by the theory of Talbot self-imaging (Talbot, 1836; Lord Rayleigh, 1881; Winthrop and Worthington, 1965). The complex amplitude $\hat{a}(x, y, z=0)$ from any periodic array of mutually coherent apertures can be expressed as a Fourier series

$$\hat{a}(x, y, z=0) = \sum_{m=-\infty}^{\infty} \sum_{n=-\infty}^{\infty} b_{mn} \exp\left[j2\pi \frac{mx+ny}{d}\right], \tag{74}$$

where b_{mn} are the complex weights of the Fourier components, d is the aperture spacing in both dimensions, and we have assumed the array to be infinite. The Fresnel transfer function for free-space propagation is given by

$$H(m, n, z) = \exp\left(j2\pi \frac{z}{\lambda}\right) \exp\left[-j\pi\lambda z \left(\frac{m^2+n^2}{d^2}\right)\right], \tag{75}$$

where z is the propagation distance, λ is the wavelength of light, and m and n are integers. The field $\hat{a}(x, y, z)$ at a distance z from the array is given by multiplying each Fourier component b_{mn} by the proper phase delay $H(m, n, z)$. Propagation of a distance $z_t = 2d^2/\lambda$ reduces $H(m, n, z)$ to a constant phase for all values of m and n. Apart from this constant phase, the distribution at this so-called Talbot plane is identical to the original near-field of the laser, and hence corresponds to a self-image. Figure 17(a) illustrates this effect for a periodic array of objects. Note that this image is distinctly different from one formed by a lens, since light from a single object period is diffracted over several periods of the image.

A Talbot cavity optical resonator can be constructed by placing a common end mirror at integer multiples of half a Talbot distance (see Fig. 17(b)).

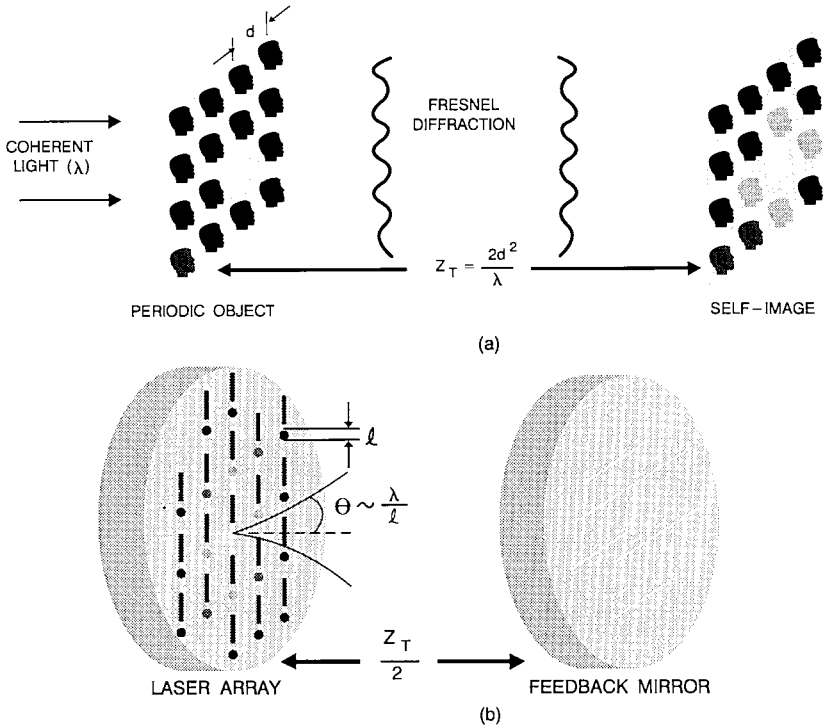

Fig. 17. Talbot self-imaging effect. (a) illustrates the self-image produced in the first Talbot plane from a coherently illuminated periodic object. Light from a single object period (white face) is spread among several image periods (white and gray faces) in the self-image plane. (b) illustrates an external cavity produced by placing the feedback mirror at one-half of a Talbot distance.

After one cavity round-trip, the feedback light forms a self-image of the array in the array plane and couples efficiently into the laser waveguides. Light from a single laser aperture is spread across several neighboring apertures and provides the required coupling to establish coherence across the laser array. Note that Talbot self-imaging requires the array to be coherent. Feedback from an incoherent array will not form a self-image at the array, and coupling from the external cavity to the optical waveguides will be inefficient. This increased loss raises the threshold of the incoherent state and promotes mutually coherent operation. In addition to equally spaced laser arrays, Talbot cavities can be constructed using hexagonal arrays and rectangular arrays with specific period ratios.

2. *Fresnel-Plane Spatial Filtering*

Lateral mode control can be accomplished by selectively increasing the loss of the undesired modes. Fresnel-plane spatial filtering and the proper choice of cavity length can both be used to select the desired mode. An understanding of these effects can be obtained by calculating the light distribution at fractional Talbot planes for specific lateral modes (Winthrop and Worthington, 1965; Golubentsev *et al.*, 1987; Leger and Holz, 1988; Roychoudhuri *et al.*, 1988; Wilcox *et al.*, 1989; Leger, 1989; D'Amato *et al.*, 1989; Leger and Swanson, 1990). For a round-trip cavity length of one-half a Talbot distance ($z = d^2/\lambda$), the Fresnel transfer function becomes

$$H\left(m, n, \frac{z_t}{2}\right) = \exp\left[j2\pi\frac{d^2}{\lambda^2}\right]\exp\left(-j\pi(m^2+n^2)\right]. \tag{76}$$

Ignoring the constant phase term again, and recognizing that $\exp(-j\pi m^2) = \exp(-j\pi m)$ for integer m, the amplitude distribution of the fundamental lateral mode becomes

$$\hat{a}\left(x, y, \frac{z_t}{2}\right) = \sum_{m=-\infty}^{\infty}\sum_{n=-\infty}^{\infty} b_{mn}\exp\left[j2\pi\frac{(mx+ny)}{d}\right]\exp\left[-j\pi(m+n)\right]$$

$$= \sum_{m=-\infty}^{\infty}\sum_{n=-\infty}^{\infty} b_{mn}\exp\left[j2\pi\frac{m(x-d/2)+n(y-d/2)}{d}\right]. \tag{77}$$

This amplitude distribution is identical to the original near-field of Eq. (74) but shifted by one-half period ($d/2$) in each direction. Feedback light from an array lasing in the fundamental lateral mode is imaged exactly in between the apertures, resulting in high cavity loss.

We now consider the self-imaging properties of the *highest-order* lateral mode. This mode is chacterized by a π phase reversal at every lasing aperture. Again, the laser apertures are assumed to be spaced by a distance d, but the period of the distribution is now $2d$ and all even harmonics of the Fourier series are zero. The field at the lasing aperture and the Fresnel transfer function are given by

$$\hat{a}(x, y, z=0) = \sum_{\substack{m=-\infty \\ \text{odd}}}^{\infty}\sum_{\substack{n=-\infty \\ \text{odd}}}^{\infty} b_{mn}\exp\left[j2\pi\frac{(mx+ny)}{2d}\right], \tag{78}$$

and

$$H(m, n, z) = \exp\left[j2\pi\frac{z}{\lambda}\right]\exp\left[-j\pi z\lambda\frac{(m^2+n^2)}{4d^2}\right]. \tag{79}$$

We would like to calculate the field at the half-Talbot plane $z = d^2/\lambda$. The Fresnel transfer function becomes (ignoring the constant phase)

$$H\left(m, n, z = \frac{d^2}{\lambda}\right) = \exp\left[-j\pi \frac{(m^2+n^2)}{4}\right], \qquad m, n = \text{odd integer.} \tag{80}$$

Since m and n are odd only, we have $m = (2p-1)$ and $n = (2q-1)$ where p and q are any integers. The transfer function becomes

$$H\left(p, q, z = \frac{d^2}{\lambda}\right) = \exp\left[-j\pi \frac{(2p-1)^2+(2q-1)^2}{4}\right]$$

$$= \exp\{-j\pi[p(p-1)+q(q-1)]\} \exp\left[-j\frac{\pi}{2}\right]. \tag{81}$$

But since p and q are integers, either p or $(p-1)$ is even and Eq. (81) reduces to a constant phase term. For the highest-order mode, we conclude that registered self-images are produced at all integer multiples of a half-Talbot distance.

In summary, an external cavity with a round-trip cavity length of a Talbot distance z_t supports both the fundamental and highest-order modes. However, a cavity with a round-trip length of $z_t/2$ preferentially supports the highest-order mode. These fractional Talbot-plane properties have been used to design external laser cavities that discriminate between the fundamental and highest-order lateral modes (Leger and Holz, 1988; Roychoudhuri *et al.*, 1988; D'Amato *et al.*, 1989; Leger and Griswold, 1990).

3. *Applications*

Figure 18 shows an external Talbot cavity designed for a linear array of seven mutually incoherent diode lasers spaced by $d = 50\ \mu\text{m}$ (Leger and Holz, 1988; Leger and Griswold, 1990). The cavity was fabricated from a single piece of fused silica, with a thickness $t = nd^2/\lambda = 4.5$ mm, where $n = 1.45$ is the refractive index of the substrate. An output mirror with 50% reflectance was deposited on the back side of the substrate. The Talbot effect produces a self-image of the array in the periodic direction (parallel to the array). Transverse to the array, the curvature of the substrate (radius of curvature = 5.0 mm) focuses the light back into the diode laser waveguides. An array of multilevel diffractive microlenses was etched onto the flat side of the cavity to collimate the individual diode lasers.

Two methods of lateral mode selection were demonstrated by modifying the output mirror in different ways. The first method utilizes the imaging

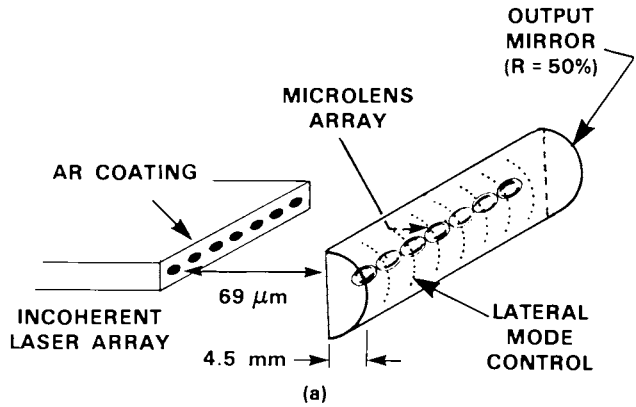

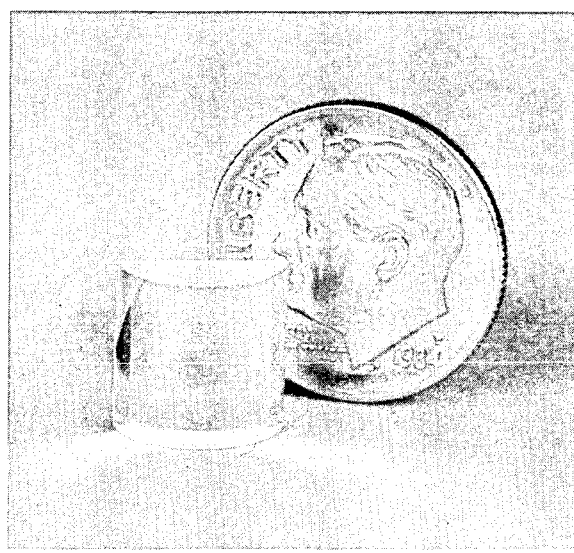

Fig. 18. Talbot cavity made from a cylindrical substrate. (a) shows the microlenses on the flat side of the cavity and the patterned mirror on the curved side. (b) is a photograph of the Talbot cavity (Leger and Griswold, 1990).

properties of the Talbot cavity at one-half of a Talbot distance ($Z_t/2$). By placing the output mirror at $Z_t/2$, the round-trip length corresponds to a full Talbot distance and both the fundamental and highest-order modes form properly registered images. At the mirror, however, a correctly registered self-image is produced for the highest-order lateral mode, whereas the fundamental lateral mode is shifted by one-half period. The output mirror was patterned to reflect light with a half-period shift corresponding to the fundamental mode. Light from the highest-order lateral mode suffers increased loss, since it passes through the removed portions of the mirror, and the mode is prevented from lasing. Figure 19 shows the far-field pattern from this cavity. The central peak has a divergence corresponding to 1.19 times the diffraction limit.

The second method of lateral mode selection was demonstrated using an external cavity with a round-trip cavity length slightly less than a Talbot distance. This cavity has a lower threshold for the highest-order lateral mode and results in a double-lobed far-field pattern. A mode correcting phase plate was fabricated on top of the 50% output mirror to convert this highest-order mode into the fundamental single-lobed mode. The phase corrector was fabricated by spinning a half-wave layer of photoresist on

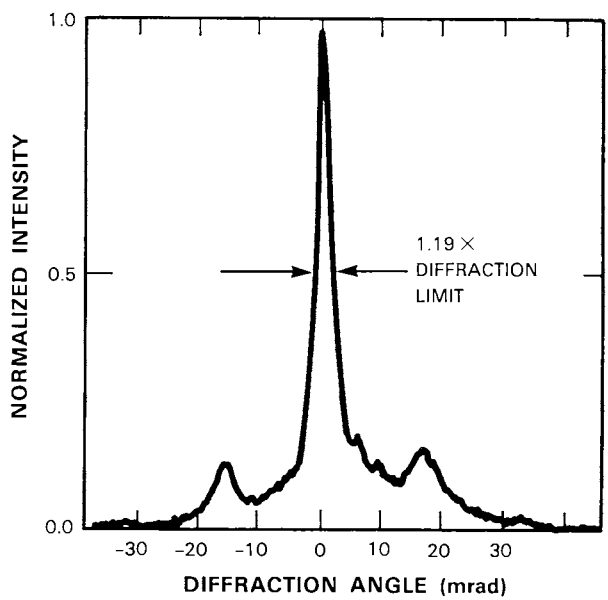

Fig. 19. Far-field diffraction pattern from Talbot cavity with patterned output mirror (Leger and Griswold, 1990).

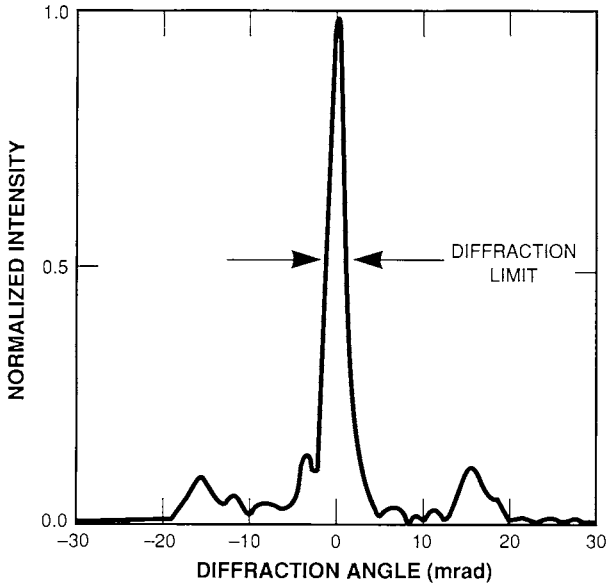

Fig. 20. Far-field diffraction pattern from Talbot cavity with phase corrector (Leger and Griswold, 1990).

top of the dielectric mirror, and applying a pattern to shift the phase of every other aperture. The resulting far-field pattern is shown in Fig. 20. The central peak was diffraction-limited with a divergence of 2.7 mrad (full width at half maximum).

C. External Master Oscillators

In the previous section, coherence and mode control were established by mutual coupling in an external optical cavity. An external master oscillator offers an alternative method of phase-locking. Light from a single master laser couples into a laser array and locks all the array elements to a common reference. One principal advantage of this method is that a spectrally pure low-power master oscillator can be used to control many slave lasers, resulting in high power emission in a narrow spectral band.

This section starts with a basic review of a Fabry–Perot laser influenced by an externally injected light source. The results of this model are extended to the locking behavior of diode lasers. Next, we review systems based on injection-locking; a master laser is used to control the frequency and phase

of each laser in the array. We end with a description of the master-oscillator-power-amplifier (MOPA) configuration, where the master laser supplies the input signal to an array of optical amplifiers.

1. *Fabry-Perot Laser Model*

Injection locking is performed by injecting a weak signal (master) into a more powerful free-running oscillator (slave). Laser injection-locking was first demonstrated with HeNe lasers (Stover and Steier, 1966) and later with diode lasers (Kobayashi and Kimura, 1980). Adler has shown that a slave oscillator can be locked in phase to a master if the natural frequency of the slave is within a prescribed frequency range of the master (Adler, 1946). This injection-locking bandwidth can be estimated by considering the Fabry-Perot laser cavity of Fig. 21. The laser cavity consists of two plane-parallel mirrors with intensity reflectance R, separated by a distance l. The cavity contains a gain medium with a round-trip amplitude gain of g. We shall calculate the output power of the cavity $P_0(\nu_i)$, which results from resonant amplification of an injected signal $P_i(\nu_i)$ incident on the left mirror (assuming 100% mode coupling efficiency).

The standard Fabry-Perot transmittance equation (Yariv, 1976) can be modified to include the round-trip amplitude gain g (Goldberg, 1990):

$$\frac{P_0(\nu_i)}{P_i(\nu_i)} = \frac{(1-R)^2 g}{(1-Rg)^2 + 4Rg \sin^2(\theta/2)}, \tag{82}$$

where θ is the round-trip phase change given by

$$\theta = 2\pi\left(\frac{2nl\nu}{c}\right), \tag{83}$$

n is the gain medium index, and ν and c are the light frequency and speed. We note that at resonance, the round-trip phase change $\theta = 2\pi M$, where M is an integer. This gives rise to the longitudinal modes of the laser at frequencies $\nu = Mc/2nl$. Near resonance, the round-trip phase change can be expressed as

$$\theta = 2\pi M + \Delta\theta \tag{84}$$

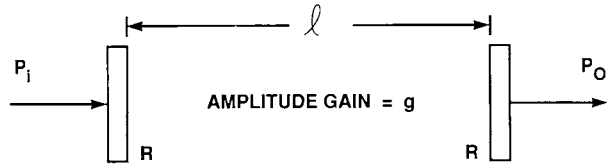

Fig. 21. Fabry-Perot laser model.

where $\Delta\theta \ll 1$. Equation (82) reduces to

$$\frac{P_0(\nu_i)}{P_i(\nu_i)} \approx \frac{(1-R)^2 g}{(1-Rg)^2 + Rg(\Delta\theta)^2}. \tag{85}$$

For lasing to occur, the round-trip gain must offset the round-trip loss. In our simple model, this implies $RG \approx 1$. Substituting this value into Eq. (85) results in

$$\frac{P_0(\nu_i)}{P_i(\nu_i)} \approx \frac{(1-R)^2}{R(\Delta\theta)^2}. \tag{86}$$

But since $\theta = 4\pi nl\nu/c$, we have $\Delta\theta = 4\pi nl\Delta\nu/c$, and

$$\frac{P_0(\nu_i)}{P_i(\nu_i)} \approx \frac{(1-R)^2 c^2}{R(4\pi nl)^2(\Delta\nu)^2}. \tag{87}$$

We can define injection locking as occurring when the output power $P_0(\nu_i)$ at frequency ν_i due to injection is greater than or equal to the maximum free-running power $P_0(\nu_0)$ at frequency ν_0. Since $P_0(\nu_i)$ is given by Eq. (87) we have

$$P_0(\nu_i) \approx \frac{P_i(\nu_i)(1-R)^2 c^2}{R(4\pi nl)^2(\Delta\nu)^2} \geq P_0(\nu_0), \tag{88}$$

and the locking is maintained when

$$|\Delta\nu| \leq \sqrt{\frac{P_i(\nu_i)}{P_0(\nu_0)}}\,\frac{(1-R)c}{\sqrt{R}(4\pi nl)}. \tag{89}$$

Recalling that the cold-cavity Q of a laser resonator is given by

$$Q = \frac{2l}{\lambda}\,\frac{\pi\sqrt{R}}{(1-R)}, \tag{90}$$

the injection-locking bandwidth B_l is given by the total frequency range allowed by Eq. (89)

$$B_l = \sqrt{\frac{P_i(\nu_i)}{P_0(\nu_0)}}\,\frac{\nu_0}{Q}. \tag{91}$$

A final useful form of this equation results from expressing the Q in terms

of the photon cavity lifetime $\tau_p = Q/(2\pi\nu_0)$:

$$B_l = \frac{1}{2\pi\tau_p}\sqrt{\frac{P_i(\nu_i)}{P_0(\nu_0)}}. \tag{92}$$

Equation (92) has been shown to describe the locking ranges of simple laser systems. Semiconductor lasers, however, are complicated by the fact that the index of refraction is not constant, but changes with carrier density and therefore laser gain. A change in the index of refraction shifts the spectral output of the laser, thereby changing the shape of the injection-locking band. This index variation is expressed by the linewidth broadening factor α, defined as (Osiński and Buus, 1987)

$$\alpha = -2k\frac{dn/dN}{dg/dN}, \tag{93}$$

where k is the free-space wave number, n is the refractive index, g is the gain per unit length, and N is the carrier density. When the gain-dependent refractive index is incorporated into the injection-locking theory, the injection-locking performance is changed in several ways. The injection-locking range is asymmetrically broadened towards the low frequency end (Lang, 1982). The locking requirement for a diode laser $\Delta\nu_d$ is given approximately by

$$-(1+\alpha^2)^{1/2}(B_l/2) < \Delta\nu_d < (B_l/2). \tag{94}$$

In addition, the high frequency part of the locking range becomes dynamically unstable, with the stable part of the range decreasing with increasing α (Lang, 1982; Henry *et al.*, 1985).

Measured values of α range from 2 to 6 for AlGaAs lasers (Osiński and Buus, 1987), with typical cavity lifetimes on the order of a few picoseconds. The full injection-locking bandwidth of a 100 mW slave laser array locked to an injected beam of 0.5 mW incident power has been measured to be 16 GHz (Goldberg *et al.*, 1982). Since the temperature tuning rate of an AlGaAs laser is on the order of 30 GHz/°C, temperature stability on the order of 0.1°C is required for both the master and the slave lasers.

2. *Injection-Locked Systems*

Injection-locking can be used to establish coherence between uncoupled lasers. More frequently, it has been used to augment the coherence of an evanescently coupled array and control the lateral mode structure (Goldberg

et al., 1985). The experimental set-up shown in Fig. 16 was used for injection-locking by replacing the optical fiber at L_4 with a separate master-oscillator laser (Goldberg and Weller, 1987b). As before, the slave laser array was composed of 40 gain-guided laser stripes spaced by 10 μm. A Faraday isolator was used to prevent coupling from the slave back into the master. The injection-locking beam was shaped by lenses L_1 and L_2 to cover most of the laser array. The optimum injection angle was approximately 4° from normal incidence in the plane of the laser junction; the injection-locked array emitted primarily along the −4° direction. This angular separation between injected light and array light allowed the array output to be picked off by a mirror and focused into a single-mode fiber by the lens L_3.

The far-field diffraction pattern of the laser array running at 510 mW is shown in Fig. 22 before and after injection-locking. Before locking, the diffraction pattern has a wide double-lobed shape. Injection-locking with a master oscillator power of 11 mW produces an output that is 1.25 times

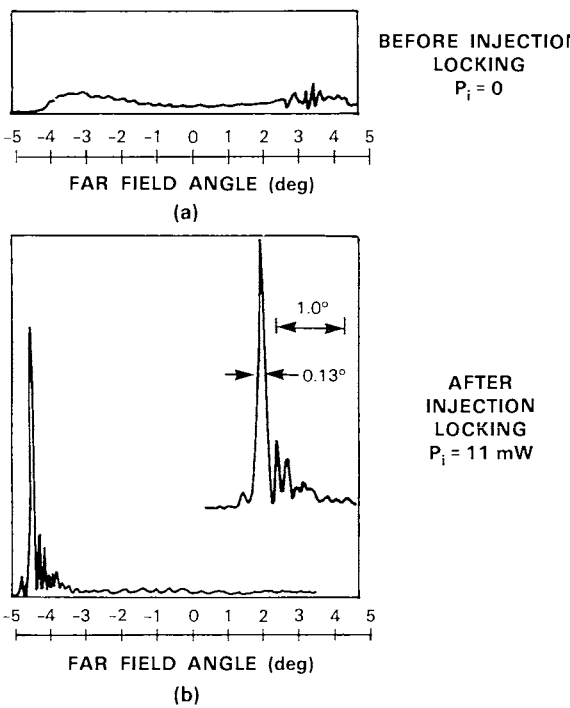

Fig. 22. Far-field patterns from array injection-locking. (a) is the far-field diffraction pattern before injection-locking. (b) is the far-field pattern after injection-locking with 11 mW of incident power (Goldberg and Weller, 1987).

the diffraction limit (0.13°). 150 mW of this light was coupled to a single-mode fiber, demonstrating the high Strehl ratio of the output. The spectrum of the original free-running laser array contained several longitudinal modes, each with a line width of approximately 40 GHz. The spectrum of the locked array consisted of a single longitudinal mode with a line width of less than 100 MHz. Similar results have been obtained with broad-area lasers (Abbas *et al.*, 1988; Goldberg and Chun, 1988).

Injection-locked, gain-guided arrays have also been shown to exhibit beam-steering. In one setup, a 100 mW 10-stripe laser array was injection-locked to a tunable dye laser (Hohimer *et al.*, 1985). The light was injected normal to the array into a single laser facet. By increasing the injection-locking power to 12 mW, continuous locking was achieved over 60 GHz. Narrow single-lobed emission was observed to occur along a specific angle determined by the array drive current and the injection frequency. Beam-steering occurred when either of these two parameters was varied. Figure 23 shows a plot of the beam angle as the injection frequency is varied over 100 GHz. The beam scans over a range of 4.7° to 7.0° with a tuning rate of 0.023°/GHz. Similar results have been obtained using a single frequency diode laser as a master oscillator (Swanson *et al.*, 1987a). The master

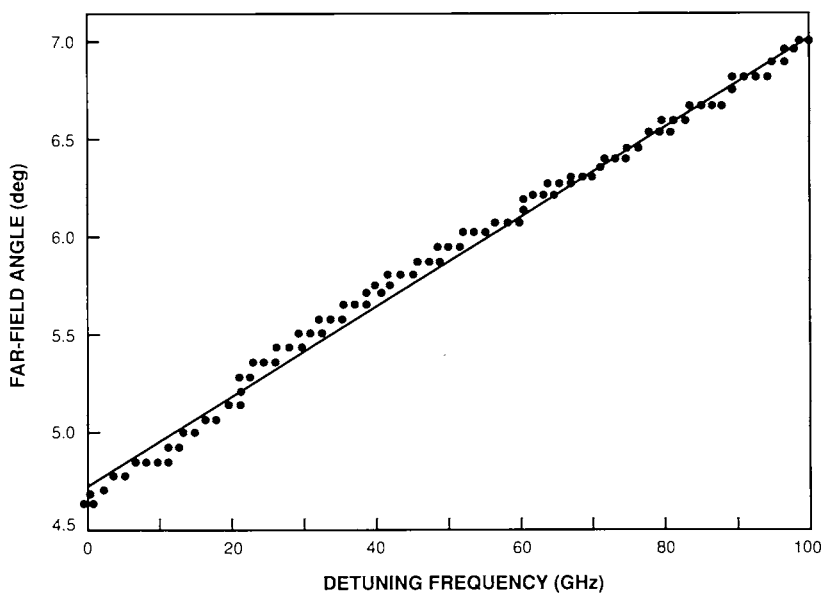

Fig. 23. Laser beam-steering from an injection-locked array. The beam is scanned by changing the frequency of the injection signal (Hohimer *et al.*, 1985).

oscillator frequency was controlled by injection-current modulation, resulting in a slave laser beam that changed in both propagation direction and frequency. An alternative method modulated the array drive current. In this configuration, the array frequency was locked to the master oscillator and did not change with beam angle.

3. *Master-Oscillator-Power-Amplifier (MOPA) Systems*

A master-oscillator-power-amplifier (MOPA) is similar to an injection-locking configuration where the slave laser array has a very low cold-cavity Q. The Q is reduced by applying an antireflection coating to the laser facets, effectively converting the lasers into amplifiers. One of the principal advantages of the MOPA technique is seen in Eq. (91). A low Q increases the locking bandwidth, and greatly relaxes the temperature and current control requirements. With a perfect AR-coating, the array operates as a traveling-wave amplifier; all longitudinal modes disappear, and the master oscillator wavelength is only required to be sufficiently close to the gain peak of the array to provide amplification.

The output beam from the MOPA does not steer appreciably with changes in drive current or injected wavelength. This can be a distinct advantage in applications such as laser ranging or optical communications, where the master or slave laser current must be modulated, but beam-steering effects are undesirable.

A MOPA system has been demonstrated using a 10-stripe, gain-guided diode laser array with an antireflection-coating applied to both facets (Andrews, 1986). Master oscillator light was injected into the amplifier to cover the entire array. By injecting 4 mW of power into the array, a single-lobed far-field pattern was observed at an angle of 2.5° from the array normal. The angle did not vary appreciably over a master oscillator tuning range of 0.5 Å and an array drive current range of 350 mA. 100 mW of coherent power were obtained from an input power of 21 mW. The measured small signal gain was 18 dB.

When MOPA systems are used in high power applications, phase aberrations can appear across the array due to thermal effects and current-induced index variations. The resulting output beam has a reduced Strehl ratio, limiting the useful output power. The double-pass MOPA illustrated in Fig. 24 compensates for these phase errors with a phase-conjugate mirror (Stephens *et al.*, 1987). The light from a single longitudinal and spatial mode master oscillator is spread across the entire front facet of an AR-coated, 10-element amplifier array by a lens system (LS_1). The amplified

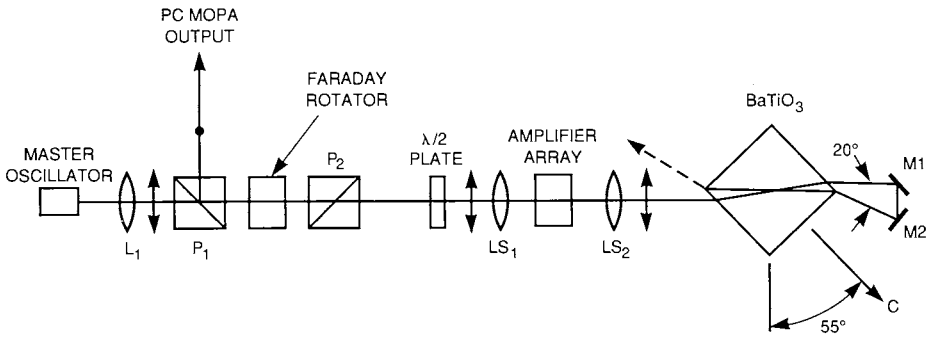

Fig. 24. Master-oscillator-power-amplifier with a phase-conjugate mirror (Stephens *et al.*, 1987).

light containing some unavoidable phase variations is presented to a phase-conjugate mirror consisting of a barium titanate crystal oriented in a self-pumped ring configuration (Cronin-Golomb *et al.*, 1985). The light exiting the crystal has a phase distribution that is the phase conjugate of the original beam. This beam retraces the original beam path through the amplifier where the same phase distortions cancel out the conjugate distortions of the beam. The double-pass light is thus restored to a flat phase front with high Strehl ratio. The Faraday rotator, two polarization-selecting prisms (P_1 and P_2), and the half-wave plate act as a nonreciprocal element that maintains the polarization for light traveling from the master oscillator to the amplifier array, but rotates it by 90° upon return. P_1 reflects the return beam with the rotated polarization and provides the output for the device.

Figure 25 compares the far-fields of the phase-conjugate MOPA with a double-pass MOPA employing an ordinary mirror. Phase errors add with

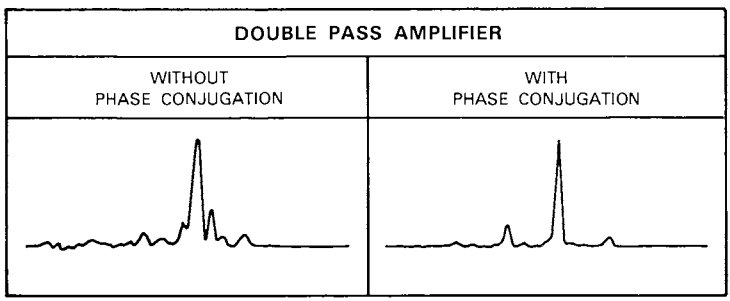

Fig. 25. Far-field patterns from phase-conjugate MOPA (Stephens *et al.*, 1987).

an ordinary mirror, producing a 1.1°-wide far-field pattern. The Strehl ratio of this pattern is estimated to be 0.51. The phase-conjugate mirror allows the phase errors to cancel, resulting in a near-diffraction-limited far-field pattern (0.58° beam width). The corresponding Strehl ratio has increased to 0.97. In similar experiments using a four-pass configuration (Stephens *et al.*, 1989), output powers as high as 100 mW were obtained.

D. Methods of Beam Combining

The radiance theorem described in Section I.B. suggested a natural way to categorize beam combining methods. Laser beam superposition is performed by directing N beams to a common point on a beam-combining element. The element directs the superimposed beams along a single direction. The resultant beam has the size and divergence of a single beam, but a near-field intensity (W/cm^2) N times greater.

Aperture filling is performed by arranging the beams in an array such that there are no gaps between the individual beams. In this case, the near-field intensity is the same as a single beam, but the area is N times greater, and the solid angle divergence is N times less.

These two methods are entirely equivalent from a radiance standpoint. The light distribution from one can be converted into the other by an appropriate afocal telescope. However, there are often practical issues that dictate the use of one over the other. Aperture-filled systems have an advantage in high-power applications since the intensity does not increase with larger number of lasers. In addition, the low divergence that results can sometimes eliminate the need for a beam-expanding telescope. Systems based on superposition are preferred for retrofitting an existing optical system with a higher power source, since the beam size and divergence are identical to the original single laser.

Laser beam superposition has been implemented in a variety of forms. Specially designed binary diffraction gratings can be used to convert multiple input beams into a common output beam with efficiencies as high as 87%. Higher efficiencies are possible with multistep gratings. These gratings have been used inside external laser cavities to superimpose light from a gain-guided laser array (Leger *et al.*, 1986, 1987*a*). It is also possible to superimpose coherent beams by using volume holograms or photorefractive crystals (Cronin-Golomb *et al.*, 1986; Christian *et al.*, 1989). Since the volume grating formed in a photorefractive crystal depends on the incident light, the photorefractive technique is able to compensate for phase drifts in the diode laser array.

Aperture filling techniques often employ arrays of microlenses to increase the fill factor and spread the light more evenly over the aperture. These lenses can be fabricated as refractive or diffractive optical elements. Refractive lenses can be made in photolytic glasses by exposing a patterned substrate to ultraviolet light (Borrelli and Morse, 1988). Subsequent heating causes the unexposed glass to be squeezed into spherical lenslets. A second technique uses selective diffusion into a planar substrate to produce arrays of planar gradient-index (GRIN) lenses (Oikawa and Iga, 1982; Oikawa *et al.*, 1990). Lenses can also be made in photoresist by fabricating an array of cylindrical shapes. Upon heating in an oven, the cylinders are pulled into a spherical shape by surface tension (Popovic *et al.*, 1988). Since photoresist has negligible absorption in the infrared, these lenses can be quite efficient. In addition, the resist technology is common to both the microlens and laser fabrication, simplifying future integration of the two structures.

In some cases, it is necessary to make aspheric microlenses. For example, collimation of high numerical aperture sources requires a lens with a nonspherical figure to control aberrations. Alternatively, the astigmatism inherent in some semiconductor lasers can be corrected by an anamorphic optical system. It is possible to make nonspherical microlenses both as refractive and diffractive elements. Refractive microlenses have been fabricated in InP and GaP by mass transport (Liau *et al.*, 1988, 1989). An approximation to an aspheric surface is etched into the substrate. The transport process uses surface diffusion to smooth local roughness while preserving the overall desired surface figure.

Diffractive microlenses have been fabricated in a large variety of materials. Efficiency can be enhanced by continuous blazing of the surface-relief structures (Fujita *et al.*, 1982; Tanigami *et al.*, 1989) or by a step-wise approximation to the continuous blaze (d'Auria *et al.*, 1972; Koronkevich *et al.*, 1984). By choosing the surface profile correctly, virtually any arbitrary phase distribution can be obtained. Diffractive lens arrays have been used inside external cavity laser arrays to increase the array fill factor (Leger *et al.*, 1988b). Figure 26 shows an array of anamorphic diffractive microlenses designed to collimate a diode laser array inside a Talbot cavity. A four-level phase profile was etched into a fused silica substrate. The spacing between the lenses is 50 μm. The focal lengths of the lens (69 μm in the transverse direction and 100 μm in the lateral direction) were chosen to correct the astigmatism of the gain-guided laser array.

Finally, there are alternative methods of aperture filling that do not use microlenses. One such method employs a Zernike phase-contrast optical

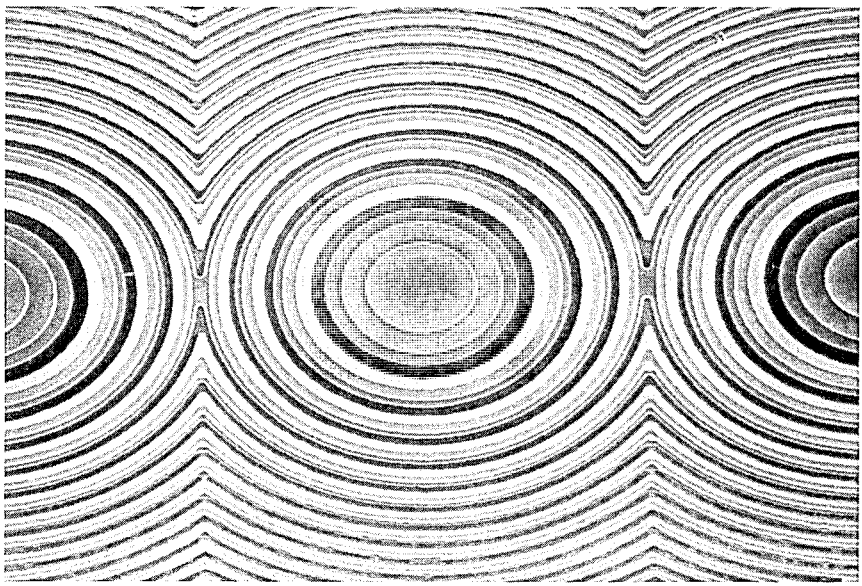

Fig. 26. SEM photograph of a four-level anamorphic diffractive lens. The lens is designed to remove the astigmatism from a gain-guided laser. The four different etch levels can be seen (Leger *et al.*, 1988).

system to convert nonuniformities in amplitude into nonuniformities in phase (Swanson *et al.*, 1987b). The phase variations are subsequently removed by a phase-correcting plate. This method has been used to eliminate the sidelobes of a Y-guide laser, resulting in a significantly improved Strehl ratio (Leger *et al.*, 1987b).

IV. CONCLUSIONS

This chapter has introduced some of the fundamental concepts of coherent beam addition. We showed in the first section that the radiance of a laser array is equal to the sum of the radiance from each element only if three requirements are satisfied: (1) mutual coherence must be established across the entire array, (2) the phases of the individual emitters must be controlled to produce an on-axis beam, and (3) the beams must be combined to produce an approximately uniform intensity profile. The consequences of failing to meet any one of these requirements was then described in terms of the Strehl ratio of the resultant beam.

The main part of the chapter described external techniques for establishing these requirements. Spatial filtering, diffractive coupling, and injection-locking were shown to establish coherence and maintain the proper phase relationships among the lasers. Beam superposition and aperture filling methods were introduced for combining individual laser beams into a single quasi-uniform beam. Although many of the methods described here have only been demonstrated in one dimension, all are extendable to two-dimensional surface-emitting arrays. As two-dimensional surface-emitting lasers become larger and more powerful in future years, it is likely that these external methods of phase-locking and coherent beam addition will become essential for generating efficient, high-radiance light sources.

V. ACKNOWLEDGMENTS

Contributions and critical reading of this manuscript by W. Goltos, M. Holz, R. Knowlden, G. Swanson, and W. Veldkamp are gratefully acknowledged.

REFERENCES

ABBAS, G. L., YANG, S., CHAN, V. W. S. AND FUJIMOTO, J. G. (1988). "Injection behavior and modeling of 100 mW broad area diode lasers," *IEEE J. Quantum Electron.* **QE-24**, 609-617.

ABELES, J. H. AND DERI, R. J. (1988). "Suppression of sidelobes in the far-field radiation patterns of optical waveguide arrays," *Appl. Phys. Lett.* **53**, 1375-1377.

ADLER, R. (1946). "A study of locking phenomena in oscillators," *Proc. IRE* **34**, 351-357.

ANDERSON, K. K. AND REDIKER, R. H. (1987). "High spectral purity cw and pulse output from an ensemble of discrete diode lasers," *Appl. Phys. Lett.* **50**, 1-3.

ANDREWS, J. R. (1986). "Traveling-wave amplifier made from a laser diode array," *Appl. Phys. Lett.* **48**, 1331-1333.

ANTYUKHOV, V. V., GLOVA, A. F., KACHURIN, O. R., LEBEDEV, F. V., LIKHANSKIĬ, V. V., NAPARTOVICH, A. P. AND PIS'MENNYĬ, V. D. (1986). "Effective phase locking of an array of lasers," *JETP Lett.* **44**, 78-81.

BASOV, N. G., BELENOV, É. M. AND LETOKHOV, V. S. (1965a). "Synchronization of oscillations in a semiconducting laser having several p-n junctions," *Sov. Phys. Solid State* **7**, 275-276.

BASOV, N. G., BELENOV, É. M. AND LETOKHOV, V. S. (1965b). "Diffraction synchronization of lasers," *Sov. Phys. Tech. Phys.* **10**, 845–850.

BERGER, J., WELCH, D., STREIFER, W. AND SCIFRES, D. R. (1988). "Narrowing the far-field of a Y-junction laser array using a customized spatial filter in an external cavity," *Appl. Phys. Lett.* **52**, 1560–1562.

BLAU, K. H., BOBB, M. A., MILLER, T. L. AND COLLISS, G. R. (1987). "Spectral multiplexing beam combiner for diode lasers," *Proc. SPIE* **740**, 48–52.

BORRELLI, N. F. AND MORSE, D. L. (1988). "Microlens arrays produced by a photolytic technique," *Appl. Opt.* **27**, 476–479.

BORN, M. AND WOLF, E. (1970). "Principles of Optics," Pergamon Press, Oxford, 462.

BOYD, R. W. (1983). "Radiometry and the Detection of Optical Radiation," Wiley, New York.

CHANG-HASNAIN, C. J., WELCH, D. F., SCIFRES, D. R., WHINNERY, J. R., DIENES, A. AND BURNHAM, R. D. (1986). "Diffraction-limited emission from a diode laser array in an apertured graded-index lens external cavity," *Appl. Phys. Lett.* **49**, 614–616.

CHANG-HASNAIN, C. J., BERGER, J., SCIFRES, D. R., STREIFER, W., WHINNERY, J. R. AND DIENES, A. (1987). "High power with high efficiency in a narrow single-lobed beam from a diode laser array in an external cavity," *Appl. Phys. Lett.* **50**, 1465–1467.

CHANG-HASNAIN, C. J., DIENES, A., WHINNERY, J. R., STREIFER, W. AND SCIFRES, D. R. (1989). "Characteristics of the off-centered apertured mirror external cavity laser array," *Appl. Phys. Lett.* **54**, 484–486.

CHEN, T. R., YU, K. L., CHANG, B., HASSON, A., MARGALIT, S. AND YARIV, A. (1983). "Phase-locked InGaAsP laser array with diffraction coupling," *Appl. Phys. Lett.* **43**, 136–137.

CHRISTIAN, W. R., BECKWITH, P. H. AND MCMICHAEL, I. (1989). "Energy transfer between injection-locked single-mode diode lasers by two-beam coupling in $BaTiO_3$," *Opt. Lett.* **14**, 81–83.

CRONIN-GOLOMB, M., LAU, K. Y. AND YARIV, A. (1985). "Infrared photorefractive passive phase conjugation with $BaTiO_3$: demonstrations with GaAlAs and 1.09 μm Ar^+ lasers," *Appl. Phys. Lett.* **47**, 567–569.

CRONIN-GOLOMB, M., YARIV, A. AND URY, I. (1986). "Coherent coupling of diode lasers by phase conjugation," *Appl. Phys. Lett.* **48**, 1240–1242.

CROWE, J. W. AND CRAIG, R. M. JR. (1964a). "Small-signal amplification in GaAs lasers," *Appl. Phys. Lett.* **4**, 57–58.

CROWE, J. W. AND CRAIG, R. M. JR. (1964b). "GaAs laser linewidth measurements by heterodyne detection," *Appl. Phys. Lett.* **5**, 72–74.

CROWE, J. W. AND AHEARN, W. E. (1966). "Semiconductor laser amplifier," *IEEE J. Quantum Electron.* **QE-2**, 283–289.

CROWE, J. W. AND AHEARN, W. E. (1968). "External cavity coupling and phase locking of gallium arsenide injection lasers," *IEEE J. Quantum Electron.* **QE-4**, 169–172.

D'AMATO, F. X., SIEVERT, E. T. AND ROYCHOUDHURI, C. (1989). "Coherent operation of an array of diode lasers using a spatial filter in a Talbot cavity," *Appl. Phys. Lett.* **55**, 816-818.

DARZNEK, S. A., ZVEREV, M. M. AND USHAKHIN, V. A. (1975). "Investigation of a multielement electron-beam-pumped semiconductor laser with an external mirror," *Sov. J. Quant. Electron.* **4**, 1272-1274.

D'AURIA, L., HUIGNARD, J. P., ROY, A. M. AND SPITZ, E. (1972). "Photolithographic fabrication of thin film lenses," *Opt. Commun.* **5**, 232-235.

EISENSTEIN, G., KOREN, U., TUCKER, R. S., RAYBON, G., DENTAI, A. G., STULZ, L. W. AND MILLER, B. I. (1987). "High-power extended-cavity laser at 1.3 μm with a single-mode fiber output port," *Appl. Phys. Lett.* **50**, 1567-1568.

FLEMING, M. W. AND MOORADIAN, A. (1981). "Spectral characteristics of external-cavity controlled semiconductor lasers," *IEEE J. Quantum Electron.* **QE-17**, 44-59.

FUHR, P. L. (1987). "Polarization power summing in laser diode communication systems," *Proc. SPIE* **740**, 70-76.

FUJITA, T., NISHIHARA, H. AND KOYAMA, J. (1982). "Blazed gratings and Fresnel lenses fabricated by electron-beam lithography," *Opt. Lett.* **7**, 578-580.

GLOVA, A. F., DREIZIN, YU. A., KACHURIN, O. R., LEVEDEV, F. V. AND PIS'MENNYĬ, V. D. (1985). "Phase locking of a two-dimensional array of CO_2 waveguide lasers," *Sov. Tech. Phys. Lett.* **11**, 102, 103.

GOLDBERG, L., TAYLOR, H. F. AND WELLER, J. F. (1982). "Locking bandwidth asymmetry in injection-locked GaAlAs lasers," *Electron. Lett.* **18**, 986-987.

GOLDBERG, L., TAYLOR, H. F., WELLER, J. F. AND SCIFRES, D. R. (1985). "Injection locking of coupled-stripe diode laser arrays," *Appl. Phys. Lett.* **46**, 236-238.

GOLDBERG, L. AND WELLER, J. F. (1987a). "Single lobe operation of a 40-element laser array in an external ring laser cavity," *Appl. Phys. Lett.* **51**, 871-873.

GOLDBERG, L. AND WELLER, J. F. (1987b). "Injection locking and single-mode fiber coupling of a 40-element laser diode array," *Appl. Phys. Lett.* **50**, 1713-1715.

GOLDBERG, L. AND CHUN, M. K. (1988). "Injection locking characteristics of a 1 W broad stripe laser diode," *Appl. Phys. Lett.* **53**, 1900-1902.

GOLDBERG, L. AND WELLER, J. F. (1989). "Narrow lobe emission of high power broad stripe laser in external resonator cavity," *Electron. Lett.* **25**, 112-114.

GOLDBERG, L. (1990). "Applications of injection-locked narrow-stripe and large active area laser diodes," *Conf. on Lasers and Electro-optics: Digest of Technical papers* (Optical Society of America, New York, 1990), 448.

GOLUBENTSEV, A. A., LIKHANSKIĬ, V. V. AND NAPARTOVICH, A. P. (1987). "Theory of phase locking of an array of lasers," *Sov. Phys. JETP* **66**, 676-682.

HARDY, A., STREIFER, W. AND OSIŃSKI, M. (1986). "Influence of external mirror on antireflection-coated phased-array semiconductor lasers," *Appl. Phys. Lett.* **49**, 185-187.

HAUS, H. A., (1984). "Waves and Fields in Optoelectronics," Prentice-Hall, Englewood Cliffs, New Jersey, 63-65.

HENRY, C. H., OLSSON, N. A. AND DUTTA, N. K. (1985). "Locking range and stability of injection-locked 1.54 μm InGaAsP semiconductor lasers," *IEEE J. Quant. Electron.* **QE-21**, 1152–1156.

HOHIMER, J. P., OWYOUNG, A. AND HADLEY, G. R. (1985). "Single-channel injection locking of a diode-laser array with a cw dye laser," *Appl. Phys. Lett.* **47**, 1244–1246.

KATZ, J., MARGALIT, S. AND YARIV, A. (1983). "Diffraction coupled phase-locked semiconductor laser array," *Appl. Phys. Lett.* **42**, 554–556.

KOBAYASHI, S. AND KIMURA, T. (1980). "Injection locking characteristics of an AlGaAs semiconductor lasers," *IEEE J. Quant. Electron.* **QE-16**, 915–917.

KORONKEVICH, V. P., KIRIYANOV, V. P., KOKOULIN, F. I., PALCHIKOVA, I. G., POLESHCHUK, A. G., SEDUKHIN, A. G., CHURIN, E. G., SHCHERBACHENKO, A. M. AND YURLOV, Y. I. (1984). "Fabrication of kinoform optical elements," *Optik* **67**, 257–266.

LANG, R. (1982). "Injection locking properties of a semiconductor laser," *IEEE J. Quant. Electron.* **QE-18**, 976–983.

LEGER, J. R. AND HOLZ, M. (1988). "Binary optical elements for coherent addition of laser diodes," *LEOS 1988 Annual Meeting Proceedings, Santa Clara, CA, Nov. 2-4* (IEEE/LEOS, Piscataway, NJ, 1988), 468–471.

LEGER, J. R., SWANSON, G. J. AND VELDKAMP, W. B. (1986). "Coherent beam addition of GaAlAs lasers by binary gratings," *Appl. Phys. Lett.* **48**, 888–890.

LEGER, J. R., SWANSON, G. J. AND VELDKAMP, W. B. (1987a). "Coherent laser addition using binary phase gratings," *Appl. Opt.* **26**, 4391–4399.

LEGER, J. R., SWANSON, G. J. AND HOLZ, M. (1987b). "Efficient side-lobe suppression of laser diode arrays," *Appl. Phys. Lett.* **50**, 1044–1046.

LEGER, J. R., SCOTT, M. L. AND VELDKAMP, W. B. (1988a). "Coherent addition of AlGaAs lasers using microlenses and diffractive coupling," *Appl. Phys. Lett.* **52**, 1771–1773.

LEGER, J. R., SCOTT, M. L., BUNDMAN, P. AND GRISWOLD, M. P. (1988b). "Astigmatic wavefront correction of a gain-guided laser diode array using diffractive microlenses," *Proc. SPIE* **884**, 82–89.

LEGER, J. R. (1989). "Lateral mode control of an AlGaAs laser array in a Talbot cavity," *Appl. Phys. Lett.* **55**, 334–336.

LEGER, J. R. AND GRISWOLD, M. P. (1990). "Binary-optics miniature Talbot cavities for laser beam addition," *Appl. Phys. Lett.* **56**, 4–6.

LEGER, J. R. AND SWANSON, G. J. (1990). "Efficient array illuminator using binary optics phase plates at fractional Talbot planes," *Opt. Lett.* **15**, 288–290.

LIAU, Z. L., DIADIUK, V., WALPOLE, J. N. AND MULL, D. E. (1988). "Large-numerical-aperture InP lenslets by mass transport," *Appl. Phys. Lett.* **52**, 1859–1861.

LIAU, Z. L., DIADIUK, V., WALPOLE, J. N. AND MULL, D. E. (1989). "Gallium phosphide microlenses by mass transport," *Appl. Phys. Lett.* **55**, 97–99.

LO, Y. T. (1963). "A mathematical theory of antenna arrays with randomly spaced elements," *IEEE Trans. Antennas and Propagation* **AP-12**, 257–268.

LO, Y. T. (1968). "Random periodic arrays," *Radio Science* **3**, 425–436.

LORD RAYLEIGH (1881). "On copying diffraction-gratings, and on some phenomena connected therewith," *Philos. Mag.* **11**, 196–205.

MAWST, L. J., BOTEZ, D., ROTH, T. J., SIMMONS, W. W., PETERSON, G., JANSEN, M., WILCOX, J. Z. AND YANG, J. J. (1989). "Phase-locked array of antiguided lasers with a monolithic spatial filter," *Electron. Lett.* **25**, 365–366.

MEHUYS, D., MITSUNAGA, K., ENG, L., MARSHALL, W. K. AND YARIV, A. (1988). "Supermode control in diffraction-coupled semiconductor laser arrays," *Appl. Phys. Lett.* **53**, 1165–1167.

MINOTT, P. O. AND ABSHIRE, J. B. (1987). "Grating rhomb diode laser power combiner," *Proc. SPIE* **756**, 38–47.

OIKAWA, M. AND IGA, K. (1982). "Distributed-index planar microlens," *Appl. Opt.* **21**, 1052–1056.

OIKAWA, M., NEMOTO, H., HAMANAKA, K. AND KISHIMOTO, T. (1990). "Light coupling between LD and optical fiber using high NA planar microlens," *SPIE OE LASE '90*, Los Angeles, CA., #1219-56.

OSIŃSKI, M. AND BUUS, J. (1987). "Linewidth broadening factor in semiconductor lasers—an overview," *IEEE J. Quant. Electron.* **QE-23**, 9–29.

PHILIPP-RUTZ, E. M. AND EDMONDS, H. D. (1969). "Diffraction-limited GaAs laser with external resonator," *Appl. Opt.* **8**, 1859–1865.

PHILIPP-RUTZ, E. M. (1972). "High-radiance room-temperature GaAs laser with controlled radiation in a single transverse mode," *IEEE J. Quantum Electron.* **QE-8**, 632–641.

PHILIPP-RUTZ, E. M. (1975). "Spatially coherent radiation from an array of GaAs lasers," *Appl. Phys. Lett.* **26**, 475–477.

POPOVIC, Z. D., SPRAGUE, R. A. AND CONNELL, G. A. N. (1988). "Technique for monolithic fabrication of microlens arrays," *Appl. Opt.* **27**, 1281–1284.

REDIKER, R. H., SCHLOSS, R. P. AND VAN RUYVEN, L. J. (1985). "Operation of individual diode lasers as a coherent ensemble controlled by a spatial filter within an external cavity," *Appl. Phys. Lett.* **46**, 133–136.

ROYCHOUDHURI, C., SIEBERT, E., D'AMATO, F., NOLL, R., MACOMBER, S., KINTNER, E. AND ZWEIG, D. (1988). "Review of compact cavities for coherent array lasers," *LEOS 1988 Annual Meeting Proceedings, Santa Clara, CA, Nov. 2-4* (IEEE/LEOS, Piscataway, NJ, 1988) 476–479.

SEO, D. S., PARK, J. D., MCINERNEY, J. G. AND OSIŃSKI, M. (1989). "Compound cavity modes in semiconductor lasers with asymmetric optical feedback," *Appl. Phys. Lett.* **54**, 990–992.

SHARFIN, W. F., SEPPALA, J., MOORADIAN, A., SOLTZ, B. A., WATERS, R. G., VOLLMER, B. J. AND BYSTROM, K. J. (1989). "High power, diffraction-limited, narrow-band external cavity diode laser," *Appl. Phys. Lett.* **54**, 1731–1733.

SMITH, R. J. (1987). "Dichroically combined diode laser transmitter," *Proc. SPIE* **756**, 25–29.

SPIEGEL, M. (1968). "Mathematical Handbook of Formulas and Tables," McGraw-Hill, Inc., New York, 107.

STEPHENS, R. R., LIND, R. C. AND GUILIANO, C. R. (1987). "Phase conjugate master oscillator-power amplifier using $BaTiO_3$ and AlGaAs semiconductor diode lasers," *Appl. Phys. Lett.* **50**, 647-649.

STEPHENS, R. R., CRAIG, R. R., NARAYANAN, A. A., LIND, R. C. AND GIULIANO, C. R. (1989). "Single and multiple element 4-pass phase conjugate master oscillator power amplifier using diode lasers," *Optics News* **15**, no. 12, 11-12.

STOVER, H. L. AND STEIER, W. H. (1966). "Locking of laser oscillators by light injection," *Appl. Phys. Lett.* **8**, 91-93.

SWANSON, E. A., ABBAS, G. L., YANG, S., CHAN, V. W. S. AND FUJIMOTO, J. G. (1987a). "High-speed electronic beam steering using injection locking of a laser-diode array," *Opt. Lett.* **12**, 30-32.

SWANSON, G. J., LEGER, J. R. AND HOLZ, M. (1987b). "Aperture filling of phase-locked laser arrays," *Optics Lett.* **12**, 245-247.

SUHRE, D. R. (1986). "Randomly phased geometrical laser array," *Appl. Opt.* **25**, 3916-3918.

TALBOT, W. H. F. (1836). "Facts relating to optical science No. IV," *Philos. Mag.* **9**, 401-407.

TANIGAMI, M., OGATA, S., AOYAMA, S., YAMASHITA, T. AND IMANAKA, K. (1989). "Low-wavefront aberration and high-temperature stability molded micro Fresnel lens," *IEEE Photonics Tech. Lett.* **1**, 384-385.

WANG, S., WILCOX, J. Z., JANSEN, M. AND YANG, J. J. (1986). "In-phase locking in diffraction-coupled phased-array diode lasers," *Appl. Phys. Lett.* **48**, 1770-1772.

WILCOX, J. Z., JANSEN, M., YANG, J. J., OU, S. S., SERGANT, M. AND SIMMONS, W. W. (1987a). "Supermode selection in diffraction-coupled semiconductor laser arrays," *Appl. Phys. Lett.* **50**, 1319-1321.

WILCOX, J. Z., JANSEN, M., YANG, J. J., PETERSON, G., SILVER, A., SIMMONS, W., OU, S. S. AND SERGANT, M. (1987b). "Supermode discrimination in diffraction-coupled laser arrays with separate contacts," *Appl. Phys. Lett.* **51**, 631-633.

WILCOX, J. Z., SIMMONS, W. W., BOTEZ, D., JANSEN, M., MAWST, L. J., PETERSON, G., WILCOX, T. J. AND YANG, J. J. (1989). "Design considerations for diffraction coupled arrays with monolithically integrated self-imaging cavities," *Appl. Phys. Lett.* **54**, 1848-1850.

WINTHROP, J. T. AND WORTHINGTON, C. R. (1965). "Theory of Fresnel images. I. Plane periodic objects in monochromatic light," *JOSA* **55**, 373-381.

YAELI, J., STREIFER, W., SCIFRES, D. R., CROSS, P. S., THORNTON, R. L. AND BURNHAM, R. D. (1985). "Array mode selection utilizing an external cavity configuration," *Appl. Phys. Lett.* **47**, 89-91.

YANG, J. J. AND JANSEN, M. (1986). "Single-lobed emission from phase-locked array lasers," *Electron. Lett.* **22**, 2-4.

YARIV, A. (1976). "Introduction to Optical Electronics," Holt, Rinehart, and Winston, New York, 60-62.

Chapter 9

COHERENCE AND ITS EFFECT ON LASER ARRAYS

M. Lurie

David Sarnoff Research Center, Princeton, New Jersey

I. INTRODUCTION TO COHERENCE

A. Discussion

The term *coherent* is often applied very casually to lasers, to distinguish them from more ordinary lamps which are called *incoherent.* But coherence is a specific, precisely defined property of radiation. Quantitative details about coherence are important for determining the performance of lasers and particularly arrays of lasers. In this chapter, we will define coherence, discuss its significance in lasers and laser arrays, and describe techniques for its measurement.

In this introduction we present a general discussion of coherence before defining it in detail later on. We apologize for the lack of rigor that creates, but it is in the interest of setting the stage for what follows.

Ideal lasers and incandescent lamps are examples of the limiting cases of complete coherence and complete incoherence. However, to completely understand the performance of more general devices, we must deal with the general case of partial coherence. We will show that coherence among the elements of an array of emitters has a strong influence on the peak intensity in the far field and on the distribution of power among the lobes.

SURFACE EMITTING
SEMICONDUCTOR
LASERS AND ARRAYS

ISBN 0-12-244070-6

High coherence, as well as uniform phase, is required to achieve a single large far-field lobe containing most of the array power. In fact, achieving high peak intensity in the far field is a major incentive for producing coherent sources. Axial intensity is sometimes specified as the Strehl ratio, the ratio of the actual peak intensity to that which would be produced by an ideal source of the same geometry, so the Strehl ratio is also strongly dependent on coherence. Surprisingly, coherence has only a weak effect on the width of the lobes. Even with coherence reduced to a low value, far-field lobes remain narrow, but are substantially reduced in intensity. It may be even more surprising that for arrays with large numbers of elements, very little coherence is needed to produce deep nulls in the far field, forming far-field patterns having high contrast, but again low intensity. We conclude from this that although coherence is necessary to produce high peak intensity, simple observation of the *shape* of the far field, without absolute intensity values, tells us very little about the degree of coherence of a source.

After we discuss partial coherence we will consider other beam properties such as phase aberrations that also degrade array performance and produce effects on far-field patterns that appear similar to reduced coherence, but are fundamentally different.

B. Importance of Coherence

A very simple list of the desirable properties of lasers would begin with:

1. Narrow beam divergence
2. Narrow spectral linewidth
3. Power
4. Efficiency

These can be produced without coherence. Coherence is important because coherence is required to produce all of them at the same time.

Narrow beam divergence and narrow spectral linewidth, in fact coherence, can be produced without lasers, both in theory and in practice. In 1934 and 1938, van Cittert and Zernicke published calculations showing how an incoherent source subtending a small enough angle at an object illuminates that object with spatially coherent light (van Cittert, 1934; Zernicke, 1938). The most universal example is starlight, which is spatially coherent over many meters when it reaches Earth, even though the star is an incoherent emitter.[1] Coherent light can be produced at normal laboratory distances

[1] The coherence of starlight has been used to measure stellar diameters. See Michelson A. A. and Pease F. G. (1921). Starlight is also an example of spatially coherent but temporally incoherent light, since it has a very broad spectrum.

with a small source like a pinhole of several microns diameter illuminated with incoherent light (Lurie, 1966). The light reaching a screen several centimeters from the pinhole will have high spatial coherence. If the light is passed through a sufficiently narrow bandpass filter it will also have temporal coherence. Then the illumination at the screen will be coherent. It could be collimated to produce a beam with narrow divergence and small spectral linewidth. However, the pinhole and the filter each transmit a very small fraction of the light. To *efficiently* produce a coherent beam, the source itself must be coherent.

C. Definition of Coherence

We will now treat coherence quantitatively.[2] Consider the electromagnetic field at point P_1 and time t. We use only a scalar electromagnetic theory here and use the complex scalar $\mathbf{V}(P_1, t)$ to represent the amplitude and phase of the field. The term mutual coherence, $\Gamma_{12}(\tau)$, is defined as the time average correlation between the electromagnetic field at that point and time, and the field at some other point and time $\mathbf{V}(P_2, t+\tau)$. That is

$$\Gamma_{12}(\tau) \equiv \langle \mathbf{V}(P_1, t)\mathbf{V}^*(P_2, t+\tau)\rangle, \tag{1}$$

where the angle brackets denote the time average.

The more common quantity, intensity I_1 at P_1, is just the time average of the amplitude squared, so

$$I_1 = \langle \mathbf{V}(P_1, t)\mathbf{V}^*(P_1, t)\rangle. \tag{2}$$

We see that mutual coherence is a generalization of intensity. If the two points and the two times are the same in the mutual coherence function, then $P_1 = P_2$, and $\tau = 0$, so $\Gamma_{11}(0) = I_1$. In general, $\Gamma_{12}(\tau)$ depends on the choice of points and times and on the time-dependent behavior of the radiation.

It is convenient to normalize Γ to get

$$\gamma_{12}(\tau) \equiv \frac{\Gamma_{12}(\tau)}{\sqrt{\Gamma_{11}(0)\Gamma_{22}(0)}} = \frac{\Gamma_{12}(\tau)}{\sqrt{I_1 I_2}}. \tag{3}$$

$\gamma_{12}(\tau)$ is called the complex degree of coherence. The magnitude $|\gamma_{12}(\tau)|$ is called simply the coherence, the subject of this chapter. When $|\gamma_{12}(\tau)| = 1$ we say that the radiation is coherent; when $|\gamma_{12}(\tau)| = 0$, we say it is incoherent; in between we say it is partially coherent.

[2] For more details of the theory used here, see Born and Wolf (1964).

It is sometimes convenient to consider the spatial and temporal dependence separately, although that is an approximation. Spatial coherence is the time average correlation between fields at separate points in space, but measured at the same time, that is the correlation between $\mathbf{V}(P_1, t)$ and $\mathbf{V}(P_2, t)$. Similarly, temporal coherence is the time average correlation between fields measured at the same point but at different times, $\mathbf{V}(P_1, t)$ and $\mathbf{V}(P_1, t+\tau)$. Clearly, temporal coherence is closely related to spectral width, but spatial coherence is not. Using the definitions above, spatial coherence is $|\gamma_{12}(0)|$ and temporal coherence is $|\gamma_{11}(\tau)|$.

The time over which the averages are taken affects the result. In a measurement, the time is the duration of the measurement itself. Until recent years that duration was always understood to be a very large number of cycles of optical radiation. Today that is not necessarily so. In the domain of measurements using only a few cycles of radiation, coherence is not a useful concept any more than monochromaticity. In this discussion, we will assume that measurements occupy enough time for the quantities frequency, phase and time average to be meaningful. On the other hand, even in this classical regime, one can imagine situations in which the coherence would be different if the measurement took 1 s or 1 μs to complete.

D. Coherent and Incoherent Light, the Limiting Cases

The limiting cases are the easiest to illustrate. A simple example of completely coherent radiation is a plane monochromatic wave. By definition, both amplitude and phase (and, therefore, frequency) are constant for all time. The field at one point and time, $\mathbf{V}(P_1, t)$, is completely correlated with that at any other pont and time, $\mathbf{V}(P_2, t+\tau)$. Then

$$\begin{aligned}\Gamma_{12}(\tau) &= \langle \mathbf{V}(P_1, t)\mathbf{V}^*(P_2, t+\tau)\rangle \\ &= |\mathbf{V}(P_1, t)|\,|\mathbf{V}^*(P_2, t+\tau)|\langle \arg \mathbf{V}(P_1, t) \arg \mathbf{V}^*(P_2, t+\tau)\rangle \\ &= \sqrt{\Gamma_{11}(0)\Gamma_{22}(0)} \cdot \text{const phase term}, \end{aligned} \tag{4}$$

since the amplitudes are independent of time. Then,

$$\gamma_{12}(\tau) = \frac{\Gamma_{12}(\tau)}{\sqrt{\Gamma_{11}(0)\Gamma_{22}(0)}} = 1 \cdot \text{const phase term} \tag{5}$$

and

$$|\gamma_{12}(\tau)| = 1. \tag{6}$$

Even if the wavefront had a highly irregular shape, as might be produced by a high-order *spatial* mode of a laser or by a perfect beam passing through stationary ground glass, it would still be coherent. It might not be a useful wave because it would diverge, have low Strehl ratio and be difficult to focus to a small spot, but it would still yield $|\gamma_{12}(\tau)| = 1$ and be coherent. That is because the phase variations across the wavefront would not vary with time, so the correlations over time would be high. In theory at least, the phase variations for this coherent radiation could be cancelled with a suitable correction plate to restore the quality of the beam.

At the other extreme, consider a wave in which the phase varies randomly with time and position across the wavefront. Then $\mathbf{V}(P_1, t_1)$ and $\mathbf{V}(P_2, t_2)$ are uncorrelated and it is clear that

$$\Gamma_{12}(\tau) = \langle \mathbf{V}(P_1, \tau)\mathbf{V}^*(P_2, t+\tau)\rangle = 0 \tag{7}$$

for any choice of P_1, P_2 and τ, making $\gamma_{12}(\tau) = 0$. The radiation is incoherent. Black body radiation fits that description.

As an example of spatial (only) coherence, consider an emitter producing a wave that is plane, but having a frequency that varies randomly with time. Each propagating wavefront has uniform phase, but there is no correlation of phase among the wavefronts emitted at different times. The fields $\mathbf{V}(P_1, t)$ and $\mathbf{V}(P_2, t)$, measured at *different positions* along a single wavefront, but which were emitted by the source at the *same time*, are correlated. (This implies that the points P_1 and P_2 are equidistant from the source). Then $\gamma_{12}(0) = 1$ and this radiation is spatially coherent. The fields emitted at *different times*—which are the fields that would be measured at unequal distances from the source—are uncorrelated whether or not they are measured at the same point. Then $\gamma_{11}(\tau) = 0$ for $\tau \neq 0$ and the radiation is temporally incoherent.

It is more difficult to imagine an emitter having only temporal coherence. Consider an emitter producing a phase that varies across the wavefront, but a frequency that is nearly constant. That is possible if the phase variation is slow compared to the frequency of the radiation, implying that $\Delta\lambda \ll \lambda$. Radiation of that form is called quasimonochromatic. A simple example is monochromatic radiation that has passed through moving ground glass. Then the fields at two *different times*, but measured at the *same position*, $\mathbf{V}(P_1, t)$ and $\mathbf{V}(P_1, t+\tau)$, are correlated and $\gamma_{11}(\tau) = 1$. (There is a limitation on τ, called the coherence time, inversely related to the rate of the phase variations. See the section below on linewidth.) However, if the radiation is measured at *different positions*, $\gamma_{12}(0) = 0$ because of the phase variations. Therefore the radiation is spatially incoherent but temporally coherent.

E. Interference Between Two Partially Coherent Point Sources

To illustrate a calculation with partially coherent light, consider the simple interference between two partially coherent point sources in Fig. 1.

Using Eqs. (2) and (3) we can show that the intensity in the interference pattern formed by the two points S_1 and S_2 can be written as

$$I = I_1 + I_2 + 2\sqrt{I_1 I_2}\,|\gamma_{12}(\tau)| \cos\left[k(s_2 - s_1) - \alpha_{12}(\tau)\right], \tag{8}$$

where $\tau = (s_2 - s_1)/c$ is the difference in the times that the interfering radiation left the sources, I_1 and I_2 are the intensities of the sources S_1 and S_2 by themselves, and $k = 2\pi/\lambda$. This is true in general, but we will now assume that the radiation is quasimonochromatic, meaning that the linewidth $\Delta\lambda \ll \lambda$. Then $\alpha_{12}(\tau)$, which is the phase of $\gamma_{12}(\tau)$ and is also the phase difference between the radiation from S_1 and S_2, varies slowly with $\tau = (s_2 - s_1)/c$, compared to the variation of $k(s_2 - s_1)$. Therefore, we let $\alpha_{12}(\tau) = \alpha_{12}$. The effect of $k(s_2 - s_1)$ is to produce a set of cosinusoidal fringes with varying $s_2 - s_1$, while the effect of α_{12} is to shift the entire fringe pattern.

If $\gamma_{12}(\tau) = 1$, then Eq. (8) becomes the elementary expression for the interference between two points radiating with phase difference α_{12},

$$I = I_1 + I_2 + 2\sqrt{I_1 I_2} \cos\left[k(s_2 - s_1) - \alpha_{12}\right], \tag{9}$$

which shows the well-known cosinusoidal variation as the path difference changes.

If $\gamma_{12}(\tau) = 0$, then instead of Eq. (9) we get

$$I = I_1 + I_2, \tag{10}$$

the obvious result of simply summing the individual intensities in the incoherent case.

The result in Eq. (8) can be used to measure the coherence between two small sources by measuring the maxima and minima of the fringes in their

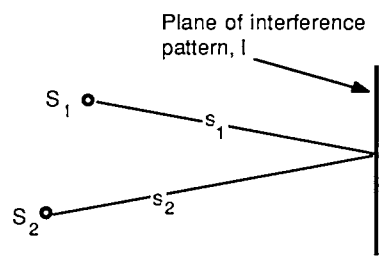

Fig. 1. Interference between two partially coherent point sources.

interference pattern. This forms the basis of a technique for measuring coherence, described in detail in Section IV.

II. THE FAR FIELD OF A 1-D ARRAY OF EMITTERS HAVING ARBITRARY COHERENCE PLUS PHASE AND INTENSITY VARIATIONS

We will now generalize the preceding calculation to include a source with any number of emitters, each having finite extent. The assumptions are:

1. Any number of emitters, each with finite size, each coherent by itself.
2. Any degree of coherence γ_{mn} between emitter pairs.
3. Arbitrary intensities across the array, but constant across each emitter.
4. Arbitrary phases across the array, but either constant (piston phase) or linear phase (beam tilt) across each emitter.

We consider only the one-dimensional case. We characterize the array coherence in terms of the coherence γ_{mn} between emitters m and n. We further assume that the intensity of each emitter is constant across that emitter although the intensity can vary from one emitter to the next. The latter restriction is not a severe one because the far field is not highly sensitive to intensity variations. We limit the phase across each emitter to be either constant, producing what are called piston phase variations among emitters, or varying linearly with position, producing variations in beam pointing angles for each emitter. Of course statistical phase fluctuations are permitted or else the radiation would necessarily be coherent. Finally, we again assume the radiation is quasi-monochromatic.

The result of this calculation allows us to predict the far-field patterns of many actual laser arrays (Carlson *et al.*, 1987). Some of the restrictions can be removed easily, requiring only more computation.

A. Calculation of the Far Field

Consider the linear array of emitters described in the introduction to this section, having length a and center to center distance b, so the near field is as shown in Fig. 2. Our assumption of quasi-monochromatic radiation means that effects of spectral linewidth are negligible. That is true in the far field of nearly all diode laser arrays, even for lasers with linewidths of a few Ångströms, as shown in Section D on linewidth.

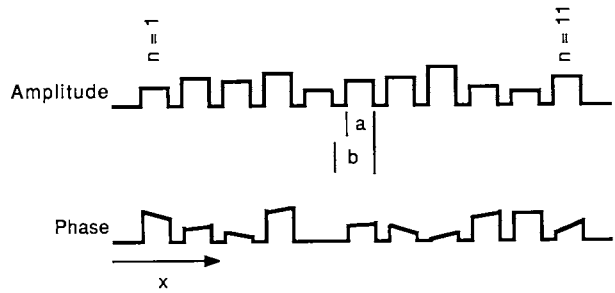

Fig. 2. A linear array of N emitters. Amplitudes and phases can vary among emitters, but amplitude is constant within each emitter and phase is either constant or linear with distance within each emitter. The coherence between element pairs is γ_{mn}.

The amplitude of the diffraction pattern of the nth emitter alone, at distance r_n from the source, can be written as

$$\mathbf{V}_n(\theta) = (I_n)^{1/2} F_n(\theta - \rho_n, r_n)\, U_n\left(t - \frac{r_n}{c}, \phi_n\right) \tag{11}$$

I_n is the intensity of the nth emitter. $F_n(\theta - \rho_n, r_n)$ contains the diffraction pattern shape as a function of θ, the $1/r_n$ amplitude dependence and various constants. It is centered at angle ρ_n due to the phase tilt of the nth source. U_n contains the time dependence and the constant (piston) phase ϕ_n of the radiation at the source.

For uniform emitters, F_n in the far field is given by $F_n(\theta - \rho_n, r_n) = K \operatorname{sinc}[a \sin(\theta - \rho_n)/\lambda]$. The quantity $1/r_n$ is absorbed into K because r_n is approximately constant in the far field for all θ of interest. By superposition, the total far-field amplitude due to the N emitters is

$$\mathbf{V}(\theta) = \sum_{n=1}^{N} (I_n)^{1/2} F_n(\theta - \rho_n, r_n)\, U_n\left(t - \frac{r_n}{c}, \phi_n\right). \tag{12}$$

The far-field intensity of the partially coherent array, $I_{\text{pcoh}}(\theta)$, is

$$\begin{aligned} I_{\text{pcoh}}(\theta) &= \langle \mathbf{V}(\theta)\mathbf{V}^*(\theta) \rangle \\ &= \left\langle \sum_{n=1}^{N} (I_n)^{1/2} F_n(\theta - \rho_n, r_n)\, U_n\left(t - \frac{r_n}{c}, \phi_n\right) \right. \\ &\quad \left. \times \sum_{m=1}^{N} (I_m)^{1/2} F_m^*(\theta - \rho_m, r_m)\, U_m^*\left(t - \frac{r_m}{c}, \phi_m\right) \right\rangle. \end{aligned} \tag{13}$$

This reduces to

$$I_{\text{pcoh}}(\theta) = \sum_{n=1}^{N} F_n^2 I_n + 2 \sum_{n=1}^{N} \sum_{m=n+1}^{N} (I_n I_m)^{1/2} F_n F_m \gamma_{mn} \cdot \cos\left[kb(m-n) \sin(\theta + \phi_m - \phi_n)\right]. \quad (14)$$

Equation (14) gives $I_{\text{pcoh}}(\theta)$, the intensity distribution in the far field of a partially coherent array of N emitters. The coherence between emitter pairs is γ_{mn}. Each emitter is itself coherent, has uniform intensity I_n, piston phase ϕ_n and beam tilt angle ρ_n with respect to $\theta = 0$, the normal to the array. γ_{mn} is the degree of coherence between emitters m and n. $F_n = K \operatorname{sinc}(a \sin(\theta - \rho_n)/\lambda)$ is the shape of the far field of the nth emitter.

Note that the first sum term in (14) is just the far field of an incoherent array of N emitters. If $\gamma_{mn} = 0$ for all m, n, the second term drops out.

Equation (14) can be used to calculate many properties of a variety of emitter arrays having any degree of coherence.

B. Far Field of a Typical Partially Coherent Array

We now use (14) to calculate several far field properties of arrays as a function of coherence. We use as an example an array consisting of 11 emitters, each with uniform intensity and phase, 300 μm long, with 150 μm spaces, for a total length of 4800 μm. Those are typical values for the grating surface emitting laser arrays discussed in other chapters. We also assume that the array is operating in the in-phase mode producing a single major lobe on the axis. The near field is shown in Fig. 3. Other modes can be treated just as easily. For example the anti-phase mode that produces two symmetric major lobes requires only letting $\phi_1 = 0$, $\phi_2 = \pi$, etc. in Eq. (14).

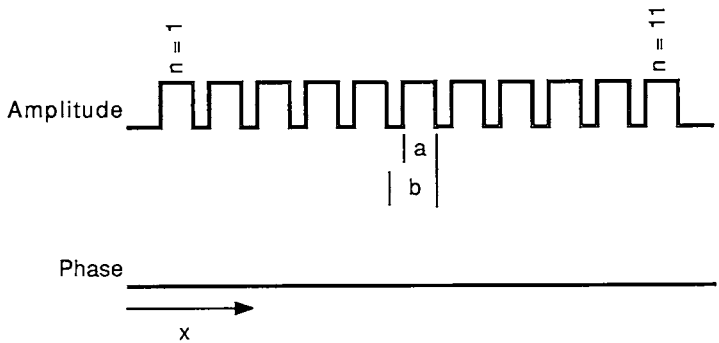

Fig. 3. Near field of a typical linear grating surface emitting laser array. $N = 11$, $a = 300$ μm, $b = 450$ μm, and $\lambda = 0.84$ μm. This near field shows uniform intensity and no phase or tilt variations.

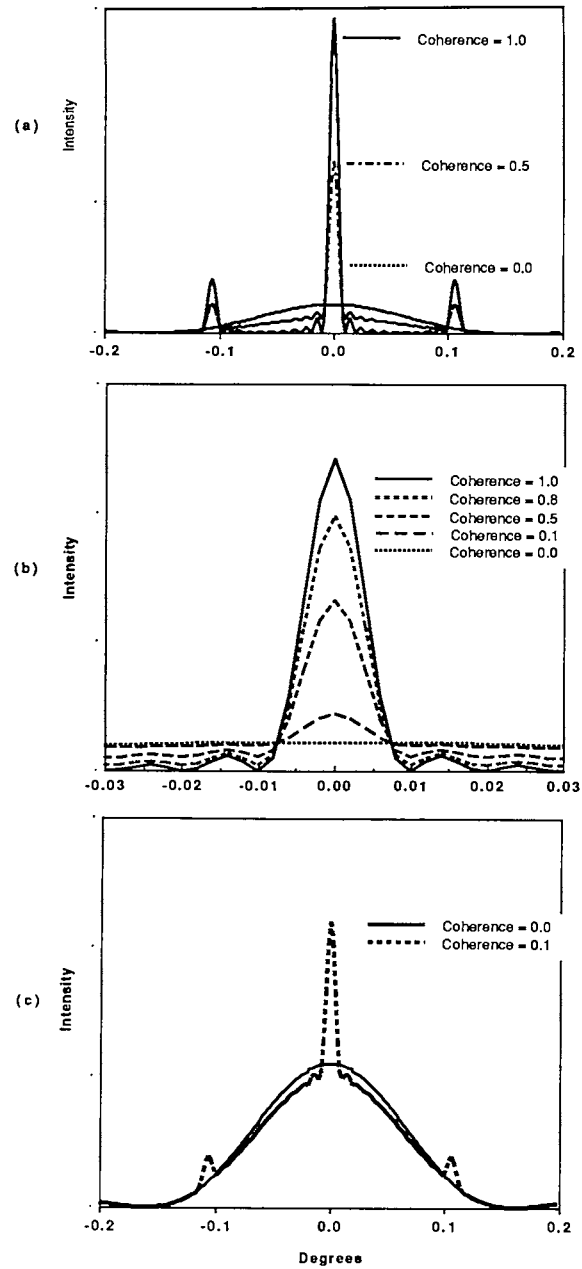

Fig. 4. Far field patterns of the array in Fig. 3 for various degrees of coherence between emitters. (a) First three lobes for incoherence, 50% coherence, and 100% coherence. (b) Detail of the central lobe showing that its general shape is established for low values of coherence. (c) Initial development of the narrow central lobe as coherence increases from 0 to 10%.

Figure 4 shows far fields of the array indicated in Fig. 3 for several degrees of coherence, calculated using Eq. (14). Note that the dimensions appear in (14) only in the function F_n and as a scaling factor in the argument of the cosine, so the results are more general than this specific example.

In this calculation, coherence between all pairs of emitters was assumed to be the same, although (14) is more general. That is, 50% coherence means that $\gamma_{1\text{-}2} = \gamma_{1\text{-}3} = \cdots = \gamma_{1\text{-}N} = \gamma_{2\text{-}3} = \cdots = 0.5$. The trends are the same if the coherence falls off for larger separations between emitters, i.e., if $\gamma_{1\text{-}4} < \gamma_{1\text{-}3} < \gamma_{1\text{-}2}$, as one might expect in a coupled array.

A surprising result of this calculation is that the general shape and half-width of the central lobe are largely independent of coherence. At 10% coherence, the lobe is only a small spike poking up above the incoherent background, but has approximately its ideal width.

That is shown more clearly in the next example. Equation (14) was applied to a similar array with 21 elements. The variation of the central lobe with coherence is shown in Fig. 5. The peak intensity varies linearly with coherence but the full width at half maximum (FWHM) of the lobe changes only slightly. The width to the first minima is independent of coherence.

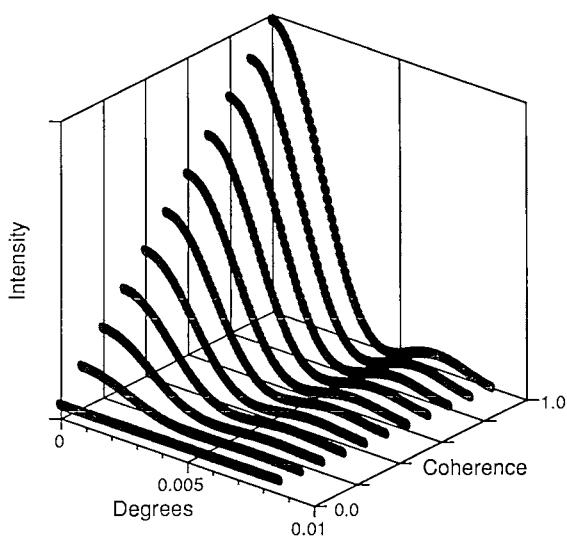

Fig. 5. The far field of an array showing the variation of the central lobe with coherence. The array consists of 21 emitters, each 300 μm long on 600 μm centers. $\lambda = 1.0$ μm. Note that the location of the first minimum of the pattern is independent of coherence, the lobe FWHM and the depth of the nulls change only slightly, and the peak intensity varies linearly with coherence.

C. Effects of Partial Coherence on Far-Field Properties

1. Lobe Width as a Function of Coherence

It may be surprising to see from Figs. 4 and 5 that the width of the central lobe is nearly independent of coherence. It may be less surprising if we point out that the location of the first minimum of the far-field pattern is determined by the emitter geometry. With the onset of coherence, the central lobe begins to rise out of the incoherent background as a small spike that is no wider than the fully coherent lobe. As coherence increases, more energy goes into the central lobe, but the width and general shape do not change much. This is emphasized in Fig. 6 which shows the FWHM of the central lobe as a function of coherence for two 11-emitter arrays. The FWHM changes very little for coherence between 20% and 100%. The figure also shows that the fill factor[3] affects the lobe width only at very low coherence.

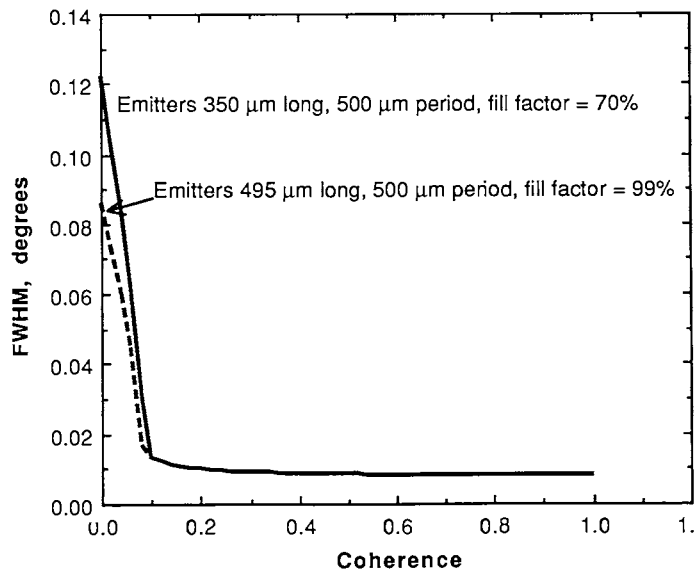

Fig. 6. The FWHM of the central far-field lobe as a function of coherence for an array of 11 emitters, based on the calculations described in the text. In this example the coherence is the same for all emitter pairs. Emitters are 350 μm long on 500 μm centers yielding a fill factor of 70%. Overall length is 5350 μm. $\lambda = 0.84$ μm. The 99% fill factor array is a good simulation of a single, continuous emitter.

[3] Fill factor is the ratio of the emitting area of a source to its total area.

2. *Peak Power on Axis as a Function of Coherence: Strehl Ratio and Power-in-the-Bucket*

Although the *width* of the central lobe does not depend strongly on coherence, the *height* or peak intensity does. As we have pointed out, the need for high peak intensity is a major motivation for producing coherent beams. Peak intensity is sometimes specified as the Strehl ratio, defined as the ratio of the actual peak intensity in the far field to that of an ideal emitter. The meaning of ideal emitter is subject to interpretation. We will assume for these arrays that the ideal emitter has the same geometry as the actual array, but produces uniform plane monochromatic (coherent) waves from all emitting elements. Figure 7 shows the dependence of Strehl on coherence. It is linear in this simple example in which the coherence is always assumed to be the same for all pairs of emitters, regardless of their separation. The Strehl ratio is independent of fill factor, although the actual intensity on axis is larger for higher fill factor.

Another measure of useful power is power-in-the-bucket (PIB), defined as the fraction of the total emitted power that falls within a given aperture, or bucket. We define that aperture here as the angle between the first zeros of the far-field pattern of an ideal emitter defined just as in the preceding paragraph. PIB is then the fraction of the total power within an aperture

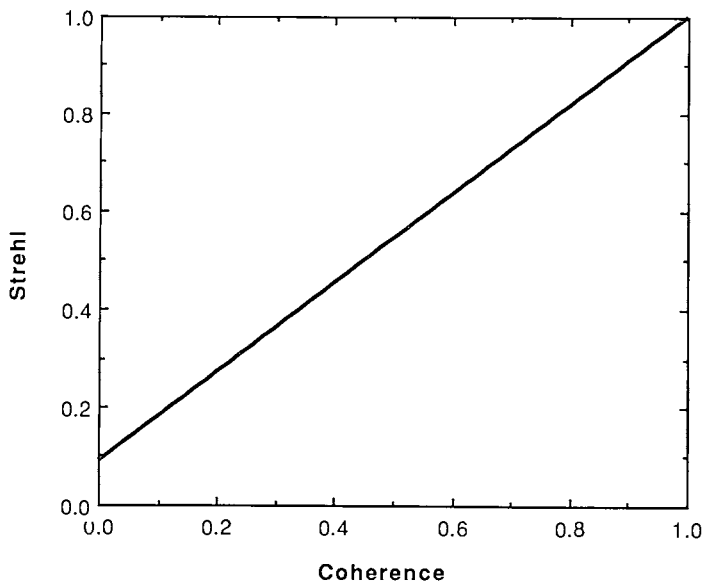

Fig. 7. Strehl ratio versus coherence for the same 11-emitter array as in Fig. 6.

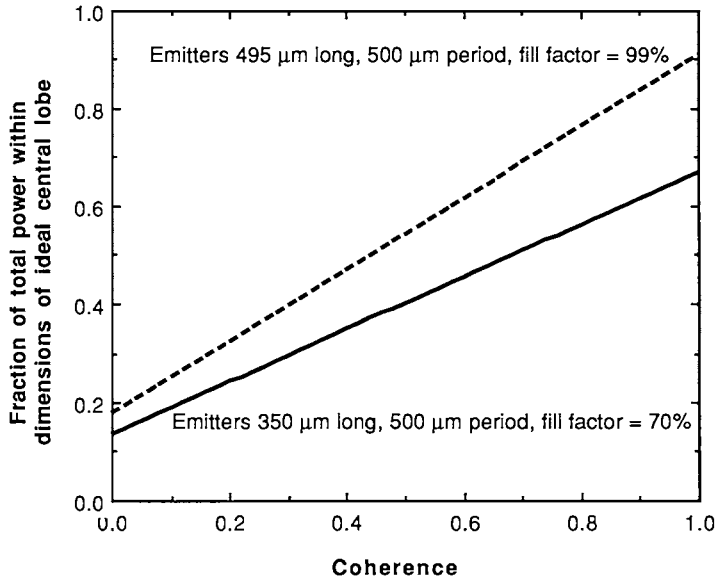

Fig. 8. Power-in-the-bucket versus coherence for the 11-emitter linear array in Fig. 6. The bucket here is an aperture the size of the diffraction limited central lobe between its zeros.

the size of the ideal central lobe. The effect of coherence on PIB for the 11-emitter array above is shown in Fig. 8. PIB depends linearly on coherence in this case, as did the Strehl. However, PIB also depends on fill factor, since the energy in the side lobes increases with lower fill factor. The maximum PIB for a single uniform, coherent emitter with length equal to the entire 11-emitter array is easily shown analytically to be 90.3%. That corresponds closely to the $\gamma = 1$, 99% fill factor array, confirming these numerical calculations for that case.

Note that all the previous calculations apply to linear arrays. If a two-dimensional array had the same geometry and coherence extended to both dimensions, then the results would have to be squared. For example, an ideal square array with 99% fill factor and coherence = 1 would have PIB = $0.90^2 = 0.81$.

3. Contrast in the Far-Field Pattern as a Function of Coherence

We showed earlier that the FWHM of an array far-field pattern does not depend strongly on coherence. The contrast, or the fringe visibility in the far field, does depend on coherence, but that dependence varies strongly

with the number of elements in the emitting array. Let us define a normalized contrast, C, in the intensity distribution as

$$C = \frac{I_{\max}}{I_{\min}}, \tag{15}$$

and the visibility, V, as

$$V = \frac{I_{\max} - I_{\min}}{I_{\max} + I_{\min}}. \tag{16}$$

The dependence of C and V on coherence can be calculated using Eq. (14) for specific cases. The relation of either of these to coherence depends on N, the number of elements in the array, and on the details of the distribution of coherence in the array, as well as on aberrations. For a two-element array with equal intensities, which is the same as the well known two-slit experiment of elementary optics, we will show later that V is a good approximation to γ. An example of that is shown in Fig. 9.

For comparison, Fig. 10 shows far field patterns for an array of 21 emitters having coherence between all pairs of 100%, 80% and 20% ($\gamma = 1.0$, 0.8 and 0.2), and no amplitude or phase aberrations. Although one can distinguish between these extreme cases, notice that the visibility is higher than the coherence for the $\gamma = 0.8$ case, and much higher for the $\gamma = 0.2$ case. For large N the incoherent component of the intensity is spread over such a large angle compared to the narrow coherent component that its effect even at the nulls is small, so the visibility and contrast remain high even for low coherence. However, the total integrated incoherent energy is significant and reduces the energy in the central lobe as has been shown.

It is even more misleading to interpret the quality of an emitted beam from a measurement of only the central region of a far-field pattern. Figure 11 shows the central lobe of the same 21-emitter array with $\gamma = 1$, 0.8 and 0.2, plotted with approximately equal peak heights on the page, as one might take this data in a laboratory. Without knowing the absolute intensities shown on the vertical axis, the patterns reveal little about the coherence or Strehl rato, particularly if there is some uncertainty about the zero level.

Figure 12 shows V as a function of γ for various values of N, the number of emitters in the array, assuming that the coherence $\gamma_{mn} = \gamma$ is the same between all pairs of emitters and there there are no intensity or phase variations across the array. For arrays with more than 20 elements, we see that $V > 90\%$ for any $\gamma > 50\%$.

An important conclusion of this is that visibility and contrast are not good measures of coherence except for arrays with few elements.

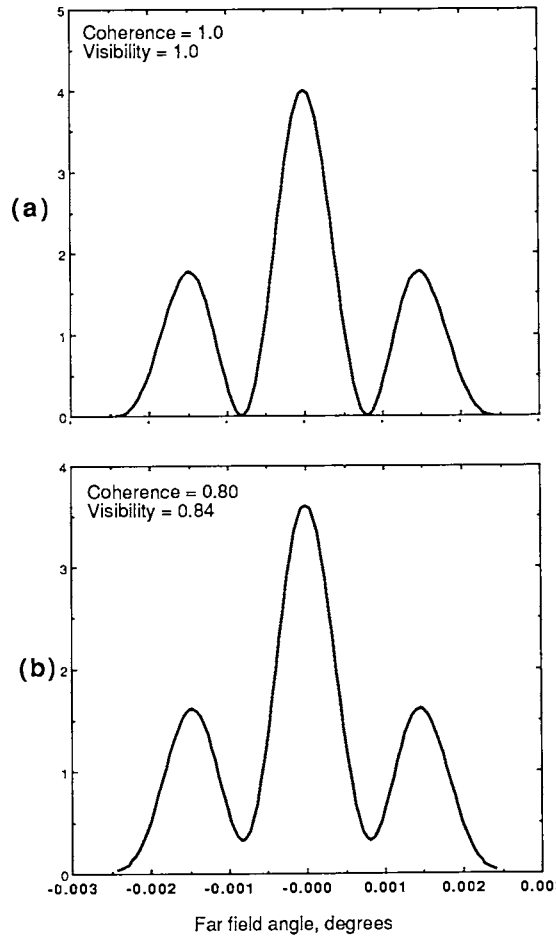

Fig. 9. Far fields of an array of only two emitters with equal intensity, showing that the visibility V is approximately equal to the coherence γ. (a) $\gamma = 1.0$, $V = 1.0$. (b) $\gamma = 0.80$, $V = 0.84$.

D. Effect of Linewidth

The preceding calculations assumed quasi-monochromatic light, i.e., that the linewidth could be ignored. We will show here that this is true in the far field of most lasers and arrays.

For any linewidth Δf, we would expect intuitively that fields emitted by the source at times differing by τ would remain at constant phase difference, or be temporally coherent, as long as $\tau \ll 1/\Delta f$. That corresponds to observing the fields emitted by two points on the source having different optical path

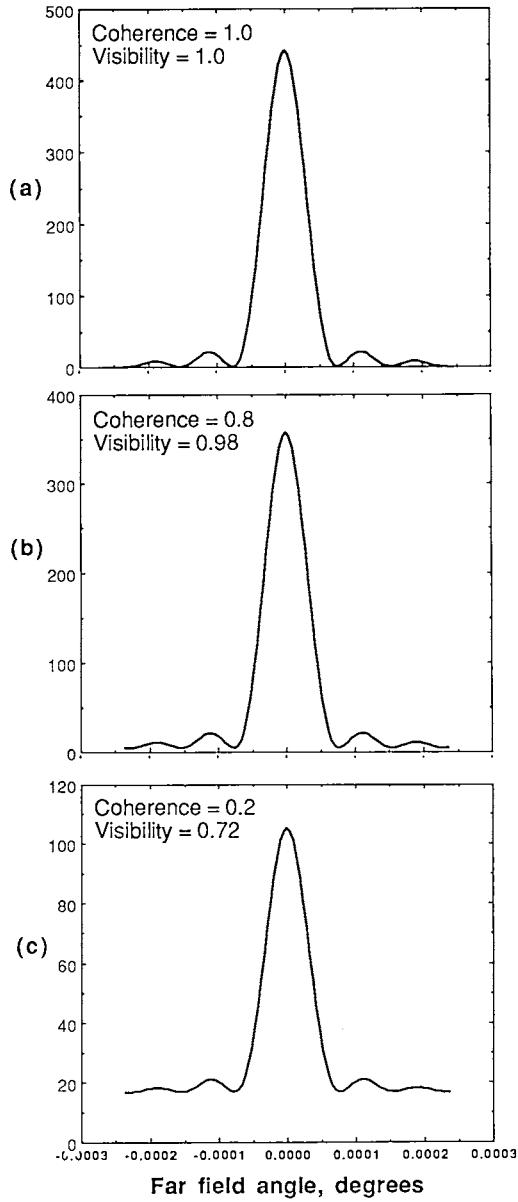

Fig. 10. Far fields of a 1-D array of 21 emitters showing that for this array neither the visibility nor depth of the nulls indicates coherence. In this array, when the coherence is reduced to 20% the visibility of the pattern is still 72%. Each emitter is 300 μm long on 600 μm centers, is coherent, and has uniform amplitude and phase. Wavelength is 972 nm.

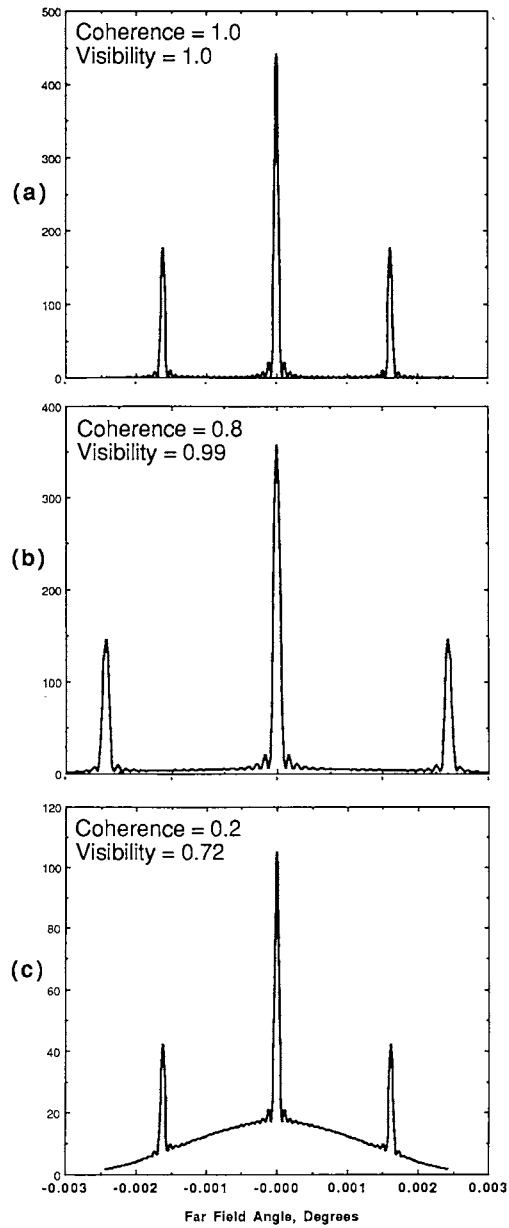

Fig. 11. The central lobe of the far field of the 21-emitter array for $\gamma = 1$, 0.8 and 0.2, showing that the shape of the pattern, without absolute intensity information, is not a good indicator of coherence or Strehl.

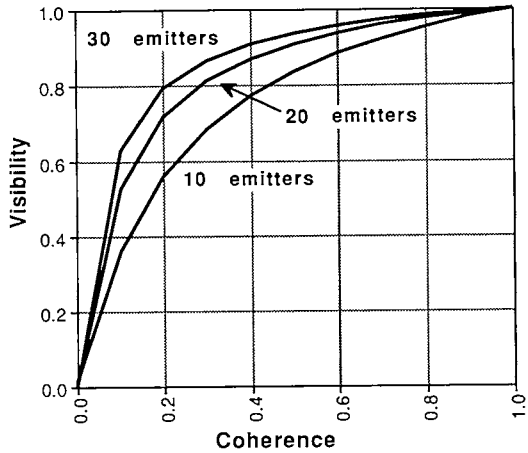

Fig. 12. The dependence of visibility V on coherence γ for various values of N, the number of emitters in the array, for an array in which coherence $\gamma_{mn} = \gamma$ is the same between all pairs of emitters and in which there are no intensity or phase variations across the array.

lengths to the observer, s_j and s_i, such that $s_j - s_i = c\tau \ll c/\Delta f$. The path difference $s_j - s_i$ at which the beam loses coherence is called the coherence length l. In this intuitive case, $l = c/\Delta f$. More precisely, we define coherence length as $l = c\tau$ where τ is the value that yields $\gamma_{11}(\tau) = 0$ or $1/e$ or some other small value chosen for a particular case. Then as long as the path differences $s_j - s_i \ll l$, we have $\gamma_{11}(\tau) \gg 0$ and the effect of temporal coherence or spectral linewidth is negligible. (One can show that $\gamma_{11}(\tau)$ is a constant times the Fourier transform of the line spectrum, which allows us to calculate actual values for τ and l. The results are close to the intuitive $l = c/\Delta f$.) Table I illustrates some typical values of coherence length, using the approximation

$$l \approx \frac{c}{\Delta f}. \tag{17}$$

For the dimensions of most diode lasers, and even arrays, path differences from any point on the array to any point in the far field receiving significant intensity are usually <1 mm. According to Table I, temporal coherence (and linewidth) has negligible effect on those far fields for linewidths of even 1 Å. For the same reason, measuring coherence by observing far-field interference patterns yields only the spatial coherence. Of course there are examples in which path differences can be much larger, in which case extremely high values of temporal coherence are required.

Table I

Linewidth and coherence length for a spectrum centered at $\lambda = 850$ nm ($f = 3.5 \times 10^{14}$ Hz)

$\Delta\lambda$	Δf	Coherence Length, l
1.0 nm (10 Å)	400 GHz	0.7 mm
0.1. nm (1 Å)	40 GHz	7 mm
2.0×10^{-6} nm	1 MHz	300 meters

There are simple demonstrations of the fact that the far-field pattern of a typical laser or array is independent of linewidth. For example, consider that the first zero of the far-field pattern of a uniform source with length $D \gg \lambda$ is located at

$$\sin \theta_0 = \frac{\lambda}{D} \approx \theta_0 \tag{18}$$

so

$$\frac{d\theta_0}{\theta_0} = \frac{d\lambda}{\lambda}. \tag{19}$$

The quantity $d\lambda/\lambda$ is usually much less than one for any laser. For example, if $d\lambda = 10$ Å and $\lambda = 1$ μm, then 10 Å/1 μm = 0.001. Then $d\theta_0/\theta_0 \ll 1$ and the zeros of the far field pattern essentially overlap for the entire range of wavelengths, yielding a total far-field pattern nearly identical to that of a source with zero linewidth. That is true even for this broad linewidth of 10 Å.

This does not contradict the fact that different laser modes produce different far fields. Although the modes have different wavelengths, it is the difference in spatial distribution that is responsible for the different far-field patterns.

E. Effects of Aberrations Not Related to Coherence

Lasers may have defects that alter the output in ways that resemble partial coherence, but are independent of it. Since coherence is a correlation over time, it is not affected by any stationary aberration in a beam. Stationary aberrations, such as a distorted wavefront, do not imply low coherence.

The important distinction between the two is that the stationary aberrations can be fixed by stationary corrections, at least in principle, like a suitably figured transmitting correction plate, whereas low coherence cannot be improved by any stationary element. High peak intensity can be restored, at least in principle, for a laser with a badly distorted wavefront. But nothing can be done to restore the peak intensity of a laser with low coherence.

1. *Phase and Tilt Errors*

Figure 13 shows an example of the effects of random piston phase errors among the array elements. The far field of our earlier 21-element array is shown, assuming $\gamma = 1$ and no tilts in the outputs. The array is ideal except for the piston phase errors among the emitters. In this example, the Strehl ratio is reduced to 0.5, and there is a shift of the peak to a small positive angle because of the phases. Many extra peaks are formed, but many of the nulls between them remain deep. Tilt angles among the emitters of up to a few lobe widths produce only small shifts in the lobes because the main steering effect is from interference. However, adding tilt to the piston phase errors of Fig. 13 increases the deterioration slightly. Figure 14 shows the result of piston phase similar to that used in the previous figure, but

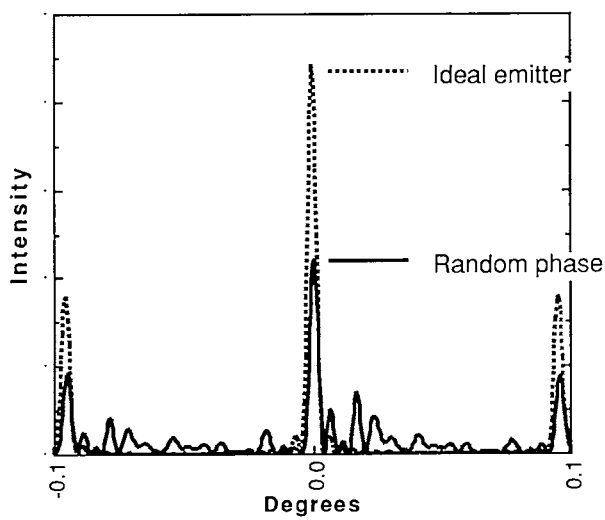

Fig. 13. Far field of a 21-element array that is ideal except for random piston phase errors among the emitters, compared to the array without phase errors. Strehl ratio = 0.5. The array elements are 300 μm long on 600 μm centers. Wavelength is 1.0 μm. The peak random phase error is 3.0 radians.

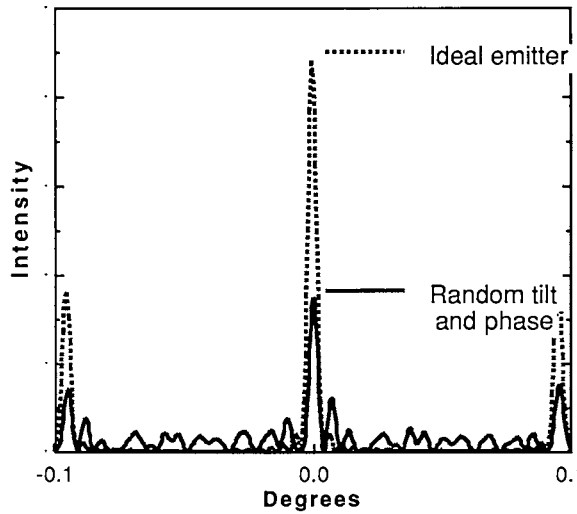

Fig. 14. Far field of the 21-element array with both random tilt (beam-pointing) errors and piston phase errors, as described in the text. Strehl ratio is reduced to 0.4.

with the required tilt added to make the phases constant across the gaps between the emitters (the gain sections in the case of a GSE array). The Strehl ratio is reduced from 0.5 to 0.4.

The effects of these phase errors are similar to partial coherence, in that they reduce Strehl and power in the bucket, and alter the far-field pattern, but they do not imply low coherence (Evans *et al.*, 1989).

In both of these examples the far fields could be restored to the ideal values by placing suitable phase-correcting plates, time invariant, in front of the arrays, because the coherence is one. Of course for that to be practical, the aberrations would have to be stable, and the correcting plates would have to be manufacturable. On the other hand, degradation caused by partial coherence can never be eliminated with any stationary correction.

2. *Nonuniform Intensities*

The effects of nonuniform intensity on far-field patterns of emitting arrays are much smaller than those of phase aberrations, so much so that in some cases uniform intensities can be used in calculations with acceptable errors. This follows from the fact that the Fourier transform of a function is much less sensitive to amplitude variations than to phase variations. Figure 15

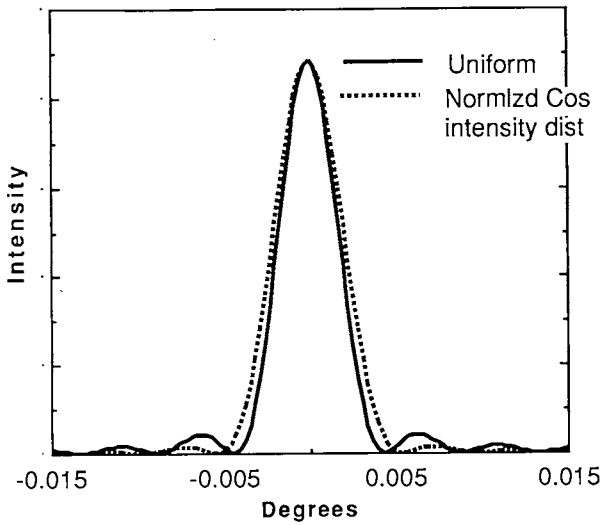

Fig. 15. Far field of the 1-D, 21-emitter coherent array with (a) uniform intensity, and (b) cosinusoidal variation of intensity from element to element, as in an evanescently coupled array. The peaks have been normalized.

compares the far fields of an ideal array of 21 emitters in which the near field intensity is uniform to one in which it is a cosinusoidal distribution typical of an evanescently coupled array. In this example, the far field produced by the cosine distribution is very slightly wider and has reduced side lobes as expected.

III. FAR FIELD PROPERTIES OF COHERENT AND INCOHERENT 2-D ARRAYS

Before leaving the subject of the effects of coherence on array properties, it is useful to go through one more example, a simple calculation of the peak power of a 2-D array for the coherent and incoherent cases, which clearly shows the importance of high coherence (Lurie *et al.*, 1988).

Consider a rectangular array of $N = n_x \times n_y$ emitters, each with dimensions $s_x \times s_y$, and periodicity $l_x \times l_y$ as in Fig. 16. As before, we assume that each emitter is itself a coherent source, uniform in intensity and phase. In the coherent case all the lasers are also coherent with each other. If $\gamma_{ij}(\tau)$ is the coherence between the ith and jth lasers, then $\gamma_{ij}(\tau) = 1$ for the coherent

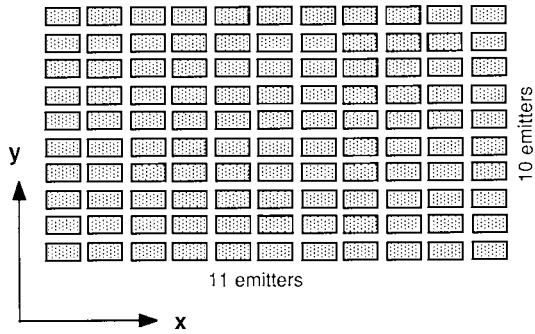

Fig. 16. A rectangular array of $N = n_x \times n_y$ lasers, or any emitters. The dimensions of each emitter are $s_x \times s_y$, with spacings of d_x and d_y along the corresponding axes. The periodicity is $l_x \times l_y$, where $l_x = s_x + d_x$, etc. Values for a typical laser array of the grating surface emitting (GSE) type used in several numerical examples here are $n_x = 11$, $n_y = 10$, $s_x = 300\ \mu\text{m}$, $s_y = 3\ \mu\text{m}$, $d_x = 150\ \mu\text{m}$, and $d_y = 3\ \mu\text{m}$. Then $N = 110$ and the overall size of the array is $4800\ \mu\text{m} \times 57\ \mu\text{m}$. The figure does not represent the true aspect ratio of this array.

array, and $\gamma_{ij}(\tau) = 0$ for the incoherent array, for all i, j, and τ. We will calculate the far fields, particularly the peak intensities.

If the array is incoherent, then the outputs of the component lasers are independent and interference effects are not possible. The far-field pattern is then just the sum of the intensities of the patterns of the individual lasers. In this example all the individual rectangular emitters are identical so each produces a far-field intensity $I_1(f_x, f_y)$ given by

$$I_1(f_x, f_y) = P_1 \cdot \left(\frac{s_x s_y}{\lambda z}\right)^2 \operatorname{sinc}^2(s_x f_x) \operatorname{sinc}^2(s_y f_y)$$

where P_1 is the power per area of each emitter, s_x and s_y are its dimensions, and $f_x = x_0/\lambda z, f_y = y_0/\lambda z$ indicate position in the far field, with z the distance to the far field plane and x_0, y_0 the coordinates in the far field. The intensity I_{incoh} of the incoherent array is just N times that of one emitter, so

$$I_{\text{incoh}}(f_x, f_y) = N \cdot I_1(f_x, f_y). \tag{21}$$

At the peak at $f_x = f_y = 0$,

$$I_{\text{incoh}}(0, 0) = N \cdot I_1(0, 0) = N P_1 \left(\frac{s_x s_y}{\lambda z}\right)^2. \tag{22}$$

The low, broad curves in Fig. 17 show the intensity along the f_x axis for the incoherent 110-element array of Fig. 16. The beam divergence of the array, determined by $I_1(f_x,f_y)$, is the same as that of any one emitter or laser, but the intensity, and of particular interest the axial intensity

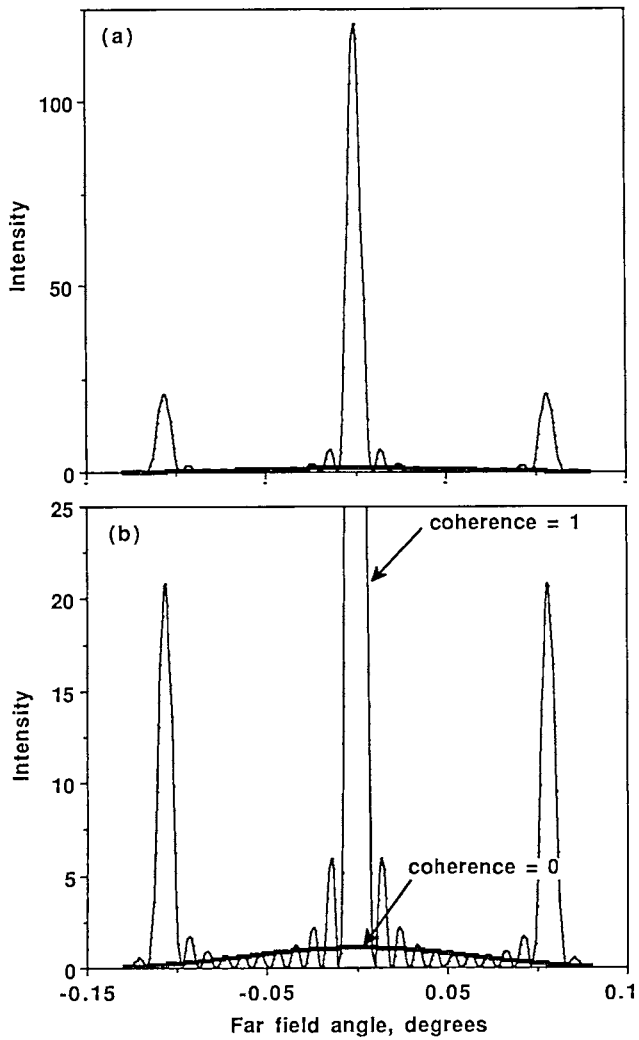

Fig. 17. Calculated far fields along the longitudinal (long) axis of the array of 110 emitters in Fig. 16 showing the difference betweeen the coherent and incoherent arrays. The lower figure is expanded to show the incoherent peak, 110 times lower than the coherent peak.

$I_{\text{incoh}}(0, 0)$, is N times larger. The spectrum of the array will contain the frequencies of each emitter.

If the same array is perfectly coherent, meaning here that all the individual emitters are coherent with each other, then the output is again easy to calculate, although the expression contains more terms. For the coherent array of $N = n_x n_y$ uniform emitters,

$$I_{\text{coh}}(f_x, f_y) = N^2 P_1 \cdot \left(\frac{s_x s_y}{\lambda z}\right)^2 \operatorname{sinc}^2(s_x f_x) \operatorname{sinc}^2(s_y f_y) \times \left(\frac{\sin \pi n_x l_x f_x}{n_x \sin \pi l_x f_x}\right)^2 \left(\frac{\sin \pi n_y l_y f_y}{n_y \sin \pi l_y f_y}\right)^2. \tag{23}$$

In terms of $I_1(f_x, f_y)$, the far field of one of the emitters,

$$I_{\text{coh}}(f_x, f_y) = N^2 \cdot I_1(f_x, f_y) \cdot \left(\frac{\sin \pi n_x l_x f_x}{n_x \sin \pi l_x f_x}\right)^2 \left(\frac{\sin \pi n_y l_y f_y}{n_y \sin \pi l_y f_y}\right)^2 \tag{24}$$

Now the peak at $f_x = f_y = 0$ is,

$$I_{\text{coh}}(0, 0) = N^2 \cdot I_1(0, 0) = N I_{\text{incoh}}(0, 0). \tag{25}$$

This is similar to the incoherent case, but the intensity of each emitter is now multiplied by N^2 instead of N. The pattern is also modulated by the two sine terms that come from the interference among the emitters and produce the comb functions along both array axes. The comb lies within the envelope that is the far-field pattern of any one emitter. The x_0 dependence of this pattern is also shown in Fig. 17 using the scaled parameter f_x. The increase in axial intensity by an additional N times is a major incentive for making large arrays coherent.

IV. MEASUREMENT OF COHERENCE

Techniques for measuring coherence follow directly from the effects we have calculated. Several tempting approaches are not suitable. We showed in a previous section that for an array with more than two elements, the visibility in the far-field pattern can remain high even with low coherence. Similarly, the width of the central lobe remains narrow as coherence decreases. Furthermore, broadened lobes can be produced by an array with high coherence if it has phase aberrations. The conclusion is that the far

field of an array with $N > 2$ tells us very little about coherence unless we know the Strehl ratio and all the aberrations.

The most straightforward way to measure the coherence of a source (Carlson *et al.*, 1987) is to measure the visibility V of the fringes produced by interfering just pairs of points across its surface, as indicated in Fig. 18. For an array, one forms interference between pairs of emitters, or portions of emitters. A mask with apertures to transmit the outputs of any two emitters is placed in front of the array. The resulting interference pattern can be calculated from Eq. (14) although it reduces to a very simple result in this two-emitter case. Using the definition of V from Eq. (16),

$$V = \frac{I_{\max} - I_{\min}}{I_{\max} + I_{\min}},$$

we can show that for two emitters

$$V = 2|\gamma_{12}(\tau)| \frac{\sqrt{I_1 I_2}}{I_1 + I_2} \tag{26}$$

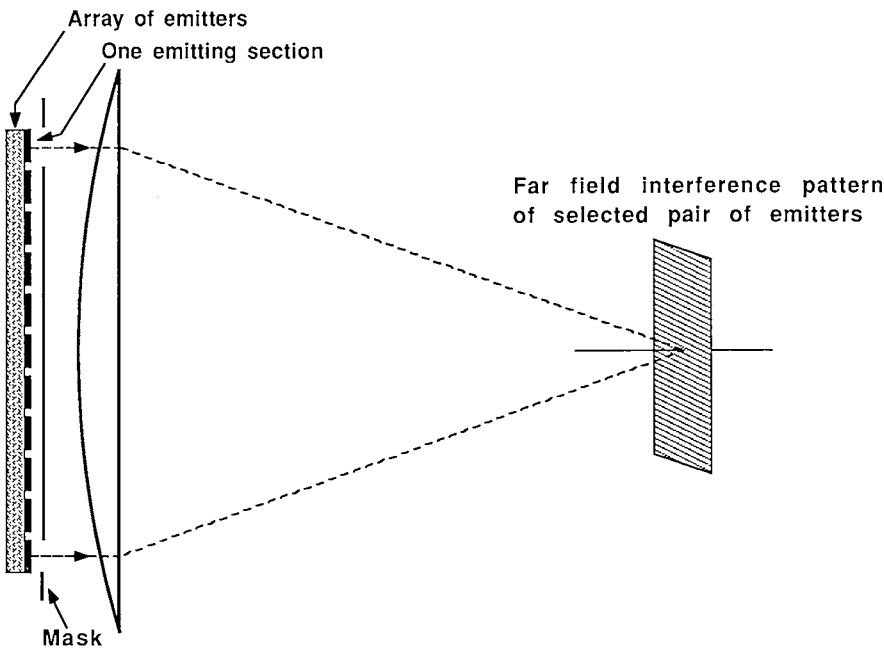

Fig. 18. A method for measuring coherence.

and

$$|\gamma_{12}(\tau)| = V\frac{I_1 + I_2}{2\sqrt{I_1 I_2}} \tag{27}$$

where I_1 and I_2 are the intensities due to the individual emitters measured separately. If $I_1 = I_2$, then we have simply

$$|\gamma_{12}(\tau)| = V. \tag{28}$$

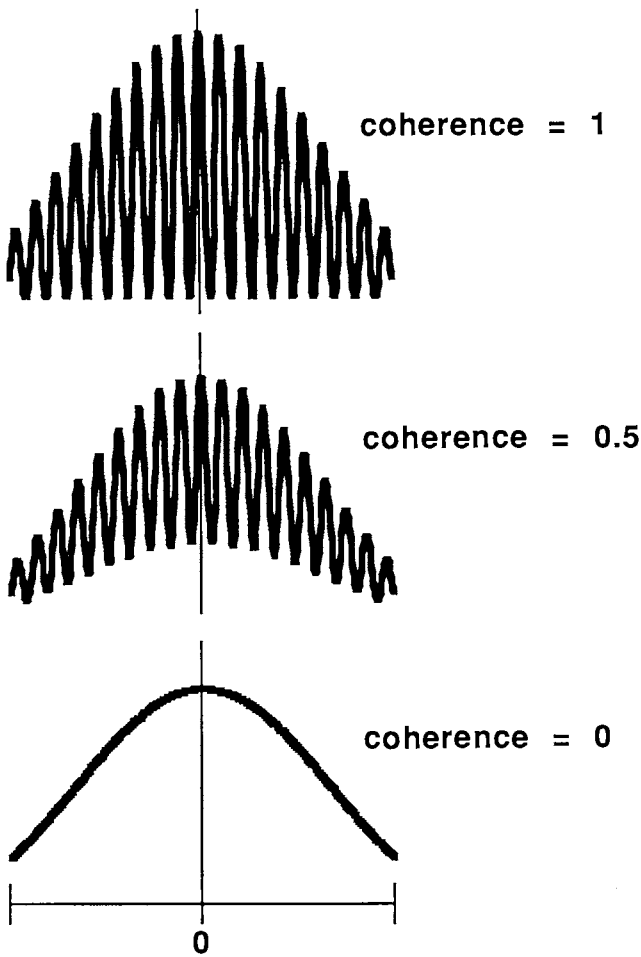

Fig. 19. Calculated interference patterns formed by two emitters with various degrees of coherence, illustrating a method for measuring coherence.

Even if the intensities are quite different, V is still a good approximation to $|\gamma_{12}(\tau)|$. For example, if $I_1 = 2I_2$, then $|\gamma_{12}(\tau)| = 1.06\ V$.

Calculated fringe patterns for two emitters with equal intensities are shown in Fig. 19, for three values of coherence.

The lens in Fig. 18 is not necessary. The shape of the interference pattern will be changed by removing the lens, because the pattern will not necessarily be in the far field, but the visibility will remain the same. The lens is sometimes required simply to cause the two outputs to overlap.

Because the two path lengths from the emitters to the interference pattern are nearly equal, effects of temporal coherence are negligible and the quantity measured is the spatial coherence, $\gamma_{12}(0)$, as discussed above. The spectral linewidth, or the presence of many lines, has little effect on the interference pattern unless path differences approach the coherence length of the radiation, shown in Table I to be millimeters or more for most lasers.

Figure 20 shows a measurement of coherence between two emitting sections of a GSE laser array using this method. The two low, broad curves are I_1 and I_2, the measured intensities in the diffraction patterns of the individual emitters, which of course show no interference. The fringes are the interference pattern of the two emitters. The measured visibility is $V = 0.86$, so $\gamma \cong 0.86$ for those two emitters, where the approximation is

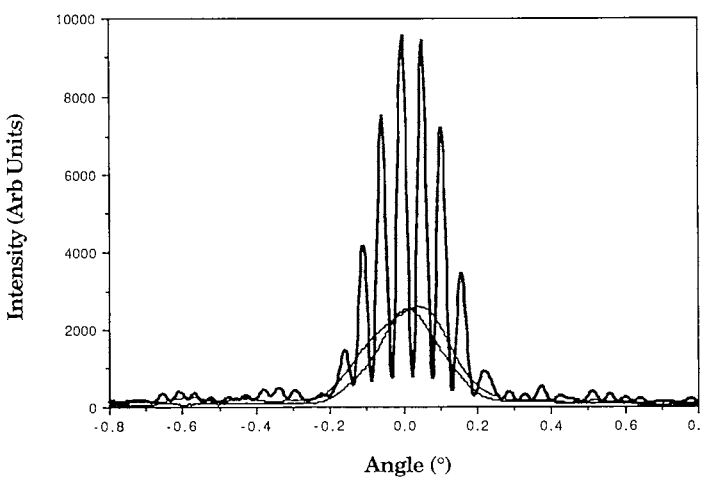

Fig. 20. Measurement of coherence between two emitting sections of a GSE laser array by observing their interference pattern. The two low broad curves are the diffraction patterns of the individual emitters. Emitters are 300 μm long on 450 μm centers. This measurement is of emitters 3 and 5. They are 900 μm apart.

very good. In this measurement $\tau = 0$ because the path lengths from the two emitters to the detector are equal. Coherence between other pairs of emitters is obtained by moving the masks or using masks with other spacings between the apertures.

V. SUMMARY

We defined coherence and presented a general expression for the far field of a linear array of emitters having any degree of coherence among them. Other variables such as nonuniform emitter intensity and phase were included. We also calculated the far field of a 2-D array for the special cases of coherence and incoherence. The analysis demonstrated that an important motivation for producing arrays having high coherence is to obtain high peak beam intensity. For an array of N emitters, all in phase, each producing axial intensity I at some distant point, the axial intensity produced by the entire array is NI if the array is incoherent, but is N^2I if the array is completely coherent. Between these extremes, the axial intensity and Strehl ratio vary approximately linearly with coherence. However, the width of the central lobe does not depend strongly on coherence. We showed that the FWHM of the central far-field lobe of an in-phase array is nearly unchanged as coherence decreases from one to nearly zero at which point the lobe disappears completely. Similarly, for a large array ($N \gg 2$) the degree of coherence of the array has only a small effect on the intensity in the minima (not the peaks) and on the visibility of the pattern. It follows that the degree of coherence is not obvious from far-field observations unless you also know what the peak intensity would be for coherence equal to one. In practice, that is often hard to know because so many properties besides coherence affect that peak. It follows that measurement of the far-field pattern usually tells us very little about the coherence of the source array. Finally, we distinguished between coherence phenomena, which are related to correlations over time, and stationary phenomena such as nonuniform intensity or phase across an array, which do not affect coherence. Stationary effects can be corrected with stationary components such as phase correction plates, at least in principle, whereas reduced coherence cannot.

Finally, we described a straightforward if tedious method for measuring coherence, and showed an example of a measurement for two elements of a GSE laser array.

A few important conclusions are summarized below, particularly because they are not all intuitive.

1. High coherence is essential in an array of emitters to produce the expected high peak intensity in the far field, high Strehl ratio and large power in the bucket.
2. The shape of the far-field pattern is not a good measure of coherence unless the Strehl ratio is known. Even with low coherence, an array will produce nearly the ideal shape in the far field. In particular, for arrays with more than a few elements, neither the width of the far-field lobes nor the intensities of the minima nor the visibility of the fringes is strongly dependent on coherence. But the intensities of the maxima are strongly dependent.
3. A badly distorted shape in the far field does not indicate low coherence. Other aberrations can disturb the far field.
4. The most direct way to measure the spatial coherence of an array is to measure the visibility in interference patterns produced by pairs of emitting elements. Spatial coherence is completely characterized by making this measurement for all pairs of emitters, although that is a tedious task for a large array.
5. Temporal coherence or linewidth is not a factor in determining the far-field pattern in most lasers or arrays. Path length differences are generally much smaller than the coherence length, even for broad linewidth lasers.
6. The term *diffraction-limited* should not be applied to a laser or array based only on the FWHM of a far-field lobe. *Diffraction-limited* implies that the performance of a source approaches that of an ideal source, limited only by the laws of diffraction. We have seen that a source can produce far-field lobes with FWHM approximately the same width as the ideal case, but having lower intensity, lower Strehl ratio and lower power in the bucket. High coherence and an aberration-free beam are both required to produce true diffraction-limited performance.

REFERENCES

BORN, M. AND WOLF, E. (1964). *Principles of Optics*, Macmillan, London, 2nd ed, Sect. 10.3 and 10.4.

CARLSON, N. W., MASIN, V. J., LURIE, M., GOLDSTEIN, B. AND EVANS, G. A. (1987). "Measurement of the coherence of a single-mode phase-locked diode laser array," *Appl. Phys. Lett.* **51**, 643-645.

EVANS, G. A., CARLSON, N. W., HAMMER, J. M., LURIE, M., BUTLER, J. K., PALFREY, S. L., AMANTEA, R., CARR, L. A., HAWRYLO, F. Z., JAMES, E. A., KAISER, C. J., KIRK, J. B. AND REICHERT, W. F. (1989). "Two-Dimensional Coherent Laser Arrays Using Grating Surface Emission," *IEEE J. Quantum Electron.* **25**, 1525-1538.

LURIE, M. (1966). "Effects of partial coherence on holography with diffuse illumination," *J. Opt. Soc. Am.* **56**, 1369-72.

LURIE, M., AMANTEA, R., BUTLER, J. K., CARLSON, N. W., EVANS, G. A., HAMER, J. M. AND PALFREY, S. L. (Nov. 1988). *Proc. of LEOS Annual Meeting*, p. 429.

MICHELSON, A. A. AND PEASE, F. G. (1921). *Astrophys. J.* **53**, 249.

VAN CITTERT, P. H. (1934). *Physica* **1**, 201.

ZERNICKE, F. (1938). *Physica* **5**, 785.

Chapter 10

MICROCHANNEL HEAT SINKS FOR TWO-DIMENSIONAL DIODE LASER ARRAYS

J. N. Walpole and **L. J. Missaggia**

Lincoln Laboratory, Massachusetts Institute of Technology, Lexington, Massachusetts

I. INTRODUCTION

In high average power applications the output power of two-dimensional arrays of diode lasers, with array dimensions on the order of 1 cm^2 or larger, is limited by the ability of the heat sink to extract waste heat. For most types of surface emitting devices, power conversion efficiency on the order of 50–60% is feasible, but not much higher. Hence, if 100 W/cm^2 of average optical output is desired, then about 100 W/cm^2 of waste heat must be dissipated while maintaining an acceptably small temperature rise. Such a heat sink is possible only when the thickness of layers of thermally conducting material along the direction of the heat flux is made very small. As a matter of definition, we will describe heat sinks with millimeter or larger thickness as conventional heat sinks, while water-cooled heat sinks, discussed in the next paragraph with submillimeter thickness will be described as microchannel heat sinks. The term microchannel actually refers to the physical dimensions of the cross sections of the channels through which the cooling fluid flows, which also typically are submillimeter.

In conventional heat exchangers, a fluid or a gas (usually water or air) is used to cool a heat sink, which may include fin structures for increased heat-exchange efficiency. As described above, the thickness of the thermally

ISBN 0-12-244070-6

conducting material on which the active devices are mounted (from the heated surface to the plane of heat extraction by the coolant) is at least a few millimeters. Consider, for example, a uniform two-dimensional heat load of 100 W/cm^2 into a Cu heat sink consisting of a layer of Cu, 4 mm thick, followed by an ideal heat exchanger, i.e., no thermal resistance is associated with the heat extraction by the coolant. The solution to this simple heat flow problem of uniform one-dimensional heat flow across a uniform medium and into an isothermal heat reservoir is

$$R = t/\kappa, \tag{1}$$

where R is the thermal resistance of a unit area (1 cm^2) of the Cu layer, $t = 0.4$ cm is the thickness of the Cu, and $\kappa = 4.0$ W/°C cm is the thermal conductivity of the Cu. In this example, R has a value of 0.1°C cm^2/W, which means that the temperature rise at the surface of the heat sink for the 100 W/cm^2 heat load is 10°C. Note that R in Eq. (1) is the product of the thermal resistance and the heated area (analogous to the specific resistance used to describe electrical contracts). It is convenient to refer to this product as simply the thermal resistance rather than the product of thermal resistance and area. The distinction between these quantities can usually be made, when necessary, by quoting the relevant dimensions, i.e., °C/W or °C cm^2/W.

Of course, an ideal heat exchanger does not exist. However, the microchannel heat sinks discussed here may be good approximations to the ideal. For an area on the order of 1 cm^2 or larger, the thermal resistance of a microchannel heat sink is on the order of 0.1 °C cm^2/W, if the mechanical energy supplied to pump the coolant is kept below about 10 W/cm^2, and can be even lower for larger mechanical power. Hence, in our example, the optimum total thermal resistance would be the sum of the resistance calculated from Eq. (1) plus the resistance of the heat exchanger for a total of approximately 0.2°C cm^2/W. The corresponding temperature rise would be 20°C.

Clearly, a better thermal design would eliminate the layer of Cu, along with its 10°C temperature rise, if possible. Otherwise, as this example illustrates, a conventional heat sink design in which several millimeters or more of conducting material is used is at best on the order of two times higher in thermal resistance than a microchannel heat sink. Because of their relative thermal conductivities, a thickness of 4 mm of Cu, 2 cm of diamond, or about 1.5 mm of Si is thermally equivalent and equal to 0.1°C cm^2/W, or about the minimum practical thermal resistance that can be easily achieved in one-dimensional heat flow. Any practical heat sink for minimum thermal resistance should utilize material thicknesses in the heat sink much smaller than the above thicknesses.

In microchannel heat sinks, heat extraction occurs at distances on the order of 100 μm from the surface of the heat sink. The structure first proposed, built and analyzed by Tuckerman and Pease (1981a,b) and Tuckerman (1984), is simply a water-cooled heat sink with ordinary cooling fins but scaled down in size. Figure 1 shows a schematic illustration of such a structure. The heat sink has usually been made in Si though other

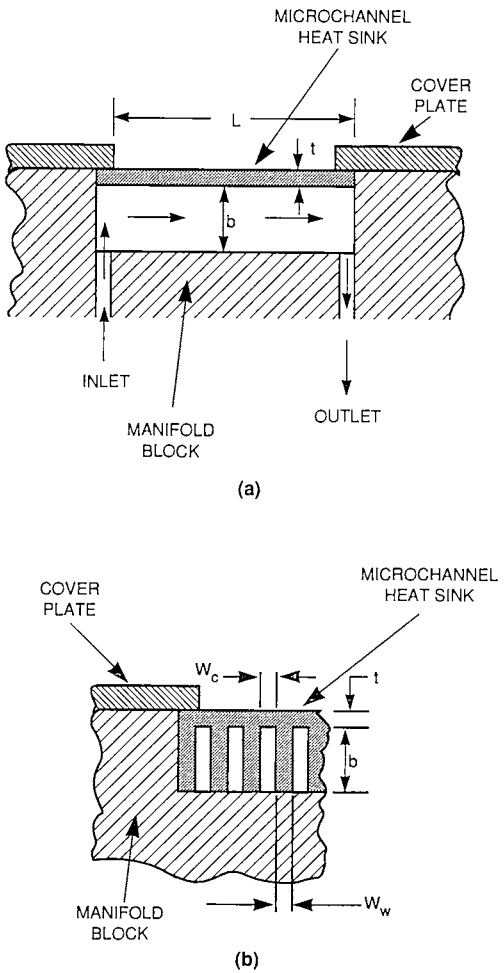

Fig. 1. Top view of microchannel heat sink in longitudinal cross section showing flow of coolant through a heat sink with channel length L. The bottom view shows a lateral cross section with channel width labeled W_c, fin width W_w, channel height b, and substrate thickness t. (Not to scale; L is typically much larger than the other dimensions.)

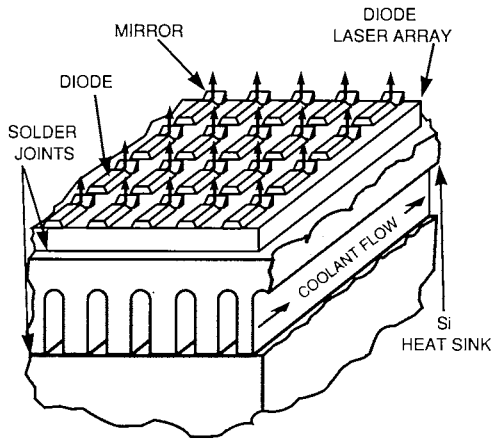

Fig. 2. Schematic illustration of a microchannel heat sink with a two-dimensional array of surface emitting diode lasers.

materials can be used. Silicon is easily etched or cut to form channels, it has relatively high thermal conductivity (~1.5 W/°C cm), and its thermal expansion coefficient is close to that of semiconductor materials. After channels are etched or cut into the heat sink material the heat sink is bonded to the manifold, and a cover plate is attached to seal the fluid. Fluid enters at one end of the channels and exits at the other. The channel length is L. The manifold includes connectors and other details to control and direct the fluid flow. In Fig. 1 the fin width is designated W_w and the channel spacing W_c. The thickness of the heat sink material above the channels is denoted by t.

Figure 2 is a schematic depiction of a monolithic two-dimensional diode laser array mounted on a microchannel heat sink. The array is shown with monolithically integrated external 45° beam deflectors, but any type of surface emitting geometry could obviously be used. The performance of such microchannel heat sinks will be analyzed here, and experimental measurements will be discussed. A design to improve temperature uniformity, in which the water flow direction alternates between adjacent channels, will be presented.

II. STATIC THERMAL CHARACTERIZATION OF MICROCHANNEL HEAT SINKS

Phillips has given a very thorough treatment of heat flow in microchannel heat sinks (Phillips, 1987; Phillips *et al.*, 1987; Phillips, 1988). Here, the

treatment will be brief. In the following, we use Phillips' notation to the extent possible. Figure 3 shows the major components of thermal resistance as identified by Phillips.

For a two-dimensional laser array, heat production near the surface of the laser wafer is generally nonuniform. In Fig. 3, the source of the heat flux is shown as localized in the solid rectangular areas on the surface of the wafer. There is an increase in the spatially averaged thermal resistance for a nonuniform heat flux compared to a uniform one because the heat must spread laterally. In most cases, as heat diffuses into the heat sink the heat flux develops into a uniform one-dimensional flow. When the flux becomes uniform within the laser wafer (before it enters the heat sink), the spreading resistance can be included as part of the resistance of the laser

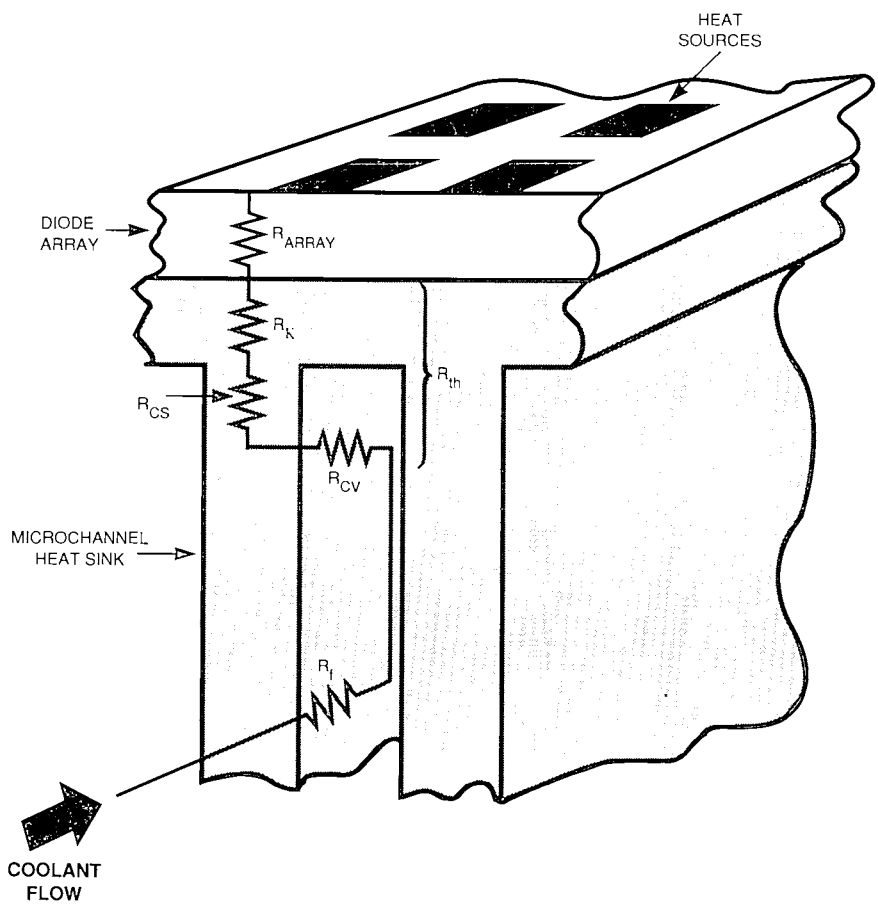

Fig. 3. Major components of thermal resistance.

array wafer R_{array} and dealt with separately. If the array is mounted junction side down, then the spreading resistance must be included as part of the heat sink resistance.

For the case in which the active laser regions are in long periodic stripes, heat spreading is essentially in two dimensions and can be calculated using the methods of Joyce and Dixon (1975) or employing the analytic approximation of Liau *et al.* (1988). This approach is discussed here since it also can be used to calculate the resistance associated with the constriction of heat flow into the fins. More generally, for other geometries, such numerical techniques as finite difference can be used. There is, in principle, an interface resistance between the laser wafer and the heat sink at the solder joint. Experimentally, this resistance appears to be negligible for thin solder joints. Note that the heat sink could be fabricated on the back side of the laser array wafer. This may not be useful in practice, since it is difficult to fabricate lasers and heat sinks on different sides of the same wafer and since the thermal conductivity of the laser wafer is generally poorer than that of other suitable heat sink material.

The heat sink itself has four major components of resistance, which will be denoted by R_κ, R_{cs}, R_{cv}, and R_{f}. The component R_κ is due to the finite conductivity κ_{w} of the heat sink material of thickness t. This component has the same form as (1),

$$R_\kappa = t/\kappa_{\text{w}}. \tag{2}$$

The next component, R_{cs}, is the resistance due to the constriction of the heat flux into the fins. As mentioned above, this component represents the inverse of the spreading resistance problem and can be calculated using the same techniques. Conformal mapping has been used (Liau *et al.*, 1988) to find the thermal resistance for a long striped heat source $2W$ wide, as shown in Fig. 4, spreading into a wider stripe $2s$ wide and v tall, which is (for a unit area)

$$R = \frac{2s}{\pi\kappa} \sinh^{-1}\left[\frac{\sinh(\pi v/2s)}{\sin(\pi W/2s)}\right] \approx \frac{2s}{\pi\kappa}\left[\frac{\pi v}{2s} + \ln\frac{1}{\sin(\pi W/2s)}\right] \tag{3}$$

for $v \geq s$. Hence, the increase in resistance due to the spreading (or constriction) is the difference between (3) and the resistance without constriction v/κ, and thus

$$R_{\text{cs}} = \frac{2s}{\pi\kappa} \ln\frac{1}{\sin(\pi W/2s)} \tag{4a}$$

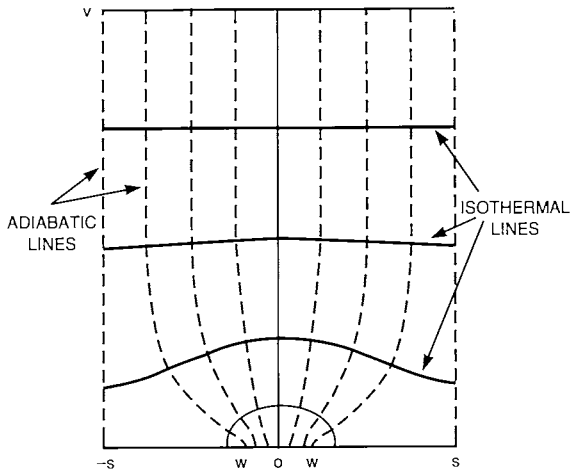

Fig. 4. Geometry for two-dimensional spreading resistance due to constriction, with the heat spreading from a width $2W$ into a width $2s$ over a distance v. The solid and dashed lines indicate the isotherms and adiabats, respectively.

$$R_{cs} \approx \frac{W_w + W_c}{\pi\kappa} \ln \frac{1}{\sin\left[\pi W_w/(2W_w + 2W_c)\right]}. \tag{4b}$$

(The result in Eq. (4a) was given by Kraus and Bar-Cohen (1983) without discussion of its derivation or the condition that $v \geq s$.) For our problem, $2s$ becomes $(W_w + W_c)$ and $2W$ becomes W_w, and hence Eq. (4a) becomes Eq. (4b). In any practical design, R_{cs} is small and not important except for precise evaluation of the thermal resistance.

The most important component, usually, is R_{cv}. It is determined by the convection heat transfer coefficient h, a function of fluid parameters which is most often experimentally determined. Once a value for h is obtained, the analysis is straightforward. The convection heat transfer coefficient is defined by the following relationship:

$$q = h(T_s - T_f), \tag{5}$$

in which q is the heat flux (in W/cm^2) from the fin surface at temperature T_s, and T_f is the mean fluid temperature. Hence, h has units of W/cm^2 °C. The heat flux can also be expressed as

$$q = \kappa_f \nabla T, \tag{6}$$

where κ_f is the thermal conductivity in the fluid and the gradient of T is evaluated in the fluid at the surface of the fin. If we define a thermal boundary layer δ_t as the width of the region across which the thermal

gradient is appreciable, then the thermal gradient can be expressed approximately as $(T_s - T_f)/\delta_t$. Hence, the convection heat transfer coefficient is on the order of κ_f/δ_t. This relationship shows explicitly that the thermal boundary layer should be thin for good convection heat transfer.

Since the experimental values of h are usually determined for flow in an enclosed channel, the channel surface is characterized by a single value of h. The total heat flow per unit length into a single channel is then given by

$$Q = h(W_c + 2b\eta_F)(T_s - T_f). \tag{7}$$

Here, the factor $(W_c + 2b\eta_F)$ is the effective inside perimeter of a channel, assuming that no heat flows through the bottom of the channel (a worst case). The fin efficiency η_F is given by the standard expression for cooling fins,

$$\eta_F = \tanh(N)/N, \tag{8}$$

where $N = (2hb^2/\kappa_w W_w)^{0.5}$. The heat flux q, which results from Q defined by (7) flowing in a width $W_w + W_c$, is given by $q = Q/(W_w + W_c)$. Hence, the thermal resistance component for a unit area due to convection heat transfer at the fins is

$$R_{cv} = (W_w + W_c)/[h(W_c + 2b\eta_F)]. \tag{9}$$

In order to develop appropriate values for h it is necessary to examine carefully the fluid flow conditions. As Phillips (1987, 1988) has explored in detail, for typical microchannel dimensions and fluid velocities there are three regimes of interest. These are fully developed laminar flow, developing laminar flow, and turbulent flow.

A. Fully Developed Laminar Flow

The simplest analysis of the heat flow in microchannel heat sinks assumes that the fluid flow condition in the microchannels is laminar and fully developed (Tuckerman and Pease, 1981a, 1981b; Tuckerman, 1984; Samalam, 1989). Fully developed implies that the width of the thermal boundary layer is fully established in a distance from the inlet (the thermal entrance length) that is short compared to the overall length of the channels. This case is particularly simple because for fully developed laminar flow between two walls spaced by W_c, the thermal boundary layer thickness is about a quarter of W_c. The thermal profiles developing from each wall meet in the middle to establish fully developed flow. As discussed previously, the thermal boundary layer must be small for good heat transfer. Therefore,

in fully developed laminar flow the width of the channels determines the heat transfer coefficient, which is thus independent of fluid velocity. However, channel width cannot be made arbitrarily small and flow cannot be reduced to zero, as will be shown later.

B. Developing Laminar Flow

In the developing laminar flow regime the thermal profiles either never reach the middle of the channels or meet there after developing for a significant fraction of the channel length. The onset of this regime occurs as fluid velocity or channel width is increased. The entrance length for laminar flow is given by

$$Le \approx 0.05 \text{ Re Pr } D. \tag{10}$$

Here, D is the hydraulic diameter, a characteristic dimension calculated from the cross-sectional area A and perimeter p of the channel, and given by

$$D = 4A/p = 2bW_c/(b + W_c) = 2W_c\alpha/(1+\alpha) \tag{11}$$

with α being the aspect ratio equal to b/W_c; Pr is the Prandtl number, which has a value of 6.4 for water at room temperature; and Re is the Reynolds number given by

$$\text{Re} = VD/\nu \tag{12}$$

with V being the mean velocity of the fluid and ν the kinematic viscosity.

From Eqs. (10–12) it can be seen that the entrance length increases nearly as the square of the channel width for large α and linearly with V. (It is important to note that ν is a significant function of temperature and should be carefully evaluated to accurately calculate the Reynolds number. Phillips (1987) found that ν and T_f should be determined self-consistently, which he did by numerically iterating in his calculations until a self-consistent value of $\nu(T_f)$ was obtained.) In the developing flow regime the value of R_{cv} will vary with length, becoming larger as the outlet is approached. Both this effect and a longitudinal variation of R_f, discussed below, lead to longitudinal temperature gradients. These may be troublesome for temperature uniformity, but the longitudinal heat flux generated by longitudinal gradients can usually be neglected in calculations of heat flow. The reason for this is that the vertical gradients (between the surface of the heat sink and the coolant) are much larger than the longitudinal gradients, except near the edges of the heated regions of the heat sink where diffusion of

heat into the unheated regions or into the package containing the heat sink may occur. This matter is also discussed in later sections.

It is convenient to introduce the dimensionless Nusselt number Nu given by

$$\mathrm{Nu} = hD/\kappa_f. \tag{13}$$

Using the approximate relationship $\delta_t \approx \kappa_f/h$, we have, in terms of the Nusselt number, $\delta_t \approx D/\mathrm{Nu}$. For fully developed laminar flow the maximum Nusselt number for rectangular channels is 8.23, which occurs for large values of α where D approaches $2W_c$. Hence, $\delta_t \approx W_c/4.1$, as stated above for fully developed laminar flow, and $h = 4.1\kappa_f/W_c$. These values are independent of the Reynolds number as long as fully developed laminar flow applies. The thermal entrance length Le is dependent on Reynolds number, however, as seen in Eq. (10). Turbulent flow in channels is considered to be established when the Reynolds number is greater than about 2300. As the turbulent transition is approached, Eq. (10) gives for water at room temperature

$$Le \approx 736D, \tag{14}$$

which, for a typical value of $D = 100$ μm, gives a thermal entrance length of 7.36 cm. Hence, undeveloped laminar flow occurs in heat sinks on the order of a centimeter or so in length well before the transition to turbulence.

C. Turbulent Flow

In turbulent flow the thermal boundary layer can become fully developed with a thickness that is a small fraction of the channel wall separation W_c. This is because turbulent motion is very effective in mixing the fluid inside the turbulent core of the channel, thus making velocity and temperature quite uniform in the core but with much sharper gradients in the boundary layer and much smaller boundary layers than in fully developed laminar flow. For turbulent flow the empirical correlation used by Phillips for the Nusselt number is given by

$$\mathrm{Nu}\,(z) = 0.012[1.0 + (D/z)^{2/3}](\mathrm{Re}^{0.87} - 280)\mathrm{Pr}^{0.4}. \tag{15}$$

For flow conditions just at the turbulent transition, i.e., $\mathrm{Re} = 2300$, and for large z (fully developed flow), (15) gives $\mathrm{Nu} = 14.1$, and hence $\delta_t \approx W_c/7.05$ and $h = 7.05\,\kappa_f/W_c$ in the limit of large α. The thermal boundary layer is a smaller fraction of the channel width than for fully developed laminar flow. For larger Reynolds numbers still smaller values for the thermal boundary layer and larger values of h will result. The thermal entrance length for

turbulent flow can be seen from (15) to be about

$$Le \approx 10D. \tag{16}$$

Hence, for channels that are on the order of a centimeter in length and have $D \approx 100\ \mu m$, the value of h is nearly constant over about 80 to 90% of the length in turbulent flow.

The final thermal resistance component R_f arises from the fact that the cooling fluid absorbs heat and the mean fluid temperature $T_f(z)$ increases in an approximately linear fashion as the fluid moves along the channel with an average velocity V in the z direction. For narrow channels this component can become more important than R_{cv}. From conservation of energy, the heat exchange equation is

$$\dot{m}[c_p(dT_f(z)/dz) + \rho_f^{-1}(dP(z)/dz)] = Q(z). \tag{17}$$

Here, $\dot{m}$ is the mass flow rate, given by $\dot{m} = \rho_f AV$, where ρ_f is the fluid density, A is given by $A = bW_c$; c_p is the heat capacity of the fluid; and $Q(z)$ is the rate at which heat enters a channel per unit length and is a constant for a uniform applied heat flux q given by $Q(z) = q(W_c + W_w)$, neglecting longitudinal diffusion of heat. The term in Eq. (17) involving the pressure gradient $dP(z)/dz$ represents the mechanical energy due to friction that is dissipated as heat in the fluid. Since the gradient is negative, this term adds to the temperature rise but is independent of the applied heat load. Hence, it is not a part of the thermal resistance and is included separately below. If we neglect that term and take Q as a constant, Eq. (17) can be integrated along the length of the fin z (which varies from 0 to L) to obtain for the temperature rise at any point z, $\Delta T_f = Qz/(\rho_f AVc_p)$. The thermal resistance per unit area contributed at any point z is obtained by

$$R_f(z) = \Delta T_f/q = z(W_c + W_w)/(\rho_f bW_c Vc_p). \tag{18}$$

This component varies from zero at the inlet to the maximum value for $z = L$ at the outlet. Diffusion of heat into unheated areas or into the package containing the heat sink reduces the maximum value of R_f and modifies the linear dependence on length as discussed later. If the term involving the pressure gradient is similarly integrated a temperature rise due to the hydrodynamic power (or the mechanical pump power) results that is clearly proportional to R_f. Hence, the additional rise in temperature of the water is given by

$$\Delta T_{mech}(z) = R_f(z)\frac{\Delta PVA}{(W_w + W_c)L} = R_f(z)p_H, \tag{19}$$

where ΔP is the total pressure drop and p_H is the total hydraulic (or

mechanical) power per unit area. Strictly speaking, Eq. (19) includes only the pressure drop integrated along the channels and not pressure drops due to bends or restrictions in the manifolds and connectors. These other pressure drops will nevertheless heat the water and can be approximately accounted for by including them here.

It is significant that the hydraulic power causes a temperature rise which is proportional to only one of the components of the thermal resistance. As a consequence the hydraulic power, in principle, can be larger than the heat load but still be effective in reducing the temperature at the surface of the heat sink.

In summary, the total thermal resistance from the junctions of the laser array devices to the inlet water includes the thermal resistance of the array and the heat sink

$$R_{\text{total}} = R_{\text{array}} + R_{\text{heat sink}}, \tag{20}$$

where the thermal resistance of the heat sink is composed of four terms:

$$R_{\text{heat sink}} = R_{\kappa} + R_{\text{cs}} + R_{\text{cv}} + R_{\text{f}}. \tag{21}$$

For later convenience, the first three of these components can be grouped and defined as $R_{\text{th}} = R_{\kappa} + R_{\text{cs}} + R_{\text{cv}}$, so that we have

$$R_{\text{heat sink}} = R_{\text{th}} + R_{\text{f}}. \tag{22}$$

Finally, the total maximum temperature rise is

$$\Delta T_{\max} = qR_{\text{total}}(L) + \Delta T_{\text{mech}}(L). \tag{23}$$

III. NUMERICAL TECHNIQUES

The theory outlined in the previous section uses several different approximations to model the complete three-dimensional problem of heat flow in microchannel heat sinks. A different approach is to simplify the modeling and use numerical calculations such as finite difference techniques to solve the heat flow problem.

In principle, even the fluid can be treated by finite difference equations in which heat is convected as well as conducted into and out of each finite difference unit cell. Two possible problems are encountered in treating the fluid by finite difference techniques. First, velocity profiles of the fluid must be known to properly treat both the developing laminar flow and the turbulent flow regimes. Especially in the turbulent flow regime, such profiles are not as well understood for a variety of different dimensions and fluid velocities as are the Nusselt number correlations used to determine the

convection heat transfer coefficient h. Moreover, the problem automatically becomes three-dimensional when the fluid flow is included in this fashion. As discussed below, only a two-dimensional treatment may be needed for most problems. Hence, it is simpler to treat the heat sink fins using finite difference techniques but model the fluid as before with boundary conditions determined by h. The finite difference calculation or other numerical technique will yield R_{th} as given in Eq. (22) rather than separate values for the components discussed earlier. The R_f is found independently as before from Eq. (18) and added to R_{th} to obtain $R_{heatsink}$.

Numerical techniques provide an alternative to the approximations used in Phillips' approach, i.e., the constriction approximation for heat entering the fin and the approximations involved in the standard fin equations. Three-dimensional flow in the fins would allow treatment of lateral and longitudinal heat diffusion. Here, lateral refers to the direction along the surface of the heat sink perpendicular to the direction of water flow, and longitudinal refers to the direction parallel to the water flow (the streamwise direction). The use of three dimensions instead of two greatly increases the number of calculations and hence both computer programming and running time. If linear superposition can be used, it is simpler to treat a two-dimensional model at any cross section of the heat sink to obtain R_{th} and then solve a differential equation for heat flow for variations along the length or width of the heat sink. The nonlinearities, which are thus neglected, include the variation with temperature of the thermal conductivities of the heat sink material and the water as well as other fluid parameters such as density and kinematic viscosity.

In a later section, the results of finite difference calculations in two dimensions are used to obtain parameters for a solution to a differential equation along the length of the channels when water is made to flow in alternating directions in adjacent channels.

Although transient heat flow in microchannel heat sinks is not treated here, it should be noted that, with the addition of thermal capacity to the finite difference equations, it is straightforward to model the transient problem. Some examples of transient solutions are included in Donnelly (1990).

IV. LONGITUDINAL DIFFUSION OF HEAT

As has been mentioned several times, at the edges of the heated regions of the heat sink the diffusion of heat laterally and longitudinally through the

heat sink and its fin may be important. The flow of heat results from the strong thermal gradients at the edges of the heat sink. Heat flow in the lateral direction can be treated in a manner similar to heat flow in the longitudinal direction. However, the lateral direction may not be as important for two reasons. First, the heat sink is thin in the channel regions, which reduces lateral heat conduction compared to longitudinal, i.e., heat must flow laterally through the portion of the heat sink that is only t in thickness. In the longitudinal direction, however, the average thermal path has a thickness $H = t + b/2$ when $W_w = W_c$. A second reason that the lateral diffusion may be less important is that it is not difficult to design the heat sink and its manifold so that there is very little unheated region at the lateral edges into which heat can flow. In the longitudinal direction, however, the requirements for the fluid manifold, water connectors, and electrical connectors may make termination of the structure in a small distance from the heated array difficult in practice. For this reason, we treat here a model for longitudinal heat flow to demonstrate the effects that occur.

The model used is based on an approach suggested by Phillips' (1987) handling of this problem. Since the real boundary conditions at the edge of the heated portion of a heat sink can involve heat flow through the manifold or other parts of the packaging, as well as conduction and convection cooling of the manifold and package parts by supporting structures and the air, the problem cannot be addressed in a universal way. Instead, Phillips treated the heat sink as very long (infinite) compared to the heated length in the longitudinal direction. The only flow of heat outside the heated length is conduction through the heat sink, including the fins, and the convection of the water flowing through the channels. Otherwise the system is considered adiabatic. With this idealization the problem can be solved for a linear system with constant h along the channels.

Conservation of energy implies the following coupled differential equations for the temperature at the surface of the heat sink $T(z)$ and the temperature of the water $T_f(z)$ (if the hydrodynamic power is neglected):

$$-\kappa_w H \frac{d^2T}{d^2z} + (T - T_f)/R_{th} = q \tag{24a}$$

$$\dot{m} c_p \frac{dT_f}{dz} = (T - T_f)(W_w + W_c)/R_{th}, \tag{24b}$$

where H is the average thickness of the heat sink and its fin in the longitudinal direction and the other symbols have already been defined. Note that R_{th} is defined by (22) and must be treated here as a constant,

i.e., independent of z, which is approximately true for fully developed laminar flow and for turbulent flow conditions. For developing flow it is necessary to use an average value for R_{th}. In (24a) the first term on the left is the longitudinal flow of heat and the second is the heat conducted to the water, while Eq. (24b) is the same equation as Eq. (17). It is straightforward to show that (24b) can be used to express T in terms of T_f and its derivative. Then, Eq. (24a) can be integrated once to obtain a second-order differential equation for T_f. This equation can be solved by standard techniques, which then permit the use of (24b) to obtain a result for $T(z)$. An approximate expression for $T(z)$ within the heated length is

$$T(z) = T_{inlet} + q\{[R_f(L)](z/L + \tfrac{1}{2}) + R_{th}[1 - e^{-(\gamma z + \beta L/2)} \cosh(\beta z + \gamma L/2)]\}. \tag{25}$$

Here, the origin of the z-axis is taken in the middle of the heated length ($-L/2 \le z \le L/2$), in contrast to the assumption used in Eqs. (18)-(23) ($0 \le z \le L$). The boundary conditions that have been applied are $T_f(-\infty) = T_{inlet}$ and $T_f(+\infty) = T_{inlet} + qR_f(L)$. The parameters γ and β are given by

$$\gamma = R_f(L)/(2LR_{th}) \tag{26a}$$

$$\beta = [\gamma^2 + 1/(\kappa_w H R_{th})]^{1/2}. \tag{26b}$$

The expression given by Eq. (25) is obtained by neglecting γ/β and $1/\beta L$ compared to unity, a good approximation for most cases. Outside the heated region, $T(z)$ decays exponentially as $(-\gamma + \beta)z$ for negative z and $(-\gamma - \beta)z$ for positive z and is continuous with (25) at $z = \pm L/2$. Since $\gamma \ll \beta$ in most cases, the thermal decay constant, or the thermal diffusion length, is approximately $1/\beta$. Plots of $[T(z) - T_{inlet}]$ with and without longitudinal diffusion are shown in Fig. 5 for the following parameter values: $R_f(L) = 0.03/L$°C cm^2/ W, $R_{th} = 0.08$°C cm^2/W, $\kappa_w = 1.5$ W/cm °C, $H = 350$ μm, and $L = 1.0$, 0.5, and 0.1 cm. This figure makes clear that measurements made for very short heated lengths must be properly interpreted if extrapolations to large lengths are to be made. For very short lengths the contribution of R_f can be neglected, and as seen in Fig. 5, the maximum value of resistance occurs near $z = 0$. When Eq. (25) is evaluated at $z = 0$, it can be seen that R_{th} with diffusion is given by

$$R_{th,d} \approx [1 - \exp(-\beta L/2)]R_{th}. \tag{27}$$

However, Eq. (25) was found with the assumption that $\beta L \gg 1$, and for small enough L this assumption is no longer valid. In that case, though, (25) underestimates the effect of diffusion and even smaller values of thermal resistance would be obtained than predicted by Eq. (27). In addition real

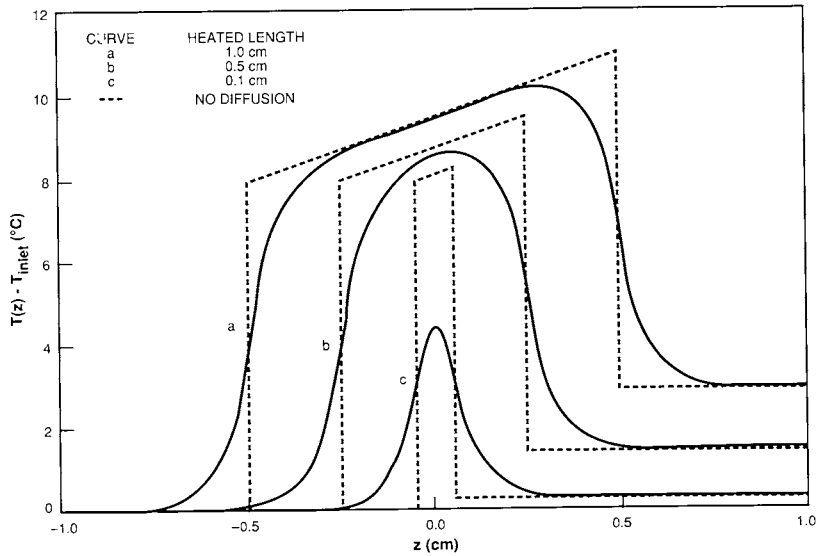

Fig. 5. Effects of longitudinal heat diffusion on the thermal distribution for various heated lengths.

boundary conditions rather than idealized ones at the edges of the heat sink may remove even more heat. For example, if the manifold is made of copper or another good thermal conductor, this would enhance cooling at the edges.

V. THEORETICAL PREDICTIONS OF PERFORMANCE

For proper heat sink design the overall resistance should be dominated by R_{cv}, i.e., the extraction of the heat should be limited by the convection cooling rate of the fins. In order to optimize heat sink performance, it is helpful to first consider that the values of the channel aspect ratio α and channel width W_c are fixed and find an optimum for W_w in terms of those parameters. R_{cv} can be written as

$$R_{cv} = (1/h)(1 + W_w/W_c)/(1 + 2\alpha\eta_F)$$
$$= (1/h)(1 + W_w/W_c)/\{1 + (2\kappa_w W_w/hW_c^2)^{0.5} \tanh [\alpha(2hW_c/\kappa_w)^{0.5}]\}. \quad (28)$$

With the value of α and W_c fixed, setting the derivative of Eq. (28) with respect to W_w equal to zero, we find the minimum value of R_{cv} occurs when

$$W_w/W_c = 1 - 2/a(1+1/a^2)^{0.5} + 2/a^2, \tag{29}$$

where $a = (2\kappa_w/hW_c)^{0.5} \tanh[\alpha(2hW_c/\kappa_w)^{0.5}]$. Since $a \gg 1$ for most practical ranges of parameters, the minimum resistance is when $W_w \approx W_c$. If R_{cv} is now written with $W_c = W_w$, we have

$$R_{cv} = (1/h)2/\{1 + (2\kappa_w/hW_c)^{0.5} \tanh[\alpha(2hW_c/\kappa_w)^{0.5}]\}. \tag{30}$$

If we now ask for an optimum value of the channel aspect ratio α, we see that α appears only in the term $\tanh[\alpha(2hW_c/\kappa_w)^{0.5}]$, which monotonically increases with α so that there is no optimum. Nevertheless, there is a point where increasing α yields very little further improvement in R_{cv}. When the argument of the hyperbolic tangent is 1.0, the value of the hyperbolic tangent is over 0.76 and becomes greater than 0.9 for an argument greater than 1.5. Hence, when

$$\alpha \approx (\kappa_w/2hW_c)^{0.5} = (\kappa_w/\kappa_f \mathrm{Nu})^{0.5}, \tag{31}$$

there is little advantage in a further increase in α. The extra fluid flow only costs mechanical energy to pump it. For most ranges of other parameters, a typical value for α determined from Eq. (31) is in the range of 3 to 8. Phillips' (1987) detailed calculations show, for a wide variety of the parameters W_w, W_c, and α that low values of thermal resistance occur. Hence, there are no clearly optimum parameters. Samalam (1989) addressed the issue of optimal dimensions, but only for the case of fully developed laminar flow. His theoretical analysis is interesting and provides some new analytic expressions for the case considered but is of limited applicability since it does not apply to developing laminar flow or turbulent flow.

In order to have a complete theoretical model it is necessary to model the pressure drop versus fluid flow in the channels as well as in the manifold where bends and changes in flow cross-sectional profiles occur. The reader is referred to Phillips (1987, 1988) for these details, which again depend upon the regime of fluid flow. The minimum mechanical power required (for 100% pump efficiency) is determined by the product of the pressure across the heat sink and the volumetric flow rate given by VA times the number of channels, i.e., volume of fluid pumped per second. A typical heat sink may operate at 10–100 psi (68.9–689 kPa) with flow rates of 5–30 cm^3/s requiring 0.5–20 W of mechanical power to cool a 1×1 cm^2 area.

Figure 6 shows calculated thermal resistance versus channel width for Si microchannel heat sinks with an aspect ratio $\alpha = 4$. The heat sink is assumed

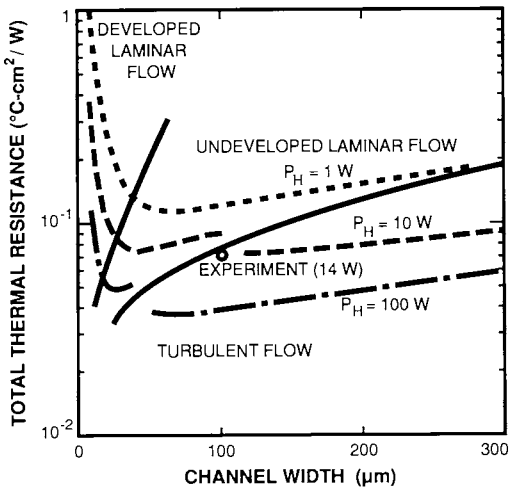

Fig. 6. Calculated thermal resistance versus channel width for the conditions: 300 K water, fin width equal to channel width, channel height equal to four times channel width, 1 cm-long channels, and 1 cm-wide heat sinks. The dashed curves represent the thermal resistance for constant hydraulic power P_H, and the solid lines delineate the regions of the various flow regimes: developed laminar flow, undeveloped laminar flow, and turbulent flow. (Based on unpublished calculations of R. J. Phillips.)

to be 1 cm wide by 1 cm long with water coolant entering at room temperature. These calculations were made by Phillips (1987, 1988) for comparison with an experiment that will be described later. In the present context, we point out the three regimes of fluid flow, shown by dashed curves with solid lines separating the different regimes. Three different sets of dashed curves were calculated for three assumed mechanical pump powers indicated by the labels $P_H = 1$, 10, and 100 W. There are breaks in the curves at the transition to turbulent flow because the calculation arbitrarily assumes an abrupt transition at $\mathrm{Re} = 2300$. In reality, that transition would be expected to be smoother.

A better understanding of the trends shown in Fig. 6 can be obtained by considering the decomposition of the thermal resistance for the $P_H = 10$ W case shown in Fig. 7. Here, the thermal resistance components arising from the heating of the fluid R_f and the convective component R_{cv} are plotted versus channel width for the same heat sink as in Fig. 6 with $\alpha = 4.0$. The total resistance is also shown, which includes the small additional terms R_κ ($t = 175$ μm) and R_{cs}. As expected, for very narrow channels the convective

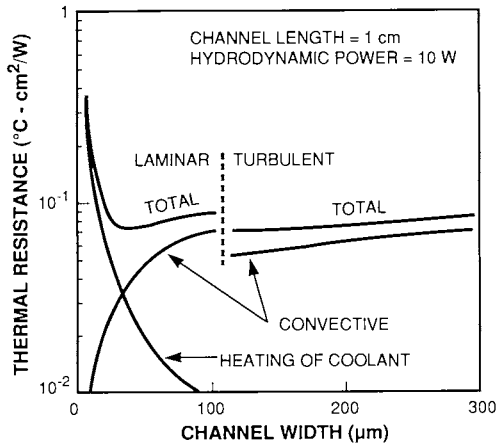

Fig. 7. Components of the thermal resistance for 1 cm-long channels at constant hydraulic power of 10 W/cm^2. (Based on unpublished calculations of R. J. Phillips.)

term becomes very small since the boundary layer is also very small. On the other hand, for narrow channels the heating of the fluid becomes dominant. The best channel aspect ratio is no longer determined by R_{cv} but rather by R_f as given by Eq. (18), where we see that either a shorter channel length or a larger aspect ratio or both could be used to reduce R_f so that R_{cv} dominates the resistance. Either solution leads to extra mechanical power. Breaking a long channel into many short channels requires complex manifolding and increases the overall hydrodynamic power needed. For high-aspect-ratio channels, extra fluid must be pumped. In addition, very high aspect ratio channels are difficult to make in practice and they must have good mixing from the top to the bottom of the fluid in order to absorb heat, since the fin efficiency becomes low for α much greater than the value given by Eq. (20) and little heat reaches the bottom of the fin. Good vertical mixing is not likely to occur for laminar flow.

VI. EXPERIMENTAL MEASUREMENTS

There have been a number of experimental demonstrations of microchannel heat sinks since Tuckerman and Pease (1981a,b) first proposed and demonstrated their usefulness (Goldberg, 1984; Mahalingam, 1985; Sasaki and Kishimoto, 1986; Kishimoto and Sasaki, 1987; Hwang *et al.*, 1987; and

Nayak *et al.*, 1987). The lowest values of thermal resistance reported prior to 1988 were 0.072, 0.08, and 0.083°C cm^2/W for Phillips (1987, 1988), Kishimoto and Sasaki (1987), and Tuckerman (1984), respectively. Kishimoto and Sasaki's and Tuckerman's best results were for interrupted fins. In these heat sinks the fins are not continuous along the channel length but rather exist for a short distance and then are absent for a short distance. In this way the buildup of the thermal boundary layer can be interrupted before it reaches too large a value. After the interruption the buildup must begin again where the fins are reintroduced. Phillips (1987) showed that there should be little if any thermal advantages for interrupted fins, but they may be useful for a practical reason. When a channel becomes clogged at some point in its length, the interruptions allow for a detour path (or bypass), which is useful if clogging of channels is a problem.

Tuckerman (1984) used very narrow high-aspect-ratio channels (W_c = 55 μm, W_w = 35 μm, b = 400 μm) with mechanical pump power of 1.73 W/cm^2. Kishimoto and Sasaki (1987) do not give the pump pressure used but they give channel dimensions (W_c = 150 μm, W_w = 150 μm, b = 400 μm). Phillips (1987, 1988) used relatively wide low-aspect-ratio channels (W_c = 200 μm, W_w = 155 μm, b = 165 μm) with mechanical pump power of 3.02 W/cm^2. Most of the microchannel heat sinks have been made in Si. Phillips' work differed in this respect since he used InP, which has less than one-half the thermal conductivity of Si (κ_{InP} = 0.6°C cm/W). Phillips as well as Kishimoto and Sasaki used heated lengths of only 0.25 cm, while Tuckerman used a heated length of 1 cm. Hence, Phillips' and Kishimoto and Sasaki's thermal resistance would be larger than Tuckerman's for the same heated length.

The use of microchannels as heat sinks for diode laser arrays was first described by Walpole (1988). A more detailed description of the work is provided in a report by Missaggia *et al.* (1989). The heat sink and laser array configuration reported was similar to that shown in Fig. 2. The two-dimensional surface emitting array has monolithically integrated beam deflectors (Liau and Walpole, 1987) fabricated in a GaInAsP/InP double-heterostructure wafer. The dimensions and construction of the Si heat sink can be seen in Fig. 8. Forty channels (400 μm deep, 100 μm wide, and on 200 μm centers) were cut in a 575 μm-thick Si wafer with a dicing saw. The channels covered an area 8 mm wide by 10 mm long. A second Si wafer was soldered to the first wafer to cover the channels and form the heat sink. The heat sink was then mounted into an aluminum manifold, and water was forced through the microchannels at pressures up to 517 kPa (75 psi). A flow rate of 20 cm^3/s through the microchannels with a pressure drop of

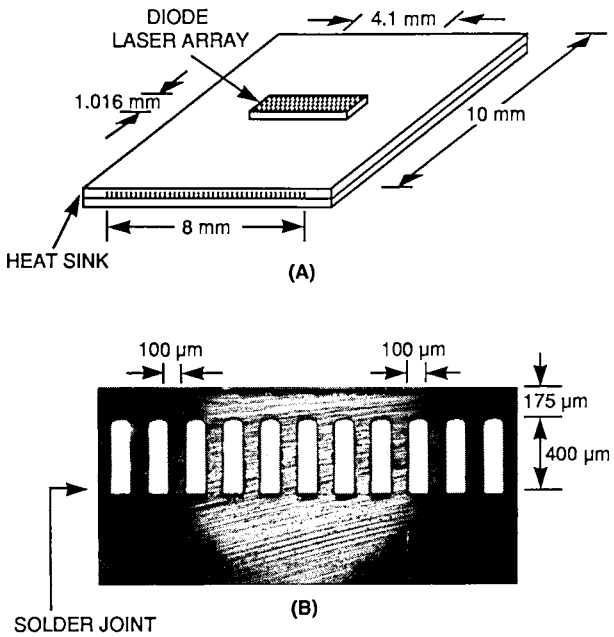

Fig. 8. Dimensions and configuration of microchannel heat sink used for the two-dimensional diode laser array experiment.

482 kPa (70 psi) across the microchannels were the standard experimental conditions. The average velocity of the coolant through each channel was 1.25×10^3 cm/s, corresponding to an average Reynolds number of approximately 2000, a value near the transition between laminar and turbulent flow regimes. The range of Reynolds numbers was 1650 to 2350 because of variations in coolant kinematic viscosity with temperature.

The surface emitting laser array used to characterize the heat sink consisted of 41 rows of lasers with four lasers in each row, with a row spacing of 100 μm and row length of approximately 1.02 mm. The area of the array (~ 0.04 cm^2) was considerably less than that of the heat sink (0.8 cm^2). The heat delivered to the array was determined by measuring the current-voltage characteristic of the array, calculating the electrical input power, and subtracting the optical output power. The laser array was used both to apply a heat load (up to 500 W/cm^2 heat loads were applied in the 0.1×0.4 cm^2 heated area) and to sense the operating temperature from the temperature dependence of the threshold current. In this manner the total thermal resistance R_{total} from the laser junctions to the inlet water was determined to be 0.079°C cm^2/W.

Further analysis showed that the thermal resistance of the heat sink R_{heatsink} accounted for 0.04°C cm^2/W of the total resistance and the rest, 0.039°C cm^2/W, was the thermal resistance of the laser array itself, R_{array}. The calculated value of R_{heatsink} was 0.035°C cm^2/W for the geometry shown in Fig. 8, in which the heated length is only approximately 1 mm. The thermal diffusion length along the direction of flow was calculated to be 0.60 mm, and the projected value of R_{heatsink} for a 1×1 cm^2 heated area was 0.07°C cm^2/W, which includes the maximum value of R_f calculated near the outlet. The calculated Reynolds number for the 1 cm heated length is just slightly larger than the 2300 required to be within the turbulent flow regime. Mechanical power dissipation was about 12 W/cm^2. The data point in Fig. 6 represents this extrapolated value of 0.07°C cm^2/W for the thermal resistance of a full 1 cm^2 area and for 12 W/cm^2 mechanical power. A very similar heat sink has been used for experiments with hybrid arrays of diode lasers as described in Chapter 5 of this volume (Williamson *et al.*). In these experiments the heated length was 1 cm, and the thermal resistance data obtained, $R_{\text{heatsink}} = 0.074$°C cm^2/W, is in close agreement with the numbers extrapolated here (Donnelly, 1990).

A low value for the thermal resistance of a microchannel heat sink was also reported by Mundinger *et al.* (1988), who demonstrated a single edge-emitting linear array (a bar of lasers) bonded between a diamond heat sink bar and electrode bar. This assembly was then attached to a microchannel heat sink in such a way that the axes of the lasers were perpendicular to the surface of the heat sink. Heat flowed into the diamond heat sink and from there into the microchannel heat sink. This technique allows, in principle, a large stack of laser bars separated by diamond heat sinks and electrodes to be attached simultaneously to a microchannel heat sink. The channel widths were 75 μm, and an aspect ratio of five and a value of $t = 175$ μm were used. A pump pressure of 20 psi was used for a flow rate of 10 cm^3/s per square centimeter, which is equivalent to 1.38 W/cm^2 of mechanical power dissipation. The heated length in this case was the width of the diamond heat sink, 300 μm.

The value reported by Mundinger *et al.* (1988) for the thermal resistance is 0.04°C cm^2/W. For the microchannel heat sink parameters listed above, the thermal diffusion length, $1/\beta$ in Eq. (27), is approximately 1 mm. Hence, because of diffusion as given by (27), the measured value of thermal resistance is approximately a factor of 0.2 lower than that which would result for the same heat sink with a long heated length. For a 1 cm length, a thermal resistance of at least 0.2°C cm^2/W would be expected with additional temperature rise due to heating of the fluid along the length.

A later paper by some of the same authors (Beach *et al.*, 1990) reports microchannel heat sink performance for 295 μm heated lengths in which a very small channel width was used, $W_c = W_w = 25$ μm. The other cross-sectional dimensions were $b = 200$ μm and $t = 181$ μm. The thermal resistance reported, 0.014°C cm^2/W, is slightly larger than 0.011°C cm^2/W, the value predicted by Eq. (27) using $R_{th} = 0.036$°C cm^2/W as calculated by Beach *et al.* (1990) without diffusion, and $\beta = 25.7$ cm^{-1} as calculated from Eq. (26b) with $H = 281$ μm and neglecting γ. This heat sink demonstrates the very small values that can be obtained for thin channels with very small heated length. It should be clear, however, that such low values of thermal resistance cannot easily be maintained for longer heated lengths because of the heating of the coolant which dominates the thermal resistance as illustrated earlier in Fig. 7. Although, in principle, it is possible to provide a heat sink for a large area using many short channels placed end to end, a practical mechanism for distributing the coolant without large manifold losses has not been demonstrated. One of the solutions that has been suggested is the use of manifolds, which are equivalent to another set of relatively long, wide microchannels, to feed the coolant to the relatively short, narrow microchannels (Harpole and Eninger, 1991). It is unclear how large the overall manifold losses would be in such a scheme.

Beach *et al.* (1992) also discuss an approach in which one-dimensional arrays of edge-emitting lasers are mounted on short, narrow microchannel modules. These modules can then be stacked together to provide a large light emitting area where the light emerges from the stacked ends of the modules. This approach, of course, cannot be used for two-dimensional arrays of surface emitting elements, but it is interesting as a means of achieving cooling of a large area. The data presented, however, are for only one module and hence do not address the issue of the actual thermal performance of a stack. The performance of such a stack would be measured by the ratio of the temperature rise at the surface of the heat sink to the power removed per unit of emitting area. The individual modules may be considerably thicker than the laser bars themselves, which may limit the packing density of emitters and hence the optical output density and the thermal heat load density.

Mott and Macomber (1989) and Macomber and Mott (1990) have measured the thermal resistance for a microchannel heat sink with a two-dimensional surface emitting diode laser array. They obtained a thermal resistance of 0.04°C cm^2/W, which is much smaller than their theoretical prediction. Consistent with our previous explanation, the discrepancy was attributed to diffusion of heat.

VII. ALTERNATING DIRECTIONS OF WATER FLOW IN ADJACENT CHANNELS

In the discussion so far it has been assumed that water flows in the same direction in all the channels. This is the simplest configuration to achieve experimentally. However, there are advantages if the direction of water flow could alternate in adjacent channels. As will be shown, the maximum temperature rise is reduced and temperature uniformity can be improved (Missaggia and Walpole, 1990, 1991). Figure 9 shows a design for an alternating channel flow (ACF) heat sink. In Fig. 9(a) the heat sink is shown schematically with its fins. The heat sink is attached on the channeled side to a manifold plate, depicted in Fig. 9(b), which contains holes to direct the flow of water.

The dotted lines represent the location of the channels with respect to the holes in the plate. The positions of inlet and outlet plenums, which would be provided in a surrounding package, are also indicated. Inlet water flows into the circular holes B and C in the manifold plate. The coolant entering row B exits at row D, while coolant entering row C exits at row

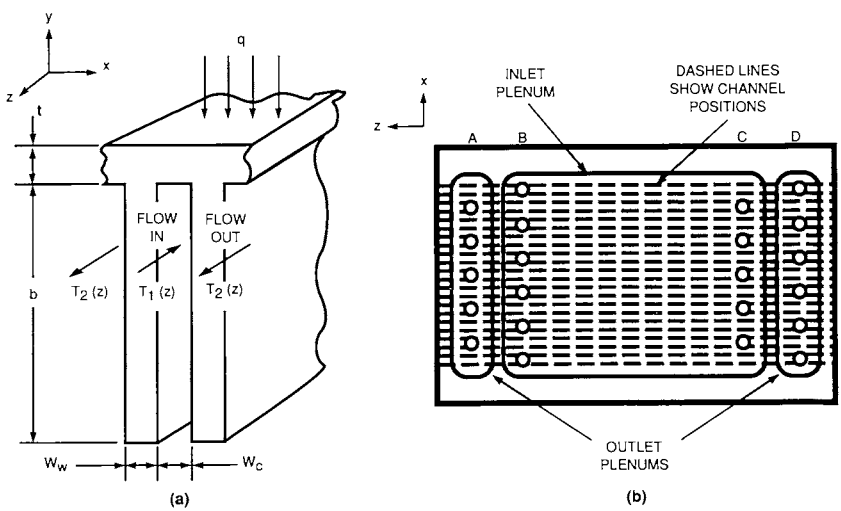

Fig. 9. Alternating channel flow design: (a) schematic of Si microchannel fins showing coolant flow directions, and (b) schematic of manifold plate showing alignment with microchannels and inlet and output plenums.

A. Hence, water flows from B to D and from C to A in alternating channels. Thus, the average temperature of the coolant is nearly constant, providing a more nearly uniform thermal resistance over the surface of the heat sink.

To determine the coolant temperatures in adjacent channels, T_1 and T_2 in Fig. 9(a), a set of coupled differential equations based on an energy balance of the coolant is required. These equations include the effect of lateral heat flux from one channel to another but neglect longitudinal heat flux. (Diffusion of heat could also be treated using the same approximations as in Eqs. (24-26), but the algebra is very tedious.) From these equations, T_1 and T_2 can be determined at any position in the streamwise direction. The equations can be written as

$$\frac{\dot{m}}{2} c_p \, dT_1/dz = Q_1(z) \tag{32}$$

and

$$\frac{\dot{m}}{2} c_p \, dT_2/dz = -Q_2(z), \tag{33}$$

where $\dot{m}$ is the mass flow rate of the water per channel, c_p is the specific heat of water, and Q_1 and Q_2 are the heat flows per unit length per channel into the channels whose temperatures are denoted by T_1 and T_2, respectively. The difference between (32) and (33) yields

$$\frac{\dot{m}}{2} c_p \, d(T_1 - T_2)/dz = Q, \tag{34}$$

where $Q = q(W_w + W_c)$ is the total heat flow per unit length per channel, assumed to be constant along the channel. If the assumptions are made that a linear regime of heat flow applies and that h is constant with z, it can be shown that the sum of Eq. (32) and Eq. (33) yields

$$\frac{\dot{m}}{2} c_p \, d(T_1 + T_2)/dz = (2/R_{fin})(T_2 - T_1). \tag{35}$$

Here, R_{fin} is the thermal resistance between the two channels, i.e., $R_{fin} = 2(T_1 - T_2)/(Q_2 - Q_1)$. The parameter R_{fin} can be calculated using the finite-difference techniques described earlier at the same time that the parameter R_{th} is calculated.

Equation (34) can be integrated immediately and substituted into (35), which after integration and some manipulation yields

$$T_1(z) = Q/(\dot{m}c_p)[z + 2zL/(R_{fin}\dot{m}c_p) - 2z^2/(R_{fin}\dot{m}c_p)] + T_{inlet} \tag{36}$$

and

$$T_2(z) = Q/(\dot{m}c_p)[L - z + 2zL/(R_{fin}\dot{m}c_p) - 2z^2/(R_{fin}\dot{m}c_p)] + T_{inlet}. \tag{37}$$

The average water temperature is

$$T_{ave} = (T_1 + T_2)/2 = Q/(\dot{m}c_p)[L/2 + 2zL/(R_{fin}\dot{m}c_p) - 2z^2/(R_{fin}\dot{m}c_p)] + T_{inlet}. \quad (38)$$

For longer channels the ACF design is particularly attractive, and it is interesting to consider a large-area heat sink with high-flow conditions. Therefore, a projected 10×10 cm^2 heat sink with 10 cm-long channels is theoretically modeled for a heat flux of 100 W/cm^2 and a flow rate corresponding to a Reynolds number of 2500 (just within the turbulent regime for rectangular channels). For 33 channels per centimeter with $\alpha = 4$, the flow rate was 44.4 cm^3/s, and the convection heat transfer coefficient calculated was 3.0 W/cm^2°C. For turbulent flow, the value of h remains constant along the channel except for a negligible entrance length. The calculated temperature rise above the inlet water temperature of both the heat sink surface and the water (average temperature) in the streamwise direction can be seen in Fig. 10. The thermal resistance of the heat sink $R_{heatsink}$ is 0.13°C cm^2/W. The maximum surface temperature differential, which occurs between the inlet/outlet and the center of the heat sink, is 0.85°C. Therefore, the maximum variation in thermal resistance is 0.0085°C cm^2/W, and the contribution to $R_{heatsink}$ due to the temperature rise of the water is R_f = 0.038°C cm^2/W. For a conventional heat sink of 10-cm length, the longitudinal variation in temperature would be 6°C (a variation in $R_{heatsink}$ of 0.06°C cm^2/W), and the maximum contribution due to the water temperature rise R_f would be 0.06°C cm^2/W.

For the conditions of the projected 10×10 cm^2 model, a finite-difference calculation was also used to generate a heat-flux plot for a cross section of

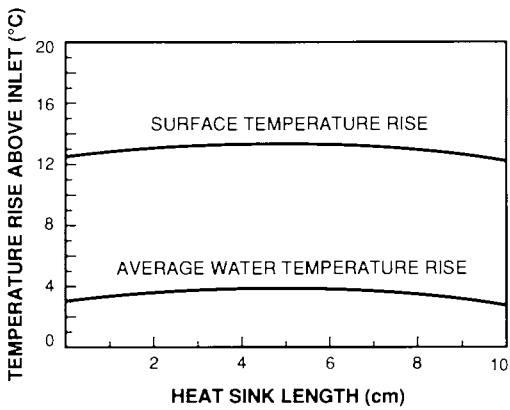

Fig. 10. Calculated temperature variations for a 10×10 cm^2 heat sink with streamwise profiles of surface temperature rise and average water temperature rise above the inlet temperature.

the fin, taken at the inlet/output position where the maximum difference in adjacent channel water temperatures occurs, as shown in Fig. 11. Isotherms are drawn for temperature increments of 0.25°C together with adiabatic lines. The lateral temperature variation at the surface of the fin is less than 0.05°C. Most of the heat entering the top of the fin exits to the inlet side as expected. A similar cross section taken at the center of the heat sink (5 cm position) would show a symmetric heat flux plot with no lateral surface temperature variation since the adjacent water temperatures T_1 and T_2 are the same.

The pressure drop that would be created by the friction losses in the 10 cm-long channels was calculated and found to be 452 kPa. The corres-

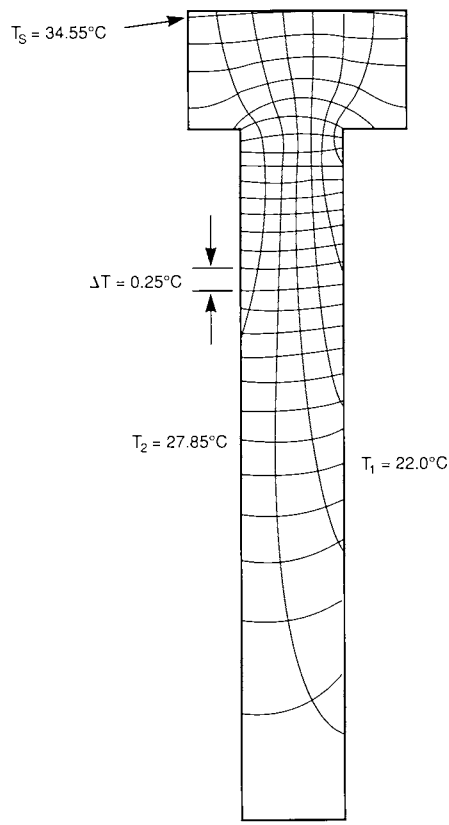

Fig. 11. Calculated heat flux plot with isotherms and adiabats, illustrating the transfer of heat from the hotter channel to the colder one. The inlet and outlet temperatures (T_1 and T_2) and the heat sink surface temperature (T_S) directly above the fin are indicated. Isotherms are shown in increments of 0.25°C.

ponding mechanical power generated by the flow of water through the microchannels would be 2.0 W/cm^2, only 2% of the assumed heat load.

The experimental characterization of an ACF heat sink was done on a heat sink with a 2.3 cm heated length (Missaggia and Walpole, 1990, 1991). The heat sink was fabricated in Si with 33 microchannels in a width of 1 cm and with an aspect ratio $\alpha = 4$. A device for supplying a uniform heat flux was obtained by fabricating a thin-metal-film resistor on the surface of the heat sink. First, a 5000 Å layer of SiO_2 was deposited to provide electrical insulation between the resistor and the Si. Then, a thin film of titanium (1000 Å) was deposited over the SiO_2. Finally, electrical contacts were formed at each end of the thin film. The heated area was 2.3 cm long (streamwise direction) and 1 cm in width.

A thermal image processsing system was used to determine the temperature rise and uniformity over the heat sink. Data were obtained with the heat sink operating at two different fluid flow conditions (case one and case two) with an applied heat load of 18.6 W/cm^2 (the maximum load that could be applied without dielectric breakdown of the SiO_2 insulator) and an initial coolant temperature of 22°C. The surface temperature rise and streamwise temperature uniformity under the thermal load were documented for each case. For the experiments described here, relatively small flow rates were intentionally used, since low flow enhances the small temperature variations which were otherwise difficult to measure accurately on relatively short channel lengths. In case one, the flow rate of the coolant was 15.8 cm^3/s with a pressure drop across the heat sink of 73 kPa. The flow rate and pressure drop for case two were 28 cm^3/s and 248 kPa, respectively.

The experimental results are compared with theoretical predictions in Fig. 12. For case one, the surface temperature rise was approximately 2.6°C above the coolant temperature, which results in an experimental thermal resistance R_{th} of 0.14°C cm^2/W. A significant experimental effect causing nonuniformity and not included in the theoretical modeling is the diffusion of heat at the perimeter of the heat sink into the adjacent brass package. This effect was negligible in the lateral directions because the package was only slightly wider than the heat sink. In the longitudinal directions, however, the effect was large near the ends. The use of additional heaters at the perimeter of the heat sink to reduce these end effects has been proposed (Phillips, 1987). Alternatively, thermal insulation to prevent heat loss at the perimeter could be used. For a sufficiently large heat sink, as discussed in the following paragraphs, the end effects may not be important.

Except for the end effects, the experimental streamwise surface temperature profile is nearly constant (±0.1°C). Nevertheless, a consistent trend is detectable in the data suggesting a small slope (approximately 13%/cm

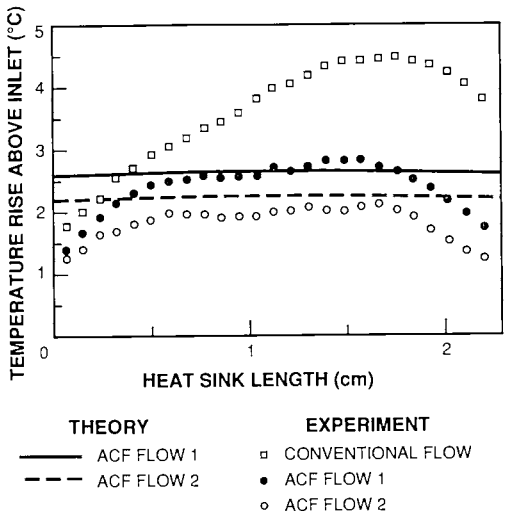

Fig. 12. Experimental and theoretical profiles shown by data points and solid curves, respectively. Conventional flow denotes coolant flow in one direction through half the channels, and ACF denotes alternating channel flow at two flow conditions.

in case one) in the profile at the center of the heat sink. This may be due to either a gradient in the heat load, i.e., resistor thickness, or to a variance in the flow rates in the two directions. For case two, the measured maximum surface temperature rise was 2.0°C, corresponding to $R_{\text{heatsink}} = 0.11°\text{C cm}^2/\text{W}$. The profile is similar to that of case one with the center of the profile essentially constant with only a small slope (<6%/cm), which suggests that the stronger gradient observed for the lower total flow rate (case one) is a result of a variance in the flow rates for the two directions. This slope can easily be eliminated by adjustment of the flow rates.

In order to demonstrate the effects of the ACF design, one-directional flow was also measured. The design of the manifold plate, which directs the flow of the water, did not allow for one-directional flow in all the channels simultaneously, but the flow in one of the directions could be shut down. Therefore, the heat sink was operated under the same flow conditions as for case one but with one-directional water flow in half the channels and stagnant water in alternating channels. As expected, this resulted in a streamwise surface temperature gradient. It should be noted that if it were not for the diffusion of heat at the ends of the heat sink, the temperature variation seen (~2.4°C) would be larger.

The convective heat transfer coefficient was dependent upon the flow regime present in the channels for each experimental case. The Reynolds numbers for the experimentally demonstrated flow conditions of case one

two were 843 and 1494, respectively. Therefore, the flow regime present in both cases was laminar flow. (For rectangular channels with an aspect ratio of six, the Reynolds number for turbulent flow would be approximately 2500 [Phillips, 1987].) Also, because of the dimensions of the channel, the flow is not fully developed over the channel length. For this type of flow (thermally developing laminar flow), the convective heat transfer coefficient h varies along the length. Therefore, an approximation was used, and an average h value was determined for each flow condition. The average h values used in the model for the flow conditions of case one and case 2 were 1.90 and 2.24 W/cm^2°C, respectively.

The theoretical surface temperature profiles can be seen in Fig. 12. The lower flow (case one) data and theory are in close agreement. The higher flow data and theory differ slightly in that the theoretical thermal resistance is higher than the experimental. This discrepancy may result from the use of a constant h, an approximation that is poorer for case two than for case one, where the thermal boundary layer is more developed.

This work was sponsored by the Department of the Air Force.

REFERENCES

BEACH, R., MUNDINGER, D., BENETT, W. J., SPERRY, V., COMASKEY, B. J. AND SOLARZ, R. (1990). "High-reliability silicon microchannel submount for high average power laser diode arrays," *Appl. Phys. Lett.* **56**, 2065.

BEACH, R., BENETT, W. J., FREITAS, B. L., MUNDINGER, D., COMASKEY, B. J., SOLARZ, R. and EMANUEL, M. A. (1992). "Modular microchannel cooled heatsinks for high average power laser diode arrays," *IEEE J. Quantum Electron.* **28**, 966.

DONNELLY, J. P. (1990). "Two-dimensional surface-emitting arrays of GaAs/AlGaAs diode lasers," *Lincoln Lab. J.* **3**, 361.

GOLDBERG, N. (1984). "Narrow channel forced air heat sink," *IEEE Trans. Compon. Hybrids Manuf. Technol.* **CHMT-7**, 154.

HARPOLE, G. M. AND ENINGER, J. E. (1991). "Micro-channel heat exchanger optimization," in *Proc. 7th Annual IEEE Semiconductor Thermal Measurement and Management Symposium.*

HWANG, L. T., TURLIK, I. and REISMAN, A. (1987). "A thermal module design for advanced packaging," *J. Electron. Mater.* **16**, 347.

JOYCE, W. B. and DIXON, R. W. (1975). "Thermal resistance of heterostructure lasers," *J. Appl. Phys.* **46**, 855.

KISHIMOTO, T. and SASAKI, S. (1987). "Cooling characteristics of diamond-shaped interrupted cooling fin for high-power LSI devices," *Electron. Lett.* **23**, 456.

KRAUS, A. D. and BAR-COHEN, A. (1983). *Thermal Analysis and Control of Electronic Equipment*, McGraw-Hill, New York.

LIAU, Z. L. and WALPOLE, J. N. (1987). "Large-monolithic two-dimensional arrays of GaInAsP/InP surface-emitting lasers," *Appl. Phys. Lett.* **50**, 528.

LIAU, Z. L., WALPOLE, J. N., TSANG, D. Z., and DIADIUK, V. (1988). "Characterization of mass-transported *p*-substrate GaInAsP/InP buried-heterostructure lasers with analytical solutions for electrical and thermal resistances," *IEEE J. Quantum Electron.* **QE-24**, 36.

MACOMBER, S. H. and MOTT, J. S. (1990). "Recent developments in surface emitting distributed feedback arrays," *Proc. SPIE* **1219**, 228.

MAHALINGAM, M. (1985). "Thermal management in semiconductor device packaging," *Proc. IEEE* **73**, 1396.

MISSAGGIA, L. J. AND WALPOLE, J. N. (1990). "Microchannel heat sink with alternate directions of water flow in adjacent channels," *Solid State Research Report*, Lincoln Laboratory, MIT, **4**, p. 1.

MISSAGGIA, L. J. AND WALPOLE, J. N. (1991). "A microchannel heat sink with alternating directions of water flow in adjacent channels," *Proc. SPIE* **1582**, 106.

MISSAGGIA, L. J., WALPOLE, J. N., LIAU, Z. L. AND PHILLIPS, R. J. (1989). "Microchannel heat sinks for two-dimensional high-power-density diode laser arrays," *IEEE J. Quantum Electron.* **25**, 1988.

MOTT, J. S. AND MACOMBER, S. H. (1989). "Two-dimensional surface emitting distributed feedback arrays," *IEEE Photon. Technol. Lett.* **1**, 202.

MUNDINGER, D., BEACH, R., BENNETT, W., SOLARZ, R., KRUPKE, W., STAVER, R. AND TUCKERMAN, D. (1988). "Demonstration of high-performance silicon microchannel heat exchangers for laser diode array cooling," *Appl. Phys. Lett.* **53**, 1030.

NAYAK, D., HWANG, L. T., TURLIK, I. AND REISMAN, A. (1987). "A high-performance thermal module for computer packaging," *J. Electron. Mater.* **16**, 357.

PHILLIPS, R. J. (1987). *Forced-Convection, Liquid-Cooled Microchannel Heat Sinks*, Master's Thesis, Massachusetts Institute of Technology, Cambridge, MA.

PHILLIPS, R. J. (1988). "Microchannel heat sinks," *Lincoln. Lab. J.* **1**, 31.

PHILLIPS, R. J., GLICKMAN, L. R. AND LARSON, R. (1987). "Forced-convection, liquid-cooled, microchannel heat sinks for high-power-density microelectronics," in *Proc. Int. Symp. on Cooling Technology for Electronic Equipment.*

SAMALAN, V. K. (1989). "Convection heat transfer in microchannels," *J. Electron. Mater.* **18**, 611

SASAKI, S. AND KISHIMOTO, T. (1986). "Optimal structure for microgrooved cooling fin for high-power LSI devices," *Electron. Lett.* **22**, 1332.

TUCKERMAN, D. B. (1984). *Heat-Transfer Microstructures for Integrated Circuits*, Ph.D. Thesis, Stanford University, Stanford, CA.

TUCKERMAN, D. B. and PEASE, R. F. W. (1981a). "High performance heat sinking for VLSI," *IEEE Electron Device Lett.* **EDL-2**, 126.

TUCKERMAN, D. B. AND PEASE, R. F. W. (1981b). "Ultrahigh thermal conductance microstructure for cooling integrated circuits," *Proc. 32nd Electronics Components Conf.*

WALPOLE, J. N. (1988). "Two-dimensional laser array technology comparison: stack-and-rack versus monolithic," Panel Discussion. *Proc. SPIE* **893**, 131.

Index

Quantum Electronics—Principles and Applications

Edited by Paul F. Liao, *Bell Communications Research, Inc., Red Bank, New Jersey*
Paul L. Kelley, *Electro-Optics Technology Center, Tufts University, Medford, Massachusetts*

N. S. Kapany and J. J. Burke, *Optical Waveguides*
Dietrich Marcuse, *Theory of Dielectric Optical Waveguides*
Benjamin Chu, *Laser Light Scattering*
Bruno Crosignani, Paolo DiPorto and Mario Bertolotti, *Statistical Properties of Scattered Light*
John D. Anderson, Jr., *Gasdynamic Lasers: An Introduction*
W.W. Duly, *CO_2 Lasers: Effects and Applications*
Henry Kressel and J. K. Butler, *Semiconductor Lasers and Heterojunction LEDs*
H. C. Casey and M. B. Panish, *Heterostructure Lasers: Part A. Fundamental Principles; Part B. Materials and Operating Characteristics*
Robert K. Erf, editor, *Speckle Metrology*
Marc D. Levenson, *Introduction to Nonlinear Laser Spectroscopy*
David S. Kliger, editor, *Ultrasensitive Laser Spectroscopy*
Robert A. Fisher, editor, *Optical Phase Conjugation*
John F. Reintjes, *Nonlinear Optical Parametric Processes in Liquids and Gases*
S. H. Lin, Y. Fujimura, H. J. Neusser and E. W. Schlag, *Multiphoton Spectroscopy of Molecules*
Hyatt M. Gibbs, *Optical Bistability: Controlling Light with Light*
D. S. Chemla and J. Zyss, editors, *Nonlinear Optical Properties of Organic Molecules and Crystals, Volume 1, Volume 2*
Marc D. Levenson and Saturo Kano, *Introduction to Nonlinear Laser Spectroscopy, Revised Edition*
Govind P. Agrawal, *Nonlinear Fiber Optics*
F. J. Duarte and Lloyd W. Hillman, editors, *Dye Laser Principles: With Applications*
Dietrich Marcuse, *Theory of Dielectric Optical Waveguides, 2nd Edition*
Govind P. Agrawal and Robert W. Boyd, editors, *Contemporary Nonlinear Optics*
Peter S. Zory, Jr., editor, *Quantum Well Lasers*
Gary A. Evans and Jacob M. Hammer, editors, *Surface Emitting Semiconductor Lasers and Arrays*
John E. Midwinter, editor, *Photonics in Switching, Volume I, Background and Components*
John E. Midwinter, editor, *Photonics in Switching, Volume II, Systems*

Yoh-Han Pao, Case Western Reserve University, Cleveland, Ohio, Founding Editor 1972-1979

ISBN 0-12-244070-6

ISBN 0-12-244070-6